

A framework for the study of physical conditions in astrophysical plasmas through radio and optical polarization

Application to extragalactic jets

INAUGURAL-DISSERTATION

zur
Erlangung des Doktorgrades
der Mathematisch-Naturwissenschaftlichen Fakultät
der Universität zu Köln



vorgelegt von

Ioannis Myserlis
aus Thessaloniki, Griechenland

Köln 2015

Berichtersteller:

Prof. Dr. Andreas Eckart
Prof. Dr. J. Anton Zensus

Tag der letzten mündlichen Prüfung: 30. Oktober 2015

ABSTRACT

This work presents a framework for the study of the physical conditions in astrophysical plasma elements through linear and circular, radio and optical polarization monitoring. The term “framework” is meant to describe the self-consistent character of the work which contains all necessary elements to:

1. Design and conduct high-cadence, multi-frequency polarimetric observations.
2. Reconstruct the Stokes 4-vector of the observed radiation with high accuracy.
3. Interpret polarimetric observations based on the theoretical predictions of several emission, absorption and propagation effects which can generate, modify, or eliminate the Stokes parameters of the radiation.
4. Reproduce the observed characteristics in the complete Stokes parameters set using a radiative transfer code we developed on the basis of the model of Hughes et al. (1989a).

The development of the machinery of this framework was based on data obtained within the *F-GAMMA* monitoring program. Our polarimetric methodology eliminates a number of sources of uncertainty and is directly applicable to radio telescopes equipped with circularly polarized feeds.

Using this methodology we recovered the polarization characteristics for a sample of 87 AGNs at 4 bands: 2.64, 4.85, 8.35 and 10.45 GHz. Our analysis focuses on observations conducted with the 100-m Effelsberg telescope between July 2010 and January 2015 with a mean cadence of 1.6 months.

We used these datasets to characterize the observed sample in terms of linear and circular radio polarization. The computed polarization parameters were subsequently used as the basis for the computation of the magnetic field strength of those jets and the rotation measure which is attributed to the low energy magnetized plasma located in regions where the radiation is emitted or propagated through. The theoretical predictions for the emission, absorption and propagation of radiation were used to perform a thorough correlation analysis between several observed characteristics in order to investigate the physical conditions of the emitting plasma elements.

Multi-frequency, high cadence observations are essential in the study of the pronounced variability these sources usually show. This variability was found to follow repeating patterns in the F_ν - ν domain for many sources, a prototype of which is the blazar 3C 454.3. In many cases, these patterns agree with the predictions of the “shock-in-jet” model (Marscher and Gear, 1985) which attributes them to the evolution of physical conditions at shocked regions as they propagate downstream the jet. Our results showed coordinated changes of the polarization characteristics which mark the transitions between the optically thick and thin regimes of synchrotron emission. Assuming that these transitions are due to the optical depth evolution of the propagated shocks, we used our radiative transfer code to emulate them and reproduce the variability observed in all Stokes parameters in the case of the prototype source 3C 454.3. We followed the strict requirement to reproduce this variability just by evolving the physical characteristics of the emitting region according to the predictions of the “shock-in-jet” model. This approach resulted in a number of estimates for the physical conditions of this jet, like its particle number density, magnetic field coherence length and Doppler factor.

Finally, we characterized our sample in terms of optical linear polarization using the data obtained with the RoboPol monitoring program between May 2013 and July 2015. The comparison of those partially simultaneous, radio and optical polarization datasets did not show any correlation between the two bands, suggesting that the physical conditions at the two emission sites are different. We detected 60 EVPA rotation events in the examined radio bands, that occurred in 22 sources of our sample, 6 of which have also shown such events in the optical

wavelengths. Assuming that these rotations are caused by the helical motion of emission elements propagating downstream the jet, we used the rotation rates and the linear polarization degree measurements in both the radio and optical bands to compare the (tangential) velocities and hence the kinetic energies of those emission elements while they are propagating through the radio and optical emission sites in the jet.

This thesis is structured as follows; In Chapter 1 we give a brief overview of the AGN structure and the theoretical predictions for the polarization properties necessary throughout the rest of the thesis. In Chapters 2 and 3 we describe the machinery of our framework used to extract and calibrate all the Stokes parameters for radio telescopes equipped with circularly polarized feeds. In Chapter 4 we characterize the linear and circular radio polarization properties of our sample of AGNs. Those are later used to calculate other physical parameters at the emission or propagation regions and to perform a correlation analysis investigating the underlying physical mechanisms. In Chapter 5 we describe our radiative transfer code and its application on the radio polarimetric data of 3C 454.3 to reproduce the observed variability and extract a number of its physical parameters. In Chapter 6 we characterize the optical polarization properties of our sample, correlate them with the ones found in the radio bands and use the combined information to compare the physical conditions in the two emission sites in the jet. Finally, in Chapter 7, we summarize the results and conclusions reached throughout this thesis.

KURZZUSAMMENFASSUNG

Diese Arbeit präsentiert ein Rahmenwerk zur Studie physikalischer Zustände in astrophysikalischen Plasmaelementen durch die langfristige Beobachtung linearer und zirkularer Polarisation im Radio- und optischen Wellenlängenbereich. Der Begriff “Rahmenwerk” soll hierbei den selbstkonsistenten Charakter dieser Arbeit verdeutlichen, welche alle nötigen Elemente enthält um:

1. Polarisationsmessungen in mehreren Frequenzbändern mit hoher Beobachtungsrate zu konzipieren und durchzuführen;
2. Den Stokes-4-Vektor der beobachteten Strahlung mit hoher Genauigkeit zu rekonstruieren;
3. Polarisationsdaten basierend auf den theoretischen Vorhersagen verschiedener Emissions-, Absorptions-, und Ausbreitungsmechanismen zu interpretieren, welche die Stokes-Parameter generieren, modifizieren oder auslöschen können;
4. Die beobachteten Charakteristika des vollständigen Stokes-Vektors mittels einer Strahlungstransfer-Codes zu reproduzieren, welcher auf der Basis des Models von Hughes et al. (1989a) im Rahmen dieser Arbeit entwickelt wurde.

Die Basis zur Entwicklung der Methodik dieses Rahmenwerks bilden Daten, die als Teil des *F-GAMMA* Beobachtungsprogramms gemessen wurden. Die hier beschriebene Methodik eliminiert eine Reihe von Fehlerquellen und lässt sich direkt auf beliebige Radioteleskope anwenden, welche mit zirkular polarisiertem Feed ausgerüstet sind.

Durch die Anwendung dieser Methode wurden die Polarisationscharakteristika von 87 aktiven Galaxienkernen in vier Frequenzbändern rekonstruiert: 2,64, 4,85, 8,35 und 10,45 GHz. Die entsprechenden Daten wurden mit dem Effelsberg-100m-Teleskop zwischen Juli 2010 und Januar 2015 mit einer mittleren Wiederholungsrate von 1,6 Monaten gemessen.

Basierend auf diesen Daten wurden die linearen und zirkularen Polarisationszustände der Objekte in der Stichprobe untersucht. Die erhaltenen Polarisationsparameter wurden daraufhin verwendet, um die magnetische Feldstärke dieser Jets zu errechnen sowie das Rotationsmaß, welches auf das niedrigenergetische, magnetisierte Plasma zurückzuführen ist, welches sich in den Regionen befindet, in denen die Strahlung erzeugt oder durch diese transmittiert wird. Theoretische Vorhersagen über die Emission, Absorption und Transmission wurden verwendet, um verschiedene Kombinationen von gemessenen Größen auf Korrelationen zu untersuchen, um Rückschlüsse auf das emittierende Plasmaelement zu ziehen.

Wiederholte Beobachtungen in mehreren Frequenzbändern in kurzen Zeitintervallen sind nötig, um die ausgeprägte Variabilität, die diese Objekte typischerweise zeigen, untersuchen zu können. Es ist bekannt, dass diese Variabilität einem wiederholenden Muster im F_ν - ν -Raum folgt. Blazar 3C 454.3 ist hierfür ein Prototyp. In vielen Fällen stimmt dieses Muster mit den Vorhersagen des “shock-in-jet”-Modells (Marscher and Gear, 1985) überein, welches dieses auf die Entwicklung des physikalischen Zustandes der schockkomprimierten Region zurückführt, während diese durch den Jet propagiert. Hier präsentierte Resultate zeigen schematische Änderungen des Polarisationszustandes, welche den Übergang von der optisch dicken zur optisch dünnen Synchrotronemission darstellen. Unter der Annahme, dass diese Übergänge durch die Änderung der optischen Tiefe des propagierenden Schocks beschrieben werden können, wurde für das Objekt 3C 454.3 ein Strahlungstransfer-Code angewendet, um die beobachtete Variation in allen vier Stokes-Parametern nachzubilden. Hierbei wurde der strikten Bedingung Folge geleistet, dass die beobachtete Variation lediglich aus der Entwicklung der physikalischen Charakteristika der Emissionsregion resultiert, gemäss den Vorhersagen des “shock-in-jet”-Modells. Aus diesem Ansatz resultiert die Schätzung einer Reihe von physikalischen Parametern, darunter die Partikelanzahldichte, die Kohärenzlänge des magnetischen Feldes und der Dopplerfaktor des Jets.

Des Weiteren wurde die lineare Polarisation im optischen Frequenzbereich der gesamten Objektstichprobe untersucht, basierend auf den Daten, die im Rahmen des RoboPol Beobachtungsprogramms zwischen May 2013 und Juli 2015 gemessen wurden. Der Vergleich der zum Teil zeitgleichen Daten im optischen und im Radiobereich zeigte keinerlei Korrelation zwischen den zwei Frequenzbändern. Dies deutet darauf, dass die physikalischen Bedingungen in den zwei Emissionsregionen verschieden sind. Insgesamt 60 EVPA-Rotationen wurden in den untersuchten Frequenzbändern beobachtet. Diese traten in 22 Objekten aus der gesamten Stichprobe auf, sechs davon zeigten ebenfalls Rotationen im optischen Wellenlängenbereich. Unter der Annahme, dass diese Rotationen aus der Bewegung von spiralförmig durch den Jet propagierenden Emissionselementen resultiert, wurden die Rotationsraten und der lineare Polarisationsgrad in beiden Frequenzbereichen verwendet, um die (tangentialen) Geschwindigkeiten und somit die kinetische Energie der Emissionselemente zu vergleichen, während diese durch das Radio- bzw. optische Emissionsgebiet propagieren.

Diese Arbeit gliedert sich wie folgt: Kapitel 1 gibt eine kurze Einleitung in die Struktur von aktiven Galaxienkernen und theoretische Vorhersagen über die Polarisationseigenschaften, die in der weiteren Arbeit benötigt werden. In den Kapiteln 2 und 3 wird die Methodologie zur Kalibrierung und Messung von Stokes-Parametern für mit zirkular polarisierten Feeds ausgestattete Radioteleskope beschrieben. In Kapitel 4 werden die linearen und zirkularen Polarisationseigenschaften der untersuchten Stichprobe von aktiven Galaxienkernen charakterisiert. Diese Ergebnisse werden dann verwendet, um zum einen weitere physikalische Parameter der Emissionsregion abzuleiten, zum anderen mittels Korrelationsanalyse die grundlegenden physikalischen Mechanismen zu untersuchen. In Kapitel 5 wird der Strahlungstransfer-Code beschrieben und auf die polarimetrischen Daten von 3C 454.3 angewandt, um die beobachtete Variabilität zu rekonstruieren und daraus verschiedene physikalische Parameter abzuleiten. Die optischen Polarisationseigenschaften der untersuchten Stichprobe von Objekten werden in Kapitel 6 untersucht und mit den entsprechenden Radiopolarisationsdaten korreliert, um die physikalischen Bedingungen der beiden Emissionsregionen im Jet, verantwortlich für die optische und die Radio-Emission, zu vergleichen. Zuletzt werden die Ergebnisse und Schlussfolgerungen dieser Arbeit in Kapitel 7 zusammengefasst.

ACKNOWLEDGEMENTS

This work would not have been completed without the essential contribution of many people who I would like to acknowledge here.

First and foremost I would like to express my sincere gratitude to my PhD adviser Dr. Emmanouil (Manolis) Angelakis for his continuous support, patience and motivation. Our frequent, thorough and multi-disciplinary discussions had a deep impact on this work, my scientific and personal development throughout the last three years. I could not have imagined having a better adviser and mentor for my PhD study.

I would like to express the deepest appreciation to my supervisors. First, to the director of the VLBI group at the Max Planck Institute for Radio Astronomy, Prof. Dr. J. Anton Zensus, for his support in a number of ways and his insightful comments and encouragement. I would also like to express my gratitude to Prof. Dr. Andreas Eckart at the I. Physikalisches Institut for reviewing this work.

Moreover, I appreciate the feedback offered by the other members of my thesis advisory committee: Dr. Alex Kraus for his suggestions and comments which were invaluable for the completion of this thesis, Prof. Vasiliki Pavlidou for her dedicated encouragement and guidance as well as Dr. Lars Fuhrmann for his constructive comments.

I want to thank all the members of the VLBI group which provided a productive environment to conduct research and our secretary Frau Beate Naunheim for her prompt support. My sincere thanks goes to Dr. Richard Porcas for our many fruitful and stimulating discussions.

I am also grateful to all the members of the RoboPol collaboration. Being part of such an international collaboration has been a very inspiring experience. Special thanks goes to Prof. A. N. Ramaprakash, Prof. Iossif Papadakis, Dr. Oliver G. King, Dr. Dmitry Blinov, Dr. Talvikki Hovatta and Dr. Pablo Reig for having numerous stimulating and constructive discussions.

A large part of this work is based on observations with the 100-m telescope of the MPIfR (Max-Planck-Institut für Radioastronomie) at Effelsberg. Thus, my thanks goes also to the personnel of the telescope who were always very helpful, keeping me company during the long nights of observations and supporting in any way possible. Advice and comments given by Dr. Peter Müller has been a great help in discovering the workings of the 100-m telescope.

I express my gratitude also to all friends and colleagues who made my PhD life easier and pleasant: Vassilis Karamanavis, Ioannis Antoniadis, Ioannis Nestoras, Sebastian Kiehlmann, Jeffrey Hodgson, Florent Mertens, Bindu Rani, Biaginna Boccardi, Behnam Javanmardi, Fateme Kamali, Miguel Requena Torres, Macarena García-Marín, Kostas Markakis, Anastasia Tsitali and Dhanya Nair.

I thank also the administration of the International Max Planck Research School for Astronomy and Astrophysics. Both the coordinators Dr. Emmanouil Angelakis and Priv.-Doz. Dr. Rainer Mauersberger as well as their assistant Dr. Simone Pott were always caring and made studying in Germany a creative learning experience.

I owe my deepest gratitude to my first mentor Prof. John H. Seiradakis at the Aristotle University of Thessaloniki for enlightening me at the first steps of research and Dr. Anastasios Molochidis for showing me the beauty of natural sciences.

Finally, I would like to thank my parents Valia and Grigorios as well as my siblings Evi, Pavlos and Ilias for the continuous support they have given me as well as my soul mate Hariklia for her caring love and patience throughout this effort.

Contents

Contents	viii
List of Figures	xi
List of Tables	xv
1 Synchrotron emission and radiative transfer	1
1.1 Active Galactic Nuclei: The big picture	1
1.1.1 The “central engine” and the obscuring torus	1
1.1.2 The narrow and broad line regions	2
1.1.3 The jet	3
1.2 Synchrotron emission	5
1.2.1 Emission from a single particle	5
1.2.2 Emission and absorption from an ensemble of particles	10
1.2.3 Self-absorption	11
1.2.4 Emission and absorption for an ensemble of particles with power law energy distribution	12
1.2.5 Emission and absorption from an ensemble of mildly relativistic particles	15
1.3 Polarized radiative transfer	17
1.4 Propagation effects	19
1.4.1 Synchrotron Self Absorption (SSA) and polarization characteristics	21
1.4.2 Faraday rotation	23
1.4.3 Faraday pulsation	23
1.4.4 Circular repolarization	25
1.5 From the source to the observer’s rest frame	25
2 High precision, full-Stokes radio polarimetry	29
2.1 The method	29
2.2 The R matrix	30
2.3 The M matrix	33
2.4 The measured Stokes vector	34
2.4.1 Stokes parametrization for circularly polarized feeds	36
2.4.2 Extracting the observables	36
2.4.3 Cross-channel calibration	38
2.4.4 Corrections	42
2.4.5 Stokes <i>Q</i> and <i>U</i> instrumental artifacts	50
3 Full-Stokes polarimetry calibration	59
3.1 Introduction	59

3.2	Full-Stokes calibration techniques	59
3.2.1	4x4 Müller matrix calibration	59
3.2.2	Full-Stokes sensitivity calibration	60
3.2.3	Our approach	60
3.3	Stokes V calibration	61
3.4	System stability	63
4	Radio linear and circular polarization of AGN jets	67
4.1	Introduction	67
4.2	The dataset	67
4.2.1	Quality Checks and data operations	68
4.2.2	Demographics of polarized sources	72
4.2.3	Linearly and circularly-only polarized sources	72
4.2.4	Linear polarization per observing frequency	73
4.2.5	Circular polarization per observing frequency	74
4.2.6	Polarized state duration	74
4.2.7	Total flux and linear polarization spectra	74
4.3	Derivative quantities	79
4.3.1	Magnetic field magnitude	79
4.3.2	Rotation measure	82
4.4	Correlation analysis	85
4.4.1	EVPA versus AGN jet position angle	87
4.4.2	Linear versus circular polarization degree	88
4.4.3	Linear and circular polarization versus RM	90
4.4.4	Polarization degree versus low and high frequency emission characteristics	90
4.4.5	Polarization characteristics and source type	94
4.4.6	Polarization degree and flux density state	97
5	Full-Stokes radiative transfer modelling of shocked jets	103
5.1	Introduction	103
5.2	Radio variability of AGN jets	103
5.2.1	The shock-in-jet model	106
5.2.2	The evolutionary path signature in the polarization characteristics	107
5.3	Full-Stokes radiative transfer code of shocked jets	107
5.3.1	A short overview of the code	108
5.3.2	The building blocks of the modeled jet	108
5.3.3	Full-Stokes radiative transfer	109
5.3.4	Emulating the jet	110
5.3.5	Relativistic shock jump conditions	112
5.4	A study case: the blazar 3C 454.3	113
5.4.1	Constraining the jet physical size	113
5.4.2	Constraining the particle number density	115
5.4.3	Constraining the number of cells	115
5.4.4	Reproducing the observed behavior	116
6	Optical and radio polarization studies of MeV–GeV blazars	119
6.1	Introduction	119
6.2	Optical polarization data	119
6.2.1	Demographics	120

6.2.2	Polarized state duration	120
6.3	Correlation analysis	122
6.3.1	Optical linear versus radio linear and circular polarization . . .	122
6.3.2	Optical linear polarization degree against the γ -ray energy flux .	122
6.3.3	Optical linear polarization degree and flux density state	122
6.4	Optical and radio EVPA rotations	125
6.4.1	Optical and radio emission site size from EVPA rotation rates .	128
6.4.2	The kinetic energy ratio between the radio and optical parts of the jet	128
7	Summary and conclusions	129
7.1	The framework	129
7.2	High precision linear and circular radio polarimetry	129
7.3	Linear and circular radio polarization characteristics of AGNs	130
7.3.1	Linear and circular radio polarization	131
7.3.2	Derivative quantities	131
7.3.3	Correlation analysis	132
7.4	Full-Stokes radiative transfer code	134
7.4.1	Application to shocked jets	134
7.4.2	The study case of 3C 454.3	134
7.5	Optical polarization properties of AGNs	135
7.5.1	Optical polarization	135
7.5.2	Correlation analysis	136
7.5.3	Optical and radio EVPA rotations	136
7.6	Future work	137
A	Radio polarization data	139
B	Light curves	177
C	Spectra	207
D	Rotation measure plots	237
E	Optical polarization data	253
	Bibliography	257
	Erklärung	267
	Publications / Teilpublikationen	269

List of Figures

1.1	AGN structure	2
1.2	The SED of 3C279	4
1.3	Synchrotron radiation pattern	7
1.4	Synchrotron emission solid angle	11
1.5	The functions $F(x)$ and $G(x)$	12
1.6	The $J(x, s)$ function	14
1.7	Relativistic aberration effect on EVPA	27
2.1	Parallactic angle - azimuth plot for the Effelsberg telescope	32
2.2	Simulated $ \Delta Q $ and $ \Delta U $ - azimuth plots for two measurement durations with $\phi = 50^\circ 31' 29''$ and $\delta = 40^\circ$	32
2.3	Müller matrix element histograms	35
2.4	LCP, RCP, COS and SIN channel datasets	37
2.5	Fitting method comparison	39
2.6	Phases A - D for the LCP channel	41
2.7	Differences between the phases recorded by the LCP channel	42
2.8	Pointing model amplitude improvement	45
2.9	Channel pointing offsets	45
2.10	Pointing correction amplitude scatter improvement	46
2.11	Pointing correction circular polarization degree scatter improvement	46
2.12	T_{sys} versus airmass	49
2.13	Fitted τ_z differences between LCP and RCP T_{sys} data	49
2.14	LCP and RCP channel gain curves	51
2.15	Stokes Q and U artifacts	52
2.16	Stokes Q and U artifact correction process	54
2.17	Linear polarization characteristics of the calibrator 3C 48 before and after the artifact correction	56
2.18	The generated models of the Stokes Q and U artifacts for 46 consecutive sessions.	57
3.1	Uncorrected Stokes V lightcurves	62
3.2	Sensitivity factors for the 4.85 GHz Effelsberg receiver	65
3.3	Sensitivity factors for the 8.35 GHz Effelsberg receiver	66
4.1	Histograms of total flux density for sources with either linear and/or circular polarization	73
4.2	Histograms of m_l	75
4.3	Histograms of Π_l	76
4.4	Histograms of $ m_c $	77
4.5	Histograms of $ \Pi_c $	78

4.6	Histograms of Π_l detectability	78
4.7	Histograms of Π_c detectability	79
4.8	Histograms of B-field strength	83
4.9	Rotation measure comparison plot	84
4.10	Histogram of rotation measures	86
4.11	RM celestial map	86
4.12	RM vs galactic latitude	87
4.13	EVPA vs jet PA alignment histogram	88
4.14	m_l vs $ m_c $	89
4.15	Median m_l vs RM	91
4.16	Median $ m_c $ vs RM	92
4.17	Median m_l vs γ -ray energy flux	93
4.18	Median $ m_c $ vs γ -ray energy flux	94
4.19	Median m_l vs synchrotron peak	95
4.20	Median $ m_c $ vs synchrotron peak	96
4.21	m_l at total flux extrema	98
4.22	Π_l at total flux extrema	99
4.23	$ m_c $ at total flux extrema	100
4.24	$ \Pi_c $ at total flux extrema	101
5.1	Multi-frequency radio variability of the FSRQ 3C 454.3	104
5.2	Multi-frequency radio variability pattern of the blazar 3C454.3	105
5.3	"Shock-in-jet" model evolutionary stages	106
5.4	3C 454.3 Full Stokes lightcurves.	108
5.5	The broadband total flux and polarization characteristics of a synchrotron self-absorbed (SSA) emitting modelled cell as generated with our code. The linear and circular polarization degrees, m_l and m_c , are normalized to 1.	110
(a)	SSA Stokes parameters	110
(b)	SSA polarization characteristics	110
5.6	A modeled jet profile	112
5.7	The dependence of the linear polarization degree m_l for an optically thin, synchrotron emitting compressed plasma cell with tangled magnetic field as a function of the compression factor, k , and the angle between the line of sight and the compression plane, ϕ (Hughes et al., 1985).	114
(a)	m_l vs compression k	114
(b)	m_l vs angle to compression plane	114
5.8	The unshocked flow of modeled jet for 3C454.3	116
5.9	Simulated Full Stokes lightcurves	117
6.1	Histogram of optical m_l	121
6.2	Histograms of optical m_l detectability	121
6.3	R band median m_l versus radio median m_l	123
6.4	R band median m_l versus radio median $ m_c $	124
6.5	R band median m_l versus γ -ray energy flux	124
6.6	R-band m_l and Π_l at low and high flux density state	125
6.7	Radio EVPA rotation ranges and rates	126
B.1	Radio linear and circular polarization lightcurves	178
B.2	continued	179
B.3	continued	180

B.4	continued	181
B.5	continued	182
B.6	continued	183
B.7	continued	184
B.8	continued	185
B.9	continued	186
B.10	continued	187
B.11	continued	188
B.12	continued	189
B.13	continued	190
B.14	continued	191
B.15	continued	192
B.16	continued	193
B.17	continued	194
B.18	continued	195
B.19	continued	196
B.20	continued	197
B.21	continued	198
B.22	continued	199
B.23	continued	200
B.24	continued	201
B.25	continued	202
B.26	continued	203
B.27	continued	204
B.28	continued	205
B.29	continued	206
C.1	Radio total flux density and linear polarization spectra	208
C.2	continued	209
C.3	continued	210
C.4	continued	211
C.5	continued	212
C.6	continued	213
C.7	continued	214
C.8	continued	215
C.9	continued	216
C.10	continued	217
C.11	continued	218
C.12	continued	219
C.13	continued	220
C.14	continued	221
C.15	continued	222
C.16	continued	223
C.17	continued	224
C.18	continued	225
C.19	continued	226
C.20	continued	227
C.21	continued	228
C.22	continued	229
C.23	continued	230

C.24	continued	231
C.25	continued	232
C.26	continued	233
C.27	continued	234
C.28	continued	235
C.29	continued	236
D.1	EVPA versus λ^2 , rotation measure and zero-wavelength EVPA variability plots	238
D.2	continued	239
D.3	continued	240
D.4	continued	241
D.5	continued	242
D.6	continued	243
D.7	continued	244
D.8	continued	245
D.9	continued	246
D.10	continued	247
D.11	continued	248
D.12	continued	249
D.13	continued	250
D.14	continued	251
D.15	continued	252

List of Tables

2.1	Fitting method comparison for circular polarization measurements	38
2.2	The setup of the different phases in the measurement cycle	40
2.3	LCP and RCP gain curve parameters	50
2.4	The initial values of the Stokes Q and U artifact model parameters	53
2.5	Stokes Q and U artifact fitted parameter values	55
3.1	Calibrated Stokes V and I of standards	63
3.2	Polarization characteristics of calibrators	64
4.1	Source list	69
4.1	continued.	70
4.1	continued.	71
4.2	Demographics of polarized sources	71
4.3	Linearly and/or circularly polarized sources	72
4.4	Magnetic field strengths	80
4.4	continued.	81
4.4	continued.	82
4.5	Rotation measures and 0-wavelength EVPAs	84
4.5	continued.	85
4.6	FSRQs vs BL Lacs in polarization	96
4.6	continued.	97
6.1	Demographics of polarized sources in radio and optical	120
6.2	The list of sources which have shown radio or optical EVPA rotations	127
A.1	Radio total flux density, linear and circular polarization characteristics	139
A.1	continued.	140
A.1	continued.	141
A.1	continued.	142
A.1	continued.	143
A.1	continued.	144
A.1	continued.	145
A.1	continued.	146
A.1	continued.	147
A.1	continued.	148
A.1	continued.	149
A.1	continued.	150
A.1	continued.	151
A.1	continued.	152
A.1	continued.	153

A.1	continued.	154
A.1	continued.	155
A.1	continued.	156
A.1	continued.	157
A.1	continued.	158
A.1	continued.	159
A.1	continued.	160
A.1	continued.	161
A.1	continued.	162
A.1	continued.	163
A.1	continued.	164
A.1	continued.	165
A.1	continued.	166
A.1	continued.	167
A.1	continued.	168
A.1	continued.	169
A.1	continued.	170
A.1	continued.	171
A.1	continued.	172
A.1	continued.	173
A.1	continued.	174
A.1	continued.	175
A.1	continued.	176
E.1	Optical polarization characteristics	253
E.1	continued.	254
E.1	continued.	255
E.1	continued.	256

Chapter 1

Synchrotron emission and radiative transfer

Abstract

In the current thesis, we apply the framework we developed to study the physical conditions in extragalactic jets, hosted by AGNs. Those jets are radiating in the radio and optical bands through the incoherent synchrotron mechanism. In this chapter we give a brief overview of the AGN structure and we provide the theoretical predictions for a number of synchrotron emission, absorption, and propagation effects which can also modify the polarization characteristics. Such effects will be used in the following chapters to interpret the observed behaviour.

The information presented in this chapter is text-book knowledge and can be found at, (e.g. Pacholczyk, 1970, 1977; Ginzburg, 1979; Rybicki and Lightman, 1979). Here we provide it however to establish a common nomenclature throughout this thesis and accumulate the part of theory relevant to this work. Most analysis is taken from Pacholczyk (1970) and Pacholczyk (1977).

1.1 ACTIVE GALACTIC NUCLEI: THE BIG PICTURE

The term Active Galactic Nucleus (AGN) is used in modern Astrophysics to describe the central regions of galaxies which exhibit immense energy production. AGNs radiate over an extreme range of frequencies with bolometric luminosities higher than their host galaxies up to a factor of ~ 100 . The typical AGN bolometric luminosities are of the order of $10^{11} - 10^{13} L_{\odot}$, i.e. $\sim 10^{44} - 10^{46} \text{ erg s}^{-1}$ (e.g. Peterson, 1997). Furthermore, the AGN emission is highly variable over a very broad range of time scales, from minutes to years. According to coherence arguments, the short time scales indicate that most of the radiated energy is produced in a region of linear scale comparable the size of our Solar system. This extreme energy production in such compact regions supports the current consensus that the energy source of AGNs are supermassive black holes (SMBHs) with masses of the order of $10^{9 \pm 1} M_{\odot}$ (e.g. Peterson, 1997).

The typical structure of an AGN is shown in Fig. 1.1 and its main constituents are described in the following subsections.

1.1.1 The “central engine” and the obscuring torus

The main energy source – “central engine” – of all AGNs is considered to be a supermassive black hole (SMBH) of $\sim 10^9 M_{\odot}$ located at their centres. Its gravitational field accretes matter from the inner part of the host galaxy, surrounding the AGN, and an accretion disk is created as a result of the angular momentum conservation of the infalling material. Part of

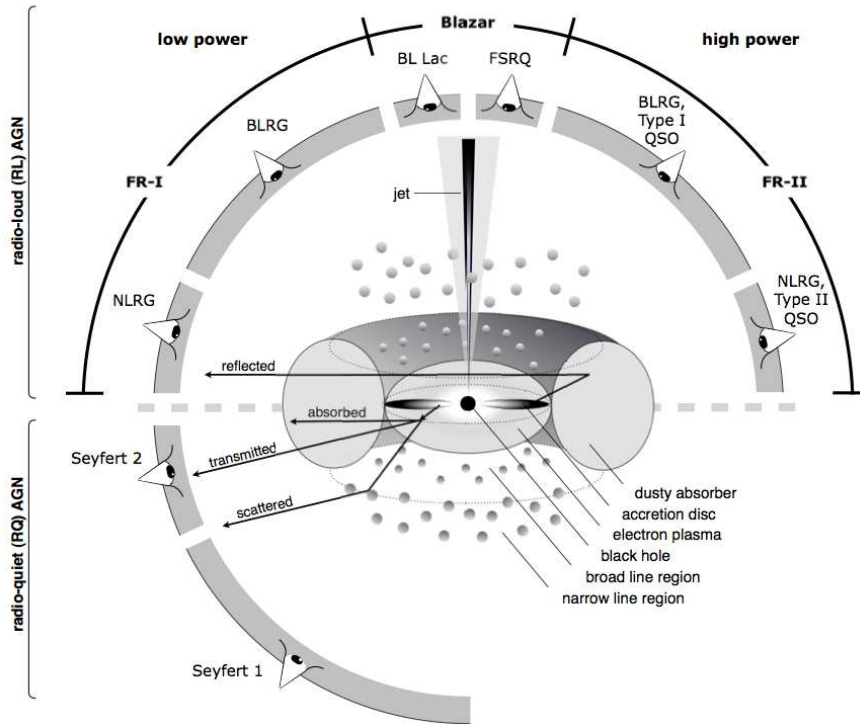


Figure 1.1: A schematic representation of the AGN structure. The different types of AGN are labeled according to the unification scheme. Figure taken from Beckmann and Shrader (2012)

the gravitational potential energy released through the accretion process is radiated away and the accretion disk becomes extremely hot and luminous due its viscosity. The accretion disk radiation is responsible for the thermal component of the AGN emission and peaks around the extreme ultraviolet and X-ray wavelengths (e.g. Begelman, 1985; Peterson, 1997).

The flow of material onto the SMBH is provided by an optically thick torus which surrounds the radiating accretion disk. Depending on the orientation of the AGN with respect to our line of sight (LoS), this torus may obscure the “central engine” from our view.

1.1.2 The narrow and broad line regions

The optical and ultraviolet parts of AGN spectra host a series of broad and narrow lines. Measurements of their Full Width at Half Maximum (FWHM) reveal that the regions where broad lines are emitted have average speeds of the level of 5000 km s^{-1} while the ones producing the narrow lines of the order of 400 km s^{-1} . Furthermore, in the cases where the “central engine” was obscured by the torus, the broad lines appeared much fainter and more polarized than the narrow lines (Antonucci and Miller, 1985).

These observations were interpreted as an AGN orientation effect. The broad lines are produced from clouds moving at high velocities because they orbit the SMBH at a close distance. When the AGN orientation conceals the central region from our LoS, these clouds are not seen directly but only after their emission is scattered in the outer parts of the AGN or the innermost part of the host galaxy. Thus, their lines appear faint and highly polarized due to scattering. On the other hand, narrow lines are produced by low velocity clouds orbiting the SMBH at greater distances. They are observed directly independently of the AGN orientation and thus their lines are not polarized (Antonucci and Miller, 1985).

These findings led to the unification scheme of AGNs (Urry and Padovani, 1995) which attributes the various types of AGN we observe to their orientation with respect to our LoS. For example, the fact that broad lines are observed for Seyfert 1 but not Seyfert 2 galaxies is explained in this scheme by the obscuration of the central part of the latter type by the torus. The different classifications of AGN and their explanation according to the unification scheme are shown in Fig. 1.1.

1.1.3 The jet

In about 10 % of AGNs, the so-called radio-loud (RL) ones, a relativistic, collimated, bipolar flow of material appears to be ejected from the “central engine”, known as the jet (e.g. Beckmann and Shrader, 2012). Jets can reach distances of the order of hundreds of kpc or even Mpc and are often terminated in extended regions where material and energy is dissipated. Those regions are very bright radio sources, called “hot spots”. Jets appear to be very collimated with opening angles $\theta \leq 15^\circ$. Furthermore, the fact that they emit from radio to optical or even X-ray wavelengths with the incoherent synchrotron mechanism becomes evident from the continuum, non-thermal appearance of their spectra and the high linear polarization observed (e.g. Boettcher et al., 2012).

Although the composition of jets is an open question, the flow is thought to be described by a charge-neutral plasma of a roughly equal admixture of electrons and protons or electrons and positrons which have similar densities. The typical densities of jets are of the order of $10^{-3} - 10^{-2} \text{ cm}^{-3}$ (e.g. Begelman et al., 1984). The relativistic motion of jets is supported by a number of observational facts, one of which is that they often appear one-sided. This is attributed to the Doppler beaming effect which enhances the radiation towards the direction of motion of the emitter, due to the relativistic aberration and time dilation effects. Thus, although jet flows are bipolar, in the case of their close alignment with our LoS the flow directed away from us becomes unobservable (e.g. Boettcher et al., 2012).

The spectral energy distributions (SEDs) of AGN jets span from the radio up to TeV energies and contain usually two broad components (Fig. 1.2). The low energy component is attributed to the incoherent synchrotron emission of the jet particle population. The strongest argument in favor of this interpretation is the high linear polarization degree observed at these frequencies. The high frequency component on the other hand is attributed to two competing interpretations or models, the leptonic and the hadronic one. The leptonic model attributes the emission to the inverse Compton up-scattering of the low frequency synchrotron photons to high energies by the relativistic particles that emit them, (e.g. Bednarek et al., 1996). The hadronic model predicts that the high energy photons are produced by electromagnetic cascades which are triggered by photo-pion production from the interaction of ultra-relativistic protons with the ambient synchrotron photons, (e.g. Kazanas and Mastichiadis, 1999; Mücke et al., 2003).

Although the exact processes to form, collimate and sustain jets are not yet fully understood, jets can be adequately described as relativistic magnetized plasma systems. Such systems are expected to emit radiation with linearly and circularly polarized components (*vide infra*). The polarized emission is later propagated through the magnetized jet plasma, i.e. a magneto-ionic medium which, under certain circumstances, can change its polarization characteristics. The initial polarization state as well as the changes it undergoes as the emission propagates through the jet are unique probes to estimate many physical parameters of the emitting and transmitting jet plasma. This approach is similar to the techniques used to study many systems that can not be simulated *in vitro* (e.g. the Earth’s magma or the Sun’s plasma). The knowledge of these physical parameters helps to create or improve theoretical jet models by narrowing their parameter spaces. Furthermore, they offer the potential to investigate the physical conditions in the vicinity of the AGN’s “central engine” which is physically and causally connected with the jet itself.

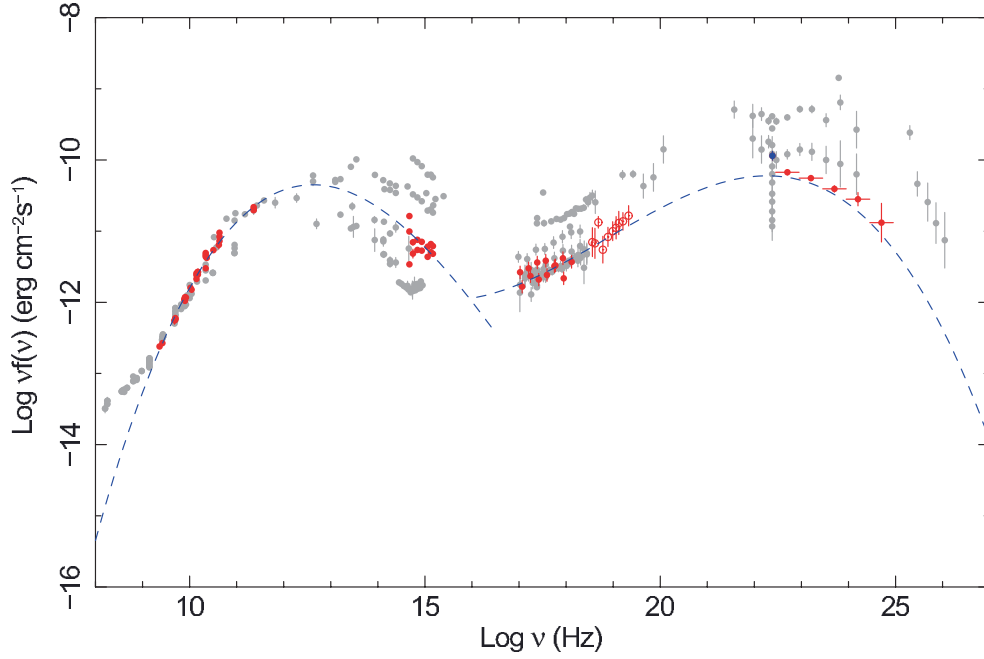


Figure 1.2: The SED of the blazar 3C279. The pronounced variability is evident by the large scatter of data points across the whole electromagnetic spectrum. Figure taken from Boettcher et al. (2012).

Another important characteristic of the AGN jet emission is its pronounced variability across the electromagnetic spectrum, as shown in the example of Fig. 1.2. This variability is often manifested in the synchrotron part of the jet emission by strong flares which are caused by the appearance of SED components at the high frequencies which usually propagate later towards the lower frequencies, (e.g. Marscher and Gear, 1985). These components are often attributed to confined particle “clouds” of higher densities or magnetic field strengths as compared to the large scale flow of the jet. Most of the times these particle “clouds” are correlated with localized emission elements in VLBI radio maps of jets. The evolution of their physical characteristics as they propagate downstream the jet is imprinted on their spectral variability as well the changes of their polarization state. Thus, multi-frequency, high cadence observations of their total flux and polarization are powerful probes to study the physical parameters of these systems.

This work is concentrated on the study of the AGN jet emission and variability in the radio and optical parts of the electromagnetic spectrum by means of high cadence, multi-frequency linear and circular radio as well as linear optical polarimetry. We exploit the invaluable tool of polarimetry primarily because such information are a direct measure of the physical parameters of the emitting regions, like their magnetic field strength and uniformity. In the following sections, we will describe the emission processes which produce the polarized radio and optical jet radiation as well as the effects which can potentially change the polarization characteristics of the emission during its propagation through the jet’s magnetized plasma.

1.2 SYNCHROTRON EMISSION

As discussed above, we focus on the radio and optical parts of the AGN jet emission, considered to be generated by the incoherent synchrotron mechanism. In this section, we describe briefly the synchrotron emission from a single particle as well as from an ensemble of particles embedded in large scale magnetic fields. This setup can be considered as the first order approximation of a synchrotron emitting AGN jet as well as the high density "clouds" which cause the flaring behavior as described in subsection 1.1.3. The predictions of synchrotron theory presented here provide a link between the physical conditions of the emitting regions and the total flux as well as linear and circular polarization characteristics of the emitted radiation.

The information presented in the following sections is text-book knowledge and can be found at, e.g. Pacholczyk (1970, 1977); Ginzburg (1979); Rybicki and Lightman (1979). Here we provide it however to make sure we have a common nomenclature throughout this thesis and also gather together the part of theory relevant to this work. Most analysis is taken from Pacholczyk (1970) and Pacholczyk (1977). Here, we present the properties of synchrotron radiation and focus on its linear and circular polarization characteristics.

When charged particles move through regions with magnetic fields, they follow helical trajectories due to the Lorentz force that acts on them as a form of centripetal force. The centripetal acceleration results to the emission of electromagnetic radiation, called cyclotron. If the particles are moving with relativistic velocities, the emission is called synchrotron.

1.2.1 Emission from a single particle

Here we discuss the details of synchrotron emission from a single particle gyrating a magnetic field. The equations are directly applicable for radiating electrons. However, they can be easily recalculated for particles of any mass or charge.

The synchrotron emission from a single particle can be studied by solving the vector and scalar Liénard-Wiechert potentials for the special case of a single particle moving on a helical trajectory. These potentials are solutions of Maxwell's equations and they are used to calculate the electric and magnetic fields of the particle's radiation as

$$\begin{aligned} \mathbf{E} &= -\frac{1}{c} \frac{\partial \mathbf{A}}{\partial t} - \nabla \phi \\ \mathbf{H} &= \nabla \times \mathbf{A} \end{aligned} \quad (1.1)$$

where,

- \mathbf{E} the electric field of the radiation
- \mathbf{H} the magnetic field of the radiation
- \mathbf{A} the vector Liénard-Wiechert potential
- ϕ the scalar Liénard-Wiechert potential and
- c the speed of light

It is important to emphasize that the Liénard-Wiechert potentials of the emitting charge and current distributions are evaluated at the time that the radiation is emitted and not at the time it is observed. This time is called the retarded time and is given by

$$t' = t - \frac{R_0(t')}{c} \quad (1.2)$$

where,

- t' the retarded time
- t the time of observation and
- $R_0(t')$ is the vector distance from the observer to the emitting element at the retarded time t'

The Liénard-Wiechert potentials at that time are given by the following expressions

$$\begin{aligned} \mathbf{A}(\mathbf{R}, t) &= \frac{1}{c} \int R_0^{-1} \mathbf{j}(\mathbf{r}', t') \delta \left(t' - t + \frac{R_0(t')}{c} \right) d\tau' dt' \\ \phi(\mathbf{R}, t) &= \int R_0^{-1} Q(\mathbf{r}', t') \delta \left(t' - t + \frac{R_0(t')}{c} \right) d\tau' dt' \end{aligned} \quad (1.3)$$

where,

- \mathbf{j} the current density of the emission element at the retarded time t'
- Q the charge density of the emission element at the retarded time t'
- τ' the volume containing \mathbf{j} and Q at the retarded time t'

In the case of a single particle moving with high velocity, the generic solution of Eq. 1.1 takes the form

$$\begin{aligned} \mathbf{E} &= \frac{e}{R_0'} \frac{\hat{\mathbf{R}}_0' \times [(\hat{\mathbf{R}}_0' - \boldsymbol{\beta}') \times \dot{\boldsymbol{\beta}}']}{c(1 - \boldsymbol{\beta}' \cdot \hat{\mathbf{R}}_0')^3} \\ \mathbf{H} &= \hat{\mathbf{R}}_0' \times \mathbf{E} \end{aligned} \quad (1.4)$$

where,

- e the elementary charge
- $\hat{\mathbf{R}}_0'$ the unit vector of the distance vector \mathbf{R}_0 at the retarded time t'
- $\boldsymbol{\beta}'$ the velocity vector of the moving particle in units of c at the retarded time t'
- $\dot{\boldsymbol{\beta}}'$ the acceleration vector of the moving particle at the retarded time t'

Eq. 1.4 is valid only for large distances from the moving particle. See also Eqs. 3.8 of Pacholczyk (1970).

Using Eq. 1.4, we calculate the radiated power of synchrotron emission per unit solid angle, \tilde{p}_Ω , as

$$\begin{aligned} \tilde{p}_\Omega &= \frac{c}{4\pi} E^2 R_0'^2 \\ &= \frac{e^2}{4\pi c} \left[\frac{(\dot{\boldsymbol{\beta}}')^2}{(1 - \boldsymbol{\beta}' \cdot \hat{\mathbf{R}}_0')^4} + \frac{2(\hat{\mathbf{R}}_0' \cdot \dot{\boldsymbol{\beta}}')(\boldsymbol{\beta}' \cdot \dot{\boldsymbol{\beta}}')}{(1 - \boldsymbol{\beta}' \cdot \hat{\mathbf{R}}_0')^5} - \frac{(\hat{\mathbf{R}}_0' \cdot \dot{\boldsymbol{\beta}}')^2}{\gamma^2 (1 - \boldsymbol{\beta}' \cdot \hat{\mathbf{R}}_0')^6} \right] \end{aligned} \quad (1.5)$$

where,

- γ the particles's Lorentz factor

$$\gamma = (1 - \beta^2)^{-1/2} \quad (1.6)$$

- β the velocity of the moving particle in units of c

See also Eqs. 3.9 of Pacholczyk (1970). As shown in Eq. 1.5, the radiated power per unit solid angle has a strong inversely proportional dependence on the quantity $(1 - \boldsymbol{\beta}' \cdot \hat{\mathbf{R}}_0')$ and it becomes significant when

$$\boldsymbol{\beta}' \cdot \hat{\mathbf{R}}_0' \approx 1 \Rightarrow \beta' \cos \psi \approx 1 \Rightarrow \beta' + \frac{\beta' \psi^2}{2} \approx 1 \Rightarrow \psi \approx \frac{2}{\beta'} \sqrt{(1 - \beta')} \sim \frac{1}{\gamma} \quad (1.7)$$

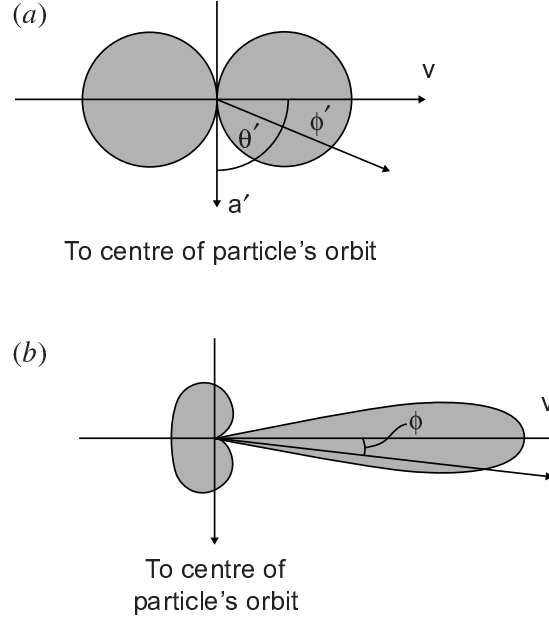


Figure 1.3: The polar diagram of the radiated power from a single moving particle with perpendicular velocity and acceleration vectors when it moves with (a) low and (b) high velocity. Figure taken from Longair (2011).

where ψ is the angle between the particle velocity vector, β' , and the unit vector, $\hat{\mathbf{R}}'_0$, of the observer's LoS at the retarded time t' . In the second step of the derivation 1.7, we used the first terms of the Taylor expansion of the cos function. As a consequence, the radiated power is concentrated within a small angle around the velocity vector of the emitting particle when $\beta' \approx 1$, i.e. when the particle is moving at relativistic velocities (synchrotron radiation). The polar diagram of the radiated power for the cases of low and high particle velocities are shown in Fig. 1.3.

Spectral distribution and polarization characteristics

The conclusions of the previous discussion are valid for any set of particle velocity, β' , and acceleration, $\dot{\beta}'$, vectors. In other words, Eq. 1.5 can be used to estimate the radiated power per unit solid angle of radiating moving particles as long as their velocity and acceleration vectors are provided.

In the case of synchrotron radiation, the particle is moving on a helical path and its motion is easily described in a reference system with one axis parallel to the magnetic field direction. Furthermore, the radiation is concentrated within a small angle around the velocity vector because the particles are moving at high velocities. Thus, a distant observer will sense periodic pulses of radiation as the particle gyrates the magnetic field lines. It can be shown that the period of these pulses is

$$T \approx \frac{2\pi}{\omega_H} \sin^2 \theta \quad (1.8)$$

where,

- θ the particle's pitch angle, i.e. the angle between its velocity vector and the magnetic field direction
- ω_H the relativistic particle gyrofrequency. If the particles are electrons it is given by

$$\omega_H = \frac{eH}{\gamma m_e c} \quad (1.9)$$

where m_e is the electron mass

Thus, the received power per unit solid angle will be modulated by the fundamental frequency, given by the inverse of Eq. 1.8, and its higher harmonics. Using a similar definition to Eq. 1.5, the received power per unit solid angle for an observer located at distance R from the emitting particle and for each of these harmonics, n , is given by

$$\tilde{p}_{n\Omega} = \frac{c}{2\pi} |\mathbf{E}_n|^2 R^2 \quad (1.10)$$

This is larger than Eq. 1.5 by a factor of 2 because both the n th and $(-n)$ th harmonics of the electric field contribute equally to the power in the n th harmonic, since $\tilde{p}_{n\Omega} \propto \mathbf{E}_n \mathbf{E}_n^*$ and $\mathbf{E}(t)$ is a real function, i.e. $\mathbf{E}_n^* = -\mathbf{E}_{-n}$ (see also Eq. 1.11). We have to take this fact into consideration for our calculations even though negative harmonics have no physical meaning.

In order to evaluate Eq. 1.10, we need an expression for the harmonics of the electric field, \mathbf{E}_n . First, we estimate the electric field, $\mathbf{E}(t)$, of a synchrotron emitting particle by replacing the velocity and acceleration vectors for its helical trajectory in Eq. 1.4 and then we calculate its harmonics, given by the Fourier transform

$$\mathbf{E}_n = \frac{\omega_H}{2\pi \sin^2 \theta} \int_0^{\frac{2\pi \sin^2 \theta}{\omega_H}} \mathbf{E}(t) \exp\left(i \frac{\omega_H}{\sin^2 \theta} nt\right) dt \quad (1.11)$$

where n is the number of the harmonic. A detailed derivation can be found in Pacholczyk (1970).

The above steps give

$$\mathbf{E}_n = n \frac{e}{\sqrt{3}\pi R c \sin^5 \theta} \exp\left(i n \frac{\omega_H}{\sin^2 \theta} \frac{R}{c}\right) \left[\hat{\mathbf{l}} \frac{1}{\gamma^2} (1 + \gamma^2 \psi^2) K_{2/3}(y) + i \hat{\mathbf{m}} \frac{\psi}{\gamma} \sqrt{1 + \gamma^2 \psi^2} K_{1/3}(y) \right] \quad (1.12)$$

where,

- R the distance between the observer and the particle
- $K_{2/3}$ and $K_{1/3}$ are Bessel functions of the second kind with imaginary arguments of the quantity

$$y = \frac{n}{3\gamma^3 \sin^3 \theta} (1 + \gamma^2 \psi^2)^{3/2} \quad (1.13)$$

- $\hat{\mathbf{l}}$ and $\hat{\mathbf{m}}$ are unit vectors which form a reference frame together with the radiation propagation unit vector $\hat{\mathbf{k}}$ towards the observer. In this frame, $\hat{\mathbf{m}}$ is aligned with the projection of the magnetic field onto the plane perpendicular to the unit vector $\hat{\mathbf{k}}$. In the context of celestial observations, $\hat{\mathbf{m}}$ and $\hat{\mathbf{l}}$ are aligned parallel and perpendicular to the projection of the magnetic field on the plane of the sky respectively.

We want to emphasize that Eq. 1.12 is derived using the assumption that the quantity $1/\gamma$ can be neglected when compared with unity, i.e. second and higher order terms of this quantity have been excluded from the calculations. Therefore this condition is also assumed for all the expressions presented until subsection 1.2.5. This assumption is valid in the case that the emitting particles are moving at very high velocities, but it cannot be used without consequences in the case of particles of lower, but still relativistic speeds. This fact becomes particularly important for polarization studies since the conclusions using this assumption are incomplete, especially considering the circular polarization characteristics of synchrotron radiation, as discussed in subsection 1.2.5.

Since the electric field of Eq. 1.12 has two components in the \hat{l} and \hat{m} directions, the radiated power can be split in two components along the same directions. Furthermore, the fact that Eq. 1.12 is roughly $\propto n/\gamma^3$ means that for large γ values the electric field amplitude and consequently the radiated power of higher harmonics are more significant compared to the lower ones. This results in the broadening of the emitted power spectrum to the point that becomes practically continuous (see also section 6.6 of Rybicki and Lightman (1979)). Under these circumstances, we can substitute the harmonic number n with the frequency

$$\nu = n \frac{\omega_H}{2\pi \sin^2 \theta} \quad (1.14)$$

The final expressions of the radiated powers per unit solid angle and frequency over directions \hat{l} and \hat{m} are given by

$$\begin{aligned} \tilde{p}_{\nu\Omega}^{(\hat{l})} &= \frac{3e^2}{4\pi^2 c} \frac{\omega_H}{\sin^2 \theta} \gamma^2 (1 + \gamma^2 \psi^2)^2 x^2 K_{2/3}^2(y) \\ \tilde{p}_{\nu\Omega}^{(\hat{m})} &= \frac{3e^2}{4\pi^2 c} \frac{\omega_H}{\sin^2 \theta} \gamma^4 \psi^2 (1 + \gamma^2 \psi^2) x^2 K_{1/3}^2(y) \end{aligned} \quad (1.15)$$

where,

x is the frequency normalized to a critical frequency ν_c , which is of the same order of magnitude as the peak frequency of the single particle synchrotron radiation spectrum.

$$\nu_c = \frac{3}{4\pi} \omega_H \sin \vartheta \gamma^3 \quad (1.16)$$

and ϑ is the angle between the magnetic field direction and the line of sight. For very high particle velocities, $\theta \approx \vartheta$.

It is of special interest to estimate the energy losses of the emitting particle due to synchrotron radiation by integrating the expressions in Eqs. 1.15 over all solid angles and frequencies. When we take into account properly the velocity of the emitting particle along the line of sight (Ginzburg, 1979) we find that

$$-\frac{dE}{dt} = \frac{2(Ze)^4}{3m^4 c^7} H^2 \sin^2 \vartheta E^2 \quad (1.17)$$

where,

Ze the charge of the emitting particle
 m the mass of the emitting particle

The above equation shows that the power of synchrotron radiation of electrons or positrons is $\sim 1840^4 \approx 1.1 \times 10^{13}$ greater when compared to that of protons of the same energy!

Another interesting conclusion is that the synchrotron radiation of a single particle is elliptically polarized. This is discerned from the fact that its electric field has two unequal complex amplitudes of the same argument (Eq. 1.12). The amplitudes of the two electric field components are used to calculate its ellipticity b as

$$\tan b = \psi \frac{\gamma K_{1/3}(y)}{\sqrt{1 + \gamma^2 \psi^2 K_{2/3}(y)}} \quad (1.18)$$

The major axis of the polarization ellipse is perpendicular to the projection of the magnetic field on the plane of the sky (i.e. parallel to the unit vector \hat{l}). We see from Eq. 1.18 that the ellipticity is an odd function of the angle ψ which means that its sense of rotation depends on the angle between the line of sight and the velocity vector of the radiating particle, being left-handed when $\psi > 0$ and right-handed in the opposite case. Positive ψ angles are considered when the line of sight forms a greater angle with respect to the magnetic field as compared to the particle pitch angle. When the line of sight is aligned with the particle velocity, $\psi = 0$ and its emission is linearly polarized with the electric vector position angle (EVPA) being perpendicular to the projection of the magnetic field on the plane of the sky.

1.2.2 Emission and absorption from an ensemble of particles

The next step in our approach to emulate the conditions of the synchrotron emitting regions in AGN jets is to generalize the previous equations for an ensemble of synchrotron emitting particles of various energies. We do that by integrating the spectral power per unit solid angle radiated from a single particle (Eqs. 1.15) over the energy, E , and solid angle, Ω , for the emitting particle population. For an isotropic distribution of particle velocities, the integration takes the form:

$$\varepsilon_{\nu}^{(i)} = \frac{1}{4\pi} \int_0^{\infty} N(E) \left(\int_{4\pi} p_{\nu\Omega}^{(i)} d\Omega \right) dE \quad (1.19)$$

where,

- $N(E)$ the energy distribution of the emitting particles
- $i = \hat{l}, \hat{m}$ the component of the integrated spectral power. This distinction is based on the fact that synchrotron radiation has two components, parallel and perpendicular to the projection of the magnetic field on the plane of the sky (see Sect. 1.2.1).

The expression of Eq. 1.19 is the spectral emission coefficient of synchrotron radiation from a stationary region of omnidirectional particle velocities.

Since the radiation is beamed within small angles around the velocity vector of the emitting particles, the expression in the parenthesis of Eq. 1.19 will be performed over the solid angle $d\Omega \approx 2\pi \sin \vartheta d\psi$ which defines a ring where most of the synchrotron radiation is concentrated during the gyration of the emitting particle around the magnetic field (Fig. 1.4). Thus, in order to estimate the spectral emission coefficients over the directions $i = \hat{l}, \hat{m}$, we need to solve Eq. 1.19 for the radiated powers of Eqs. 1.15, which yields

$$\varepsilon_{\nu}^{(i)} = \frac{1}{2} \frac{\sqrt{3}}{4\pi} \frac{e^3}{mc^2} H \sin \vartheta \int_0^{\infty} N(E) [F(x) \pm G(x)] dE \quad (1.20)$$

where,

$$\begin{aligned} F(x) &= x \int_x^{\infty} K_{5/3}(z) dz \\ G(x) &= x K_{2/3}(x) \end{aligned} \quad (1.21)$$

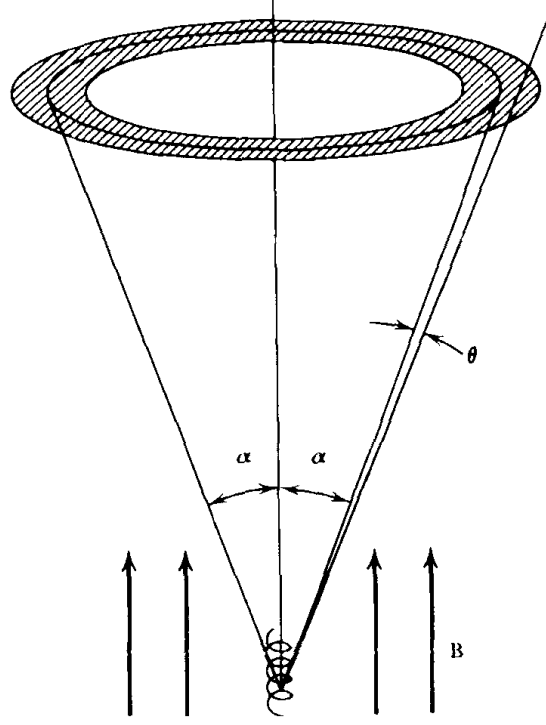


Figure 1.4: The solid angle covered by synchrotron emitting particles of pitch angle α . Figure taken from Rybicki and Lightman (1979).

and the \pm signs refer to directions \hat{l} and \hat{m} respectively. Finally, the total emission coefficient can be calculated as the sum of the coefficients over all directions. Therefore, in the total coefficient, the contribution of the function $G(x)$ vanishes. The functions $F(x)$ and $G(x)$ are shown in Fig. 1.5.

1.2.3 Self-absorption

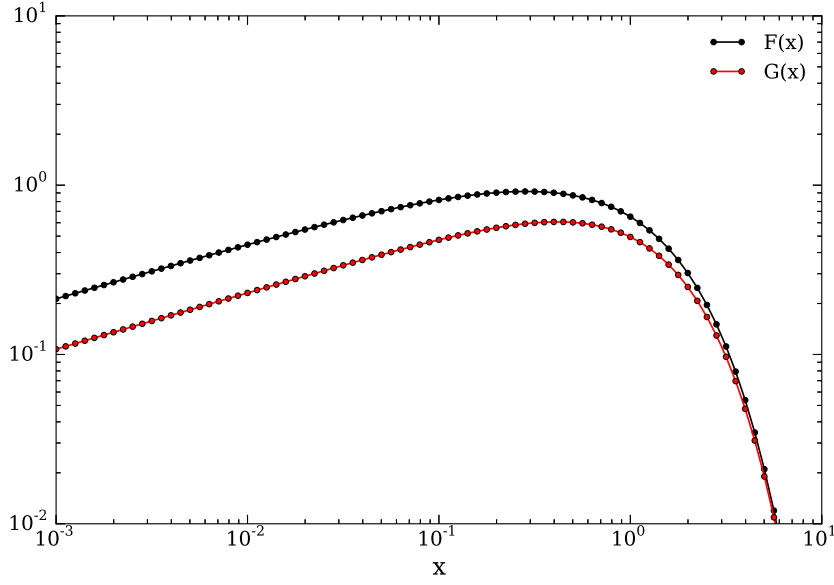
Under certain conditions, the synchrotron photons emitted from a particle population can be absorbed by the emitting particles themselves. A convenient and elegant approach to estimate the absorption of a synchrotron emitting source, is through the utilization of the Einstein coefficients which follow the relation

$$B_{12}^{(i)} = B_{21}^{(i)} = A_{21}^{(i)} \frac{c^2}{h\nu^3} \quad (1.22)$$

where,

B_{12}	the Einstein coefficient for absorption between energy levels 1 and 2
B_{21}	the Einstein coefficient for stimulated emission
A_{21}	the Einstein coefficient for spontaneous emission
$i = \hat{l}, \hat{m}$	the component of the polarized emission/absorption parallel and perpendicular to the projection of the magnetic field on the plane of the sky respectively

The above relation provides a way to estimate the absorption of a synchrotron emitting source. Given that the emission has two distinct components with respect to the direction of the magnetic field on the plane of the sky (Eq. 1.20), it is expected that the absorption coefficients will

Figure 1.5: The functions $F(x)$ and $G(x)$

also follow this dichotomy. The absorption coefficients for an isotropic distribution of particles are

$$\kappa_{\nu}^{(i)} = -\frac{\sqrt{3}e^3}{8\pi m\nu^2} H \sin \vartheta \int_0^{\infty} E^2 \frac{d}{dE} \left(\frac{N(E)}{E^2} \right) [F(x) \pm G(x)] dE \quad (1.23)$$

The detailed derivation of Eq. 1.23 can be found in Pacholczyk (1970); Ginzburg (1979); Rybicki and Lightman (1979).

1.2.4 Emission and absorption for an ensemble of particles with power law energy distribution

In many astrophysical contexts, the particle energies follow a power law distribution. This is the case also for AGN jets, where one of the main particle acceleration processes is thought to be Fermi acceleration, which gives power law energy distributions.

Emission and absorption coefficients

We can calculate the emission and absorption coefficients for an ensemble of synchrotron emitting particles with power-law energy distribution of the form

$$N(E) = N_0 E^{-s} \quad (1.24)$$

by substituting 1.24 in expressions 1.20 and 1.23. These calculations yield

$$\begin{aligned} \varepsilon_{\nu}^{(i)} &= \frac{1}{2} C_3(s) N_0 (H \sin \vartheta)^{(s+1)/2} \left(\frac{\nu}{2C_1} \right)^{(1-s)/2} \left(1 \pm \frac{s+1}{s+7/3} \right) \\ \kappa_{\nu}^{(i)} &= C_4(s) N_0 (H \sin \vartheta)^{(s+2)/2} \left(\frac{\nu}{2C_1} \right)^{-(s+4)/2} \left(1 \pm \frac{s+2}{s+10/3} \right) \end{aligned} \quad (1.25)$$

where,

$$\begin{aligned}
 C_1 &= \frac{3e}{4\pi m^3 c^5} = 6.27 \times 10^{18} \\
 C_2 &= \frac{\sqrt{3}e^3}{4\pi m c^2} = 1.87 \times 10^{-23} \\
 C_3(s) &= \frac{1}{4} C_2 \left(\frac{s + 7/3}{s + 1} \right) \Gamma\left(\frac{3s - 1}{12}\right) \Gamma\left(\frac{3s + 7}{12}\right) \\
 C_4(s) &= \frac{1}{32} \left(\frac{c}{C_1} \right)^2 C_2 \left(s + \frac{10}{3} \right) \Gamma\left(\frac{3s + 2}{12}\right) \Gamma\left(\frac{3s + 10}{12}\right)
 \end{aligned} \tag{1.26}$$

These relations can be used to estimate the coefficients per direction, $i = \hat{l}, \hat{m}$, as well as the total coefficients as their sum.

Spectral intensity

Expressions 1.25 can be used as input to the radiative transfer equation in order to estimate the spectral intensity for a synchrotron emitting and absorbing ensemble of particles. If we assume that there is no incident radiation and the emission and absorption coefficients are constant throughout the emitting region, the radiative transfer equation can be written as

$$I_\nu(\tau_\nu) = S_\nu(1 - e^{-\tau_\nu}) \tag{1.27}$$

where,

- I_ν the spectral intensity of the emitting region
- τ_ν the optical depth
- S_ν the source function of the emitting region, defined as

$$S_\nu = \frac{\varepsilon_\nu}{\kappa_\nu} \tag{1.28}$$

The solution of Eq. 1.27 for a power law energy distribution is

$$I_\nu = S(\nu_1) \cdot J\left(\frac{\nu}{\nu_1}, s\right) \tag{1.29}$$

where,

- ν_1 the frequency where the optical depth of the emitting region becomes unity, $\tau(\nu_1) = 1$. It is given by

$$\nu_1 = 2 C_1 [z C_4(s)]^{2/(s+4)} N_0^{2/(s+4)} (H \sin \vartheta)^{(s+2)/(s+4)} \tag{1.30}$$

with z being the size of the emitting region

and also

$$\begin{aligned}
 S(\nu_1) &= \frac{C_3(s)}{C_4(s)} (H \sin \vartheta)^{-1/2} \left(\frac{\nu_1}{2C_1} \right)^{5/2} \\
 J(x, s) &= x^{5/2} [1 - \exp(-x^{-(s+4)/2})]
 \end{aligned} \tag{1.31}$$

Expression 1.29 shows that the spectral intensity of a synchrotron emitting and self-absorbing ensemble of particles has the form of the function $J(x, s)$, given in Eq. 1.31, and its location is determined by the values of ν_1 and $S(\nu_1)$. A plot of the $J(x, s)$ function for various values of the power law index, s , are shown in Fig. 1.6.

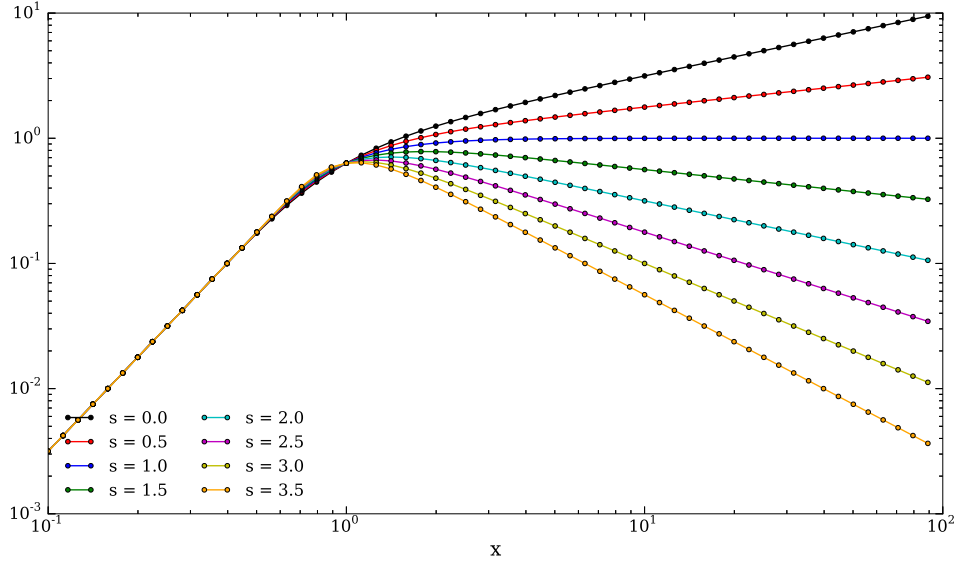


Figure 1.6: The $J(x, s)$ function for various values of the power law particle energy distribution index, s .

At high frequencies, the emission is optically thin and the absorption coefficient becomes insignificant. In this spectral region the intensity follows a frequency dependence similar to that of the emission coefficient (Eq. 1.25)

$$I_\nu \propto \nu^{-(s-1)/2} = \nu^{-\alpha} \quad (1.32)$$

where,

α the power law index of the spectral intensity in the optically thin part of the emission, given by

$$\alpha = \frac{s-1}{2} \quad (1.33)$$

At low frequencies, the emission is optically thick and the intensity follows the frequency dependence of the source function, S_ν (Eq. 1.28)

$$I_\nu \propto \nu^{5/2} \quad (1.34)$$

For $s > 1$, the intensity has a maximum value at a certain frequency, ν_m , which is also seen in Fig. 1.6. The optical depth of the emitting region at this point, τ_m , can be calculated from

$$e^{\tau_m} = 1 + \frac{s+4}{5} \tau_m \quad (1.35)$$

Evidently, the frequency ν_m is not coincident with the frequency where the optical depth of the emitting region is unity, ν_1 and their ratio can be calculated as

$$\frac{\nu_1}{\nu_m} = \tau_m^{2/(s+4)} \quad (1.36)$$

1.2.5 Emission and absorption from an ensemble of mildly relativistic particles

In the above discussion, only particles moving at very high velocities were considered, as it was also mentioned in subsection 1.2.1. The Lorentz factors γ , of those particles are so large that terms of the order of $1/\gamma$ can be neglected. In fact, that was one of the main assumptions to derive Eq. 1.12, on which all the expressions discussed so far are based. Here, we show how the derived expressions, and the corresponding conclusions, are affected when this assumption is relaxed and higher orders of γ^{-1} are considered non-negligible. The calculations are described extensively in Chapter 2 of Pacholczyk (1977).

It is clear that we need to repeat the derivation of all relations and expressions. This is due to the fact that, under the new assumption, even the period of the received pulses from a single synchrotron radiating particle, changes. It is now given by

$$T = \frac{2\pi}{\omega_H}(1 - \beta_{\parallel} \cos \vartheta) = \frac{2\pi}{\omega_H}(1 - \beta \cos \theta \cos \vartheta) \quad (1.37)$$

where,

- ω_H the relativistic particle gyrofrequency (Eq. 1.9)
- β_{\parallel} the magnitude of the velocity vector component parallel to the magnetic field
- ϑ the angle between the magnetic field, \mathbf{H} , and the LoS
- θ the pitch angle of the emitting particle gyrating the magnetic field

In the case of highly relativistic particles, $\beta \approx 1$ and $\vartheta \approx \theta$ and Eq. 1.37 reduces to Eq. 1.8. Instead, if we consider just one more order of γ^{-1} in the calculations we get

$$T = \frac{2\pi}{\omega_H} \sin^2 \theta (1 + \psi \cot \theta) \quad (1.38)$$

where ψ the angle between the direction of the particle velocity and the LoS at the moment they are both coplanar with the magnetic field direction. This change in period is crucial since it alters all the expressions derived from that. For example, the the n th harmonic of the electric field becomes

$$\mathbf{E}_n = n \frac{e}{\sqrt{3}\pi R c} \frac{\omega_H}{\sin^5 \theta} \exp \left(i n \frac{\omega_H}{\sin^2 \theta (1 - \psi \cot \theta)} \frac{R}{c} \right) \left[\hat{\mathbf{l}} w^2 K_{2/3}(y) + i \hat{\mathbf{m}} w \left(\psi + \frac{1}{2} w^2 \right) \cot \theta K_{1/3}(y) \right] \quad (1.39)$$

where,

$$w^2 = \frac{1 + \gamma^2 \psi^2}{\gamma^2 (1 - 2\psi \cot \theta)} \quad (1.40)$$

$$y = \frac{n}{3\gamma^3 \sin^3 \theta} (1 + \gamma^2 \psi^2)^{3/2} (1 + \psi \cot \theta)^{3/2}$$

instead of Eq. 1.13. Therefore, in this case, the ellipticity of the radiation emitted by a single particle is

$$\tan b = \frac{\psi + \frac{1}{2} w^2 \cot \theta}{w} \frac{K_{1/3}(y)}{K_{2/3}(y)} \quad (1.41)$$

Eq. 1.41 contains both odd and even terms with respect to the angle ψ while Eq. 1.18 had only odd terms. This fact implies that, for the usual assumption of synchrotron emitting particle populations having an isotropic distribution velocities with respect to our line of sight (LoS), the net ellipticity will not cancel out when these particles have mildly relativistic velocities.

The even terms of ψ will add up and thus their emission will be circularly polarized to some extent. This is the major difference compared to the results of highly relativistic particles, the emission of which is circularly unpolarized due to the even cancellation of the ellipticities from particles having velocities with positive and negative ψ values (see Eq. 1.18).

Another interesting effect which increases even more the circular polarization of synchrotron emission from a particle population of mildly relativistic velocities becomes important when we consider non-uniform energy distributions. Assuming that we are observing at the critical frequency, which is close to the peak frequency of the synchrotron radiation spectrum, we can correlate the pitch angle, θ , with the velocity or energy of the emitting particles, quantified by the Lorentz factor, γ , using Eq. 1.16

$$\nu_c \propto \gamma^3 \omega_H \sin \theta = \gamma^2 \omega_g \sin \theta \quad (1.42)$$

where ω_g is the particle gyrofrequency which is constant for a given magnetic field, H . Eq. 1.42 shows that particles of small pitch angles need large γ values to contribute to the radiation at the observing frequency and vice versa. Thus, for non-uniform energy distributions, like the power law one, the number of particles with velocity vectors on either side of the LoS which contribute to the observed emission at the critical frequency is unequal, even in the case of isotropic particle velocity distributions. Therefore, there is an inexact cancellation even of the odd terms of the ellipticities in Eqs. 1.18 & 1.41 and the net circular polarization would be further increased. This effect is also applicable to particle populations of highly relativistic velocities, although less important since the range of pitch angles for the particles which contribute to the emission at a given LoS is smaller. Detailed calculations can be found in Legg and Westfold (1968) but an interesting result which worth further investigation is that the circular polarization expected from this effect is roughly about γ^{-1} of the linear polarization.

Since the electric field of a mildly relativistic particle is different from a highly relativistic one, we expect that the emission and absorption coefficients for an ensemble of such particles will also be different from the expressions we described in the previous subsection. There, we presented the emission and absorption coefficients along the two directions of the electric field components, i.e. parallel and perpendicular to the projection of the magnetic field on the plane of the sky. We can modify this description to express the coefficients in the four Stokes parameters, I, Q, U and V which provide a complete characterization for the polarization state of the emission. To do that, we need to form the polarization tensor

$$P_{ij} = \frac{c}{4\pi} (E_i E_j^*) \quad (1.43)$$

where $i, j = \hat{l}, \hat{m}$ denote the electric field components along the two orthogonal directions. According to theory, the polarization tensor is connected with the Stokes parameters through

$$P_{l\hat{m}} = \frac{c}{4\pi} \begin{bmatrix} E_{\hat{l}} E_{\hat{l}}^* & E_{\hat{l}} E_{\hat{m}}^* \\ E_{\hat{m}} E_{\hat{l}}^* & E_{\hat{m}} E_{\hat{m}}^* \end{bmatrix} = \frac{1}{2} \begin{bmatrix} I + Q & U - iV \\ U + iV & I - Q \end{bmatrix} \quad (1.44)$$

Using Eq. 1.44, we can estimate the radiated power for all Stokes parameters and subsequently follow the arguments of subsection 1.2.2 to calculate their emission and absorption coefficients. The general expressions of the coefficients for a given particle energy distribution, $N(E)$, can be found in Chapter 2 of Pacholczyk (1977). The solutions for the case of power law energy distributions are:

Emission coefficients:

$$\begin{aligned}
\varepsilon_I &= C_3(s) (H \sin \vartheta)^{(s+1)/2} [4\pi N_0 \phi(\vartheta)] \left(\frac{\nu}{2C_1} \right)^{-(s-1)/2} \\
\varepsilon_Q &= \frac{s+1}{s+7/3} \varepsilon_I \\
\varepsilon_U &= 0 \\
\varepsilon_V &= -C_5(s) (H \sin \vartheta)^{(s+2)/2} [4\pi N_0 \phi(\vartheta)] \left[(s+2) \cot \vartheta + \frac{\phi'}{\phi} \right] \left(\frac{\nu}{2C_1} \right)^{-s/2}
\end{aligned} \tag{1.45}$$

Absorption coefficients:

$$\begin{aligned}
\kappa_I &= \kappa = C_4(s) (H \sin \vartheta)^{(s+2)/2} [4\pi N_0 \phi(\vartheta)] \left(\frac{\nu}{2C_1} \right)^{-(s+4)/2} \\
\kappa_Q &= q = \frac{s+2}{s+10/3} \kappa \\
\kappa_U &= u = 0 \\
\kappa_V &= v = -C_6(s) (H \sin \vartheta)^{(s+3)/2} [4\pi N_0 \phi(\vartheta)] \left[(s+2) \cot \vartheta + \frac{\phi'}{\phi} \right] \left(\frac{\nu}{2C_1} \right)^{-(s+5)/2}
\end{aligned} \tag{1.46}$$

where,

N_0 the normalization factor of the energy distribution, $N(E) = N_0 E^{-s}$
 $\phi(\vartheta)$ the distribution of angles ϑ over which the radiation is propagated
 $C_1, C_3(s)$ and $C_4(s)$ are given in Eq. 1.26

and

$$\begin{aligned}
C_5(s) &= \frac{\sqrt{3}e^3}{12\pi s} \Gamma\left(\frac{3s+8}{12}\right) \Gamma\left(\frac{3s+4}{12}\right) \\
C_6(s) &= \frac{\sqrt{3}\pi}{54} em^6 c^{12} \left(\frac{s+3}{s+1}\right) \Gamma\left(\frac{3s+11}{12}\right) \Gamma\left(\frac{3s+7}{12}\right)
\end{aligned} \tag{1.47}$$

1.3 POLARIZED RADIATIVE TRANSFER

The next step of our investigation is to understand how the AGN jet emission is affected by the matter which lies between the emitting region and the observer, whether this is the jet itself, intergalactic plasma “screens”, our Galaxy or even Earth’s atmosphere. All these systems can potentially alter the total intensity or polarization characteristics of the propagated radiation and these effects can be studied in detail with the invaluable tool of polarized radiative transfer.

In order to study the propagation of electromagnetic radiation through a certain material, we need to solve Maxwell’s equations for a propagating electromagnetic (plane) wave into the material in study. The problem usually boils down to the determination of the permittivity tensor, which connects the electric displacement, \mathbf{D} , with the electric field, \mathbf{E} , in the material.

The media through which the radiation propagates can be both isotropic and anisotropic in terms of their permittivity. Isotropic media “react” in the same way for any orientation with respect to the direction of the propagated electric field, thus their permittivity is simplified to a scalar relation between the displacement and the electric field magnitudes, $D = \epsilon E$. In this case, the problem takes the form of simple radiative transfer since the incident radiation intensity can only be decreased due to the medium’s absorption or increased due to radiation sources present inside the medium.

In this section, we focus in the general case of anisotropic materials because the radiation of AGN jets is usually propagated through magnetoactive plasmas, i.e. plasma systems embedded in large scale magnetic fields, including the the AGN jet itself, our Galaxy and the upper layer's of Earth's atmosphere. Since the magnetic field interacts with the propagated radiation, its presence sets a preferred direction in space and renders the material anisotropic, i.e. its permittivity depends on the direction of propagation inside the material. For anisotropic media, the permittivity is a transformation tensor between the vector forms of the displacement and the propagated electric field, $\mathbf{D} = \bar{\epsilon} \mathbf{E}$.

The permittivity tensor can be derived from the generalized Ohm's law which connects the electric currents with the electric and magnetic fields which are present inside the medium. Once the permittivity tensor of the medium is known, we solve Maxwell's equations for a plane electromagnetic wave propagating through the material. In the case of magnetoactive plasmas, there are two accepted solutions which are called ordinary and extraordinary modes of propagation. These modes propagate with different speeds through the anisotropic medium which is also called birefringent.

The polarization properties of the two propagation modes depend on the direction of propagation with respect to the magnetic field of the magnetoactive medium. In the general case, they are elliptically polarized with opposite handednesses, their major axes are perpendicular to each other and the major axis of the ordinary mode is parallel to the projection of the magnetic field on the plane of the sky. A detailed derivation can be found in Chapter 3 of Pacholczyk (1977). In the context of astrophysical magnetoactive plasmas, two cases are usually considered for the propagation of electromagnetic radiation. The first is called Quasi-Longitudinal (QL) propagation approximation for which

$$\frac{u_T^2}{4u_L} \ll 1 \quad (1.48)$$

where

$$\begin{aligned} u_L &= u \cos^2 \theta && \text{is proportional to the component of the propagated electromagnetic wave} \\ &&& \text{which is parallel to the magnetic field direction} \\ u_T &= u \sin^2 \theta && \text{is proportional to the component of the propagated electromagnetic wave} \\ &&& \text{which is perpendicular to the magnetic field direction and} \\ u &= \frac{\omega_G^2}{\omega^2} && \text{relates the propagated electromagnetic wave frequency, } \omega, \text{ with the gyrofrequency, } \omega_G, \text{ in the magnetoactive plasma} \end{aligned}$$

In the QL approximation, the modes of propagation are circularly polarized with the extraordinary one rotating in the same sense as the electrons in the magnetoactive plasma. The second propagation approximation is called Quasi-Transverse (QT) and the following relation holds

$$\frac{u_T^2}{4u_L} \gg 1 \quad (1.49)$$

In the QT approximation, the modes are linearly polarized with the ordinary one being parallel to the projection of the magnetic field. The relations of Eqs. 1.48 and 1.49 are valid for an almost collisionless magnetoactive plasma and for frequencies of the propagated wave which are much larger than the plasma frequency.

The incident electromagnetic waves on the magnetoactive medium, independently of their polarization state, can be described as the sum of an ordinary and an extraordinary wave due to the fact that the two modes are orthogonally polarized. This is particularly useful for the investigation of the polarized radiative transfer through the medium because we can construct the

polarization tensor of the propagated wave using Eq. 1.44 and replacing $E_{\hat{l},\hat{m}}$ with $E_{o,e}$, where o,e denote the ordinary and extraordinary modes of the propagated radiation respectively.

Finally, the polarized radiative transfer expression can be derived by the differentiation of the resulting Stokes parameters with respect to the direction of propagation and has the general form

$$\left(\frac{1}{c} \frac{\partial}{\partial t} + \frac{\mathbf{k}}{k}\right) \begin{bmatrix} I \\ Q \\ U \\ V \end{bmatrix} = \begin{bmatrix} \varepsilon_I \\ \varepsilon_Q \\ \varepsilon_U \\ \varepsilon_V \end{bmatrix} - \begin{bmatrix} \kappa & q & 0 & v \\ q & \kappa & f & 0 \\ 0 & -f & \kappa & h \\ v & 0 & -h & \kappa \end{bmatrix} \begin{bmatrix} I \\ Q \\ U \\ V \end{bmatrix} \quad (1.50)$$

where,

- \mathbf{k} the vector along the direction of propagation
- ε_i the emission coefficient of the Stokes parameter, i with $i = I, Q, U, V$, derived from the polarization tensor
- κ, q, v the absorption coefficients of the Stokes parameters I, Q and V respectively
- f, h the propagation coefficients which alter the polarization state of the propagated radiation

The emission and absorption coefficients have been already discussed in several contexts. The propagation coefficients affect only the polarization characteristics of the radiation and their roles can be discerned from Eq. 1.50. Coefficient f is changing Stokes Q to Stokes U and vice versa, which is observed as a rotation of the electric vector position angle (EVPA) as the radiation propagates through the medium and thus it is usually called rotation coefficient. Coefficient h on the other hand transforms Stokes U to Stokes V and vice versa. This is observed as an interconversion between linear and circular polarization and this coefficient is usually called conversion coefficient.

The emission, absorption and propagation coefficients depend on the physical characteristics of the magnetoactive medium as well as the direction along which the radiation is propagated with respect to the magnetic field. It is very interesting to study these coefficients in some characteristic cases because the propagation can leave an imprint on the polarization characteristics of the emerging radiation which can then be used to infer the physical characteristics of the regions where the emission was produced or propagated through. In the following we will describe a number of such cases and discuss the information we can extract from them. A detailed description of these effects can be found in Chapter 3 of Pacholczyk (1977).

1.4 PROPAGATION EFFECTS

In this section we will examine some propagation effects that may take place when polarized radiation is propagated through magnetoactive plasma systems. These effects become evident when we solve the polarized radiative transfer equation (Eq. 1.50) using the emission, absorption and propagation coefficients, the form of which depends on the physical characteristics of the propagating medium as well as the propagation direction.

In the case of cold (thermal) magnetoactive plasma systems, i.e. systems where the particle velocities are much smaller than the speed of light, the propagation and absorption coefficients

are given by

$$\begin{aligned}
 f &= \frac{\omega_0^2 \omega_G \cos \vartheta}{c(\omega^2 - \omega_G^2)} \\
 h &= \frac{\omega_0^2 \omega_G^2 \sin^2 \vartheta}{2c\omega(\omega^2 - \omega_G^2)} \\
 \kappa &= \frac{\omega_0^2 \left[\omega^2 + \omega_G^2 - \frac{3}{2} \omega_G^2 \sin^2 \vartheta + \left(\frac{\omega_G^4 \sin^2 \vartheta}{2\omega^2} \right) \right]}{c(\omega^2 - \omega_G^2)^2} \nu_c \\
 q &= \frac{\omega_0^2 \omega_G^2 \sin^2 \vartheta (3\omega^2 - \omega_G^2)}{2c\omega^2 (\omega^2 - \omega_G^2)^2} \nu_c \\
 v &= -\frac{2\omega\omega_0^2 \omega_G \cos \vartheta}{c(\omega^2 - \omega_G^2)^2} \nu_c
 \end{aligned} \tag{1.51}$$

where,

- ω_0 the plasma frequency in the magnetoactive medium
- ω_G the particle gyrofrequency in the magnetoactive medium
- ω the frequency of the propagated electromagnetic wave
- ν_c the collision frequency in the magnetoactive medium, which can be calculated using

$$\nu_c = 3.6 \frac{N}{T^{3/2}} \left(17.7 + \ln \frac{T^{3/2}}{\nu} \right) \tag{1.52}$$

where N is the particle density and T the temperature of the magnetoactive plasma and ν the frequency of the propagated electromagnetic wave

(Pacholczyk, 1977) Combining Eqs. 1.51, 1.48 and 1.49 we can see that in the QL approximation coefficients h and q are vanishing while in the QT approximation the ones which vanish are f and v .

In the case of relativistic magnetoactive plasma systems with power law particle energy distributions of index s , the emission and absorption coefficients are already given in Eqs. 1.45 and 1.46. The propagation coefficients are given by

$$\begin{aligned}
 h &= C_7(s) \left[\left(\frac{\nu}{\nu_L} \right)^{(s-2)/2} - 1 \right] [4\pi N_0 \phi(\vartheta)] (H \sin \vartheta)^{(s+2)/2} \left(\frac{\nu}{2C_1} \right)^{-(s+4)/2} \\
 f &= C_8(s) \frac{\ln \gamma_L}{\gamma_L^{s+1}} [4\pi N_0 \phi(\vartheta)] \left(\cot \vartheta + \frac{\phi'}{\phi} \right) H \sin \vartheta \left(\frac{\nu}{2C_1} \right)^{-2}
 \end{aligned} \tag{1.53}$$

with,

$$\begin{aligned}
 C_7(s) &= -8.5 \times 10^{-3} \frac{2}{s-2} (mc^2)^{1-s} \left(\frac{e}{mc} \right)^{\frac{(s+2)}{2}} (2C_1)^{\frac{-(s+4)}{2}} \left[\left(\frac{\nu}{\nu_L} \right)^{\frac{(s-2)}{2}} - 1 \right] \\
 C_8(s) &= 1.7 \times 10^{-2} \frac{1}{s+1} (mc^2)^{1-s} \frac{e}{mc} (2C_1)^{-2}
 \end{aligned} \tag{1.54}$$

where,

- γ_L the Lorentz factor of the low energy cut-off for the particles in the magnetoactive medium
- ν_L the critical frequency of the particles with γ_L in the medium

Practically, the propagation coefficients of Eq. 1.53 are much smaller than the ones of Eq. 1.51 and become dominant only in the absence thermal plasma in the propagating medium. Under these circumstances, the polarization state of the ordinary and extraordinary modes in the magnetoactive plasma depend on ν_L . They are linearly and circularly polarized if the ν_L is large or small respectively (Pacholczyk, 1977).

Now that we have seen the form of the emission, absorption and propagation coefficients with respect to the characteristics of the magnetoactive medium and the direction of propagation, we focus on some interesting propagation effects.

1.4.1 Synchrotron Self Absorption (SSA) and polarization characteristics

First, we show the effects that occur when synchrotron radiation is propagated through the emitting medium itself. In this case, the thermal plasma is considered to be absent and for the sake of simplicity we will disregard any propagation effects due to the relativistic plasma of the source (Eqs. 1.53). Thus, we will take into account only the emission and absorption coefficients of Eqs. 1.45 and 1.46 in the polarized radiative transfer problem (Eq. 1.50) which is now formulated as

$$\begin{aligned}\frac{dI}{dz} &= \varepsilon_I - \kappa I - qQ - \nu V \\ \frac{dQ}{dz} &= \varepsilon_Q - qI - \kappa Q \\ \frac{dV}{dz} &= \varepsilon_V - \nu I - \kappa V\end{aligned}\tag{1.55}$$

where z is the direction of propagation and the equation for Stokes U is absent because $\varepsilon_U = 0$. The solutions of Eqs. 1.55 are given in Pacholczyk (1977):

$$\begin{aligned}I &= I_p + Ge^{-(\kappa-g)z} + He^{-(\kappa+g)z} \\ Q &= Q_p - \frac{q}{g}Ge^{-(\kappa-g)z} + \frac{q}{g}He^{-(\kappa+g)z} + De^{-\kappa z} \\ V &= V_p - \frac{\nu}{g}Ge^{-(\kappa-g)z} + \frac{\nu}{g}He^{-(\kappa+g)z} - \frac{q}{\nu}De^{-\kappa z}\end{aligned}\tag{1.56}$$

with,

$$\begin{aligned}g &= \sqrt{q^2 + \nu^2} \\ G &= \frac{1}{2g}[g(I_0 - I_p) - q(Q_0 - Q_p) - \nu(V_0 - V_p)] \\ H &= \frac{1}{2g}[g(I_0 - I_p) + q(Q_0 - Q_p) + \nu(V_0 - V_p)] \\ D &= \frac{\nu}{g^2}[\nu(Q_0 - Q_p) - q(V_0 - V_p)]\end{aligned}\tag{1.57}$$

and

$$\begin{aligned}I_p &= \frac{\kappa\varepsilon_I - q\varepsilon_Q - \nu\varepsilon_V}{\kappa^2 - q^2 - \nu^2} \\ Q_p &= \frac{(\kappa^2 - \nu^2)\varepsilon_Q - \kappa q\varepsilon_I + q\nu\varepsilon_V}{\kappa(\kappa^2 - q^2 - \nu^2)} \\ V_p &= \frac{(\kappa^2 - q^2)\varepsilon_V - \kappa\nu\varepsilon_I + q\nu\varepsilon_Q}{\kappa(\kappa^2 - q^2 - \nu^2)}\end{aligned}\tag{1.58}$$

where I_0 , Q_0 and V_0 are the Stokes parameters of the incident radiation.

At the two extreme cases of optically thin and thick synchrotron sources, the polarization characteristics can be described as follows. If we neglect ν and ε_V in comparison with κ , q and

$\varepsilon_I, \varepsilon_Q$ respectively, the linear polarization degree of an *optically thin* source is given by

$$\pi_L = \frac{qI_p + \kappa Q_p}{\kappa I_p + qQ_p} = \frac{\varepsilon_Q}{\varepsilon_I} = \frac{s+1}{s+7/3} \quad (1.59)$$

where s is the index of the power law particle energy distribution. In the case of an *optically thick* source ($\kappa z \gg 1$), the linear polarization degree is given by

$$\pi_L = \frac{Q_p}{I_p} = -\frac{3}{6s+13} \quad (1.60)$$

where the minus sign indicates that the linear polarization angle in the thick case is perpendicular to that of the thin case. Since we know that the major axis of the polarization ellipse for an optically thin synchrotron source is perpendicular to the projection of the magnetic field on the plane of the sky, when the same source is optically thick to its own emission, the polarization angle is parallel to that direction.

A detailed investigation of the linear polarization degree at various optical depths would show that this transition happens smoothly, which means that at a certain optical depth, τ_Q , the linear polarization degree becomes zero. This happens at a frequency, ν_Q , in the vicinity of ν_m , where the source intensity is maximized and the optical depth is τ_m . The relation that connects these quantities is

$$\frac{\nu_Q}{\nu_m} = \left(\frac{\tau_m}{\tau_Q} \right)^{2/(s+4)} \quad (1.61)$$

The circular polarization degree for an *optically thin* synchrotron source can be calculated with Eqs. 1.45

$$\pi_C = \frac{\varepsilon_V}{\varepsilon_I} = -\frac{C_5(s)}{C_3(s)} (H \sin \vartheta)^{1/2} \left[(s+2) \cot \vartheta + \frac{\phi'}{\phi} \right] \left(\frac{\nu}{2C_1} \right)^{-1/2} \quad (1.62)$$

and for an *optically thick* one it is

$$\pi_C = \frac{V_p}{I_p} = \frac{(\kappa^2 - q^2)\varepsilon_V - \kappa v \varepsilon_I + q v \varepsilon_Q}{\kappa(\kappa \varepsilon_I - q \varepsilon_Q - v \varepsilon_V)} \quad (1.63)$$

Using similar assumptions as the ones to derive Eq. 1.59, we can show that

$$\pi_C^{(\text{thick})} = -C_9(s) \cdot \pi_C^{(\text{thin})} \quad (1.64)$$

where,

$$C_9(s) = \frac{C_6(s)C_3(s)}{C_4(s)C_5(s)} - \frac{\left(s + \frac{7}{3}\right) \left[\left(s + 2^2 - \left(s + \frac{10}{3}\right)^2\right) \right]}{\left(s + \frac{10}{3}\right) \left[(s+1)(s+2) - \left(s + \frac{7}{3}\right) \left(s + \frac{10}{3}\right) \right]} \quad (1.65)$$

As we can see from Eqs. 1.62 - 1.65, there is a frequency dependence of the circular polarization degree of $\nu^{-1/2}$ in both optically thin and thick regimes. The only difference between them is the sign, i.e. the sense of rotation of the circular polarization. This change happens also gradually and at a certain frequency, ν_V , at which the optical depth is τ_V , the circular polarization degree becomes zero. At that point the following relation holds

$$\frac{\nu_V}{\nu_m} = \left(\frac{\tau_m}{\tau_V} \right)^{2/(s+4)} \quad (1.66)$$

Numerical results of $\pi_L, \tau_Q, \tau_m, \nu_Q/\nu_m$ and ν_V/ν_m for various values of the index s can be found in Table 3.1 of Pacholczyk (1977).

1.4.2 Faraday rotation

For the next case we will consider the propagation of an electromagnetic wave in a cold magnetoactive plasma medium under the QL propagation approximation. As we show above, under this approximation the coefficients h and q are vanishing. If we focus only on linear polarization, the polarized radiative transfer problem 1.50 takes the form

$$\begin{aligned}\frac{dI}{dz} &= \varepsilon_I - \kappa I \\ \frac{dQ}{dz} &= \varepsilon_Q - \kappa Q - fU \\ \frac{dU}{dz} &= -\kappa U + fQ\end{aligned}\tag{1.67}$$

the solution of which is

$$\begin{aligned}I &= \varepsilon_I z + I_0 \\ Q &= \left(U_0 + \frac{\varepsilon_Q}{f}\right) \sin 2\eta + Q_0 \cos 2\eta \\ U &= \left(U_0 + \frac{\varepsilon_Q}{f}\right) \cos 2\eta - Q_0 \sin 2\eta - \frac{\varepsilon_Q}{f}\end{aligned}\tag{1.68}$$

where $\eta = \frac{1}{2}fz$. When we neglect the emission within the medium and consider only the absorption and propagation coefficients the linear polarization degree remains unchanged while the polarization angle rotates during the propagation. The amount of rotation is $\chi = 2\eta = fz$ and this quantity is proportional to

$$\chi = fz \propto N_c H_{\parallel} z \nu^{-2}\tag{1.69}$$

where,

- N_c the particle number density in the propagating medium
- H_{\parallel} the magnetic field component of the magnetoactive medium parallel to the line of sight
- ν the observed frequency

This effect is known as *Faraday rotation*.

Assuming that the radiation is emitted at various depths, z , of the propagating medium, the different amounts of rotation for various depths can decrease the net linear polarization degree of the emerging radiation. We can evaluate this depolarization effect if we assume no incident radiation to the medium, i.e. $I_0 = Q_0 = U_0 = 0$. Under this assumption and using Eqs. 1.68 we get:

$$\pi_L = \frac{\varepsilon_Q}{\varepsilon_I} \left| \frac{\sin \eta}{\eta} \right|\tag{1.70}$$

which gives the net linear polarization degree as a function of the quantity η , also known as *Faraday rotation depth*.

1.4.3 Faraday pulsation

We now consider the propagation of an electromagnetic wave through a cold plasma region under the QT propagation approximation. Under this approximation, the coefficients f and ν vanish and assuming that the emission coefficients for Stokes V and U are consistent with

zero, the polarized radiative transfer problem (Eq. 1.50) is formulated as

$$\begin{aligned}\frac{dI}{dz} &= \varepsilon_I - \kappa I - qQ \\ \frac{dQ}{dz} &= \varepsilon_Q - qI - \kappa Q \\ \frac{dU}{dz} &= -\kappa U - hV \\ \frac{dV}{dz} &= hU - \kappa V\end{aligned}\tag{1.71}$$

The last two expressions in Eq. 1.71 are coupled and the solution for Stokes U and V yields

$$\begin{aligned}U &= [U_0 \cos(hz) - V_0 \sin(hz)]e^{-\kappa z} \\ V &= [U_0 \sin(hz) + V_0 \cos(hz)]e^{-\kappa z}\end{aligned}\tag{1.72}$$

If we assume also no absorption in the propagating medium ($\kappa = q = 0$), the first two expressions of Eq. 1.71 acquire the simple solutions

$$\begin{aligned}I &= I_0 + \varepsilon_I z \\ Q &= Q_0 + \varepsilon_Q z\end{aligned}\tag{1.73}$$

The previous set of equations reveal a very interesting phenomenon. As it is shown in the expressions below, the position angle, χ , and the ellipticity, δ , of the polarization ellipse “oscillate” with respect to the propagated depth, z , in a coupled manner:

$$\begin{aligned}\tan 2\chi &= \frac{U}{Q} = \frac{U_0 \cos(hz) - V_0 \sin(hz)}{Q_0 + \varepsilon_Q z} \\ \sin 2\delta &= \frac{V}{I} = \frac{U_0 \sin(hz) + V_0 \cos(hz)}{I_0 + \varepsilon_I z}\end{aligned}\tag{1.74}$$

If the propagated emission is initially linearly polarized and there is no emission within the propagating medium, we need to set V_0 , ε_Q and ε_I to zero in the above expressions. In this case, the position angle, χ , and the ellipticity, δ , oscillate interchangeably between two extreme values of χ_0 and $-\chi_0$. If the emission coefficients of the medium are not equal to zero, these oscillations gradually fade out as the radiation is propagated through it.

If the propagated emission is initially circularly polarized, we can set Q_0 , U_0 to zero and $V_0 = I_0$ in Eqs. 1.74 which now take the form

$$\begin{aligned}\tan 2\chi &= -\frac{I_0}{\varepsilon_Q z} \sin(hz) \\ \sin 2\delta &= \frac{I_0}{I_0 + \varepsilon_I z} \cos(hz)\end{aligned}\tag{1.75}$$

In this case the emission changes from circular to linear with position angle $\chi = 45^\circ$ and back to circular as it propagates. If the emission coefficients are non-zero, these transformations gradually fade out. The effect we describe can generate circular from linear polarization and vice versa, keeping the total polarization degree (linear and circular) constant. This effect is called *Faraday pulsation*. As we saw from Eqs. 1.74, the effect needs a non-zero U_0 to occur. This happens when the linear polarization angle of the incident radiation is neither parallel nor perpendicular to the magnetic field of the medium but at an intermediate value. The effects maximize when this angle is 45° with respect to the magnetic field direction. Thus, a synchrotron source cannot cause Faraday pulsation on its own emission since it is linearly polarized either perpendicular or parallel to the magnetic field in the optically thin and thick cases respectively.

1.4.4 Circular repolarization

This effect produces circular polarization during the propagation when the propagating medium contains both thermal and low-energy relativistic particles. The latter should be at an adequately low energy level, γ_L , that makes the coefficient f of Eq. 1.53 significant. If we neglect the propagation coefficients of the relativistic particles in the polarized radiative transfer problem and consider the QL approximation, the circular polarization degree in the optically thin case of strong Faraday rotation ($f \gg \kappa$) is given by Pacholczyk (1977):

$$\pi_C = \frac{\varepsilon_V}{\varepsilon_I} - \frac{\varepsilon_Q}{\varepsilon_I} \frac{h}{f} \left[1 - \frac{\sin(fz)}{fz} \right] \quad (1.76)$$

where,

$$h = C(s, \gamma_L) N_r (H \sin \vartheta)^{-1} \quad (1.77)$$

$$f = f_c + f_r = -5 \times 10^4 (N_c + N_r \frac{s-1}{s+1} \frac{\ln \gamma_L}{\gamma_L^2} \cot \vartheta) \frac{H \sin \vartheta}{\nu^2}$$

the subscripts c and r denote the cold and relativistic components of the magnetoactive medium respectively and $N_{c,r}$ are their particle densities.

In the described setup, the circular polarization of Eq. 1.76 has three components. The first one is the result of the circularly polarized emission coefficient, ε_V , which may be present from the synchrotron emitting particles in the medium. The second and third terms of Eq. 1.76 describe the circular repolarization effect. For $fz \geq 3$, the third term can be neglected and the circular polarization, assuming $\varepsilon_V = 0$ and $s = 2$ is calculated as

$$\pi_C = 2.6 \times 10^7 \ln \left(\frac{\nu}{\nu_L} \right) N_r H_{\perp}^{3/2} f^{-1} \left(\frac{\nu}{\nu_L} \right)^{-1/2} \nu^{-5/2} \quad (1.78)$$

where,

$$f = 5 \times 10^4 \left[N_c + 7 \times 10^5 N_r \left(\ln \frac{\nu_L}{H_{\perp}} - 15 \right) \frac{H_{\parallel}}{\nu_L} \right] \frac{H_{\perp}}{\nu^2} \quad (1.79)$$

In general the frequency dependence of the circular polarization degree produced with this effect is steeper than $\nu^{-1/2}$ and for $s \geq 1$, it is ν^{-1} . Additionally, the circular polarization degree produced in this way should not be correlated with the linear polarization degree. In comparison, we described above that in the case of a synchrotron source of mildly relativistic emitting particles without the presence of thermal plasma, the observed circular polarization degree should be correlated with the linear polarization degree according to $\pi_C = \gamma^{-1} \pi_L$ (subsection 1.2.5). These theoretical prediction can be compared against observational data to examine the physical characteristics of the emitting and/or propagating media.

1.5 FROM THE SOURCE TO THE OBSERVER'S REST FRAME

The results discussed above are expected to be observed at the rest frame of the emitting region. There are two major parameters though that affect the observed characteristics. The first is the relativistic motion of the emitting region in the AGN jet itself and the second is the vast distance that the radiation has to travel before it reaches the observer. Both of them introduce a number of effects that need to be taken into account for the interpretation of the measured quantities. These effects are caused by the relativistic light aberration, time dilation as well as the relativistic and classical Doppler effects. In the following we describe how the measured physical parameters are affected by these effects.

Frequency

The observed frequency is different from the emitted one due to two main reasons. The first one is the relativistic Doppler effect in the case that the emitting region is moving at high velocities. This acts like

$$f_o = \frac{f_e}{\gamma(1 - \beta \cos \phi)} f_e = D f_e \quad (1.80)$$

where,

- $f_{o,e}$ the observed and the emitted frequency of the radiation
- ϕ the angle between the velocity vector of the emitting region and the line of sight
- D the Doppler factor of the emitting region

The second one is the classical Doppler effect due to the source's redshift which acts like

$$f_o = (z + 1)f_e \quad (1.81)$$

where,

- z the redshift of the source

Total and polarized intensities

The intensity is expected to be boosted by the relativistic beaming effect which acts as

$$S_o = S_e D^{3-\alpha} \quad (1.82)$$

where,

- $S_{o,e}$ the observed and the emitted (polarized) intensity of the source
- α the spectral index of the source's SED

Electric vector position angle (EVPA)

The effect expected to modify the observed EVPA is the relativistic aberration. The light rays bend towards the direction of the (relativistic) motion and the emitted EVPA may be dragged by them from its original position. Ignoring this effect may lead to misunderstandings. For example we discussed earlier that in the synchrotron self-absorbed (SSA) case, the EVPA is parallel or perpendicular to the projection of the magnetic field on the plane of the sky. However, this holds true only at the source rest frame. In the observer's frame the EVPA is shifted preventing us to draw the magnetic field orientation without additional knowledge.

The effect of relativistic aberration on EVPA has been studied for a variety of emitting region setups, including various for relativistic AGN jets (Blandford, R. D.; Königl, 1979; Lyutikov et al., 2003, 2005). According to these studies, the prediction for the EVPA shift from its initial position at the rest frame *requires in general knowledge of the velocity vector of the emitting region as well as its magnetic field vector*. For example Blandford, R. D.; Königl (1979) calculate that

$$\tan \xi = \frac{\cos \psi [\beta - \cos \theta (1 - \tan \psi \tan \theta)]}{\tan \eta (\beta - \cos \theta - 1)} \quad (1.83)$$

with the related angles shown in Fig. 1.7

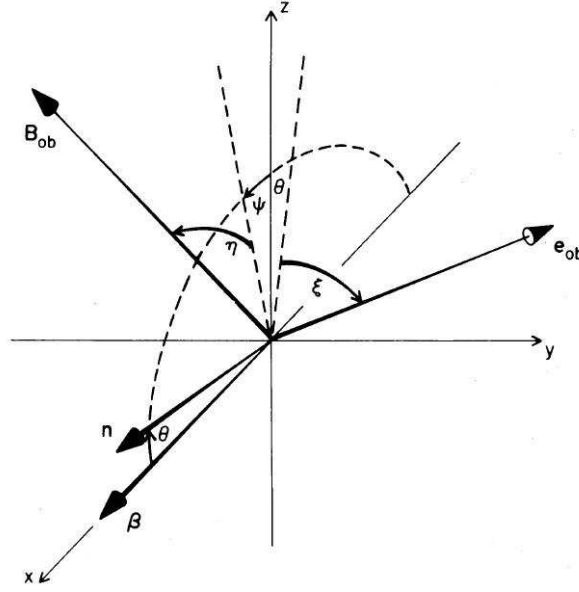


Figure 1.7: The relativistic aberration effect and the modification of the EVPA. Figure taken from Blandford, R. D.; Königl (1979).

Another relation is given in Appendix C of Lyutikov et al. (2003), where they calculate the Lorentz transformation of EVPA. According to their calculations

$$\hat{e} = \frac{\mathbf{n} \times \mathbf{q}}{\sqrt{q^2 - (\mathbf{n} \cdot \mathbf{q})^2}} \quad (1.84)$$

$$\mathbf{q} = \hat{\mathbf{B}} + \mathbf{n} \times (\mathbf{v} \times \hat{\mathbf{B}})$$

where,

- \hat{e} the unit vector along the EVPA direction
- \mathbf{n} the vector along the line of sight
- $\hat{\mathbf{B}}$ the unit vector along the magnetic field direction
- \mathbf{v} the velocity vector of the emitting region

and all quantities are referring to the observer frame. The above relations show that the velocity vector of the emitting region (or flow) is needed in order to correctly interpret the data and infer the magnetic field direction from the measured EVPA.

Linear and circular polarization degree

Both the total and the polarized flux density are subject to the same effects. Furthermore, these effects are usually multiplicative and hence we expect that for the polarization degree, which is calculated as their ratio, they would cancel out. Thus, the polarization degree we observe is most likely the same as the rest frame. There may however be cases that this simplistic interpretation does not hold. One such case could be the relativistic light aberration which would rotate different parts of the jet we observe (different \mathbf{n} 's according to Eq. 1.84) for different angles. This may cause a depolarization to the observed degree as compared to the emitted one.

Another effect may be that the nominator and the denominator in the degree calculation have come from regions with different intrinsic speeds and thus different Doppler factors. This

would cause also a difference between the observed and emitted degrees. In any case all these effects are worth a more detailed investigation.

Time

Assuming that the emitting region is moving relativistically towards the observer, the time scales are compressed for the latter. This change though is not expected to cause a misinterpretation since all lightcurves (total flux, polarization degree, EVPA, etc.) are squeezed the same way. So the events are much shorter in the observer's frame but no time shift between e.g. total flux and polarization is expected to be introduced.

Chapter 2

High precision, full-Stokes radio polarimetry

Abstract

In this chapter we describe the methodology we have developed for high-cadence, high-precision linear and circular radio polarimetry, using the data obtained with the 4.85-GHz secondary focus receiver of the 100-m Effelsberg telescope. Furthermore, the methodology was successfully applied to the 8.35-GHz receiver data. These systems are equipped with circularly polarized feeds and hence the details of our methodology are immediately applicable to this type of receivers. The general conclusions can be easily generalized to telescopes with linearly polarized feeds.

2.1 THE METHOD

The polarization characteristics of an electromagnetic wave are fully described by its Stokes 4-vector,

$$S = \begin{bmatrix} I \\ Q \\ U \\ V \end{bmatrix} \quad (2.1)$$

where,

I the total intensity of the radiation
 Q and U describe the linear polarization characteristics. The linearly polarized intensity Π_L and the electric vector position angle (hereon EVPA or χ):

$$\Pi_L = \sqrt{Q^2 + U^2}, \chi = \frac{1}{2} \arctan\left(\frac{U}{Q}\right) \quad (2.2)$$

The reference frame we adopt for measuring EVPA angles is the one defined by the North and East (N-E) directions. Positive angles are measured counter clock-wise (CCW) and negative clock-wise (CW) (Saikia and Salter, 1988)

V describes the circular polarization characteristics. Its modulus is the circularly polarized intensity, Π_C , and its sign defines the sense of rotation or handedness. For this work, we adopt the positive V sign for the left-handed circularly polarized radiation.

A polarimetric device provides a set of Stokes parameters which, unless corrected automatically, are different from the incident ones due to two main reasons:

1. *The misalignment of the device reference frame with respect to the absolute one (N–E direction).* For example, in the case of a telescope oriented at a certain celestial position, the measured EVPA would be rotated by the angle between the telescope's Stokes Q – U reference frame and the default N–E reference frame. This angle depends on the telescope's mounting design. For alt-azimuthally mounted telescopes, it is equal to $2q$, where q is the parallactic angle of the source at the time of the observation. For equatorially mounted telescopes, on the other hand, the EVPA reference frame is always aligned with the N–E one and no correction is needed. Conventionally, this rotation is formulated in terms of a matrix \mathbf{R} (see Eq. 2.3).
2. *The device's response to the incident Stokes parameters.* Any device used for the detection of electromagnetic waves introduces some instrumental polarization. The instrumental polarization depends on a number of parameters like the mechanical and/or electrical design of the device or the level of symmetry in the signal path. It can be fully described with a 4x4 matrix, which acts as a transfer function between the incident and the measured Stokes 4-vector and is called Müller matrix.

The expression that describes both effects can be written as:

$$S_{\text{obs}} = \mathbf{M} \cdot \mathbf{R} \cdot S_{\text{real}} \quad (2.3)$$

where,

- S_{obs} are the measured Stokes parameters
- \mathbf{M} is the device's Müller matrix
- \mathbf{R} is a rotation matrix for the angle between the telescope's Q - U reference frame and the N-E one and
- S_{real} are the incident Stokes parameters

In the following sections, we will examine the different parts of Eq. 2.3 for telescopes with circularly polarized feeds and describe a data reduction pipeline that minimizes the effect of systematic errors, resulting in high-precision linear and circular polarization measurements.

2.2 THE \mathbf{R} MATRIX

The \mathbf{R} matrix is necessary to express all the observed Stokes Q and U parameters to a common reference frame in order to compare them. For alt-azimuthally mounted telescopes the rotation matrix is given by:

$$\mathbf{R} = \begin{bmatrix} 1 & 0 & 0 & 0 \\ 0 & \cos 2q & \sin 2q & 0 \\ 0 & -\sin 2q & \cos 2q & 0 \\ 0 & 0 & 0 & 1 \end{bmatrix} \quad (2.4)$$

where q is the parallactic angle of the source at the time of the observation.

Parallactic rotation of the measured Stokes Q and U

In order to study the behavior of the \mathbf{R} matrix independently, we will consider the ideal case of an alt-azimuthally mounted telescope which does not alter the polarization characteristics of the incident radiation otherwise, i.e. its Müller matrix is reduced to the unity matrix and Eq. 2.3 is reduced to

$$S_{\text{obs}} = \mathbf{R} \cdot S_{\text{real}} \quad (2.5)$$

or

$$\begin{bmatrix} I_{\text{obs}} \\ Q_{\text{obs}} \\ U_{\text{obs}} \\ V_{\text{obs}} \end{bmatrix} = \begin{bmatrix} 1 & 0 & 0 & 0 \\ 0 & \cos 2q & \sin 2q & 0 \\ 0 & -\sin 2q & \cos 2q & 0 \\ 0 & 0 & 0 & 1 \end{bmatrix} \cdot \begin{bmatrix} I_{\text{real}} \\ Q_{\text{real}} \\ U_{\text{real}} \\ V_{\text{real}} \end{bmatrix} \quad (2.6)$$

Equation 2.6 shows that the measured Stokes I and V are not affected by the \mathbf{R} matrix. Stokes Q and U on the other hand change according to:

$$\begin{aligned} Q_{\text{obs}} &= \cos 2q \cdot Q_{\text{real}} + \sin 2q \cdot U_{\text{real}} \\ U_{\text{obs}} &= -\sin 2q \cdot Q_{\text{real}} + \cos 2q \cdot U_{\text{real}} \end{aligned} \quad (2.7)$$

The parallactic angle of a source changes continuously while it is being tracked on the sky (Fig. 2.1) and its value depends on the telescope's latitude ϕ , the source's declination, δ and the source's hour angle H at the time of the observation as:

$$q = \arctan \left(\frac{\sin H \cos \phi}{\sin \phi \cos \delta - \cos \phi \sin \delta \cos H} \right) \quad (2.8)$$

This change affects the measured Stokes Q and U in accordance with Eq. 2.7. Since every measurement has a finite duration, the Stokes Q and U change during the integration. This effect will be transferred to the final uncertainty of the measurement. Thus, it is important to account for this factor in order to fine-tune the observing strategy and estimate the final uncertainty of the measured Stokes parameters Q and U . One way for example is to minimize the measurement integration. It is clear that shorter measurement durations result to better accuracy of the measured Stokes parameters Q and U . In Fig. 2.2 for example, we show simulated absolute differences in the measured Stokes Q (circles) and U (triangles) between the beginning and the end of a measurement for two different measurement durations and a source with declination $\delta = 40^\circ$ observed from the Effelsberg 100-m Radio Telescope (latitude, $\phi = 50^\circ 31' 29''$). In this example, the simulated data were generated for a source with $Q_{\text{real}} = U_{\text{real}} = 1$, so the plotted values in Fig. 2.2 represent also the fractional absolute differences in the Stokes Q and U measurements which have a maximum of 7.6% for a measurement duration of $\Delta t = 120$ s and 1.9% for a shorter integration of $\Delta t = 30$ s.

Correcting Stokes Q and U measurements obtained with the cross-scan observing mode

All the observations shown here were conducted with the Effelsberg 100-m Radio Telescope employing the “cross-scan” observing mode. The telescope scans over the targeted source for a number of cycles (sub-scans) in the azimuth and elevation directions. The duration of each sub-scan was tuned to 30 s, which means that the total measurement (scan) duration was $N \cdot 30$ s with N the number of sub-scans.

Traditionally, it is the mean parallactic angle over the scan that has been used as input for the \mathbf{R} matrix. According to the above analysis, this approach ignores the change of Stokes Q and U throughout the scan, resulting in an increase of the final uncertainties. This effect becomes more significant as the number of the subscans increases. The approach we follow in the current work is

1. rotate the measured Stokes Q and U of each subscan using its own “instantaneous” parallactic angle and
 2. calculate the final Stokes Q and U by averaging the rotated parameters of all subscans
- This way we eliminate the contribution of the parallactic angle to the parameter uncertainty achieving a better accuracy of our measurements.

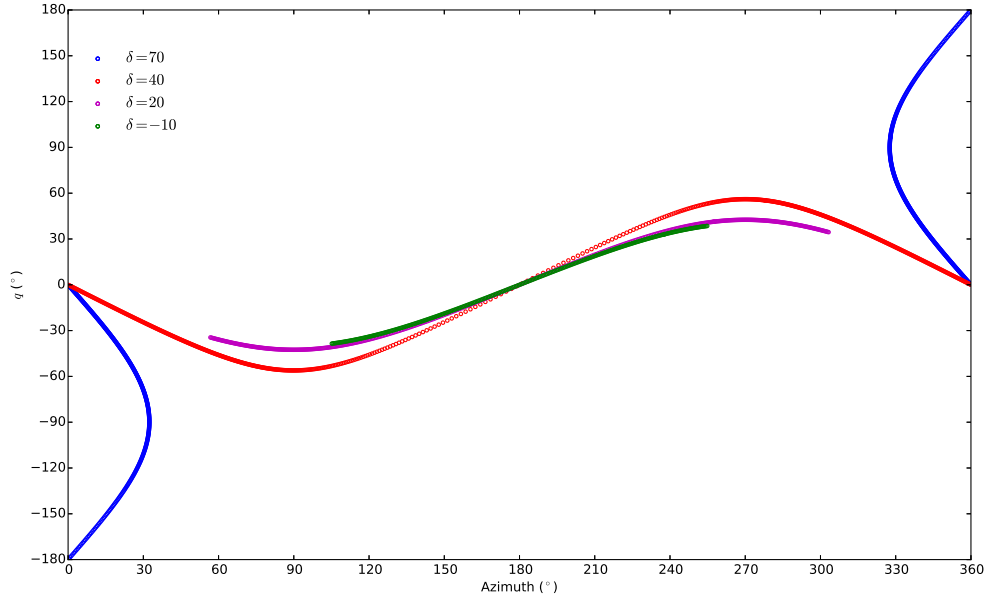


Figure 2.1: The parallactic angle, q , as a function of azimuth for the Effelsberg 100-m Radio Telescope for sources with different declinations, δ .

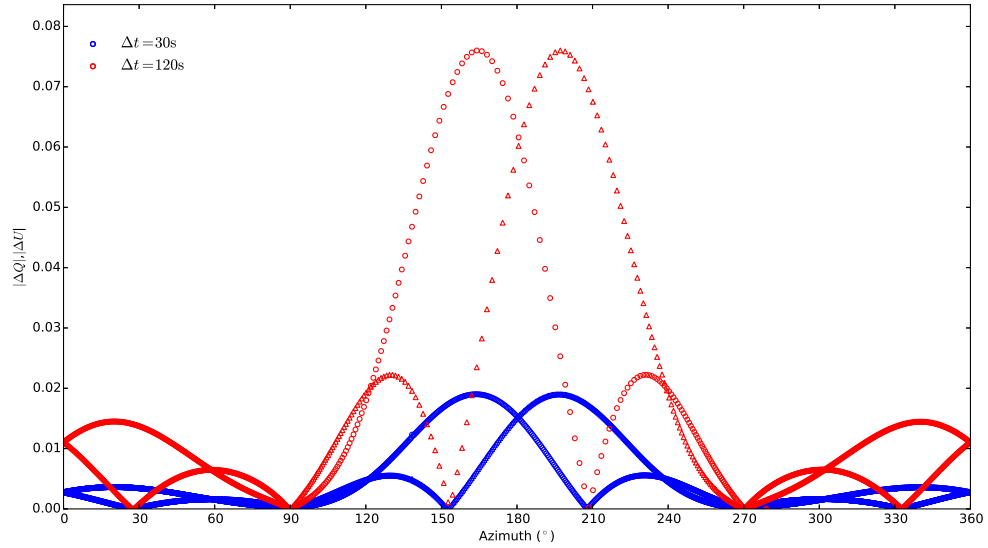


Figure 2.2: Simulated absolute differences in the measured Stokes Q (circles) and U (triangles) between the beginning and the end of a measurement for two different measurement durations, Δt . The simulations were generated with $\delta = 40^\circ$ and $\phi = 50^\circ 31' 29''$.

An example. For 20 consecutive 30-second sub-scans of the polarized source 3C 286 using the Effelsberg 100-m telescope at $q \simeq 16^\circ.5$, the fractional absolute difference was measured to be 10.6% for Stokes Q and 13.7% for Stokes U . Simulations under the same conditions yield a fractional absolute difference of 13.1% for Stokes Q and 13.6% for Stokes U . Considering the total length of the 20 subscans as a single measurement, the major contribution to the Stokes Q and U uncertainties would come from the Q and U variations as the parallactic angle of the source changes during the scan, a factor which can be corrected for using the above methodology. After this correction, the scatter of the Stokes Q and U measurements reduced to 9.7% peak-to-peak for Stokes Q and 6.1% peak-to-peak for Stokes U .

2.3 THE M MATRIX

The path of the incident radiation is interrupted by the telescope's optical elements which change the wavefront of the incident radiation redirecting it to the polarimetric detector. Each redirection modifies the polarization characteristics of the radiation and the change can be described by a 4x4 transformation matrix between the Stokes 4-vectors, before and after the interruption, as it was discussed in Eq. 2.3. The matrices of ideal optical elements can be estimated theoretically by the methods of Müller calculus. Finally, the net effect of all matrices on the incident radiation is calculated as their product, a 4x4 matrix enclosing all instrumental effects within its elements, the Müller (or **M**) matrix.

M matrix element description

Once the incident and the measured Stokes parameters have been rotated to a common reference frame, using the **R** matrix (section 2.2), Eq. 2.3 can be reduced to

$$S_{\text{obs}} = \mathbf{M} \cdot S_{\text{rot}} \quad (2.9)$$

where S_{rot} , in this example, are the rotated incident Stokes parameters. Equation 2.9 can be rewritten as

$$\begin{bmatrix} I_{\text{obs}} \\ Q_{\text{obs}} \\ U_{\text{obs}} \\ V_{\text{obs}} \end{bmatrix} = \begin{bmatrix} m_{II} & m_{IQ} & m_{IU} & m_{IV} \\ m_{QI} & m_{QQ} & m_{QU} & m_{QV} \\ m_{UI} & m_{UQ} & m_{UU} & m_{UV} \\ m_{VI} & m_{VQ} & m_{VU} & m_{VV} \end{bmatrix} \cdot \begin{bmatrix} I_{\text{rot}} \\ Q_{\text{rot}} \\ U_{\text{rot}} \\ V_{\text{rot}} \end{bmatrix} \quad (2.10)$$

where m_{ij} ($i, j = I, Q, U, V$) are the elements of the Müller matrix.

The representation of Eq. 2.10 shows how the different Müller matrix elements connect the incident and the measured Stokes parameters. In this notation, part of the radiation intensity which reaches the telescope as Stokes parameter j is measured as Stokes i intensity and the Müller matrix element m_{ij} provides a quantitative description of this cross-talk. The elements can be described qualitatively as follows:

m_{II}	Stokes I efficiency
m_{VV}	Stokes V efficiency
$m_{QQ}, m_{QU}, m_{UQ}, m_{UU}$	Instrumental rotation matrix
m_{IQ}, m_{IU}	Linear depolarization
m_{IV}	Circular depolarization
m_{VQ}, m_{VU}	Linear to circular polarization conversion
m_{QV}, m_{UV}	Circular to linear polarization conversion
m_{QI}, m_{UI}	Spurious linear polarization
m_{VI}	Spurious circular polarization

M matrix correction

In order to correct the measured Stokes parameters for instrumental effects, it is crucial to determine the complete set of parameters m_{ij} . There are two major schools of thought for the solution of this problem. The first treats the problem step by step. One should study the radiation path in the instrument in detail, find all the interruptions from the moment the radiation reaches the telescope until it is recorded, study their transformation matrices and calculate their product, i.e. the Müller matrix.

The second approach utilizes sources of radiation of which the incident polarization characteristics S_{real} are known independently, i.e. polarization calibrators. First the calibrators are observed as if they were targets. After performing at least four such measurements the system of equations 2.10 can be determined and one can estimate the elements of the Müller matrix. In case more measurements are available a fit can determine even better the elements of the matrix. That is the approach we follow in this work.

The set of main polarization calibrators we have used are given in Table 3.2 along with their reference polarization characteristics at 4.85 and 8.35 GHz. The circular polarization degrees, m_c , reported in Table 3.2 have been extracted from a large part of our dataset of monthly measurements over the last 4.5 years (see also Sect. 3.3).

Müller matrix of the 4.85-GHz secondary focus Effelsberg receiver

We performed the fitting approach described above to estimate the Müller matrix of this system for each of the 59 consecutive monthly observing sessions we analyzed. This was done to eliminate possible fluctuations of the Müller matrix elements as a source of uncertainty in our Stokes parameter measurements. Most of the Müller matrix elements remained stable over this period as shown in Fig. 2.3.

Using the most significant ($\geq 3\sigma$) results of the fitted Müller matrix elements, we can write down a representative matrix which describes the average behavior of the 4.85 GHz receiver of the Effelsberg telescope over this period. This representative Müller matrix is

$$\begin{bmatrix} 0.846 \pm 0.019 & -0.064 \pm 0.214 & 0.056 \pm 0.385 & 2.607 \pm 2.428 \\ -0.002 \pm 0.003 & 0.853 \pm 0.018 & -0.085 \pm 0.036 & -0.170 \pm 0.552 \\ 0.000 \pm 0.002 & 0.058 \pm 0.010 & 0.841 \pm 0.044 & 0.235 \pm 0.295 \\ -0.008 \pm 0.003 & -0.015 \pm 0.020 & -0.021 \pm 0.008 & 0.876 \pm 0.251 \end{bmatrix} \quad (2.11)$$

This **M** matrix is a very useful result of our analysis because it can be used directly to correct Stokes parameter measurements, performed with this system, for instrumental polarization as well as express them in physical units (see also Sect. 3.2.1).

2.4 THE MEASURED STOKES VECTOR

The last step needed to calculate in detail the incident Stokes parameters, S_{real} , using Eq. 2.3, is the extraction of the measured Stokes parameters, S_{obs} , from the available datasets. The methodology described below was developed using datasets obtained with the 4.85 GHz receiver, located at the secondary focus of the 100-m Effelsberg telescope, but it can easily be generalized for any receiver equipped with circularly polarized feeds. For the sake of fluency, the section has been split into the following subsections:

1. Stokes parametrization for circularly polarized feeds
2. Extracting the observables
3. Cross-channel calibration
4. Corrections
5. Stokes Q and U instrumental artifacts

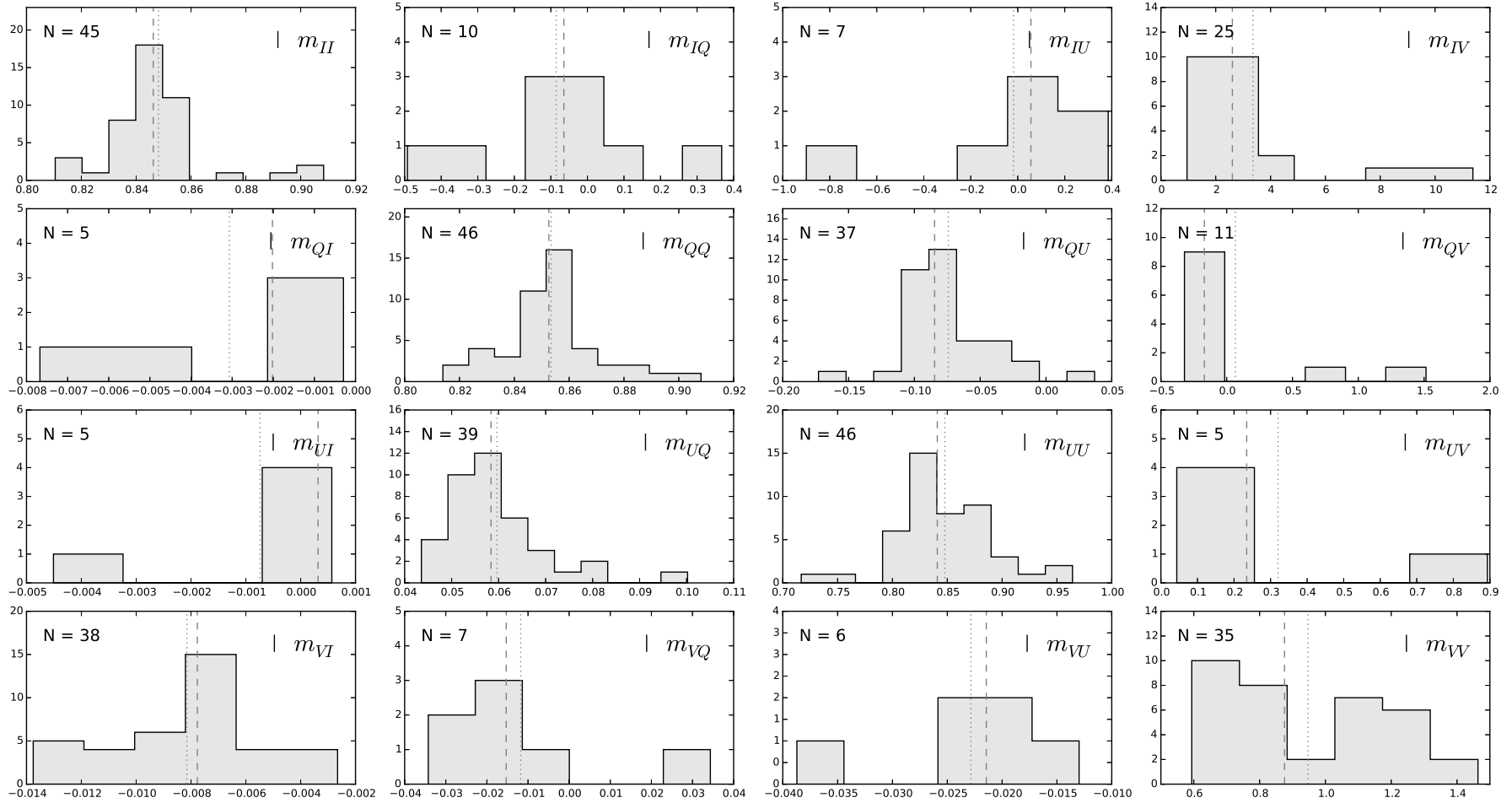


Figure 2.3: The Müller matrix element histograms. The data acquisition and reduction is described in the text. The median and average values are indicated by the dashed and dotted vertical lines respectively.

2.4.1 Stokes parametrization for circularly polarized feeds

Telescopes with circularly polarized feeds record the left and right-handed circularly polarized electric field components of the incident radiation, E_l and E_r , respectively. The Stokes parametrization with a circularly polarized orthogonal base is given by:

$$\begin{aligned} I &= \langle E_l^2 \rangle + \langle E_r^2 \rangle \\ Q &= 2 \langle E_l \rangle \langle E_r \rangle \cos \theta \\ U &= 2 \langle E_l \rangle \langle E_r \rangle \sin \theta \\ V &= \langle E_l^2 \rangle - \langle E_r^2 \rangle \end{aligned} \quad (2.12)$$

where θ is the phase difference between E_l and E_r and $\langle \rangle$ denotes the averages of the enclosed quantities in time.

Eq. 2.12 shows that Stokes I and V can be calculated as the sum and difference of the radiation intensities, recorded by the Left and Right (LCP and RCP) Circular Polarization channels of the receiver, $\langle E_l^2 \rangle$ and $\langle E_r^2 \rangle$, respectively. Stokes Q and U , on the other hand, are measured directly by correlating the LCP and RCP electric field components of the incident radiation in the receiver's (correlation) polarimeter. The only difference between the latter two is the introduction of a 90° phase delay between E_l and E_r to measure Stokes U (Turlo et al., 1985).

This parametrization favors linear polarization measurements. Stokes Q and U are measured through a correlation process, and thus they are less affected by noise-like, uncorrelated components which may be present in the LCP and RCP signals. Stokes V , on the other hand, is usually the difference of two very little – if at all – different numbers because celestial sources are generally weakly circularly polarized. This makes the measurement of circular polarization with circularly polarized feeds extremely challenging. The Stokes parametrization which favors circular polarization measurements is the one having a linearly polarized orthogonal base, for which the Stokes V is measured by a correlation operation. Thus, telescopes equipped with linearly polarized feeds are optimized for circular polarization measurements.

Channel nomenclature

The Effelsberg telescope records the polarization characteristics in four channels following the formalism of Eq. 2.12. The left and right-handed circularly polarized components are recorded by the LCP and RCP channels of the receiver and the linearly polarized part of the radiation is recorded by channels labeled as COS and SIN. The COS and SIN channels form an orthogonal base which is rotated by ϕ degrees with respect to the Q – U reference frame. The COS and SIN data can be transferred to the Q and U domain using

$$\begin{pmatrix} Q \\ U \end{pmatrix} = \begin{pmatrix} \cos \phi & -\sin \phi \\ \sin \phi & \cos \phi \end{pmatrix} \cdot \begin{pmatrix} \text{COS} \\ \text{SIN} \end{pmatrix} \quad (2.13)$$

This channel nomenclature will be adopted from here on.

2.4.2 Extracting the observables

The cross-scan observing method

The data of this work have been obtained using the cross-scan technique which can be described as follows: After moving to the commanded celestial coordinates, the telescope scans over the source in two perpendicular directions, e.g. over azimuth and elevation, for a number of cycles (sub-scans). During each sub-scan, the system is recording the incident power in all polarization channels (LCP, RCP, COS and SIN) at a cadence of 64 ms. Thus, the recorded datasets consist of pairs of counts and positional coordinate (offset) from the center of the cross-scan, i.e. the assumed position of the source.

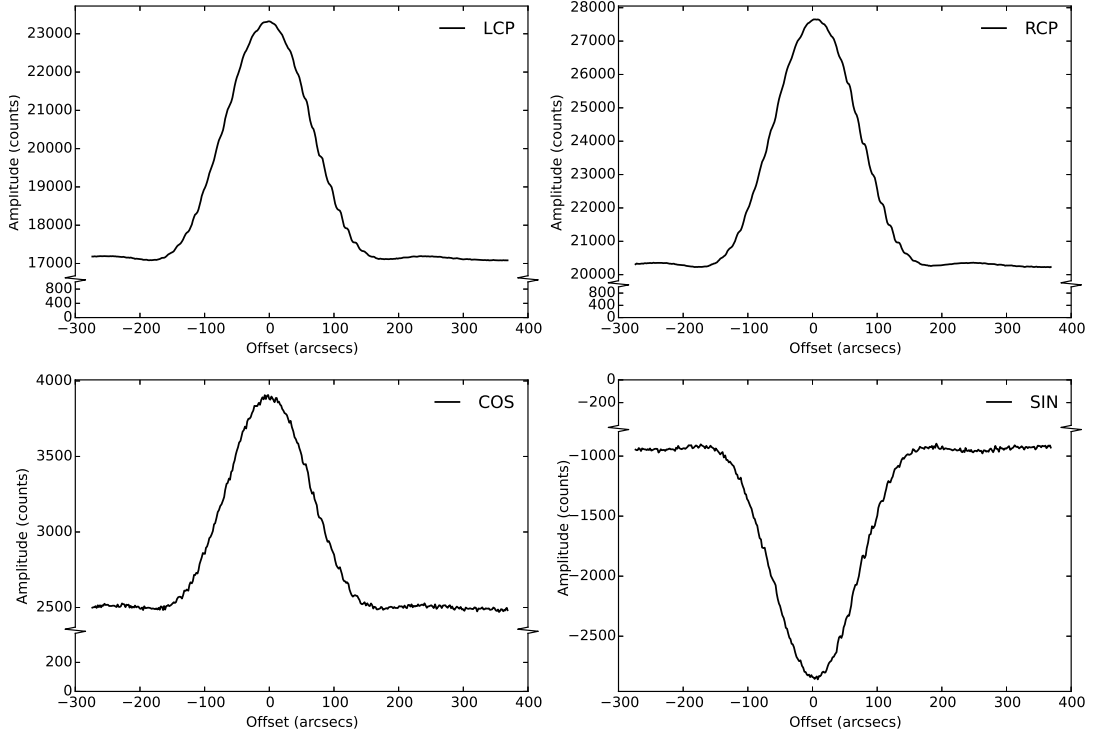


Figure 2.4: Example of the same sub-scan in all channels obtained with the 4.85 GHz receiver of the 100-m Effelsberg telescope. The LCP and RCP channel datasets are shown in the upper row while the COS and SIN datasets in the lower row.

According to antenna theory, the series of data points of each sub-scan comprise the convolution of the antenna pattern and the source brightness distribution over the subscan path. In the case of point sources the latter is a δ function with an amplitude equal to the source power in a certain polarization mode, on top of an (ideally constant) background emission level. That background emission has several constituents like the atmospheric emission, the receiver noise level, CMB, etc. The recorded power then have the form of the antenna pattern, normalized to the source power, on top of a background emission.

Datasets recorded with the LCP, RCP, COS and SIN channels of the 4.85 GHz receiver of the Effelsberg telescope for a polarized source are shown in Fig. 2.4. Since Stokes Q and U can have both positive and negative signs, the COS and SIN datasets can have both positive and negative amplitudes, like the example of this figure.

Extracting the Stokes parameters of a subscan

Stokes Q and U are measured by fitting a proper function to the COS and SIN channel datasets. The COS and SIN amplitudes are then rotated to the Q – U plane using Eq. 2.13. Following the same procedure, we can measure the LCP and RCP amplitudes which are then used to calculate Stokes I and V according to the Stokes parametrization described in subsection 2.4.1.

The sources of our sample are expected to have low circular polarization degrees, which makes Stokes V measurements extremely difficult. For example, assuming a typical value for the degree of circular polarization of $m_c \approx 0.5\%$, a source with a typical amplitude of the order of 2500 counts in the LCP and RCP channels would have a Stokes V amplitude of 25 counts. For a $5\text{-}\sigma$ detection limit level, one needs a Stokes V uncertainty level of only 5 counts

which means that the uncertainty of the measured LCP and RCP amplitudes should be of the level of 3.5 counts! It is clear that the method that is used for fitting the recorded datasets, especially those of the LCP and RCP channels, is crucial for reaching the desired reliability in the polarization measurements.

Fitting functions and their errors

The common practice for cross-scan datasets is fitting a Gaussian function to the data with the addition of a linear function for the removal of the baseline. This method is suitable for estimating the source amplitude but it becomes very imprecise outside the receiver's Full Width at Half Maximum (FWHM). Because the telescope response is not described by a Gaussian profile, fitting such a function to the entire dataset clearly results to uncertainties in the amplitudes much higher than the desired ones. Thus, we sought alternative functional forms that could provide a better description of the telescope response and allow us to more accurately estimate the response amplitudes.

Basic antenna theory predicts that the zeroth order approximation of an antenna pattern is a $\text{sinc}^2(x)$ function. We soon realized that the fit indeed describes well the main lobe area but fails to do so for the side lobes. Furthermore, the amplitude uncertainty level was turning out again much higher than our goal.

A better approximation of the antenna pattern of a circular parabolic antenna – like the one at Effelsberg – is the diffraction pattern of a circular aperture, i.e. the Airy disk pattern:

$$I = I_0 \left(\frac{2J_1(x)}{x} \right)^2 \quad (2.14)$$

where I_0 is the maximum response level of the pattern at the center of the main lobe and J_1 is the Bessel function of the first kind. We found out that *the Airy disk pattern fits describe the whole area of the dataset with high accuracy and the fitted amplitude errors are small enough to accommodate reliable low circular polarization degree measurements.* An example of the different fitting methods along with their residuals from the data is shown in Fig. 2.5. The amplitudes of the respective Stokes I and V and their signal to noise ratios (SNRs) predicted for $m_c \approx 0.5\%$ are given in Table 2.1.

Table 2.1: The measured Stokes I and the predicted Stokes V along with its signal-to-noise ratio (SNR) assuming $m_c \approx 0.5\%$ using the different fitting methods shown in Fig. 2.5.

Fitting method	Stokes I (counts)	Stokes V (counts)	Stokes V SNR
Gaussian	6391.55 ± 20.42	31.96 ± 20.42	1.6
$\text{sinc}^2(x)$	6315.22 ± 17.69	31.58 ± 17.69	1.8
Airy disk pattern	6277.46 ± 7.69	31.39 ± 7.69	4.1

2.4.3 Cross-channel calibration

The receiver channels that record the polarization characteristics of the incident radiation have different gains, i.e. they convert the same number of incident photons to different number of counts. Thus, we need to cross-calibrate them before we could compare the recorded power. This is done with a known calibration signal, generated by a noise diode. The reference signal is injected at the receiver feed and hence it is following the same path that the incoming celestial signal follows as it travels along the receiver signal path. The noise diode is designed to imitate a signal which

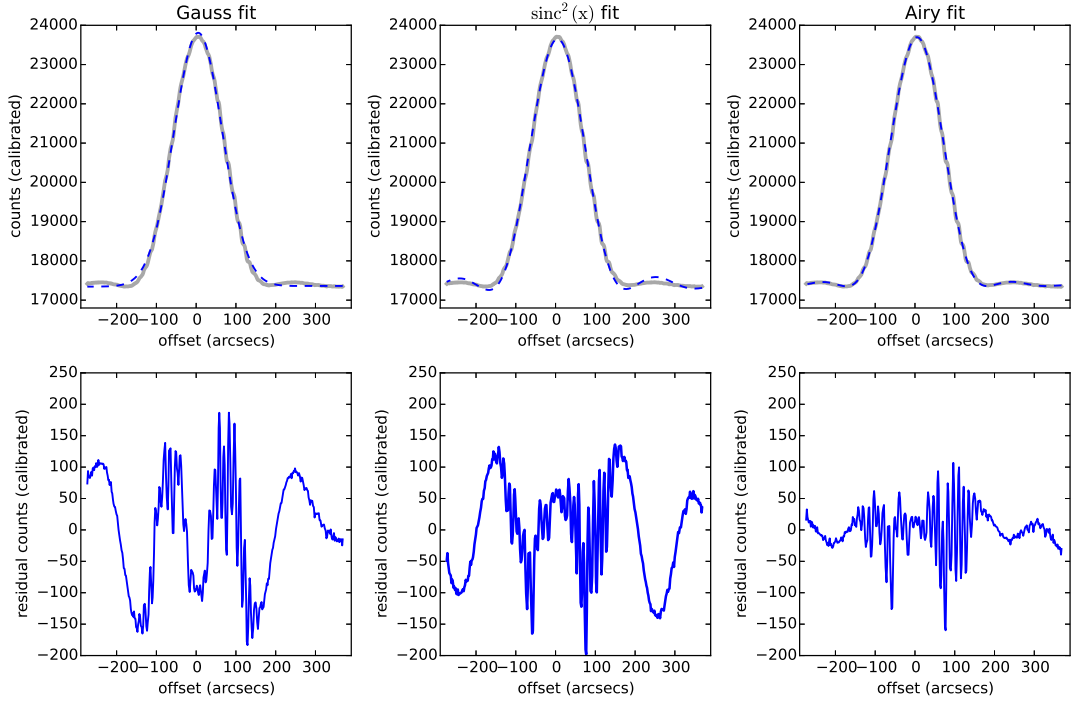


Figure 2.5: The different methods used to fit the recorded datasets (grey lines) are shown in the top row. Their residuals, i.e. the differences between the data and their fitted values, are given in the bottom row for a direct comparison between the fitting methods.

- is circularly unpolarized, i.e. the noise diode transmits the same signal to both LCP and RCP channels

$$E_l^d = E_r^d$$

- is 100% linearly polarized. Assuming that it has only Stokes Q , the phase difference, θ , between its E_l and E_r is 0° , or

$$Q^d = 2 \langle E_l^d \rangle \langle E_r^d \rangle \cos \theta = 2 \langle E_l^d \rangle \langle E_r^d \rangle$$

$$U^d = 2 \langle E_l^d \rangle \langle E_r^d \rangle \sin \theta = 0$$

where the letter d denotes the noise diode values.

Data point phase packet

Each data point of the recorded datasets is obtained in a 4-phase sequence. Each phase lasts for 16 ms and the noise diode is turned on for the last two phases of this sequence. Furthermore, a phase difference of 180° between E_l and E_r is introduced during the A and C phases. This rotates the incoming EVPA by 180° and it is used to remove instrumental systematic errors that may affect the linear polarization characteristics of the recorded signal. The different characteristics of the four phases (A-D) are given in Table 2.2.

The fact that the measured counts of each phase and for each channel are recorded in the raw data files provides a powerful handle to cross-calibrate the recorded datasets. The manipulation of the different phases can be fine-tuned to accommodate the requirements of each project. The fact that our sample consists of weakly polarized radio sources led us to take advantage of this information redundancy to calibrate our data acquisition method with high accuracy. In the following we describe the specifics of our strategy.

Table 2.2: The setup of the different phases in the measurement cycle

Phase:	A	B	C	D
Noise diode	off	off	on	on
Phase difference between E_l and E_r	$\theta + 180^\circ$	θ	$\theta + 180^\circ$	θ

LCP and RCP channel measurement

The LCP and RCP datasets are not affected by the phase difference between E_l and E_r , thus there is no difference between the datasets obtained during phases A and B or C and D. Furthermore, the datasets obtained in phases C and D are just a parallel displacement of the ones obtained in phases A and B respectively with the injection of the noise diode signal atop the celestial signal as shown in Fig. 2.6. Thus, in order to extract the noise diode signal as that is recorded by the LCP and RCP channels, one needs to subtract any of the phase A or B datasets from any of the phase C or D datasets. All the possible combinations are plotted in Fig. 2.7 for datasets obtained by the LCP channel of the 4.85 GHz receiver.

The sinusoidal pattern around the middle of the dataset differences in Fig. 2.7 is caused by the fact that the receiver is recording the counts of phases A to D continuously while the telescope moves over the source position. This means that the celestial signal recorded at each phase has a slightly larger or smaller value than the previous phase, depending on whether the telescope is moving towards or away from the source, respectively. These small differences in the recorded amplitudes become evident as the derivative of a Gaussian (sinusoidal) pattern when we subtract the data points recorded between phases. In the example of Fig. 2.7, the telescope was moving from the negative towards the positive offset positions. This is why when we subtract the counts recorded during any earlier from any later phase, we see an excess of counts before the telescope reaches the source position (at an offset $\sim 0''$) and a lack after it has passed that point. Also, this is the reason for the larger amplitude of the sinusoidal pattern when we subtract phases which are more distant in time, like phase A from phase D. The symmetry of the effect (for the case of point sources) allows us to use the average value of any difference combination along a subscan as a good estimate of the noise diode's amplitude as recorded by the LCP and RCP channels. In order to (1) smear out possible random errors that may be present in the datasets of certain phases, (2) utilize all the available information that the telescope provides us with and (3) improve the detection rate of faint sources, we use all the datasets obtained during the phase cycle from A to D.

In the following, we term the incident signal without the noise diode's power as "sky" and the diode's signal as "diode". Assuming that the phase switch that introduces the 180° phase difference between E_l and E_r during phases A and C affects the gain of the respective channel as an additional element in the signal path, we can write the four phases in the LCP and RCP channels as

$$\begin{aligned}
 \text{phase A} &= g \cdot \text{sky} \\
 \text{phase B} &= g_a \cdot \text{sky} \\
 \text{phase C} &= g \cdot (\text{sky} + \text{diode}) \\
 \text{phase D} &= g_a \cdot (\text{sky} + \text{diode})
 \end{aligned} \tag{2.15}$$

where g is the receiver's gain with the 180° phase switch "on", g_a is the gain with the switch "off". We now define the calibration signal in the LCP and RCP channels using the phase combination

$$\text{Cal} = (D + C - A - B) = (g + g_a) \cdot \text{diode} \tag{2.16}$$

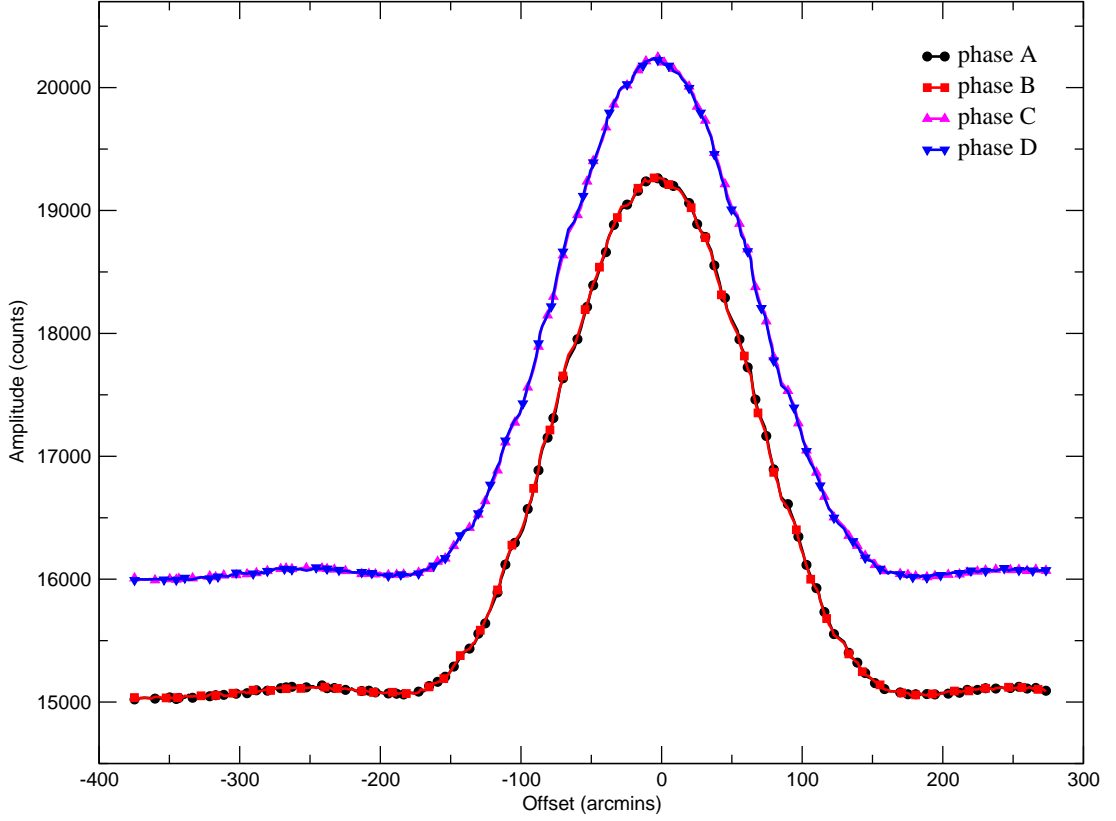


Figure 2.6: Datasets obtained through phases A to D for the LCP channel of the 4.85 GHz Effelsberg receiver.

and the signal used to measure the celestial source's LCP and RCP amplitudes, as

$$\text{Sky} = A + B + C + D = (g + g_a) \cdot (2\text{sky} + \text{diode}) \quad (2.17)$$

Then we use an Airy disk profile fit (subsection 2.4.2) to measure the amplitude, A_{Sky} , of the “sky” signal (Eq. 2.17) in counts and we take the average of the “Cal” signal (2.16) over the whole subscan as the amplitude, A_{Cal} , of the calibration signal.

Finally, the incident celestial source's LCP and RCP amplitudes, calibrated in terms of the noise diode's amplitude, is calculated as

$$\frac{A_{\text{Sky}} - A_{\text{Cal}}}{2A_{\text{Cal}}} = \frac{\text{sky}}{\text{diode}} \quad (2.18)$$

COS and SIN channel measurement

For the channels that measure the linear polarization the situation is slightly different. The 180° phase difference between E_l and E_r during phases A and C, changes the sign of the COS and SIN signal amplitudes. Thus, the four phases of the measurement in the COS and SIN channels can be written as

$$\begin{aligned} \text{phase A} &= -g \cdot \text{sky} \\ \text{phase B} &= g_a \cdot \text{sky} \\ \text{phase C} &= -g \cdot (\text{sky} + \text{diode}) \\ \text{phase D} &= g_a \cdot (\text{sky} + \text{diode}) \end{aligned} \quad (2.19)$$

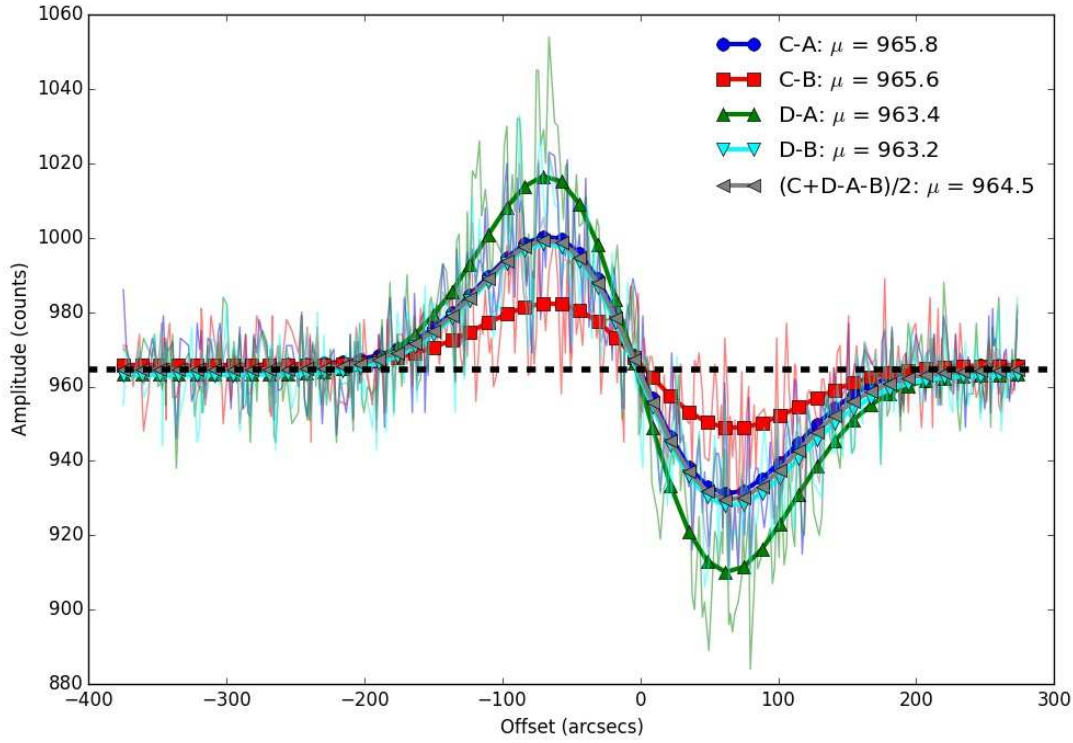


Figure 2.7: Differences between the datasets obtained throughout the different phases of the measurement cycle as recorded by the LCP channel of the 4.85 GHz Effelsberg receiver. A fit is also plotted for each difference using a Gaussian derivative function. The average values, μ , of all datasets are in good agreement and provide an estimate of the noise diode's LCP amplitude.

We can now define the calibration signal in the COS and SIN channels using the phase combination

$$\text{Cal} = -A + B + C - D = -(g + g_a) \cdot \text{diode} \quad (2.20)$$

and the signal used to extract the celestial source's COS and SIN amplitudes as

$$\text{Sky} = A - B + C - D = -(g + g_a) \cdot (2\text{sky} + \text{diode}) \quad (2.21)$$

The phase combinations of the expressions 2.20 and 2.21 produce datasets of the same form as the ones obtained with expressions 2.16 and 2.17. Thus, we can use the same procedure followed for the LCP and RCP channels and calibrate the incident celestial source's COS and SIN amplitudes according to Eq. 2.18.

Following the methodology described above and the expressions 2.16 - 2.21 we are able to express the fitted LCP, RCP, COS and SIN source amplitudes in terms of the noise diode amplitude. This is an essential step because it allows us to calculate the complete Stokes 4-vector of the observed sources and perform calculations using its parameters correctly since it ensures the cross-calibration of the data obtained with the different receiver channels.

2.4.4 Corrections

The fitted amplitudes of the LCP, RCP, COS and SIN channels are corrected for a number of systematic errors. In the following, we describe the origin of these errors and the methodology we follow to correct for them.

Telescope pointing

When the telescope is commanded to observe at a certain position in the sky, the given celestial coordinates are recalculated by the pointing model of the telescope's control software which, among others:

- Transforms them from their reference epoch (J2000, B1950 etc.) to the date and time of observation
- Corrects them for the Earth precession and nutation
- Corrects them for light aberration effects etc.

Then the telescope uses these recalculated coordinates to center the azimuth and elevation sub-scan paths over which the source is measured. Several factors, like the atmospheric conditions or the accuracy of the telescope's pointing model, can cause small deviations of the recalculated coordinates with respect to the actual position of the source on the sky. In this case, the telescope will be slewing over a position slightly off the actual source position in the sky. This misplacement is manifested as an offset of the peak of the dataset from the zero position in azimuth or elevation offset in the recorded datasets.

If the observed source is measured repeatedly, for the cross-scans following the first one, the telescope can use, upon the observer's request, the azimuth and elevation offsets measured in the previous cross-scan to align better the telescope's beam with the source position. For our project and for most of the observed frequencies we measured the sources repeatedly, including this option. In order to quantify the improvement of the beam alignment with respect to the actual source position, one can compare the mean amplitude (over all sub-scans) between the first and the second consecutive scans. Histograms of the fractional differences in the mean amplitudes of the first and the second consecutive scans for the LCP and RCP channels are shown in Fig. 2.8 for a large number of scans. The fact that the mean amplitude increases only for $\sim 50\%$ of the scans by a small fraction (maximum $\sim 1 - 2\%$) points towards the conclusion that the pointing model of the Effelsberg telescope is very accurate and the deviation of the recalculated coordinates from the actual source position is very small.

Beam separation

Despite the automatic correction for the telescope pointing described above, the recorded datasets of at least one of the telescope channels will be misaligned with respect to the source position. This happens because telescopes use feed pairs with separate polarization characteristics (e.g. left and right-handed circular or vertical and horizontal linear polarization) which are physically separated in the receiver construction. This results to separate locations of the corresponding beam patterns of each polarization on the plane of the sky.

For example, in the case of the 4.85 GHz, secondary focus receiver of the Effelsberg telescope, the LCP and RCP beams are separated by $\sim 8''$ and since the linear polarization characteristics are recorded by a correlation of the signals recorded by the LCP and RCP channels (Eq. 2.12), the COS and SIN beams are usually located between the LCP and RCP ones (Fig. 2.9). This means practically that independently of which beam the telescope is using to calibrate its pointing model all the others will be misaligned with respect to the source position. In this example, the 4.85 GHz receiver of the Effelsberg telescope is using the LCP feed as the reference point of its pointing model and the rest of the beams are always misaligned as it can be seen in Fig. 2.9.

Correcting for the beam separation

The beam separation on the plane of the sky alters the polarization characteristics of the observed source in a systematic way which can be corrected. For example, a circularly unpolarized point source (LCP amplitude = RCP amplitude) observed by the cross-scan method would appear circularly polarized. This happens because it would be measured by different "slices"

of the LCP and RCP patterns in the azimuth and elevation direction, i.e. beam pattern regions with different gains. To compensate for this effect, we use the average absolute pointing offset in the azimuth and elevation directions of each scan to correct the source amplitude as measured in the other direction, using an Airy disk beam pattern model (see subsection 2.4.2). This way, we recalculate the amplitude of the source as if it would be observed at the maximum response point of the beam pattern. To do that we use the following expression

$$A_{\text{corr}}^{\text{azi,elv}} = A_{\text{obs}}^{\text{azi,elv}} \cdot \left(\frac{2J_1(w \cdot p_{\text{off}}^{\text{elv,azi}})}{w \cdot p_{\text{off}}^{\text{elv,azi}}} \right)^{-2} \quad (2.22)$$

where,

- azi, elv denotes the scanning direction
- A_{poi} is the source amplitude corrected for pointing offset
- A_{obs} is the measured source amplitude
- p_{off} is the average absolute pointing offset in arcsecs on the other direction
- w is the Full Width at Half Maximum of the Airy disk pattern in units of the telescope beam pattern Full Width at Half Maximum, FWHM, at the observing frequency in arcsecs

$$w = \frac{3.23266}{\text{FWHM}} \quad (2.23)$$

This operation is called *pointing correction* and it is valid under the following assumptions:

1. The pointing model of the telescope is accurate, i.e. the zero positions in azimuth and elevation correspond to the actual source position
2. The source's Stokes parameters are all maximized at the same position on the sky, which is always true for unresolved sources and
3. The beam pattern of each channel can be accurately modeled with an Airy disk pattern

Pointing correction quality check

In order to check the quality of the pointing correction, one can compare the scatter of the measured amplitudes in the different sub-scans of the same cross-scan before and after the correction, for a beam with different azimuth and elevation pointing offsets. According to Fig. 2.9, the most extreme case of that for the 4.85 GHz Effelsberg receiver is the RCP channel with beam position at $7.10''$ and $1.43''$ in azimuth and elevation respectively. Since the beam offset in elevation is smaller, before the pointing correction, the measured amplitudes over the azimuth direction should be larger than the ones over the elevation direction and this discrepancy should become smaller after the pointing correction.

Histograms of the fractional differences in the standard deviation of the scan amplitudes before and after the pointing correction for the LCP and RCP channels and for a large number of scans are shown in Fig. 2.10. For this plot, we excluded all the first scans in order to check the quality of the pointing correction alone. For 3 out of 4 cross-scans, the pointing correction improves the scatter of the measured amplitudes in both channels and the correction is more significant for the RCP channel with a mean fractional decrease of the scatter by $\sim 25\%$ as opposed to $\sim 2 - 4\%$ for the LCP channel. The improvement in the scatter of the amplitudes in the RCP channel affects also the scatter of the circular polarization measurements. Using the same dataset as Fig. 2.10, we created Fig. 2.11 which shows that for $\sim 70\%$ of the scans the scatter on the circular polarization degree measurements decreases with an average decrease of $\sim 15\%$.

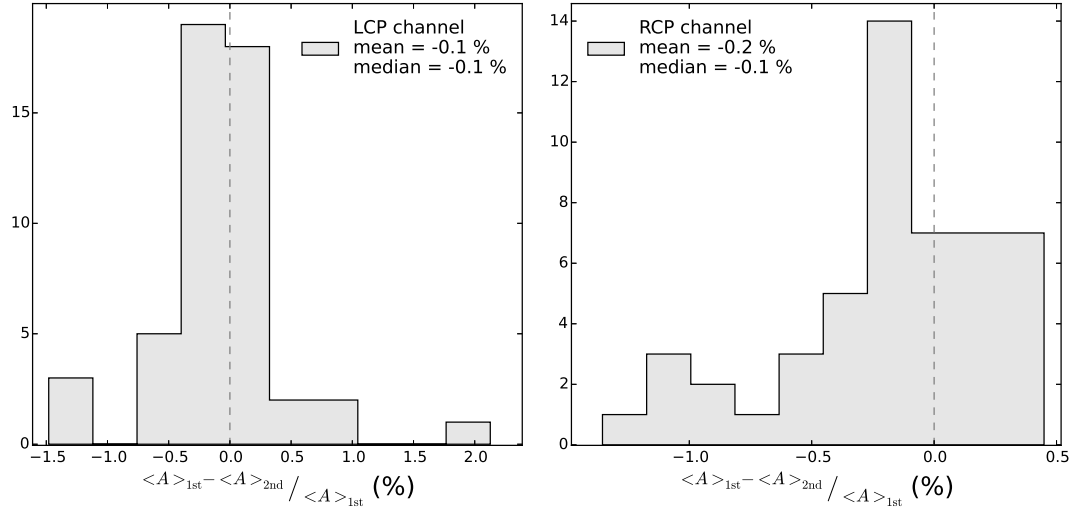


Figure 2.8: The fractional differences in the mean amplitudes of the first and the second consecutive scans for the LCP and RCP channels. The positive values contain 42% and 32% of the LCP and RCP histograms respectively.

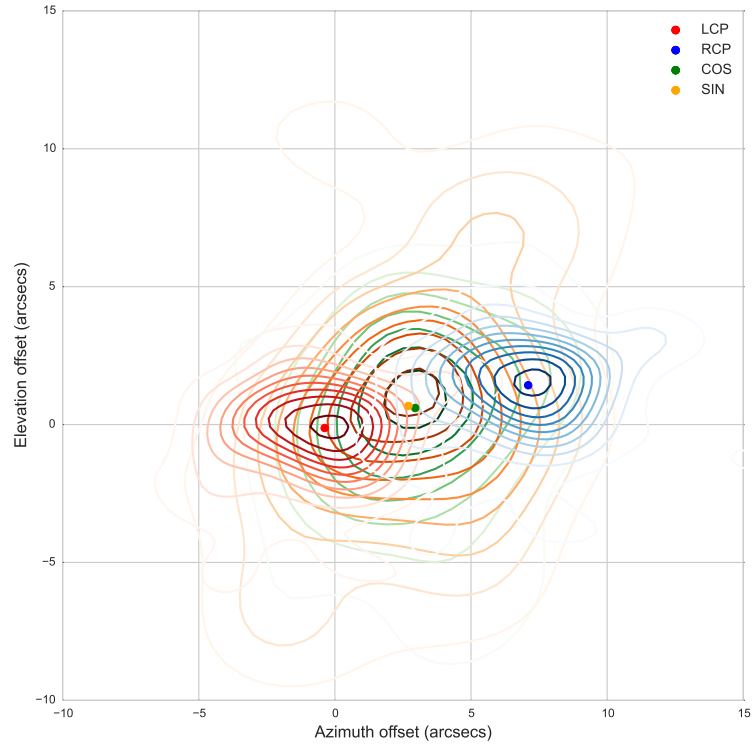


Figure 2.9: Pointing offset density plots for the LCP, RCP, COS and SIN channels of the 4.85 GHz Effelsberg receiver. The beam separation between these channels can be clearly seen.

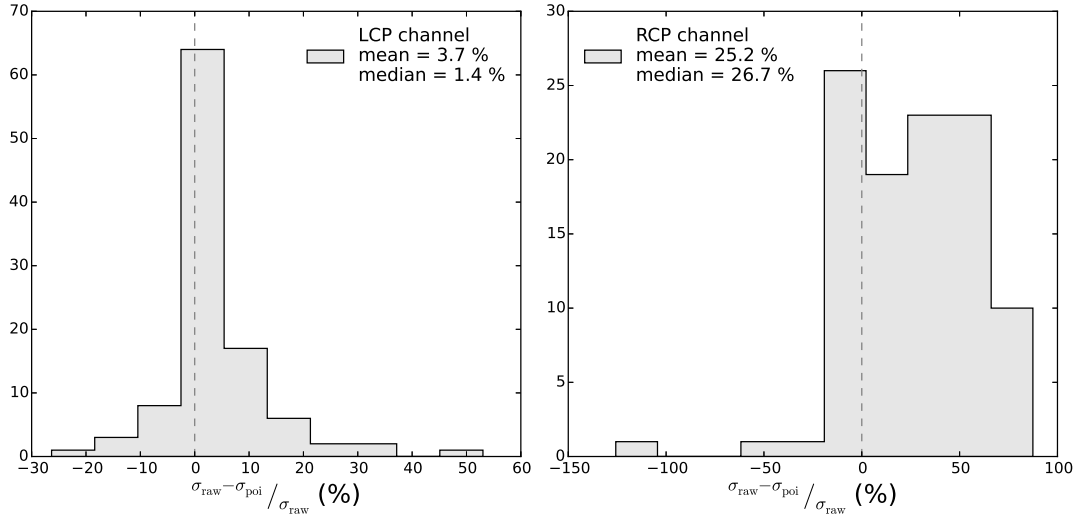


Figure 2.10: The fractional differences in the standard deviation of the scan amplitudes before and after the pointing correction for the LCP and RCP channels. For 72% and 78% of the cases it is positive for the LCP and RCP channel respectively.

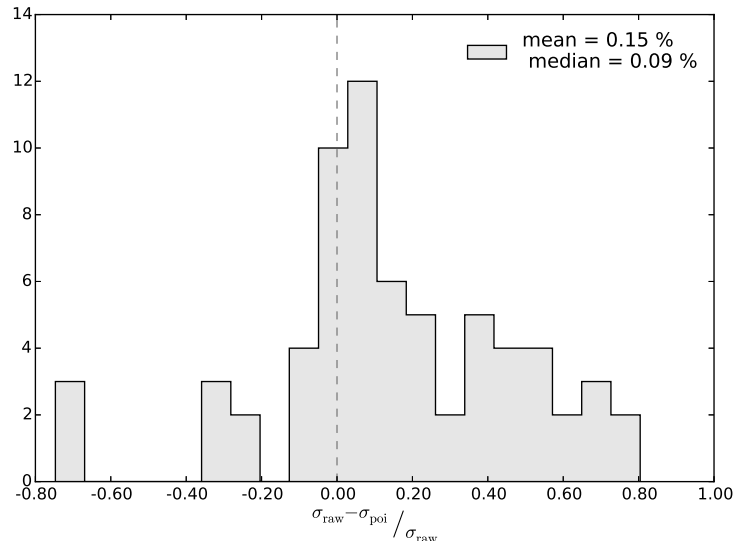


Figure 2.11: The fractional differences in the standard deviation of the scan circular polarization degree before and after the pointing correction. For 72% of the cases it is positive.

Opacity correction

Earth's atmosphere changes the incident signal by acting both as an attenuator and emitter. The emission of the atmosphere contributes to the background level of the subscan and thus it is not affecting the measured source amplitude which is estimated by fitting the part of the datasets above it (subsection 2.4.2). This is done by including a linear function to the fitting expression assuming that the local background level emission shows a linear behavior. For the cases that the assumption fails, we disregard the subscan. The measured amplitudes though are decreased due to atmospheric absorption and the correction for this effect, described below, is called opacity correction. A detailed description can be found in Angelakis (2007); Angelakis et al. (2009).

Using basic radiative transfer theory, we can express the source's amplitude, corrected for atmospheric absorption, with the following expression:

$$A_{\text{opc}} = A_{\text{obs}} \cdot e^{\tau_{\text{atm}}} \quad (2.24)$$

where,

- A_{opc} is the source amplitude corrected for atmospheric absorption
- A_{obs} is the measured source amplitude
- τ_{atm} is the atmospheric opacity at the elevation of the observation. Using a simple atmosphere model, we can express the dependance of the opacity on elevation as

$$\tau_{\text{atm}} = \tau_z AM = \tau_z \frac{1}{\sin(ELV)} \quad (2.25)$$

where τ_z is the opacity at zenith and ELV is the elevation at the time of the observation

The correction can be easily applied once the atmospheric opacity term τ_{atm} has been estimated. This term can be extracted from the atmospheric emission, recorded in the background level, because it is also regulated by τ_{atm} but in a sense opposite to the absorption.

Using the fitted linear function of the subscan's background level, we calculate the background emission called the system temperature, T_{sys} . Most of the components contributing to this background signal level are elevation-independent except for the atmospheric emission. We can write the system temperature as follows:

$$T_{\text{sys}} = T_0 + T_{\text{atm}} (1 - e^{-\tau_{\text{atm}}}) \quad (2.26)$$

where,

- T_0 includes the elevation-independent contributors, like the receiver noise temperature, the antenna temperature, the cosmic microwave background emission etc.
- T_{atm} is the effective temperature of the atmosphere, i.e. a measure of the atmosphere's emissivity assuming black-body behavior. The effective temperature can be calculated as

$$T_{\text{atm}} = 1.12 \cdot T_{\text{ground}} - 50K \quad (2.27)$$

- where T_{ground} is the ground temperature at the time of the observation
- τ_{atm} atmospheric opacity at the elevation of the observation

Earth's atmosphere is optically thin for most of the radio frequencies, which means that τ_{atm} is much less than unity and we can Taylor expand Eq. 2.26 so that

$$T_{\text{sys}} \simeq T_0 + T_{\text{atm}}\tau_{\text{atm}} = T_0 + T_{\text{atm}}\tau_z \frac{1}{\sin(ELV)} \quad (2.28)$$

Assuming that T_0 , T_{atm} and τ_z are stable, the above equation dictates that the system temperature should be in an inverse proportional relation with elevation. We use then T_{sys} measurements over various elevations to extract the parameters of the above linear relation, i.e. T_0 and τ_z .

An example plot of the T_{sys} measurements over various airmass values for the LCP and the RCP channels of the 4.85 GHz Effelsberg receiver is shown in Fig. 2.12. T_{sys} values that don't follow the linear relation are attributed mainly to weather effects which can change instantaneously T_{atm} or τ_z and increase the measured T_{sys} . Datasets like the one depicted in Fig. 2.12 are created from the measurements of each observing session and a lower-envelope linear fit is used to estimate the parameters of Eq. 2.28, namely τ_z from the slope of the fit and T_0 from the value of the fit at zero airmass. Then, using the fitted T_0 value, we estimate the atmospheric opacity, τ_{atm} , at the time of the observation from Eq. 2.26 as

$$\tau_{\text{atm}} = -\ln \left(1 - \frac{T_{\text{sys}} - T_0}{T_{\text{atm}}} \right) \quad (2.29)$$

where T_{atm} is calculated from Eq. 2.27. Finally, the calculated atmospheric opacity is used to perform the opacity correction according to Eq. 2.24.

Opacity correction in different polarization modes

Assuming the atmosphere is totally unpolarized, the calculated atmospheric opacity term should be the same for the datasets obtained with all the channels of the receiver (LCP, RCP, COS and SIN). This assumption is supported by the parallel displacement of the LCP and RCP data points in Fig. 2.12 which means that although the T_0 value is different for each channel, the τ_z values are the same for both the LCP and RCP channels. Furthermore, since the COS and SIN signals are proportional to a $\langle E_{(l,r)}^2 \rangle$ term, similar to the LCP and RCP signals (see Eq. 2.12), the same atmospheric opacity term can be used to correct also their measured amplitudes for atmospheric attenuation.

As a quality check, the differences between the fitted τ_z using either LCP or RCP T_{sys} measurements for all the observed epochs are shown in Fig. 2.13. The very low average value of -0.0003 indicates that the atmospheric opacity values obtained by the two channels independently are consistent. Thus, we use the average atmospheric opacity of the LCP and RCP channels to correct for atmospheric absorption the amplitudes measured in all polarization modes.

Gain curve correction

The weight of a telescope causes the deformation of its surface in a way which depends on the elevation angle. For the 100-m Effelsberg telescope, any attempt to minimize this effect by making its construction unbendable would result in an extremely cumbersome design. Instead, this was the first telescope designed to follow the homology principle, i.e. the controlled deformation of its surface (von Hoerner, 1967). According to the design, the surface deformation results always to a paraboloidal shape with different focal positions at different elevation angles. The telescope then moves the receiver in real time during the observations to obtain the correct focal position. Nevertheless, the change of the surface shape alter the effective aperture and consequently the sensitivity of the telescope in a way which is elevation-dependent. The

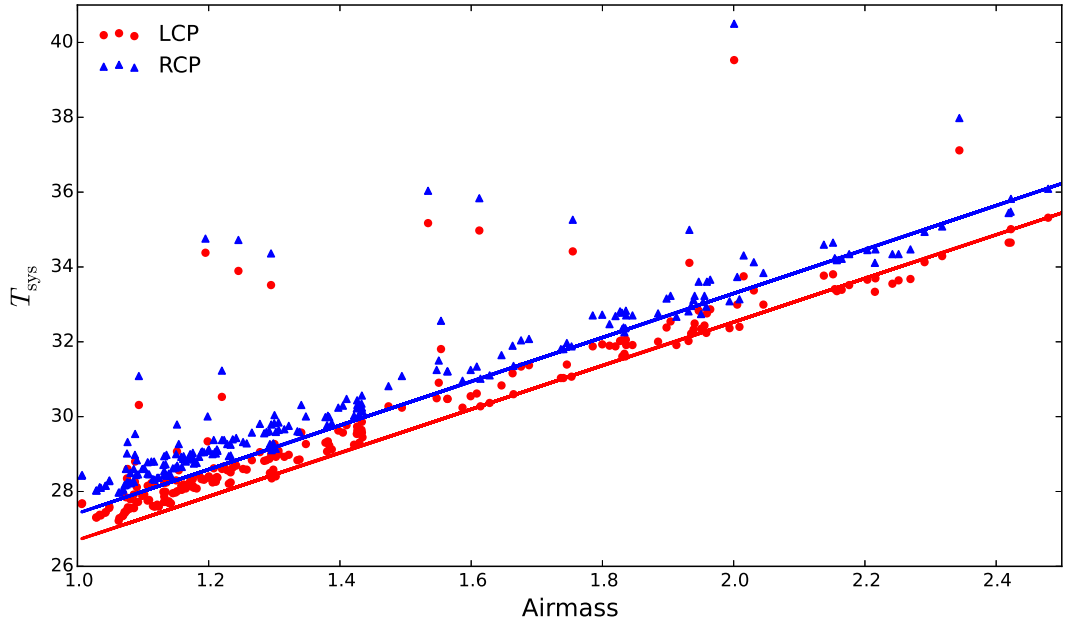


Figure 2.12: T_{sys} versus airmass for the LCP and RCP channels of the 4.85 GHz Effelsberg receiver

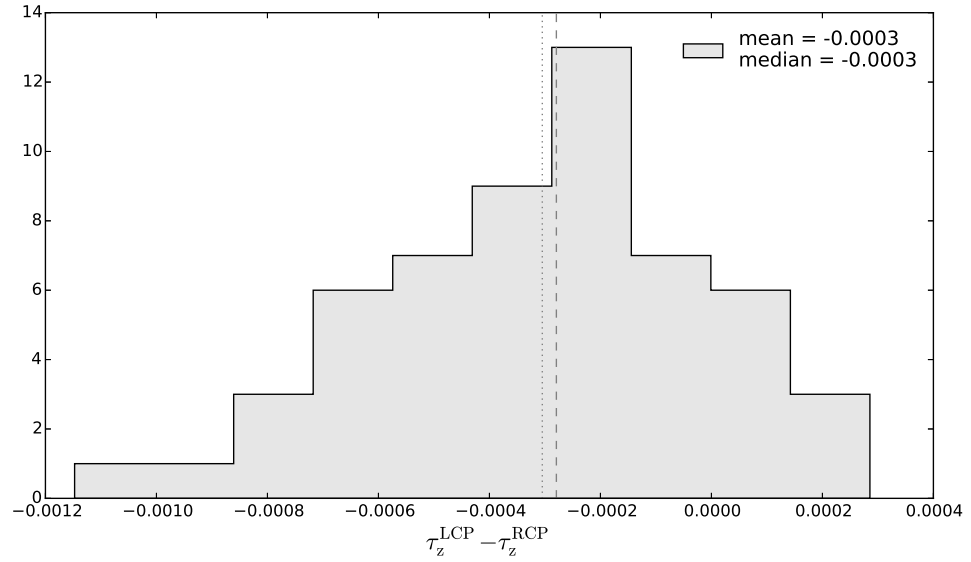


Figure 2.13: Fitted τ_z differences by using the LCP and RCP T_{sys} data independently. The median and average values are indicated by the dashed and dotted vertical lines respectively.

correction of the measured amplitudes at different elevations for the latter effect is called gain curve correction (Angelakis, 2007; Angelakis et al., 2009).

Strong, non-variable sources are observed in order to determine the change of the telescope sensitivity at different elevations. The effect can be revealed then by plotting the measured amplitudes of these sources as a function of elevation, normalized to the average amplitude of each source. An example plot for the 4.85 GHz receiver is shown in Fig. 2.14. The data points can be fitted by a parabola of the form:

$$G(ELV) = A_0 + A_1 \cdot ELV + A_2 \cdot ELV^2 \quad (2.30)$$

which connects the telescope gain, G , at a given elevation, ELV , and is called “gain curve”. Knowing the parameters of Eq. 2.30, we can correct all measured amplitudes according to:

$$A_{gc} = \frac{A_{obs}}{G(ELV)} \quad (2.31)$$

where,

- A_{gc} is the source amplitude corrected for the telescope gain dependance on elevation
- A_{obs} is the measured amplitude of the source and
- ELV is the elevation at the time of the observation

Gain curve correction in different polarization modes

The change in telescope sensitivity due to the deformation of its surface is expected to affect all the recorded polarized signals the same way. Thus, the same G value is used to correct the amplitudes in LCP, RCP, COS and SIN channels. This assumption is supported by the fact that when we use the LCP and RCP channel data separately for fitting the gain curve, we get almost the same parameter values. The LCP and RCP gain curves for the 4.85 GHz Effelsberg receiver are shown in Fig. 2.14 and their calculated parameters are given in Table 2.3. The parameters which we applied to all our datasets were obtained by the Effelsberg telescope staff members in a dedicated observing session back in February 2008 and are shown in the same table for comparison.

Table 2.3: LCP and RCP gain curve parameters fitted by the datasets shown in Fig. 2.14. The February 2008 gain curve parameters are given for comparison.

Channel	A_0	A_1	A_2
LCP	1.01390	$4.9817 \cdot 10^{-4}$	$-1.3239 \cdot 10^{-5}$
RCP	1.02122	$1.7028 \cdot 10^{-4}$	$-0.9814 \cdot 10^{-5}$
Stokes I (2008)	0.99500	$5.2022 \cdot 10^{-4}$	$-1.2787 \cdot 10^{-5}$

2.4.5 Stokes Q and U instrumental artifacts

According to the Stokes parametrization 2.12, the COS and SIN channels record the linearly polarized part of the incident radiation by cross-correlating its LCP and RCP components. The cross-correlation process is filtering out the part of the radiation which reaches the telescope with a random phase difference between E_l and E_r , θ , and comprises the linearly unpolarized (or better randomly polarized) part of the incident radiation. The part of the radiation that reaches the telescope with constant phase difference θ comprises the linearly polarized part with EVPA

$$\chi = \frac{1}{2}\theta \quad (2.32)$$

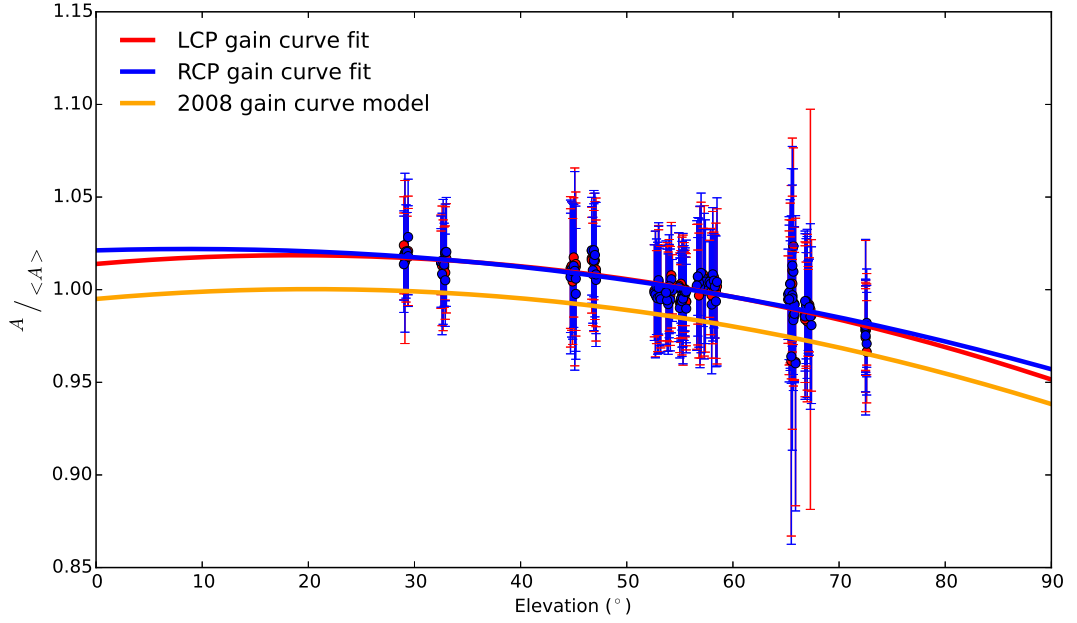


Figure 2.14: LCP and RCP channel gain curves for the 4.85 GHz Effelsberg receiver.

For a linearly unpolarized source, the observed COS and SIN (or Q and U) datasets should be consistent with a noise signal. The COS and SIN datasets of unpolarized sources that we obtained though contain some spurious signals of strange shapes (artifacts) which are different for each scanning direction. The fact that these spurious signals were the same for

1. different observed sources
2. different parallactic angles
3. different times of observation

led us to realize the systematic nature of the effect that causes them. The different forms of artifacts we encountered after rotating the COS and SIN datasets of unpolarized sources to the Q and U domain using Eq. 2.13 are shown in Fig. 2.15.

Correcting the artifacts

The only factors affecting these artifacts are (1) the Stokes I amplitude of the observed source and (2) the position of the peak in the LCP and RCP channel datasets. The artifacts become more prominent for sources of high Stokes I amplitudes and their location in the COS and SIN datasets are correlated with the peak position in the LCP and RCP datasets. Using this information and the fact that their shapes are always the same and can be reproduced by smooth functions (e.g. sums of Gaussians or Gaussian derivatives) we model them using the recorded datasets of unpolarized sources observed in each observing session. We use a different set of functions to fit each artifact and we estimate the fit parameters by stitching all unpolarized source Q and U datasets together and performing a simultaneous fit in order to minimize the parameter errors. The functional forms we use to fit the artifacts are:

$$Q_{\text{azi}} = -\alpha I e^{\frac{-[x-(x_I-x_\alpha)]^2}{2(\sigma_\alpha\sigma)^2}} - \beta I e^{\frac{-[x-(x_I-x_\beta)]^2}{2(\sigma_\beta\sigma)^2}} \quad (2.33)$$

$$Q_{\text{elv}} = \alpha I e^{\frac{-[x-(x_I-x_\alpha)]^2}{2(\sigma_\alpha\sigma)^2}} - \beta I e^{\frac{-[x-(x_I-x_\beta)]^2}{2(\sigma_\beta\sigma)^2}} + \gamma I e^{\frac{-[x-(x_I-x_\gamma)]^2}{2(\sigma_\gamma\sigma)^2}} \quad (2.34)$$

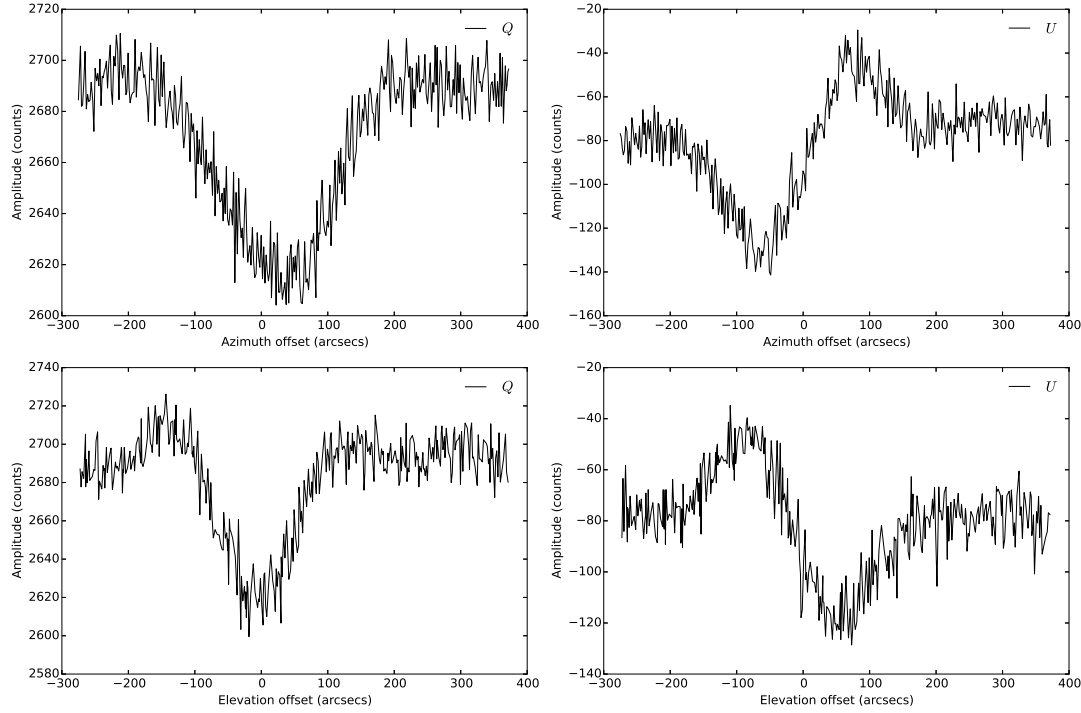


Figure 2.15: Stokes Q and U artifacts as observed for an unpolarized source in the two scanning directions, the azimuth in the top and the elevation in the bottom panels.

$$U_{\text{azi}} = -\frac{\alpha I(x - (x_I - x_\alpha))e^{\frac{-(x_I - x_\alpha)^2}{2(\sigma_\alpha \sigma)^2}}}{(\sigma_\alpha \sigma)^2} - \beta I e^{\frac{-[x - (x_I - x_\beta)]^2}{2(\sigma_\beta \sigma)^2}} \quad (2.35)$$

$$U_{\text{elv}} = -\frac{\alpha I(x - (x_I - x_\alpha))e^{\frac{-(x_I - x_\alpha)^2}{2(\sigma_\alpha \sigma)^2}}}{(\sigma_\alpha \sigma)^2} - \beta I e^{\frac{-[x - (x_I - x_\beta)]^2}{2(\sigma_\beta \sigma)^2}} \quad (2.36)$$

where,

azi, elv	denotes the scanning direction that the functional form of the Q or U artifact is referring to
I	is the Stokes I amplitude, calculated from the LCP and RCP fitted amplitudes
x_I	is the mean offset of the LCP and RCP fitted offsets
σ_I	is the average FWHM of the LCP and RCP fitted FWHMs
i, x_i, σ_i with $i = \alpha, \beta$ or γ	are the parameters of the model which are fitted with the unpolarized source datasets of the session

The fitting functions have a large number of parameters and thus the fitting algorithm may run in different local minima of the parameter space every time we run it. In order to avoid this, we feed the algorithm with the initial parameter values shown in Table 2.4.

Finally, in order to remove these artifacts from the Q and U datasets of the observed sources, we use their LCP and RCP amplitudes and peak positions, to reproduce the artifacts using the generated model of each session (Eqs.2.33-2.36), and we subtract the modeled Q and U artifacts from the corresponding datasets. The recorded Q and U datasets are improved in many ways after this subtraction:

Table 2.4: The initial values of the Stokes Q and U artifact model parameters. The functional form of the model is given in Eqs.2.33-2.36.

Parameter	Q_{azi}	Q_{elv}	U_{azi}	U_{elv}
α	0.005	0.003	-0.3	0.3
x_α	-70	110	0	5
σ_α	0.5	0.2	0.9	0.3
β	0.002	0.010	0.002	0.002
x_β	-5	0	0	-50
σ_β	0.5	0.2	0.5	0.2
γ	...	0.002
x_γ	...	-110
σ_γ	...	0.2

1. Their peak is better aligned with the LCP/RCP peaks
2. Their FWHM value approaches the one expected at the observing frequency
3. Faint or erratic Stokes Q and U datasets obtain the expected shape (e.g. more similar to an Airy disk pattern)

An example. An example of the artifact correction for a polarized target source is shown in Fig. 2.16. The top panels show the LCP and RCP datasets with their fits. The dashed gray line notes the mean offset of their peaks. In the bottom panels the steps of the correction are shown. The COS and SIN datasets as well as their rotated forms to the Stokes Q and U domain are colored red before and blue after the correction. First, we rotate the observed COS and SIN datasets to the Q and U domain using the expressions of Eq. 2.13. Then, using the fitted amplitudes and positions of the LCP and RCP peaks, we generate the predicted artifact form from the model of the corresponding epoch which is shown here with the black lines within the red Q and U dataset plots of the bottom panels. After the removal of the artifacts (blue Q and U datasets in the bottom panels), we rotate the raw data back to the COS and SIN domain to fit an Airy disk pattern and extract their amplitudes which we correct for the effects discussed in subsection 2.4.4.

In Fig. 2.18, the generated models for 38 sessions are plotted. The shape of the artifacts is very stable in time which is another indication for their systematic character. The averages and the standard deviations of the fitted parameters over all 38 sessions are given in Table 2.5. An idea that worths further investigation is that these artifacts are just “slices” of the Stokes Q and U beams of the Effelsberg telescope at the observing frequency along the azimuth and elevation axis (A. Kraus, priv.comm.).

Artifact correction quality check

Although the artifact correction affects only a small part of the radiation recorded in the COS and SIN channels (the maximum amplitude of the artifacts is $\sim 0.4\%$ of the Stokes I amplitude), it is important for both weakly and strongly polarized sources. This is due to the fact that even for the latter ones, there are certain crucial parallactic angles where the amplitude of the recorded Q and U datasets becomes comparable to the artifact amplitude level (section 2.2).

As an example, we show in Fig. 2.17 the scatter of the linear polarization characteristics, before and after the artifact correction, of the polarized source 3C 48 as measured several times in one session. The scatter is greatly reduced after the correction, showing that its main contribution comes from the way that the recorded Q and U datasets in various parallactic angles

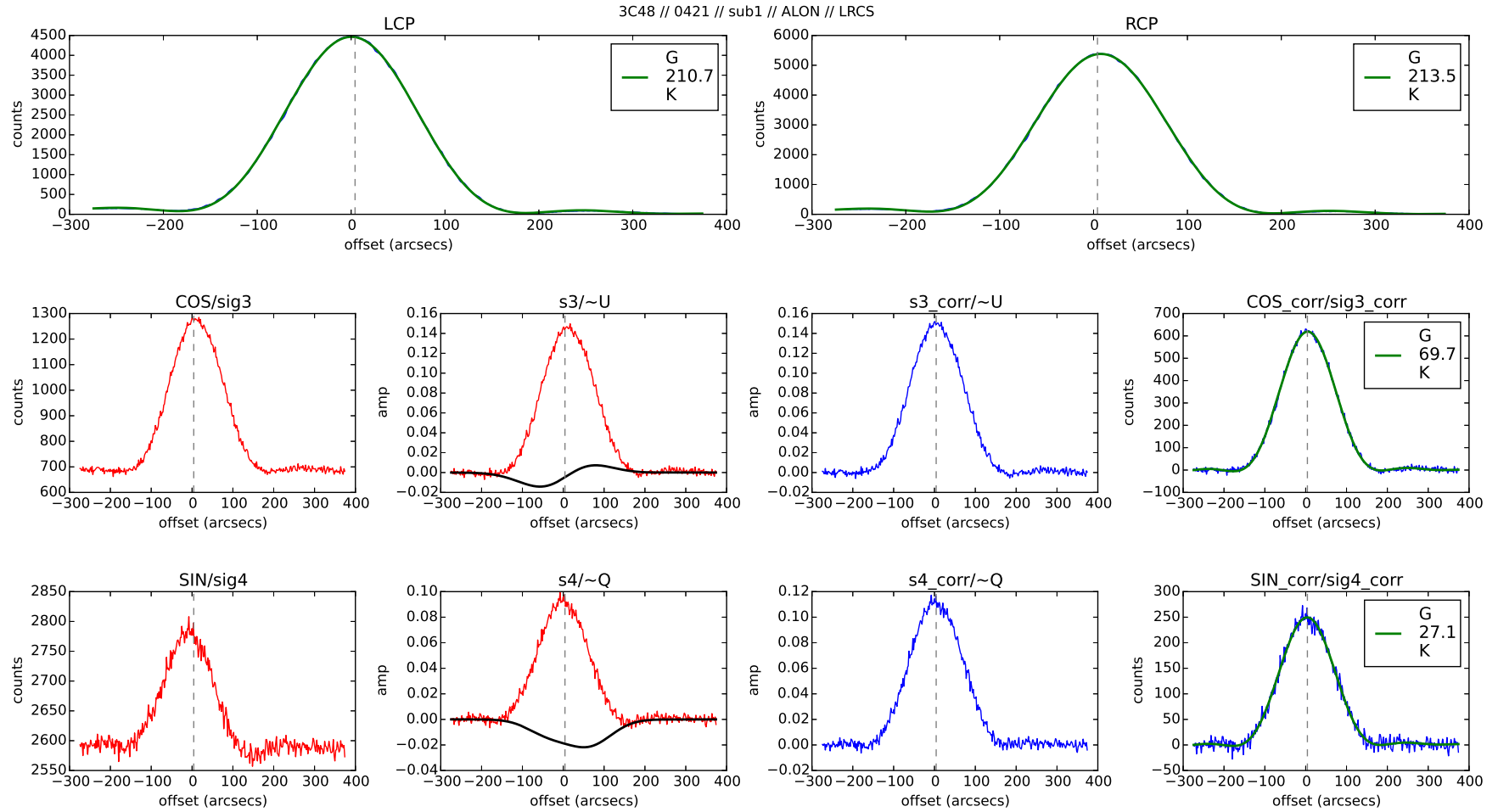


Figure 2.16: Stokes Q and U artifact correction process as described in the text.

Table 2.5: Stokes Q and U artifact fitted parameter values averages and standard deviations.

Parameter	Q_{azi}	Q_{elv}	U_{azi}	U_{elv}
α	0.004 ± 0.001	0.002 ± 0.001	-0.3 ± 0.1	$0.2 \pm 0.0(4)$
x_α	-65 ± 7	128 ± 8	-8 ± 12	20 ± 8
σ_α	$0.3 \pm 0.0(2)$	$0.26 \pm 0.0(4)$	0.9 ± 0.4	0.9 ± 0.1
β	$0.003 \pm 0.000(4)$	0.004 ± 0.001	0.002 ± 0.001	0.001 ± 0.001
x_β	29 ± 15	5 ± 8	3 ± 77	-81 ± 26
σ_β	$0.3 \pm 0.0(2)$	0.36 ± 0.1	0.2 ± 0.3	0.3 ± 0.1
γ	...	0.001 ± 0.001
x_γ	...	-108 ± 8
σ_γ	...	0.2 ± 0.1

were affected from the artifacts. Furthermore, the improvement in the stability of the measured Stokes parameters during a session becomes even more important when it comes to standard sources since their measurements are used to estimate the Müller matrix elements for that session and their scatter will affect also the accuracy of the fit.

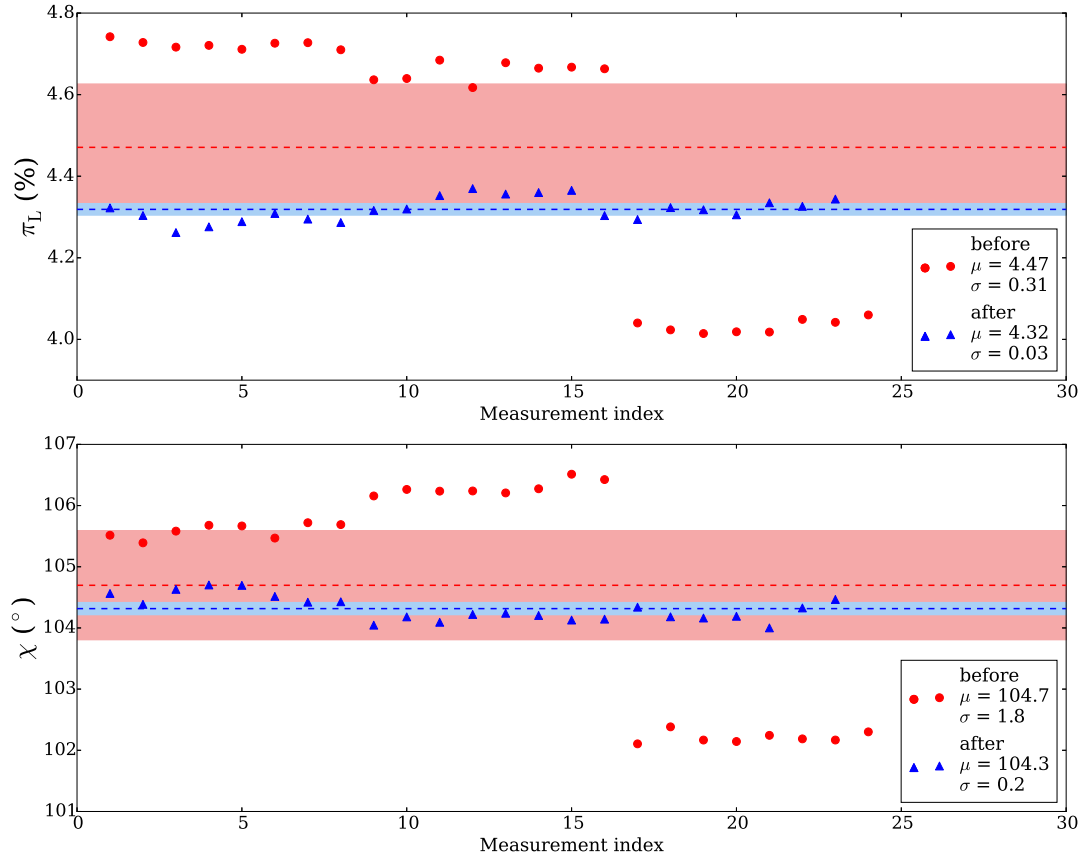


Figure 2.17: Linear polarization characteristics of the calibrator 3C 48 before and after the artifact correction. The data refer to 24 subscans of the source during one observing session. The average values are indicated by dotted lines and the highlighted areas indicate the $1-\sigma$ region around them. The respective values are shown in the legend.

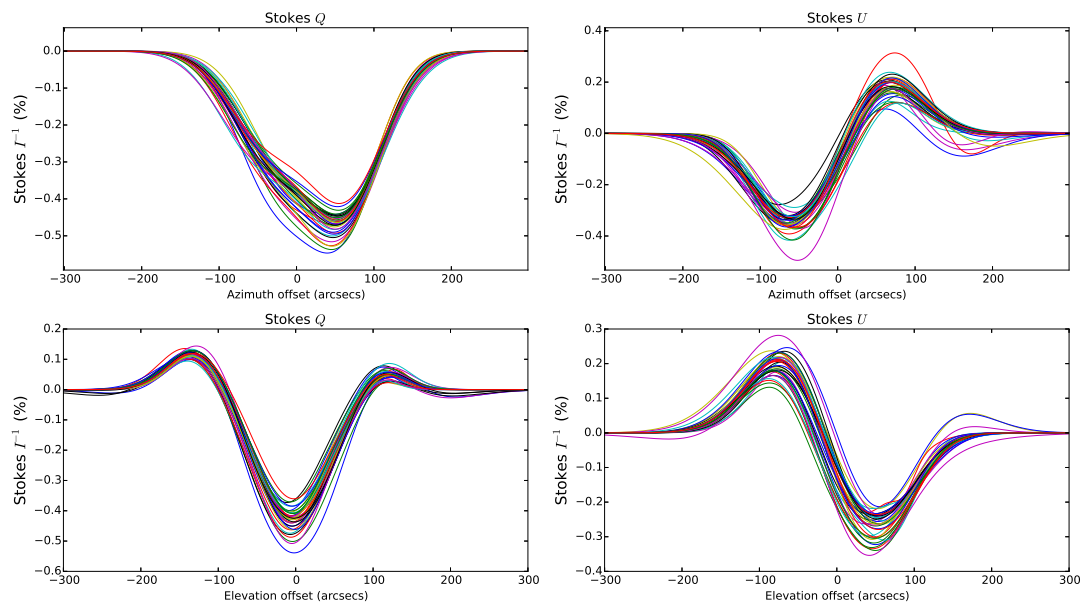


Figure 2.18: The generated models of the Stokes Q and U artifacts in the two scanning directions, the azimuth in the top and the elevation in the bottom panels. The models were generated for 38 sessions.

Chapter 3

Full-Stokes polarimetry calibration

Abstract

Here, we present two methodologies for calibrating all four Stokes parameters, we obtained at 4.85 and 8.35 GHz. Two additional techniques are presented for the correction of the spurious instrumental Stokes V . Finally, the stability of the observing system, in terms of polarization, is presented for the period between July 2010 and January 2015.

3.1 INTRODUCTION

The detailed data reduction methodology described in chapter 2, allows us to recover the Stokes parameters of point sources observed with the Effelsberg 100-m or any other telescope with circularly polarized feeds, with high accuracy. The parameters recovered with this methodology are expressed in diode amplitude units and the last step required is to express them in physical units with the aid of standard sources (calibrators), i.e. sources with preferably stable Stokes parameters which are either already known or can be derived independently on the basis of physical arguments.

In this chapter, we present the two different methodologies we followed in order to calibrate all four Stokes parameters of the observed sources. Furthermore, we show the technique we developed to correct the instrumental effects and calibrate the Stokes V parameter given that there are no standard sources available. Finally, we study the stability of the observing system in terms of polarization using the by-products of the Full-Stokes calibration procedure we followed.

3.2 FULL-STOKES CALIBRATION TECHNIQUES

We have followed two separate methodologies to calibrate the Stokes parameters of the observed sources. The first makes use of the 4x4 Müller matrix which describes the instrumental effects that may alter the polarization characteristics of the incident radiation. The second methodology is a generalization of the sensitivity correction which is usually applied to the observed Stokes I in order to convert its value from diode units or Kelvins (K) to Jansky units (Jy) (Angelakis, 2007; Angelakis et al., 2009). The latter takes into account also the polarization characteristics of the standard sources to perform a detailed step-by-step calibration of the Stokes parameters, as described below.

3.2.1 4x4 Müller matrix calibration

The Müller matrix calibration of the observed Stokes parameters is described in subsection 2.3. Using an adequate number of observations for the available standard sources, we can estimate the elements of the 4x4 Müller matrix by multi-dimensional least-square fits for the

set of equations 2.9 and 2.10, where S_{obs} are the observed Stokes parameters of the calibrators and S_{rot} are their known Stokes parameters, rotated accordingly to match S_{obs} at the time of observation (see also section 2.2).

Once the Müller matrix elements are known, we multiply its inverse with the Stokes parameters of the observed sources, rotated at a common reference frame, S_{rot}

$$S_{\text{real}} = \mathbf{M}^{-1} \cdot S_{\text{rot}} \quad (3.1)$$

This operation has a double benefit:

1. We correct the observed Stokes parameters for instrumental effects which may cause cross-talk between them, i.e. partial conversion of one Stokes parameter to another. This is done by the off-diagonal elements of the Müller matrix.
2. We express the measured Stokes parameters in physical units. This is performed by the diagonal elements. This is the reason for the great similarity of the diagonal elements in the representative Müller matrix of Eq. 2.11 which show an average conversion ratio between the diode amplitude units and Jy of ~ 0.86 for all Stokes parameters.

It is noteworthy that the fits that we ran to estimate the elements of the Müller matrix for 59 consecutive monthly sessions (at 4.85 GHz), returned systematically significant measurements only for certain matrix elements. Those are $m_{II}, m_{IV}, m_{QQ}, m_{QU}, m_{UQ}, m_{UU}, m_{VI}$ and m_{VV} , according to the notation introduced in section 2.3 (see also Fig. 2.3). This fact is a strong indication that there is only cross-talk between the Stokes parameter pairs of I – V and Q – U which is expected since they are calculated by the information delivered by the LCP–RCP and COS–SIN receiver channel pairs respectively (see also section 2.4). Thus, we conclude that instrumental effects which transform Stokes I/V to Q/U are insignificant and the corresponding off-diagonal Müller matrix elements are usually consistent with zero.

3.2.2 Full-Stokes sensitivity calibration

The second methodology we followed can be applied whenever the number of the available calibrators observations is inadequate for a meaningful fit that could estimate the Müller matrix elements as described above. In this case, the observation of at least one polarization standard source is needed.

The first step of the methodology is the estimation of the sensitivity factor which transforms the Stokes I and V measurements from diode amplitude units to Jy. To do that, we collect all the Stokes I measurements of the calibrators we observed in each session and we divide them with their corresponding known Stokes I values, expressed in Jy. The final sensitivity factor with which we correct the Stokes I and V measurements of the observed sources is the weighted average of these ratios. We use as weights the errors of the observed Stokes I parameters for the calibrators.

Before we use the same approach to estimate the sensitivity factors of the Stokes parameters Q and U , we need to correct the observed ones for instrumental rotations. We do that, by calculating the angle between the EVPA we observe and the one we expect for the standard sources using the observed and known Stokes Q and U parameters. The instrumental rotation is calculated as the weighted average of these angles and applied to all Stokes Q and U measurements. After this step, we calculate the sensitivity factors for Stokes Q and U , following the same approach as for Stokes I and V above. The observed Stokes parameters are finally corrected with the estimated sensitivity factors for each session.

3.2.3 Our approach

We have used the above techniques combined in order to calibrate our datasets. Generally the calibrated data agree very well. Specifically, using the average of the measured Stokes

parameters for 2630 measurements we find a median difference of 13.5, 1.6, 1.5 and 2.5 mJy for Stokes I , Q , U and V respectively, calibrated by the two techniques. We noticed though that the 4x4 Müller matrix technique was very sensitive to the number of calibrator observations needed to get a sensible fit.

In general we need 4–5 calibrator measurements at different parallactic angles. Fitting for the Stokes I , Q and U part of the Müller matrix (also known as solving the 3x3 Müller matrix problem) is relatively easy even by observing one polarized calibrator at various parallactic angles. The rotated Stokes Q and U at the different source positions, cover the corresponding parameter spaces well. This is unfortunately not the case for Stokes V which does not depend on the parallactic angle. For including also Stokes V in the fitting, i.e. solving the complete 4x4 Müller matrix problem, we need at least 3–4 observations of calibrators with different circular polarization characteristics in order to adequately cover the Stokes V parameter space. Preferably, one of those sources should be circularly unpolarized in order to calibrate the zero level of Stokes V .

The demand for large numbers of calibrator observations, limited the sessions that the 4x4 Müller matrix technique could be applied. For most of these sessions though the Full-Stokes sensitivity calibration technique was able to deliver good results. Thus, in order to include as many datasets as possible to our analyses we also used data calibrated with the latter method. The results and conclusions of this thesis are based on them.

3.3 STOKES V CALIBRATION

Both calibration techniques described above are based on the assumption that all the Stokes parameters are known for the calibrators. Such sources are generally known and have been used routinely for the calibration of Stokes I , Q and U . These are usually steep spectrum quasars or planetary nebulae which remain unchanged for very long periods of time. One example is the quasar 3C 286 that remains stable within 1% in Stokes I for over 30 years (Perley and Butler, 2013a) and its linear polarization degree is increasing for $0.015\% \text{ yr}^{-1}$ (Perley and Butler, 2013b).

The set of sources we used for calibrating Stokes I , Q and U are the quasars 3C 286, 3C 295, 3C 48 and the planetary nebula NGC 7027. For the latter we use the model presented in Zijlstra et al. (2008) to calculate its total flux at the time of observation since it changes over time. The total flux and linear polarization characteristics of these sources are given in Table 3.2.

The situation becomes somehow more difficult when we need to calibrate the Stokes V parameter. First, there is no such information readily available in the relevant literature. Furthermore, the fact that the Effelsberg telescope has circularly polarized feeds deteriorates the quality of circular polarization measurements by introducing spurious Stokes V . Nevertheless, since we are interested also in the circular polarization characteristics of the observed sources, we developed a methodology to recover it. In this section we describe the technique we developed to correct the spurious Stokes V introduced by the observing system and the steps we followed to recover the circular polarization information for the set of calibrators mentioned above.

Searching for circular polarization calibrators

Since we were interested in finding a set of sources with stable circular polarization characteristics, we focused our efforts on sources which are already used as calibrators for the rest of the Stokes parameters. After the initial inspection of their uncalibrated Stokes V lightcurves (Fig. 3.1), we realized that the telescope was introducing spurious and variable Stokes V to the observations. The former is indicated by the fact that all sources have negative Stokes

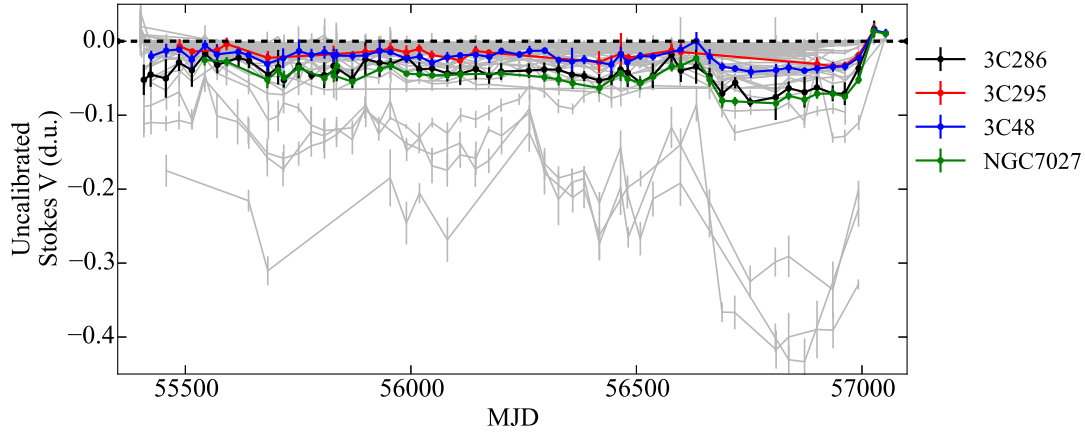


Figure 3.1: Lightcurves of the uncorrected and uncalibrated Stokes V in diode amplitude units (d.u.) for all the sources. The calibrators are marked with colors.

V values and the latter by the fact that they appeared correlated, especially for the standard sources. Spearman ρ tests were performed to quantify the correlations for all the pairs of the standard sources. The correlation is very significant with p values in the range of $0.03 - 10^{-6}$ and corresponding ρ values in the range of $0.57 - 0.92$.

In order to correct this instrumental effect, we followed two independent techniques:

1. The first uses the assumption that the planetary nebula NGC 7027, is unpolarized both linearly and circularly, since it emits thermal radiation. This means that we can set the Stokes V measurement of this nebula as the zero level and calibrate all the other measurements by a subtraction of its value.
2. The second technique is based on the assumption that the average Stokes V for a large number of randomly selected celestial sources is zero, since there should be no preferred handedness for the circular polarization. Thus, since we observed ~ 60 sources in every session, we can use their average Stokes V as the zero level.

The Stokes V level for the standard sources, estimated with both the above techniques for the 4.85 GHz data are shown in Table 3.1. The levels are consistent within the errors between the two techniques but the one using the Stokes V of NGC 7027 as the zero level gives systematically more stable results. Using these results we estimated the average Stokes V and its standard deviation for each calibrator which is also shown in Table 3.1 (labeled as "comb."). This exercise, showed that the calibrators 3C 295 and 3C 48 have significant and stable Stokes V at 4.85 GHz. The significance and stability was estimated by dividing the weighted average Stokes V with its weighted standard deviation over the observing period (columns 4 and 5 of Table 3.1) and accepting values ≥ 3 .

Using the Stokes V values that we estimated by the combination of the above calibration techniques and the corresponding weighted average Stokes I over the observing period (both given in Table 3.1), we calculate the level of circular polarization degree for the sources which showed significant and stable Stokes V . Furthermore, we followed the same procedure for the datasets at 8.35 GHz, where we found significant Stokes V for the calibrators 3C 286 and 3C 48. The results are shown in Table 3.2 (column m_c). The polarization characteristics given in this table are the ones we used to calibrate our datasets and perform the analyses presented in the following chapters.

Table 3.1: The 4.85 GHz calibrated Stokes V parameters of the calibrators along with the estimates of their Stokes I , both expressed in diode amplitude units (d.u.). The calibration technique for which we use the Stokes V of the planetary nebula NGC 7027 as the zero level is labeled as "NGC7027" and the one we use the average Stokes V of all the observed sources in a session as "Average V ". The final Stokes V estimated from the combination of both techniques are labeled as "comb."

Source	Stokes parameter	Calibration technique	Weighted average (d.u)	Weighted σ (d.u)	N
3C286	V	NGC7027	0.011	0.015	40
	V	Average V	-0.007	0.019	50
	V	comb.	-0.003	0.006	...
	I	...	6.207	0.408	55
3C295	V	NGC7027	0.029	0.008	21
	V	Average V	0.036	0.025	25
	V	comb.	0.034	0.005	...
	I	...	5.830	0.260	26
3C48	V	NGC7027	0.027	0.009	37
	V	Average V	0.018	0.015	49
	V	comb.	0.022	0.006	...
	I	...	4.472	0.359	54
NGC7027	V	NGC7027	42
	V	Average V	-0.007	0.013	38
	V	comb.	-0.007	0.013	...
	I	...	4.694	0.258	41

3.4 SYSTEM STABILITY

The various Stokes parameter sensitivity factors and the instrumental EVPA rotation we calculated for all the sessions can be used to quantify the observing system stability in both total intensity and polarization characteristics. In Figures 3.2 and 3.3, we show their histograms for the 4.85 and 8.35 GHz receivers respectively.

The scatter of the instrumental rotation remains as low as $1.2 - 2^\circ$ for the total observing period of 4.5 years and the Stokes parameter sensitivity factors remain stable within $1 - 2\%$ and $1 - 7\%$ for the 4.85 and 8.35 GHz data respectively. We conclude that the observing system is very stable and can deliver high accuracy results for total intensity, linear and circular polarization observations. Such results for the datasets we obtained, recovered and calibrated with the techniques described in Chapters 2 and 3 are presented in the second half of this thesis.

Table 3.2: Polarization characteristics for the standard sources (calibrators). The given Stokes parameters Q and U are expressed in the North–East (N–E) reference frame.

Source	Freq. (GHz)	Stokes				$m_l^{(1)}$ (%)	$\chi^{(1)}$ (°)	m_c (%)
		$I^{(1)}$ (Jy)	Q (Jy)	U (Jy)	V (Jy)			
3C286	4.85	7.48	0.340	0.765	0.000	11.19	33.0	0.00
	8.35	5.22	0.238	0.534	0.003	11.19	33.0	0.06
3C295	4.85	6.56	0.000	0.000	0.038	0.00	0.0	0.58
	8.35	3.47	0.017	0.027	0.000	0.93	28.9	0.00
3C48	4.85	5.48	-0.192	-0.126	0.027	4.19	106.6	0.50
	8.35	3.25	-0.115	-0.132	-0.007	5.39	114.5	-0.20
NGC7027	4.85	5.48	0.000	0.000	0.000	0.00	0.0	0.00
	8.35	5.92	0.000	0.000	0.000	0.00	0.0	0.00

(1) Dr. A. Kraus (priv.comm.)

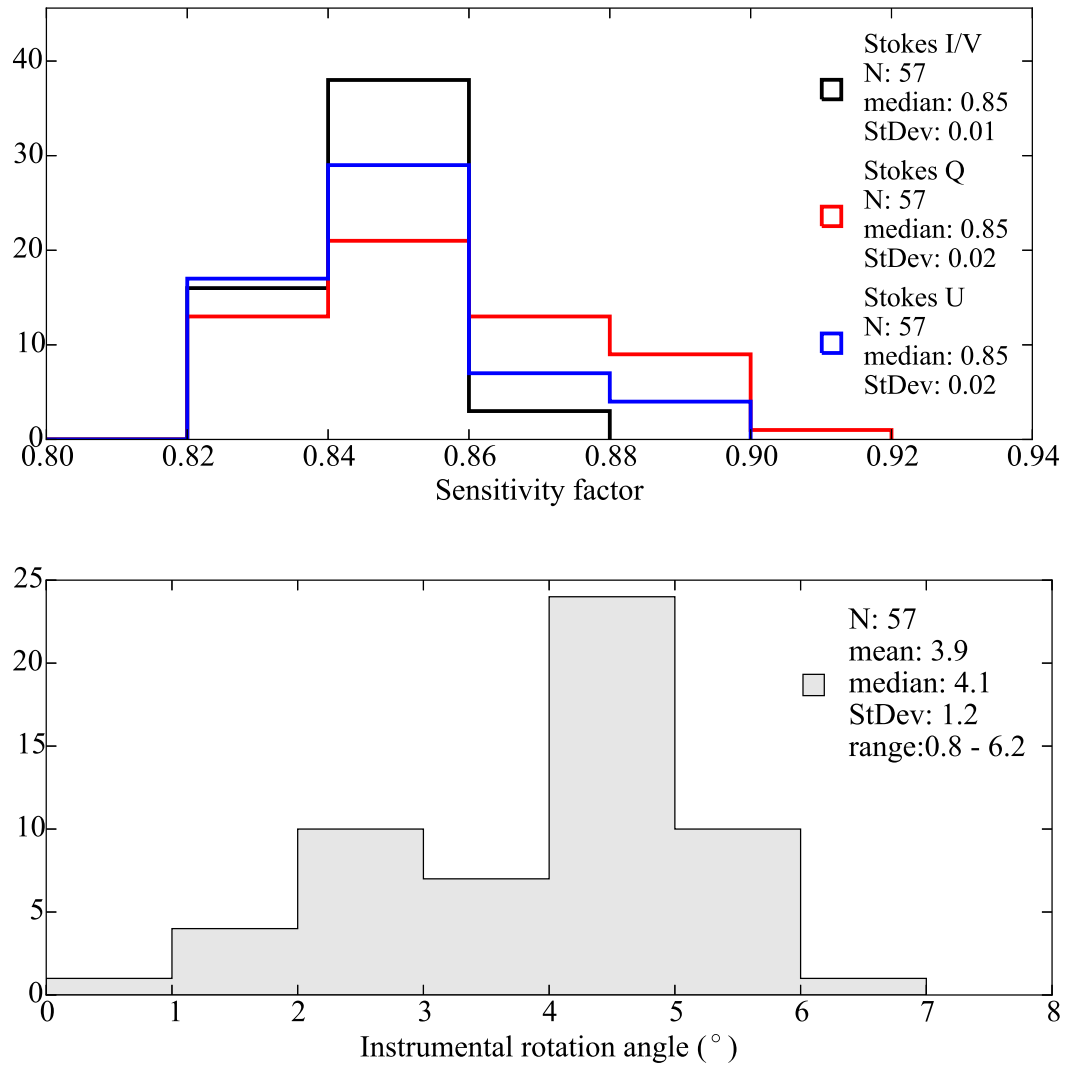


Figure 3.2: Histograms of the Stokes parameter sensitivity factors and the instrumental EVPA rotation angle for the 4.85 GHz system over the observing period.

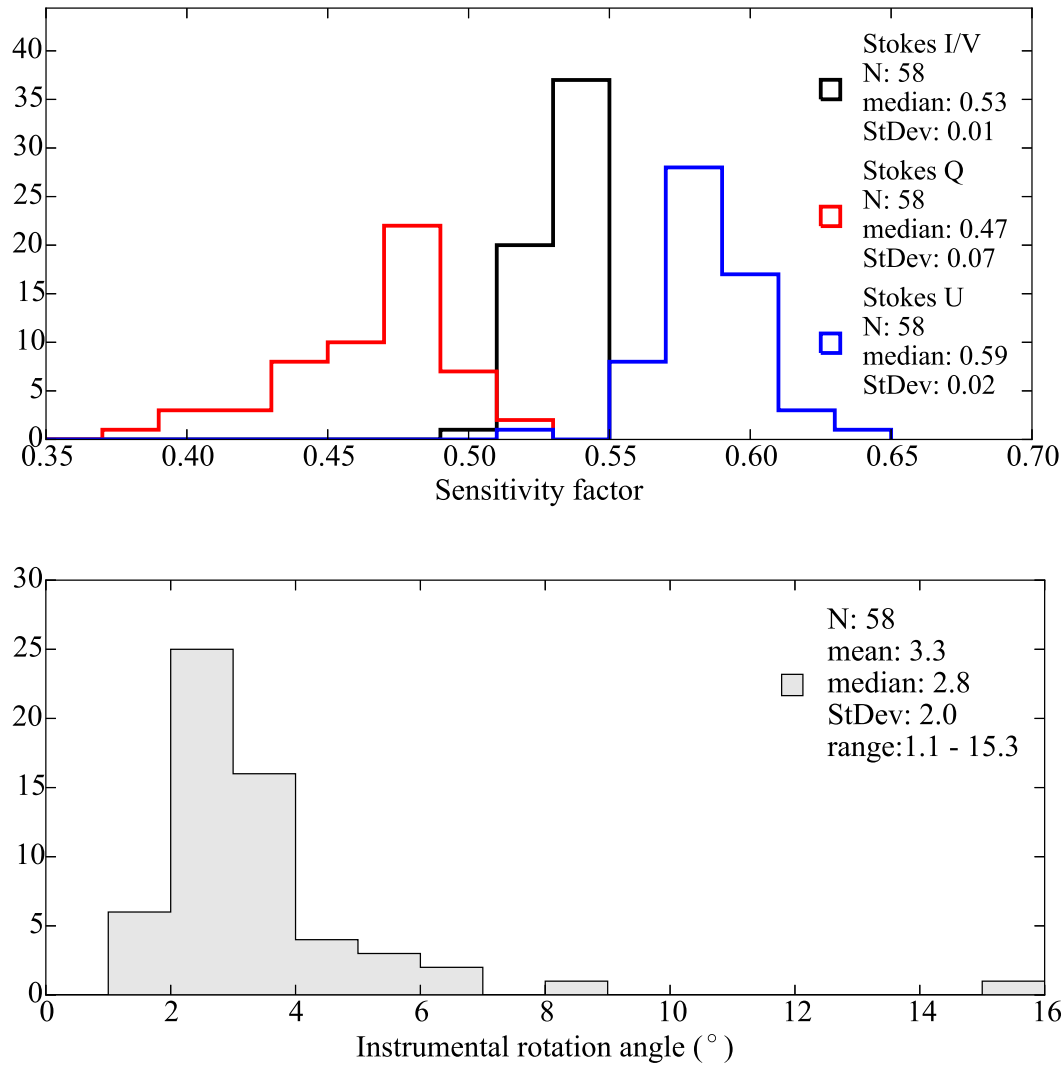


Figure 3.3: Histograms of the Stokes parameter sensitivity factors and the instrumental EVPA rotation angle for the 8.35 GHz system over the observing period.

Chapter 4

Radio linear and circular polarization of AGN jets

Abstract

The methodology described in Chapter 2 was developed specifically for the purposes of this thesis. It was used for the entire analysis of the part of the *F-GAMMA* dataset that is discussed here (2010.6 - 2015.1), in terms of both total flux, linear and circular polarization. The current chapter is meant to present the analysis of the polarization data of the *F-GAMMA* sources. After the presentation of the data we present some correlation analyses and attempt an answer to some relevant “key” questions.

4.1 INTRODUCTION

In this chapter we describe the linear and circular polarization properties of a large sample of AGNs consisting mostly of blazars – i.e. the ones with the jet axis almost aligned to our line of sight. We managed to recover their linear and circular polarization properties over four different radio frequencies and over a large number of observing sessions which cover the last 4.5 yrs, using the methodologies described in Chapters 2 and 3. This high-cadence and multi-frequency approach allows us to study also the frequency and time dependence of those characteristics, which show pronounced variability as discussed below.

The prerequisite conditions for the emergence of significant polarization, provide a unique handle on the physical conditions at the emitting element. In the current chapter we investigate two of them, namely the magnetic field of the emitting (and transmitting) plasma and its low energy particle content. Finally, we investigate a number of relations between different observed properties such as the position angle of their jet, their linear and circular polarization, rotation measure, magnetic fields or flux density state. Such relations can be connected with the corresponding theoretical predictions to provide an insight onto the physical mechanisms that govern these sources.

4.2 THE DATASET

Our sample includes 87 radio-loud AGNs which have been observed with the 100-m Effelsberg telescope in the framework of the *F-GAMMA* monitoring program¹ (Fuhrmann et al., 2007; Angelakis et al., 2010). A list of the observed sources is given in Table 4.1 along with some useful information. Although the program has been observing in total flux density and polarization mode since January 2007, this thesis deals with a subset of these observations covering

¹<http://www.mpifr-bonn.mpg.de/div/vlbi/fgamma>

the period from July 2010 until January 2015. The observations have been conducted over 56 sessions with a median cadence of 49.4 days (1.6 months). For four of the 8 receivers, the total power is paired with polarization information. For the receivers operating at 2.64, 4.85, 8.35 and 10.45 GHz linear polarization information has been recovered. At 4.85 and 8.35 also circular polarization has been reduced.

In Table A.1 we give some representative statistical moments for the total flux density and polarization characteristics of the observed sources. For each source and observing frequency we provide the number of data points which passed our selection criteria, N_{sign} , over the total number of data points obtained and some basic descriptive statistics for a number of observed quantities shown in the third column with the title x . These quantities are:

- the linear polarization degree, m_l , and flux density Π_l
- the absolute circular polarization degree, $|m_c|$, and flux density $|\Pi_c|$
- the total flux density, S
- the electric vector position angle (EVPA), χ

Note that in some cases the total number of points that passed the quality checks for the m_l may be different from those for the Π_l . In those cases, Π_l has been measured (from COS and SIN channels) while m_l has been corrupted because of corrupted total flux density measurement. EVPA measurements are reported for all successful Π_l measurements.

For each of the above quantities we provide the total number of measurements that passed a set of quality checks, the weighted average, $\langle x \rangle$, and standard deviation, σ_x , over the time that the quantity has been observed. The modulation index, $\frac{\sigma_x}{\langle x \rangle}$, as a measure of the variability amplitude of the source in that quantity as well as the median, minimum and maximum values.

4.2.1 Quality Checks and data operations

The data quality limits, depend on the measured quantity and are briefly described as follows:

- For the total flux density, S , we rejected data with
 1. signal-to-noise ratio < 3
 2. extreme values for which the absolute deviation from the median value of the corresponding dataset was larger than 10 times the standard deviation of the rest of the dataset (if number of measurements ≥ 2)
- For the linear polarization degree, m_l , and flux density, Π_l we rejected data with
 1. signal-to-noise ratio < 3
 2. extreme values defined as above
 3. *Only for m_l :* values associated with corrupted corresponding total flux density measurements
- For the EVPA, we rejected data with
 1. signal-to-noise ratio of the corresponding linear polarization flux density < 3
 2. values associated with corrupted corresponding linear polarization flux density
- For the circular polarization degree, m_c , and flux density, Π_c we rejected data with
 1. extreme values defined as above
 2. signal-to-noise ratio < 3
 3. values associated with corrupted corresponding total flux density measurements

The EVPA datasets have been corrected for the $n\pi$ ambiguity with the methodology described in Kiehlmann et al. (2013): stating from the first data point in time, we calculate the absolute EVPA difference between two adjacent data points, taking into account their errors, σ , as

$$\Delta\chi = |\chi_{i+1} - \chi_i| - \sqrt{\sigma_{\chi_{i+1}}^2 + \sigma_{\chi_i}^2} \quad (4.1)$$

If $\Delta\chi$ is found to be more than $\pi/2$, we subtract n times π from the latter data point, χ_{i+1} , with n selected so that the difference 4.1 is minimized.

The corresponding lightcurves for the quantities described in Table A.1 are shown in Figures B.1-B.29.

Table 4.1: The list of the observed sources.

<i>F-GAMMA</i> source ID	Catalog name	RA hh:mm:ss.s	DEC dd:mm:ss.s	Class ^(a)	redshift ^(b)
3C 48	3CR 48	01:37:41.3	+33:09:35.1	QSO ⁹	0.367
3C 161	3C 161	06:27:10.1	-05:53:05	Quasar ¹¹	...
3C 286	3CR 286	13:31:08.3	+30:30:33.0	QSO ⁹	0.850
3C 295	3C 295	14:11:20.5	+52:12:09.5	Radio Galaxy ¹⁰	0.464
J0006-0623	PKS 0003-066	00:06:13.9	-06:23:35.3	FSRQ	0.347
J0050-0929	FBQS J0050-0929	00:50:41.3	-09:29:05.2	BL Lac	0.634
J0102+5824	87GB 0059+5808	01:02:45.8	+58:24:11.1	FSRQ ¹	0.644
J0136+4751	0133+476	01:36:58.6	+47:51:29.1	FSRQ	0.859
J0217+0144	0215+015	02:17:49.0	+01:44:49.7	FSRQ	1.715
J0221+3556	B2 0218+35	02:21:05.5	+35:56:13.9	Blazar	0.944
J0222+4302	3C 066A	02:22:39.6	+43:02:07.8	BL Lac	0.444
J0237+2848	0234+285	02:37:52.4	+28:48:09.0	FSRQ	1.213
J0238+1636	0235+164	02:38:38.9	+16:36:59.3	BL Lac	0.940
J0241-0815	NGC 1052	02:41:04.8	-08:15:20.8	Seyfert 2 ⁷	0.005
J0303+4716	0300+470	03:03:35.2	+47:16:16.3	BL Lac	0.475
J0319+1845	0317+185	03:19:51.8	+18:45:34.2	BL Lac	0.190
J0319+4130	3C 084	03:19:48.2	+41:30:42.1	Blazar	0.018
J0324+3410	1H 0323+342	03:24:41.2	+34:10:45.1	NLSy1 ⁸	0.061
J0336+3218	0333+321	03:36:30.1	+32:18:29.3	FSRQ	1.259
J0339-0146	0336-019	03:39:30.9	-01:46:35.8	FSRQ	0.850
J0349-2102	PKS 0347-211	03:49:57.9	-21:02:47.7	FSRQ	2.944
J0359+5057	4C +50.11	03:59:29.7	+50:57:50.2	FSRQ ⁵	1.520
J0418+3801	3C 111	04:18:21.3	+38:01:35.8	Seyfert 1 ²	0.049
J0423-0120	0420-014	04:23:15.8	-01:20:33.1	FSRQ	0.916
J0433+0521	3C 120	04:33:11.1	+05:21:15.6	Blazar	0.033
J0507+6737	1ES 0502+675	05:07:56.2	+67:37:24.4	BL Lac	0.416
J0530+1331	PKS 0528+134	05:30:56.4	+13:31:55.1	FSRQ	2.070
J0654+4514	B3 0650+453	06:54:23.6	+45:14:22.9	Blazar	0.933
J0719+3307	B2 0716+33	07:19:19.4	+33:07:09.7	Blazar	0.779
J0721+7120	0716+714	07:21:53.4	+71:20:36.4	BL Lac	0.328
J0730-1141	0727-115	07:30:19.0	-11:41:13.0	FSRQ	1.589
J0738+1742	0735+178	07:38:07.4	+17:42:19.0	BL Lac	0.424
J0750+1231	0748+126	07:50:52.0	+12:31:04.8	FSRQ	0.889
J0808-0751	0805-077	08:08:15.5	-07:51:09.9	FSRQ	1.837
J0818+4222	B3 0814+425	08:18:16.0	+42:22:45.4	BL Lac	0.530
J0824+5552	0820+560	08:24:47.2	+55:52:42.7	FSRQ	1.417
J0830+2410	0827+243	08:30:52.1	+24:10:59.8	FSRQ	0.939
J0841+7053	0836+710	08:41:24.4	+70:53:42.2	FSRQ	2.218
J0849+5108	SBS 0846+513	08:49:58.0	+51:08:29.0	NLSy1 ^{3,4}	0.584
J0854+2006	OJ +287	08:54:48.9	+20:06:30.6	BL Lac	0.306
J0920+4441	0917+449	09:20:58.3	+44:41:53.9	FSRQ	2.190
J0948+0022	0946+006	09:48:57.3	+00:22:25.6	FSRQ,NLSy1 ⁴	0.585

Table 4.1: continued.

<i>F-GAMMA</i> source ID	Catalog name	RA hh:mm:ss.s	DEC dd:mm:ss.s	Class ^(a)	redshift ^(b)
J0958+6533	0954+658	09:58:47.2	+65:33:54.8	BL Lac	0.367
J1041+0610	1038+064	10:41:17.2	+06:10:16.9	FSRQ	1.264
J1104+3812	MRK 0421	11:04:27.3	+38:12:31.8	BL Lac	0.030
J1128+5925	1125+596	11:28:13.3	+59:25:14.8	FSRQ	1.795
J1130-1449	1127-145	11:30:07.1	-14:49:27.4	FSRQ	1.184
J1136+7009	MRK 0180	11:36:26.4	+70:09:27.3	BL Lac	0.045
J1159+2914	1156+295	11:59:31.8	+29:14:43.8	FSRQ	0.729
J1217+3007	BZB J1217+3007	12:17:52.1	+30:07:00.6	BL Lac	0.130
J1221+2813	W Com	12:21:31.7	+28:13:58.5	BL Lac	0.102
J1224+2122	PG 1222+216	12:24:54.5	+21:22:46.4	FSRQ	0.435
J1229+0203	3C 273	12:29:06.7	+02:03:08.6	FSRQ	0.158
J1230+1223	M 087	12:30:49.4	+12:23:28.0	Radio Galaxy ¹	0.004
J1246+0238	...	12:46:34.7	+02:38:09.1	NLSy1 ⁴	0.363
J1256-0547	3C 279	12:56:11.2	-05:47:21.5	FSRQ	0.536
J1310+3220	OP +313	13:10:28.7	+32:20:43.8	Blazar	0.997
J1332-0509	PKS 1329-049	13:32:04.3	-05:09:42.9	FSRQ	2.150
J1345+4452	1343+451	13:45:33.2	+44:52:59.6	FSRQ	2.534
J1354-1041	PKS 1352-104	13:54:46.5	-10:41:02.7	FSRQ	0.330
J1408-0752	PKS B1406-076	14:08:56.5	-07:52:26.7	FSRQ	1.494
J1428+4240	H 1426+428	14:28:32.7	+42:40:20.6	BL Lac	0.129
J1504+1029	PKS 1502+106	15:04:25.0	+10:29:39.0	FSRQ	1.839
J1505+0326	PKS 1502+036	15:05:06.5	+03:26:31.0	FSRQ,NLSy1 ⁸	0.409
J1512-0905	PKS 1510-089	15:12:50.5	-09:05:59.8	FSRQ	0.360
J1522+3144	B2 1520+31	15:22:10.0	+31:44:14.4	FSRQ	1.487
J1540+8155	1ES 1544+820	15:40:16.0	+81:55:05.5	BL Lac	0.000
J1542+6129	1542+616	15:42:56.8	+61:29:54.9	BL Lac	0.000
J1553+1256	1551+130	15:53:32.7	+12:56:51.7	FSRQ	1.308
J1555+1111	1ES 1553+113	15:55:43.0	+11:11:24.4	BL Lac ¹	0.360
J1613+3412	1611+343	16:13:41.1	+34:12:47.9	FSRQ	1.397
J1635+3808	4C +38.41	16:35:15.5	+38:08:04.5	FSRQ	1.814
J1642+3948	3C 345	16:42:58.8	+39:48:37.0	FSRQ	0.593
J1653+3945	MRK 0501	16:53:52.2	+39:45:36.6	BL Lac	0.033
J1733-1304	PKS 1730-13	17:33:02.7	-13:04:49.5	FSRQ	0.902
J1751+0939	OT +081	17:51:32.8	+09:39:00.7	Blazar	0.322
J1800+7828	S5 1803+78	18:00:45.7	+78:28:04.0	BL Lac	0.680
J1806+6949	3C 371	18:06:50.7	+69:49:28.1	BL Lac	0.046
J1824+5651	4C +56.27	18:24:07.1	+56:51:01.5	BL Lac	0.664
J1848+3219	1846+322	18:48:22.0	+32:19:01.9	FSRQ	0.798
J1849+6705	S4 1849+670	18:49:16.1	+67:05:41.7	FSRQ	0.657
J1911-2102	1908-211	19:11:53.9	-21:02:43.8	FSRQ	1.420
J1923-2104	1920-211	19:23:32.2	-21:04:33.3	FSRQ	0.874
J1959+4044	Cyg A	19:59:28.4	+40:44:02.1	FRII ⁶	0.056
J1959+6508	1ES 1959+650	19:59:59.9	+65:08:54.7	BL Lac	0.047

Table 4.1: continued.

<i>F-GAMMA</i> source ID	Catalog name	RA hh:mm:ss.s	DEC dd:mm:ss.s	Class ^(a)	redshift ^(b)
J2025-0735	2022-077	20:25:40.6	-07:35:52.0	FSRQ	1.388
J2143+1743	2141+175	21:43:35.5	+17:43:48.0	FSRQ	0.213
J2147+0929	2144+092	21:47:10.0	+09:29:45.9	FSRQ	1.113
J2158-1501	PKS 2155-152	21:58:06.3	-15:01:09.3	FSRQ	0.672
J2158-3013	PKS 2155-304	21:58:52.0	-30:13:32.0	BL Lac	0.116
J2202+4216	BL Lacertae	22:02:43.3	+42:16:40.0	BL Lac	0.069
J2203+1725	2201+171	22:03:27.0	+17:25:48.2	FSRQ	1.076
J2203+3145	2201+315	22:03:15.0	+31:45:38.3	FSRQ	0.295
J2225-0457	3C 446	22:25:47.3	-04:57:01.4	FSRQ	1.404
J2229-0832	2227-088	22:29:40.1	-08:32:54.4	FSRQ	1.560
J2232+1143	CTA 102	22:32:36.4	+11:43:50.9	FSRQ	1.037
J2253+1608	3C 454.3	22:53:57.7	+16:08:53.6	FSRQ	0.859
J2325+3957	B3 2322+396	23:25:17.9	+39:57:37.0	BL Lac	0.000
J2327+0940	2325+093	23:27:33.4	+09:40:09.0	FSRQ	1.843
J2347+5142	1ES 2344+514	23:47:04.8	+51:42:17.9	BL Lac	0.044
J2348-1631	PKS 2345-16	23:48:02.6	-16:31:12.0	FSRQ	0.576
NGC 7027	NGC 7027	21:07:01.6	+42:14:10.2	Pl. Nebula ¹²	...

(a) Taken from the 3rd online edition of the “The Roma BZCAT Multi-frequency Catalogue of Blazars” (original paper, Massaro et al. (2009)) unless otherwise noted with a superscript according to one of the references below. The classes “FSRQ” and “Blazar” stand for the “QSO RLOud flat radio sp.” and “Blazar Uncertain type” in the catalog.

(b) Taken from the same catalog as before. If the source was not in the catalog, we searched the NASA/IPAC Extragalactic Database (NED) for a redshift measurement.

References. (1) Nolan et al. (2012), (2) Véron-Cetty and Véron (2006), (3) Zhou et al. (2005), (4) Yuan et al. (2008), (5) Acosta-Pulido et al. (2010), (6) Leahy and Williams (1984), (7) Maia et al. (2003), (8) Angelakis et al. (2015), (9) Hewitt and Burbidge (1980), (10) Perley and Butler (2013a), (11) Souchay et al. (2012), (12) Zijlstra et al. (2008)

Table 4.2: The numbers of sources with at least 1 significantly polarized data point (i.e. $N_{\text{sign}} \geq 1$) for each frequency.

Freq. (GHz)	Quantity	Detected sources	Percentage (%)	$\langle m_{l,c} \rangle$ (%)
2.64	Π_l	72/79	91.1	3.0
4.85	Π_l	67/85	78.8	3.1
	Π_c	44/85	51.8	0.5
8.35	Π_l	73/84	86.9	3.1
	Π_c	48/84	57.1	0.4
10.45	Π_l	61/79	77.2	3.2

4.2.2 Demographics of polarized sources

The demographics of the observed sources in terms of their polarization characteristics are shown in Table 4.2. In the third column, we report the number of sources we measured the corresponding quantity at least once over the total number of sources except for the planetary nebula NGC7027 which was observed as calibrator. These sources have $N_{\text{sign}} \geq 1$ in Table A.1. In column 4 we give the same number as a percentage and in column 5 the average value of the linear and circular polarization degree of our dataset for each frequency.

A large fraction, around 80-90 %, of the observed AGNs were found to be linearly polarized at least once. Concerning the circular polarization, a mere 55% showed significant circular polarization degree at least once; i.e. signal-to-noise ratio ≥ 3 . As we discuss later, the main reason for this is the intrinsically lower degree of circular polarization ($\sim 0.4 - 0.5\%$) which makes the detection of circularly polarized flux extremely challenging, especially for sources with comparatively low flux density.

4.2.3 Linearly and circularly-only polarized sources

There are 40 and 46 sources that show both linear and circular polarization characteristics in our 4.85 and 8.35 GHz data respectively. Here we are focusing on the sources that show either linear or circular only polarization. The numbers of sources which were found either linearly or circularly polarized in any combination are shown in Table 4.3.

Table 4.3: Combined linear and circular polarization characteristics. Number of sources found either linearly or circularly polarized in any combination.

Freq. (GHz)	LP	CP	Number
4.85	Y	Y	40
	Y	N	27
	N	Y	4
	N	N	14
8.35	Y	Y	46
	Y	N	27
	N	Y	2
	N	N	9

As shown in that table, there are 27 sources in both 4.85 and 8.35 GHz datasets which show linear but no circular polarization. One possible explanation for the m_c deficiency for these sources is that they show lower levels of total flux density, S , and hence they do not satisfy the detection limits of circular polarization for our system. Since the m_c levels are usually in the range of 0.2 - 1. %, their circularly polarized flux density (Π_c) is possibly not detected. This interpretation is supported by the histograms shown in Fig. 4.1, where we plot the median total flux densities for sources which show both linear and circular polarization (LP and CP) and the ones which show only linear polarization. The two distributions have different median values, in accordance to our interpretation that sources which show only linear polarization have systematically lower total flux levels than the ones that show both linear and circular polarization. The 2 sample KS test results support that the two distributions are indeed different with confidence level of 99.9 and 99.4 % for the 4.85 and 8.35 GHz data respectively.

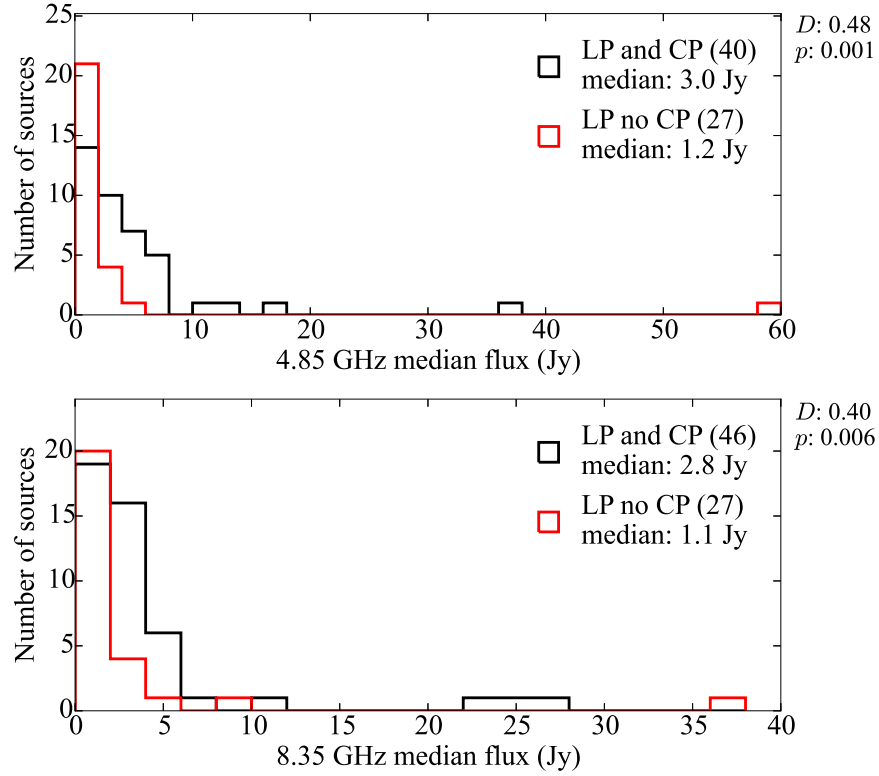


Figure 4.1: Histograms of the flux densities for sources which show both linear and circular polarization as well as the ones which show linear but no circular polarization. The results support that the two samples are drawn from two different distributions with median total flux densities which are shown in the legend of each graph.

Only circularly polarized sources

There is also a very interesting subgroup of sources for which, we have detected circular polarization at least once with 3 sigma significance, but no linear polarization. Their number is very small. 4 sources in the 4.85 GHz data and 2 for the 8.35 GHz. Other than the simplistic interpretation that these are false-positive detections of circular polarization, this observable should be connected with the physical characteristics of these sources. For example, Very Long Baseline Interferometry (VLBI) observations of these sources show either very compact configurations or double sided jets which appear to lie on the plane of the sky. If the observed emission is coming from an ultra-compact, point-like jet, then the excess of circular polarization, could be explained by depolarization effects which affect the linear polarization characteristics more than the circular ones. In other words, this may be an indication that circular polarization “survives” various depolarization effects as we show also in subsection 4.4.3.

4.2.4 Linear polarization per observing frequency

In Fig. 4.2 we show with grey color the distribution of the median linear polarization degree for all sources and for each of the four frequencies. The red and blue histograms show the corresponding distributions for the Flat Spectrum Radio Quasars (FSRQs) and the BL Lac sources respectively for a direct comparison. Since there are sources classified as neither FSRQ nor BL Lac in our sample (see also Table 4.1), the number of the ones in the grey histograms is always greater than the sum of those in the red and blue ones (given in the corresponding parentheses). This representation is followed for all the plots shown in this chapter. The total

number of sources with $N_{\text{sign}} \geq 1$ is given in the legend of each plot as N , along with the mean, median and standard deviation for each dataset. The average linear polarization degrees for each frequency were also reported in Table 4.2. Finally, in order to disentangle the polarized from the total flux density, we give in Fig. 4.3 the corresponding histograms for the median linearly polarized flux density.

Judging from either the median or the mean values, we observe that the linear polarization degree and flux appear to be correlated with the observing frequency. A similar result is found by Agudo et al. (2014) where they compare their polarization data at 86 and 229 GHz with the ones measured by the MOJAVE program at 15 GHz (Lister et al., 2009). They argue that the increase of the linear polarization degree with increasing frequency is due to the better ordering of the magnetic field closer to the central engine. The higher the frequency the closer we look at the central engine due to opacity effects. Additionally, the increased depolarization due to the Faraday rotation effect is expected towards lower frequencies.

4.2.5 Circular polarization per observing frequency

In Fig. 4.4 we show the distribution of the median absolute circular polarization degree, m_c , at 4.85 and 8.35 GHz. We perform our analysis for the absolute values of circular polarization in order to avoid cancellations due to the different handedness (sign) of the measured circular polarization. We remind that for our analysis, we adopt the positive circular polarization degree sign for the left-handed circularly polarized radiation. Furthermore, we plot in Fig. 4.5 the corresponding distribution of the median absolute circular polarization flux density.

No significant difference was found between the 4.85 and 8.35 GHz circular polarization information for our sample. The difference was insignificant between those two frequencies also for the linear polarization parameters. We interpret this result as a consequence of the fact that the emission is coming from neighboring regions in the jet with similar physical conditions.

4.2.6 Polarized state duration

Since we are working with monitoring data, we can tackle the question of what fraction of their activity the sources remain in states of significant polarization. In order to solidify the results of this analysis, we consider sources that have been observed at least 10 times. For each source, we compute the fraction of the number of times it was found to be polarized over the total number of times it was measured. The results are shown in Figures 4.6 and 4.7.

The majority of the linearly polarized sources are found at significantly polarized state for 80 - 90 % of the time they were observed. Interestingly, this is not the case for the highest observing frequency at 10.45 GHz, where the corresponding fraction has a median of 28 %. A possible interpretation for this peculiar behavior is the increased variability of the sources at higher frequencies. If the variability is caused by the optical depth and spectral evolution of emitting elements, as described in Chapter 5, their linear polarization degree is often minimized or vanishes when they change from optically thick to thin. Thus intense variability can render the polarized part of the jet emission unobservable for at least part of the time that it is observed.

On the other hand, sources which were measured to be circularly polarized at least once, acquire this state only for a small fraction of the time (median: 7 %). This is expected for variable sources since the intrinsically low fraction of circular polarization (Table 4.2) restricts our capacity to measure it to only the brief periods the source remains at a high total flux state.

4.2.7 Total flux and linear polarization spectra

In subsection 4.2.4, we showed that there is a weak correlation between the linear polarization degree and the observing frequency. Since we acquired monitoring data, we can show that this “static” approach is not valid when the dynamics of the relation is investigated. In fact we

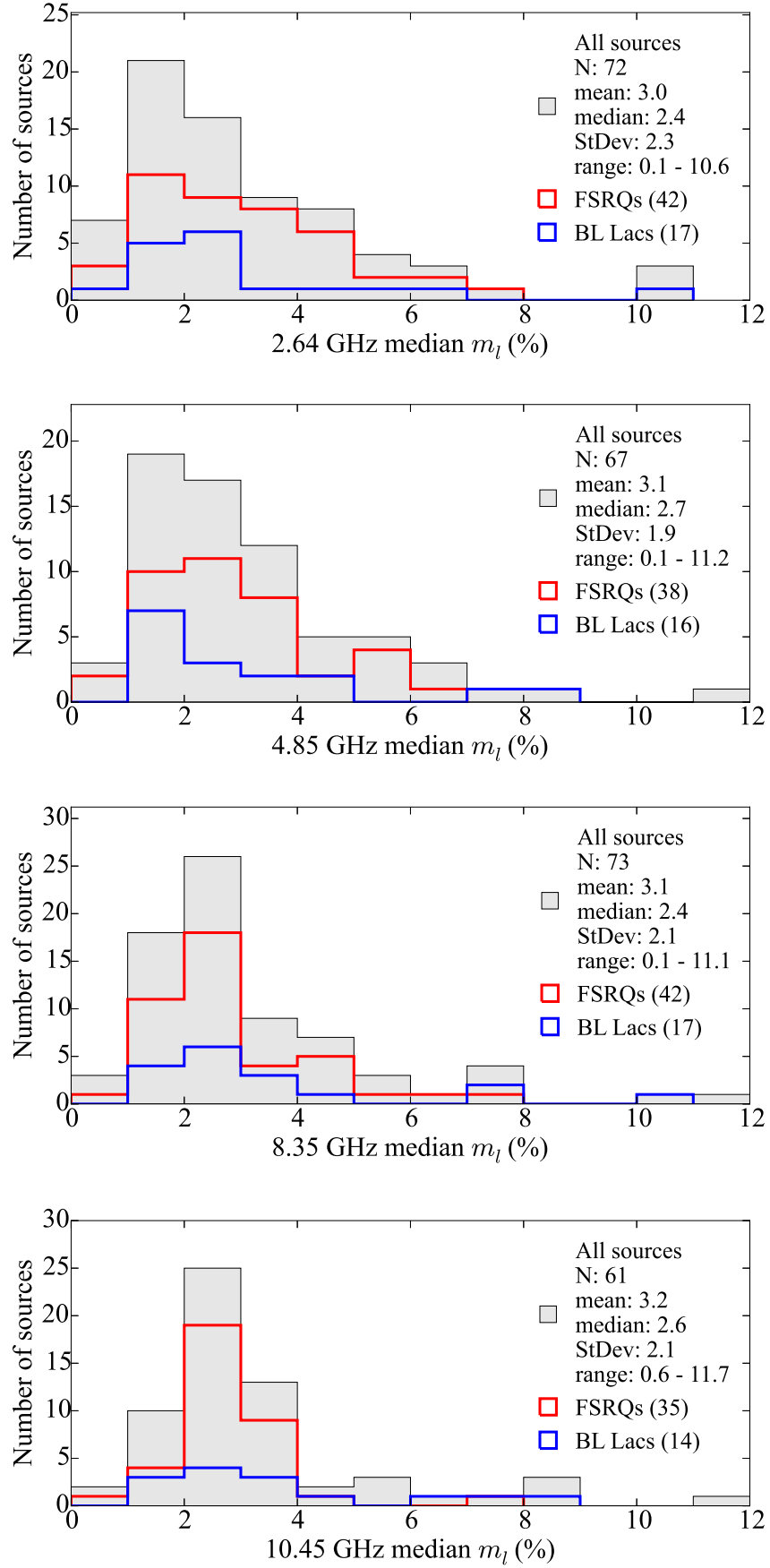


Figure 4.2: The distribution of the linear polarization degree, m_l , for sources with at least one significantly detected polarization data point at each observing frequency.

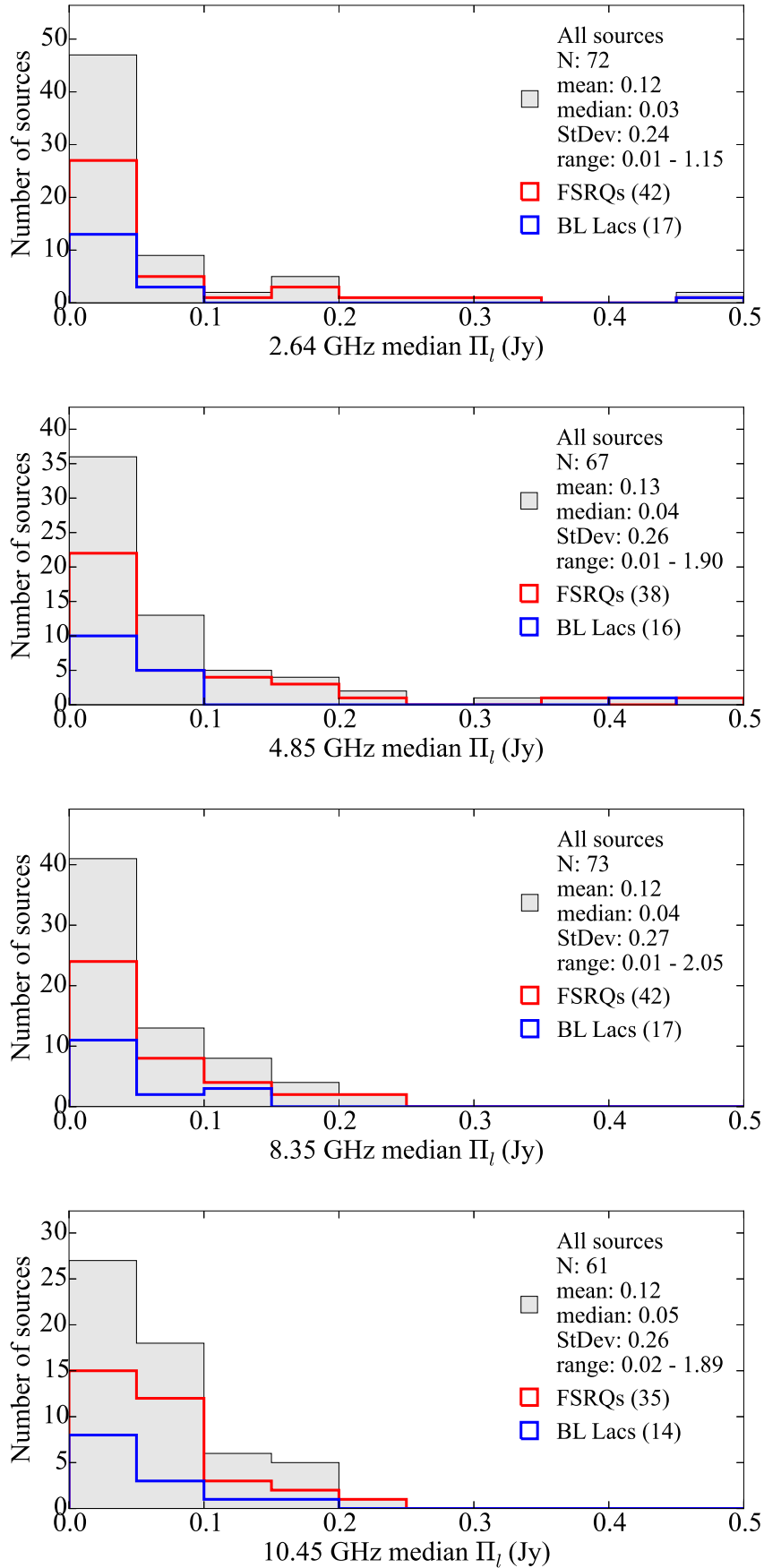


Figure 4.3: The distributions of the linearly polarized flux density, Π_l , for sources with at least one significant polarization data point at each observing frequency. The plots have been truncated to 0.5 Jy to ease reading. There are a small number of data points outside this range.

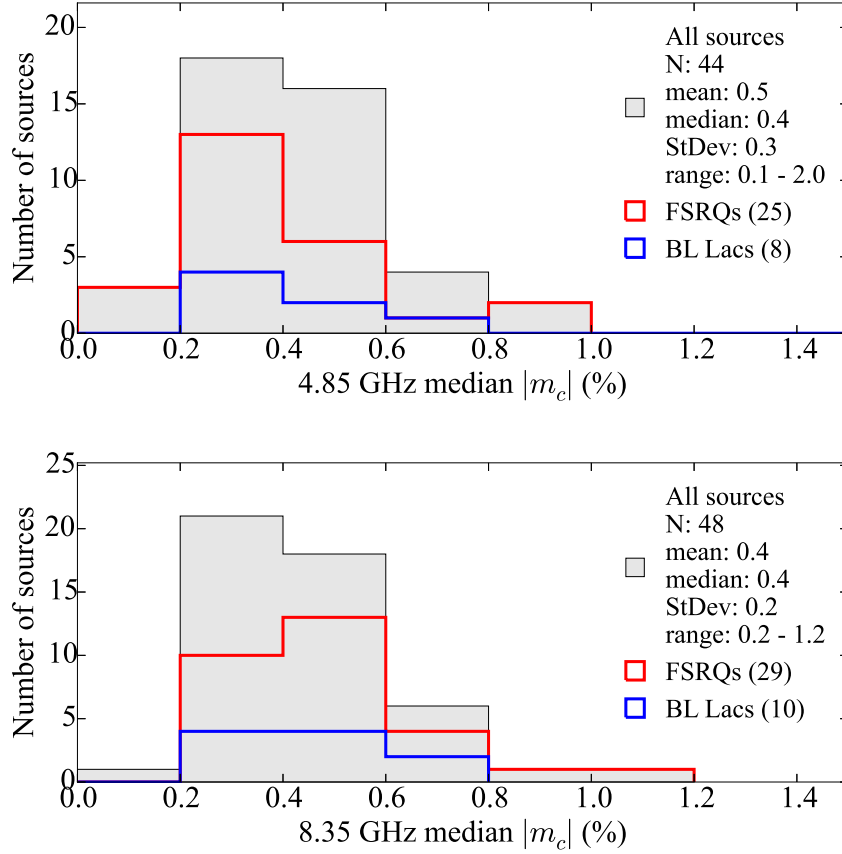


Figure 4.4: The distribution of the absolute circular polarization degree, m_c , for sources with at least one significantly detected polarization data point at each observing frequency. The plots have been truncated to 1.5 % to ease reading. There is one data point outside this range for the 4.85 GHz histogram.

observed significant variability in the frequency dependence of the linear polarization characteristics (m_l versus frequency) for the majority of the sources. This is expected since, in the case of (incoherent) synchrotron emission, the linear polarization degree is a function of the spectral index (see also subsection 1.4.1) and most of these sources show pronounced spectral variability (e.g. Angelakis et al., 2012).

In Figures C.1 - C.29, we show the spectral variations of the total flux density as well as the linear polarization degree along with the temporal variations of the corresponding fitted power-law spectral indices. The indices were measured by fitting a single power-law function for each spectrum using:

$$\log S = \alpha_S \log \nu + \text{const.} \quad (4.2)$$

$$\log m_l = \alpha_l \log \nu + \text{const.} \quad (4.3)$$

In the bottom panels of each plot we give the lightcurves of α_S and α_l .

For a subset of sources like J1256-0547 (3C 279) or J2253+1608 (3C 454.3) and for a number of measurements, the m_l versus ν curve is not described by a single power law. In these cases, we measure a clear minimization of m_l at one of the observed frequencies. This fact, combined with the concurrent rotation of the EVPA by 90° , points towards the fact that we observe a clear transition between the optically thick and thin regimes of a component emitting

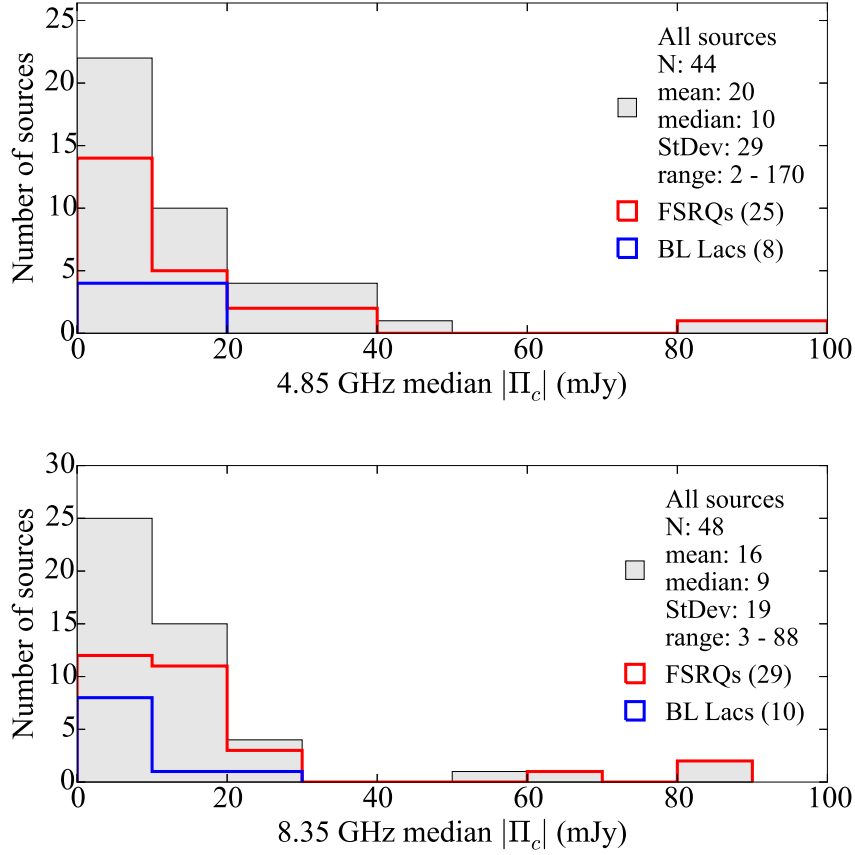


Figure 4.5: The distributions of the absolute circularly polarized flux density, Π_c , for sources with at least one significant polarization data point at each observing frequency. The plots have been truncated to 100 mJy to ease reading. There is one data point outside this range for the 4.85 GHz histogram.

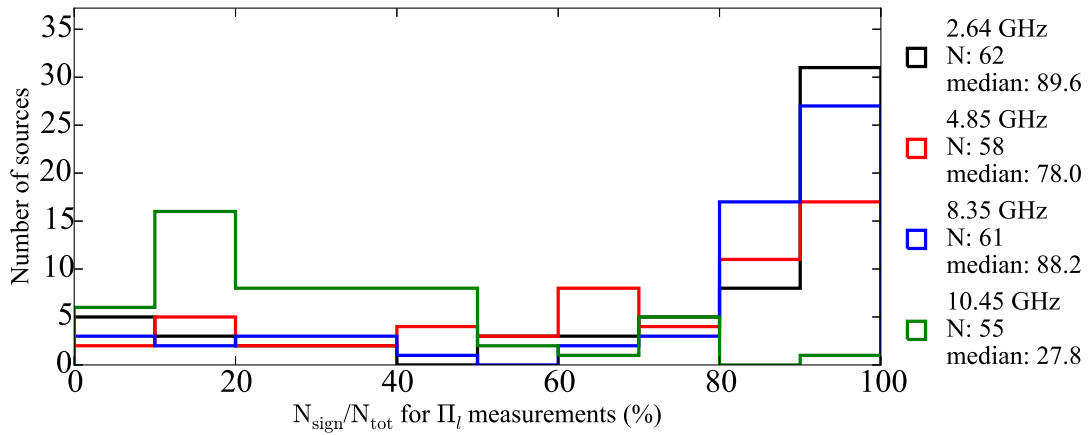


Figure 4.6: Histograms of the fraction of the number of times the sources were detected to be linearly polarized over the number of times they were observed. The analysis was performed for sources that were observed at least 10 times.

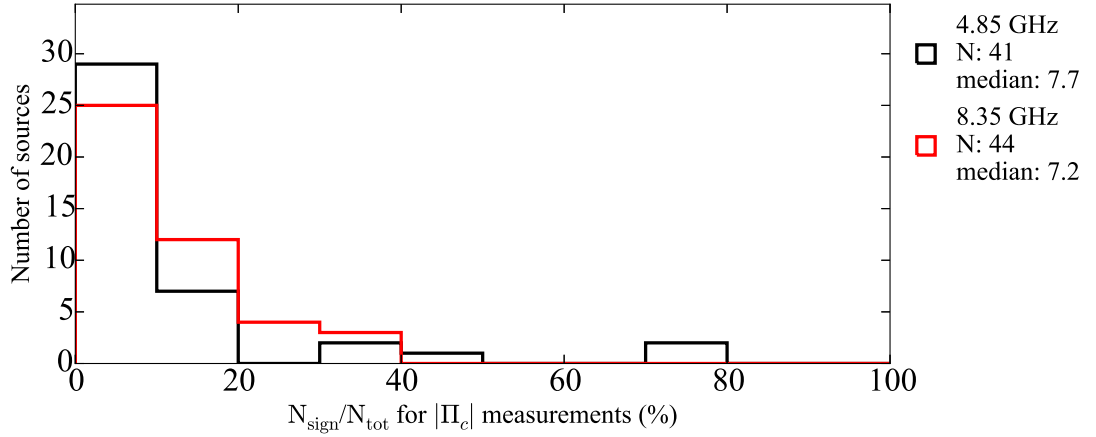


Figure 4.7: Histograms of the fraction of the number of times the sources were detected to be circularly polarized over the number of times they were observed. The analysis was performed for sources that were observed at least 10 times.

a synchrotron self-absorbed spectrum. These transitions can provide a wealth of information for the physical conditions of the emitting components as it is discussed in detail in Chapter 5.

4.3 DERIVATIVE QUANTITIES

The prerequisite conditions for the emergence of significant linear polarization and even more so for circular polarization, provide a unique handle on the physical conditions at the emitting element. Here we examine only two examples: The magnetic field magnetizing the emitting (and transmitting) plasma and the low energy particle content (through rotation measure studies) of that plasma. In separate publications we explore the full potential of the technique by studying other parameters that can reveal through polarization.

4.3.1 Magnetic field magnitude

The degree of circular polarization allows us to have a direct estimate of the magnetic field strength at the emission site. Under the assumptions that

1. the observed circular polarization degree is attributed to the intrinsic synchrotron emission mechanism and not other polarization modifying effects such as Faraday conversion
 2. the emitting particles are electrons
 3. the magnetic field is uniform at least at the linear scales of the emitting region,
- the degree of circular polarization is directly related to the magnetic field strength by

$$m_c \sim \sqrt{\frac{\nu_B}{\nu_{\text{em}}}} \quad (4.4)$$

(Homan et al., 2009) where,

- ν_{em} the frequency of emission
 $\nu_B = 2.8 B$ the electron gyro-frequency in a magnetic field of strength B , given in MHz

If we use the Eq. 4.4 to estimate the magnetic field strength, we need to account for the fact that the frequency of emission is usually not the one we observe. There are two major effects that can alter this frequency. The first one is the cosmological redshift and the second is the relativistic Doppler effect as a result of special relativity, caused by the relativistic motion of the emitting element. These two effects act reversely to each other. The former causes a redshift

of the observed frequency relative to the emitted. The latter on the other hand blueshifts the observing frequency. Assuming that the emission region is traveling along the jet axis we can recover the emitted frequency from the observed one using

$$\nu_{\text{em}} = \frac{\nu_{\text{obs}}(1+z)}{\delta} \quad (4.5)$$

where,

ν_{obs}	the observing frequency
z	the redshift of the source
$\delta = \frac{\sqrt{1-\beta^2}}{1-\beta \cos \theta}$	the relativistic Doppler factor of the emission region which is moving with speed β (in units of c) on a path with angle θ to our line of sight (LoS)

Using the median of the absolute circular polarization degree measurements for the sources which had at least one m_c data point with high significance (signal-to-noise ratio ≥ 3), we calculated the magnetic field strength of sources for which both the redshift and the Doppler factor could be calculated independently. The Doppler factor estimates are taken from the variability studies presented in Hovatta et al. (2009). The results can be found in Table 4.4 as well as in Fig. 4.8.

The magnetic field strengths estimated with the above technique are of the order of a few to a few tens of mG. There is a slight increase of the median magnetic field strength from ~ 3 to ~ 6 mG with increasing observing frequency which can be seen as an indication that at higher frequencies we observe regions of the jet where the magnetic field becomes more uniform. Our magnetic field estimates are in good agreement with other studies. For example O’Sullivan and Gabuzda (2009a) calculate equipartition magnetic field strengths of the order of 10 – 100 mG in the radio cores of four AGN jets using the frequency dependence of their VLBI core positions (core-shifts) from 4.6 to 43 GHz. They argue that extrapolating these results back to the accretion disc and black hole jet-launching distances, the magnetic field strengths are consistent with those expected from theoretical predictions of magnetically powered jets.

Table 4.4: Magnetic field strength estimates using the median circular polarization degree. Column 2 is the observing frequency, column 3 is the number of $|m_c|$ data points with signal-to-noise ratio ≥ 3 and column 4 the median value of $|m_c|$ using these data points. Columns 5, 6 and 7 are three different estimates for the magnetic field strength. Column 5 is the estimate after correcting the observing frequency for both the cosmological redshift and the relativistic Doppler effect. Column 6 is the estimate after correcting the observing frequency only for the cosmological redshift and column 7 the estimate without applying any correction to the observing frequency.

Source	Freq. (GHz)	N _{sign}	median $ m_c $ (%)	B (mG)	$B_{z \text{ corr}}$ (mG)	B_{uncorr} (mG)
J0102+5824	4.85	2	0.25	1.3	17.8	10.8
	8.35	3	0.36	4.5	63.5	38.6
J0136+4751	4.85	1	0.42	2.7	56.8	30.6
J0237+2848	4.85	5	0.38	3.4	55.4	25.0
	8.35	13	0.40	6.6	105.6	47.7
J0238+1636	8.35	1	0.32	2.5	59.2	30.5
J0319+4130	4.85	10	0.80	371.5	111.4	109.5

Table 4.4: continued.

Source	Freq. (GHz)	N _{sign}	median m_c (%)	B (mG)	$B_{z\ corr}$ (mG)	B_{uncorr} (mG)
	8.35	3	0.23	53.5	16.1	15.8
J0339-0146	8.35	1	0.54	9.2	160.9	87.0
J0359+5057	4.85	1	0.47	7.4	96.4	38.3
J0418+3801	4.85	26	0.46	13.5	39.3	37.5
	8.35	4	0.31	10.0	29.1	27.7
J0423-0120	4.85	4	0.23	0.9	18.3	9.6
	8.35	2	0.32	3.0	60.4	31.5
J0530+1331	8.35	4	0.68	13.6	423.3	137.9
J0721+7120	4.85	3	0.67	9.5	103.3	77.8
	8.35	6	0.40	5.8	63.4	47.7
J0818+4222	4.85	3	0.33	6.3	28.9	18.9
	8.35	3	0.51	25.8	118.7	77.6
J0841+7053	8.35	5	0.44	11.4	185.8	57.7
J0854+2006	4.85	6	0.32	1.4	23.2	17.7
	8.35	5	0.31	2.2	37.4	28.7
J0958+6533	4.85	2	0.41	6.6	40.8	29.8
	8.35	3	0.78	40.0	248.0	181.4
J1159+2914	4.85	2	0.29	0.9	25.2	14.6
J1221+2813	8.35	1	0.64	112.2	134.6	122.1
J1224+2122	8.35	3	0.70	40.3	209.7	146.1
J1229+0203	4.85	6	0.28	0.9	15.2	13.1
	8.35	4	0.28	1.6	27.1	23.4
J1256-0547	4.85	19	0.55	3.4	80.5	52.4
	8.35	10	0.48	4.4	105.5	68.7
J1310+3220	4.85	4	0.33	2.4	37.7	18.9
	8.35	2	0.47	8.7	134.4	67.3
J1504+1029	4.85	2	0.28	3.1	37.2	13.1
	8.35	3	0.40	11.3	135.5	47.7
J1512-0905	4.85	2	0.29	1.2	19.8	14.6
	8.35	5	0.46	5.1	85.8	63.1
J1635+3808	4.85	1	0.18	0.7	15.8	5.6
	8.35	7	0.30	3.5	75.5	26.8
J1642+3948	4.85	2	0.18	1.2	9.4	5.9
	8.35	13	0.32	6.2	48.6	30.5
J1733-1304	8.35	2	0.36	7.1	75.6	39.7
J1751+0939	4.85	7	0.42	3.4	40.4	30.6
	8.35	4	0.34	3.8	45.6	34.5
J1800+7828	4.85	1	0.48	5.5	67.0	39.9
	8.35	8	0.32	4.2	51.3	30.5
J1806+6949	4.85	1	0.33	17.9	19.7	18.9
J2202+4216	4.85	3	0.31	2.4	17.8	16.6
	8.35	16	0.38	6.3	46.0	43.1
J2203+3145	8.35	1	0.44	11.2	74.8	57.7
J2225-0457	4.85	1	0.37	3.6	57.0	23.7

Table 4.4: continued.

Source	Freq. (GHz)	N_{sign}	median m_c (%)	B (mG)	$B_{z \text{ corr}}$ (mG)	B_{uncorr} (mG)
J2232+1143	4.85	6	0.29	1.8	28.7	14.1
	8.35	2	0.23	2.2	33.5	16.5
J2253+1608	4.85	5	0.33	1.1	35.1	18.9
	8.35	9	0.50	4.2	138.6	74.6

4.3.2 Rotation measure

As described in subsection 1.4, Faraday rotation occurs when electromagnetic radiation passes through a region of low energy magnetized plasma. As a result, the EVPA is rotated by an angle $\Delta\chi$ given in Eq. 1.69 which can be also written as

$$\Delta\chi \propto N_e B_{\parallel} \lambda^2 \quad (4.6)$$

The magnitude of the rotation is proportional to the electron number density in the propagating medium, N_e , and the magnetic field component of the magnetized region parallel to the line of sight, B_{\parallel} . In fact, $\Delta\chi$ is proportional to the integral of their product along the propagating medium – termed Rotation Measure (RM). The rotation measure, has units of [rad m^{-2}] and it can be estimated by a linear fit of the EVPA measurements plotted against the square of the wavelength, λ , at various observed wavelengths.

The fact that we acquired multi-frequency, high cadence polarization data gives the unique opportunity to study the rotation measure and its variability for the observed sources. Using the EVPA measurements for each epoch, we constructed the rotation measure (RM) plots (i.e. EVPA versus λ^2). In order to solidify the results of this analysis we constricted ourselves to the sources which had EVPA data for at least 3 different wavelengths with at least 10 data points each.

As a first step of this analysis, we corrected the RM plots for the $n\pi$ ambiguities of the EVPA values between the observing bands. To do that, we started from the EVPA data at the highest frequencies (8.35 or 10.45 GHz) which is less likely to be affected by the Faraday rotation effect, and progressively corrected the lower frequencies (8.35, 4.85 and 2.64 GHz). The correction applies integer multiples of π since we expect a linear relation between EVPA and λ^2 . In order to compensate for the high EVPA variability, we performed the above correction only when the difference between the median EVPAs of two adjacent frequencies are larger than $\frac{\pi}{2}$. After visual inspection of the corrected EVPA datasets, we changed this limit to $\frac{\pi}{3}$ only for one source, namely J2202+4216 (BL Lacertae), which was still suffering from the $n\pi$ ambiguity at the lowest frequency (2.64 GHz).

Once the EVPA vs λ^2 datasets were corrected, we performed a linear fit through the EVPA measurements of each epoch. We consider as low significance those fits that used only two EVPA measurements and of high significance the ones with 3 or more EVPA measurements. The slope of the fitted lines are the RM calculated for each epoch and the point where they pass through the y-axis is the corresponding zero-wavelength EVPA, χ_0 , or the EVPA of the radio emission free of the Faraday rotation effect. The RM plots along with lightcurves of both the RM and χ_0 are given in Figures D.1 - D.15. In Table 4.5 we collect the median values of the RMs and χ_0 measured for all sources with at least one observing session with a 3-point fit. In the same table, we provide the jet position angle on the plane of the sky, calculated as the median of the various VLBI components position angles, given in Lister et al. (2013), for all the available sources.

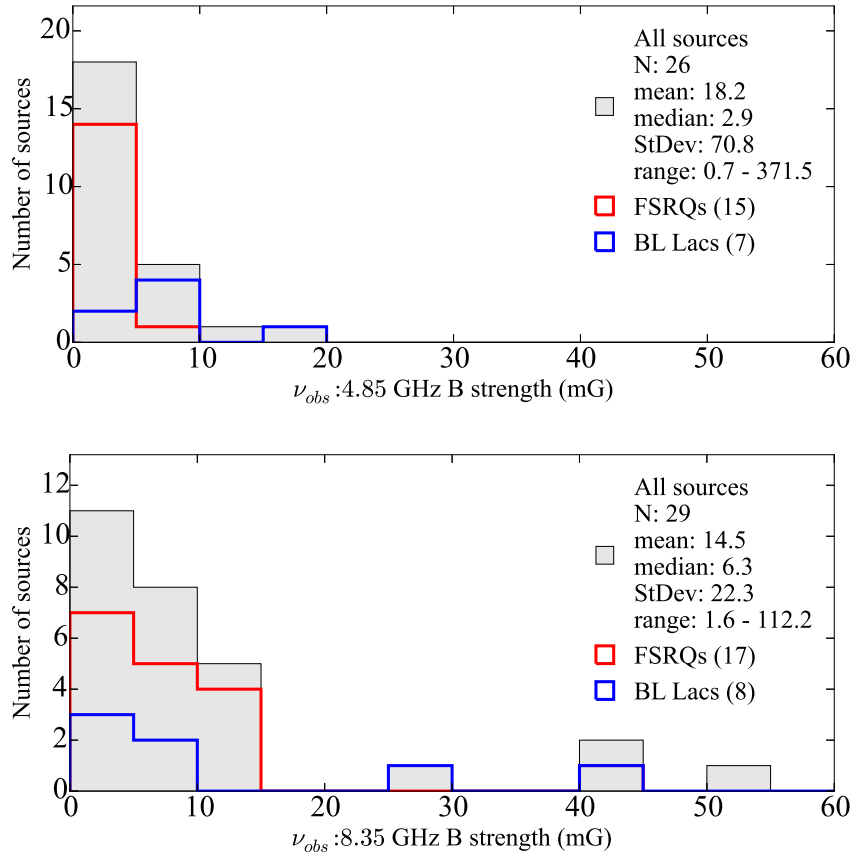


Figure 4.8: Histograms of the magnetic field strength for sources with at least one $|m_c|$ data point of high significance (signal-to-noise ratio ≥ 3). The plots have been truncated to 60 mG to ease reading. There is one data point outside the given ranges for the 4.85 GHz data.

As a cross-check we compared our median RM values with the ones given in Taylor et al. (2009) which were computed from the NVSS data. The comparison plot is shown in Fig. 4.9. The RM differences between the two projects have a median value of 19.7 rad m^{-2} . A Spearman ρ test reveals a very significant correlation ($p = 2 \cdot 10^{-5}$) of $\rho = 0.63$, suggesting a good agreement between the two projects.

The physical interpretation of the RM

A histogram of the RM values we estimated for all sources is given in Fig. 4.10. The majority of the estimated RM values lie in the range between $\pm 100 \text{ rad m}^{-2}$. Those levels are consistent with the interpretation that the Faraday effect mainly takes place in the magnetized plasma of our Galaxy, since the observed rotation measures are similar to the galactic levels (Taylor et al., 2009). In Fig. 4.11, we give a celestial map for the sources we estimated the rotation measure in galactic coordinates and in Fig. 4.12 we plot the absolute rotation measure as a function of the absolute galactic latitude, $|b|$ for each source. We performed a Spearman ρ test for the latter datasets which showed a very significant correlation of $\rho = -0.58$ with a 99.99 % confidence level. This is in accordance with the assumption for the galactic origin of the rotation measure.

RM variability

We observe significant variability of the rotation measure which seems to be correlated with the source variability. This fact is also the reason for the large errorbars in Fig. 4.9 which are

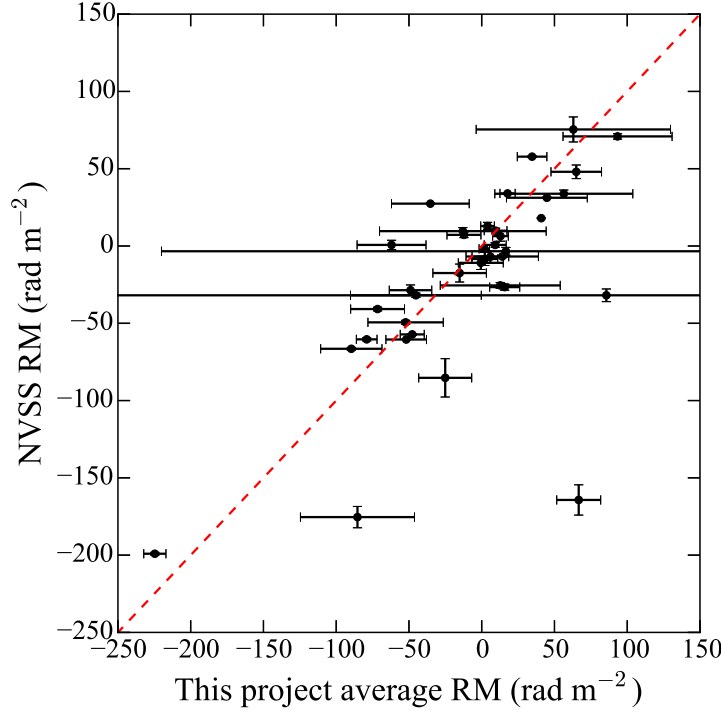


Figure 4.9: Comparison between the rotation measure values estimated with our methodology and the ones given in Taylor et al. (2009).

the standard deviations of the measured RMs for each source. If the above interpretation of the galactic origin of Faraday rotation holds, this variability can be used as a powerful probe to study the plasma content and magnetic field variations of our Galaxy with a high temporal resolution. A careful inspection of our results showed a sudden increase of RM variability when a number of sources showed transitions between the optically thick and thin regimes of the synchrotron spectrum in their polarization characteristics (see also subsection 4.2.7), e.g. J1512-0905, J2253+1608 (3C 454.3) and J1256-0547 (3C 279). If this is the case, RM variability can be also an important diagnostic tool for the intrinsic physical properties of the source, e.g. its opacity or the magnetic field geometry through the correlation of the jet position angle, ϕ_{jet} , with the zero-wavelength EVPA χ_0 .

Table 4.5: The median values of the RMs and the χ_0 values for sources with at least one session for which a 3-point fit could be made. The second column gives the number of sessions fulfilling the latter condition. The fifth column lists the jet position angle on the plane of the sky as reported in Lister et al. (2013).

Source	N_{sign}	RM (rad m^{-2})	χ_0 ($^\circ$)	ϕ_{jet} ($^\circ$)
3C286	32	0.2 ± 0.3	32.9 ± 0.2	...
3C48	29	-64.9 ± 5.8	-60.5 ± 0.6	...
J0102+5824	11	-85.0 ± 39.0	90.4 ± 30.3	-147.7 ± 3.0
J0217+0144	10	-15.2 ± 18.5	19.9 ± 20.1	107.5 ± 0.9

Table 4.5: continued.

Source	N_{sign}	RM (rad m^{-2})	χ_0 ($^\circ$)	ϕ_{jet} ($^\circ$)
J0221+3556	10	-84.0 ± 16.3	37.0 ± 4.4	...
J0237+2848	14	-52.2 ± 25.9	87.1 ± 22.9	-50.0 ± 2.2
J0324+3410	19	65.5 ± 17.5	30.6 ± 2.3	...
J0359+5057	16	15.7 ± 10.3	100.8 ± 6.2	100.0 ± 6.1
J0418+3801	9	-62.7 ± 9.8	-10.8 ± 5.1	65.9 ± 1.0
J0423-0120	17	-10.5 ± 37.6	79.2 ± 21.5	-157.5 ± 3.3
J0530+1331	17	66.5 ± 15.2	-34.6 ± 3.7	52.2 ± 2.7
J0721+7120	17	85.6 ± 536.9	-50.8 ± 82.8	18.8 ± 1.6
J0730-1141	9	93.4 ± 37.4	-28.8 ± 14.0	-72.8 ± 4.0
J0808-0751	5	-49.0 ± 14.6	61.6 ± 12.9	-29.7 ± 0.4
J0818+4222	9	-12.9 ± 57.3	-89.6 ± 51.8	100.2 ± 2.4
J0841+7053	15	1.7 ± 3.6	-81.4 ± 1.7	-145.4 ± 0.8
J0854+2006	22	44.7 ± 27.9	-53.5 ± 15.1	-113.0 ± 3.3
J0920+4441	11	2.1 ± 8.9	-60.9 ± 4.6	178.3 ± 1.2
J0958+6533	12	-12.2 ± 11.6	-3.2 ± 10.0	-37.9 ± 1.7
J1130-1449	21	17.8 ± 5.2	-28.0 ± 2.6	81.3 ± 1.0
J1159+2914	14	-45.2 ± 45.0	-227.5 ± 49.7	8.9 ± 1.8
J1217+3007	10	4.0 ± 4.7	53.6 ± 3.2	144.5 ± 0.2
J1229+0203	24	34.6 ± 10.2	-36.1 ± 2.8	-125.0 ± 3.0
J1256-0547	24	-35.3 ± 26.7	-33.7 ± 15.7	-124.0 ± 2.2
J1310+3220	14	-62.0 ± 23.7	47.7 ± 11.4	-58.8 ± 3.0
J1332-0509	6	9.5 ± 7.8	-74.4 ± 2.2	16.0 ± 0.4
J1504+1029	13	8.5 ± 7.5	23.3 ± 4.7	115.8 ± 1.3
J1512-0905	18	14.1 ± 25.0	37.7 ± 13.4	-32.3 ± 1.2
J1553+1256	7	-0.6 ± 15.4	88.0 ± 14.8	11.1 ± 0.8
J1635+3808	14	56.7 ± 47.4	-7.7 ± 39.2	-78.9 ± 3.1
J1642+3948	24	37.4 ± 11.6	40.3 ± 2.8	-88.6 ± 2.6
J1653+3945	16	12.8 ± 5.7	-13.7 ± 3.9	160.0 ± 3.2
J1733-1304	19	-47.6 ± 8.3	57.9 ± 4.6	7.7 ± 1.7
J1751+0939	24	63.6 ± 66.6	301.3 ± 33.8	17.6 ± 2.6
J1800+7828	13	-89.4 ± 21.1	-83.7 ± 21.8	-89.9 ± 1.2
J1849+6705	7	16.3 ± 236.7	-129.3 ± 39.6	-45.2 ± 0.7
J2025-0735	13	-71.3 ± 18.5	73.4 ± 11.7	-12.8 ± 0.4
J2147+0929	5	-25.1 ± 18.2	55.4 ± 6.8	78.5 ± 0.1
J2202+4216	28	-224.7 ± 7.6	16.0 ± 3.0	-171.0 ± 2.4
J2229-0832	10	6.1 ± 12.3	79.9 ± 10.2	-10.4 ± 1.4
J2232+1143	26	-79.1 ± 7.1	69.5 ± 4.5	152.2 ± 2.8
J2253+1608	28	-52.0 ± 13.9	17.8 ± 8.2	-76.8 ± 5.7

4.4 CORRELATION ANALYSIS

The linear and circular radio polarization datasets we have reduced as well as their derivative quantities that we present in subsection 4.3 provide a unique framework to study the physical parameters of AGN jets. In this section, we utilize the tool of correlation analysis to investigate

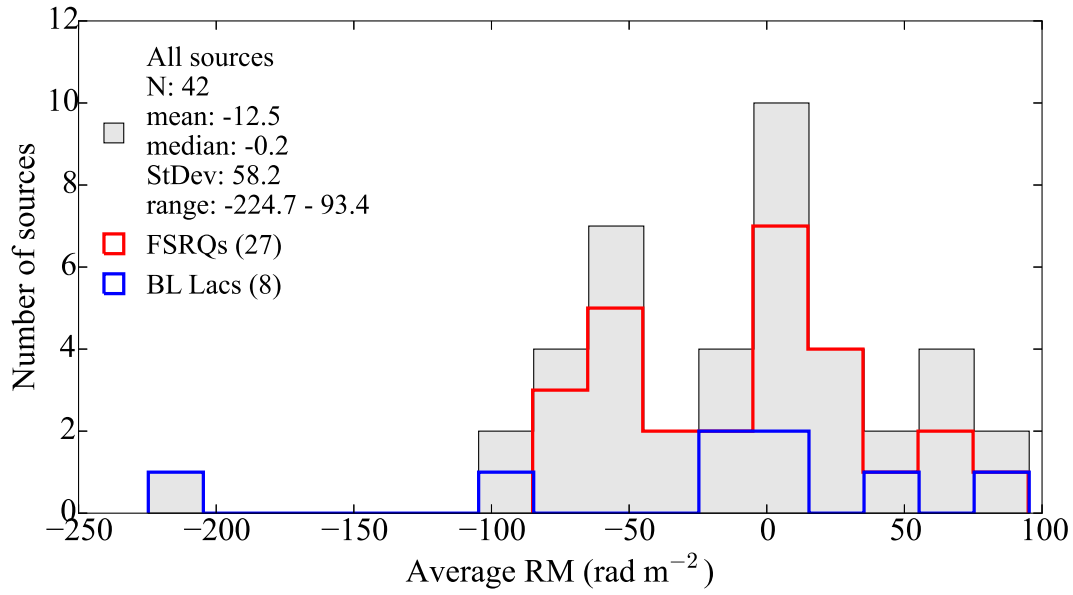


Figure 4.10: Histogram of the rotation measure values estimated with our methodology.

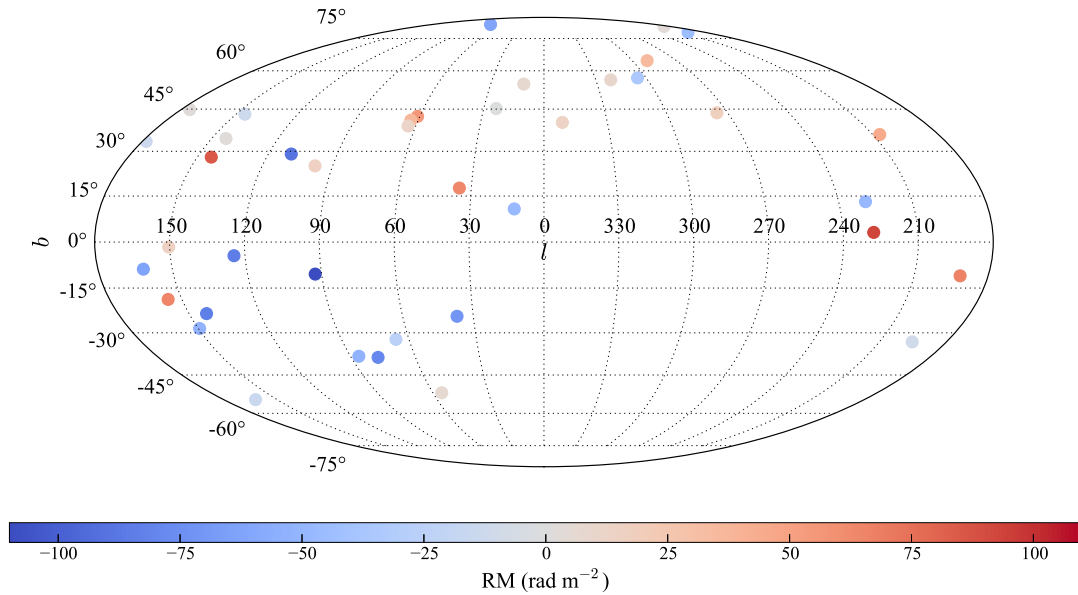


Figure 4.11: A celestial map of the sources for which we estimated the rotation measure in galactic coordinates. The rotation measure is color-coded.

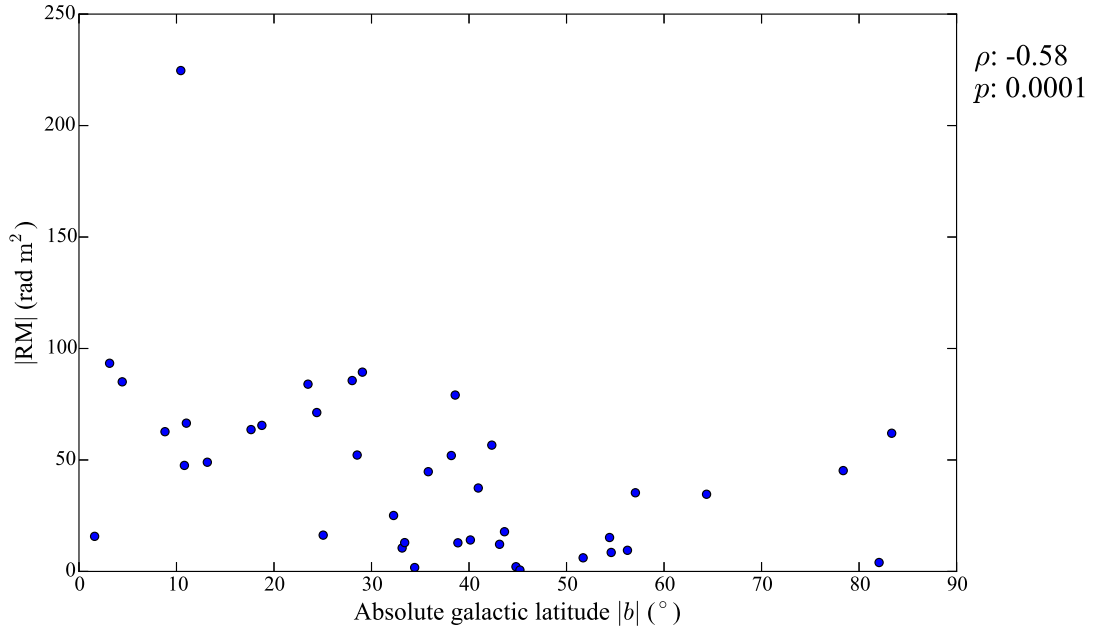


Figure 4.12: The absolute rotation measure versus the absolute galactic latitude of our sources. The Spearman ρ test results are shown on the side of the plot.

various relations between the observed characteristics of jets that can be used to probe the underlying physical conditions and variability mechanisms that govern them.

4.4.1 EVPA versus AGN jet position angle

One of the usual applications of linear polarization studies for a variety of astrophysical sources is the investigation of the magnetic field geometry at the emission region, (e.g. O’Sullivan and Gabuzda, 2009b; Gabuzda et al., 2006). The probe used for such studies is the EVPA and its orientation with respect to the local magnetic field according to theoretical predictions (e.g. Lyutikov et al., 2005). In the case of the radio emission from AGN jets, the emission is generated by the incoherent synchrotron mechanism, where the EVPA lies perpendicular to the projected magnetic field on the plane of the sky when the emission is optically thin and along that direction when it is optically thick (see also subsection 1.4). In order to set a common reference frame for the observed AGN jets, we estimate the deviation of the measured EVPAs with respect to the jet position angle (PA), given in Table 4.5. Furthermore, we perform this analysis using the zero-wavelength EVPA, χ_0 , since it is corrected for the Faraday rotation effect.

We performed this analysis for the 38 sources we have both the jet PA and χ_0 available. The results are shown in Fig. 4.13 where we plot the histogram of the alignment between χ_0 and the jet PA (ϕ_{jet}). We can deduce from that plot that there is a slight bi-modality of χ_0 to be oriented either parallel or perpendicular to ϕ_{jet} with a preference to the latter. This means that a poloidal component of the jet’s magnetic field is slightly dominant at the emission regions we probe. The bi-modality of the distribution comes in agreement with the theoretical work in this field, (e.g. Lyutikov et al., 2005). Of course the reader must be cautioned of (a) the bias of our sample and (b) that this result refers to the population in hand and hence cannot be specified for each source.

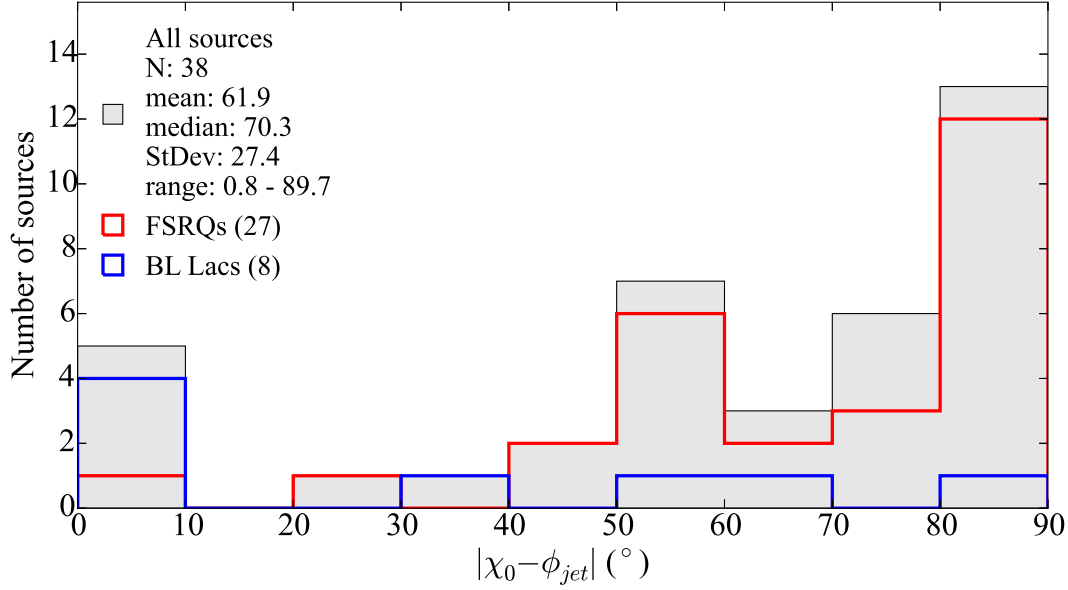


Figure 4.13: Histogram of the alignment between the EVPA at zero-wavelength (χ_0) and the jet PA (ϕ_{jet}).

4.4.2 Linear versus circular polarization degree

Here we compare the linear and circular polarization degree for sources which are detected in both modes. In Fig. 4.14 we plot the median m_l against the median absolute m_c for the 4.85 and 8.35 GHz datasets. Both plots were created by taking only high significance m_l and m_c measurements. The errorbars in both plots give an estimate for the variability of each source at the corresponding quantity since they are equal to the standard deviation of the significant data points for that quantity over the observing period. Spearman ρ test shows a correlation between the two for the 4.85 GHz data (excluding the outlier m_c data point at 2 %) of $\rho = 0.32$ with a 95 % confidence level. The corresponding dataset at 8.35 GHz shows no correlation (confidence level 17 %).

Assuming that both the linear and circular polarization degrees are attributed to the intrinsic synchrotron emission of the sources and not to propagation effects, we can calculate the linear regression between the m_l and m_c and compare it with the predictions of synchrotron theory. In order to take into account the errorbars in both x and y axes, we used the methodology described in Akritas and Bershadsky (1996) (BCES method) to perform the linear regression which gives:

$$m_l = (13.3 \pm 19.2) \cdot m_c + (-2.2 \pm 7.8) \quad (4.7)$$

The errors of the fitted parameters are remarkably large due to the scatter of the data points as it was also evident from the low Spearman's ρ value. Nevertheless, the slope provides an estimate for the relation between the observed m_l and m_c .

Using our Full-Stokes radiative transfer code, described in section 5.3, we examined the theoretical predictions. According to synchrotron theory, the optically thin circular polarization degree, m_c , has a frequency dependence of $\nu^{-0.5}$, while the linear polarization degree, m_l , is stable over frequency. This means that the ratio m_l/m_c is increasing with frequency. Our calculations show that in the ideal case of a synchrotron emitting element with uniform magnetic field, this ratio is ~ 10 at the frequency of the order of a few tens of MHz, while at

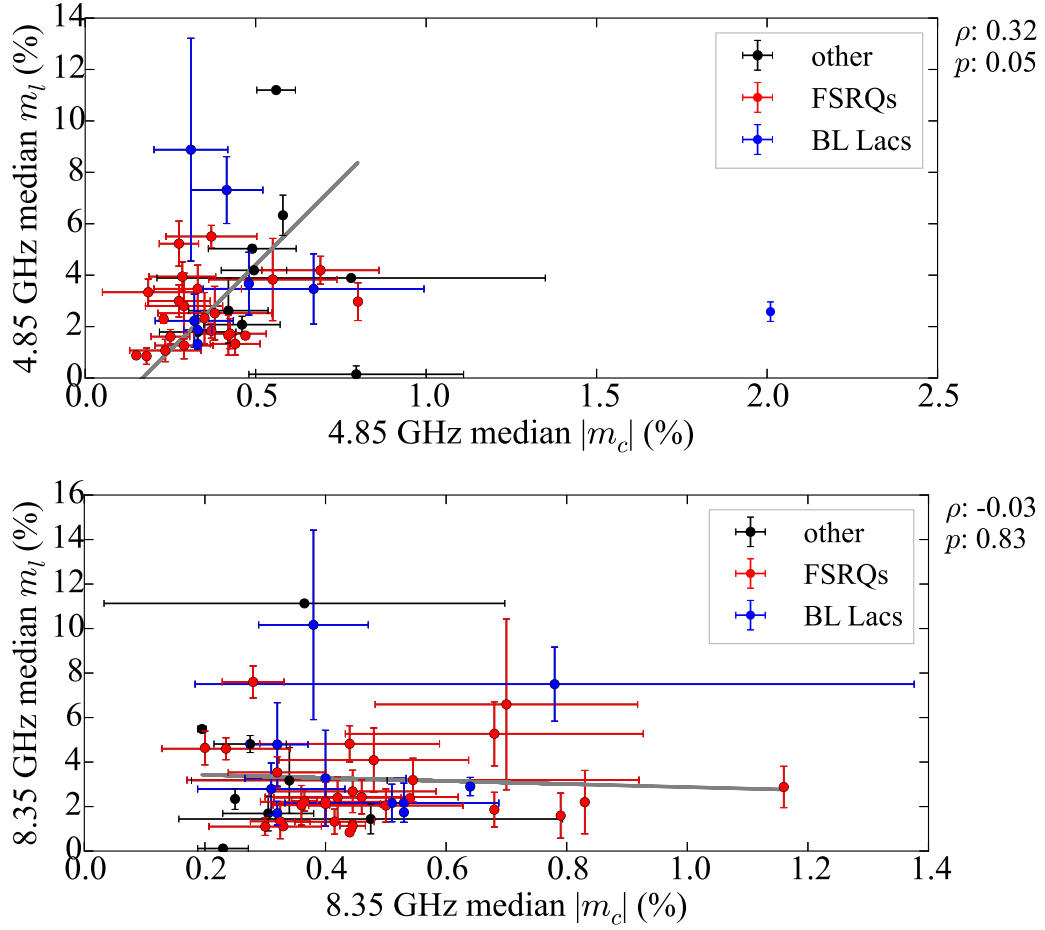


Figure 4.14: Median m_l vs median absolute m_c for the frequencies with available circular polarization information. The Spearman's ρ and p values are shown on the side of each plot.

the (observing) frequency of 4.85 GHz it is expected to be ~ 230 , i.e. one order of magnitude larger than the observed.

One explanation of this discrepancy is that several depolarization effects like Faraday Rotation or the non-uniformity of the magnetic field in the emission region can decrease the linear polarization degree of the radiation much more than its circular one. The decrease of the linear polarization degree is supported by our observations (subsection 4.2.2), which show that $m_l \approx 3\%$, one order of magnitude less than the theoretical value of the ideal case described above ($m_l \approx 70\%$). The fact then that the observed ratio m_l/m_c is less than the one predicted by theory supports our view that the circular polarization degree is not decreased as much as the linear one. This means that circular polarization “survives” better the radiation propagation through the tangled magnetic field of the emitting region and other magnetized plasma clouds which may lie between the source and the observer. This makes circular polarization observations a direct probe of the emitting region.

Finally, the fact that there is no evident correlation between the observed m_l and m_c at 8.35 GHz is not necessarily contradicting the above interpretation. One possible explanation is that the m_c we observe at 8.35 GHz is not attributed (only) to the intrinsic synchrotron emission but also to certain propagation effects, like circular repolarization, which predict the observed lack of correlation between m_l and m_c (see also subsection 1.4.4).

4.4.3 Linear and circular polarization versus RM

In Figures 4.15 and Fig. 4.16, we plot the median m_l and the median absolute m_c against the estimated absolute rotation measure values for our sources. We have considered only the data points with absolute RM less than 200 rad m^{-2} . Faraday rotation theory predicts an anti-correlation of the observed m_l and the RM if the effect is taking place in the source (internal Faraday Rotation) due to differential rotations of the EVPAs for radiation emitted at the same frequency but different depths. If not, the Faraday rotation effect is taking place mainly externally to the source in a magnetized plasma region along the light path.

For the m_l data, we observe a slight anti-correlation with RM only at the the lowest observing frequency with confidence level of 91 %. For the higher frequencies, no correlation is found. This result suggests that at the lowest frequencies we may be affected by internal Faraday rotation in the vicinity of the emitting region, while at the higher ones, the observed RM is caused by external Faraday rotation, possibly due to the low energy magnetized plasma content of our Galaxy as found also in subsection 4.3.2. The fact that we may observe internal Faraday rotation at the lowest frequency may be an indication of the presence of low energy plasma at the outer parts of the AGN jets where this emission is mainly coming from.

For the m_c data, we don't get a significant correlation or anti-correlation with RM. The fact that m_c is not correlated with RM, speaks in favor of the observed m_c being intrinsic to the synchrotron emission. If it were created by propagation effects it would require low energy magnetized plasma which would cause also the observed Faraday rotation. This fact is in accordance with the findings of subsection 4.4.2.

Jet plasma composition

In the light of the previous discussion one can argue that the magnetic field strengths calculated in subsection 4.3.1 are direct estimates of the magnetic field at the emission region, under the assumption that the emitting plasma is purely consisting of electrons. We can compare these values with the ones predicted by theory under the same assumptions. If the measured m_c is less than expected, we can attribute this discrepancy to the presence of positrons in the emitting plasma particles which lower the emitted circular polarization due to their reverse rotation in the source's magnetic field.

Finally using the theoretical predictions, we can estimate the ratio of electrons to positrons we need to have in the emitting region to get the observed m_c values. This ratio is usually expressed as by the lepton number

$$\ell = \frac{n_- - n_+}{n_- + n_+} \quad (4.8)$$

(Homan et al., 2009) with n_- and n_+ the electron and positron number density respectively. In this case the observed m_c is proportional to ℓ , which makes the magnetic field strength proportional to ℓ^2 . Since we considered only the median of the absolute m_c to estimate the magnetic field strength, we cannot discern between electron or positron dominated plasmas but we can estimate the absolute value of number ℓ . For example, if we assume that theory predicts a magnetic field strength of $10 - 100 \text{ mG}$ for an electron plasma (O'Sullivan and Gabuzda, 2009a), and we observe a median value of $\sim 3 \text{ mG}$ at 4.85 GHz (subsection 4.3.1), we calculate that $|\ell| \sim 0.2 - 0.5$. This lepton number range shows that for every particle of one population there are $1.5 - 2$ particles of the other (electrons or positrons). In other words, the admixture of positrons in electron-dominated jet plasmas or electrons in positron-dominated ones is $\sim 33 - 40\%$.

4.4.4 Polarization degree versus low and high frequency emission characteristics

The AGN jet emission is extremely broadband and contains two dominant components. The low frequency component is attributed to the incoherent synchrotron emission mechanism

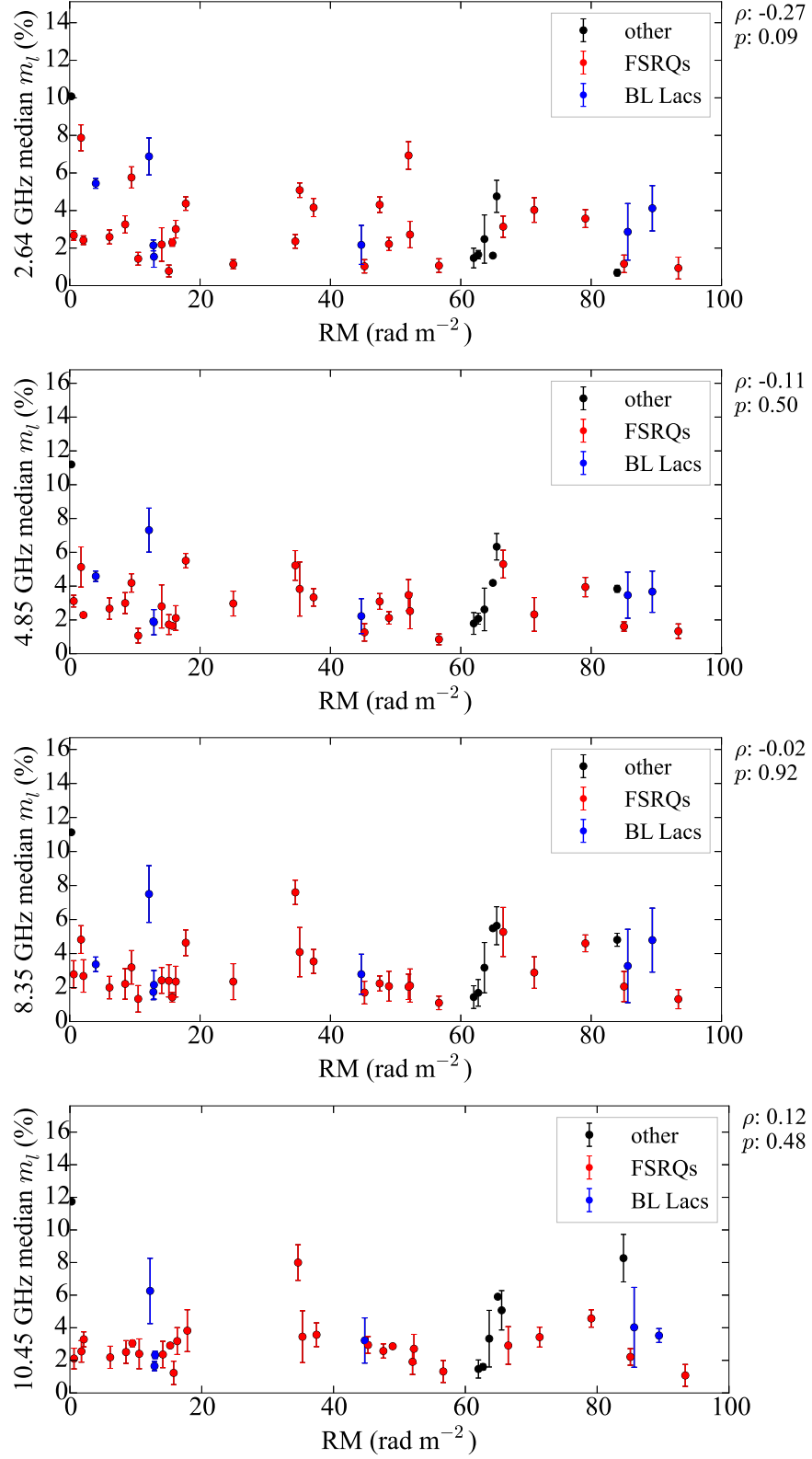


Figure 4.15: Median m_l versus RM. The Spearman's ρ and p values are shown on the side of each plot.

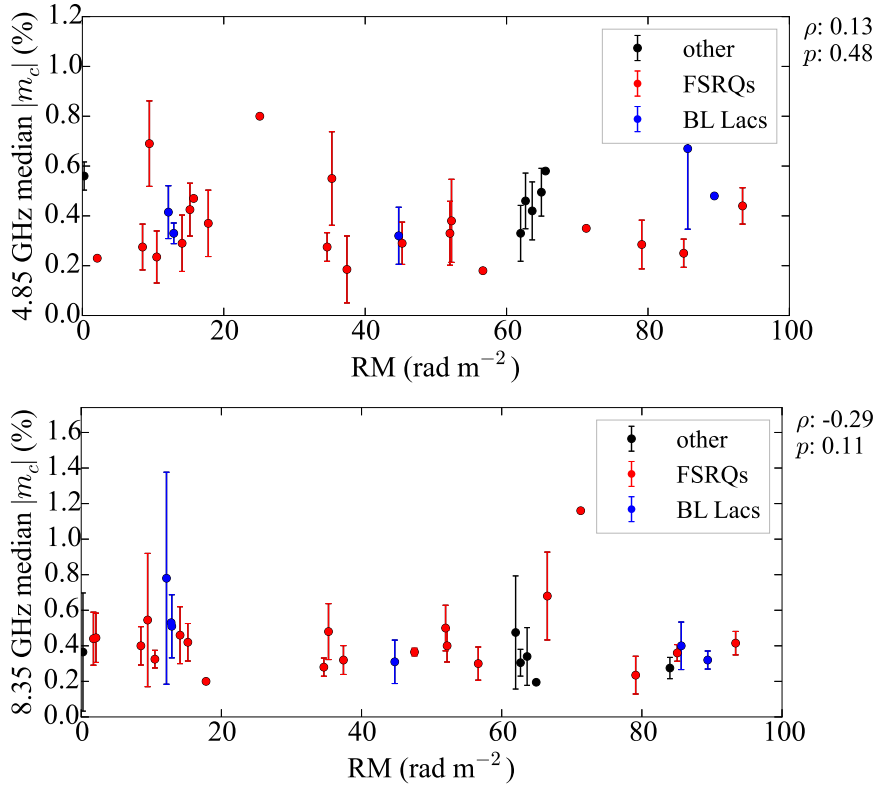


Figure 4.16: Median absolute m_c versus RM. The Spearman's ρ and p values are shown on the side of each plot.

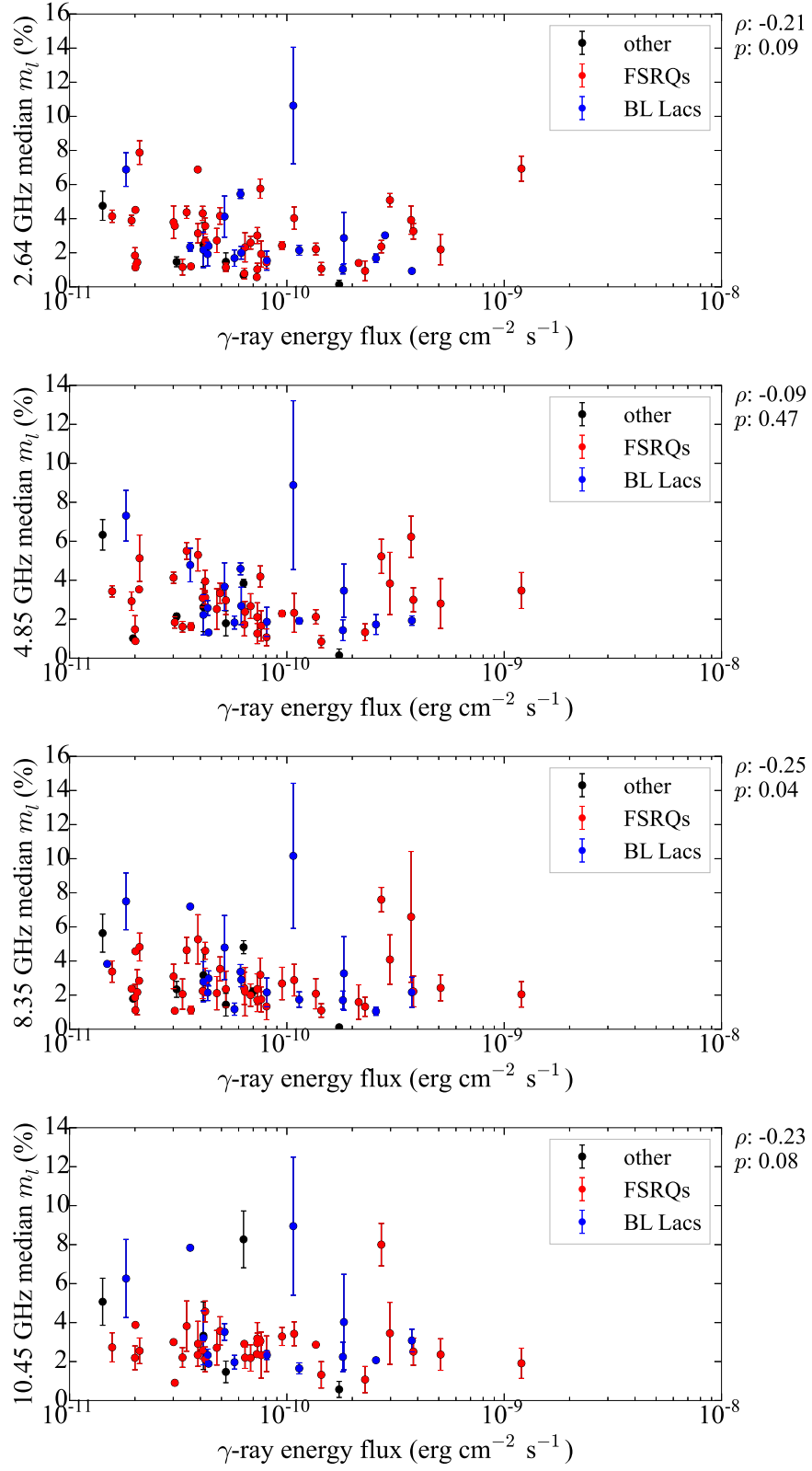
while the details of the physical processes which produce the high frequency one is an active field of research (see also subsection 1.1.3). Here we seek some phenomenological correlations between the radio linear and circular polarization characteristics and those broadband emission components. We investigate their correlation with the peak frequency of synchrotron emission as well as the γ -ray energy flux as representative quantities of the two emission components.

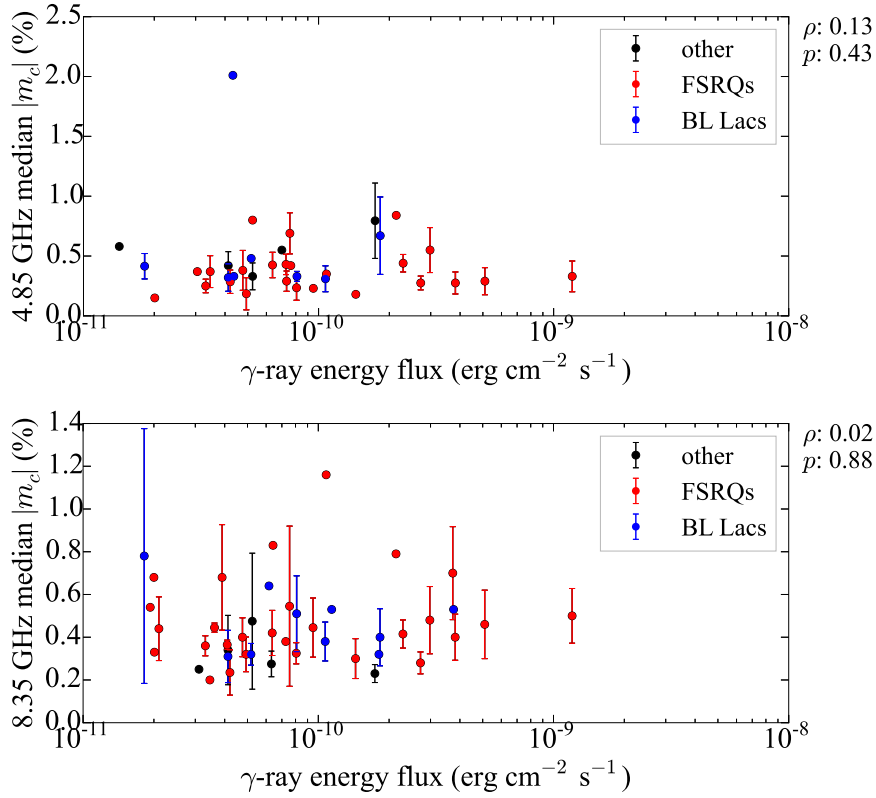
Polarization degree versus γ -ray energy flux

In Figures 4.17 and 4.18, we plot of the median m_l and absolute m_c values against the gamma ray energy flux, taken from the 2FGL catalog (Nolan et al., 2012). On the side of each plot, we give the estimated Spearman ρ and p values as an indication for the goodness of the correlation. There seems to be an anti-correlation of m_l and the γ -ray energy flux which becomes more significant for the 8.35 GHz data with corresponding $\rho = -0.25$ at a confidence level of 96 %. The Spearman ρ test results show no clear correlation between the median absolute m_c and the γ -ray energy flux. These results can be tested against the competing theoretical predictions for the high-energy emission of AGN jets.

Polarization degree versus synchrotron peak

In Figures 4.19 and 4.20 we plot the median m_l and absolute m_c values against the logarithm of the peak frequency of for the synchrotron part of the source SED, ν_s , taken from the 3LAC catalog (Ackermann et al., 2015). We performed Spearman ρ tests to quantify the correlations. There only significant anti-correlation is found for the 4.85 GHz m_l data with $\rho = -0.35$ at a confidence level of 96 %. This anti-correlation shows that the linear polarization degree is increased for sources with synchrotron peaks close to the lower part of the spectrum which we probe with our observations.

Figure 4.17: Median m_l versus γ -ray energy flux.

Figure 4.18: Median absolute m_c versus γ -ray energy flux.

4.4.5 Polarization characteristics and source type

We performed a population study for the polarization characteristics and their derived quantities described in the previous sections for two of the major populations of the AGN family, those known as Flat Spectrum Radio Quasars (FSRQs) and BL Lac objects. We quantified this comparison by performing a Kolmogoroff-Smirnov (KS) test. The results are shown in Table 4.6.

We find that there is no significant difference between FSRQ and BL Lac populations in the majority of the characteristics we tested. The only two parameters for which the two populations were found to be different at are the magnetic field magnitude at the observing frequency of 4.85 GHz and the χ_0 vs ϕ_{jet} alignment with confidence levels of 98 and 97 %. The latter is also clearly discerned from Fig. 4.13, where BL Lac objects peak at 0° and FSRQs at 90° . This preference of the BL Lac EVPA values to be aligned with the jet position angle is also reported in Agudo et al. (2014). Furthermore, the fact that the two populations don't differ in most of their physical characteristics can also be discerned from the majority of the plots shown in this chapter where FSRQ sources are denoted with red and BL Lac ones with blue color.

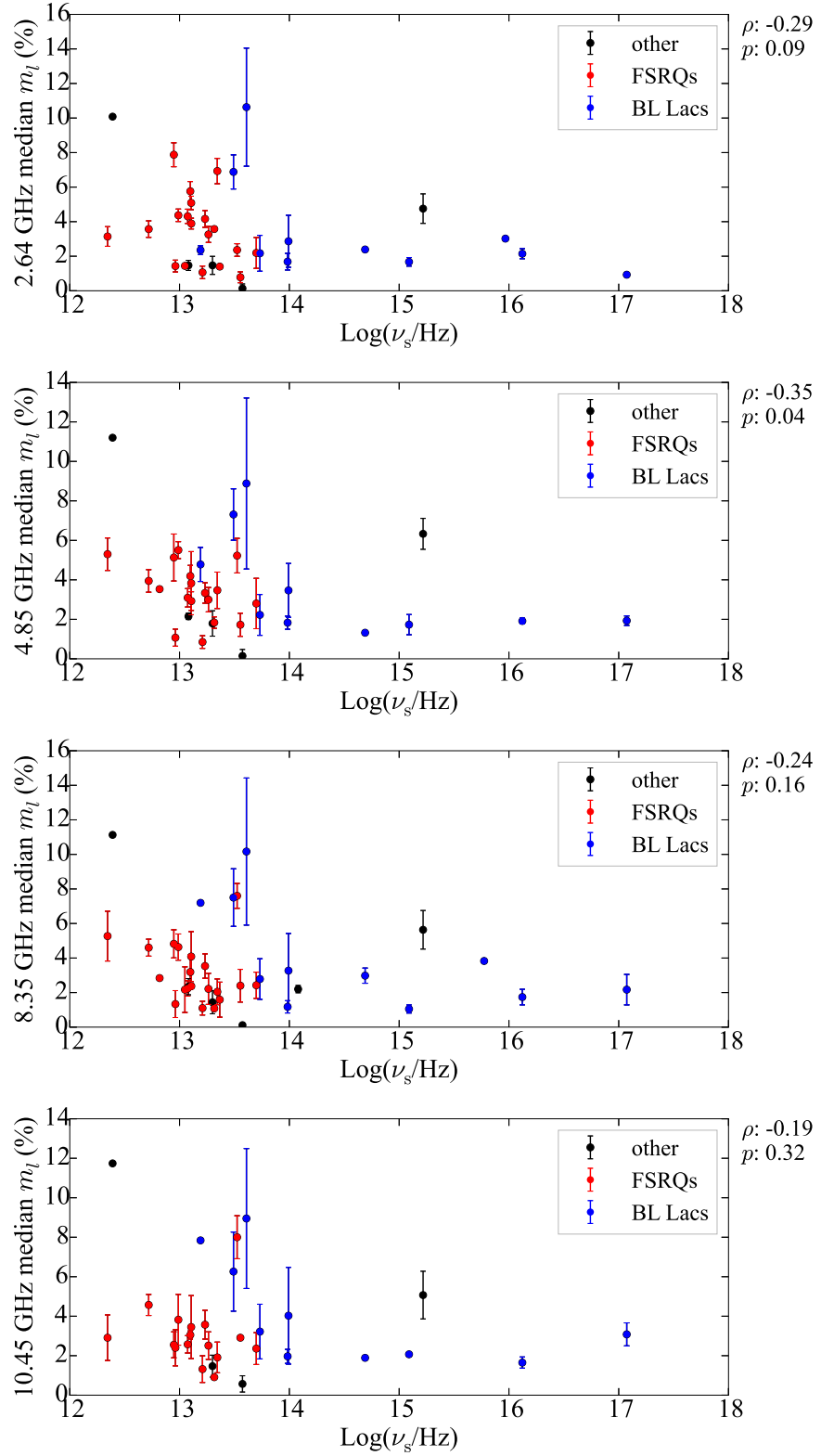


Figure 4.19: Median m_l versus logarithm of the peak frequency for the synchrotron part of the sources' SED.

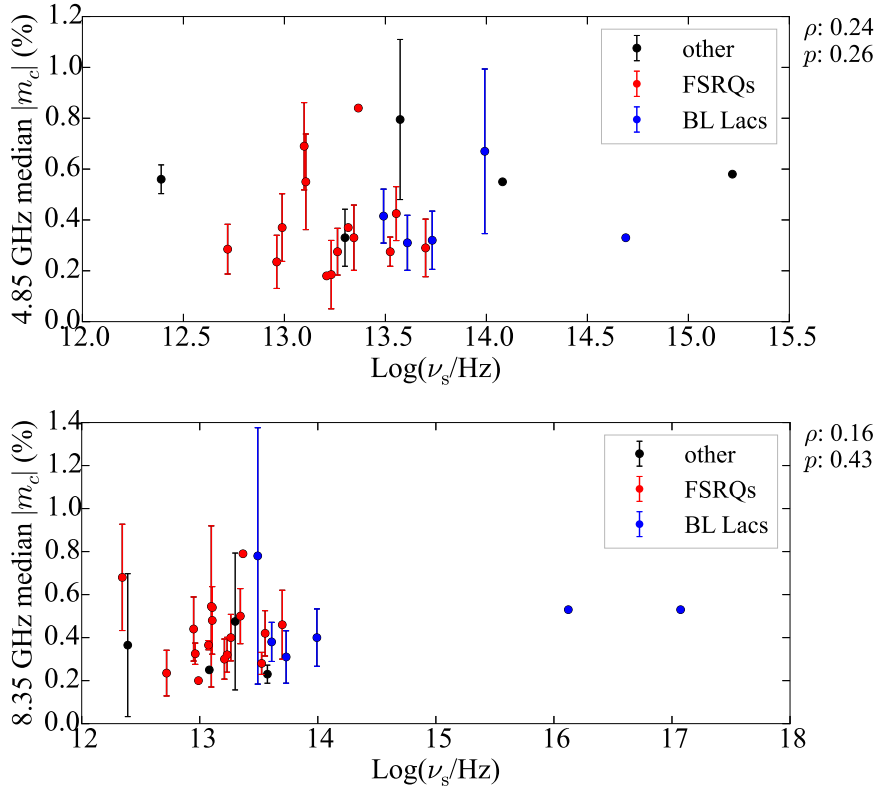


Figure 4.20: Median absolute m_c versus logarithm of the peak frequency for the synchrotron part of the sources' SED.

Table 4.6: Table with the statistical moments (descriptive statistics) and KS test results for the different physical characteristics of FSRQs and BL Lacs

x		Freq. (GHz)	Type	N	\tilde{x}	$\langle x \rangle$	σ_x	min	max	KS-test	
										D	p
m_l	(%)	2.64	FSRQ	42	2.6	3.0	1.7	0.6	7.9	0.20	0.69
			BL Lac	17	2.2	3.1	2.4	0.9	10.6		
m_l	(%)	4.85	FSRQ	38	2.7	2.9	1.4	0.8	6.2	0.16	0.89
			BL Lac	16	2.4	3.3	2.1	1.3	8.9		
m_l	(%)	8.35	FSRQ	42	2.3	2.7	1.5	0.8	7.6	0.26	0.36
			BL Lac	17	2.9	3.6	2.4	1.1	10.2		
m_l	(%)	10.45	FSRQ	35	2.6	2.8	1.2	0.9	8.0	0.24	0.54
			BL Lac	14	2.7	3.7	2.3	1.6	8.9		
m_c	(%)	4.85	FSRQ	25	0.3	0.4	0.2	0.1	0.8	0.44	0.14
			BL Lac	8	0.4	0.6	0.5	0.3	2.0		
m_c	(%)	8.35	FSRQ	29	0.4	0.5	0.2	0.2	1.2	0.22	0.80
			BL Lac	10	0.5	0.5	0.1	0.3	0.8		
B	(mG)	4.85	FSRQ	15	1.3	2.2	1.7	0.7	7.4	0.65	0.02
			BL Lac	7	6.3	7.1	5.1	1.4	17.9		
B	(mG)	8.35	FSRQ	17	6.2	8.5	8.7	1.6	40.3	0.32	0.56
			BL Lac	8	6.1	24.9	35.4	2.2	112.2		

Table 4.6: continued.

x		Freq. (GHz)	Type	N	\tilde{x}	$\langle x \rangle$	σ_x	min	max	KS-test	
										D	p
RM	$(\frac{rad}{m^2})$...	FSRQ	27	34.6	35.1	27.1	0.6	93.4	0.34	0.40
			BL Lac	8	28.8	60.8	69.6	4.0	224.7		
$ \chi_0 - \phi_{jet} $	$(^\circ)$...	FSRQ	27	71.2	68.2	22.3	0.8	89.7	0.55	0.03
			BL Lac	8	22.2	35.3	31.2	6.2	89.1		

4.4.6 Polarization degree and flux density state

As a last study, we compare the polarization degree when the sources are in “quiescent” as well as “flaring” states. The comparisons are shown for m_l and the absolute m_c in Figures 4.21 and 4.23 respectively.

The m_l plots show more points below the $x = y$ line for all the observing frequencies but the 10.45 GHz ones. This means that when the total flux density peaks, the polarized flux density usually stays at a low state. One interpretation that can explain this behavior is that the total flux density increase at the lower frequencies is mainly caused by synchrotron self absorbed (SSA) spectra which approach that frequency range from their optically thick regime side, i.e. from higher frequencies. A back-of-the-envelope calculation predicts a decrease of m_l when an optically thick part of an SSA spectrum which can cause the total flux density increase is added to an optically thin SSA spectrum, possibly attributed to a “quiescent” state large scale jet. This interpretation is also supported by the reverse picture we see at the highest frequency (10.45 GHz) where it seems that – at least for 50% of the times – the total flux density is increased by a flux component which has high linear polarization degree and thus it is most likely attributed to the optically thin part of an SSA spectrum.

For the absolute m_c data the situation looks slightly more “balanced”. Contrary to the m_l results, the total flux density increase seems to be concurrent with a respective circularly polarized flux increase for half of the sources.

In any case, the increase in total flux density is caused by a non-thermal emission element independently of its optical depth. This is supported by the information presented in Figures 4.22 and 4.24 where we plot the linearly and circularly polarized flux density at the high versus low total flux density state, respectively. The number of data points above the $x = y$ line is more than the ones below, indicating that the polarized flux density is usually increased during the flaring state.

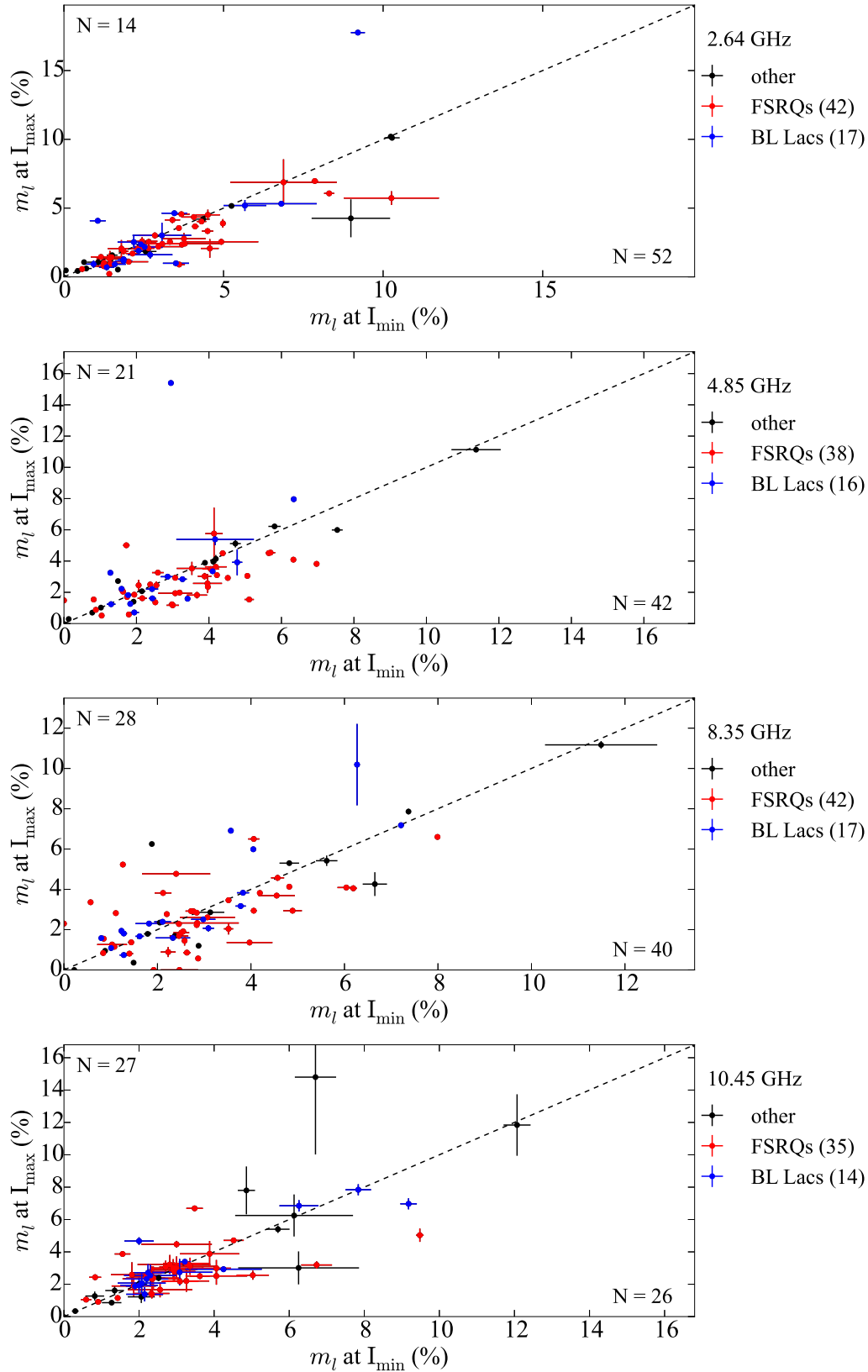


Figure 4.21: m_l at maximum versus m_l at minimum total flux density. The number of data points above and below the $x=y$ line are given in the top left and bottom right parts of the plots respectively.

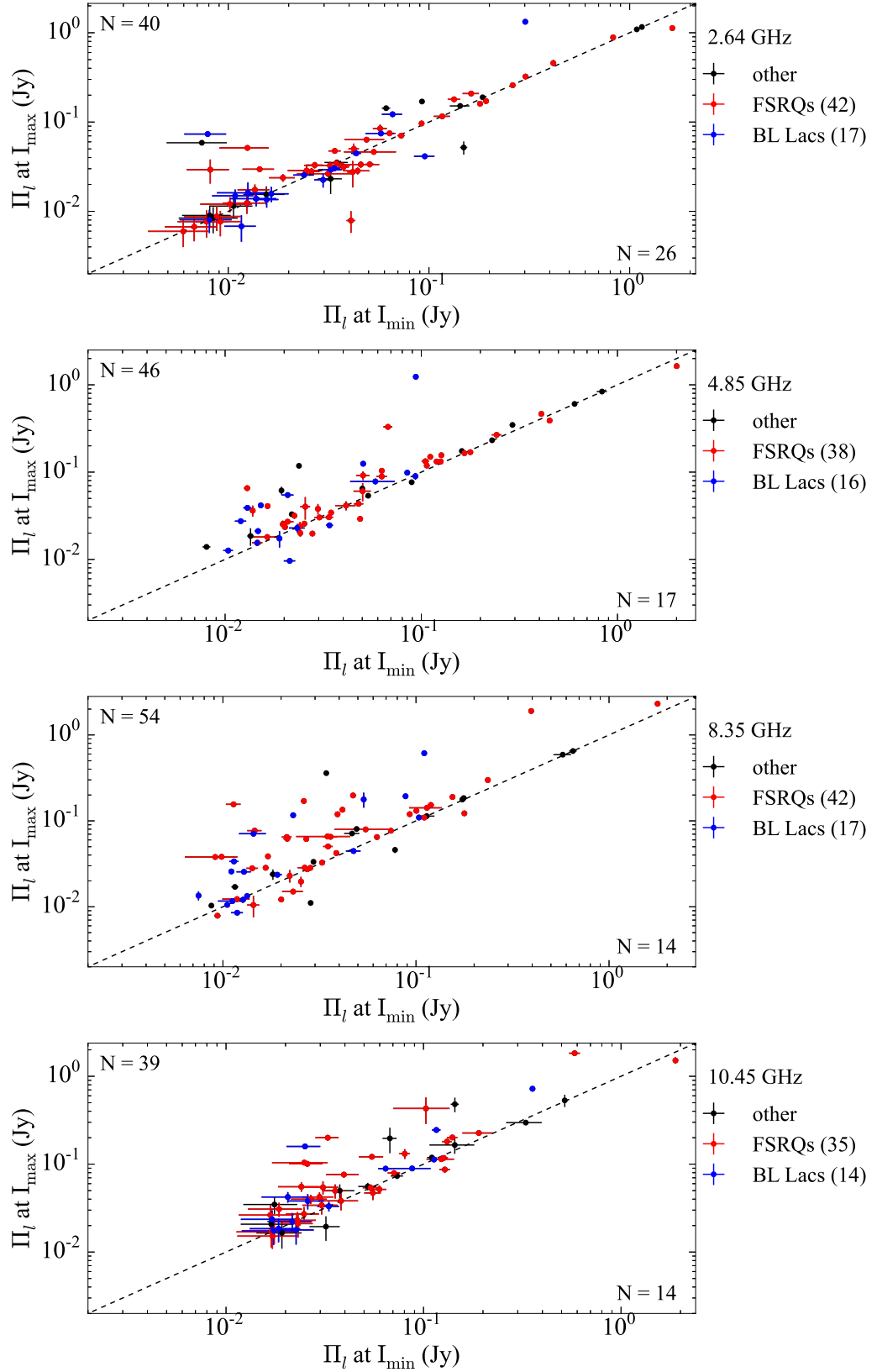


Figure 4.22: Π_l at maximum versus Π_l at minimum total flux density. The number of data points above and below the $x=y$ line are given in the top left and bottom right parts of the plots respectively.

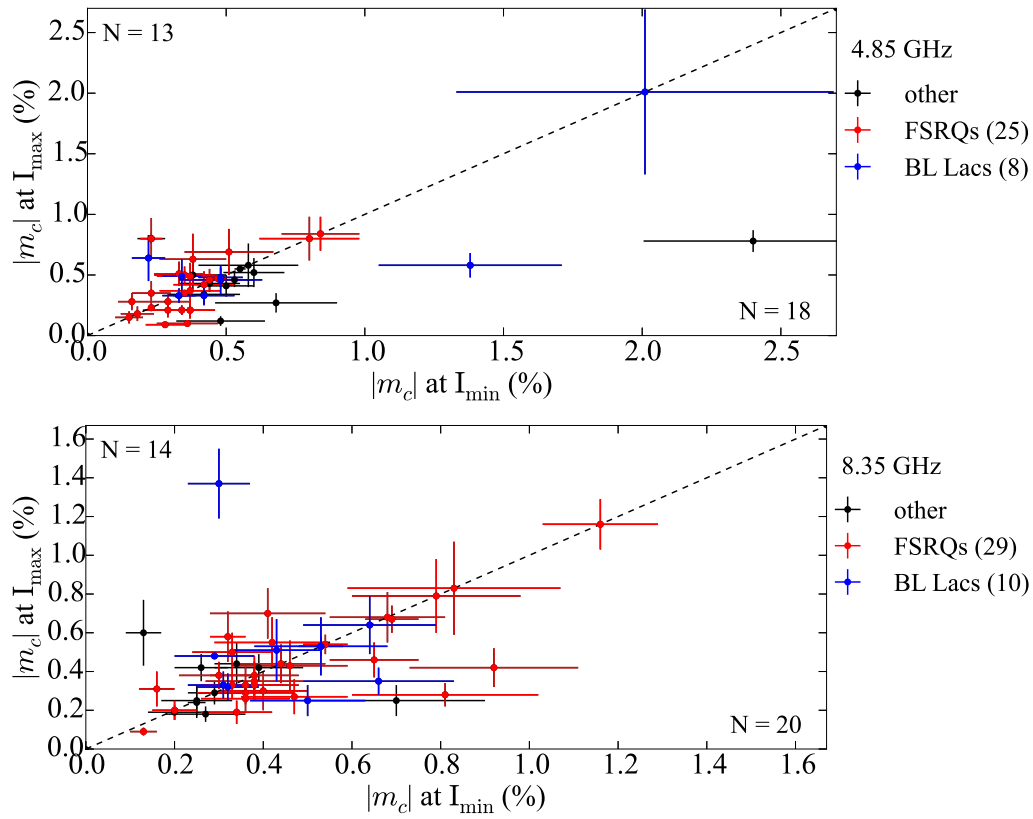


Figure 4.23: Absolute m_c at maximum versus m_c at minimum total flux density. The number of data points above and below the $x=y$ line are given in the top left and bottom right parts of the plots respectively.

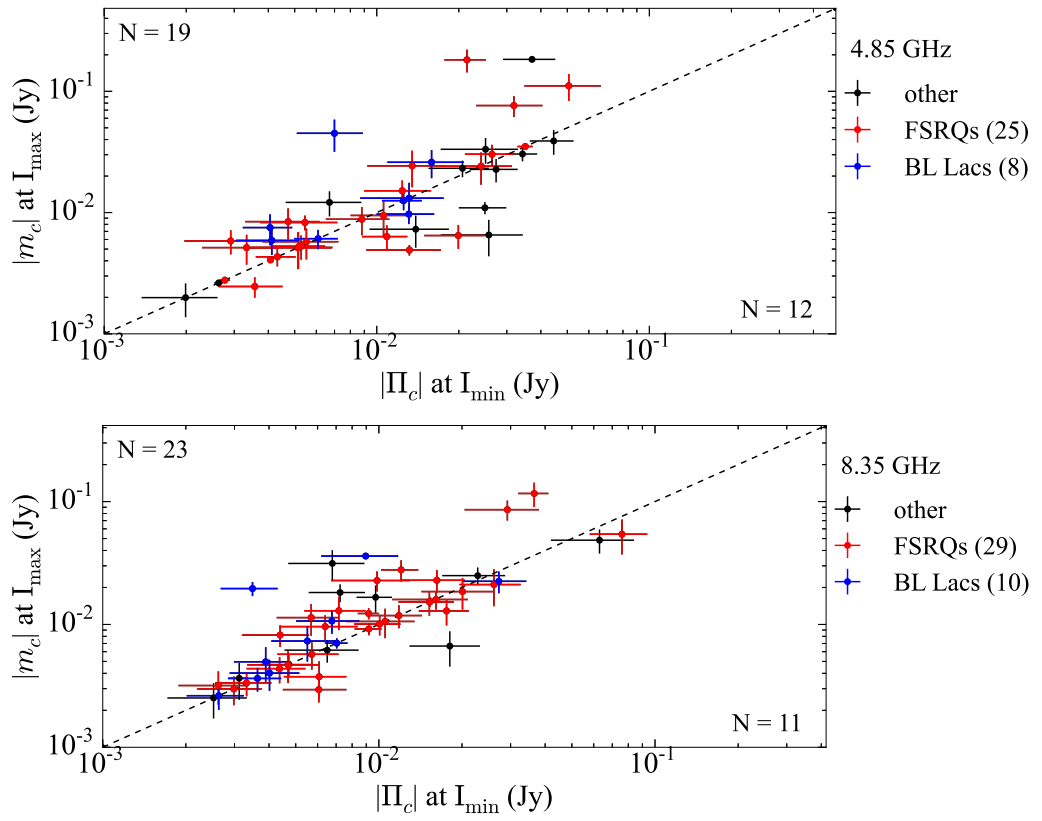


Figure 4.24: Absolute Π_c at maximum versus Π_c at minimum total flux density. The number of data points above and below the $x=y$ line are given in the top left and bottom right parts of the plots respectively.

Chapter 5

Full-Stokes radiative transfer modelling of shocked jets

Abstract

In this chapter we study the pronounced variability of AGN jets. This variability often follows repeating patterns in the F_ν - ν domain which agree with the predictions of the “shock-in-jet” model. Our observations revealed also the coordinated changes of the polarization characteristics which mark the transitions between the optically thick and thin regimes of synchrotron emission. Assuming that these transitions are due to the optical depth evolution of the propagated shocks, we use a radiative transfer code to emulate them and reproduce the variability observed in all Stokes parameters in the case of the prototype source 3C 454.3. This approach resulted in a number of estimates for the physical conditions of this jet, like its particle number density, magnetic field coherence length and Doppler factor.

5.1 INTRODUCTION

AGN jets show pronounced total flux and polarization variability over a broad energy range as well as a wide range of timescales spanning from minutes to years, (e.g. Aller et al., 1999; Quirrenbach et al., 1992). As we discuss in Chapter 4, it is not surprise that this phenomenology dominates also the *F-GAMMA* data set. Here we focus on the details of the variability characteristics we observe both in total flux density as well as linear and circular polarization in order to recover physical parameters for the emitting elements and thus the observed sources. We developed a computer code which is based on the theoretical framework of propagating shock fronts downstream the jet as the underlying mechanism for the observed variability. The theoretical mechanism has been introduced by Marscher and Gear (1985). Our code is based on earlier works which developed similar codes, primarily the work of Hughes et al. (1989a). The aforementioned “shock-in-jet” model has been successfully tested in several cases to mostly explain the total flux density variability patterns observed in AGN jets, (e.g. Hughes et al., 1989b; Aller et al., 2014; Hughes et al., 2015). The main goal for our study is to reproduce the behavior we see both in linear and circular polarization. Such a model can then be utilized to estimate physical parameters of AGN jets, simply by a parameter space survey.

5.2 RADIO VARIABILITY OF AGN JETS

The variability of AGN jets in the radio band has been studied in detail since the 1960s, (e.g. Pauliny-Toth and Kellermann, 1966). Generally, it spans across the whole radio window and becomes more pronounced at higher frequencies in the mm and sub-mm wavelength range. An

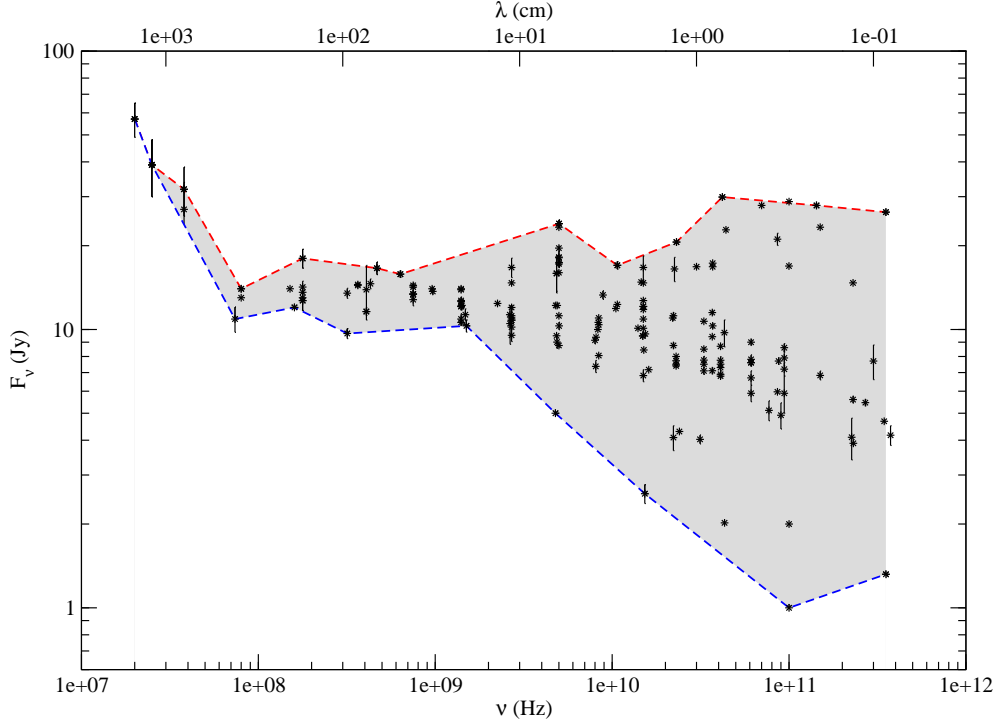


Figure 5.1: An example of the variability seen in radio bands. Broad band radio SEDs observed over a period of more than 45 years of the FSRQ 3C 454.3. Data obtained by the NED online database.

example is shown in Fig. 5.1, where we plot the flux density, F_ν , as a function of the observing frequency, ν , of the FSRQ 3C 454.3 for data obtained over a period of more than 45 years and retrieved from the NASA/IPAC Extragalactic Database (NED).

The defining property of blazars is the rather small angles of the jet axis to the line of sight. Using the variability Doppler factors from Hovatta et al. (2009) and the median values of the apparent speeds for a number of identified jet emission components with the MOJAVE monitoring program from Lister et al. (2013), we calculated a median viewing angle of 5.3° for the blazar 3C 454.3. This suggests that the radio observations are dominated by the boosted jet emission as a result of the relativistic aberration and time dilation effects. Thus, we believe that the observed variability is the manifestation of variable emission components located in the AGN jet as discussed below. In certain cases, these components can be resolved and identified by high angular resolution observational techniques like VLBI.

Similar variability patterns – as the example in Fig. 5.1 – are observed for all blazar sources in different timescales and frequency ranges (e.g. Angelakis et al., 2012). Using high cadence, multi-frequency datasets as the ones of the *F-GAMMA* program, we can decompose the spectral shape of the flux density into its main constituents. The first one is a stable steep power-law spectrum, usually attributed to the optically thin incoherent synchrotron emission of the “quiescent” AGN jet flow. The typical value for the index of this spectral component is of the order of $\alpha \approx -0.7$ (defined as $F_\nu \propto \nu^\alpha$) and it should also show high linear polarization degree (see also subsection 1.4). We believe that this component is observed at the lowest frequencies in Fig. 5.1 because they show the most stable behavior. A power-law fit for the data points with frequency values up to 10^8 Hz yields an index of -1.1 ± 0.2 which is close to the typical value.

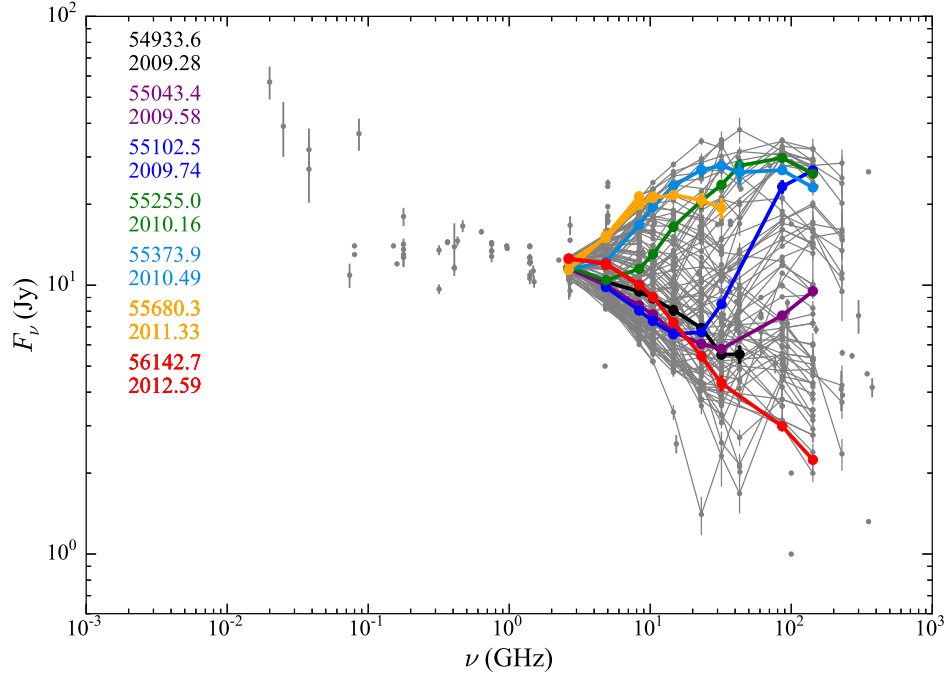


Figure 5.2: Multi-frequency radio variability pattern of the blazar 3C454.3. Data obtained by both the NED online database and the *F-GAMMA* monitoring program are plotted. *F-GAMMA* data are shown by connected lines which mark spectral “snapshots” of the source with coherency time of ~ 3 days. The highlighted spectral “snapshots” are given to demonstrate the spectral variability pattern of the source.

The second constituent is thought to be causing the increased spectral variability at the highest frequencies. The details of its emission are difficult to be discerned from plots like the one of Fig. 5.1 which do not show (quasi-)simultaneous data points. Temporal information is essential in order to illuminate the spectral evolution of the observed sources, especially the ones which evolve rapidly.

In Fig. 5.2, we overplot the 3C 454.3 data taken from the *F-GAMMA* monitoring program to the ones shown in Fig. 5.1. This time, we use the temporal information from the *F-GAMMA* program to connect the data points with lines to show different “snapshots” of the source. Data points connected by one line are coherent in time within ~ 3 days. We have highlighted a small number of consecutive spectra to show the typical variability cycle that they follow in the F_ν - ν plane. Such variability cycles are common among blazars and they are recorded by the *F-GAMMA* program both in time and in frequency.

The most common interpretation is that the variability is caused by evolving synchrotron self-absorbed (SSA) spectral components which propagate through the radio bands as they evolve. Such spectral components can be attributed to individual, confined plasma clouds of high particle density or magnetic field strengths as compared to the “quiescent” large scale plasma flow of an AGN jet. Such emitting components are also associated with localized emission elements seen in VLBI maps. Their creation and evolution is an active field of research. Some theoretical predictions attribute them to evolving small scale instabilities either at the onset of the flow or further downstream, (e.g. Blandford and Konigl, 1979; Lind and Blandford, 1985). Independently of how they are formed, these plasma clouds exhibit a convex SSA spec-

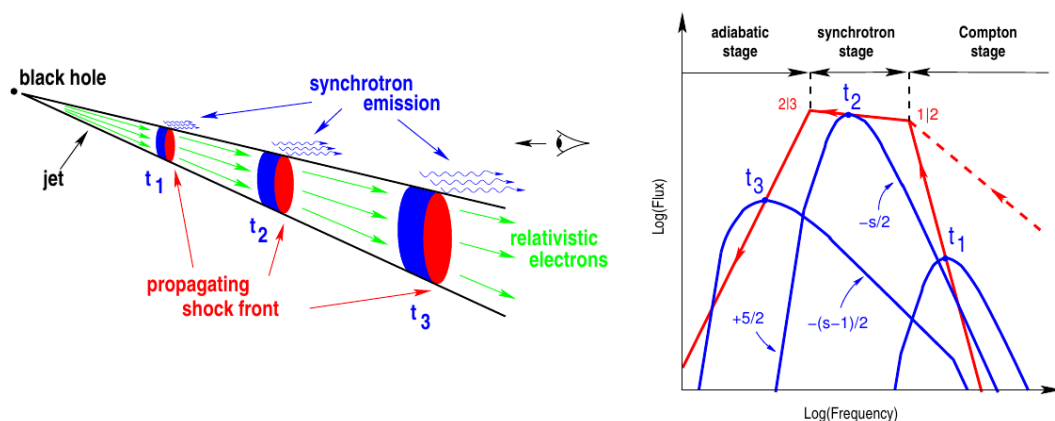


Figure 5.3: The evolutionary stages of the SSA spectrum emitted by the high energy plasma cloud which is formed in the AGN jet and evolve according to the "shock-in-jet" model. Figure taken from Turler (2010)

trum. The peak frequency of this spectrum corresponds to an optical depth of the emitting cloud of about 1 and depends on its magnetic field strength and particle density (see also subsection 1.2.4). In the general case, this spectrum evolves in the $F_\nu - \nu$ plane. Several physical processes are believed to be driving this evolution. Adiabatic expansion of the corresponding plasma cloud as it travels downstream the jet flow may be the dominant mechanism inducing a number of effects among which the optical depth evolution.

5.2.1 The shock-in-jet model

One of the most successful theoretical frameworks developed to extract physical characteristics of jets from the total flux variability studies is the "shock-in-jet" model (Marscher and Gear, 1985). It was introduced to improve previous models that rely merely on the role of the adiabatic expansion of high energy particle clouds, (e.g. Van der Laan, 1966). Those models could not reproduce the observed spectral evolution at its initial evolutionary stages (i.e. the onset of the variability event). Apart from its ability to reproduce the total intensity evolution, the "shock-in-jet" model has been used to provide the framework for explaining the behavior of the linear polarization variability in jets, (e.g. Hughes et al., 1989a). For all these reasons we selected to adopt this model for our investigations.

According to the shock-in-jet model (Marscher and Gear, 1985; Turler, 2010) the evolution in the $F_\nu - \nu$ plane happens in three stages which are also shown in Fig. 5.3:

- First, the maximum of the SSA spectrum increases in flux while drifting towards lower frequencies. Practically, unless a fine – and possibly very specific – tuning of the involved parameters is assumed, adiabatic expansion alone fails to reproduce this stage (Marscher and Gear, 1985). The "shock-in-jet" model predicts that during this stage, the emitting cloud is losing energy by the Compton scattering mechanism. Thus it is termed as "the Compton stage".
- Later, the peak of the SSA spectrum moves almost horizontally towards the lower frequencies. At that stage, the cloud of particles is losing energy due to its own synchrotron emission only and it is termed "the Synchrotron stage".
- Finally, during the last part of the spectral evolution, the peak of the SSA component decreases in both flux density and frequency. This part of the evolutionary path is easily reproduced by a simple adiabatic expansion of the emitting cloud of particles, (e.g. Van der Laan, 1966; Pauliny-Toth and Kellermann, 1966). Thus the dominating energy

loss mechanism this time is the adiabatic expansion and this part is known as “the Adiabatic stage”.

The several characteristics and the plurality of phenomenologies are then easily explained with reoccurring activity of such events so that at any given time the observer sees the superposition of events, each one at a different evolutionary stage. In the general case, the physical characteristics of the clouds that produce each event can differ. Thus, the plurality and complexity of the observed variability cycles maximizes even in the same source.

5.2.2 The evolutionary path signature in the polarization characteristics

Since we observe the spectral variability cycle for a large number of sources, and we know that the polarization characteristics of an SSA component are different between its optically thick and thin regimes (see also subsection 1.4), we expect to observe these discrepancies when the evolving SSA component passes through our observing bandpass (2.64 – 143 GHz). These changes are expected at specific instances that correspond to certain optical depths of the emitting region according to theory (see also subsection 1.4.1 and Pacholczyk, 1977). Specifically, as the component transverses from the optically thick to the thin regime we expect to observe:

1. First a minimization of the linear polarization degree, concurrent with an EVPA rotation of exactly 90° . After that point, the linear polarization degree should obtain gradually its optically thin value which is usually much larger than the optically thick one. In the ideal case of an SSA emitting cloud of particles embedded in a uniform magnetic field, this is expected to happen when the optical depth of the emitting region is ~ 7 and the linear polarization degree in the optically thick and thin regimes are $\sim 10\%$ and $\sim 70\%$, respectively (subsection 1.4.1).
2. Soon after that, we expect to observe the minimization of the circular polarization degree, followed by a change in the circular polarization handedness. In the ideal case described above, this is expected to happen when the optical depth of the emitting region is ~ 5 .
3. The last step of this characteristic signature is the maximization of the total flux when the peak of the SSA spectrum matches the observing frequency.

The “signature” described above has been observed in our polarimetric datasets for at least a few of our sources. For example, in Fig. 5.4, the data set of 3C 454.3 shows at MJD ~ 55650 and 56350, two EVPA rotations of exactly 90° are concurrent with a minimization of the linear polarization degree at the corresponding observing frequencies and an indication of a change in the handedness of the circular polarization is evident close to those dates.

Such among other indications motivate attributing the observed variability, in both total flux density and polarization, with the shock-in-jet model. We use its predictions to investigate the physical characteristics of the emitting plasma elements (clouds) which cause the spectral evolution. We do that by utilizing a computer code we developed which is described in detail in the following section.

5.3 FULL-STOKES RADIATIVE TRANSFER CODE OF SHOCKED JETS

After the discovery that the series of events described in subsection 5.2.2 are observed for a number of sources in our polarimetric datasets, we initiated the construction of a computer code which would be assigned the task to reproduce the observed variability based on the theoretical framework described in subsections 5.2.1 and 5.2.2. One of the requirements of this attempt was to reproduce the spectral behavior assumed by Marscher and Gear (1985) by evolving only the physical characteristics of the emitting region according to a physical model, rather than assuming any *ad hoc* evolutionary path during this process. The reason for this approach is that it would allow us to understand directly the physical parameters that affect the spectral

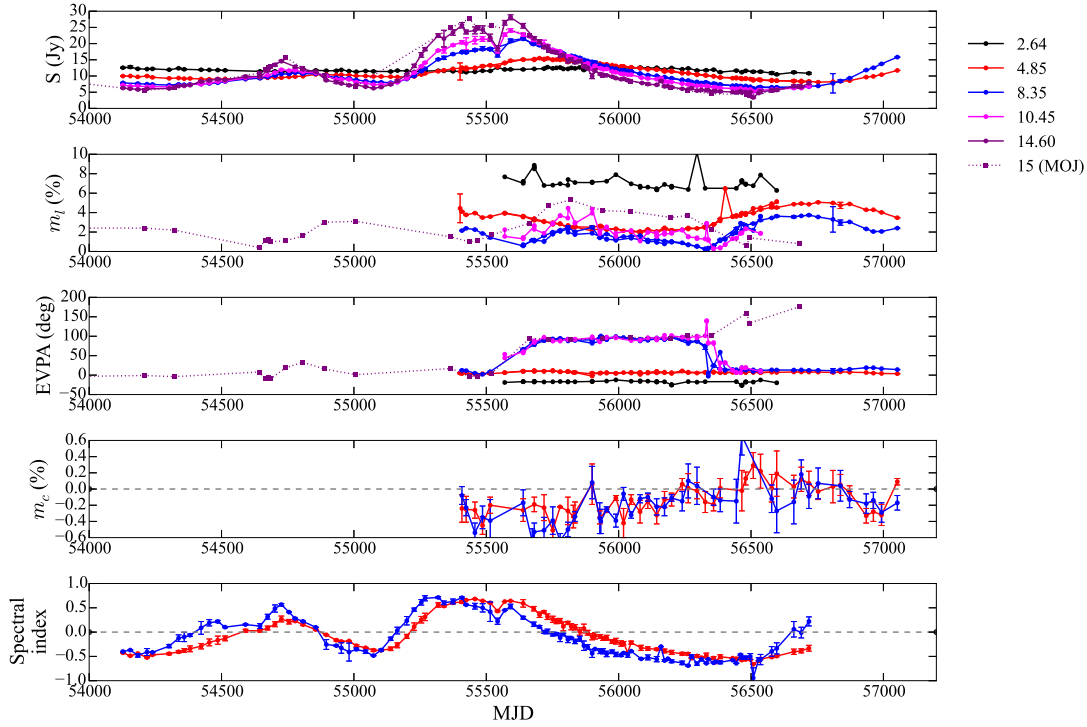


Figure 5.4: Full-Stokes lightcurves for the blazar 3C 454.3. From top to bottom we plot: Stokes I at 2.64, 4.85, 8.35, 10.45 and 14.6 GHz; the degree of linear polarization m_l ; the linear polarization angle (EVPA); the degree of circular polarization m_c and the spectral index at two overlapping bands: 4.85, 8.35, 10.45 (red) and 8.35, 10.45, 14.6 GHz (blue). In the Stokes I , m_l and EVPA plots, we have included the information at 15 GHz, taken from the MOJAVE monitoring program.

shape and evolution. Thus, we developed our own computer code based on the one described in Hughes et al. (1989a).

5.3.1 A short overview of the code

This code emulates the emission in terms of all four Stokes parameters (I , Q , U and V), for regions in AGN jets which we observe at the radio frequencies at their “quiescent” state. Furthermore, by using a set of known jump conditions, valid for relativistic shock fronts, the code calculates the corresponding emission for shocked regions in the jet which propagate downstream the “quiescent” flow in predefined time steps. These jump conditions are the relativistic limit of the Rankine-Hugoniot relations of non-relativistic shock fronts. These relations prescribe the sudden changes of the physical characteristics (density, magnetic field, spectral index) between the shocked and unshocked parts of the flow. As the shock travels downstream, it changes the local physical characteristics of the jet and this change is imprinted on the emitted spectrum which follows the shock evolution. The spectra are obtained by solving the full-Stokes radiative transfer problem for radiation emitted and propagated across the jet.

5.3.2 The building blocks of the modeled jet

The emulated part of the AGN jet is constructed as a set of homogeneous relativistic plasma cells. Since the large scale magnetic field of AGN jets is considered to be highly non-uniform

(Jones et al., 1985), the cell size is equal to the maximum scale that would still allow the (local) magnetic field to be uniform, termed here as the coherence length of the jet magnetic field.

Each cell is filled with particles with power-law energy distribution:

$$n(\gamma)d\gamma = n_0\gamma^{-\delta}d\gamma, \quad \gamma > \gamma_i \quad (5.1)$$

where,

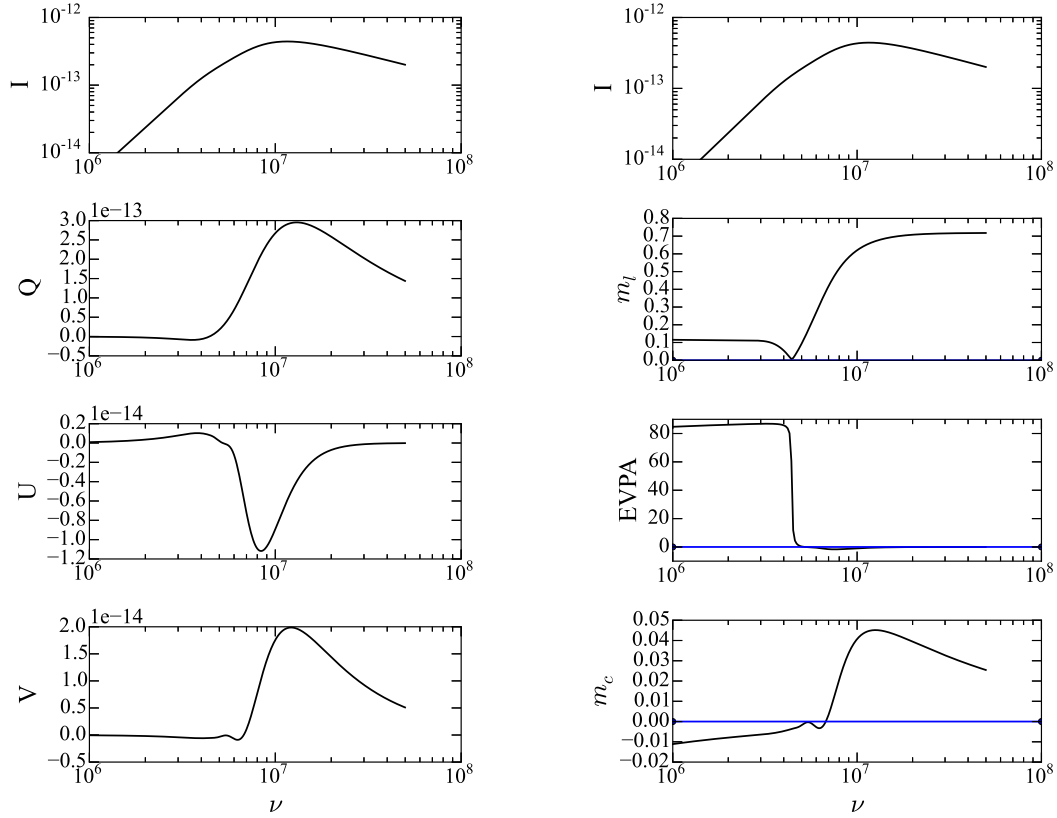
γ	the lorentz factor for the emitting particles of energy $E = \gamma mc^2$
$n(\gamma)$	the number of particles with lorentz factor, γ
n_0	the number density normalization factor
γ_i	the low-energy cut-off of the emitting particles
δ	the power-law index of the energy distribution

We specify that the number density normalization factor, n_0 , is set individually for each cell according to the local jet conditions. In our case we consider that there is a density gradient along the jet axis described by Eq. 5.6. The physical conditions of each cell then, i.e. relativistic plasma embedded in a uniform magnetic field, are enough for it to emit an SSA spectrum with the theoretical linear and circular polarization characteristics (see also subsection 1.4).

5.3.3 Full-Stokes radiative transfer

The Stokes parameters of each cell are calculated at a predefined set of frequencies using the full-Stokes radiative transfer solutions given in Jones and Odell (1977); Hughes et al. (1989a). These solutions contain coefficients which affect the Stokes parameters emerging from each cell. These coefficients are:

1. Emission and absorption coefficients of the four Stokes parameters. These are used to calculate the emission of each Stokes parameter which depends on the physical characteristics of the emitting plasma as well as the emitted frequency. These coefficients depend mainly on the particle density in the emitting cell, the magnetic field strength and the angle between the magnetic field vector and the line of sight (LoS). These parameters define the location of the peak of the emitted SSA spectrum in the $F_\nu - \nu$ plane. The total flux density as well as the linear and circular polarization characteristics we finally observe depend on the value of the observing frequency relative to that position.
2. Faraday rotation coefficient. This coefficient do not affect the total emission but only the polarized one. It is attributed to the Faraday rotation effect which may occur in magnetized plasmas (see also subsection 1.4.2). Faraday rotation is the rotation of the plane of linear polarization due to the the material birefringence between the two circularly polarized normal modes, the left handed (LHC) and the right handed circular (RHC) one. The normal modes are valid solutions of the Maxwell's equations for the propagating plane electromagnetic waves only in the case that the energy distribution of the cell particles is extended towards the lower energies ($\gamma_i \approx 10 - 100$) or if there is significant presence of non-relativistic (cold) particles in the jet plasma. Under these conditions, the Faraday rotation coefficient becomes significant and the plane of linear polarization is rotated when the emission is propagated through the cell, i.e. Stokes Q is transformed into Stokes U and vice versa.
3. Faraday conversion coefficient. The Faraday conversion effect is responsible for the inter-conversion of linear and circular polarization due to the birefringence of magnetized plasma between two linearly polarized normal modes. These normal modes are valid in the case of relativistic plasmas which is usually the case for AGN jets. When the Faraday conversion coefficient becomes significant, it may increase the amount of circular polarization (Stokes V) that emerges from the emitting cell.



(a) SSA Stokes parameters

(b) SSA polarization characteristics

Figure 5.5: The broadband total flux and polarization characteristics of a synchrotron self-absorbed (SSA) emitting modelled cell as generated with our code. The linear and circular polarization degrees, m_l and m_c , are normalized to 1.

The radiative transfer equations take also into account the emission incident to the cell which can be affected by the physical characteristics of the emitting cell, for which they are solved. As an example, we show the broadband picture of the Stokes parameters and the polarization characteristics for radiation emitted from a cell of high energy plasma in Fig 5.5. The physical parameters we selected to generate these plots are:

- Particle number density normalization factor, n_0 : 10 cm^{-3}
- Linear scale of the emitting region: 10^{14} cm
- Magnetic field strength: 5 mG
- Angle θ between the magnetic field direction and the LoS: 135°
- Angle ϕ between the projection of the magnetic field direction on the plane of the sky in the EVPA reference frame, N – E: 90°
- Index of the power-law energy distribution of the emitting particles: $\delta = 2.4$
- Low energy cut-off of the emitting particles: $\gamma_i = 10^4$
- Incident Stokes vector: $I_0 = Q_0 = U_0 = V_0 = 0$

5.3.4 Emulating the jet

As discussed above, the notion of cells is introduced because observations of extragalactic jets indicate that their (large scale) magnetic fields are non-uniform (Jones et al., 1985). This interpretation is discerned by the low levels of linear polarization degree we observe for these

sources, at least during their “quiescent” state. Thus, we assume that the modeled jet is an ensemble of cells with uniform magnetic field components which are randomly distributed in space. The magnetic field orientations are selected using a random number generator to decrease the uniformity of the total magnetic field and lower the linear polarization degree level to the observed values of $\sim 3\%$ (see also Chapter 4). Theory predicts that the number of cells, N , is connected with the observed total linear polarization degree, m_l , through the relation

$$m_l \approx \frac{m_l^{\text{th}}}{\sqrt{N}} \quad (5.2)$$

where m_l^{th} is the theoretical value of m_l . Thus, if $m_l^{\text{th}} = 70\%$, in order to observe $m_l \approx 3\%$ we need to introduce ~ 540 cells.

The cells are organized in slabs of increasing radius which are finally arranged in a row to form the modeled jet. All slabs have the same number of cells and the overall jet geometry is dictated by the following formula

$$r = r_0 \left(\frac{d}{d_0} \right)^p, \quad d_i < d < d_f \quad (5.3)$$

where,

- r the slab radius. r_0 is the radius of first slab of the jet, located at the fiducial distance d_0
- d the distance along the jet, measured from d_0
- p the index that defines the jet shape

For example, for a conical jet, $p = 1$ and for a parabolic one $p = 0.5$.

For an expanding jet, the magnetic field strength decreases as we move downstream. The prescription for that is

$$B = B_0 \left(\frac{r}{r_0} \right)^{-q} \quad (5.4)$$

where,

- B the magnetic field strength at a slab of radius r
- q the index to quantify the magnetic field strength decrease along the jet axis

Assuming an adiabatically expanding flow, the perpendicular component of the magnetic field with respect to the jet axis, decreases as $B_{\perp} \propto r^{-1}$ and the parallel one as $B_{\parallel} \propto r^{-2}$, so that generally we expect $q > 1$ (Hughes et al., 1989a). Furthermore, if we want to increase the alignment of the “quiescent” state EVPA with the direction perpendicular to the jet axis (see subsection 4.4.1), we have implemented the option to add a uniform magnetic field component, parallel to the jet axis and of magnitude $\epsilon_B \cdot B$ with $\epsilon_B \ll 1$.

The assumption of adiabatic expansion for the flow dictates the relation between the plasma density normalization factor and the low-energy cut-off of the emitting particles and the location along the jet axis. These quantities are calculated using

$$\gamma_i = \gamma_{i0} \left(\frac{r}{r_0} \right)^{-2/3} \quad (5.5)$$

where,

- γ_i the low-energy cut-off of the emitting particles and
- γ_{i0} the same cut-off for the particles located at the fiducial distance d_0

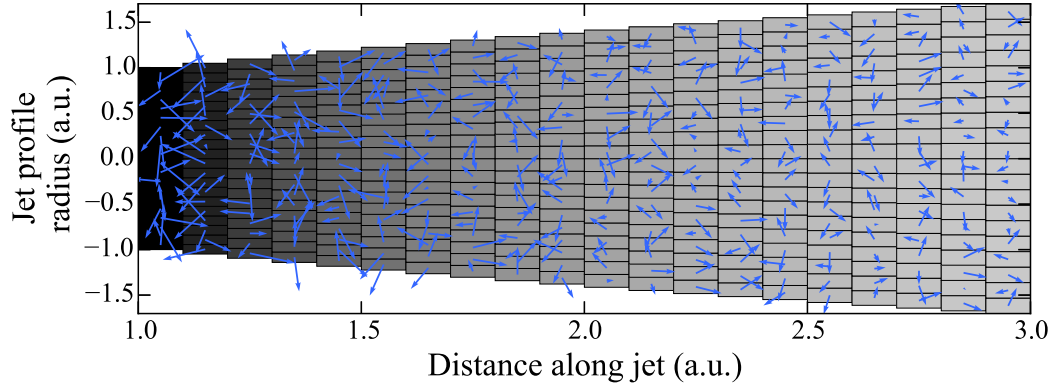


Figure 5.6: A modeled jet profile. The density gradient along the jet axis is demonstrated by the greyscale shading of the cells. The blue arrows show the projection of magnetic field on the plane of the sky. The radius and distance along the jet are expressed in arbitrary units (a.u.).

and

$$n_0 = n_{00} \left(\frac{r}{r_0} \right)^{-2(\delta+2)/3} \quad (5.6)$$

where,

- n_0 the local number density normalization factor of the emitting particles
- n_{00} the number density normalization factor for the particles located at the fiducial distance d_0
- δ the index of the power-law energy distribution of the emitting particles

As an example, we show in Fig. 5.6 a realization of the modeled jet at its “quiescent” state. This realization was modeled using the following set of parameters.

- $d_0 = 1$ (arbitrary units)
- $p = 0.5$
- Slab thickness $\Delta d = 0.1$ (arbitrary units)
- $B_0 = 5$ mG
- $q = 1.5$
- $\epsilon_B = 0.2$
- $\gamma_{i0} = 10^4$
- $n_{00} = 10 \text{ cm}^{-3}$
- $\delta = 2.4$

5.3.5 Relativistic shock jump conditions

As mentioned above, our code is following the model described in Hughes et al. (1989a). According to their approach, as the shocks travel downstream, they modify the local physical conditions of the flow. The main modifications they cause, are:

- The low energy cut-off of the particle energy distribution increases. An adiabatic compression changes the local γ_i to $\gamma_i k^{-1/3}$, where k is the compression factor. This factor is defined as the unit length at the direction of compression, which is reduced to length k (Hughes et al., 1985).
- The number density of the emitting particles is increased from the local n_0 to $n_0 k^{-(\delta+2)/3}$, where δ is the index of the power-law energy distribution of the emitting particles.

- The magnetic field components perpendicular to the compression direction are increased by a factor of $1/k$, while the one parallel to that remains unchanged. Assuming that the compression is always perpendicular to the jet axis, the magnetic field components that increase are the ones perpendicular to that direction. This phenomenon has two consequences:

1. The first is the increase of the magnetic field uniformity (perpendicular to the source axis) which causes in turn an increase of the observed linear polarization degree. The observed linear polarization degree in this case is a function of the compression factor, k , and the angle between the LoS and the compression plane, ϕ , and it is given by

$$m_l = \frac{\delta + 1}{\delta + \frac{7}{3}} \frac{(1 - k^2) \cos^2 \phi}{2 - (1 - k^2) \cos^2 \phi} \quad (5.7)$$

where,

δ the index of the power-law particle energy distribution

In Fig. 5.7, we plot the linear polarization degree against ϕ and k for various combinations of the two.

2. The second is the sudden increase of the magnetic field strength for the shocked part of the flow.

The magnetic field compression induced by the shock, is manifested through the displacement of the emitted SSA spectrum towards higher frequencies. At the same time, it also imposes a drift of the SSA spectral component towards higher flux densities. As the traveling shock passes through regions of the jet with different physical characteristics, the SSA component of the shocked flow evolves, moving in general towards lower flux densities and frequencies. The parameters of our model can be adjusted then to emulate the evolutionary path of the “shock-in-jet” model as described in subsection 5.2.1.

Finally, the Stokes parameters of the modeled jet are estimated by integrating the ones that emerge from the side of each slab, i.e. perpendicular to the flow axis at the co-moving reference frame of the flow. With this approach, we assume that:

- the shocked and unshocked parts of the flow have (almost) the same Doppler factors and thus, also the same relativistic aberration angles
- the source is observed at the critical angle $\psi_{\text{crit}} \sim \arcsin(1/\Gamma)$, where Γ is the Lorentz factor of the jet’s downstream velocity.

5.4 A STUDY CASE: THE BLAZAR 3C 454.3

The first source for which we tried to reproduce the observed behavior both in total flux and polarization, using our code is 3C 454.3. In the following paragraphs we describe the methodology we followed and give the first results of our study.

5.4.1 Constraining the jet physical size

First, we need to estimate the physical size for the cells of our modeled jet. We can get an impression of this scale, using VLBI maps. A close inspection of the available MOJAVE monitoring data¹ (Lister et al., 2009) revealed that the majority of the observed emission is coming from the inner part of the jet, its core, which spans over a region of about 19 pc. This size corresponds to ~ 850 pc after correcting for projection effects, using a viewing angle of 1.3° (Hovatta et al., 2009). Nevertheless, this size is comparable to the map beam size, thus we consider it as an upper limit for the size of our modeled jet.

¹<http://www.physics.purdue.edu/MOJAVE/>

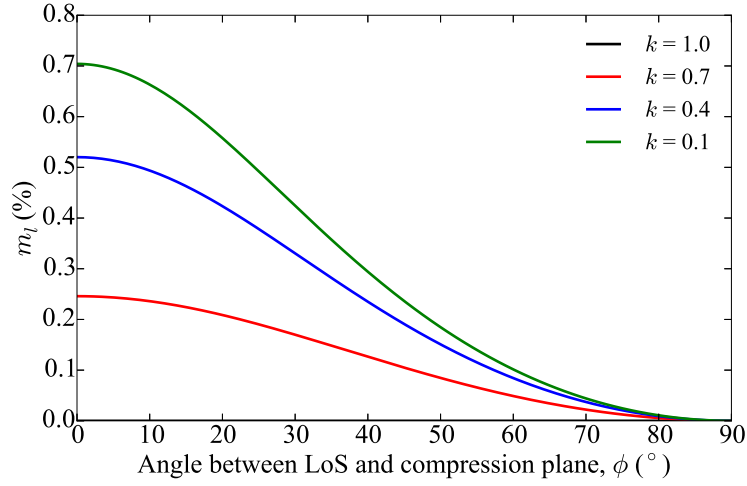
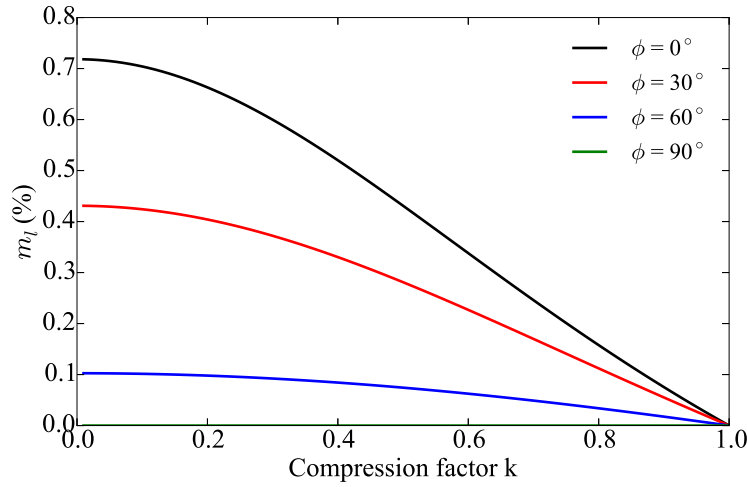
(a) m_l vs compression k (b) m_l vs angle to compression plane

Figure 5.7: The dependence of the linear polarization degree m_l for an optically thin, synchrotron emitting compressed plasma cell with tangled magnetic field as a function of the compression factor, k , and the angle between the line of sight and the compression plane, ϕ (Hughes et al., 1985).

5.4.2 Constraining the particle number density

Next, we want to estimate the particle number density normalization factor, n_{00} , which is needed to model the density gradient of the jet according to Eq. 5.6. This parameter can be estimated from the magnetic field strength and the jet size upper limit we calculated in the previous subsection (5.4.1). The magnetic field strength can be estimated by our circular polarization observations as discussed in subsection 4.4.2. Using the values we calculated in subsection 4.3.1, we estimate a magnetic field magnitude of ~ 3 mG for 3C 454.3. In order to estimate then the parameter n_{00} , we ran our computer code several times using different values in the range of a few to a few hundred particles per cubic cm and tried to reproduce the observed flux of the jet at its “quiescent” state. Using the 14.5 GHz data as a pivot frequency, we managed to reach the observed flux density levels of $\sim 4 - 5$ Jy with number densities of $\sim 10 - 10^2 \text{ cm}^{-3}$.

5.4.3 Constraining the number of cells

The next step was to set a number of cells for the modeled jet. This was done by utilizing the linear polarization degree we observe. When the source is optically thin, we observe the emission generated and propagated through the whole modeled jet. Thus, the linear polarization degree when the source is optically thin can be used to estimate the total number of cells in the jet using Eq. 5.2. On the other hand, when the source is optically thick, we observe only the radiation emitted from the row of cells on the facing side of the jet and we can use the polarization degree at those moments to estimate the number of slabs for the modeled jet. Our observations show that when the source is optically thin, its linear polarization degree has a median value of 3 % and when it is optically thick it is 1 %. Using these values and the theoretical predictions of ~ 70 and ~ 10 % at the optically thin and thick regimes respectively we estimate a total number of 540 cells, organized in ~ 100 slabs. This result, in combination with the linear scale of the source, gives a cell linear scale of ~ 9 pc. Since we expect that the magnetic field of each cell is uniform, we argue that this size is equivalent to the coherence length of the magnetic field in the modeled jet.

This size comes in agreement with the linear scale we get using the variability we observe in the polarized flux. Assuming that the polarized flux is coming from the most compact emission components of the jet region, we can estimate their size by light-travel arguments. The main idea is that we can use the timescale of the variability and the speed of light to estimate a linear scale of the region of the jet where this variability takes place. Quantifying the variability timescale as the half-period between two consecutive minimizations of the polarized flux, we estimate it to be ~ 400 days (see also Fig. 5.4). These observer’s frame time scales however must be corrected for cosmological redshift and relativistic bulk motion. It will then be

$$t' = \frac{\delta}{1+z} t \quad (5.8)$$

where,

- t' time in the emission element frame
- t time in the observer’s frame
- δ the doppler factor of the emission element
- z the redshift of the source

Using $\delta = 33$ (Hovatta et al., 2009) and $z = 0.859$, we calculate the variability timescale at the emission frame to be ~ 7100 days, which corresponds to a linear scale of ~ 6 pc. This size is comparable to the estimated cell size above.

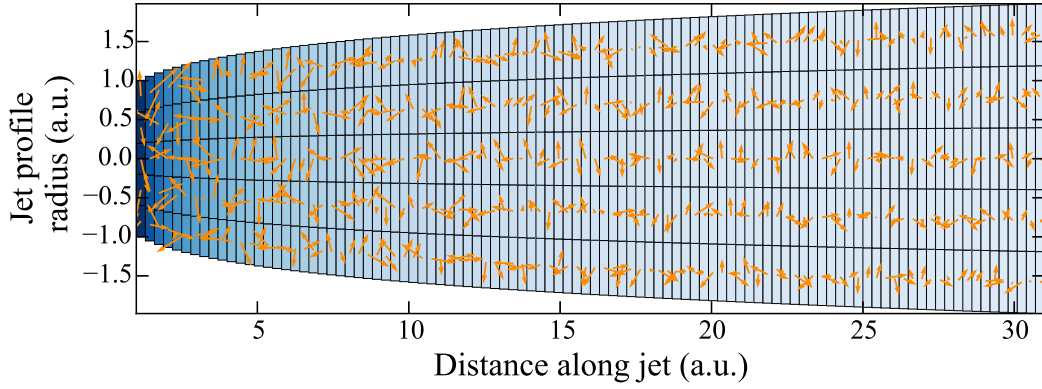


Figure 5.8: The unshocked flow of modeled jet for 3C454.3. The parameters used to construct this model are described in the text.

5.4.4 Reproducing the observed behavior

The above estimates for the cell number and size, the magnetic field strength and the particle density normalization factor were used for the consequent runs of our computer code. The remaining results were made possible by these runs. First, we explored the parameter space of the compression factor and found out that in order to reach the observed maximum polarization degree of $\sim 6\%$ during the polarized flare at MJD ~ 56800 , the compression factor, k , should be ~ 0.8 .

Next, we tried to reproduce the variability pattern with a traveling shock of $k = 0.8$. Using our code, we realized that the variability pattern was reproduced but the propagated SED component was transversing within a small frequency range of a few tens of GHz. In order to transfer the variability pattern to the higher frequencies it is observed ($\sim 20 - 150$ GHz, Fig. 5.2), without changing the parameters estimated above, we increased the Doppler factor of the propagating shock. An exploration of the parameter space showed that the Doppler factor should be ~ 30 for the variability to be observed at that frequency range. This number comes in agreement with the Doppler factor estimates for this source in the literature, (e.g. Sasada et al., 2014; Zhou et al., 2015; Hovatta et al., 2009), calculated by different methodologies.

Finally, we used typical values for a number of parameters which we were not able to constrain observationally. The first is the parameter p which changes the shape of the modeled jet and has anyhow a minor influence on the results. We selected $p = 0.2$ to give a parabolic shape to the modeled jet. The second parameter is q and defines the gradient of the magnetic field strength along the jet. We selected $p = 1$. The third is the index of the power-law particle energy distribution which was assigned the canonical value of 2.4 which yields a spectral index of -0.7 in the optically thin part of the synchrotron spectrum. In Fig. 5.8, we show a profile of the modeled jet using all the parameters discussed above.

The “shock-in-jet” signature in the polarization characteristics generated by our code

In Fig. 5.9, we show a simulated set of lightcurves for the total flux and polarization characteristics of a modeled jet in the case of propagation of one relativistic shock front. The generated lightcurves are very similar with the one we observe for sources which show transitions from the optically thick to the optically thin regime, like 3C 454.3. The signature behavior for this transition (see also subsection 5.2.2) is clearly discerned from the linear polarization datasets, since we observe a 90° rotation of the EVPA, concurrent with a minimization of the linear

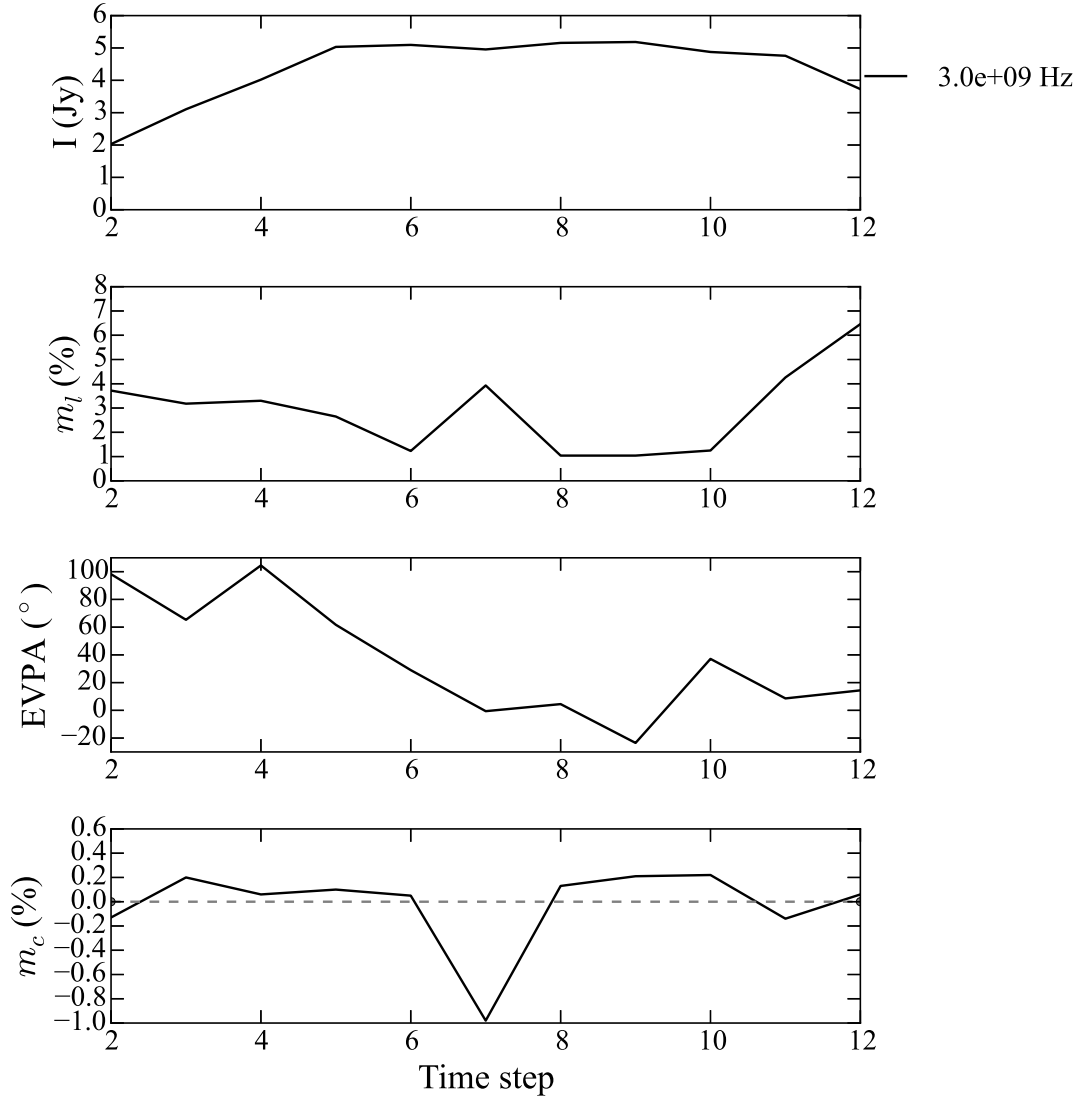


Figure 5.9: Simulated Full Stokes lightcurves as generated with our computer code.

polarization degree, m_l . The corresponding change in handedness for the circular polarization is also observed in the specific example, although the dataset is very noisy and the circular polarization degree remains in general very low.

In conclusion, we believe that the computer code we developed is a powerful tool for the investigation of the physical characteristics of AGN jets. The combination of total flux density and polarization information we observe puts strict constraints on the parameters of the code which in turn can be used directly to extract information for the shock compression factor, Doppler factor and the density of the shocked material. Furthermore, the code can be used to study the influence of Faraday effects on the emitted radiation since these radiative transfer parameters are coded at its core. Finally, this framework can be enriched by useful modifications, like the addition of the lepton number which is discussed in subsection 4.4.3, which can be used to answer fundamental open questions of AGN jets like their composition (electron–proton or electron–positron).

Chapter 6

Optical and radio polarization studies of MeV–GeV blazars

Abstract

In this chapter, we characterize our sample in terms of optical linear polarization using the data obtained with the RoboPol monitoring program between May 2013 and July 2015. Furthermore, the comparison of our partially simultaneous, radio and optical polarization monitoring datasets does not show any correlation between the two bands, suggesting that the physical conditions at the two emission sites are different. We report 60 EVPA rotation events in the radio bands we examined, performed by 22 sources of our sample. A small number of those (6) have also shown such events in the optical wavelengths. Assuming that these rotations are caused by the helical motion of emission elements propagating downstream the jet, we use the rotation rates and the linear polarization degree measurements in both the radio and optical bands to compare their (tangential) velocities and hence their kinetic energies while they propagate through the radio and optical emission sites in the jet.

6.1 INTRODUCTION

One of the defining characteristics of blazars is the high and variable optical linear polarization degree. This characteristic has been used early on as an important probe of the physical parameters of jets and several observing campaigns have been initiated with the mere goal to collect as much polarization information as possible from such sources, (e.g. Smith et al., 2009).

One of the optical polarization blazar monitoring campaigns which is currently running is the RoboPol program (King et al., 2014; Pavlidou et al., 2014). RoboPol monitors the linear polarization parameters of an unbiased sub-set of a gamma-ray flux limited sample (selected from the second Fermi-LAT source catalog, (Nolan et al., 2012)) that includes ~ 65 gamma-ray blazars. The cadence ranges between a fraction of a night to 3 nights. The program uses the Skinakas 1.3m optical telescope and a 4-channel polarimeter that can measure instantaneously three Stokes parameters I , Q and U .

The current chapter is discussing the combined radio and optical polarization properties of the *F-GAMMA* sources. Assuming that the radio and optical photons are produced in separate emission sites in the AGN jets, the results can provide us with valuable information for the physical characteristics at the two jet regions.

6.2 OPTICAL POLARIZATION DATA

In this section we introduce the sub-set of common sources between the radio polarization sample discussed in Chapter 4 and the RoboPol source sample. We present their optical polar-

ization characteristics along with some basic descriptive statistics and compare them with the ones found in radio.

6.2.1 Demographics

There are 49 sources in the RoboPol data, collected between May 2013 and July 2015, which have been also observed at least once at any of the four radio frequencies discussed in chapter 4. These sources, along with a number of descriptive statistics for their R band magnitude, linear polarization degree and EVPA measurements obtained over the last ~ 2.2 years are given in Table E.1.

In Table 6.1, we present the fractions of these sources which were found to be polarized at least once in the RoboPol optical data as well as the radio data of the previous chapter. In the last column of that table, we give the average value of the median linear and circular polarization degrees of the corresponding sources. Finally, in Fig. 6.1, we show the histogram of the median linear polarization degrees for the 44 sources which were found to be polarized at least once in the R band.

In Fig. 6.1 we have also included the histograms separately for the sources labelled as Flat Spectrum Radio Quasars (FSRQs) and BL Lac in Table 4.1. A direct visual inspection of the two histograms does not show a significant difference between the two source types which is also verified by a 2 sample Kolmogorov-Smirnov (KS) test ($D = 0.14$ and $p = 0.96$).

Table 6.1: The fraction of sources which were observed in both radio and optical bands and were found to be polarized along with the average polarization degrees in each band.

Band	Quantity	Detected sources	Percentage (%)	$\langle m_{l,c} \rangle$ (%)
R	m_l	44/49	89.8	8.4
2.64 GHz	m_l	40/44	90.1	3.2
4.85 GHz	m_l	37/49	75.5	3.2
	m_c	24/49	49.0	0.4
8.35 GHz	m_l	40/48	83.3	3.4
	m_c	25/48	52.1	0.4
10.45 GHz	m_l	33/45	73.3	3.5

6.2.2 Polarized state duration

In order to investigate whether the polarized state is a transient event for the R-band data of the observed sources, possibly connected with their prominent flaring behaviour, we calculate the fraction of the number of times they were detected to be significantly polarized, N_{sign} (signal-to-noise ratio ≥ 3), over the total number of times they were observed, N_{tot} . These fractions are shown as percentages in Fig. 6.2. In order to solidify our results, we perform our analysis with the 29 sources which were measured at least 10 times over the observing period.

We conclude that the sources remain polarized most of the time (median: 91%), independently of whether they are in a “flaring” or “quiescent” state. A detailed discussion for the polarization characteristics of the source at those two states can be found in subsection 6.3.3. Furthermore, these results are also in agreement with the same study for the radio bands, described in subsection 4.2.6.

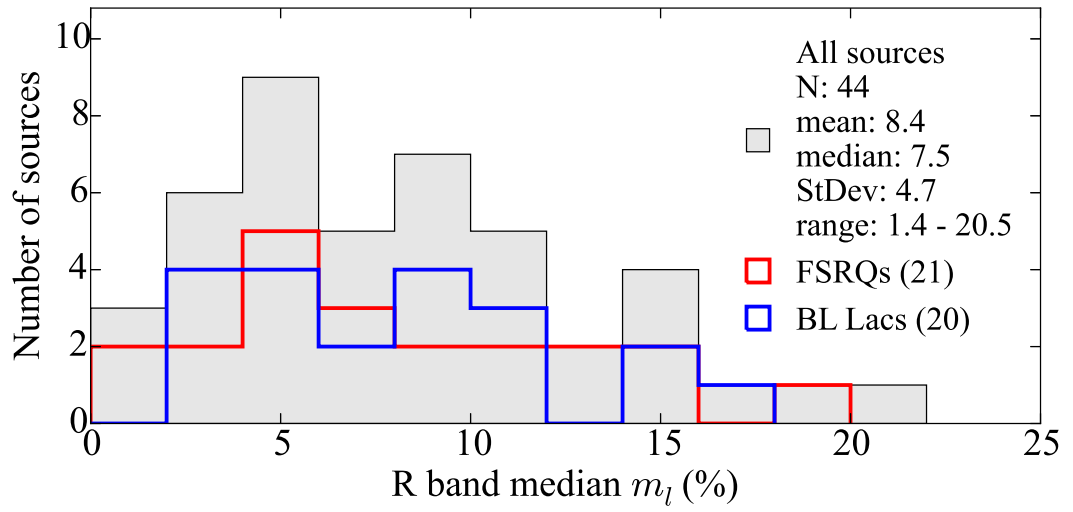


Figure 6.1: The distribution of the R band median linear polarization degree measured by the RoboPol program.

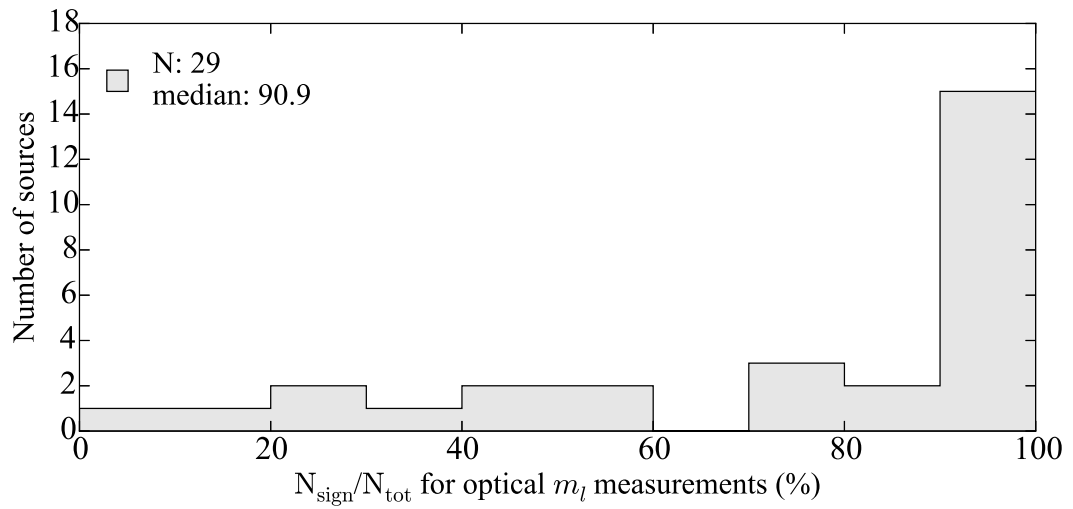


Figure 6.2: Histograms of the fraction of the number of times the sources were detected to be linearly polarized, N_{sign} , over the number of times they were observed, N_{tot} . The analysis was performed for sources that were observed at least 10 times.

6.3 CORRELATION ANALYSIS

In this section, we utilize the tool of correlation analysis to quantify the relations between the optical linear polarization and other observational characteristics for the sources in our sample. Such relations are either dictated from existing theoretical models or can be used in the development of new ones.

6.3.1 Optical linear versus radio linear and circular polarization

The average values of the linear and circular polarization degrees, reported in Table 6.1, show that the linear polarization degree at optical bands is more than double the one we observe at radio. One possible interpretation is that the magnetic field at the jet regions we probe with the optical observations is more ordered than the one we probe with the radio observations. This can be attributed to less randomization of the magnetic field in the optical part of the jet or to frequent compressions of that field, possibly due to propagating shock fronts, which would lead to an apparent uniformity, even if the randomization is similar in both radio and optical parts (see also subsection 5.3.5).

Here we investigate further the correlation of the linear polarization degree at the optical and radio bands, by comparing them at the source level. In Fig. 6.3, we plot the linear polarization degree as measured in the two bands for all applicable cases. A similar plot is shown in Fig. 6.4, where we compare the optical linear polarization degree with the radio circular polarization degree. Interestingly, no correlation is found between the optical linear and radio linear and circular polarization degrees in any of the bands we tested. This is supported by the Spearman ρ test results (ρ and p values) attached on the side of each plot.

This result can be attributed to the difference of the physical parameters between the two source regions. For example, if we consider the difference in the magnetic field uniformity as the reason for the difference of the linear polarization degrees as discussed above, there are sources with both higher and lower uniformity in the optical part of the jet as compared with the radio one. The former is expected since we believe that the optical emission of the jet is coming from the part closer to the “central engine” where theory predicts better ordering of the magnetic field. Thus, sources which show lower ordering of the magnetic field in the optical than the radio part are very interesting cases and need further investigation.

6.3.2 Optical linear polarization degree against the γ -ray energy flux

In Fig. 6.5, we plot the optical linear polarization degree as a function of the γ -ray energy flux, taken from the 2FGL catalog (Nolan et al., 2012). We report that we find no correlation between these two quantities, which is also supported by the Spearman ρ test results, attached to the plot.

This is opposite to what we found for the radio data in subsection 4.4.4, where we noted an anti-correlation between the linear polarization degree and the γ -ray energy flux. This fact can be used as a constrain for the various theoretical frameworks which attempt an interpretation of the origin of γ -rays observed from AGN jets.

6.3.3 Optical linear polarization degree and flux density state

In Fig. 6.6, we plot the linear polarization degree and polarized flux density at the low and high optical flux density state of the sources. For the majority of data points, the linearly polarized flux density is increased when the sources are at high total flux density state. This is an indication of the non-thermal origin of the emission component responsible for the flux density increase and it is similar to the results at radio as shown in subsection 4.4.6.

On the other hand, the optical linear polarization degree is not always higher at the high flux state. The results of Fig. 6.6 show that the probabilities of the degree to be higher and

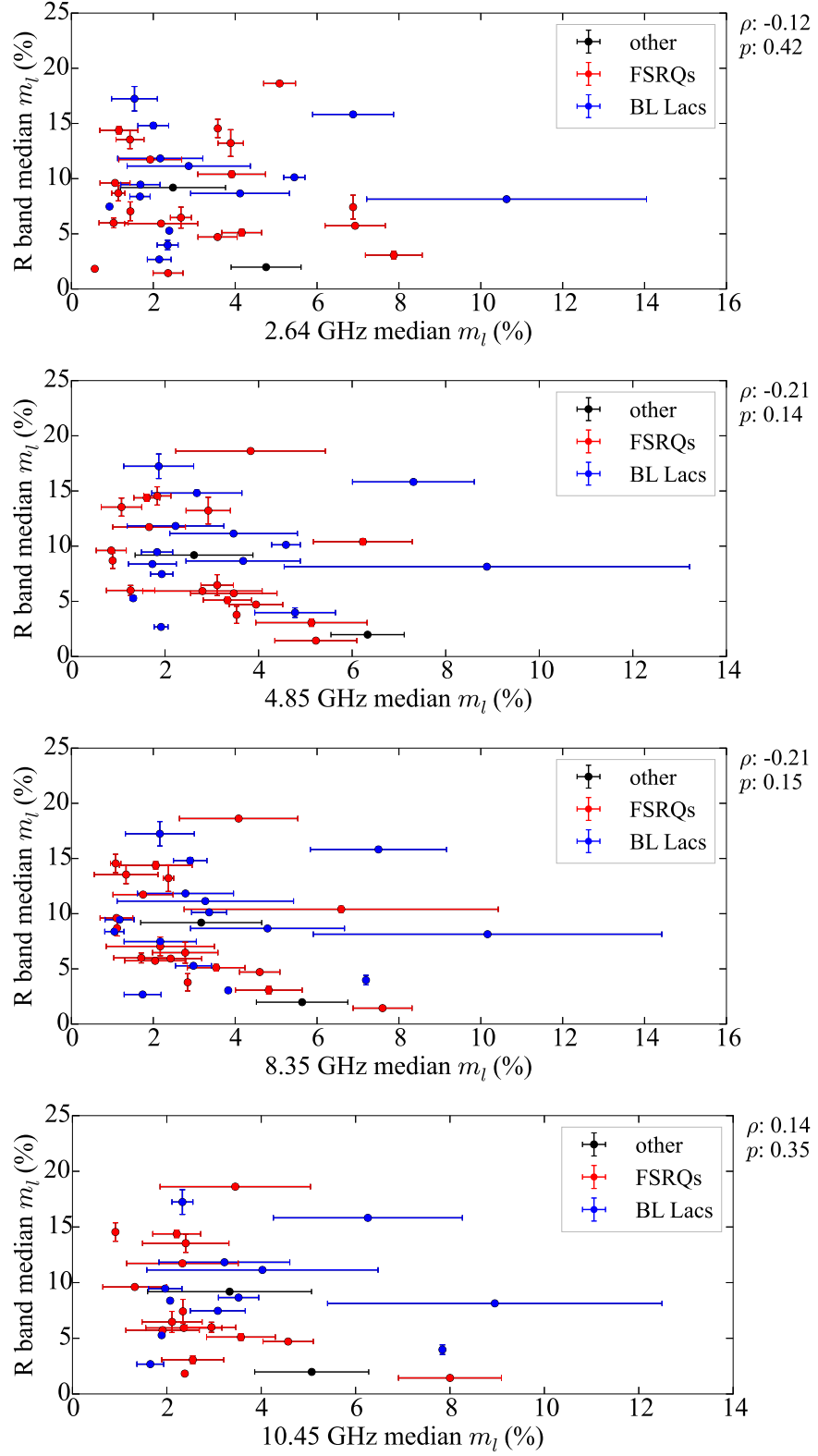


Figure 6.3: R band median m_l against radio median m_l . The Spearman ρ and p values are shown on the side of each plot.

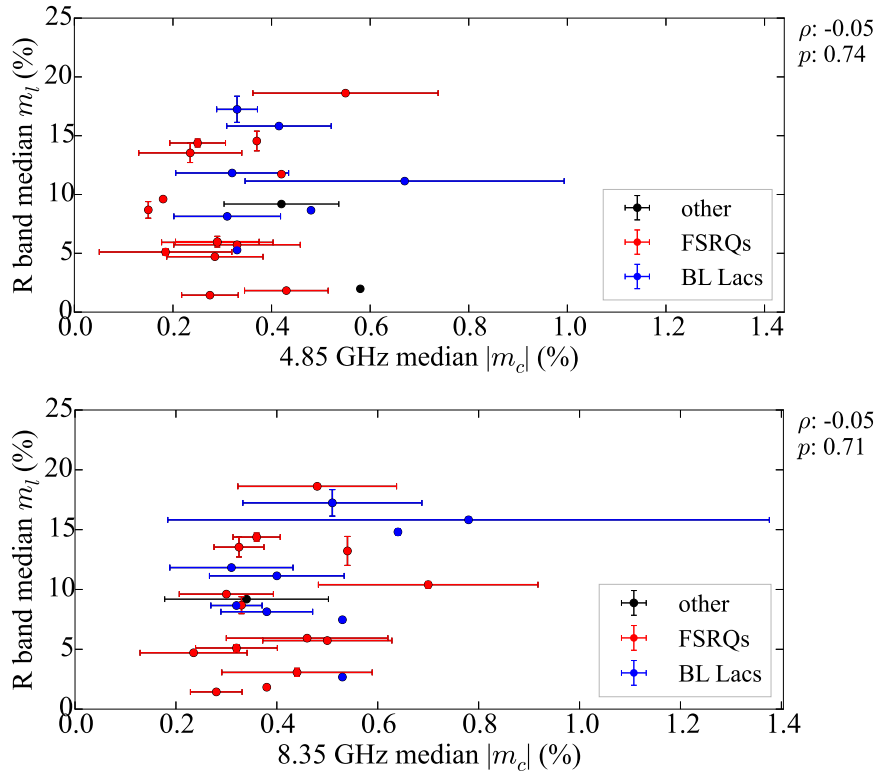


Figure 6.4: R band median m_l against radio median absolute m_c . The Spearman ρ and p values are shown on the side of each plot.

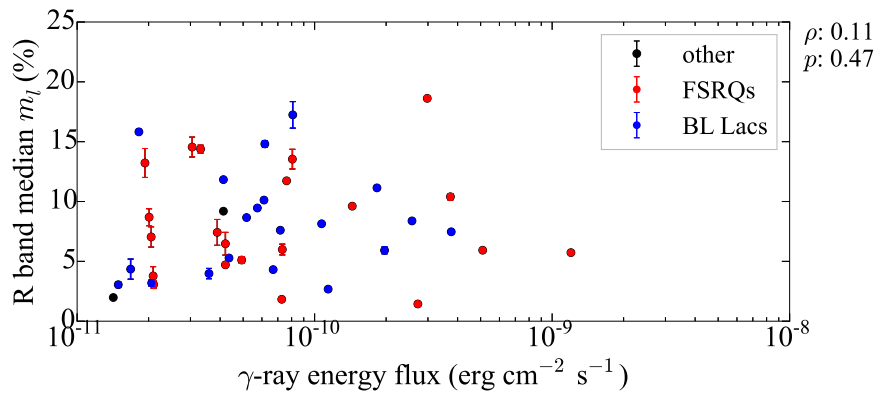
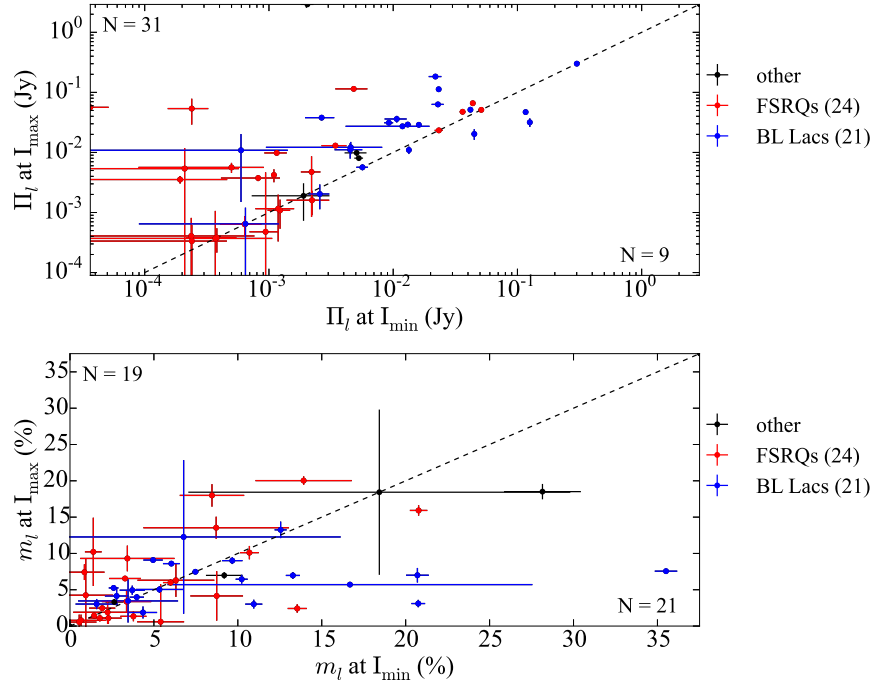


Figure 6.5: R band median m_l against γ -ray energy flux.

Figure 6.6: R-band m_l and Π_l at low and high flux density state.

lower are almost equal. The optical results are very similar to the radio only at 10.45 GHz. The interpretation we presented there was that for half of the times the flux increase at 10.45 GHz was due to optically thick emission components and optically thin for the other half. This interpretation though is inadequate for the optical data, since we expect that the optical emission remains always optically thin. An alternative interpretation would be that for the data points above the $x = y$ line in Fig. 6.6, where the linear polarization degree is higher at the high flux state, the flux increase is caused by an emission component with higher magnetic field uniformity, while for the ones below the $x = y$ line it is caused by an emission component with lower uniformity.

The former case is easily supported by the majority of theoretical interpretations for the emission components which cause the observed variability. One such example is the “shock-in-jet” model, according to which the variability is caused by a travelling shock front which compresses the ambient magnetic field and thus results to an (apparent) increase of the uniformity as discussed in subsection 5.3.5. The latter case however is difficult to be explained and further investigation is needed.

6.4 OPTICAL AND RADIO EVPA ROTATIONS

One essential advantage of high-cadence, polarization monitoring programs like RoboPol, is the capacity to densely sample smooth EVPA rotations which have been reported for AGN jets, (e.g. Marscher et al., 2008; Abdo et al., 2010; Marscher et al., 2010). High cadence observations is a necessity if we want to remove the $n\pi$ ambiguity between consecutive EVPA data points correctly. The ranges of optical EVPA rotations vary from a few tens to a few hundreds of degrees and the rotation rates are $\sim 10^\circ/\text{day}$ (Blinov et al., 2015). It has been suggested that these rotations are correlated with flares of the high energy jet emission (Marscher et al., 2008) but the systematic study of Blinov et al. (2015) showed that no such exclusive correlation exists.

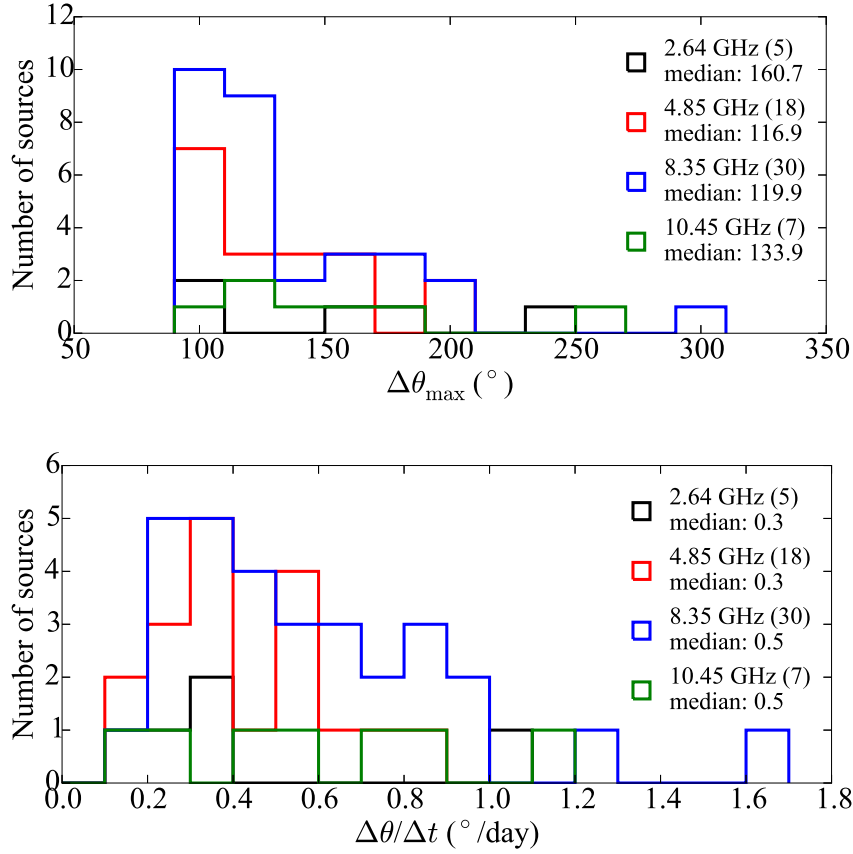


Figure 6.7: Histograms of the radio linear polarization EVPA rotation ranges, $\Delta\theta_{\max}$, and rates, $\Delta\theta/\Delta t$, for four different bands.

We applied the methodology developed by Kiehlmann et al., (*in prep*) and presented in Blinov et al. (2015) for the optical EVPA datasets obtained by RoboPol, to search for EVPA rotations in the radio bands. We used the criteria described in Blinov et al. (2015) to define an EVPA rotation. We considered:

- monotonous rotations with ranges $\Delta\theta \geq 90^\circ$ and
- measured with at least 4 significant data points

There are 60 such rotations detected in the radio polarization datasets we analyzed. The histograms of the EVPA rotation ranges, $\Delta\theta_{\max}$, and the rotation rates, $\Delta\theta/\Delta t$, in the four different radio bands are shown in Fig. 6.7. Although the EVPA rotations at radio bands have similar ranges as the ones in optical, their rates are much lower (median: $0.4^\circ/\text{day}$).

The radio EVPA rotations we report were observed for 22 sources in our sample. These sources are shown in Table 6.2, along with the number of rotations observed in any of the radio bands we examined. We also give the median value of all the observed rotation ranges, $\Delta\theta_{\max}$, as well as the median value of their rates, $\Delta\theta/\Delta t$. Sources with detected optical EVPA rotations have a second entry in Table 6.2, starting with the label “R band”. The corresponding optical EVPA rotation ranges and rates are taken from Blinov et al. (2015). There are 6 sources with EVPA rotations detected at least once in both the optical and radio bands, independently of whether they were concurrent.

Table 6.2: The list of sources which have shown radio or optical EVPA rotations. The second column is the number of detected rotations, the third is the median value of the ranges of these rotations, $\Delta\theta_{\max}$, and the fourth column the corresponding median value of the rotation rates, $\Delta\theta/\Delta t$.

Source	Rotations	Median $\Delta\theta$	Median $\frac{\Delta\theta}{\Delta t}$
J0050-0929	3	177.1	0.31
J0102+5824	1	90.8	0.17
J0217+0144	3	133.6	0.69
J0237+2848	2	199.4	0.72
J0238+1636	1	106.6	0.25
J0319+4130	3	121.4	0.51
J0423-0120	6	124.8	0.52
R band	1	110.0	11.10
J0721+7120	9	122.6	0.58
R band	2	194.0	72.40
J0730-1141	4	166.1	0.35
J0738+1742	1	109.6	0.37
J0818+4222	3	119.8	0.30
J0854+2006	2	155.4	1.13
R band	2	167.0	11.85
J1159+2914	1	132.3	0.69
J1256-0547	2	116.0	0.31
R band	3	180.0	4.70
J1310+3220	1	128.3	0.30
J1512-0905	2	102.2	0.64
R band	4	450.0	13.80
J1635+3808	1	120.0	0.34
J1751+0939	5	107.6	0.51
J1848+3219	2	103.2	0.45
J1849+6705	4	160.2	0.38
J2203+1725	2	142.8	0.36
J2253+1608	2	103.3	0.59
R band	3	130.0	16.30

The interpretation of EVPA rotations in both the radio and optical bands is an active field of research. There are several theoretical frameworks which can explain the observed behaviour and they can be split into two major categories, the radiative and the geometrical rotations (Myserlis et al., 2014). The former attribute the observed rotations to changes of the physical characteristics of the emission components which in turn change the polarization characteristics of the observed emission. One example is the transitions between the optically thin and thick regimes for a synchrotron emitting component, which rotate its EVPA by exactly 90° as described in subsection 5.2.2. The latter attribute the observed EVPA rotations to geometrical characteristics of the emitting source, such as bend jet geometries and curved trajectories of moving emission elements (e.g. Marscher et al., 2008; Nalewajko, 2010; Cawthorne and Cobb, 1990).

One of the geometrical interpretations of EVPA rotations predicts that large scale

monotonous rotations are caused by the helical motion of emission components as they propagate downstream the jet (Marscher et al., 2008). Assuming that this is the cause of EVPA rotations in both radio and optical bands, we can use our findings to constrain some of the basic physical characteristics of jets.

6.4.1 Optical and radio emission site size from EVPA rotation rates

In the following analysis we use the observed radio and optical EVPA rotation rates independently of whether the rotations appear simultaneously in the two bands. As discussed above, for the sources which show both radio and optical EVPA rotations, the former ones have much lower rotation rates than the latter as shown in Table 6.2. The median value of the ratios of EVPA rotation rates between radio and optical is 0.05, i.e. the optical EVPAs rotate 20 times faster.

Assuming now a stable tangential speed, v , for the helically moving emission components, we can estimate the ratio of the jet cross-section radii at the optical and radio emitting parts of the jet using the conservation of angular momentum argument. If the angular speed of the emission element, ω , is equal to the EVPA rotation rate, we estimate that the jet radius at the radio emitting part of the jet should be 20 times larger than the one at the optical emitting part. This size ratio is not only very large but it should be manifested through much higher linear polarization degree ratios between the optical and radio bands than the ones observed. That is, under the assumption of a self-similar jet magnetic field structure for which the only difference between the optical and radio emitting parts is a 3-dimensional “compression”.

6.4.2 The kinetic energy ratio between the radio and optical parts of the jet

The only assumption in all the above, besides the interpretation of the EVPA rotation, is the stable tangential speed, and thus kinetic energy, of the helically moving emission component. If we drop this and use the observed linear polarization degree ratio between the optical and radio observations, we can estimate the size ratio between the radio and optical emission sites assuming the self-similar magnetic field structure discussed above. This in turn will provide an estimate for the tangential speeds when we combine it with the angular ones, deduced from the EVPA rotation rates in the two bands. Using only the set of sources which show both optical and radio EVPA rotations, we estimate that the ratio of radio over optical linear polarization degree is ~ 0.26 .

Assuming that this difference of linear polarization degrees is due to a 3-dimensional compression of the optically emitting jet part as compared to the radio emitting one, we can generalize Eq. 5.7 to estimate the linear compression factor that could cause this difference. Then, a 3-dimensional linear polarization degree ratio of ~ 0.26 would correspond to a 1-dimensional of $\sqrt[3]{0.26} = 0.64$, which in turn corresponds to a compression factor of 0.47 (assuming the ideal case of $\phi = 0$ in Eq. 5.7). This would also be the ratio of the jet cross-section radii, R , between the optical and the radio emitting parts of the jet.

The latest finding, combined with the observed ratio of the angular speeds of the emission component can be used to estimate the ratio of tangential speeds:

$$\frac{v_r}{v_o} = \frac{\omega_r}{\omega_o} \frac{R_r}{R_o} = 0.05 \cdot \frac{1}{0.47} = 0.05 \cdot 2.1 = 0.105 \quad (6.1)$$

where the subscripts “r” and “o” refer to the radio and optical emitting part of the jet. This would correspond to a kinetic energy ratio of 0.011 between the two parts of the jet. A comparison of this results with the current theoretical predictions is among our immediate next steps.

Chapter 7

Summary and conclusions

7.1 THE FRAMEWORK

This work presented a framework for the study of the physical conditions in astrophysical emitting plasma elements through linear and circular polarization monitoring. This framework includes all necessary elements to:

1. Design and conduct high-cadence, multi-frequency polarimetric observations.
2. Recover the complete Stokes 4-vector of the observed radiation with high accuracy.
3. Interpret polarimetric observations on the basis of the theoretical predictions that include emission, absorption and propagation effects that can generate, modify or eliminate the Stokes parameters of the radiation.
4. Reproduce the observed characteristics in the complete Stokes parameters set using a radiative transfer code we developed on the basis of the model of Hughes et al. (1989a).

In this chapter we give an overview of the different elements of the framework and summarize the conclusions reached throughout this thesis.

7.2 HIGH PRECISION LINEAR AND CIRCULAR RADIO POLARIMETRY

We have developed the machinery of our framework using a large fraction of the data obtained with the *F-GAMMA* monitoring program. The methodology was based on the data obtained with the 4.85 GHz secondary focus receiver of the 100-m Effelsberg telescope and it can be easily generalized to accommodate the needs of any radio telescope equipped with circularly polarized feeds. This methodology is described in Chapters 2 and 3.

The low circular polarization degree ($\sim 0.5\text{--}1\%$) of the observed sources renders their Stokes V measurements extremely challenging, especially with telescopes equipped with circularly polarized feeds. The development of a methodology to extract all four Stokes parameters was essential for our project since it eliminates a number of uncertainty sources. The most important of which, are:

1. The variability of Stokes Q and U during the measurement integration, caused by the parallactic rotation of the source. We minimize this contribution by rotating the Stokes parameters Q and U to the default North–East reference frame in the minimum possible quantum of time. In our case, this was the duration of one sub-scan (~ 30 s) for the cross-scan observing method we followed.
2. The spurious linear and circular polarization as well as the cross-talk between Stokes parameters induced by the observing system, collectively known as instrumental polarization. We followed two methodologies to correct this effect. For the first one, we estimated the elements of the 4×4 Müller matrix for each observing session and multiplied its inverse matrix with the observed Stokes vector to correct them. For the second

one, we performed a detailed calibration of all the Stokes parameters compensating for the instrumental cross-talk between Stokes Q and U (instrumental rotation).

Both methodologies require linear and circular polarization standards. The former are usually known while the latter are almost nonexistent in the available literature. After a careful examination of the Stokes V for the sources in our sample, we discovered a number of them which showed significant and stable circular polarization after removing the spurious Stokes V introduced by the instrument. We used the known linear polarization and the discovered circular polarization standards to correct the instrumental polarization and calibrate the observe Stokes parameters with the above methodologies. The linear and circular polarization standards we used are given in Table 3.2.

3. The uncertainty introduced by the fitting algorithm that we use to compute the Stokes parameter amplitudes. Since most of our sources are unresolved, the datasets obtained during each sub-scan yield the beam pattern of the telescope, normalized to the corresponding amplitude of the observed source. In order to compensate for the low Stokes V of our sources, measured as the difference between the fitted left and right circularly polarized (LCP and RCP) source amplitudes, we adopted the Airy disk function (Eq. 2.14) which describes the whole area of the scan with high accuracy and delivers small enough fitted amplitude errors.
4. The spurious Stokes V introduced by the LCP and RCP beam separation on the plane of the sky, which introduces a gain difference between the two channels. We compensate for this difference by recalculating the LCP and RCP amplitudes as if they were measured at the center of each beam using the pointing offsets in the two scanning directions and the Airy disk function which describes the beams. Our results show that the Stokes V variability introduced by this effect due to the different LCP to RCP gain ratios over the two scanning directions, is decreased for $\sim 70\%$ of our measurements with an average decrease of $\sim 15\%$.
5. The instrumental artifacts of the Stokes Q and U beam patterns. We model those for each observing session using the Stokes Q and U datasets of unpolarized sources. Afterwards, we subtract the constructed models from the corresponding datasets of all the observed sources. The benefits are manifold, including the improvement of the FWHM and the recovery of faint or corrupted Stokes Q and U datasets. After this correction, the scatter of linear polarization degree and EVPA for the standard sources we measure was found to be reduced by as much as up to 10 times.

We also studied the multiplicative factors used to correct the measured amplitudes for the attenuation of the incident radiation through the atmosphere as well as the telescope's gain variability due to deviations of its surface from the ideal parabolic shape at different observing elevations. We did not find any significant difference of those factors between the different polarization modes; subsequently, the same factors were used for all Stokes parameters.

Finally, our examination of the polarimetric datasets obtained over more than 4.5 years showed that the observing system is very stable and can deliver high accuracy results in all Stokes parameters (Sect. 3.4).

7.3 LINEAR AND CIRCULAR RADIO POLARIZATION CHARACTERISTICS OF AGNS

We used the above methodology to recover the polarization parameters for a sample of 87 AGNs at 4 bands between 2.64 and 10.45 GHz. Stokes I, Q and U were recovered at 2.64, 4.85, 8.35 and 10.45 GHz and Stokes V at 4.85 and 8.35 GHz. Our results concern monitoring observations conducted with the 100-m Effelsberg telescope between July 2010 and January 2015 with a mean cadence of 1.6 months and they are presented in Chapter 4.

7.3.1 Linear and circular radio polarization

Around 80–90% of the sources were found to be linearly polarized at least once. On the other hand, 55% of the sample showed significant circular polarization degree, m_c , at least once. The distributions of the median linear and circular polarization degrees, m_l and m_c , have average values of $\sim 3.1\%$ and $\sim 0.5\%$ respectively. Our measurements yield a mean uncertainty of 0.2% and 0.1% for m_l and m_c respectively.

Linearly and circularly-only polarized sources

There are 27 sources in our sample which showed only linear polarization. They were found to populate the lower part of the flux density distribution of our sample and thus their circularly polarized fluxes most probably do not pass the detection limits of our system. There are also 4 sources which show only circular polarization. Since such behaviour is not expected from the synchrotron emission mechanism, those sources may be an indication that circular polarization “survives” better the various propagation effects which depolarize the radiation or of another emission mechanism at play.

Linear and circular polarization per observing frequency

We found a correlation between the average m_l and the observing frequency. This result can be attributed to a better ordering of the magnetic field upstream the AGN jet or to the depolarization due to internal Faraday rotation which should be more prominent at the lower frequencies. No significant difference was found between the 4.85 and 8.35 GHz m_c distributions. This is an indication that the emission is coming from neighboring regions in the jet with similar physical conditions.

Duration of polarized state

Most of the linearly polarized sources were found at a significantly polarized state for 80–90% of the time. Interestingly, this is not the case for the 10.45 GHz data, where this fraction is $\sim 28\%$. This result can be attributed to the intense variability at that frequency. Assuming that the variability is caused by emitting elements which undergo transitions between the optically thick and thin regimes of synchrotron emission, their linear polarization degree is often minimized and renders the linearly polarized part of the emission unobservable. On the other hand, the circularly polarized sources, acquire that state only for a small fraction of the time (median: 7 %). This is expected, since our sources are very variable and the intrinsically low fraction of circular polarization (Table 4.2) restricts our capacity to measure it to only the brief periods the source remains at a high total flux density state.

Total flux density and linear polarization spectra

We observed significant variability in the frequency dependence of the linear polarization characteristics (m_l versus frequency) for most of our sources. This is expected in the case of (incoherent) synchrotron emission since the linear polarization degree depends on the spectral index (see also subsection 1.4.1) and most of the sources show pronounced spectral evolution (Angelakis et al., 2012). Furthermore, for a subset of sources like J1256-0547 (3C 279) or J2253+1608 (3C 454.3) we measure clear minimizations of m_l versus frequency which propagates to lower frequencies. The fact that we observe also a concurrent rotation of the EVPA by 90° , indicates that we observe transitions between the optically thick and thin regimes of synchrotron emission which has been one of the main drives for the current work.

7.3.2 Derivative quantities

We used the linear and circular polarization characteristics described above to calculate the magnetic field strength in our sources. We also compute the rotation measure which is at-

tributed to the low energy magnetized plasma located in regions where the radiation is emitted or propagated through.

Magnetic field magnitude

We calculated the magnetic field strength by utilizing their circular polarization degrees and the observing frequency, corrected for the relativistic Doppler and the cosmological redshift effects. The magnetic field strengths estimated with the above technique are of the order of a few to a few tens of mG (Table 4.4 and Fig. 4.8). There is an increase of the median magnetic field strength from ~ 3 to ~ 6 mG with increasing observing frequency which might be an indication that we observe regions of the jet where the magnetic field becomes more uniform. Our magnetic field estimates are in good agreement with other studies and they are consistent with those expected from theoretical predictions of magnetically powered jets.

Rotation measure

Our EVPA measurements at various frequencies allowed us to recover also the rotation measure and the zero-wavelength EVPA, χ_0 , for each session. Their median values are reported in Table 4.5. Our RM measurements are significantly correlated with the ones estimated by NVSS data in Taylor et al. (2009) ($p = 2 \cdot 10^{-5}$, $\rho = 0.63$), suggesting a good agreement between the two projects. Most of the RM values lie in the range between $\pm 100 \text{ rad m}^{-2}$ which is an indication that the Faraday rotation effect mainly takes place in the magnetized plasma of our Galaxy, since they are consistent with the Galactic RM (Taylor et al., 2009). This interpretation is supported by the fact that we find a significant anti-correlation between the RM and the galactic latitude of our sources ($p = 10^{-4}$, $\rho = -0.58$, Fig. 4.12).

We found also significant variability of RM which seems to be correlated with the source variability. If the above interpretation for the galactic origin of Faraday rotation holds, we can use this variability to probe the plasma content and magnetic field variations of our Galaxy. Furthermore, a careful inspection of our results showed a sudden increase of RM when the sources showed transitions between the optically thick and thin regimes of synchrotron emission. Therefore, RM variability is also an important diagnostic tool for the intrinsic physical conditions of the source which may cause such transitions, like the particle density of the emitting region or its magnetic field strength.

7.3.3 Correlation analysis

The theoretical predictions for the emission, absorption and propagation of polarized radiation were used to perform a thorough correlation analysis between several observed characteristics in order to investigate the physical conditions of the emitting plasma elements.

EVPA versus AGN jet position angle

We found a bimodality in the distribution of angles between χ_0 and the jet position angle (ϕ_{jet}). The peaks of the distribution are located at 0° and 90° with the latter being more significant. This result is consistent with the poloidal component of the jet's magnetic field being slightly dominant. The bimodality of the distribution comes in agreement with the theoretical work in this field, (e.g. Lyutikov et al., 2005) but a repeat of this experiment with an unbiased sample is needed in order to generalise the conclusions.

Linear versus circular polarization degree

Our 4.85 GHz data show that m_l is correlated with m_c and it is about 10 times larger while no significant correlation is found for the 8.35 GHz data. The correlation is predicted by the synchrotron theory but the ratio is expected to be one order of magnitude larger ($m_l/m_c \approx 230$) at those frequencies. We attribute this discrepancy to depolarization effects – Faraday

Rotation or the non-uniformity of the magnetic field – which decrease the linear polarization degree much more than the degree of circular polarization. Our linear polarization degree results ($m_l \approx 3\%$) which are one order of magnitude less than the ones predicted by theory ($m_l \approx 70\%$) support this interpretation. This means that circular polarization “survives” better the transmission of radiation through the tangled magnetic field of the emitting region and other magnetized plasma clouds which may lie between the source and the observer. This makes circular polarization observations a direct probe of the emitting region properties.

Finally, the fact that there is no evident correlation between the observed m_l and m_c at 8.35 GHz is not necessarily contradicting the above interpretation. One possible explanation is that the m_c we observe at 8.35 GHz is not attributed (only) to the intrinsic synchrotron emission but also to certain propagation effects, like circular repolarization, which predict the observed lack of correlation between m_l and m_c (see also subsection 1.4.4).

Linear and circular polarization versus RM

For the m_l data, we observe a slight anti-correlation with RM only at 2.64 GHz with confidence level of 91%. For the higher frequencies (4.85–10.45 GHz), no correlation is found. This result suggests that the low frequencies may be affected by internal Faraday rotation caused by low energy magnetized plasma at the outer parts of the AGN jets where this emission is mainly coming from. The lack of correlation at the higher frequencies, shown that the observed RM is caused by external Faraday rotation, possibly caused by our Galaxy. For the m_c data, we don’t get a significant correlation or anti-correlation with RM which indicates that the observed m_c is intrinsic to synchrotron emission and not generated by propagation effects which require low energy magnetized plasma.

Jet plasma composition

The magnetic field strengths were calculated under the assumption that the emitting plasma is purely made of electrons or positrons. We compared them against theoretical predictions under the same assumption to estimate, in the case they are different, the content of positrons or electrons respectively in the emitting plasma, quantified by the lepton number, ℓ (Eq. 4.8). Assuming that the theory predicts a magnetic field strength of 10–100 mG for an electron plasma (O’Sullivan and Gabuzda, 2009a) and given the fact that we observe a median value of ~ 3 mG at 4.85 GHz (subsection 4.3.1), we calculate that $|\ell| \sim 0.2$ –0.5. This lepton number range shows that for every particle of one population there are 1.5 – 2 particles of the other (electrons or positrons). In other words, the admixture of positrons in electron-dominated jet plasmas or electrons in positron-dominated ones is ~ 33 –40%.

Polarization degree versus γ -ray energy flux and synchrotron peak

We found an anti-correlation between m_l and the γ -ray energy flux (Nolan et al., 2012) which is more significant for the 8.35 GHz data ($\rho = -0.25$, $p = 0.04$, Fig. 4.17). We also found an anti-correlation between m_l and the logarithm of the peak frequency of for the synchrotron part of the source SED, ν_s , taken from Ackermann et al. (2015) ($\rho = -0.35$, $p = 0.04$, Fig. 4.19).

Polarization parameters and source type

We did not find a significant difference between the two major source types, namely Flat Spectrum Radio Quasars (FSRQs) and BL Lac objects, for the majority of the characteristics we examined, except for two: the magnetic field strength at the observing frequency of 4.85 GHz and the angle between χ_0 and ϕ_{jet} with confidence levels of 98 and 97% respectively. For the latter, BL Lac objects peak at 0° and FSRQs at 90° . This can be attributed to the difference in redshift between those two populations. The cosmological redshift affects the emitted frequency and we may probe different regions of the jet at the same observing frequency. A

potential difference in the magnetic field geometry between those regions would then be imprinted in the angle distributions between χ_0 and ϕ_{jet} .

Polarization degree and flux density state

Finally, we compared the polarization when the sources are in “quiescent” and “flaring” states. Although the linearly polarized flux density is always increased in the “flaring” state, indicating that the flare is caused by a non-thermal emission element, the linear polarization degree was found most of the times lower at the “flaring” state for the majority of the frequencies we examined (2.64–8.35 GHz). We interpret this behavior by attributing the total flux density increase at these frequencies to optically thick synchrotron components. The situation is reversed at 10.45 GHz where the m_l is mostly increased during the “flaring” state which we attribute to optically thin synchrotron components. The circularly polarized flux density also seems to increase at the “flaring” state confirming the non-thermal character of the component which causing the flare.

7.4 FULL-STOKES RADIATIVE TRANSFER CODE

An essential part of our framework, presented in Chapter 5, is the computer code we developed based on the equations given in Hughes et al. (1989a) to yield the solution of the radiative transfer problem in the complete set of Stokes parameters accounting for all formal emission, absorption and propagation effects. This code can be used to investigate the physical conditions in astrophysical plasmas since the radiative transfer coefficients depend on those conditions.

7.4.1 Application to shocked jets

Multi-frequency, high cadence observations are essential in the study of the pronounced variability our sources usually show. This variability was found to follow repeating patterns in the F_ν – ν domain for many sources, a prototype of which is the blazar 3C 454.3. In many cases, these patterns agree with the predictions of the “shock-in-jet” model (Marscher and Gear, 1985) which attributes them to the evolution of physical conditions at shocked regions as they propagate downstream the jet.

Our results revealed the coordinated changes of the polarization parameters that mark the transition from the optically thick to thin regimes of synchrotron emission. Assuming that these transitions are due to the optical depth evolution of the propagated shocks, we used our radiative transfer code to emulate them and reproduce the variability observed in all Stokes parameters in the case of the prototype source 3C 454.3. We followed the strict requirement to accomplish that just by evolving the physical characteristics of the emitting region according to the predictions of the “shock-in-jet” model. The reason for this approach is that it allows us to understand directly the physical parameters that affect emitted radiation and its variability.

7.4.2 The study case of 3C 454.3

The approach described above resulted in a number of estimates for the physical conditions of in the jet of the blazar 3C 454.3.

Jet physical size

A close inspection of the MOJAVE VLBI maps revealed that most of the observed emission is coming from the inner part of the jet, its core, which spans over a region of about 19 pc. This size corresponds to ~ 850 pc after correcting for projection effects, using a viewing angle of 1.3° (Hovatta et al., 2009). However, this region is comparable to the map beam size and we consider the calculated value as an upper limit for the size of our modelled jet.

Particle number density

We estimated the particle number density using the magnetic field strength and the jet size upper limit. Our observations show that the magnetic field strength is ~ 3 mG. We ran our computer code several times using different values for the particle number density in the range of a few to a few hundred cm^{-3} in order to reproduce the observed flux of the jet at its “quiescent” state. Using the 14.5 GHz data as a pivot frequency, we reached the observed flux density levels ($\sim 4\text{--}5$ Jy) with number densities of $\sim 10\text{--}10^2 \text{ cm}^{-3}$.

Magnetic field coherence length

The plasma “cells” we use to construct the emitting region with our code are embedded in uniform magnetic fields. Thus their polarization characteristics match the theoretical ones (e.g. $\sim 70\%$ in the optically thin case). In order to compensate for the low levels of linear polarization we observe, we randomize their magnetic field orientations. Therefore, the number of cells in combination with the above size estimate can provide a coherence length for the jet magnetic field.

For the case of 3C 454.3, we need a total number of 540 cells, organized in ~ 100 slabs, to reproduce the observed levels of m_l . Using this result we calculate a cell linear size of ~ 9 pc which is also the coherence length of the magnetic field. This size comes in agreement with the linear scale we estimate using the variability we observe in the polarized flux density. Assuming that the polarized flux density is coming from the most compact emission components of the jet region, we can estimate their size by light-travel arguments. Quantifying the variability time scales as the half-period between two consecutive minimizations of the polarized flux density, we estimate it to be ~ 400 days (see also Fig. 5.4). After correcting for cosmological redshift and relativistic Doppler factor, this time scale becomes ~ 7100 days which corresponds to a linear scale of ~ 6 pc.

Reproducing variability with propagating shocks

Using the above estimates, we ran our code several times to reproduce the observed variability with propagating shocked regions downstream the jet. First, we explored the compression factor, k , parameter space and found out that the observed maximum polarization degree of $\sim 6\%$ during the polarized flare at MJD ~ 56800 , is reached with $k \sim 0.8$.

Although we managed to reproduce the variability pattern with a propagating shock of $k = 0.8$, its corresponding SED component was transversing within a small frequency range of a few tens of GHz. In order to transfer the variability pattern to the higher frequencies it is observed ($\sim 20\text{--}150$ GHz), without changing the parameters estimated above, we increased the Doppler factor of the propagating shock. An exploration of the parameter space showed that its Doppler factor should be ~ 30 to accomplish that. This number comes in agreement with the Doppler factor estimates for this source in the literature, (e.g. Sasada et al., 2014; Zhou et al., 2015; Hovatta et al., 2009), calculated by different methodologies.

7.5 OPTICAL POLARIZATION PROPERTIES OF AGNS

Finally, in Chapter 6, we studied the cross-band polarization properties of AGN jets comparing the datasets obtained with the *F-GAMMA* and RoboPol monitoring programs. This plurality of information allows us to compare also the physical characteristics of the radio and optical emitting parts of the jet.

7.5.1 Optical polarization

There are 49 sources in the RoboPol data, obtained between May 2013 and July 2015, which have been also observed at least once, at at least one of the four radio frequencies we examined.

44 out of those were found to be linearly polarized at least once in the optical wavelengths. The average value of the distribution of median optical m_l is 8.4%, hence more than double the one in radio ($\sim 3\%$). No significant difference were found between FSRQ and BL Lac objects in the optical polarization characteristics.

Polarized state duration

We found that the sources remain optically polarized most of the time (median: 91%), independently of whether they are in a “flaring” or “quiescent” state. These results are also in agreement with the same study in most of the radio bands, described in subsection 4.2.6.

7.5.2 Correlation analysis

We also performed a correlation analysis between the optical and radio polarization characteristics as well as other observational properties.

Optical linear versus radio linear and circular polarization

Interestingly, no correlation was found between the optical linear and radio linear and circular polarization degrees in any of the bands we tested (Figs. 6.3 and 6.4). This result can be attributed to the difference of the physical parameters between the two source regions. Assuming that the linear polarization degree measurements probe the magnetic field uniformity, there are sources with both higher and lower uniformity in the optical part of the jet as compared with the radio one. The former is expected since the optical emission of the jet is believed to originate closer to the “central engine” where the theory predicts better ordering of the magnetic field. Consequently, sources that show the opposite result are very interesting cases and need further investigation.

Optical linear polarization degree versus γ -ray energy flux

We found no correlation between these two quantities. This is opposite to the corresponding result for the radio data, where we found an anti-correlation between the linear polarization degree and the γ -ray energy flux. Both these findings can be used as constraints for the various theoretical interpretations for the origin of γ -rays of AGN jets.

Optical linear polarization degree and flux density state

In most of the cases, the optical linearly polarized flux density is increased when the sources are at a “flaring” state. This is an indication of the non-thermal character of the emission for the component responsible for the flux density increase and it is similar to the results at radio bands as shown in subsection 4.4.6. On the other hand, the optical linear polarization degree is not always higher during the “flaring” state. This is similar to the corresponding result at 10.45 GHz. However, our interpretation that in those cases the flux increase at 10.45 GHz was due to optically thick emission components is not applicable for the optical data. We expect that the optical emission remains mostly optically thin. An alternative interpretation would be that for sources with higher or lower m_l at the “flaring” state, the flux density increase is caused by an emission component with higher or lower magnetic field uniformity respectively. The former case is easily supported by existing theoretical interpretations for the emission components which cause the observed variability, like the “shock-in-jet” model. However, the latter case is difficult to be explained and further investigation is needed.

7.5.3 Optical and radio EVPA rotations

We looked for EVPA rotations in our radio data and compared them with the optical ones. We found that several physical characteristics of jets can be discerned from such comparisons.

Assuming that these rotations are caused by the helical motion of emission elements propagating downstream the jet, we used the rotation rates and the linear polarization degree measurements in both the radio and optical bands to compare the (tangential) velocities and furthermore the kinetic energies of those emission elements while they are propagating through the radio and optical emission sites in the jet.

Radio EVPA rotations

We applied the methodology developed by Kiehlmann et al., (*in prep*) and presented in Blinov et al. (2015), to search for EVPA rotations in the radio bands. There are 60 such rotations detected in 22 sources. Although the EVPA rotations in radio bands have similar ranges as the ones in the optical, their rates are much lower (median: $0.4^\circ/\text{day}$, Fig. 6.7). Six of these sources showed optical EVPA rotations independently of whether they were concurrent with the radio ones.

Optical and radio emission site size from EVPA rotation rates

As we discussed already, one of the interpretations for EVPA rotations is that they are caused by the helical motion of emission components as they propagate downstream the jet (Marscher et al., 2008). Under this assumption, the angular speed of those elements, ω , is equal to the observed EVPA rotation rate. Assuming the same tangential speed, v , for the helically moving components as they propagate through the radio and optical emitting parts of the jet, we estimate that the jet cross-section radius in the radio part is 20 times larger than the one in the optical part, using the conservation of angular momentum argument. We expect that this large size ratio should be manifested through much higher linear polarization degree ratios between the optical and radio bands than the ones observed. That is, under the assumption of a self-similar jet magnetic field structure for which the only difference between the optical and radio emitting parts is a 3-dimensional “compression”.

The kinetic energy ratio between the radio and optical parts of the jet

The only assumption used above is the stable tangential speed, and the kinetic energy, of the helically moving emission component. If we drop this and use the observed linear polarization degree ratio between the optical and radio observations, we estimate that the radio emission site size is 2.1 times larger than the optical one. We used this estimate in combination with the angular speed ratio to calculate that the tangential speed in the radio part of the jet is ~ 10 times lower than in the optical, which corresponds to the kinetic energy being ~ 100 times lower in the radio part.

7.6 FUTURE WORK

Our immediate next steps would be to:

1. Apply our radiative transfer code in order to reproduce the observed behaviour in all Stokes parameters and extract the physical conditions for more sources in our sample.
2. Expand our linear and circular radio polarimetric dataset in both frequency and time domains by applying the machinery of our framework to the entirety of the *F-GAMMA* dataset.
3. Combine our results with observations in other parts of the electromagnetic spectrum to acquire a broadband view of the emitted radiation which is essential to discern the underlying physical mechanisms. Such a panchromatic analysis will become particularly valuable in the light of the upcoming high energy (e.g. X-ray) polarization-sensitive satellites (e.g. ASTRO-H).

Finally, we believe that our framework can be applied to study the physical conditions of other astrophysical magnetized plasma systems like protostellar outflows, galactic halos, or the interstellar medium. It is within our scope to expand our understanding towards those directions as well.

Appendix A

Radio polarization data

Table A.1: Representative statistical moments for the total flux density and polarization characteristics of the observed sources in the radio bands. The quantities we examined are given in the third column (x) and they are: the linear polarization degree, m_l , and flux density Π_l , the absolute circular polarization degree, $|m_c|$, and flux density $|\Pi_c|$, the total flux density, S , and the electric vector position angle (EVPA), χ . N_{sign} is the number of data points which passed a number of quality criteria over the total number of data points. For each quantity we provide the weighted average, $\langle x \rangle$, and standard deviation, σ_x , over the time that the quantity has been observed. The modulation index, $\frac{\sigma_x}{\langle x \rangle}$, as a measure of the variability amplitude of the source in that quantity as well as the median, minimum and maximum values are reported. Note that in some cases the N_{sign} for the m_l and Π_l may differ. In those cases, Π_l has been measured while m_l has been corrupted because of corrupted total flux density measurement. EVPA measurements are reported for all successful Π_l measurements.

Source	Freq. (GHz)	x		N_{sign}	$\langle x \rangle$	σ_x	mi (%)	median	min	max
3C161	2.64	S	(Jy)	8/8	11.296	0.046	0.4	11.308	11.235	11.376
		Π_l	(Jy)	8/8	1.152	0.003	0.3	1.151	1.149	1.160
		m_l	(%)	8/8	10.2	0.0	0.3	10.2	10.2	10.2
		χ	($^\circ$)	8/8	-4.2	0.2	...	-4.3	-4.4	-3.9
	4.85	S	(Jy)	17/17	6.638	0.093	1.4	6.640	6.165	6.782
		Π_l	(Jy)	17/17	0.331	0.008	2.5	0.334	0.292	0.347
		$ \Pi_c $	(Jy)	6/17	0.030	0.009	28.0	0.033	0.017	0.041
		m_l	(%)	17/17	5.0	0.1	2.6	5.0	4.7	5.3
		$ m_c $	(%)	6/17	0.5	0.1	28.0	0.5	0.2	0.6
		χ	($^\circ$)	17/17	-56.6	1.3	...	-56.6	-60.9	-55.1
		S	(Jy)	14/14	3.800	0.051	1.3	3.781	3.632	3.973
	8.35	Π_l	(Jy)	14/14	0.117	0.011	9.1	0.117	0.107	0.158
		$ \Pi_c $	(Jy)	0/14	nan	nan	nan	nan	nan	nan
		m_l	(%)	14/14	3.1	0.3	9.5	3.1	2.9	4.1
		$ m_c $	(%)	0/14	nan	nan	nan	nan	nan	nan
		χ	($^\circ$)	14/14	-79.0	1.1	...	-78.5	-81.0	-77.0
	10.45	S	(Jy)	9/9	2.992	0.066	2.2	2.977	2.917	3.081
		Π_l	(Jy)	5/9	0.074	0.003	3.4	0.074	0.072	0.079

Table A.1: continued.

Source	Freq. (GHz)	x		N _{sign}	$\langle x \rangle$	σ_x	mi (%)	median	min	max	
3C286	2.64	m_l	(%)	5/9	2.5	0.1	5.2	2.5	2.4	2.7	
		χ	($^\circ$)	5/5	-86.3	1.0	...	-87.0	-87.2	-85.1	
		S	(Jy)	30/31	10.679	0.026	0.2	10.684	10.551	10.788	
		Π_l	(Jy)	30/31	1.076	0.002	0.2	1.076	1.071	1.091	
		m_l	(%)	30/31	10.1	0.0	0.3	10.1	10.1	10.3	
		χ	($^\circ$)	30/30	33.0	0.1	...	33.0	32.8	33.1	
	4.85	S	(Jy)	55/56	7.489	0.040	0.5	7.463	7.335	7.522	
		Π_l	(Jy)	55/56	0.837	0.004	0.5	0.836	0.827	0.852	
		$ \Pi_c $	(Jy)	2/56	0.042	0.004	9.5	0.042	0.039	0.045	
		m_l	(%)	55/56	11.2	0.1	0.7	11.2	11.1	11.4	
		$ m_c $	(%)	2/56	0.6	0.1	10.0	0.6	0.5	0.6	
		χ	($^\circ$)	55/55	32.8	0.5	...	32.9	31.6	33.7	
	8.35	S	(Jy)	53/53	5.211	0.038	0.7	5.210	5.009	5.279	
		Π_l	(Jy)	53/53	0.577	0.007	1.2	0.579	0.555	0.593	
		$ \Pi_c $	(Jy)	2/53	0.008	0.017	215.6	0.019	0.007	0.031	
		m_l	(%)	53/53	11.1	0.1	0.9	11.1	10.6	11.5	
		$ m_c $	(%)	2/53	0.2	0.3	214.9	0.4	0.1	0.6	
		χ	($^\circ$)	53/53	32.8	0.3	...	32.9	30.8	38.2	
3C295	10.45	S	(Jy)	36/36	4.446	0.020	0.5	4.444	4.273	4.491	
		Π_l	(Jy)	34/36	0.521	0.001	0.3	0.521	0.514	0.532	
		m_l	(%)	34/36	11.7	0.1	0.5	11.7	11.6	12.1	
		χ	($^\circ$)	34/34	33.0	0.1	...	33.0	32.3	33.5	
	2.64	S	(Jy)	12/14	12.404	0.068	0.5	12.399	12.226	12.493	
		Π_l	(Jy)	2/14	0.023	0.036	158.4	0.033	0.007	0.059	
		m_l	(%)	2/14	0.2	0.3	155.7	0.3	0.1	0.5	
		χ	($^\circ$)	2/2	22.6	28.6	...	41.6	21.4	61.9	
		4.85	S	(Jy)	26/26	6.559	0.047	0.7	6.559	6.462	6.608
			Π_l	(Jy)	0/26	nan	nan	nan	nan	nan	nan
	$ \Pi_c $		(Jy)	19/26	0.035	0.006	16.4	0.034	0.022	0.049	
	m_l		(%)	0/26	nan	nan	nan	nan	nan	nan	
	8.35	$ m_c $	(%)	19/26	0.5	0.1	16.3	0.5	0.3	0.7	
		S	(Jy)	22/23	3.431	0.041	1.2	3.442	3.346	3.511	
		Π_l	(Jy)	22/23	0.031	0.002	7.0	0.031	0.027	0.034	
		$ \Pi_c $	(Jy)	0/23	nan	nan	nan	nan	nan	nan	
		m_l	(%)	22/23	0.9	0.1	7.0	0.9	0.8	1.0	
		$ m_c $	(%)	0/23	nan	nan	nan	nan	nan	nan	
3C48	10.45	χ	($^\circ$)	22/22	31.3	2.6	...	31.6	26.1	40.4	
		S	(Jy)	13/15	2.591	0.136	5.2	2.656	2.421	2.760	
		Π_l	(Jy)	3/15	0.061	0.012	19.4	0.056	0.052	0.074	
		m_l	(%)	3/15	2.3	0.4	19.0	2.0	2.0	2.8	
	2.64	χ	($^\circ$)	3/3	-27.5	2.9	...	-29.5	-30.1	-25.4	
		S	(Jy)	28/29	9.525	0.028	0.3	9.511	9.472	9.591	
		Π_l	(Jy)	27/29	0.151	0.003	2.0	0.152	0.143	0.155	
		m_l	(%)	27/29	1.6	0.0	2.1	1.6	1.5	1.6	

Table A.1: continued.

Source	Freq. (GHz)	x		N _{sign}	$\langle x \rangle$	σ_x	mi (%)	median	min	max
J0050-0929	4.85	χ	($^\circ$)	27/27	70.0	0.4	...	70.0	68.8	71.3
		S	(Jy)	53/53	5.518	0.015	0.3	5.515	5.479	5.597
		Π_l	(Jy)	53/53	0.234	0.004	1.5	0.231	0.223	0.238
		$ \Pi_c $	(Jy)	20/53	0.026	0.005	20.1	0.027	0.019	0.037
		m_l	(%)	53/53	4.2	0.1	1.5	4.2	4.0	4.3
		$ m_c $	(%)	20/53	0.5	0.1	20.2	0.5	0.3	0.7
	8.35	χ	($^\circ$)	53/53	-72.8	0.5	...	-73.1	-74.8	-71.9
		S	(Jy)	54/54	3.253	0.017	0.5	3.256	3.145	3.400
		Π_l	(Jy)	54/54	0.179	0.004	2.3	0.180	0.172	0.201
		$ \Pi_c $	(Jy)	2/54	0.006	0.000	3.6	0.006	0.006	0.006
		m_l	(%)	54/54	5.5	0.1	2.2	5.5	5.3	6.1
		$ m_c $	(%)	2/54	0.2	0.0	3.7	0.2	0.2	0.2
	10.45	χ	($^\circ$)	54/54	-65.5	0.6	...	-65.2	-68.4	-64.2
		S	(Jy)	34/34	2.602	0.014	0.6	2.602	2.348	2.652
		Π_l	(Jy)	20/34	0.153	0.003	1.7	0.153	0.144	0.165
		m_l	(%)	20/34	5.9	0.0	0.7	5.9	5.8	6.2
		χ	($^\circ$)	20/20	-63.8	0.4	...	-63.8	-64.6	-63.0
		S	(Jy)	24/25	0.651	0.123	19.0	0.691	0.372	0.861
	2.64	Π_l	(Jy)	14/25	0.015	0.005	31.0	0.014	0.010	0.026
		m_l	(%)	14/25	2.1	0.7	33.4	1.9	1.4	3.4
		χ	($^\circ$)	14/14	105.9	25.7	...	109.2	54.4	153.5
		S	(Jy)	38/39	0.628	0.212	33.8	0.665	0.241	0.999
		Π_l	(Jy)	4/39	0.019	0.006	29.7	0.019	0.012	0.027
		$ \Pi_c $	(Jy)	1/39	0.013	0.000	nan	0.013	0.013	0.013
	4.85	m_l	(%)	4/39	2.4	0.4	15.9	2.6	2.2	3.0
		$ m_c $	(%)	1/39	2.0	0.0	nan	2.0	2.0	2.0
		χ	($^\circ$)	4/4	-66.2	24.6	...	-70.4	-101.6	-29.5
		S	(Jy)	37/38	0.595	0.253	42.6	0.680	0.214	1.068
		Π_l	(Jy)	14/38	0.017	0.004	25.9	0.016	0.012	0.044
		$ \Pi_c $	(Jy)	0/38	nan	nan	nan	nan	nan	nan
	8.35	m_l	(%)	14/38	2.1	0.5	22.9	2.1	1.4	4.2
		$ m_c $	(%)	0/38	nan	nan	nan	nan	nan	nan
		χ	($^\circ$)	14/14	-2.3	48.8	...	-55.2	-134.3	62.3
		S	(Jy)	24/27	0.786	0.156	19.9	0.776	0.499	1.130
		Π_l	(Jy)	5/27	0.019	0.004	18.4	0.019	0.016	0.024
		m_l	(%)	5/27	2.3	0.3	13.4	2.3	1.8	2.6
J0102+5824	2.64	χ	($^\circ$)	5/5	110.9	35.6	...	117.4	58.6	145.5
		S	(Jy)	20/20	1.844	0.622	33.7	2.025	1.074	3.539
		Π_l	(Jy)	17/20	0.024	0.010	43.2	0.021	0.012	0.065
		m_l	(%)	17/20	1.1	0.5	43.3	1.2	0.6	2.9
		χ	($^\circ$)	17/17	33.1	20.5	...	30.6	-2.1	67.7
		S	(Jy)	25/26	2.006	0.599	29.9	2.342	1.214	4.253
	4.85	Π_l	(Jy)	17/26	0.036	0.020	53.8	0.040	0.013	0.067
		$ \Pi_c $	(Jy)	2/26	0.006	0.000	2.9	0.006	0.006	0.006

Table A.1: continued.

Source	Freq. (GHz)	x	N_{sign}	$\langle x \rangle$	σ_x	mi (%)	median	min	max
J0136+4751	8.35	m_l (%)	17/26	1.5	0.3	18.2	1.6	0.6	2.3
		$ m_c $ (%)	2/26	0.2	0.1	24.1	0.2	0.2	0.3
		χ ($^\circ$)	17/17	45.8	22.2	...	53.7	-36.8	131.1
		S (Jy)	27/28	2.300	0.661	28.7	2.816	1.673	4.438
		Π_l (Jy)	24/28	0.052	0.035	67.5	0.054	0.019	0.119
		$ \Pi_c $ (Jy)	3/28	0.010	0.005	50.4	0.013	0.007	0.015
		m_l (%)	24/28	2.2	0.9	39.6	2.1	0.8	3.5
		$ m_c $ (%)	3/28	0.4	0.0	12.4	0.4	0.3	0.4
	10.45	χ ($^\circ$)	24/24	79.6	22.1	...	70.6	22.3	153.7
		S (Jy)	16/19	2.707	0.771	28.5	2.858	2.104	5.110
		Π_l (Jy)	6/19	0.073	0.031	42.5	0.065	0.038	0.121
		m_l (%)	6/19	2.3	0.5	21.9	2.2	1.4	2.8
	2.64	χ ($^\circ$)	6/6	85.7	29.5	...	84.8	15.8	116.7
		S (Jy)	8/9	1.587	0.238	15.0	1.633	1.254	2.066
		Π_l (Jy)	4/9	0.032	0.012	36.9	0.030	0.019	0.045
		m_l (%)	4/9	2.1	0.8	37.4	1.9	1.3	3.0
		χ ($^\circ$)	4/4	8.9	20.2	...	0.1	-6.6	43.1
		S (Jy)	12/12	2.202	0.704	32.0	1.956	1.597	3.702
		Π_l (Jy)	7/12	0.041	0.028	66.7	0.048	0.016	0.104
		$ \Pi_c $ (Jy)	1/12	0.009	0.000	nan	0.009	0.009	0.009
	4.85	m_l (%)	7/12	1.6	0.8	47.0	1.7	0.8	3.0
		$ m_c $ (%)	1/12	0.4	0.0	nan	0.4	0.4	0.4
		χ ($^\circ$)	7/7	22.4	16.4	...	23.9	5.4	65.4
		S (Jy)	12/12	2.163	0.467	21.6	2.158	1.698	4.639
		Π_l (Jy)	10/12	0.024	0.021	84.5	0.044	0.011	0.156
		$ \Pi_c $ (Jy)	0/12	nan	nan	nan	nan	nan	nan
		m_l (%)	10/12	1.2	0.7	62.6	1.8	0.6	3.8
		$ m_c $ (%)	0/12	nan	nan	nan	nan	nan	nan
	8.35	χ ($^\circ$)	10/10	-130.9	41.7	...	-106.3	-151.8	-55.6
		S (Jy)	10/11	2.588	0.574	22.2	2.375	1.696	5.167
		Π_l (Jy)	5/11	0.079	0.062	78.1	0.059	0.033	0.200
		m_l (%)	5/11	3.0	1.2	39.4	2.3	1.6	4.0
		χ ($^\circ$)	5/5	-142.9	26.7	...	-144.3	-151.0	-72.1
		S (Jy)	23/23	1.175	0.304	25.8	1.329	0.691	1.545
		Π_l (Jy)	14/23	0.011	0.004	37.0	0.010	0.007	0.022
		m_l (%)	14/23	0.8	0.3	39.4	0.8	0.5	1.7
J0217+0144	2.64	χ ($^\circ$)	14/14	30.3	47.5	...	27.8	-47.5	127.7
		S (Jy)	43/43	1.118	0.439	39.3	1.369	0.614	1.897
		Π_l (Jy)	24/43	0.021	0.011	51.6	0.028	0.014	0.054
		$ \Pi_c $ (Jy)	2/43	0.007	0.002	27.1	0.007	0.005	0.008
	4.85	m_l (%)	24/43	1.6	0.6	36.2	1.7	1.1	3.0
		$ m_c $ (%)	2/43	0.5	0.1	23.2	0.4	0.3	0.5
		χ ($^\circ$)	24/24	-78.4	57.8	...	-122.0	-164.7	-4.2
		S (Jy)	39/41	1.323	0.421	31.8	1.466	0.644	2.016

Table A.1: continued.

Source	Freq. (GHz)	x	N_{sign}	$\langle x \rangle$	σ_x	mi (%)	median	min	max
J0221+3556	10.45	Π_l (Jy)	27/41	0.033	0.018	54.8	0.038	0.014	0.117
		$ \Pi_c $ (Jy)	5/41	0.007	0.002	26.0	0.007	0.005	0.010
		m_l (%)	27/41	2.3	0.9	41.7	2.4	0.8	6.3
		$ m_c $ (%)	5/41	0.4	0.1	25.9	0.4	0.3	0.6
		χ ($^\circ$)	27/27	8.9	58.7	...	46.3	-64.0	105.5
		S (Jy)	28/30	1.318	0.494	37.5	1.573	0.589	1.982
		Π_l (Jy)	1/30	0.038	0.000	nan	0.038	0.038	0.038
		m_l (%)	1/30	2.9	0.0	nan	2.9	2.9	2.9
		χ ($^\circ$)	1/1	42.4	0.0	...	42.4	42.4	42.4
		S (Jy)	12/12	1.708	0.133	7.8	1.788	1.517	1.878
	2.64	Π_l (Jy)	11/12	0.012	0.003	23.1	0.012	0.008	0.017
		m_l (%)	11/12	0.7	0.2	24.1	0.7	0.4	1.0
		χ ($^\circ$)	11/11	-18.8	9.0	...	-15.4	-32.2	-5.5
		S (Jy)	19/19	1.547	0.125	8.1	1.479	1.215	1.638
		Π_l (Jy)	18/19	0.054	0.005	9.0	0.055	0.043	0.068
		$ \Pi_c $ (Jy)	0/19	nan	nan	nan	nan	nan	nan
		m_l (%)	18/19	3.8	0.2	5.3	3.8	2.9	4.2
		$ m_c $ (%)	0/19	nan	nan	nan	nan	nan	nan
		χ ($^\circ$)	18/18	6.0	4.1	...	6.3	-13.9	8.1
		S (Jy)	20/20	1.293	0.063	4.9	1.305	1.022	1.519
	4.85	Π_l (Jy)	20/20	0.061	0.008	13.2	0.060	0.046	0.081
		$ \Pi_c $ (Jy)	4/20	0.003	0.001	28.9	0.004	0.003	0.006
		m_l (%)	20/20	4.7	0.4	8.1	4.8	4.3	5.7
		$ m_c $ (%)	4/20	0.3	0.1	23.4	0.3	0.2	0.4
		χ ($^\circ$)	20/20	42.0	4.6	...	42.8	33.5	48.0
		S (Jy)	10/15	1.228	0.109	8.9	1.314	1.008	1.427
		Π_l (Jy)	3/15	0.077	0.024	31.0	0.096	0.068	0.197
		m_l (%)	3/15	7.4	1.5	19.8	8.3	6.7	14.8
		χ ($^\circ$)	3/3	39.4	6.3	...	41.8	35.0	57.1
		S (Jy)	19/19	1.654	0.055	3.3	1.645	1.587	1.758
J0222+4302	2.64	Π_l (Jy)	18/19	0.027	0.004	13.6	0.027	0.020	0.035
		m_l (%)	18/19	1.7	0.2	14.9	1.7	1.2	2.1
		χ ($^\circ$)	18/18	52.0	4.6	...	53.0	41.9	58.2
		S (Jy)	35/35	1.267	0.080	6.3	1.216	1.100	1.363
		Π_l (Jy)	15/35	0.014	0.005	36.5	0.020	0.010	0.022
		$ \Pi_c $ (Jy)	0/35	nan	nan	nan	nan	nan	nan
		m_l (%)	15/35	1.1	0.5	48.5	1.7	0.7	2.0
		$ m_c $ (%)	0/35	nan	nan	nan	nan	nan	nan
		χ ($^\circ$)	15/15	-68.3	15.0	...	-74.3	-85.0	-50.1
		S (Jy)	34/34	0.969	0.083	8.5	0.965	0.870	1.216
	4.85	Π_l (Jy)	8/34	0.010	0.002	15.3	0.010	0.009	0.013
		$ \Pi_c $ (Jy)	0/34	nan	nan	nan	nan	nan	nan
		m_l (%)	8/34	1.0	0.2	24.3	1.1	0.7	1.4
		$ m_c $ (%)	0/34	nan	nan	nan	nan	nan	nan
	8.35	Π_l (Jy)	27/41	0.033	0.018	54.8	0.038	0.014	0.117
		$ \Pi_c $ (Jy)	5/41	0.007	0.002	26.0	0.007	0.005	0.010
		m_l (%)	27/41	2.3	0.9	41.7	2.4	0.8	6.3
		$ m_c $ (%)	5/41	0.4	0.1	25.9	0.4	0.3	0.6
		χ ($^\circ$)	27/27	8.9	58.7	...	46.3	-64.0	105.5
		S (Jy)	28/30	1.318	0.494	37.5	1.573	0.589	1.982
		Π_l (Jy)	1/30	0.038	0.000	nan	0.038	0.038	0.038
		m_l (%)	1/30	2.9	0.0	nan	2.9	2.9	2.9
		χ ($^\circ$)	1/1	42.4	0.0	...	42.4	42.4	42.4
		S (Jy)	12/12	1.708	0.133	7.8	1.788	1.517	1.878

Table A.1: continued.

Source	Freq. (GHz)	x		N _{sign}	$\langle x \rangle$	σ_x	mi (%)	median	min	max
J0237+2848	10.45	χ	($^\circ$)	8/8	-41.2	25.8	...	-45.7	-67.5	9.1
		S	(Jy)	20/23	0.882	0.077	8.8	0.899	0.779	1.073
		Π_l	(Jy)	1/23	0.017	0.000	nan	0.017	0.017	0.017
		m_l	(%)	1/23	2.1	0.0	nan	2.1	2.1	2.1
	2.64	χ	($^\circ$)	1/1	-70.7	0.0	...	-70.7	-70.7	-70.7
		S	(Jy)	22/23	3.037	0.334	11.0	3.071	2.401	3.595
		Π_l	(Jy)	21/23	0.079	0.016	20.4	0.080	0.046	0.103
		m_l	(%)	21/23	2.6	0.7	27.3	2.7	1.4	3.7
	4.85	χ	($^\circ$)	21/21	52.8	11.4	...	55.2	17.9	67.7
		S	(Jy)	40/41	2.824	0.472	16.7	3.040	2.360	4.072
		Π_l	(Jy)	36/41	0.076	0.031	41.2	0.071	0.030	0.132
		$ \Pi_c $	(Jy)	5/41	0.009	0.006	65.6	0.013	0.006	0.024
		m_l	(%)	36/41	2.3	1.0	45.4	2.5	0.8	4.5
		$ m_c $	(%)	5/41	0.3	0.2	65.6	0.4	0.2	0.6
		χ	($^\circ$)	36/36	64.7	21.9	...	70.6	27.2	106.8
		S	(Jy)	40/40	3.449	0.464	13.5	3.323	2.286	4.068
	8.35	Π_l	(Jy)	38/40	0.054	0.031	58.1	0.068	0.023	0.120
		$ \Pi_c $	(Jy)	13/40	0.014	0.003	24.4	0.015	0.008	0.025
		m_l	(%)	38/40	1.5	1.0	64.8	2.1	0.7	4.1
		$ m_c $	(%)	13/40	0.4	0.1	23.5	0.4	0.2	0.7
		χ	($^\circ$)	38/38	1.6	122.0	...	26.2	-155.2	151.6
		S	(Jy)	25/26	3.555	0.470	13.2	3.648	2.546	4.278
		Π_l	(Jy)	7/26	0.078	0.033	42.3	0.080	0.034	0.131
		m_l	(%)	7/26	2.1	0.9	42.1	2.7	0.9	3.1
J0238+1636	2.64	χ	($^\circ$)	7/7	-123.1	46.9	...	-135.4	-155.2	-55.1
		S	(Jy)	23/25	0.908	0.081	8.9	0.945	0.745	1.028
		Π_l	(Jy)	7/25	0.009	0.002	23.6	0.010	0.006	0.012
		m_l	(%)	7/25	1.0	0.3	26.9	1.0	0.7	1.3
	4.85	χ	($^\circ$)	7/7	16.0	12.1	...	15.1	-0.9	35.7
		S	(Jy)	40/41	0.988	0.121	12.2	1.045	0.726	1.260
		Π_l	(Jy)	12/41	0.014	0.007	48.9	0.016	0.009	0.039
		$ \Pi_c $	(Jy)	0/41	nan	nan	nan	nan	nan	nan
		m_l	(%)	12/41	1.3	0.5	41.3	1.4	0.9	3.2
		$ m_c $	(%)	0/41	nan	nan	nan	nan	nan	nan
		χ	($^\circ$)	12/13	3.0	53.6	...	-33.6	-62.2	44.4
		S	(Jy)	38/40	1.065	0.192	18.0	1.102	0.703	1.327
	8.35	Π_l	(Jy)	26/40	0.018	0.007	38.3	0.019	0.010	0.099
		$ \Pi_c $	(Jy)	1/40	0.004	0.000	nan	0.004	0.004	0.004
		m_l	(%)	25/40	1.6	0.5	34.0	1.7	0.9	3.0
		$ m_c $	(%)	1/40	0.3	0.0	nan	0.3	0.3	0.3
		χ	($^\circ$)	26/26	-57.1	27.5	...	-52.6	-116.4	-14.0
		S	(Jy)	23/27	1.177	0.134	11.4	1.158	0.681	1.406
		Π_l	(Jy)	5/27	0.027	0.010	38.1	0.026	0.019	0.044
		m_l	(%)	5/27	2.1	0.8	36.3	2.2	1.5	3.3

Table A.1: continued.

Source	Freq. (GHz)	x		N _{sign}	$\langle x \rangle$	σ_x	mi (%)	median	min	max
J0241-0815	2.64	χ	($^\circ$)	5/5	-97.9	19.6	...	-102.9	-106.0	-48.2
		S	(Jy)	22/24	0.791	0.063	7.9	0.791	0.724	0.966
		Π_l	(Jy)	1/24	0.008	0.000	nan	0.008	0.008	0.008
		m_l	(%)	1/24	1.1	0.0	nan	1.1	1.1	1.1
	4.85	χ	($^\circ$)	1/1	50.2	0.0	...	50.2	50.2	50.2
		S	(Jy)	37/38	1.268	0.174	13.7	1.254	1.039	1.425
		Π_l	(Jy)	1/38	0.054	0.000	nan	0.054	0.054	0.054
		$ \Pi_c $	(Jy)	3/38	0.011	0.005	48.8	0.011	0.008	0.025
		m_l	(%)	1/38	3.9	0.0	nan	3.9	3.9	3.9
		$ m_c $	(%)	3/38	0.8	0.6	68.9	0.8	0.7	2.4
		χ	($^\circ$)	1/3	58.4	0.0	...	58.4	58.4	58.4
	8.35	S	(Jy)	36/37	1.527	0.133	8.7	1.476	1.116	1.692
		Π_l	(Jy)	0/37	nan	nan	nan	nan	nan	nan
		$ \Pi_c $	(Jy)	1/37	0.005	0.000	nan	0.005	0.005	0.005
		m_l	(%)	0/37	nan	nan	nan	nan	nan	nan
		$ m_c $	(%)	1/37	0.3	0.0	nan	0.3	0.3	0.3
	10.45	S	(Jy)	29/31	1.532	0.127	8.3	1.523	1.153	1.735
		Π_l	(Jy)	2/31	0.026	0.009	33.9	0.026	0.019	0.032
		m_l	(%)	2/31	1.7	0.6	35.7	1.6	1.2	2.1
		χ	($^\circ$)	2/2	55.6	62.5	...	31.9	-12.3	76.1
J0319+4130	2.64	S	(Jy)	25/26	15.044	0.262	1.7	15.098	14.298	15.864
		Π_l	(Jy)	10/26	0.037	0.039	105.0	0.020	0.011	0.170
		m_l	(%)	10/26	0.2	0.3	106.0	0.1	0.1	1.1
		χ	($^\circ$)	10/10	26.1	36.3	...	9.3	-38.0	103.2
	4.85	S	(Jy)	51/51	15.404	1.719	11.2	16.666	13.930	22.927
		Π_l	(Jy)	6/51	0.038	0.058	153.0	0.022	0.011	0.174
		$ \Pi_c $	(Jy)	10/51	0.115	0.081	71.0	0.170	0.037	0.216
		m_l	(%)	6/51	0.2	0.3	133.4	0.1	0.1	1.0
		$ m_c $	(%)	10/51	0.6	0.3	49.7	0.8	0.2	1.0
		χ	($^\circ$)	6/6	-197.4	76.4	...	-188.7	-277.2	-84.6
	8.35	S	(Jy)	48/49	27.240	2.434	8.9	27.444	20.468	36.036
		Π_l	(Jy)	11/49	0.037	0.022	58.9	0.031	0.018	0.071
		$ \Pi_c $	(Jy)	3/49	0.054	0.007	12.9	0.057	0.049	0.063
		m_l	(%)	12/49	0.1	0.1	60.1	0.1	0.0	0.3
		$ m_c $	(%)	3/49	0.2	0.0	20.3	0.2	0.2	0.3
	10.45	χ	($^\circ$)	11/11	97.4	32.4	...	84.0	68.4	156.7
		S	(Jy)	27/29	28.340	3.499	12.3	29.677	21.774	34.533
		Π_l	(Jy)	13/29	0.110	0.134	121.8	0.169	0.044	0.940
		m_l	(%)	13/29	0.3	0.4	117.6	0.6	0.1	2.9
J0324+3410	2.64	χ	($^\circ$)	13/13	-52.4	63.0	...	3.3	-122.2	69.8
		S	(Jy)	26/27	0.421	0.055	13.0	0.455	0.360	0.556
		Π_l	(Jy)	22/27	0.021	0.003	12.8	0.021	0.017	0.032
		m_l	(%)	22/27	4.7	0.9	18.1	4.8	3.7	9.0
		χ	($^\circ$)	22/22	63.3	4.7	...	65.2	48.6	74.2

Table A.1: continued.

Source	Freq. (GHz)	x	N_{sign}	$\langle x \rangle$	σ_x	mi (%)	median	min	max
J0339-0146	4.85	S (Jy)	45/47	0.408	0.050	12.2	0.393	0.290	0.549
		Π_l (Jy)	39/47	0.025	0.003	11.5	0.025	0.021	0.033
		$ \Pi_c $ (Jy)	1/47	0.002	0.000	nan	0.002	0.002	0.002
		m_l (%)	39/47	6.6	0.8	11.9	6.3	5.3	8.3
		$ m_c $ (%)	1/47	0.6	0.0	nan	0.6	0.6	0.6
		χ ($^\circ$)	39/39	47.1	5.8	...	44.5	29.5	56.9
	8.35	S (Jy)	44/45	0.377	0.092	24.3	0.359	0.273	0.561
		Π_l (Jy)	44/45	0.019	0.002	12.5	0.021	0.017	0.024
		$ \Pi_c $ (Jy)	0/45	nan	nan	nan	nan	nan	nan
		m_l (%)	44/45	5.0	1.1	22.2	5.6	3.9	7.6
		$ m_c $ (%)	0/45	nan	nan	nan	nan	nan	nan
		χ ($^\circ$)	44/44	42.3	7.9	...	35.5	25.9	49.2
	10.45	S (Jy)	29/35	0.333	0.055	16.4	0.336	0.265	0.548
		Π_l (Jy)	10/35	0.019	0.001	6.4	0.019	0.016	0.020
		m_l (%)	10/35	4.6	1.2	26.4	5.1	3.0	6.2
		χ ($^\circ$)	10/10	32.8	3.3	...	33.3	25.1	37.8
	2.64	S (Jy)	2/2	2.411	0.276	11.5	2.431	2.236	2.627
		Π_l (Jy)	2/2	0.094	0.003	3.4	0.094	0.092	0.096
		m_l (%)	2/2	3.9	0.3	8.0	3.9	3.7	4.1
		χ ($^\circ$)	2/2	-19.7	1.3	...	-19.9	-20.8	-18.9
	4.85	S (Jy)	2/2	2.708	0.214	7.9	2.579	2.428	2.731
		Π_l (Jy)	2/2	0.077	0.018	24.0	0.076	0.063	0.089
		$ \Pi_c $ (Jy)	0/2	nan	nan	nan	nan	nan	nan
		m_l (%)	2/2	3.0	0.5	15.8	2.9	2.6	3.3
		$ m_c $ (%)	0/2	nan	nan	nan	nan	nan	nan
		χ ($^\circ$)	2/2	-34.7	4.3	...	-32.5	-35.5	-29.4
	8.35	S (Jy)	2/2	2.834	0.204	7.2	2.697	2.552	2.841
		Π_l (Jy)	2/2	0.064	0.001	2.2	0.064	0.063	0.065
		$ \Pi_c $ (Jy)	1/2	0.015	0.000	nan	0.015	0.015	0.015
		m_l (%)	2/2	2.3	0.1	5.4	2.4	2.3	2.5
		$ m_c $ (%)	1/2	0.5	0.0	nan	0.5	0.5	0.5
		χ ($^\circ$)	2/2	-36.6	6.2	...	-35.0	-39.3	-30.6
J0349-2102	10.45	S (Jy)	2/2	2.864	0.307	10.7	2.654	2.437	2.871
		Π_l (Jy)	0/2	nan	nan	nan	nan	nan	nan
		m_l (%)	0/2	nan	nan	nan	nan	nan	nan
	4.85	S (Jy)	1/1	0.517	0.000	nan	0.517	0.517	0.517
		Π_l (Jy)	0/1	nan	nan	nan	nan	nan	nan
		$ \Pi_c $ (Jy)	0/1	nan	nan	nan	nan	nan	nan
		m_l (%)	0/1	nan	nan	nan	nan	nan	nan
		$ m_c $ (%)	0/1	nan	nan	nan	nan	nan	nan
		χ ($^\circ$)	0/1	nan	nan	nan	nan	nan	nan
	8.35	S (Jy)	1/1	0.484	0.000	nan	0.484	0.484	0.484
		Π_l (Jy)	0/1	nan	nan	nan	nan	nan	nan
		$ \Pi_c $ (Jy)	0/1	nan	nan	nan	nan	nan	nan
		m_l (%)	0/1	nan	nan	nan	nan	nan	nan

Table A.1: continued.

Source	Freq. (GHz)	x	N_{sign}	$\langle x \rangle$	σ_x	mi (%)	median	min	max
J0359+5057	2.64	$ m_c $	(%)	0/1	nan	nan	nan	nan	nan
		S	(Jy)	17/17	5.024	0.161	3.2	4.983	5.366
		Π_l	(Jy)	16/17	0.119	0.008	7.1	0.116	0.167
		m_l	(%)	16/17	2.3	0.2	8.5	2.3	3.3
	4.85	χ	($^\circ$)	16/16	-70.2	1.2	...	-70.0	-66.1
		S	(Jy)	33/33	7.725	0.694	9.0	7.458	8.799
		Π_l	(Jy)	33/33	0.127	0.011	8.9	0.125	0.188
		$ \Pi_c $	(Jy)	1/33	0.035	0.000	nan	0.035	0.035
	8.35	m_l	(%)	33/33	1.7	0.1	5.3	1.6	2.4
		$ m_c $	(%)	1/33	0.5	0.0	nan	0.5	0.5
		χ	($^\circ$)	33/33	-70.1	6.3	...	-73.8	-57.4
		S	(Jy)	33/33	9.353	0.874	9.3	9.097	11.174
	10.45	Π_l	(Jy)	33/33	0.110	0.030	27.2	0.130	0.187
		$ \Pi_c $	(Jy)	0/33	nan	nan	nan	nan	nan
		m_l	(%)	33/33	1.2	0.3	23.6	1.4	1.8
		$ m_c $	(%)	0/33	nan	nan	nan	nan	nan
	10.45	χ	($^\circ$)	33/33	-86.4	10.7	...	-77.2	-50.0
		S	(Jy)	22/22	9.469	0.441	4.7	9.343	10.351
		Π_l	(Jy)	10/22	0.127	0.066	51.7	0.116	0.242
		m_l	(%)	10/22	1.3	0.7	54.4	1.2	2.6
	10.45	χ	($^\circ$)	10/10	110.0	15.7	...	104.1	130.7
J0418+3801	2.64	S	(Jy)	21/22	9.175	0.235	2.6	9.198	9.790
		Π_l	(Jy)	21/22	0.153	0.020	12.8	0.150	0.191
		m_l	(%)	21/22	1.6	0.2	13.6	1.6	2.2
		χ	($^\circ$)	21/21	-52.1	5.2	...	-52.0	30.0
	4.85	S	(Jy)	38/38	5.090	0.093	1.8	5.062	5.472
		Π_l	(Jy)	26/38	0.105	0.016	15.5	0.103	0.123
		$ \Pi_c $	(Jy)	28/38	0.025	0.006	23.4	0.024	0.033
		m_l	(%)	26/38	2.1	0.3	15.9	2.1	2.5
	8.35	$ m_c $	(%)	28/38	0.5	0.1	23.4	0.5	0.7
		χ	($^\circ$)	26/26	-39.2	4.4	...	-34.7	-27.5
		S	(Jy)	36/36	3.039	0.255	8.4	3.130	3.829
		Π_l	(Jy)	32/36	0.056	0.022	39.3	0.053	0.124
	10.45	$ \Pi_c $	(Jy)	4/36	0.009	0.002	25.8	0.009	0.017
		m_l	(%)	32/36	1.7	0.8	46.9	1.7	4.0
		$ m_c $	(%)	4/36	0.3	0.1	25.0	0.3	0.4
		χ	($^\circ$)	32/32	-7.4	6.5	...	-13.6	-1.1
	10.45	S	(Jy)	17/18	2.746	0.159	5.8	2.753	3.099
		Π_l	(Jy)	5/18	0.045	0.006	14.6	0.046	0.055
		m_l	(%)	5/18	1.5	0.2	12.6	1.6	1.9
		χ	($^\circ$)	5/5	-20.4	6.4	...	-21.4	-9.7
J0423-0120	2.64	S	(Jy)	22/23	3.188	0.219	6.9	3.205	3.833
		Π_l	(Jy)	21/23	0.041	0.011	26.7	0.044	0.058
		m_l	(%)	21/23	1.3	0.3	25.9	1.4	1.9

Table A.1: continued.

Source	Freq. (GHz)	x	N_{sign}	$\langle x \rangle$	σ_x	mi (%)	median	min	max
J0433+0521	4.85	χ ($^\circ$)	21/21	70.1	14.9	...	67.5	43.3	101.5
		S (Jy)	44/44	3.960	0.390	9.8	4.200	2.725	5.019
		Π_l (Jy)	36/44	0.044	0.015	34.6	0.042	0.018	0.102
		$ \Pi_c $ (Jy)	4/44	0.005	0.004	75.8	0.010	0.005	0.014
		m_l (%)	36/44	1.1	0.4	40.6	1.1	0.4	2.2
		$ m_c $ (%)	4/44	0.1	0.1	97.3	0.2	0.1	0.4
	8.35	χ ($^\circ$)	36/36	-45.0	27.0	...	-77.3	-126.4	-18.1
		S (Jy)	42/42	4.776	0.884	18.5	4.902	2.503	6.217
		Π_l (Jy)	38/42	0.055	0.038	69.2	0.058	0.011	0.163
		$ \Pi_c $ (Jy)	2/42	0.016	0.000	0.6	0.016	0.016	0.016
		m_l (%)	38/42	1.1	0.8	72.1	1.3	0.2	3.2
		$ m_c $ (%)	2/42	0.3	0.0	16.4	0.3	0.3	0.4
	10.45	χ ($^\circ$)	38/38	85.6	104.0	...	94.0	-52.0	209.8
		S (Jy)	21/26	5.309	0.452	8.5	5.193	3.993	5.972
		Π_l (Jy)	11/26	0.112	0.049	43.4	0.132	0.044	0.255
		m_l (%)	11/26	2.1	0.9	43.6	2.4	0.8	4.7
		χ ($^\circ$)	11/11	74.5	35.7	...	83.2	-5.3	128.6
		S (Jy)	2/4	3.617	0.100	2.8	3.596	3.526	3.667
	2.64	Π_l (Jy)	3/4	0.188	0.002	1.1	0.188	0.185	0.189
		m_l (%)	2/4	5.2	0.1	1.2	5.2	5.2	5.2
		χ ($^\circ$)	3/3	-19.7	2.6	...	-20.5	-21.9	-16.8
		S (Jy)	2/3	2.780	0.025	0.9	2.789	2.771	2.807
		Π_l (Jy)	3/3	0.158	0.014	8.9	0.161	0.150	0.175
		$ \Pi_c $ (Jy)	0/3	nan	nan	nan	nan	nan	nan
	4.85	m_l (%)	2/3	6.1	0.3	4.8	6.0	5.8	6.2
		$ m_c $ (%)	0/3	nan	nan	nan	nan	nan	nan
		χ ($^\circ$)	3/3	-9.7	0.8	...	-9.5	-9.9	-7.8
		S (Jy)	3/3	1.988	0.184	9.3	2.160	1.933	2.254
		Π_l (Jy)	2/3	0.175	0.002	1.3	0.176	0.174	0.177
		$ \Pi_c $ (Jy)	0/3	nan	nan	nan	nan	nan	nan
	8.35	m_l (%)	3/3	7.6	0.4	5.7	7.9	7.4	8.1
		$ m_c $ (%)	0/3	nan	nan	nan	nan	nan	nan
		χ ($^\circ$)	2/2	-5.5	0.5	...	-5.8	-6.1	-5.4
		S (Jy)	4/6	2.120	0.098	4.6	2.038	1.933	2.204
		Π_l (Jy)	2/6	0.115	0.006	5.4	0.115	0.110	0.119
		m_l (%)	2/6	5.5	0.2	3.9	5.6	5.4	5.7
J0530+1331	2.64	χ ($^\circ$)	2/2	-9.2	0.5	...	-9.2	-9.5	-8.8
		S (Jy)	20/21	2.016	0.198	9.8	2.053	1.587	2.643
		Π_l (Jy)	19/21	0.064	0.010	15.4	0.063	0.046	0.095
		m_l (%)	19/21	2.9	0.6	19.4	3.1	2.0	4.7
		χ ($^\circ$)	19/19	6.6	5.7	...	8.5	-22.2	15.2
		S (Jy)	36/36	1.828	0.209	11.5	1.728	1.436	2.302
	4.85	Π_l (Jy)	36/36	0.090	0.015	16.3	0.098	0.063	0.109
		$ \Pi_c $ (Jy)	0/36	nan	nan	nan	nan	nan	nan

Table A.1: continued.

Source	Freq. (GHz)	x	N_{sign}	$\langle x \rangle$	σ_x	mi (%)	median	min	max	
J0654+4514	8.35	m_l	(%)	36/36	5.1	0.8	16.1	5.3	3.6	6.6
		$ m_c $	(%)	0/36	nan	nan	nan	nan	nan	nan
		χ	($^\circ$)	36/36	-25.3	3.1	...	-25.8	-32.9	-19.8
		S	(Jy)	34/35	1.442	0.204	14.1	1.507	1.198	1.897
		Π_l	(Jy)	34/35	0.068	0.018	26.5	0.077	0.036	0.094
		$ \Pi_c $	(Jy)	4/35	0.007	0.004	54.5	0.011	0.005	0.014
		m_l	(%)	34/35	4.5	1.4	31.7	5.3	2.2	6.8
		$ m_c $	(%)	4/35	0.5	0.2	51.0	0.7	0.3	0.8
	10.45	χ	($^\circ$)	34/34	-31.0	4.2	...	-31.6	-43.4	-20.1
		S	(Jy)	18/22	1.423	0.324	22.8	1.474	1.188	2.019
		Π_l	(Jy)	7/22	0.054	0.013	24.1	0.052	0.035	0.076
		m_l	(%)	7/22	3.2	1.2	35.7	2.9	2.1	5.0
		χ	($^\circ$)	7/7	-34.7	7.4	...	-34.9	-62.7	-26.8
		S	(Jy)	15/16	0.461	0.151	32.9	0.568	0.273	0.756
		Π_l	(Jy)	3/16	0.009	0.001	14.9	0.009	0.008	0.011
		m_l	(%)	3/16	1.5	0.3	19.1	1.5	1.3	1.9
	4.85	χ	($^\circ$)	3/3	36.6	28.4	...	48.6	4.4	58.5
		S	(Jy)	34/34	0.498	0.180	36.1	0.512	0.288	0.889
		Π_l	(Jy)	3/34	0.012	0.004	35.0	0.014	0.008	0.019
		$ \Pi_c $	(Jy)	0/34	nan	nan	nan	nan	nan	nan
		m_l	(%)	3/34	2.1	0.2	7.7	2.1	2.1	2.9
		$ m_c $	(%)	0/34	nan	nan	nan	nan	nan	nan
		χ	($^\circ$)	3/3	55.4	60.6	...	29.2	-21.7	67.1
		S	(Jy)	32/32	0.568	0.208	36.6	0.474	0.296	1.194
	8.35	Π_l	(Jy)	6/32	0.015	0.002	15.3	0.016	0.012	0.017
		$ \Pi_c $	(Jy)	1/32	0.003	0.000	nan	0.003	0.003	0.003
		m_l	(%)	6/32	1.9	0.5	24.2	2.3	1.6	2.8
		$ m_c $	(%)	1/32	0.2	0.0	nan	0.2	0.2	0.2
		χ	($^\circ$)	6/6	41.0	30.0	...	35.1	0.2	82.1
		S	(Jy)	16/20	0.524	0.167	31.9	0.549	0.351	1.299
		Π_l	(Jy)	0/20	nan	nan	nan	nan	nan	nan
		m_l	(%)	0/20	nan	nan	nan	nan	nan	nan
J0719+3307	2.64	S	(Jy)	8/8	0.292	0.066	22.5	0.307	0.206	0.376
		Π_l	(Jy)	0/8	nan	nan	nan	nan	nan	nan
		m_l	(%)	0/8	nan	nan	nan	nan	nan	nan
	4.85	S	(Jy)	18/19	0.364	0.074	20.2	0.347	0.198	0.525
		Π_l	(Jy)	0/19	nan	nan	nan	nan	nan	nan
		$ \Pi_c $	(Jy)	1/19	0.003	0.000	nan	0.003	0.003	0.003
		m_l	(%)	0/19	nan	nan	nan	nan	nan	nan
		$ m_c $	(%)	1/19	0.6	0.0	nan	0.6	0.6	0.6
		χ	($^\circ$)	0/1	nan	nan	...	nan	nan	nan
	8.35	S	(Jy)	19/20	0.363	0.084	23.0	0.373	0.144	0.547
		Π_l	(Jy)	2/20	0.009	0.001	12.4	0.010	0.009	0.010
		$ \Pi_c $	(Jy)	0/20	nan	nan	nan	nan	nan	nan

Table A.1: continued.

Source	Freq. (GHz)	x	N_{sign}	$\langle x \rangle$	σ_x	mi (%)	median	min	max
J0721+7120	10.45	m_l (%)	2/20	2.1	0.2	10.0	2.2	2.0	2.4
		$ m_c $ (%)	0/20	nan	nan	nan	nan	nan	nan
		χ ($^\circ$)	2/2	-23.6	5.5	...	-22.7	-26.6	-18.8
		S (Jy)	9/10	0.314	0.109	34.7	0.343	0.142	0.535
		Π_l (Jy)	0/10	nan	nan	nan	nan	nan	nan
		m_l (%)	0/10	nan	nan	nan	nan	nan	nan
	2.64	S (Jy)	22/25	1.108	0.300	27.1	1.249	0.745	1.798
		Π_l (Jy)	18/25	0.033	0.022	65.1	0.033	0.008	0.073
		m_l (%)	18/25	2.9	1.5	51.6	2.9	0.7	5.1
		χ ($^\circ$)	18/18	-20.0	30.1	...	-13.9	-80.9	19.4
		S (Jy)	44/44	1.224	0.517	42.2	1.428	0.695	2.472
		Π_l (Jy)	32/44	0.038	0.022	58.6	0.054	0.020	0.133
	4.85	$ \Pi_c $ (Jy)	3/44	0.010	0.002	18.8	0.010	0.009	0.013
		m_l (%)	32/44	2.3	1.4	59.3	3.5	1.1	6.8
		$ m_c $ (%)	3/44	0.7	0.3	49.7	0.7	0.6	1.4
		χ ($^\circ$)	32/32	-188.4	94.9	...	-170.2	-303.3	1.7
		S (Jy)	40/41	1.491	0.564	37.8	1.714	0.791	3.080
		Π_l (Jy)	38/41	0.042	0.038	91.0	0.058	0.014	0.187
	8.35	$ \Pi_c $ (Jy)	6/41	0.005	0.002	44.6	0.006	0.004	0.011
		m_l (%)	39/41	2.2	2.2	98.6	3.3	0.0	9.7
		$ m_c $ (%)	6/41	0.3	0.1	43.5	0.4	0.2	0.7
		χ ($^\circ$)	38/38	-197.4	59.2	...	-175.6	-281.5	-19.0
		S (Jy)	31/32	1.486	0.576	38.8	1.709	0.804	3.407
		Π_l (Jy)	14/32	0.087	0.060	69.1	0.076	0.025	0.222
	10.45	m_l (%)	14/32	4.2	2.5	58.4	4.0	0.8	10.1
		χ ($^\circ$)	14/14	23.9	38.1	...	15.2	-58.7	102.0
		S (Jy)	18/18	3.436	0.276	8.0	3.452	3.054	4.549
		Π_l (Jy)	18/18	0.036	0.020	56.1	0.033	0.010	0.085
		m_l (%)	18/18	1.0	0.6	57.0	0.9	0.3	2.2
		χ ($^\circ$)	18/18	28.2	52.8	...	25.2	-30.4	145.1
J0730-1141	4.85	S (Jy)	38/38	4.785	0.856	17.9	4.792	3.933	6.583
		Π_l (Jy)	33/38	0.053	0.020	37.1	0.061	0.018	0.330
		$ \Pi_c $ (Jy)	3/38	0.026	0.005	19.2	0.026	0.020	0.030
		m_l (%)	33/38	1.1	0.4	38.5	1.3	0.4	5.0
		$ m_c $ (%)	3/38	0.4	0.1	17.7	0.4	0.3	0.5
		χ ($^\circ$)	33/33	-196.2	43.2	...	-204.1	-267.4	-58.0
	8.35	S (Jy)	33/34	4.906	0.764	15.6	5.253	4.179	7.007
		Π_l (Jy)	30/34	0.064	0.029	45.0	0.071	0.023	0.198
		$ \Pi_c $ (Jy)	8/34	0.021	0.003	15.8	0.022	0.016	0.025
		m_l (%)	30/34	1.3	0.6	44.5	1.3	0.4	3.1
		$ m_c $ (%)	8/34	0.4	0.1	15.2	0.4	0.3	0.5
		χ ($^\circ$)	30/30	-55.7	122.5	...	56.0	-204.2	110.6
	10.45	S (Jy)	20/22	4.359	0.529	12.1	4.569	4.044	6.305
		Π_l (Jy)	8/22	0.063	0.030	48.1	0.056	0.024	0.118

Table A.1: continued.

Source	Freq. (GHz)	x		N _{sign}	$\langle x \rangle$	σ_x	mi (%)	median	min	max	
J0738+1742	2.64	m_l	(%)	8/22	1.3	0.7	49.8	1.1	0.6	2.6	
		χ	($^\circ$)	8/8	-37.5	70.7	...	20.1	-93.5	79.3	
		S	(Jy)	17/18	0.980	0.128	13.0	0.947	0.776	1.169	
		Π_l	(Jy)	14/18	0.015	0.004	23.2	0.015	0.009	0.021	
	4.85	m_l	(%)	14/18	1.5	0.5	31.3	1.7	0.8	2.1	
		χ	($^\circ$)	14/14	12.3	5.5	...	10.5	1.2	22.8	
		S	(Jy)	35/35	0.948	0.140	14.7	0.955	0.764	1.313	
		Π_l	(Jy)	9/35	0.016	0.003	21.7	0.016	0.013	0.024	
		$ \Pi_c $	(Jy)	0/35	nan	nan	nan	nan	nan	nan	
		m_l	(%)	9/35	1.4	0.3	23.0	1.8	1.2	2.0	
		$ m_c $	(%)	0/35	nan	nan	nan	nan	nan	nan	
		χ	($^\circ$)	9/9	-15.1	22.6	...	-1.9	-43.0	17.8	
	8.35	S	(Jy)	33/33	0.830	0.153	18.4	0.906	0.659	1.237	
		Π_l	(Jy)	16/33	0.011	0.005	41.4	0.013	0.007	0.024	
		$ \Pi_c $	(Jy)	0/33	nan	nan	nan	nan	nan	nan	
		m_l	(%)	16/33	1.2	0.4	29.6	1.2	0.9	2.0	
		$ m_c $	(%)	0/33	nan	nan	nan	nan	nan	nan	
		χ	($^\circ$)	16/16	-27.1	38.6	...	-28.4	-87.4	22.2	
	J0750+1231	10.45	S	(Jy)	21/21	0.889	0.207	23.3	0.910	0.576	1.154
			Π_l	(Jy)	4/21	0.022	0.004	17.8	0.022	0.017	0.026
m_l			(%)	4/21	2.0	0.4	17.9	2.0	1.6	2.4	
χ			($^\circ$)	4/4	-59.1	11.3	...	-60.8	-67.4	-42.5	
2.64		S	(Jy)	2/2	2.986	0.048	1.6	3.011	2.977	3.045	
		Π_l	(Jy)	2/2	0.035	0.004	12.4	0.034	0.031	0.038	
		m_l	(%)	2/2	1.2	0.2	13.9	1.1	1.0	1.3	
		χ	($^\circ$)	2/2	-27.0	3.4	...	-26.3	-28.7	-23.9	
		4.85	S	(Jy)	2/3	3.434	0.009	0.3	3.431	3.425	3.438
			Π_l	(Jy)	1/3	0.030	0.000	nan	0.030	0.030	0.030
$ \Pi_c $	(Jy)		1/3	0.005	0.000	nan	0.005	0.005	0.005		
m_l	(%)		1/3	0.9	0.0	nan	0.9	0.9	0.9		
$ m_c $	(%)		1/3	0.1	0.0	nan	0.1	0.1	0.1		
χ	($^\circ$)		1/1	45.1	0.0	...	45.1	45.1	45.1		
J0808-0751	8.35	S	(Jy)	2/3	3.604	0.060	1.7	3.623	3.580	3.665	
		Π_l	(Jy)	3/3	0.048	0.008	16.7	0.042	0.039	0.051	
		$ \Pi_c $	(Jy)	1/3	0.012	0.000	nan	0.012	0.012	0.012	
		m_l	(%)	2/3	1.1	0.0	4.5	1.1	1.1	1.1	
		$ m_c $	(%)	1/3	0.3	0.0	nan	0.3	0.3	0.3	
		χ	($^\circ$)	3/3	53.2	5.7	...	51.2	47.7	59.6	
	10.45	S	(Jy)	3/4	3.585	0.161	4.5	3.633	3.414	4.028	
		Π_l	(Jy)	0/4	nan	nan	nan	nan	nan	nan	
		m_l	(%)	0/4	nan	nan	nan	nan	nan	nan	
		2.64	S	(Jy)	12/12	1.279	0.110	8.6	1.288	1.086	1.488
Π_l	(Jy)		12/12	0.028	0.004	15.9	0.028	0.019	0.034		
m_l	(%)		12/12	2.1	0.3	16.3	2.2	1.4	3.0		

Table A.1: continued.

Source	Freq. (GHz)	x	N_{sign}	$\langle x \rangle$	σ_x	mi (%)	median	min	max
J0818+4222	4.85	χ (°)	12/12	25.4	3.3	...	27.2	21.5	35.3
		S (Jy)	19/19	1.307	0.292	22.4	1.331	0.959	1.842
		Π_l (Jy)	10/19	0.024	0.002	9.0	0.025	0.020	0.029
		$ \Pi_c $ (Jy)	0/19	nan	nan	nan	nan	nan	nan
		m_l (%)	10/19	2.5	0.4	14.8	2.1	1.4	2.5
	8.35	$ m_c $ (%)	0/19	nan	nan	nan	nan	nan	nan
		χ (°)	10/10	47.2	6.1	...	48.0	22.3	67.3
		S (Jy)	17/17	1.159	0.284	24.5	1.228	0.860	1.821
		Π_l (Jy)	15/17	0.024	0.011	44.5	0.023	0.011	0.049
		$ \Pi_c $ (Jy)	0/17	nan	nan	nan	nan	nan	nan
	10.45	m_l (%)	15/17	1.8	0.9	48.1	2.1	0.9	4.1
		$ m_c $ (%)	0/17	nan	nan	nan	nan	nan	nan
		χ (°)	15/15	65.8	14.4	...	56.2	29.7	75.2
		S (Jy)	13/15	1.235	0.294	23.8	1.176	0.830	1.591
		Π_l (Jy)	2/15	0.026	0.002	6.2	0.026	0.025	0.027
J0824+5552	2.64	m_l (%)	2/15	2.9	0.1	3.7	2.9	2.8	2.9
		χ (°)	2/2	54.1	17.5	...	55.0	42.6	67.4
		S (Jy)	20/21	1.278	0.195	15.3	1.374	1.030	1.709
		Π_l (Jy)	16/21	0.021	0.007	33.9	0.021	0.010	0.037
		m_l (%)	16/21	1.5	0.6	38.0	1.5	0.6	2.7
	4.85	χ (°)	16/16	-93.0	31.9	...	-96.9	-128.1	-10.1
		S (Jy)	43/43	1.367	0.294	21.5	1.422	0.956	1.875
		Π_l (Jy)	26/43	0.024	0.009	37.5	0.027	0.014	0.055
		$ \Pi_c $ (Jy)	3/43	0.004	0.001	26.7	0.004	0.004	0.006
		m_l (%)	26/43	1.8	0.7	41.9	1.9	0.9	3.6
	8.35	$ m_c $ (%)	3/43	0.3	0.0	12.1	0.3	0.3	0.4
		χ (°)	26/26	-51.8	40.8	...	-53.0	-150.8	-11.8
		S (Jy)	40/41	1.208	0.291	24.1	1.231	0.891	1.861
		Π_l (Jy)	33/41	0.023	0.013	57.6	0.022	0.011	0.079
		$ \Pi_c $ (Jy)	3/41	0.005	0.002	33.5	0.005	0.004	0.007
J0824+5552	10.45	m_l (%)	33/41	2.1	0.8	40.7	2.2	0.9	4.7
		$ m_c $ (%)	3/41	0.5	0.2	32.8	0.5	0.4	0.8
		χ (°)	33/33	-59.1	46.8	...	-32.0	-166.0	-8.9
		S (Jy)	21/22	1.213	0.350	28.8	1.236	0.848	1.816
		Π_l (Jy)	3/22	0.036	0.013	36.8	0.042	0.021	0.045
	2.64	m_l (%)	3/22	2.5	0.2	9.0	2.3	2.2	2.6
		χ (°)	3/3	-29.9	18.6	...	-22.3	-48.9	-19.5
		S (Jy)	8/10	1.090	0.048	4.4	1.087	0.998	1.147
		Π_l (Jy)	7/10	0.044	0.006	12.8	0.047	0.034	0.048
		m_l (%)	7/10	4.0	0.4	8.8	4.1	3.4	4.5
	4.85	χ (°)	7/7	-0.2	2.4	...	-0.2	-4.7	2.5
		S (Jy)	16/16	0.919	0.039	4.3	0.916	0.794	1.028
		Π_l (Jy)	11/16	0.030	0.003	10.8	0.032	0.029	0.037
		$ \Pi_c $ (Jy)	0/16	nan	nan	nan	nan	nan	nan

Table A.1: continued.

Source	Freq. (GHz)	x	N_{sign}	$\langle x \rangle$	σ_x	mi (%)	median	min	max		
J0830+2410	8.35	m_l	(%)	11/16	3.3	0.3	8.8	3.4	3.0	3.9	
		$ m_c $	(%)	0/16	nan	nan	nan	nan	nan	nan	
		χ	($^\circ$)	11/11	0.8	4.5	...	2.6	-6.5	12.6	
		S	(Jy)	15/15	0.826	0.065	7.9	0.793	0.660	0.962	
		Π_l	(Jy)	13/15	0.030	0.005	16.7	0.025	0.020	0.037	
		$ \Pi_c $	(Jy)	0/15	nan	nan	nan	nan	nan	nan	
		m_l	(%)	13/15	3.7	0.6	16.8	3.4	2.0	4.9	
		$ m_c $	(%)	0/15	nan	nan	nan	nan	nan	nan	
	10.45	χ	($^\circ$)	13/13	2.1	3.6	...	1.8	-9.0	12.0	
		S	(Jy)	9/11	0.780	0.091	11.6	0.734	0.656	0.958	
		Π_l	(Jy)	2/11	0.022	0.001	6.5	0.022	0.021	0.023	
		m_l	(%)	2/11	2.8	0.7	27.0	2.7	2.2	3.3	
	2.64	χ	($^\circ$)	2/2	0.2	11.5	...	1.9	-6.2	10.1	
		S	(Jy)	1/1	0.958	0.000	nan	0.958	0.958	0.958	
		Π_l	(Jy)	0/1	nan	nan	nan	nan	nan	nan	
		m_l	(%)	0/1	nan	nan	nan	nan	nan	nan	
	4.85	S	(Jy)	1/1	1.171	0.000	nan	1.171	1.171	1.171	
		Π_l	(Jy)	1/1	0.041	0.000	nan	0.041	0.041	0.041	
		$ \Pi_c $	(Jy)	0/1	nan	nan	nan	nan	nan	nan	
		m_l	(%)	1/1	3.5	0.0	nan	3.5	3.5	3.5	
		$ m_c $	(%)	0/1	nan	nan	nan	nan	nan	nan	
		χ	($^\circ$)	1/1	48.6	0.0	...	48.6	48.6	48.6	
		8.35	S	(Jy)	1/1	1.149	0.000	nan	1.149	1.149	1.149
			Π_l	(Jy)	1/1	0.033	0.000	nan	0.033	0.033	0.033
	$ \Pi_c $		(Jy)	0/1	nan	nan	nan	nan	nan	nan	
	m_l		(%)	1/1	2.8	0.0	nan	2.8	2.8	2.8	
	10.45	$ m_c $	(%)	0/1	nan	nan	nan	nan	nan	nan	
		χ	($^\circ$)	1/1	42.4	0.0	...	42.4	42.4	42.4	
		S	(Jy)	1/1	1.066	0.000	nan	1.066	1.066	1.066	
		Π_l	(Jy)	0/1	nan	nan	nan	nan	nan	nan	
	J0841+7053	2.64	m_l	(%)	0/1	nan	nan	nan	nan	nan	nan
S			(Jy)	17/19	2.503	0.113	4.5	2.505	2.316	2.827	
Π_l			(Jy)	16/19	0.197	0.009	4.7	0.194	0.172	0.214	
m_l			(%)	16/19	7.8	0.7	8.8	7.9	6.1	8.9	
4.85		χ	($^\circ$)	16/16	-80.3	1.2	...	-80.3	-82.3	-78.1	
		S	(Jy)	33/34	2.247	0.562	25.0	2.212	1.717	3.461	
		Π_l	(Jy)	33/34	0.122	0.005	4.2	0.121	0.109	0.138	
		$ \Pi_c $	(Jy)	0/34	nan	nan	nan	nan	nan	nan	
8.35		m_l	(%)	33/34	4.7	1.2	25.3	5.1	3.5	7.0	
		$ m_c $	(%)	0/34	nan	nan	nan	nan	nan	nan	
		χ	($^\circ$)	33/33	-77.8	1.9	...	-79.0	-81.2	-70.8	
		S	(Jy)	31/32	2.611	0.518	19.8	2.924	1.664	3.202	
		Π_l	(Jy)	31/32	0.126	0.015	12.2	0.118	0.093	0.172	
	$ \Pi_c $	(Jy)	5/32	0.013	0.003	22.2	0.013	0.009	0.018		

Table A.1: continued.

Source	Freq. (GHz)	x	N_{sign}	$\langle x \rangle$	σ_x	mi (%)	median	min	max
J0849+5108	10.45	m_l (%)	31/32	4.6	0.8	17.6	4.8	3.1	6.8
		$ m_c $ (%)	5/32	0.4	0.1	34.7	0.4	0.3	0.9
		χ ($^\circ$)	31/31	-83.3	1.9	...	-83.2	-86.0	-78.2
		S (Jy)	22/24	2.595	0.502	19.3	2.921	1.839	3.190
		Π_l (Jy)	8/24	0.073	0.013	18.0	0.074	0.049	0.095
		m_l (%)	8/24	2.6	0.7	25.3	2.5	1.6	3.7
	2.64	χ ($^\circ$)	8/8	-86.3	12.3	...	-81.5	-106.4	-73.2
		S (Jy)	6/8	0.200	0.016	8.0	0.205	0.191	0.228
		Π_l (Jy)	0/8	nan	nan	nan	nan	nan	nan
		m_l (%)	0/8	nan	nan	nan	nan	nan	nan
		S (Jy)	12/12	0.219	0.024	11.0	0.204	0.179	0.247
		Π_l (Jy)	0/12	nan	nan	nan	nan	nan	nan
	4.85	$ \Pi_c $ (Jy)	0/12	nan	nan	nan	nan	nan	nan
		m_l (%)	0/12	nan	nan	nan	nan	nan	nan
		$ m_c $ (%)	0/12	nan	nan	nan	nan	nan	nan
		S (Jy)	12/13	0.239	0.032	13.3	0.259	0.203	0.302
		Π_l (Jy)	0/13	nan	nan	nan	nan	nan	nan
		$ \Pi_c $ (Jy)	0/13	nan	nan	nan	nan	nan	nan
	8.35	m_l (%)	0/13	nan	nan	nan	nan	nan	nan
		$ m_c $ (%)	0/13	nan	nan	nan	nan	nan	nan
		S (Jy)	7/7	0.271	0.074	27.3	0.258	0.137	0.345
		Π_l (Jy)	0/7	nan	nan	nan	nan	nan	nan
		m_l (%)	0/7	nan	nan	nan	nan	nan	nan
		S (Jy)	20/22	3.467	0.381	11.0	3.673	2.716	4.174
J0854+2006	2.64	Π_l (Jy)	19/22	0.073	0.034	46.5	0.078	0.028	0.155
		m_l (%)	19/22	2.0	1.0	52.8	2.2	0.8	4.8
		χ ($^\circ$)	19/19	-21.2	15.1	...	-21.4	-64.2	4.2
		S (Jy)	46/47	3.929	0.956	24.3	4.156	2.737	5.650
		Π_l (Jy)	42/47	0.092	0.045	48.8	0.092	0.022	0.224
		$ \Pi_c $ (Jy)	6/47	0.007	0.005	77.0	0.013	0.003	0.026
	4.85	m_l (%)	42/47	2.3	1.0	44.6	2.2	0.4	5.3
		$ m_c $ (%)	6/47	0.1	0.1	87.6	0.3	0.1	0.5
		χ ($^\circ$)	42/42	-40.0	24.4	...	-33.8	-102.5	14.3
		S (Jy)	46/46	4.772	1.272	26.7	4.841	2.889	7.363
		Π_l (Jy)	46/46	0.094	0.063	67.1	0.129	0.023	0.384
		$ \Pi_c $ (Jy)	5/46	0.014	0.008	56.0	0.019	0.007	0.027
	8.35	m_l (%)	46/46	2.0	1.2	59.3	2.8	0.6	6.6
		$ m_c $ (%)	5/46	0.3	0.1	45.3	0.3	0.1	0.7
		χ ($^\circ$)	46/46	115.1	72.7	...	134.9	-57.6	187.3
		S (Jy)	25/26	4.991	0.989	19.8	5.314	3.607	7.228
		Π_l (Jy)	19/26	0.136	0.076	56.3	0.158	0.065	0.518
		m_l (%)	19/26	2.8	1.4	49.4	3.2	1.4	7.7
	10.45	χ ($^\circ$)	19/19	-44.9	18.0	...	-42.8	-96.2	-22.5
		S (Jy)	20/22	1.055	0.021	2.0	1.054	1.003	1.105
		Π_l (Jy)	19/26	0.136	0.076	56.3	0.158	0.065	0.518
		m_l (%)	19/26	2.8	1.4	49.4	3.2	1.4	7.7
		χ ($^\circ$)	19/19	-44.9	18.0	...	-42.8	-96.2	-22.5
		S (Jy)	20/22	1.055	0.021	2.0	1.054	1.003	1.105
J0920+4441	2.64	S (Jy)	20/22	1.055	0.021	2.0	1.054	1.003	1.105

Table A.1: continued.

Source	Freq. (GHz)	x		N _{sign}	$\langle x \rangle$	σ_x	mi (%)	median	min	max
J0948+0022	4.85	Π_l	(Jy)	17/22	0.026	0.002	8.9	0.026	0.022	0.031
		m_l	(%)	17/22	2.5	0.2	9.3	2.4	2.1	2.9
		χ	($^\circ$)	17/17	-56.6	3.0	...	-57.3	-64.7	-50.9
		S	(Jy)	35/35	1.207	0.052	4.3	1.217	1.041	1.269
		Π_l	(Jy)	28/35	0.027	0.003	9.6	0.027	0.020	0.035
		$ \Pi_c $	(Jy)	1/35	0.003	0.000	nan	0.003	0.003	0.003
		m_l	(%)	28/35	2.3	0.2	6.9	2.3	1.8	2.8
		$ m_c $	(%)	1/35	0.2	0.0	nan	0.2	0.2	0.2
	8.35	χ	($^\circ$)	28/28	-79.9	10.8	...	-75.3	-105.8	-55.1
		S	(Jy)	33/33	1.469	0.170	11.6	1.534	1.078	1.687
		Π_l	(Jy)	29/33	0.032	0.013	40.2	0.039	0.012	0.047
		$ \Pi_c $	(Jy)	4/33	0.006	0.002	39.7	0.007	0.004	0.011
		m_l	(%)	29/33	2.1	1.0	45.3	2.7	0.7	3.5
		$ m_c $	(%)	4/33	0.4	0.1	32.7	0.4	0.3	0.8
		χ	($^\circ$)	29/29	-65.0	18.3	...	-63.8	-91.4	-14.7
		S	(Jy)	22/24	1.619	0.185	11.5	1.648	1.213	1.845
	10.45	Π_l	(Jy)	6/24	0.049	0.006	12.0	0.048	0.042	0.055
		m_l	(%)	6/24	3.4	0.5	13.7	3.3	2.9	4.1
		χ	($^\circ$)	6/6	-59.1	5.5	...	-56.5	-65.8	-51.8
		S	(Jy)	21/23	0.182	0.029	16.0	0.189	0.131	0.234
		Π_l	(Jy)	1/23	0.012	0.000	nan	0.012	0.012	0.012
		m_l	(%)	1/23	6.9	0.0	nan	6.9	6.9	6.9
		χ	($^\circ$)	1/1	41.6	0.0	...	41.6	41.6	41.6
		S	(Jy)	45/47	0.286	0.056	19.7	0.271	0.163	0.460
	4.85	Π_l	(Jy)	0/47	nan	nan	nan	nan	nan	nan
		$ \Pi_c $	(Jy)	0/47	nan	nan	nan	nan	nan	nan
		m_l	(%)	0/47	nan	nan	nan	nan	nan	nan
		$ m_c $	(%)	0/47	nan	nan	nan	nan	nan	nan
		S	(Jy)	45/45	0.394	0.107	27.2	0.364	0.191	0.754
		Π_l	(Jy)	0/45	nan	nan	nan	nan	nan	nan
		$ \Pi_c $	(Jy)	0/45	nan	nan	nan	nan	nan	nan
		m_l	(%)	0/45	nan	nan	nan	nan	nan	nan
	8.35	$ m_c $	(%)	0/45	nan	nan	nan	nan	nan	nan
		S	(Jy)	28/30	0.443	0.163	36.7	0.449	0.254	0.901
		Π_l	(Jy)	1/30	0.017	0.000	nan	0.017	0.017	0.017
		m_l	(%)	1/30	2.3	0.0	nan	2.3	2.3	2.3
		χ	($^\circ$)	1/1	-80.2	0.0	...	-80.2	-80.2	-80.2
		S	(Jy)	14/15	1.124	0.160	14.3	1.135	0.846	1.401
		Π_l	(Jy)	14/15	0.078	0.013	17.1	0.079	0.058	0.102
		m_l	(%)	14/15	6.9	1.0	14.2	6.9	5.3	8.9
J0958+6533	2.64	χ	($^\circ$)	14/14	-16.0	5.4	...	-15.7	-31.0	-8.6
		S	(Jy)	26/26	1.092	0.168	15.4	1.184	0.797	1.567
		Π_l	(Jy)	25/26	0.080	0.024	29.9	0.088	0.041	0.161
		$ \Pi_c $	(Jy)	2/26	0.005	0.002	54.2	0.006	0.004	0.008

Table A.1: continued.

Source	Freq. (GHz)	x	N_{sign}	$\langle x \rangle$	σ_x	mi (%)	median	min	max
J1104+3812	8.35	m_l (%)	25/26	7.6	1.3	17.1	7.3	3.2	10.5
		$ m_c $ (%)	2/26	0.4	0.1	28.7	0.4	0.3	0.5
		χ ($^\circ$)	25/25	-9.3	4.7	...	-10.7	-33.2	4.5
		S (Jy)	25/27	1.115	0.156	14.0	1.196	0.855	1.743
		Π_l (Jy)	25/27	0.069	0.025	36.3	0.097	0.039	0.233
		$ \Pi_c $ (Jy)	3/27	0.005	0.008	154.2	0.009	0.003	0.020
		m_l (%)	25/27	6.7	1.7	25.0	7.5	3.5	15.0
		$ m_c $ (%)	3/27	0.5	0.6	126.0	0.8	0.3	1.4
	10.45	χ ($^\circ$)	25/25	-5.9	5.7	...	-4.0	-24.8	12.2
		S (Jy)	14/18	1.171	0.172	14.7	1.120	0.864	1.425
		Π_l (Jy)	3/18	0.067	0.025	37.6	0.064	0.040	0.089
		m_l (%)	3/18	5.6	2.0	35.6	6.3	3.2	6.8
	2.64	χ ($^\circ$)	3/3	-16.2	13.2	...	-5.4	-23.0	1.0
		S (Jy)	25/26	0.777	0.087	11.1	0.779	0.662	0.938
		Π_l (Jy)	1/26	0.008	0.000	nan	0.008	0.008	0.008
		m_l (%)	1/26	0.9	0.0	nan	0.9	0.9	0.9
		χ ($^\circ$)	1/1	70.2	0.0	...	70.2	70.2	70.2
		S (Jy)	43/44	0.679	0.099	14.6	0.659	0.558	0.947
		Π_l (Jy)	6/44	0.012	0.002	13.3	0.013	0.010	0.013
		$ \Pi_c $ (Jy)	0/44	nan	nan	nan	nan	nan	nan
	4.85	m_l (%)	6/44	1.9	0.2	12.6	1.9	1.6	2.1
		$ m_c $ (%)	0/44	nan	nan	nan	nan	nan	nan
		χ ($^\circ$)	6/6	46.8	6.2	...	45.2	33.6	62.0
		S (Jy)	42/44	0.588	0.098	16.6	0.597	0.462	0.916
		Π_l (Jy)	17/44	0.013	0.006	46.2	0.013	0.008	0.026
		$ \Pi_c $ (Jy)	1/44	0.004	0.000	nan	0.004	0.004	0.004
		m_l (%)	17/44	2.1	0.9	42.2	2.2	1.3	4.4
		$ m_c $ (%)	1/44	0.5	0.0	nan	0.5	0.5	0.5
	8.35	χ ($^\circ$)	17/17	-16.7	15.5	...	-20.6	-53.4	7.2
		S (Jy)	30/31	0.596	0.112	18.7	0.611	0.436	0.919
		Π_l (Jy)	3/31	0.020	0.003	14.3	0.018	0.018	0.023
		m_l (%)	3/31	3.2	0.6	18.1	3.1	2.7	3.9
		χ ($^\circ$)	3/3	-44.5	3.1	...	-45.5	-46.9	-40.7
		S (Jy)	22/22	3.819	0.075	2.0	3.826	3.624	3.938
		Π_l (Jy)	22/22	0.168	0.013	7.9	0.169	0.132	0.243
		m_l (%)	22/22	4.4	0.4	8.2	4.4	3.4	6.2
J1130-1449	2.64	χ ($^\circ$)	22/22	-14.4	3.2	...	-14.0	-22.1	-8.5
		S (Jy)	38/39	3.243	0.159	4.9	3.026	2.911	3.629
		Π_l (Jy)	38/39	0.168	0.011	6.5	0.165	0.154	0.200
		$ \Pi_c $ (Jy)	3/39	0.011	0.004	34.0	0.011	0.006	0.013
	4.85	m_l (%)	38/39	5.3	0.4	8.1	5.5	4.4	6.0
		$ m_c $ (%)	3/39	0.4	0.1	35.2	0.4	0.2	0.4
		χ ($^\circ$)	38/38	-26.7	2.5	...	-26.6	-30.6	-21.3
		S (Jy)	37/38	2.630	0.315	12.0	2.565	2.257	3.716

Table A.1: continued.

Source	Freq. (GHz)	x		N _{sign}	$\langle x \rangle$	σ_x	mi (%)	median	min	max
J1136+7009	10.45	Π_l	(Jy)	36/38	0.121	0.011	8.9	0.117	0.108	0.159
		$ \Pi_c $	(Jy)	1/38	0.006	0.000	nan	0.006	0.006	0.006
		m_l	(%)	36/38	4.3	0.8	17.5	4.6	2.9	5.6
		$ m_c $	(%)	1/38	0.2	0.0	nan	0.2	0.2	0.2
		χ	($^\circ$)	36/36	-23.8	2.9	...	-24.2	-27.8	-17.9
		S	(Jy)	23/26	2.318	0.151	6.5	2.377	1.905	2.722
	2.64	Π_l	(Jy)	11/26	0.086	0.028	32.8	0.093	0.019	0.128
		m_l	(%)	11/26	3.5	1.3	36.4	3.8	0.8	6.7
		χ	($^\circ$)	11/11	-31.5	6.3	...	-33.3	-49.5	-18.7
		S	(Jy)	1/1	0.304	0.000	nan	0.304	0.304	0.304
		Π_l	(Jy)	0/1	nan	nan	nan	nan	nan	nan
		m_l	(%)	0/1	nan	nan	nan	nan	nan	nan
	4.85	S	(Jy)	3/4	0.318	0.003	1.0	0.317	0.317	0.323
		Π_l	(Jy)	0/4	nan	nan	nan	nan	nan	nan
		$ \Pi_c $	(Jy)	0/4	nan	nan	nan	nan	nan	nan
		m_l	(%)	0/4	nan	nan	nan	nan	nan	nan
		$ m_c $	(%)	0/4	nan	nan	nan	nan	nan	nan
		S	(Jy)	3/4	0.276	0.004	1.5	0.275	0.274	0.281
	8.35	Π_l	(Jy)	1/4	0.011	0.000	nan	0.011	0.011	0.011
		$ \Pi_c $	(Jy)	0/4	nan	nan	nan	nan	nan	nan
		m_l	(%)	1/4	3.8	0.0	nan	3.8	3.8	3.8
		$ m_c $	(%)	0/4	nan	nan	nan	nan	nan	nan
		χ	($^\circ$)	1/1	-14.0	0.0	...	-14.0	-14.0	-14.0
		S	(Jy)	1/1	0.218	0.000	nan	0.218	0.218	0.218
J1159+2914	10.45	Π_l	(Jy)	0/1	nan	nan	nan	nan	nan	nan
		m_l	(%)	0/1	nan	nan	nan	nan	nan	nan
		S	(Jy)	22/24	2.029	0.260	12.8	2.168	1.547	2.401
		Π_l	(Jy)	22/24	0.023	0.007	32.9	0.023	0.009	0.034
		m_l	(%)	22/24	1.0	0.4	33.8	1.0	0.5	2.0
		χ	($^\circ$)	22/22	99.0	15.5	...	100.2	69.9	124.0
	4.85	S	(Jy)	36/36	1.947	0.521	26.8	2.080	1.164	2.824
		Π_l	(Jy)	26/36	0.023	0.007	30.6	0.025	0.011	0.042
		$ \Pi_c $	(Jy)	2/36	0.006	0.003	45.7	0.007	0.005	0.008
		m_l	(%)	26/36	1.2	0.5	44.2	1.3	0.5	3.0
		$ m_c $	(%)	2/36	0.3	0.1	31.5	0.3	0.2	0.3
		χ	($^\circ$)	26/26	-187.9	96.9	...	-219.4	-285.4	-80.7
	8.35	S	(Jy)	35/35	1.633	0.419	25.7	1.769	1.060	3.220
		Π_l	(Jy)	32/35	0.031	0.016	51.5	0.032	0.011	0.084
		$ \Pi_c $	(Jy)	0/35	nan	nan	nan	nan	nan	nan
		m_l	(%)	32/35	1.8	0.7	37.0	1.7	0.6	3.4
		$ m_c $	(%)	0/35	nan	nan	nan	nan	nan	nan
		χ	($^\circ$)	32/32	-213.2	63.8	...	-203.6	-285.1	-16.9
	10.45	S	(Jy)	23/25	1.676	0.369	22.0	1.694	1.191	2.860
		Π_l	(Jy)	4/25	0.055	0.021	38.5	0.049	0.026	0.076

Table A.1: continued.

Source	Freq. (GHz)	x	N_{sign}	$\langle x \rangle$	σ_x	mi (%)	median	min	max	
J1217+3007	2.64	m_l (%)	4/25	2.9	0.5	17.7	2.9	2.0	3.3	
		χ ($^\circ$)	4/4	33.0	12.5	...	32.0	1.1	79.6	
		S (Jy)	19/20	0.461	0.018	4.0	0.456	0.421	0.491	
		Π_l (Jy)	18/20	0.025	0.001	4.3	0.025	0.023	0.028	
		m_l (%)	18/20	5.4	0.3	4.7	5.4	5.1	5.9	
		χ ($^\circ$)	18/18	56.4	1.3	...	56.4	52.8	59.9	
	4.85	S (Jy)	39/39	0.420	0.011	2.5	0.415	0.396	0.443	
		Π_l (Jy)	27/39	0.020	0.001	7.5	0.019	0.015	0.022	
		$ \Pi_c $ (Jy)	0/39	nan	nan	nan	nan	nan	nan	
		m_l (%)	28/39	4.7	0.3	6.5	4.6	3.8	5.2	
		$ m_c $ (%)	0/39	nan	nan	nan	nan	nan	nan	
		χ ($^\circ$)	27/27	51.5	10.1	...	52.9	36.3	67.9	
	8.35	S (Jy)	37/37	0.380	0.021	5.6	0.389	0.353	0.420	
		Π_l (Jy)	32/37	0.013	0.002	12.4	0.013	0.010	0.015	
		$ \Pi_c $ (Jy)	0/37	nan	nan	nan	nan	nan	nan	
		m_l (%)	32/37	3.3	0.4	13.1	3.4	2.5	4.2	
		$ m_c $ (%)	0/37	nan	nan	nan	nan	nan	nan	
		χ ($^\circ$)	32/32	51.8	7.0	...	56.8	34.6	75.4	
	10.45	S (Jy)	18/21	0.371	0.024	6.5	0.364	0.328	0.403	
		Π_l (Jy)	0/21	nan	nan	nan	nan	nan	nan	
		m_l (%)	0/21	nan	nan	nan	nan	nan	nan	
J1221+2813		2.64	S (Jy)	18/20	0.527	0.038	7.3	0.514	0.492	0.631
			Π_l (Jy)	13/20	0.010	0.002	20.9	0.010	0.007	0.015
			m_l (%)	13/20	2.0	0.4	19.1	2.0	1.2	2.6
	χ ($^\circ$)		13/13	-7.0	9.2	...	-6.0	-24.6	13.1	
	4.85	S (Jy)	36/36	0.535	0.098	18.2	0.498	0.450	0.743	
		Π_l (Jy)	14/36	0.016	0.004	23.1	0.015	0.010	0.021	
		$ \Pi_c $ (Jy)	0/36	nan	nan	nan	nan	nan	nan	
		m_l (%)	16/36	2.4	1.0	39.4	2.7	0.0	3.3	
		$ m_c $ (%)	0/36	nan	nan	nan	nan	nan	nan	
		χ ($^\circ$)	14/14	-13.0	13.5	...	-15.1	-32.7	14.5	
	8.35	S (Jy)	35/35	0.487	0.067	13.8	0.475	0.291	0.780	
		Π_l (Jy)	3/35	0.012	0.000	3.6	0.012	0.012	0.013	
		$ \Pi_c $ (Jy)	1/35	0.003	0.000	nan	0.003	0.003	0.003	
		m_l (%)	3/35	2.9	0.4	14.4	2.9	2.1	3.1	
		$ m_c $ (%)	1/35	0.6	0.0	nan	0.6	0.6	0.6	
		χ ($^\circ$)	3/3	0.4	3.3	...	4.2	0.0	5.6	
	10.45	S (Jy)	21/21	0.484	0.068	14.1	0.474	0.428	0.685	
		Π_l (Jy)	0/21	nan	nan	nan	nan	nan	nan	
		m_l (%)	0/21	nan	nan	nan	nan	nan	nan	
J1224+2122	2.64	S (Jy)	2/2	2.055	0.353	17.2	1.866	1.616	2.115	
		Π_l (Jy)	2/2	0.072	0.002	2.3	0.072	0.070	0.073	
		m_l (%)	2/2	3.8	0.8	21.7	3.9	3.3	4.5	
		χ ($^\circ$)	2/2	-40.9	10.0	...	-41.0	-48.0	-33.9	

Table A.1: continued.

Source	Freq. (GHz)	x		N _{sign}	$\langle x \rangle$	σ_x	mi (%)	median	min	max
J1229+0203	4.85	S	(Jy)	6/6	1.993	0.494	24.8	2.802	1.634	2.928
		Π_l	(Jy)	5/6	0.152	0.030	19.8	0.177	0.126	0.192
		$ \Pi_c $	(Jy)	0/6	nan	nan	nan	nan	nan	nan
		m_l	(%)	5/6	5.5	1.1	19.4	6.2	4.5	7.0
		$ m_c $	(%)	0/6	nan	nan	nan	nan	nan	nan
		χ	($^\circ$)	5/5	-22.8	5.4	...	-20.7	-25.4	-7.5
	8.35	S	(Jy)	6/6	2.605	0.490	18.8	2.935	2.083	3.255
		Π_l	(Jy)	6/6	0.047	0.119	255.5	0.193	0.026	0.236
		$ \Pi_c $	(Jy)	3/6	0.020	0.009	44.5	0.023	0.010	0.025
		m_l	(%)	6/6	2.4	3.8	161.3	6.6	1.3	9.0
		$ m_c $	(%)	3/6	0.7	0.2	30.6	0.7	0.4	0.8
		χ	($^\circ$)	6/6	-8.7	6.8	...	-13.3	-19.9	-2.5
	10.45	S	(Jy)	2/2	2.353	0.049	2.1	2.384	2.349	2.418
		Π_l	(Jy)	0/2	nan	nan	nan	nan	nan	nan
		m_l	(%)	0/2	nan	nan	nan	nan	nan	nan
	2.64	S	(Jy)	22/23	46.310	1.243	2.7	46.734	44.082	47.936
		Π_l	(Jy)	22/23	1.141	0.158	13.8	1.098	1.015	1.631
		m_l	(%)	22/23	2.4	0.4	14.9	2.4	2.1	3.7
		χ	($^\circ$)	22/22	-15.5	4.2	...	-14.6	-27.1	-7.4
	4.85	S	(Jy)	50/52	38.253	2.442	6.4	36.725	31.639	40.074
		Π_l	(Jy)	50/52	1.795	0.199	11.1	1.905	1.490	2.143
		$ \Pi_c $	(Jy)	6/52	0.081	0.025	30.4	0.093	0.051	0.111
		m_l	(%)	50/52	4.8	0.9	18.4	5.2	3.8	6.4
		$ m_c $	(%)	6/52	0.2	0.1	23.8	0.3	0.2	0.3
		χ	($^\circ$)	50/50	-26.3	1.9	...	-25.9	-29.7	-22.2
	8.35	S	(Jy)	48/50	26.874	3.846	14.3	25.931	22.325	34.980
		Π_l	(Jy)	47/50	2.047	0.124	6.1	2.048	1.773	2.309
		$ \Pi_c $	(Jy)	4/50	0.065	0.008	12.1	0.069	0.054	0.076
		m_l	(%)	47/50	7.5	0.7	9.5	7.6	6.4	8.7
		$ m_c $	(%)	4/50	0.3	0.1	19.7	0.3	0.2	0.3
		χ	($^\circ$)	47/47	-33.9	2.0	...	-34.2	-37.7	-28.0
	10.45	S	(Jy)	24/30	23.083	3.325	14.4	23.596	19.901	30.130
		Π_l	(Jy)	23/30	1.907	0.191	10.0	1.887	1.088	2.573
		m_l	(%)	23/30	8.4	1.1	13.1	8.0	5.0	10.3
		χ	($^\circ$)	23/23	-40.4	4.9	...	-41.0	-57.6	5.6
J1230+1223	4.85	S	(Jy)	1/1	59.269	0.000	nan	59.269	59.269	59.269
		Π_l	(Jy)	1/1	0.605	0.000	nan	0.605	0.605	0.605
		$ \Pi_c $	(Jy)	0/1	nan	nan	nan	nan	nan	nan
		m_l	(%)	1/1	1.0	0.0	nan	1.0	1.0	1.0
		$ m_c $	(%)	0/1	nan	nan	nan	nan	nan	nan
		χ	($^\circ$)	1/1	26.7	0.0	...	26.7	26.7	26.7
	8.35	S	(Jy)	1/1	36.331	0.000	nan	36.331	36.331	36.331
		Π_l	(Jy)	1/1	0.650	0.000	nan	0.650	0.650	0.650
		$ \Pi_c $	(Jy)	0/1	nan	nan	nan	nan	nan	nan

Table A.1: continued.

Source	Freq. (GHz)	x	N_{sign}	$\langle x \rangle$	σ_x	mi (%)	median	min	max	
J1332-0509	2.64	m_l	(%)	7/24	1.5	0.6	35.8	1.5	0.8	2.2
		χ	($^\circ$)	7/7	47.8	15.1	...	52.6	40.0	95.9
		S	(Jy)	20/21	0.477	0.019	4.0	0.478	0.430	0.496
		Π_l	(Jy)	18/21	0.028	0.002	8.0	0.028	0.025	0.044
		m_l	(%)	18/21	5.8	0.6	9.7	5.8	5.4	10.3
	4.85	χ	($^\circ$)	18/18	-63.9	1.9	...	-64.3	-67.8	-57.3
		S	(Jy)	34/35	0.561	0.082	14.6	0.585	0.497	0.745
		Π_l	(Jy)	13/35	0.023	0.004	16.2	0.021	0.016	0.032
		$ \Pi_c $	(Jy)	3/35	0.004	0.001	33.4	0.005	0.003	0.006
		m_l	(%)	13/35	3.9	0.5	14.0	4.2	3.0	4.6
	8.35	$ m_c $	(%)	3/35	0.6	0.2	26.8	0.7	0.5	0.9
		χ	($^\circ$)	13/13	-58.3	11.2	...	-65.6	-83.5	-49.8
		S	(Jy)	27/30	0.746	0.178	23.9	0.798	0.582	1.106
		Π_l	(Jy)	24/30	0.022	0.006	28.5	0.022	0.015	0.038
		$ \Pi_c $	(Jy)	2/30	0.003	0.002	65.1	0.005	0.003	0.006
	10.45	m_l	(%)	24/30	2.5	1.0	39.0	3.2	1.4	4.0
$ m_c $		(%)	2/30	0.3	0.4	117.1	0.5	0.3	0.8	
χ		($^\circ$)	24/24	-75.6	22.5	...	-74.0	-93.5	-24.5	
S		(Jy)	21/21	0.704	0.135	19.2	0.694	0.602	1.226	
Π_l		(Jy)	3/21	0.024	0.006	27.6	0.021	0.019	0.031	
J1345+4452	2.64	m_l	(%)	3/21	3.1	0.2	6.7	3.0	2.8	3.2
		χ	($^\circ$)	3/3	-85.5	1.6	...	-85.4	-87.8	-84.7
		S	(Jy)	10/10	0.535	0.073	13.6	0.544	0.361	0.627
		Π_l	(Jy)	9/10	0.021	0.006	29.5	0.021	0.013	0.030
		m_l	(%)	9/10	4.0	1.0	23.9	3.8	2.7	5.6
	4.85	χ	($^\circ$)	9/9	54.1	10.1	...	50.7	46.1	70.4
		S	(Jy)	10/10	0.570	0.146	25.6	0.639	0.362	0.710
		Π_l	(Jy)	4/10	0.025	0.001	4.1	0.026	0.025	0.040
		$ \Pi_c $	(Jy)	0/10	nan	nan	nan	nan	nan	nan
		m_l	(%)	4/10	3.9	0.3	7.5	4.1	3.7	5.8
	8.35	$ m_c $	(%)	0/10	nan	nan	nan	nan	nan	nan
		χ	($^\circ$)	4/4	53.4	6.7	...	53.0	45.0	61.6
		S	(Jy)	10/10	0.587	0.169	28.8	0.713	0.380	0.798
		Π_l	(Jy)	8/10	0.020	0.004	18.8	0.020	0.009	0.038
		$ \Pi_c $	(Jy)	0/10	nan	nan	nan	nan	nan	nan
	10.45	m_l	(%)	8/10	3.0	0.7	23.5	3.1	1.9	5.1
$ m_c $		(%)	0/10	nan	nan	nan	nan	nan	nan	
χ		($^\circ$)	8/8	66.2	6.3	...	60.5	40.2	72.2	
S		(Jy)	9/10	0.613	0.160	26.1	0.708	0.379	0.791	
Π_l		(Jy)	1/10	0.023	0.000	nan	0.023	0.023	0.023	
J1354-1041	2.64	m_l	(%)	1/10	3.0	0.0	nan	3.0	3.0	3.0
		χ	($^\circ$)	1/1	71.6	0.0	...	71.6	71.6	71.6
		S	(Jy)	1/1	0.767	0.000	nan	0.767	0.767	0.767
		Π_l	(Jy)	1/1	0.035	0.000	nan	0.035	0.035	0.035

Table A.1: continued.

Source	Freq. (GHz)	x	N_{sign}	$\langle x \rangle$	σ_x	mi (%)	median	min	max
J1428+4240	4.85	m_l (%)	1/1	4.5	0.0	nan	4.5	4.5	4.5
		χ (°)	1/1	6.2	0.0	...	6.2	6.2	6.2
		S (Jy)	1/1	0.631	0.000	nan	0.631	0.631	0.631
		Π_l (Jy)	0/1	nan	nan	nan	nan	nan	nan
		$ \Pi_c $ (Jy)	0/1	nan	nan	nan	nan	nan	nan
		m_l (%)	0/1	nan	nan	nan	nan	nan	nan
	8.35	$ m_c $ (%)	0/1	nan	nan	nan	nan	nan	nan
		S (Jy)	1/1	0.598	0.000	nan	0.598	0.598	0.598
		Π_l (Jy)	1/1	0.027	0.000	nan	0.027	0.027	0.027
		$ \Pi_c $ (Jy)	0/1	nan	nan	nan	nan	nan	nan
		m_l (%)	1/1	4.6	0.0	nan	4.6	4.6	4.6
		$ m_c $ (%)	0/1	nan	nan	nan	nan	nan	nan
	10.45	χ (°)	1/1	1.2	0.0	...	1.2	1.2	1.2
		S (Jy)	1/1	0.588	0.000	nan	0.588	0.588	0.588
		Π_l (Jy)	1/1	0.023	0.000	nan	0.023	0.023	0.023
		m_l (%)	1/1	3.9	0.0	nan	3.9	3.9	3.9
		χ (°)	1/1	-8.6	0.0	...	-8.6	-8.6	-8.6
		S (Jy)	1/1	0.060	0.000	nan	0.060	0.060	0.060
J1504+1029	4.85	Π_l (Jy)	0/1	nan	nan	nan	nan	nan	nan
		$ \Pi_c $ (Jy)	0/1	nan	nan	nan	nan	nan	nan
		m_l (%)	0/1	nan	nan	nan	nan	nan	nan
		$ m_c $ (%)	0/1	nan	nan	nan	nan	nan	nan
	2.64	S (Jy)	24/25	1.085	0.079	7.2	1.111	0.928	1.312
		Π_l (Jy)	24/25	0.036	0.004	11.9	0.037	0.026	0.047
		m_l (%)	24/25	3.3	0.5	14.2	3.3	2.5	4.9
		χ (°)	24/24	27.9	4.6	...	28.1	21.2	39.4
	4.85	S (Jy)	41/43	1.086	0.147	13.5	1.090	0.795	1.296
		Π_l (Jy)	35/43	0.031	0.007	22.1	0.032	0.020	0.041
		$ \Pi_c $ (Jy)	2/43	0.003	0.001	29.3	0.003	0.002	0.004
		m_l (%)	34/43	2.9	0.6	21.5	3.0	1.8	3.8
		$ m_c $ (%)	2/43	0.2	0.1	39.7	0.3	0.2	0.3
		χ (°)	35/35	19.0	17.7	...	25.5	-43.5	40.4
	8.35	S (Jy)	42/42	1.190	0.202	17.0	1.200	0.762	1.414
		Π_l (Jy)	36/42	0.024	0.011	45.2	0.025	0.009	0.048
		$ \Pi_c $ (Jy)	3/42	0.005	0.001	25.5	0.005	0.004	0.006
		m_l (%)	36/42	1.9	0.9	46.4	2.2	0.7	4.0
		$ m_c $ (%)	3/42	0.4	0.1	30.2	0.4	0.3	0.5
		χ (°)	36/36	24.4	17.4	...	23.4	-28.5	52.0
	10.45	S (Jy)	23/24	1.225	0.202	16.5	1.277	0.717	1.479
		Π_l (Jy)	5/24	0.028	0.004	14.4	0.028	0.024	0.034
		m_l (%)	5/24	2.4	0.7	28.7	2.5	1.8	4.1
		χ (°)	5/5	19.7	7.5	...	22.7	10.4	27.2
J1505+0326	2.64	S (Jy)	24/25	0.430	0.076	17.6	0.433	0.286	0.609
		Π_l (Jy)	1/25	0.009	0.000	nan	0.009	0.009	0.009

Table A.1: continued.

Source	Freq. (GHz)	x	N_{sign}	$\langle x \rangle$	σ_x	mi (%)	median	min	max
J1512-0905	4.85	m_l (%)	1/25	1.4	0.0	nan	1.4	1.4	1.4
		χ (°)	1/1	60.1	0.0	...	60.1	60.1	60.1
		S (Jy)	40/44	0.562	0.079	14.1	0.505	0.391	0.696
		Π_l (Jy)	0/44	nan	nan	nan	nan	nan	nan
		$ \Pi_c $ (Jy)	0/44	nan	nan	nan	nan	nan	nan
		m_l (%)	0/44	nan	nan	nan	nan	nan	nan
	8.35	$ m_c $ (%)	0/44	nan	nan	nan	nan	nan	nan
		S (Jy)	37/41	0.514	0.088	17.2	0.499	0.410	0.694
		Π_l (Jy)	2/41	0.012	0.000	2.6	0.012	0.012	0.012
		$ \Pi_c $ (Jy)	0/41	nan	nan	nan	nan	nan	nan
		m_l (%)	3/41	1.8	1.3	73.2	2.2	0.0	2.5
		$ m_c $ (%)	0/41	nan	nan	nan	nan	nan	nan
	10.45	χ (°)	2/2	47.2	13.7	...	53.6	43.9	63.3
		S (Jy)	25/29	0.490	0.073	15.0	0.483	0.378	0.681
		Π_l (Jy)	0/29	nan	nan	nan	nan	nan	nan
		m_l (%)	0/29	nan	nan	nan	nan	nan	nan
		S (Jy)	22/23	2.125	0.871	41.0	2.569	1.405	3.737
		Π_l (Jy)	22/23	0.046	0.011	25.0	0.050	0.013	0.161
	2.64	m_l (%)	22/23	1.6	0.9	56.9	2.2	0.4	7.4
		χ (°)	22/22	63.8	10.9	...	66.4	-1.6	89.1
		S (Jy)	42/44	2.629	1.272	48.4	2.891	1.359	5.035
		Π_l (Jy)	36/44	0.051	0.026	51.2	0.065	0.025	0.170
		$ \Pi_c $ (Jy)	2/44	0.010	0.001	7.8	0.010	0.009	0.011
		m_l (%)	36/44	1.6	1.3	78.6	2.8	0.6	6.0
	4.85	$ m_c $ (%)	2/44	0.3	0.1	41.9	0.3	0.2	0.4
		χ (°)	36/36	43.1	24.7	...	55.8	-11.1	76.8
		S (Jy)	42/43	2.315	1.085	46.9	2.939	1.465	6.048
		Π_l (Jy)	42/43	0.051	0.028	54.3	0.069	0.012	0.155
		$ \Pi_c $ (Jy)	5/43	0.009	0.007	70.4	0.014	0.006	0.028
		m_l (%)	42/43	2.0	0.8	37.9	2.4	0.6	5.5
	8.35	$ m_c $ (%)	5/43	0.4	0.2	39.5	0.5	0.3	0.7
		χ (°)	42/42	47.9	32.1	...	58.9	-45.3	93.7
		S (Jy)	26/28	1.973	0.850	43.1	3.015	1.525	6.283
		Π_l (Jy)	11/28	0.064	0.027	42.2	0.058	0.031	0.114
		m_l (%)	11/28	2.4	0.8	33.6	2.4	1.0	3.6
		χ (°)	11/11	38.3	14.2	...	41.3	-19.5	69.8
J1522+3144	2.64	S (Jy)	24/25	0.488	0.020	4.2	0.489	0.445	0.541
		Π_l (Jy)	5/25	0.007	0.000	6.4	0.007	0.007	0.008
		m_l (%)	5/25	1.4	0.1	6.7	1.4	1.3	1.6
		χ (°)	5/5	-21.4	12.3	...	-18.0	-33.0	-5.9
	4.85	S (Jy)	37/38	0.485	0.031	6.3	0.492	0.418	0.548
		Π_l (Jy)	0/38	nan	nan	nan	nan	nan	nan
		$ \Pi_c $ (Jy)	1/38	0.004	0.000	nan	0.004	0.004	0.004
		m_l (%)	0/38	nan	nan	nan	nan	nan	nan

Table A.1: continued.

Source	Freq. (GHz)	x	N_{sign}	$\langle x \rangle$	σ_x	mi (%)	median	min	max
J1542+6129	8.35	$ m_c $ (%)	1/38	0.8	0.0	nan	0.8	0.8	0.8
		S (Jy)	38/38	0.464	0.035	7.6	0.486	0.364	0.576
		Π_l (Jy)	2/38	0.009	0.001	12.4	0.009	0.008	0.009
		$ \Pi_c $ (Jy)	1/38	0.004	0.000	nan	0.004	0.004	0.004
		m_l (%)	3/38	1.2	1.0	87.3	1.6	0.0	1.9
	10.45	$ m_c $ (%)	1/38	0.8	0.0	nan	0.8	0.8	0.8
		χ (°)	2/2	-46.7	1.4	...	-47.1	-48.1	-46.1
		S (Jy)	21/24	0.452	0.038	8.4	0.449	0.403	0.523
		Π_l (Jy)	0/24	nan	nan	nan	nan	nan	nan
		m_l (%)	0/24	nan	nan	nan	nan	nan	nan
	2.64	S (Jy)	1/1	0.135	0.000	nan	0.135	0.135	0.135
		Π_l (Jy)	0/1	nan	nan	nan	nan	nan	nan
		m_l (%)	0/1	nan	nan	nan	nan	nan	nan
	4.85	S (Jy)	2/2	0.133	0.011	8.5	0.133	0.125	0.141
		Π_l (Jy)	0/2	nan	nan	nan	nan	nan	nan
		$ \Pi_c $ (Jy)	0/2	nan	nan	nan	nan	nan	nan
		m_l (%)	0/2	nan	nan	nan	nan	nan	nan
		$ m_c $ (%)	0/2	nan	nan	nan	nan	nan	nan
J1553+1256	8.35	S (Jy)	1/1	0.160	0.000	nan	0.160	0.160	0.160
		Π_l (Jy)	0/1	nan	nan	nan	nan	nan	nan
		$ \Pi_c $ (Jy)	0/1	nan	nan	nan	nan	nan	nan
		m_l (%)	0/1	nan	nan	nan	nan	nan	nan
		$ m_c $ (%)	0/1	nan	nan	nan	nan	nan	nan
	10.45	S (Jy)	1/1	0.161	0.000	nan	0.161	0.161	0.161
		Π_l (Jy)	0/1	nan	nan	nan	nan	nan	nan
		m_l (%)	0/1	nan	nan	nan	nan	nan	nan
	2.64	S (Jy)	10/10	1.034	0.039	3.7	1.032	0.981	1.105
		Π_l (Jy)	10/10	0.029	0.002	7.9	0.028	0.026	0.033
		m_l (%)	10/10	2.8	0.3	9.2	2.7	2.5	3.2
	4.85	χ (°)	10/10	81.1	3.8	...	81.4	74.6	89.0
		S (Jy)	17/17	0.926	0.109	11.7	0.961	0.772	1.030
		Π_l (Jy)	14/17	0.024	0.005	18.9	0.028	0.020	0.042
		$ \Pi_c $ (Jy)	0/17	nan	nan	nan	nan	nan	nan
		m_l (%)	14/17	2.9	0.3	12.0	3.1	2.5	4.3
	8.35	$ m_c $ (%)	0/17	nan	nan	nan	nan	nan	nan
		χ (°)	14/14	89.4	6.7	...	77.2	64.5	100.1
		S (Jy)	17/17	0.950	0.088	9.3	0.921	0.601	0.977
		Π_l (Jy)	15/17	0.023	0.008	33.5	0.026	0.013	0.035
		$ \Pi_c $ (Jy)	0/17	nan	nan	nan	nan	nan	nan
	10.45	m_l (%)	15/17	2.6	0.8	30.4	2.8	1.4	3.7
		$ m_c $ (%)	0/17	nan	nan	nan	nan	nan	nan
		χ (°)	15/15	81.3	16.2	...	77.9	49.8	94.7
		S (Jy)	11/11	0.907	0.048	5.3	0.914	0.671	0.982
		Π_l (Jy)	2/11	0.016	0.001	8.9	0.016	0.015	0.017

Table A.1: continued.

Source	Freq. (GHz)	x	N_{sign}	$\langle x \rangle$	σ_x	mi (%)	median	min	max
J1555+1111	4.85	m_l (%)	2/11	1.9	0.6	34.1	2.1	1.7	2.6
		χ (°)	2/2	70.5	22.2	...	71.9	56.2	87.6
		S (Jy)	5/5	0.229	0.012	5.4	0.233	0.211	0.257
		Π_l (Jy)	0/5	nan	nan	nan	nan	nan	nan
		$ \Pi_c $ (Jy)	0/5	nan	nan	nan	nan	nan	nan
		m_l (%)	0/5	nan	nan	nan	nan	nan	nan
	8.35	$ m_c $ (%)	0/5	nan	nan	nan	nan	nan	nan
		S (Jy)	5/5	0.224	0.009	3.8	0.225	0.206	0.261
		Π_l (Jy)	0/5	nan	nan	nan	nan	nan	nan
		$ \Pi_c $ (Jy)	0/5	nan	nan	nan	nan	nan	nan
		m_l (%)	0/5	nan	nan	nan	nan	nan	nan
J1635+3808	2.64	$ m_c $ (%)	0/5	nan	nan	nan	nan	nan	nan
		S (Jy)	23/24	2.996	0.153	5.1	3.034	2.877	3.588
		Π_l (Jy)	22/24	0.030	0.010	32.9	0.031	0.008	0.062
		m_l (%)	22/24	0.9	0.4	39.8	1.1	0.2	2.0
		χ (°)	22/22	-136.9	7.4	...	-134.5	-150.1	-86.2
		S (Jy)	46/46	3.351	0.451	13.5	3.272	2.607	3.876
	4.85	Π_l (Jy)	31/46	0.026	0.010	39.9	0.026	0.013	0.077
		$ \Pi_c $ (Jy)	1/46	0.005	0.000	nan	0.005	0.005	0.005
		m_l (%)	31/46	0.8	0.3	41.1	0.8	0.4	2.2
		$ m_c $ (%)	1/46	0.2	0.0	nan	0.2	0.2	0.2
		χ (°)	31/31	-26.9	41.2	...	31.5	-45.1	69.2
	8.35	S (Jy)	44/45	3.206	0.433	13.5	3.361	2.520	4.185
		Π_l (Jy)	37/45	0.030	0.015	50.8	0.032	0.013	0.083
		$ \Pi_c $ (Jy)	7/45	0.004	0.003	73.3	0.008	0.003	0.023
		m_l (%)	37/45	0.9	0.4	43.4	1.1	0.4	2.0
		$ m_c $ (%)	7/45	0.1	0.1	79.0	0.3	0.1	0.7
	10.45	χ (°)	37/37	69.1	40.6	...	49.2	-61.6	115.3
		S (Jy)	31/32	3.409	0.538	15.8	3.614	2.535	4.275
		Π_l (Jy)	13/32	0.051	0.027	54.2	0.050	0.016	0.101
		m_l (%)	13/32	1.4	0.7	49.0	1.3	0.4	2.5
		χ (°)	13/13	-77.4	16.2	...	-79.7	-116.1	-25.4
J1642+3948	2.64	S (Jy)	22/24	7.523	0.225	3.0	7.613	7.025	8.011
		Π_l (Jy)	22/24	0.288	0.033	11.6	0.311	0.246	0.348
		m_l (%)	22/24	3.8	0.5	12.8	4.2	3.2	4.6
		χ (°)	22/22	57.5	2.6	...	57.5	54.2	68.6
	4.85	S (Jy)	38/38	7.206	0.256	3.5	7.184	5.982	7.659
		Π_l (Jy)	38/38	0.245	0.037	15.2	0.236	0.163	0.314
		$ \Pi_c $ (Jy)	2/38	0.008	0.010	126.8	0.013	0.006	0.020
		m_l (%)	38/38	3.4	0.5	15.2	3.3	2.2	4.5
		$ m_c $ (%)	2/38	0.1	0.1	128.8	0.2	0.1	0.3
	8.35	χ (°)	38/38	48.3	3.5	...	48.8	41.2	56.6
		S (Jy)	35/35	6.658	0.301	4.5	6.734	4.803	7.812
		Π_l (Jy)	34/35	0.191	0.047	24.8	0.236	0.131	0.308

Table A.1: continued.

Source	Freq. (GHz)	x	N_{sign}	$\langle x \rangle$	σ_x	mi (%)	median	min	max
J1653+3945	10.45	$ \Pi_c $ (Jy)	13/35	0.020	0.006	27.8	0.022	0.013	0.039
		m_l (%)	34/35	2.9	0.7	24.7	3.5	1.9	4.2
		$ m_c $ (%)	13/35	0.3	0.1	27.1	0.3	0.2	0.6
		χ ($^\circ$)	34/34	54.0	6.4	...	54.7	42.2	67.7
		S (Jy)	26/28	6.549	0.317	4.8	6.576	5.740	7.309
		Π_l (Jy)	18/28	0.208	0.052	25.1	0.240	0.111	0.296
		m_l (%)	18/28	3.2	0.7	23.0	3.6	1.8	4.8
		χ ($^\circ$)	18/18	51.4	9.7	...	51.6	40.6	67.4
		S (Jy)	23/24	1.541	0.040	2.6	1.550	1.447	1.597
		Π_l (Jy)	22/24	0.033	0.004	13.1	0.033	0.026	0.046
	2.64	m_l (%)	22/24	2.2	0.3	13.4	2.1	1.7	3.1
		χ ($^\circ$)	22/22	-3.6	4.9	...	-3.4	-21.4	7.1
		S (Jy)	45/46	1.457	0.026	1.8	1.456	1.395	1.543
		Π_l (Jy)	36/46	0.027	0.002	7.1	0.028	0.022	0.035
		$ \Pi_c $ (Jy)	0/46	nan	nan	nan	nan	nan	nan
		m_l (%)	36/46	1.9	0.1	7.9	1.9	1.4	2.4
		$ m_c $ (%)	0/46	nan	nan	nan	nan	nan	nan
		χ ($^\circ$)	36/36	-9.9	4.2	...	-11.4	-23.5	-2.8
		S (Jy)	43/44	1.307	0.029	2.2	1.313	1.181	1.443
		Π_l (Jy)	38/44	0.022	0.006	28.0	0.023	0.013	0.050
	8.35	$ \Pi_c $ (Jy)	1/44	0.007	0.000	nan	0.007	0.007	0.007
		m_l (%)	38/44	1.6	0.5	27.5	1.7	1.0	3.7
		$ m_c $ (%)	1/44	0.5	0.0	nan	0.5	0.5	0.5
		χ ($^\circ$)	38/38	-11.5	6.0	...	-12.2	-34.2	-5.5
		S (Jy)	29/29	1.237	0.052	4.2	1.246	1.053	1.325
		Π_l (Jy)	5/29	0.020	0.002	10.0	0.021	0.018	0.023
		m_l (%)	5/29	1.6	0.3	17.3	1.6	1.4	2.1
		χ ($^\circ$)	5/5	-31.9	19.8	...	-23.4	-59.6	-14.2
		S (Jy)	23/23	4.434	0.235	5.3	4.445	3.984	4.792
		Π_l (Jy)	23/23	0.192	0.019	9.8	0.187	0.151	0.219
J1733-1304	2.64	m_l (%)	23/23	4.3	0.4	9.7	4.3	3.2	5.0
		χ ($^\circ$)	23/23	24.6	2.3	...	24.2	18.9	30.0
		S (Jy)	33/34	4.481	0.169	3.8	4.600	4.121	5.326
		Π_l (Jy)	33/34	0.138	0.021	15.1	0.142	0.095	0.181
		$ \Pi_c $ (Jy)	0/34	nan	nan	nan	nan	nan	nan
		m_l (%)	33/34	3.0	0.5	15.5	3.1	2.1	4.1
		$ m_c $ (%)	0/34	nan	nan	nan	nan	nan	nan
		χ ($^\circ$)	33/33	48.8	8.3	...	50.8	36.7	61.9
		S (Jy)	32/33	4.839	0.254	5.3	4.796	3.713	5.435
		Π_l (Jy)	32/33	0.103	0.021	19.9	0.113	0.058	0.150
	4.85	$ \Pi_c $ (Jy)	2/33	0.019	0.001	5.8	0.019	0.019	0.020
		m_l (%)	32/33	2.1	0.4	20.7	2.2	1.3	3.4
		$ m_c $ (%)	2/33	0.4	0.0	5.8	0.4	0.3	0.4
		χ ($^\circ$)	32/32	61.1	10.1	...	59.0	35.8	78.6
		S (Jy)	32/33	4.839	0.254	5.3	4.796	3.713	5.435
		Π_l (Jy)	32/33	0.103	0.021	19.9	0.113	0.058	0.150
		$ \Pi_c $ (Jy)	2/33	0.019	0.001	5.8	0.019	0.019	0.020
		m_l (%)	32/33	2.1	0.4	20.7	2.2	1.3	3.4
		$ m_c $ (%)	2/33	0.4	0.0	5.8	0.4	0.3	0.4
		χ ($^\circ$)	32/32	61.1	10.1	...	59.0	35.8	78.6

Table A.1: continued.

Source	Freq. (GHz)	x		N _{sign}	$\langle x \rangle$	σ_x	mi (%)	median	min	max
J1751+0939	10.45	S	(Jy)	22/23	4.943	0.300	6.1	4.826	3.985	5.421
		Π_l	(Jy)	8/23	0.119	0.021	17.8	0.119	0.085	0.154
		m_l	(%)	8/23	2.4	0.4	18.1	2.6	1.8	3.1
		χ	($^\circ$)	8/8	58.3	6.6	...	54.5	52.5	67.5
	2.64	S	(Jy)	24/25	2.004	0.469	23.4	2.098	1.403	3.404
		Π_l	(Jy)	24/25	0.061	0.038	63.1	0.058	0.015	0.145
		m_l	(%)	24/25	2.9	1.3	45.0	2.5	0.8	4.6
		χ	($^\circ$)	24/24	-30.8	15.8	...	-16.0	-48.7	38.5
	4.85	S	(Jy)	46/46	2.455	0.669	27.3	2.643	1.597	4.340
		Π_l	(Jy)	46/46	0.053	0.034	64.7	0.068	0.023	0.252
		$ \Pi_c $	(Jy)	7/46	0.011	0.004	32.8	0.012	0.007	0.022
		m_l	(%)	46/46	2.1	1.3	61.2	2.6	0.9	6.8
		$ m_c $	(%)	7/46	0.4	0.1	26.6	0.4	0.3	0.7
		χ	($^\circ$)	46/46	-43.0	26.9	...	-51.2	-99.0	0.0
		S	(Jy)	44/44	3.026	0.683	22.6	3.050	1.825	5.751
		Π_l	(Jy)	42/44	0.087	0.057	65.4	0.100	0.019	0.416
		$ \Pi_c $	(Jy)	4/44	0.010	0.007	75.0	0.013	0.007	0.039
		m_l	(%)	42/44	2.9	1.5	51.8	3.2	0.5	10.2
		$ m_c $	(%)	4/44	0.3	0.2	51.8	0.3	0.2	0.9
		χ	($^\circ$)	42/42	-66.8	34.6	...	-65.8	-189.6	-2.4
	8.35	S	(Jy)	44/44	3.026	0.683	22.6	3.050	1.825	5.751
		Π_l	(Jy)	42/44	0.087	0.057	65.4	0.100	0.019	0.416
		$ \Pi_c $	(Jy)	4/44	0.010	0.007	75.0	0.013	0.007	0.039
		m_l	(%)	42/44	2.9	1.5	51.8	3.2	0.5	10.2
	10.45	S	(Jy)	26/29	3.380	1.056	31.2	3.276	2.428	6.166
		Π_l	(Jy)	16/29	0.134	0.073	54.8	0.123	0.024	0.481
		m_l	(%)	16/29	3.3	1.7	53.0	3.3	0.8	7.8
		χ	($^\circ$)	16/16	251.7	63.8	...	268.6	48.4	325.7
J1800+7828	2.64	S	(Jy)	18/19	2.277	0.210	9.2	2.283	1.903	2.638
		Π_l	(Jy)	16/19	0.085	0.030	35.3	0.087	0.039	0.122
		m_l	(%)	16/19	3.8	1.2	32.0	4.1	1.8	5.3
		χ	($^\circ$)	16/16	30.9	9.4	...	34.2	-0.1	40.9
	4.85	S	(Jy)	24/24	2.519	0.182	7.2	2.526	2.068	2.941
		Π_l	(Jy)	21/24	0.110	0.027	24.3	0.096	0.057	0.149
		$ \Pi_c $	(Jy)	1/24	0.013	0.000	nan	0.013	0.013	0.013
		m_l	(%)	21/24	4.6	1.2	26.5	3.7	2.4	6.3
		$ m_c $	(%)	1/24	0.5	0.0	nan	0.5	0.5	0.5
		χ	($^\circ$)	21/21	74.8	10.6	...	70.8	29.9	84.9
		S	(Jy)	24/24	2.768	0.162	5.8	2.730	2.180	3.230
		Π_l	(Jy)	23/24	0.099	0.055	55.4	0.116	0.037	0.200
		$ \Pi_c $	(Jy)	8/24	0.009	0.002	19.9	0.009	0.007	0.014
		m_l	(%)	23/24	3.6	1.9	52.6	4.8	1.3	7.4
		$ m_c $	(%)	8/24	0.3	0.1	15.3	0.3	0.3	0.5
		χ	($^\circ$)	23/23	-97.6	14.8	...	-95.1	-145.6	-81.5
	10.45	S	(Jy)	19/21	2.734	0.258	9.4	2.713	2.061	3.303
		Π_l	(Jy)	4/21	0.089	0.016	17.5	0.088	0.073	0.105
		m_l	(%)	4/21	3.3	0.4	12.9	3.5	2.9	4.2
		χ	($^\circ$)	4/4	60.9	28.5	...	47.7	-0.1	101.8

Table A.1: continued.

Source	Freq. (GHz)	x		N _{sign}	$\langle x \rangle$	σ_x	mi (%)	median	min	max
J1806+6949	2.64	S	(Jy)	2/3	1.833	0.058	3.2	1.843	1.802	1.884
		Π_l	(Jy)	2/3	0.044	0.001	2.0	0.044	0.043	0.045
		m_l	(%)	2/3	2.4	0.0	1.2	2.4	2.4	2.4
		χ	($^\circ$)	2/2	-6.3	0.6	...	-6.2	-6.6	-5.7
	4.85	S	(Jy)	5/5	1.825	0.034	1.9	1.815	1.784	1.846
		Π_l	(Jy)	4/5	0.024	0.001	4.4	0.024	0.023	0.026
		$ \Pi_c $	(Jy)	1/5	0.006	0.000	nan	0.006	0.006	0.006
		m_l	(%)	4/5	1.3	0.1	4.6	1.3	1.2	1.4
		$ m_c $	(%)	1/5	0.3	0.0	nan	0.3	0.3	0.3
		χ	($^\circ$)	4/4	-4.6	12.6	...	8.2	-8.5	12.3
		S	(Jy)	5/5	1.758	0.022	1.2	1.721	1.594	1.774
	8.35	Π_l	(Jy)	5/5	0.050	0.008	15.3	0.048	0.044	0.057
		$ \Pi_c $	(Jy)	0/5	nan	nan	nan	nan	nan	nan
		m_l	(%)	5/5	2.8	0.4	15.6	3.0	2.5	3.2
		$ m_c $	(%)	0/5	nan	nan	nan	nan	nan	nan
		χ	($^\circ$)	5/5	-4.6	0.8	...	-5.0	-5.5	-2.2
	10.45	S	(Jy)	3/5	1.709	0.081	4.7	1.711	1.628	1.755
		Π_l	(Jy)	1/5	0.033	0.000	nan	0.033	0.033	0.033
		m_l	(%)	1/5	1.9	0.0	nan	1.9	1.9	1.9
		χ	($^\circ$)	1/1	-16.2	0.0	...	-16.2	-16.2	-16.2
J1824+5651	2.64	S	(Jy)	2/2	1.307	0.047	3.6	1.315	1.281	1.348
		Π_l	(Jy)	2/2	0.030	0.002	7.4	0.031	0.029	0.032
		m_l	(%)	2/2	2.2	0.3	11.3	2.3	2.2	2.5
		χ	($^\circ$)	2/2	48.3	1.7	...	47.9	46.7	49.1
	4.85	S	(Jy)	2/2	1.407	0.036	2.6	1.425	1.399	1.450
		Π_l	(Jy)	2/2	0.076	0.014	18.5	0.068	0.058	0.078
		$ \Pi_c $	(Jy)	0/2	nan	nan	nan	nan	nan	nan
		m_l	(%)	2/2	5.3	0.9	16.4	4.8	4.2	5.4
		$ m_c $	(%)	0/2	nan	nan	nan	nan	nan	nan
		χ	($^\circ$)	2/2	37.7	3.9	...	35.2	32.5	38.0
		S	(Jy)	2/2	1.446	0.062	4.3	1.481	1.437	1.524
	8.35	Π_l	(Jy)	2/2	0.104	0.004	3.9	0.107	0.104	0.109
		$ \Pi_c $	(Jy)	0/2	nan	nan	nan	nan	nan	nan
		m_l	(%)	2/2	7.2	0.0	0.3	7.2	7.2	7.2
		$ m_c $	(%)	0/2	nan	nan	nan	nan	nan	nan
		χ	($^\circ$)	2/2	22.9	1.1	...	23.4	22.6	24.1
	10.45	S	(Jy)	2/3	1.448	0.069	4.7	1.490	1.441	1.538
		Π_l	(Jy)	1/3	0.113	0.000	nan	0.113	0.113	0.113
		m_l	(%)	1/3	7.8	0.0	nan	7.8	7.8	7.8
J1848+3219	2.64	S	(Jy)	23/24	0.647	0.245	37.9	0.601	0.382	1.421
		Π_l	(Jy)	14/24	0.012	0.006	50.6	0.011	0.007	0.037
		m_l	(%)	14/24	1.9	0.5	24.5	1.8	1.2	2.9
		χ	($^\circ$)	14/14	-15.6	14.0	...	-8.4	-36.9	0.3
	4.85	S	(Jy)	41/42	0.655	0.286	43.6	0.664	0.256	1.618

Table A.1: continued.

Source	Freq. (GHz)	x	N_{sign}	$\langle x \rangle$	σ_x	mi (%)	median	min	max
J1849+6705	8.35	Π_l (Jy)	7/42	0.015	0.007	44.1	0.022	0.012	0.031
		$ \Pi_c $ (Jy)	0/42	nan	nan	nan	nan	nan	nan
		m_l (%)	8/42	1.2	0.7	60.9	1.5	0.0	2.4
		$ m_c $ (%)	0/42	nan	nan	nan	nan	nan	nan
		χ ($^\circ$)	7/7	53.3	9.3	...	51.4	29.6	60.9
		S (Jy)	41/42	0.666	0.217	32.6	0.813	0.325	1.710
		Π_l (Jy)	13/42	0.016	0.011	66.7	0.020	0.009	0.062
		$ \Pi_c $ (Jy)	1/42	0.010	0.000	nan	0.010	0.010	0.010
		m_l (%)	14/42	1.3	0.8	58.4	1.9	0.0	4.2
		$ m_c $ (%)	1/42	0.7	0.0	nan	0.7	0.7	0.7
	10.45	χ ($^\circ$)	13/13	6.2	28.5	...	24.1	-19.5	94.6
		S (Jy)	26/29	0.772	0.217	28.2	0.805	0.527	1.700
		Π_l (Jy)	5/29	0.034	0.013	37.6	0.030	0.021	0.051
		m_l (%)	5/29	2.3	0.6	26.6	2.2	1.5	3.0
		χ ($^\circ$)	5/5	127.7	32.1	...	129.0	30.7	158.9
	2.64	S (Jy)	19/20	0.673	0.132	19.7	0.793	0.503	0.985
		Π_l (Jy)	13/20	0.022	0.006	28.8	0.023	0.011	0.031
		m_l (%)	13/20	3.0	0.5	15.4	3.0	1.7	3.5
		χ ($^\circ$)	13/13	-58.0	87.3	...	-101.9	-146.8	86.0
		S (Jy)	27/27	1.134	0.188	16.6	1.213	0.671	1.477
	4.85	Π_l (Jy)	18/27	0.020	0.005	27.0	0.024	0.011	0.036
		$ \Pi_c $ (Jy)	0/27	nan	nan	nan	nan	nan	nan
		m_l (%)	18/27	1.8	0.7	39.5	2.1	0.9	3.0
		$ m_c $ (%)	0/27	nan	nan	nan	nan	nan	nan
		χ ($^\circ$)	18/18	54.3	29.6	...	37.3	-83.9	84.3
	8.35	S (Jy)	26/27	1.454	0.409	28.1	1.682	0.791	2.118
		Π_l (Jy)	21/27	0.037	0.017	44.9	0.026	0.013	0.064
		$ \Pi_c $ (Jy)	0/27	nan	nan	nan	nan	nan	nan
		m_l (%)	21/27	2.1	0.9	42.5	2.4	0.7	5.0
		$ m_c $ (%)	0/27	nan	nan	nan	nan	nan	nan
	10.45	χ ($^\circ$)	21/21	-158.7	36.3	...	-135.2	-181.5	-29.3
		S (Jy)	18/22	1.333	0.489	36.7	1.577	0.801	2.330
		Π_l (Jy)	4/22	0.067	0.035	52.4	0.057	0.025	0.104
		m_l (%)	4/22	3.8	0.8	21.9	3.2	3.0	4.5
		χ ($^\circ$)	4/4	11.0	23.3	...	32.1	3.7	70.7
J1959+6508	4.85	S (Jy)	2/2	0.300	0.006	1.9	0.296	0.292	0.300
		Π_l (Jy)	0/2	nan	nan	nan	nan	nan	nan
		$ \Pi_c $ (Jy)	0/2	nan	nan	nan	nan	nan	nan
		m_l (%)	0/2	nan	nan	nan	nan	nan	nan
		$ m_c $ (%)	0/2	nan	nan	nan	nan	nan	nan
	8.35	S (Jy)	2/2	0.273	0.037	13.5	0.247	0.221	0.273
		Π_l (Jy)	0/2	nan	nan	nan	nan	nan	nan
		$ \Pi_c $ (Jy)	0/2	nan	nan	nan	nan	nan	nan
		m_l (%)	0/2	nan	nan	nan	nan	nan	nan

Table A.1: continued.

Source	Freq. (GHz)	x	N_{sign}	$\langle x \rangle$	σ_x	mi (%)	median	min	max
J2025-0735	2.64	$ m_c $	(%)	0/2	nan	nan	nan	nan	nan
		S	(Jy)	24/24	1.037	0.137	13.2	1.004	0.912
		Π_l	(Jy)	22/24	0.042	0.005	12.5	0.040	0.028
		m_l	(%)	22/24	4.0	0.7	16.3	4.0	2.1
	4.85	χ	($^\circ$)	22/22	22.7	3.9	...	22.4	11.0
		S	(Jy)	35/37	0.955	0.265	27.7	1.272	0.749
		Π_l	(Jy)	24/37	0.025	0.006	23.9	0.030	0.019
		$ \Pi_c $	(Jy)	1/37	0.004	0.000	nan	0.004	0.004
	8.35	m_l	(%)	24/37	1.9	1.0	53.8	2.3	1.3
		$ m_c $	(%)	1/37	0.3	0.0	nan	0.3	0.3
		χ	($^\circ$)	24/24	49.2	5.9	...	56.4	43.9
		S	(Jy)	37/37	1.290	0.305	23.6	1.318	0.793
	10.45	Π_l	(Jy)	34/37	0.031	0.014	47.2	0.036	0.015
		$ \Pi_c $	(Jy)	1/37	0.009	0.000	nan	0.009	0.009
		m_l	(%)	34/37	2.5	0.9	37.6	2.9	1.1
		$ m_c $	(%)	1/37	1.2	0.0	nan	1.2	1.2
J2143+1743	2.64	χ	($^\circ$)	34/34	73.8	11.3	...	74.2	55.4
		S	(Jy)	26/30	1.269	0.245	19.3	1.295	0.837
		Π_l	(Jy)	10/30	0.051	0.016	30.4	0.054	0.031
		m_l	(%)	10/30	3.5	0.6	17.4	3.4	2.7
	4.85	χ	($^\circ$)	10/10	74.7	5.9	...	73.4	60.7
		S	(Jy)	24/26	0.854	0.161	18.8	0.905	0.539
		Π_l	(Jy)	1/26	0.006	0.000	nan	0.006	0.006
		m_l	(%)	1/26	0.6	0.0	nan	0.6	0.6
	8.35	χ	($^\circ$)	1/1	-79.4	0.0	...	-79.4	-79.4
		S	(Jy)	39/40	0.869	0.166	19.1	0.872	0.630
		Π_l	(Jy)	0/40	nan	nan	nan	nan	nan
		$ \Pi_c $	(Jy)	2/40	0.004	0.002	52.8	0.004	0.003
	10.45	m_l	(%)	0/40	nan	nan	nan	nan	nan
		$ m_c $	(%)	2/40	0.4	0.1	19.5	0.4	0.4
		S	(Jy)	39/40	0.927	0.219	23.6	0.899	0.645
		Π_l	(Jy)	0/40	nan	nan	nan	nan	nan
J2147+0929	2.64	$ \Pi_c $	(Jy)	1/40	0.003	0.000	nan	0.003	0.003
		m_l	(%)	0/40	nan	nan	nan	nan	nan
		$ m_c $	(%)	1/40	0.4	0.0	nan	0.4	0.4
		S	(Jy)	32/34	0.886	0.213	24.1	0.895	0.673
	4.85	Π_l	(Jy)	1/34	0.018	0.000	nan	0.018	0.018
		m_l	(%)	1/34	2.4	0.0	nan	2.4	2.4
		χ	($^\circ$)	1/1	-64.9	0.0	...	-64.9	-64.9
		S	(Jy)	26/28	0.728	0.037	5.1	0.718	0.630
	10.45	Π_l	(Jy)	14/28	0.008	0.001	17.2	0.008	0.007
		m_l	(%)	14/28	1.1	0.2	21.4	1.1	0.9

Table A.1: continued.

Source	Freq. (GHz)	x	N_{sign}	$\langle x \rangle$	σ_x	mi (%)	median	min	max
J2158-3013	8.35	Π_l (Jy)	19/44	0.017	0.005	30.8	0.018	0.014	0.033
		$ \Pi_c $ (Jy)	1/44	0.005	0.000	nan	0.005	0.005	0.005
		m_l (%)	19/44	2.6	0.7	28.5	3.0	1.8	4.6
		$ m_c $ (%)	1/44	0.8	0.0	nan	0.8	0.8	0.8
		χ ($^\circ$)	19/19	79.4	9.7	...	75.6	62.1	93.2
		S (Jy)	41/42	0.657	0.125	19.1	0.625	0.486	1.117
		Π_l (Jy)	35/42	0.012	0.007	56.6	0.015	0.008	0.039
		$ \Pi_c $ (Jy)	0/42	nan	nan	nan	nan	nan	nan
		m_l (%)	37/42	1.4	1.1	75.0	2.4	0.0	3.9
		$ m_c $ (%)	0/42	nan	nan	nan	nan	nan	nan
	10.45	χ ($^\circ$)	35/35	30.7	12.7	...	25.2	10.5	48.1
		S (Jy)	25/31	0.653	0.171	26.3	0.688	0.465	0.993
		Π_l (Jy)	0/31	nan	nan	nan	nan	nan	nan
		m_l (%)	0/31	nan	nan	nan	nan	nan	nan
	2.64	S (Jy)	17/17	0.464	0.031	6.6	0.453	0.408	0.534
		Π_l (Jy)	3/17	0.014	0.002	13.4	0.013	0.013	0.016
		m_l (%)	3/17	3.0	0.1	2.3	3.0	2.9	3.1
		χ ($^\circ$)	3/3	-27.1	12.6	...	-20.6	-40.5	-18.2
	4.85	S (Jy)	3/27	0.374	0.034	9.0	0.374	0.358	0.415
		Π_l (Jy)	0/27	nan	nan	nan	nan	nan	nan
		$ \Pi_c $ (Jy)	0/27	nan	nan	nan	nan	nan	nan
		m_l (%)	0/27	nan	nan	nan	nan	nan	nan
	8.35	$ m_c $ (%)	0/27	nan	nan	nan	nan	nan	nan
		S (Jy)	5/26	0.232	0.100	42.9	0.391	0.211	0.452
		Π_l (Jy)	0/26	nan	nan	nan	nan	nan	nan
		$ \Pi_c $ (Jy)	0/26	nan	nan	nan	nan	nan	nan
	10.45	m_l (%)	0/26	nan	nan	nan	nan	nan	nan
		$ m_c $ (%)	0/26	nan	nan	nan	nan	nan	nan
		S (Jy)	14/17	0.367	0.038	10.3	0.376	0.311	0.452
		Π_l (Jy)	0/17	nan	nan	nan	nan	nan	nan
	2.64	m_l (%)	0/17	nan	nan	nan	nan	nan	nan
		S (Jy)	26/28	4.478	1.029	23.0	4.264	3.277	7.472
		Π_l (Jy)	26/28	0.490	0.259	52.8	0.461	0.265	1.413
		m_l (%)	26/28	11.8	3.4	28.9	10.6	7.2	19.8
J2202+4216	4.85	χ ($^\circ$)	26/26	42.5	3.8	...	43.5	35.6	48.6
		S (Jy)	53/54	4.591	0.823	17.9	4.951	3.179	8.034
		Π_l (Jy)	53/54	0.299	0.234	78.1	0.419	0.061	1.295
		$ \Pi_c $ (Jy)	3/54	0.011	0.007	63.3	0.015	0.007	0.045
	8.35	m_l (%)	53/54	7.4	4.3	58.4	8.9	1.4	17.3
		$ m_c $ (%)	3/54	0.3	0.1	36.9	0.3	0.2	0.6
		χ ($^\circ$)	53/53	-31.9	4.4	...	-32.2	-37.9	-0.9
		S (Jy)	54/54	5.443	1.301	23.9	5.329	3.091	8.871
	8.35	Π_l (Jy)	54/54	0.297	0.275	92.7	0.569	0.072	1.545
		$ \Pi_c $ (Jy)	16/54	0.030	0.011	35.5	0.024	0.009	0.036

Table A.1: continued.

Source	Freq. (GHz)	x	N_{sign}	$\langle x \rangle$	σ_x	mi (%)	median	min	max
J2203+1725	10.45	m_l (%)	54/54	7.2	4.3	59.4	10.2	1.8	18.6
		$ m_c $ (%)	16/54	0.5	0.1	20.0	0.4	0.2	0.6
		χ ($^\circ$)	54/54	1.6	3.2	...	1.4	-16.8	22.2
		S (Jy)	28/34	6.175	1.568	25.4	6.995	3.881	10.350
		Π_l (Jy)	26/34	0.629	0.308	49.0	0.640	0.310	1.183
		m_l (%)	26/34	9.6	3.5	37.1	8.9	4.8	15.7
	2.64	χ ($^\circ$)	26/26	2.1	4.1	...	3.1	-13.4	11.2
		S (Jy)	15/15	0.954	0.112	11.7	1.017	0.807	1.160
		Π_l (Jy)	15/15	0.024	0.008	31.9	0.024	0.014	0.040
		m_l (%)	15/15	2.5	0.9	34.6	2.3	1.6	4.2
		χ ($^\circ$)	15/15	-42.5	14.4	...	-47.1	-76.1	-15.6
		S (Jy)	18/19	1.051	0.256	24.4	1.175	0.503	1.271
	4.85	Π_l (Jy)	9/19	0.022	0.006	26.8	0.028	0.012	0.046
		$ \Pi_c $ (Jy)	0/19	nan	nan	nan	nan	nan	nan
		m_l (%)	9/19	2.2	0.5	23.9	2.4	1.2	3.7
		$ m_c $ (%)	0/19	nan	nan	nan	nan	nan	nan
		χ ($^\circ$)	9/9	-141.9	71.6	...	-41.3	-195.6	-1.0
		S (Jy)	20/20	1.046	0.299	28.6	1.224	0.526	1.516
	8.35	Π_l (Jy)	15/20	0.030	0.018	60.3	0.024	0.012	0.066
		$ \Pi_c $ (Jy)	1/20	0.005	0.000	nan	0.005	0.005	0.005
		m_l (%)	15/20	2.7	1.4	51.9	2.2	0.8	5.2
		$ m_c $ (%)	1/20	0.8	0.0	nan	0.8	0.8	0.8
		χ ($^\circ$)	15/15	4.9	17.8	...	8.7	-21.5	69.4
		S (Jy)	16/17	1.072	0.339	31.7	1.274	0.582	1.627
J2203+3145	10.45	Π_l (Jy)	2/17	0.020	0.007	34.4	0.022	0.017	0.026
		m_l (%)	2/17	2.1	0.6	26.5	2.2	1.8	2.6
		χ ($^\circ$)	2/2	28.8	5.6	...	28.2	24.3	32.2
		S (Jy)	2/2	1.828	0.027	1.5	1.823	1.804	1.842
		Π_l (Jy)	0/2	nan	nan	nan	nan	nan	nan
		m_l (%)	0/2	nan	nan	nan	nan	nan	nan
	2.64	S (Jy)	2/2	2.662	0.046	1.7	2.630	2.598	2.663
		Π_l (Jy)	0/2	nan	nan	nan	nan	nan	nan
		$ \Pi_c $ (Jy)	0/2	nan	nan	nan	nan	nan	nan
		m_l (%)	0/2	nan	nan	nan	nan	nan	nan
		$ m_c $ (%)	0/2	nan	nan	nan	nan	nan	nan
		S (Jy)	2/2	3.388	0.059	1.8	3.421	3.379	3.463
	8.35	Π_l (Jy)	1/2	0.028	0.000	nan	0.028	0.028	0.028
		$ \Pi_c $ (Jy)	1/2	0.015	0.000	nan	0.015	0.015	0.015
		m_l (%)	1/2	0.8	0.0	nan	0.8	0.8	0.8
		$ m_c $ (%)	1/2	0.4	0.0	nan	0.4	0.4	0.4
		χ ($^\circ$)	1/1	-80.8	0.0	...	-80.8	-80.8	-80.8
		S (Jy)	2/2	3.469	0.201	5.8	3.356	3.214	3.498
	10.45	Π_l (Jy)	0/2	nan	nan	nan	nan	nan	nan
		m_l (%)	0/2	nan	nan	nan	nan	nan	nan

Table A.1: continued.

Source	Freq. (GHz)	x		N _{sign}	$\langle x \rangle$	σ_x	mi (%)	median	min	max
J2225-0457	2.64	S	(Jy)	2/3	7.264	0.016	0.2	7.268	7.257	7.279
		Π_l	(Jy)	2/3	0.260	0.002	0.8	0.260	0.258	0.261
		m_l	(%)	2/3	3.6	0.0	1.0	3.6	3.5	3.6
		χ	($^\circ$)	2/2	-17.1	1.9	...	-17.6	-19.0	-16.3
	4.85	S	(Jy)	2/3	6.501	0.062	1.0	6.480	6.436	6.524
		Π_l	(Jy)	3/3	0.124	0.027	21.5	0.133	0.105	0.191
		$ \Pi_c $	(Jy)	1/3	0.024	0.000	nan	0.024	0.024	0.024
		m_l	(%)	2/3	1.9	0.3	15.5	1.8	1.6	2.0
		$ m_c $	(%)	1/3	0.4	0.0	nan	0.4	0.4	0.4
		χ	($^\circ$)	3/3	3.9	1.6	...	4.0	2.5	6.2
		S	(Jy)	3/3	5.615	0.531	9.5	5.523	5.327	6.309
		Π_l	(Jy)	3/3	0.061	0.014	22.9	0.060	0.055	0.079
		$ \Pi_c $	(Jy)	0/3	nan	nan	nan	nan	nan	nan
		m_l	(%)	3/3	1.1	0.1	11.6	1.1	1.0	1.3
		$ m_c $	(%)	0/3	nan	nan	nan	nan	nan	nan
		χ	($^\circ$)	3/3	-7.6	6.6	...	-9.9	-20.2	-0.6
	10.45	S	(Jy)	2/3	5.386	0.687	12.8	5.447	4.961	5.933
		Π_l	(Jy)	1/3	0.054	0.000	nan	0.054	0.054	0.054
		m_l	(%)	1/3	0.9	0.0	nan	0.9	0.9	0.9
		χ	($^\circ$)	1/1	-14.9	0.0	...	-14.9	-14.9	-14.9
J2229-0832	2.64	S	(Jy)	17/17	1.702	0.142	8.4	1.720	1.401	1.913
		Π_l	(Jy)	16/17	0.043	0.007	17.3	0.046	0.031	0.058
		m_l	(%)	16/17	2.5	0.4	15.1	2.6	1.9	3.8
		χ	($^\circ$)	16/16	86.5	3.0	...	86.5	74.1	89.4
	4.85	S	(Jy)	26/27	1.502	0.224	14.9	1.597	1.268	2.355
		Π_l	(Jy)	21/27	0.037	0.006	17.4	0.041	0.030	0.061
		$ \Pi_c $	(Jy)	0/27	nan	nan	nan	nan	nan	nan
		m_l	(%)	21/27	2.3	0.6	27.6	2.7	1.8	4.0
		$ m_c $	(%)	0/27	nan	nan	nan	nan	nan	nan
		χ	($^\circ$)	21/22	82.3	4.3	...	81.7	71.9	89.8
		S	(Jy)	24/26	1.528	0.372	24.3	1.511	1.222	2.823
		Π_l	(Jy)	21/26	0.029	0.008	26.6	0.029	0.018	0.066
		$ \Pi_c $	(Jy)	0/26	nan	nan	nan	nan	nan	nan
		m_l	(%)	21/26	1.8	0.7	36.8	2.0	0.8	3.1
		$ m_c $	(%)	0/26	nan	nan	nan	nan	nan	nan
		χ	($^\circ$)	21/21	85.0	6.0	...	83.1	67.9	97.0
	10.45	S	(Jy)	16/17	1.821	0.654	35.9	1.353	1.153	2.793
		Π_l	(Jy)	6/17	0.032	0.007	21.7	0.027	0.025	0.040
		m_l	(%)	6/17	1.8	0.7	37.9	2.2	1.4	2.9
		χ	($^\circ$)	6/6	72.5	9.5	...	77.3	61.8	81.4
J2232+1143	2.64	S	(Jy)	26/26	5.714	0.195	3.4	5.721	5.412	6.292
		Π_l	(Jy)	25/26	0.191	0.022	11.4	0.201	0.160	0.232
		m_l	(%)	25/26	3.3	0.5	14.6	3.6	2.5	4.2
		χ	($^\circ$)	25/25	13.9	3.4	...	14.7	6.6	18.6

Table A.1: continued.

Source	Freq. (GHz)	x	N_{sign}	$\langle x \rangle$	σ_x	mi (%)	median	min	max
J2253+1608	4.85	S (Jy)	44/46	4.818	0.460	9.5	4.518	4.215	5.460
		Π_l (Jy)	44/46	0.172	0.013	7.6	0.177	0.140	0.192
		$ \Pi_c $ (Jy)	6/46	0.008	0.005	55.8	0.013	0.006	0.019
		m_l (%)	44/46	3.6	0.6	15.8	3.9	2.6	4.3
		$ m_c $ (%)	6/46	0.2	0.1	54.6	0.3	0.1	0.4
		χ ($^\circ$)	44/44	48.8	3.2	...	49.5	42.8	56.1
	8.35	S (Jy)	43/45	3.686	0.337	9.1	3.606	3.207	4.589
		Π_l (Jy)	43/45	0.167	0.016	9.3	0.173	0.136	0.227
		$ \Pi_c $ (Jy)	2/45	0.007	0.004	61.1	0.009	0.006	0.011
		m_l (%)	43/45	4.5	0.5	10.8	4.6	3.5	6.7
		$ m_c $ (%)	2/45	0.2	0.1	57.4	0.2	0.2	0.3
		χ ($^\circ$)	43/43	69.2	4.2	...	68.4	59.6	77.7
	10.45	S (Jy)	29/31	3.231	0.297	9.2	3.260	2.781	4.352
		Π_l (Jy)	14/31	0.171	0.023	13.2	0.171	0.134	0.201
		m_l (%)	14/31	4.7	0.5	11.3	4.6	3.9	5.9
		χ ($^\circ$)	14/14	64.2	3.2	...	64.7	57.5	68.1
	2.64	S (Jy)	25/28	11.968	0.701	5.9	12.165	10.521	12.724
		Π_l (Jy)	25/28	0.838	0.087	10.3	0.838	0.669	1.149
		m_l (%)	25/28	7.0	0.7	10.5	6.9	6.3	10.2
		χ ($^\circ$)	25/25	-17.9	3.4	...	-17.2	-26.0	-12.3
	4.85	S (Jy)	49/51	12.008	2.096	17.5	11.673	8.090	15.239
		Π_l (Jy)	49/51	0.344	0.080	23.2	0.379	0.246	0.554
		$ \Pi_c $ (Jy)	5/51	0.031	0.017	54.7	0.037	0.014	0.076
		m_l (%)	49/51	3.1	0.9	30.1	3.5	2.0	5.1
		$ m_c $ (%)	5/51	0.2	0.1	54.3	0.3	0.1	0.5
		χ ($^\circ$)	49/49	6.2	1.9	...	6.6	2.1	10.8
	8.35	S (Jy)	46/48	10.928	3.538	32.4	10.492	6.206	21.460
		Π_l (Jy)	46/48	0.196	0.108	55.0	0.228	0.022	0.417
		$ \Pi_c $ (Jy)	9/48	0.042	0.023	54.6	0.080	0.032	0.116
		m_l (%)	46/48	1.7	0.7	44.7	2.0	0.3	3.7
		$ m_c $ (%)	9/48	0.3	0.1	38.2	0.5	0.2	0.6
		χ ($^\circ$)	46/46	51.5	41.4	...	21.9	2.0	98.3
	10.45	S (Jy)	32/35	7.718	3.176	41.2	8.731	5.530	22.773
		Π_l (Jy)	25/35	0.117	0.103	88.3	0.158	0.018	0.629
		m_l (%)	25/35	1.8	0.8	43.4	1.9	0.3	4.0
		χ ($^\circ$)	25/25	75.2	38.9	...	88.0	6.1	120.1
J2325+3957	4.85	S (Jy)	2/2	0.128	0.011	8.3	0.126	0.118	0.133
		Π_l (Jy)	0/2	nan	nan	nan	nan	nan	nan
		$ \Pi_c $ (Jy)	0/2	nan	nan	nan	nan	nan	nan
		m_l (%)	0/2	nan	nan	nan	nan	nan	nan
		$ m_c $ (%)	0/2	nan	nan	nan	nan	nan	nan
		χ ($^\circ$)	0/2	nan	nan	nan	nan	nan	nan
	8.35	S (Jy)	2/2	0.115	0.007	6.1	0.118	0.113	0.123
		Π_l (Jy)	0/2	nan	nan	nan	nan	nan	nan
		$ \Pi_c $ (Jy)	0/2	nan	nan	nan	nan	nan	nan
		χ ($^\circ$)	0/2	nan	nan	nan	nan	nan	nan

Table A.1: continued.

Source	Freq. (GHz)	x	N_{sign}	$\langle x \rangle$	σ_x	mi (%)	median	min	max
J2327+0940	10.45	m_l (%)	0/2	nan	nan	nan	nan	nan	nan
		$ m_c $ (%)	0/2	nan	nan	nan	nan	nan	nan
		S (Jy)	1/1	0.113	0.000	nan	0.113	0.113	0.113
		Π_l (Jy)	0/1	nan	nan	nan	nan	nan	nan
	2.64	m_l (%)	0/1	nan	nan	nan	nan	nan	nan
		S (Jy)	26/26	0.651	0.123	18.9	0.673	0.495	0.856
		Π_l (Jy)	9/26	0.009	0.001	13.5	0.009	0.008	0.012
		m_l (%)	9/26	1.2	0.1	11.0	1.2	0.9	1.4
	4.85	χ (°)	9/9	-11.6	7.0	...	-9.0	-19.3	-2.4
		S (Jy)	38/39	0.618	0.202	32.7	0.592	0.450	0.969
		Π_l (Jy)	7/39	0.014	0.002	11.0	0.015	0.010	0.017
		$ \Pi_c $ (Jy)	0/39	nan	nan	nan	nan	nan	nan
	8.35	m_l (%)	7/39	1.5	0.2	12.4	1.6	1.1	2.2
		$ m_c $ (%)	0/39	nan	nan	nan	nan	nan	nan
		χ (°)	7/7	-21.7	19.6	...	-10.4	-41.6	11.1
		S (Jy)	35/36	0.548	0.142	25.9	0.655	0.430	1.177
	10.45	Π_l (Jy)	8/36	0.011	0.002	17.4	0.011	0.010	0.014
		$ \Pi_c $ (Jy)	2/36	0.003	0.000	14.0	0.003	0.003	0.003
		m_l (%)	8/36	1.1	0.2	21.5	1.1	0.9	2.2
		$ m_c $ (%)	2/36	0.4	0.0	4.8	0.4	0.4	0.5
J2347+5142	8.35	χ (°)	8/8	-19.6	26.5	...	-25.8	-64.9	4.6
		S (Jy)	27/28	0.584	0.150	25.6	0.636	0.416	1.207
		Π_l (Jy)	0/28	nan	nan	nan	nan	nan	nan
		m_l (%)	0/28	nan	nan	nan	nan	nan	nan
	4.85	S (Jy)	3/3	0.219	0.006	2.7	0.221	0.215	0.233
		Π_l (Jy)	0/3	nan	nan	nan	nan	nan	nan
		$ \Pi_c $ (Jy)	0/3	nan	nan	nan	nan	nan	nan
		m_l (%)	0/3	nan	nan	nan	nan	nan	nan
	8.35	$ m_c $ (%)	0/3	nan	nan	nan	nan	nan	nan
		S (Jy)	3/3	0.178	0.002	1.2	0.179	0.177	0.184
		Π_l (Jy)	0/3	nan	nan	nan	nan	nan	nan
		$ \Pi_c $ (Jy)	0/3	nan	nan	nan	nan	nan	nan
NGC7027	2.64	m_l (%)	0/3	nan	nan	nan	nan	nan	nan
		$ m_c $ (%)	0/3	nan	nan	nan	nan	nan	nan
		S (Jy)	15/16	3.640	0.028	0.8	3.646	3.599	3.819
		Π_l (Jy)	1/16	0.015	0.000	nan	0.015	0.015	0.015
	4.85	m_l (%)	1/16	0.4	0.0	nan	0.4	0.4	0.4
		χ (°)	1/1	-42.2	0.0	...	-42.2	-42.2	-42.2
		S (Jy)	41/41	5.424	0.031	0.6	5.419	5.367	5.494
		Π_l (Jy)	0/41	nan	nan	nan	nan	nan	nan
	8.35	$ \Pi_c $ (Jy)	5/41	0.011	0.005	45.5	0.013	0.007	0.026
		m_l (%)	0/41	nan	nan	nan	nan	nan	nan
		$ m_c $ (%)	5/41	0.2	0.1	46.0	0.2	0.1	0.5
		S (Jy)	38/39	5.895	0.055	0.9	5.865	5.744	6.164

Table A.1: continued.

Source	Freq. (GHz)	x	N_{sign}	$\langle x \rangle$	σ_x	mi (%)	median	min	max
		Π_l (Jy)	0/39	nan	nan	nan	nan	nan	nan
		$ \Pi_c $ (Jy)	5/39	0.017	0.007	39.3	0.019	0.011	0.025
		m_l (%)	0/39	nan	nan	nan	nan	nan	nan
		$ m_c $ (%)	5/39	0.3	0.1	38.8	0.3	0.2	0.4
	10.45	S (Jy)	22/25	5.819	0.148	2.6	5.815	5.316	6.102
		Π_l (Jy)	5/25	0.044	0.041	93.8	0.023	0.017	0.115
		m_l (%)	5/25	0.8	0.7	92.7	0.4	0.3	1.9
		χ (°)	5/5	-81.2	50.7	...	-34.1	-125.6	9.4

Appendix B

Light curves

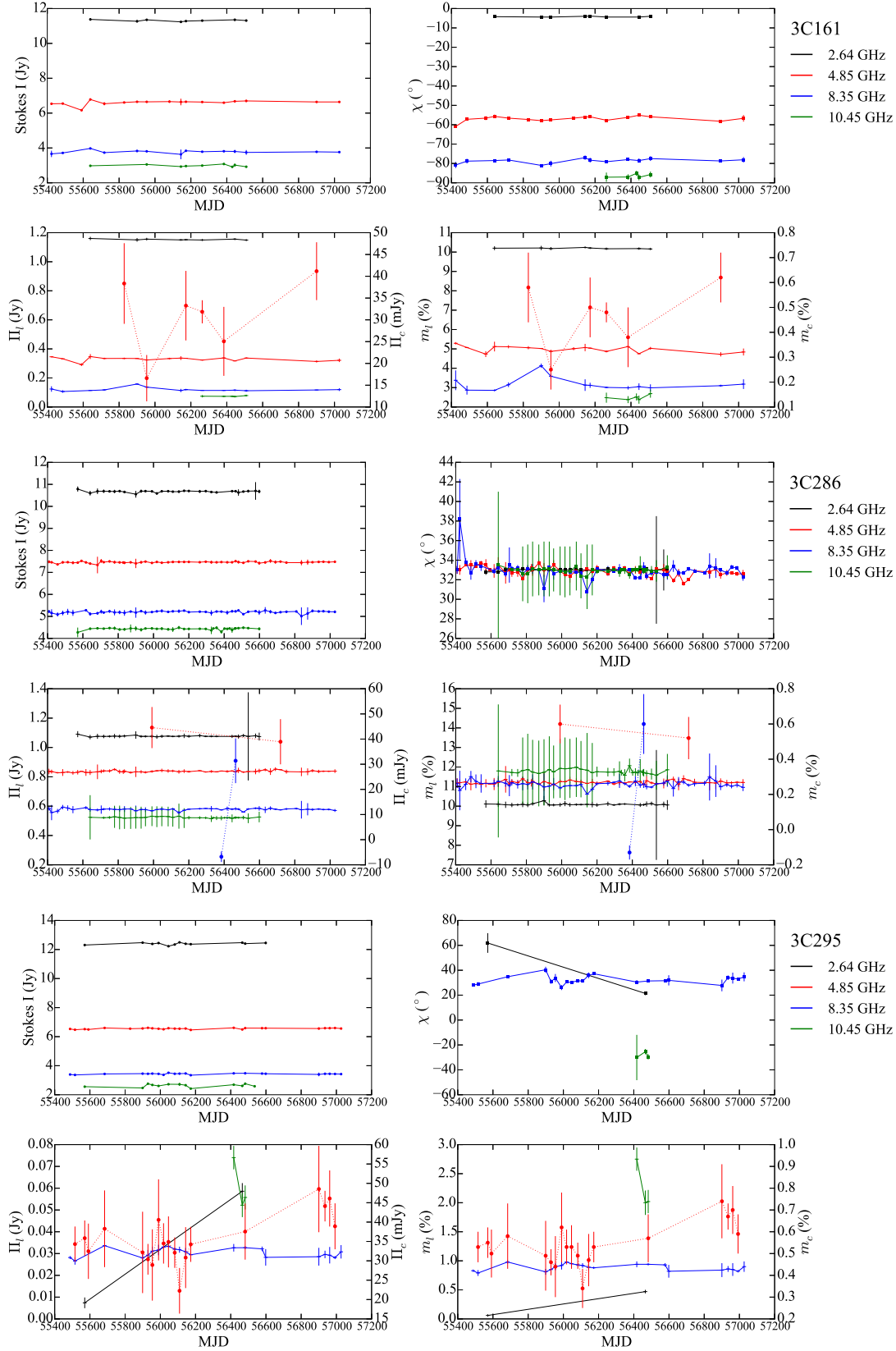


Figure B.1: The radio total flux density (I), linear and circular polarization lightcurves for all sources. Only significant measurements are shown (signal-to-noise ratio ≥ 3). The curves are color-coded according to the observed frequency as shown in the legend. In the left column, we plot the total, linearly and circularly polarized flux densities, I , Π_l and Π_c respectively. In the right column, we plot the EVPA, linear and circular polarization degrees, χ , m_l and m_c respectively. The linear and circular polarization information are shown in the bottom row by the continuous and dotted lines respectively.

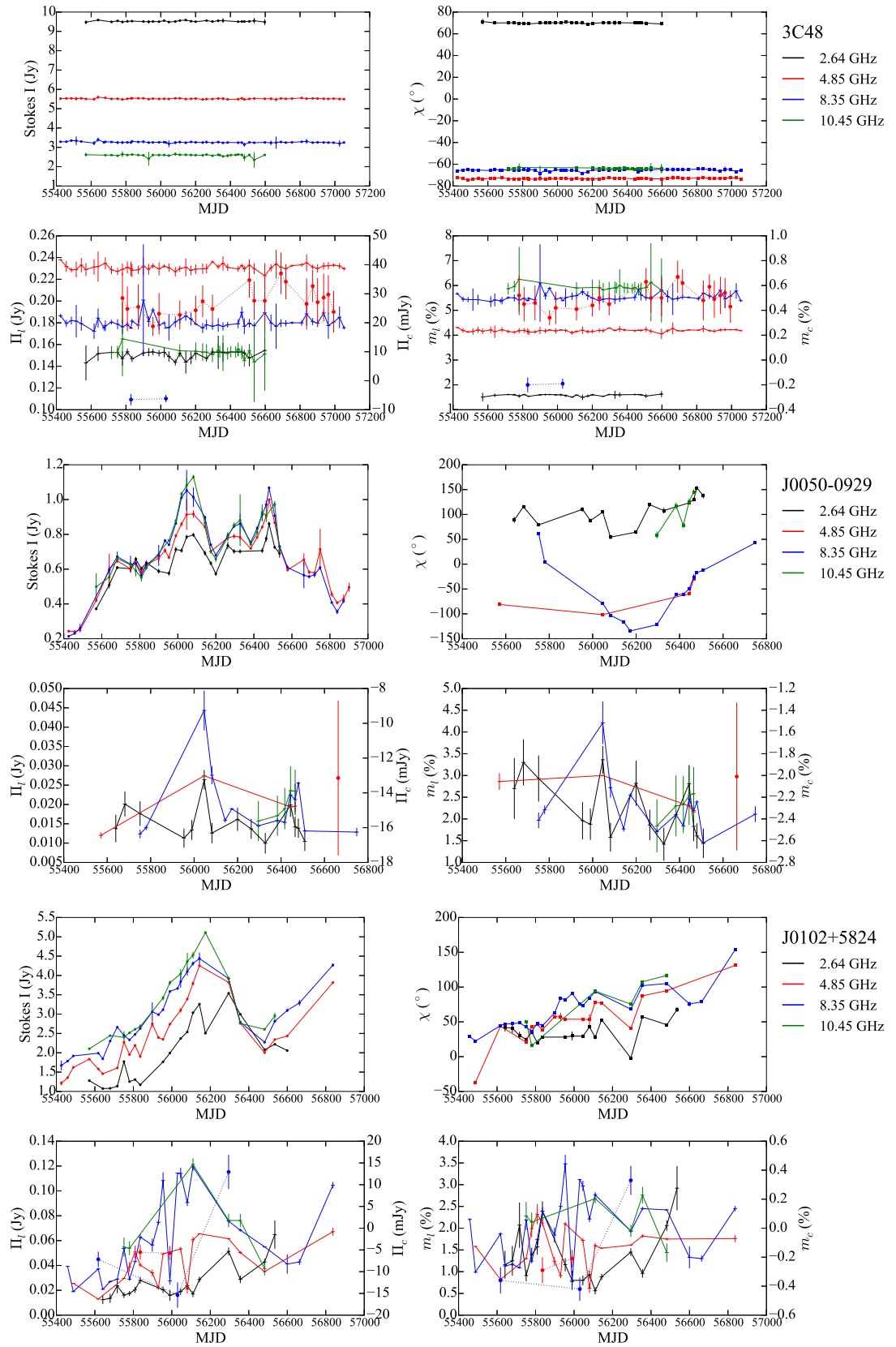


Figure B.2: continued

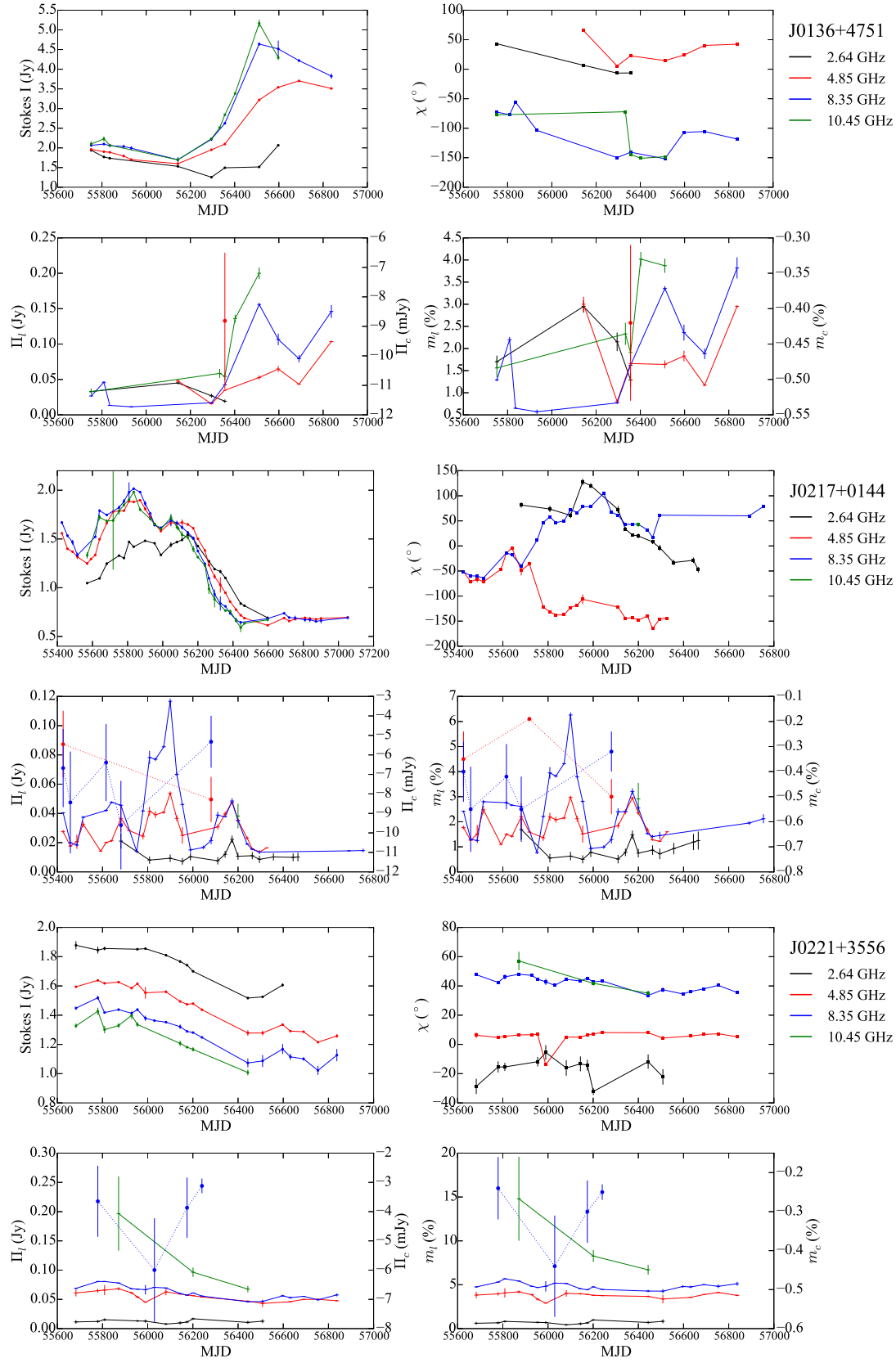


Figure B.3: continued

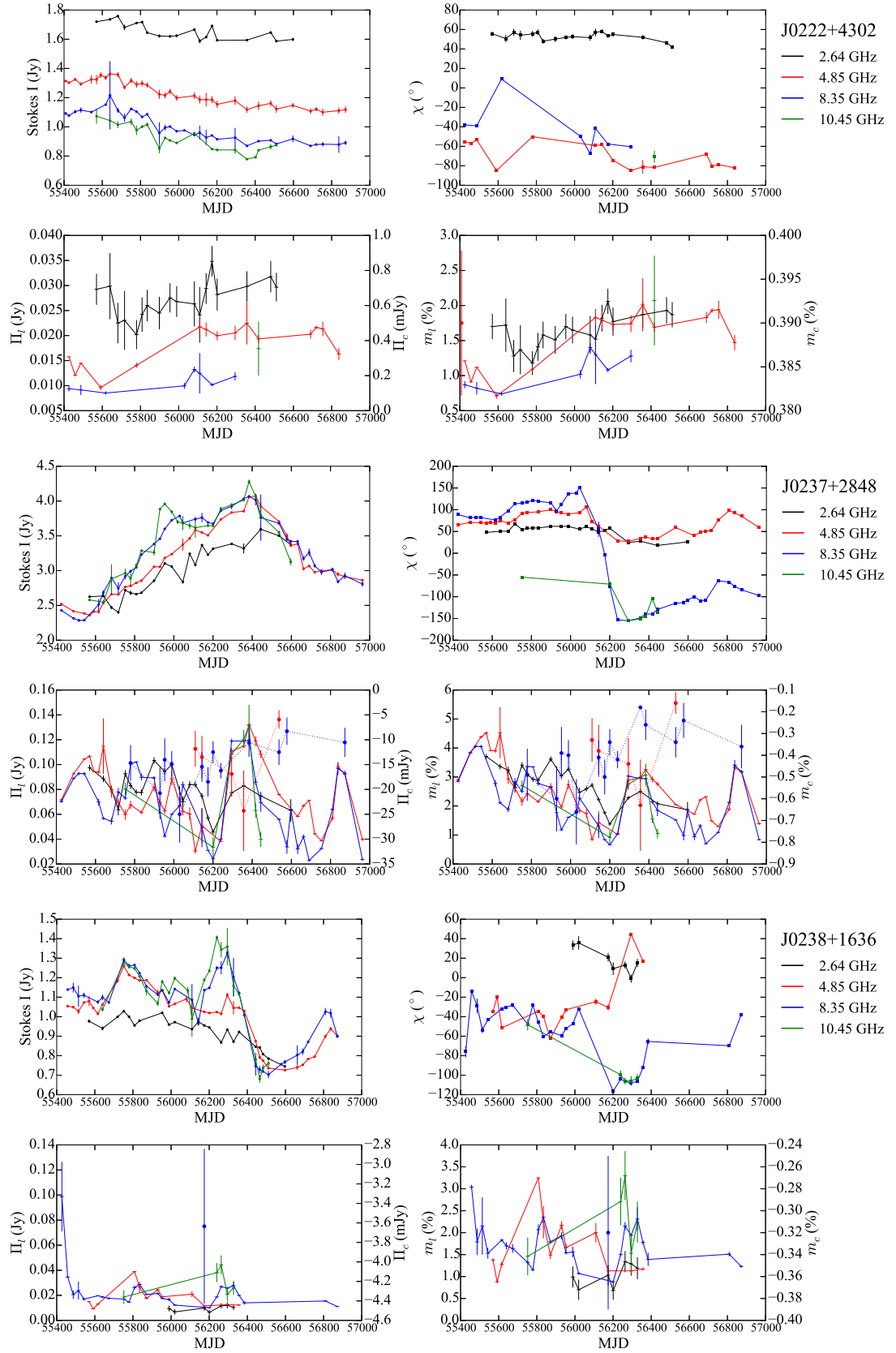


Figure B.4: continued

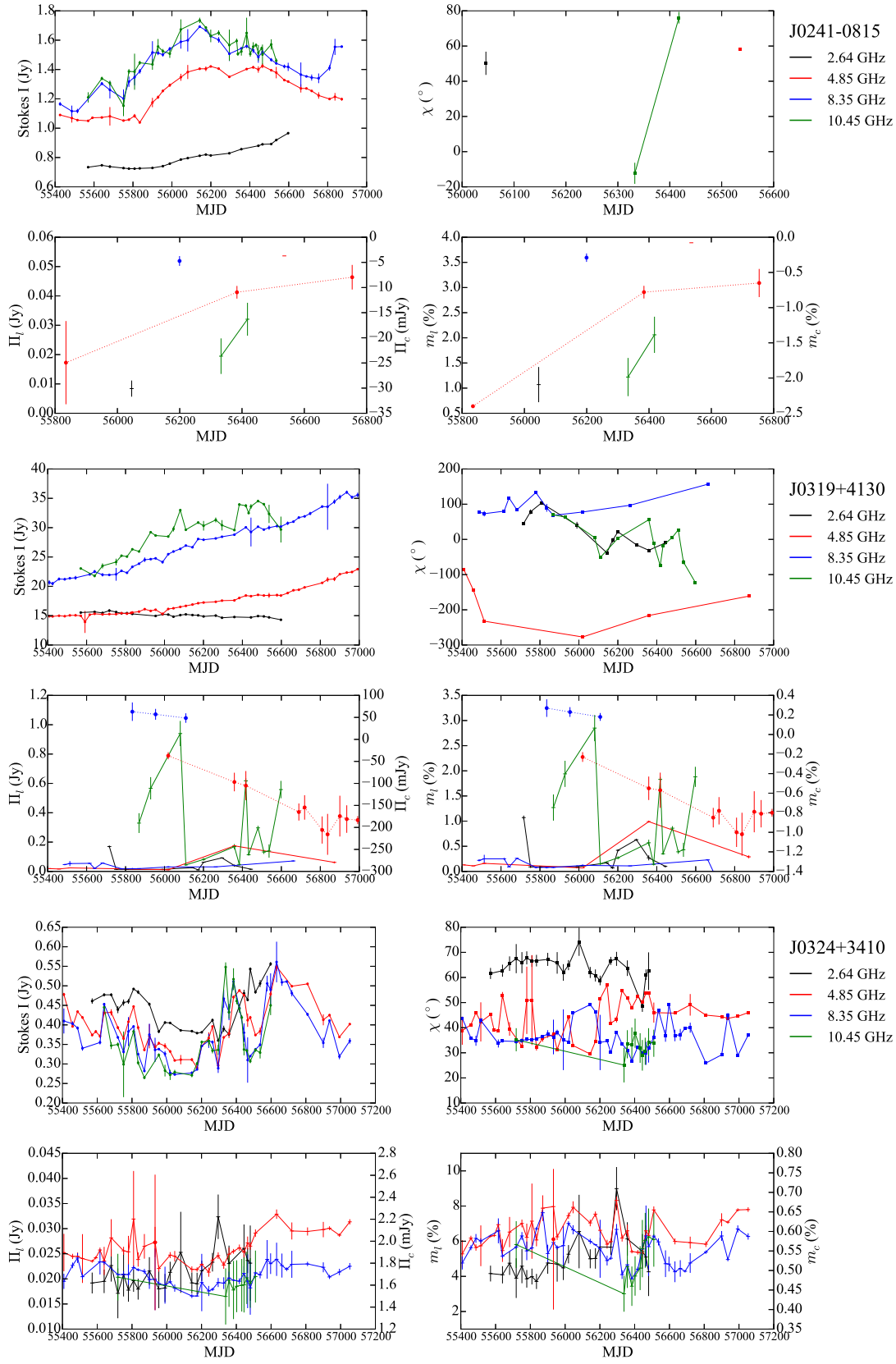


Figure B.5: continued

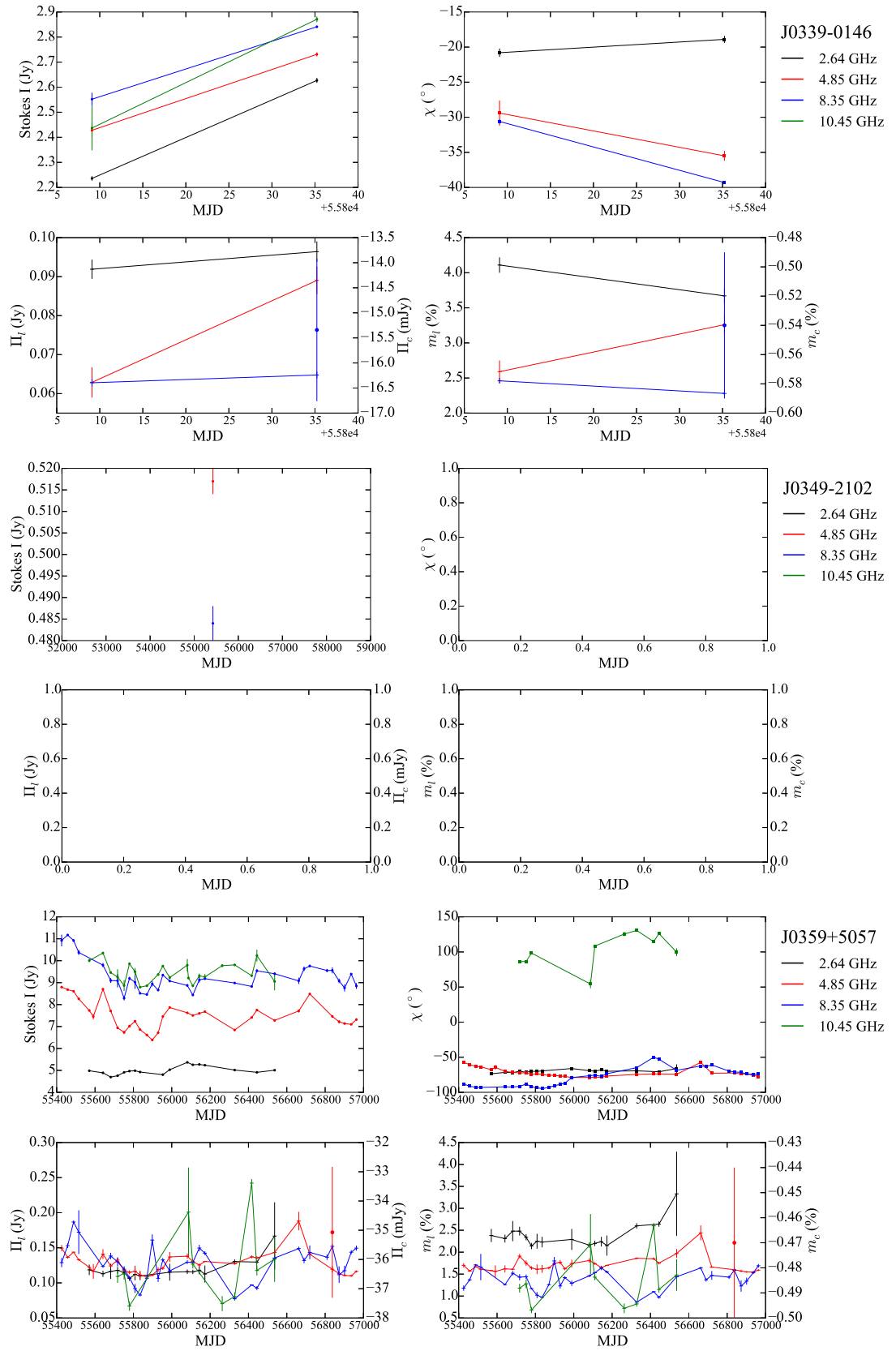


Figure B.6: continued

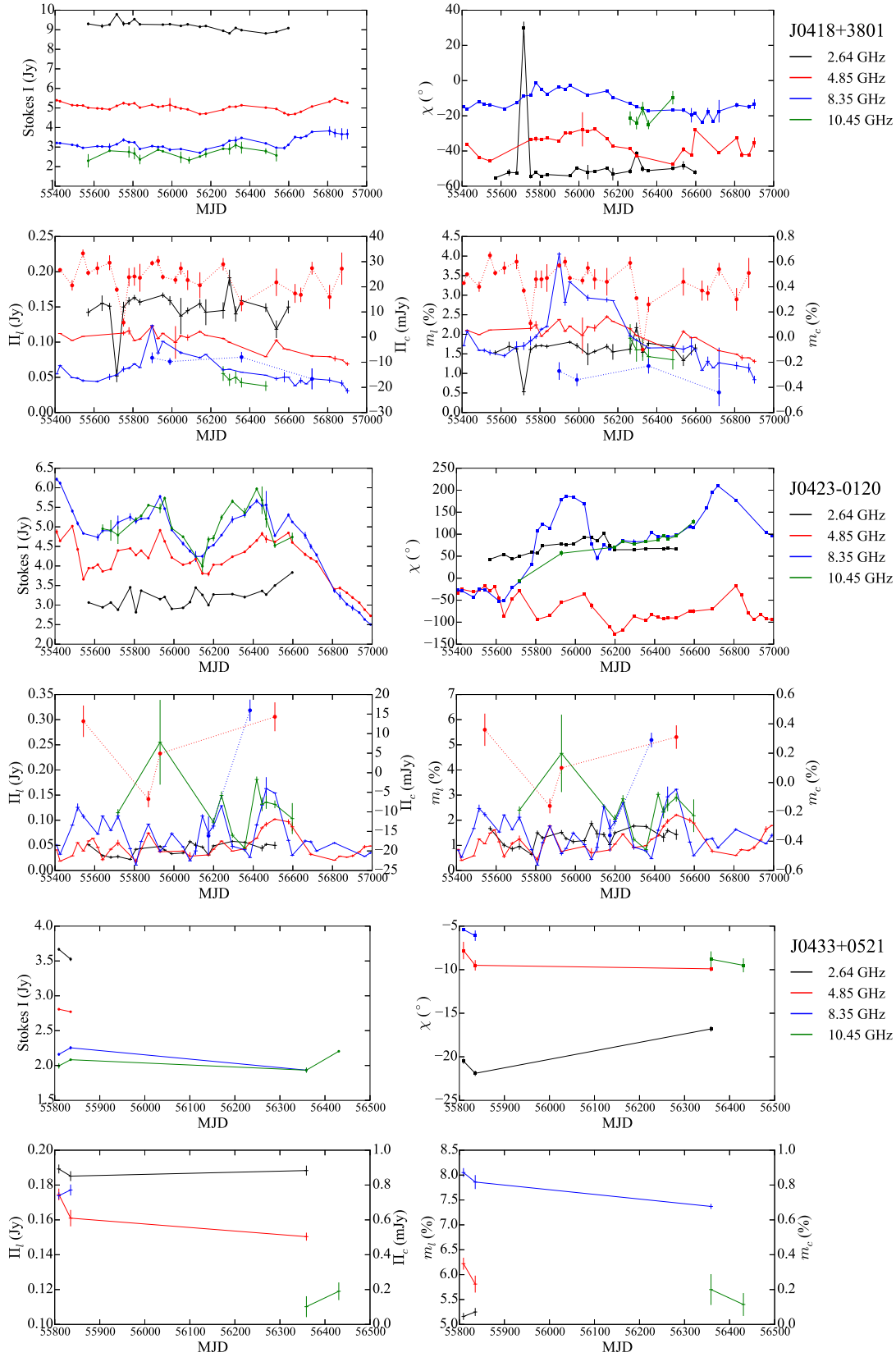


Figure B.7: continued

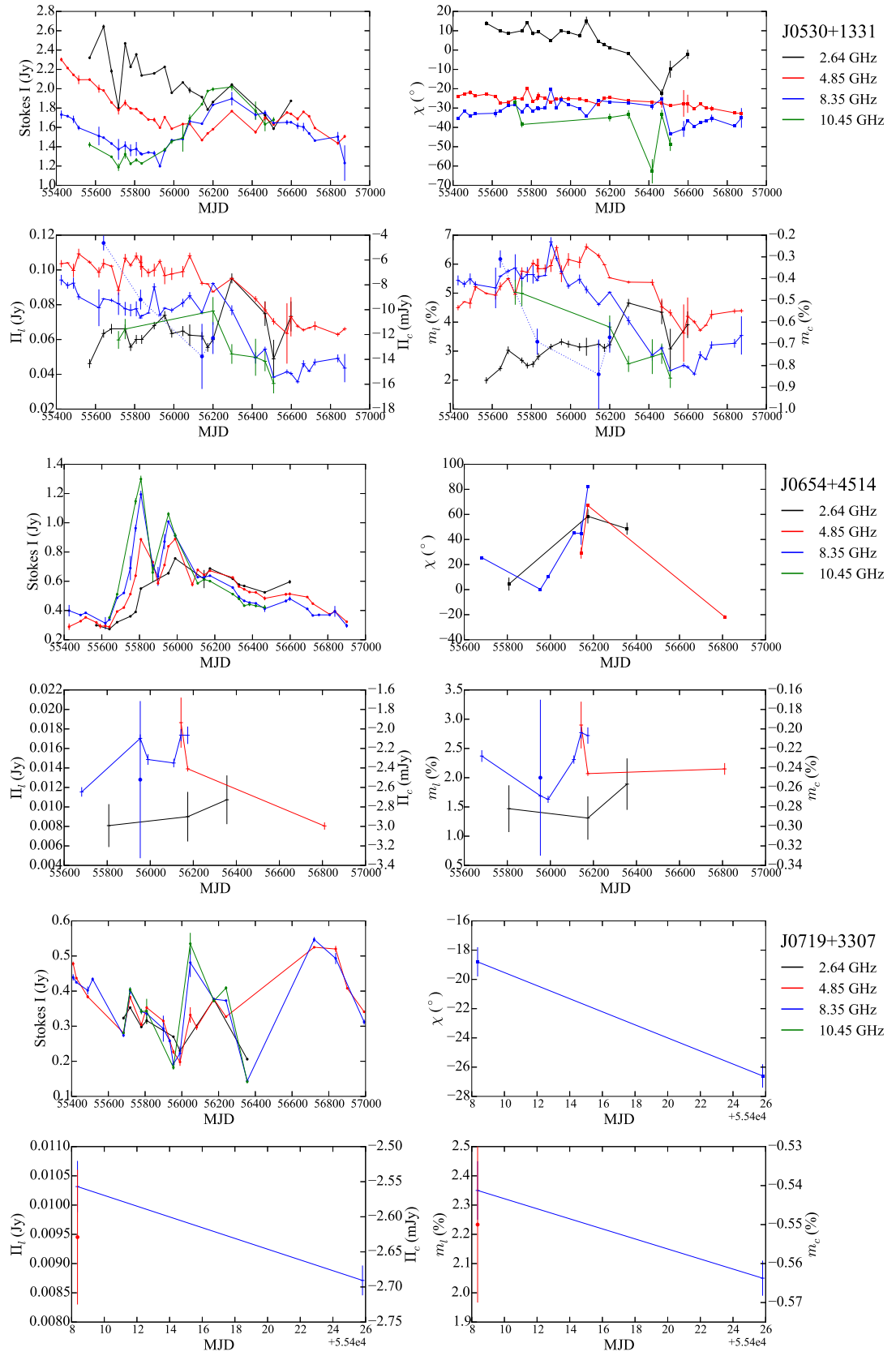


Figure B.8: continued

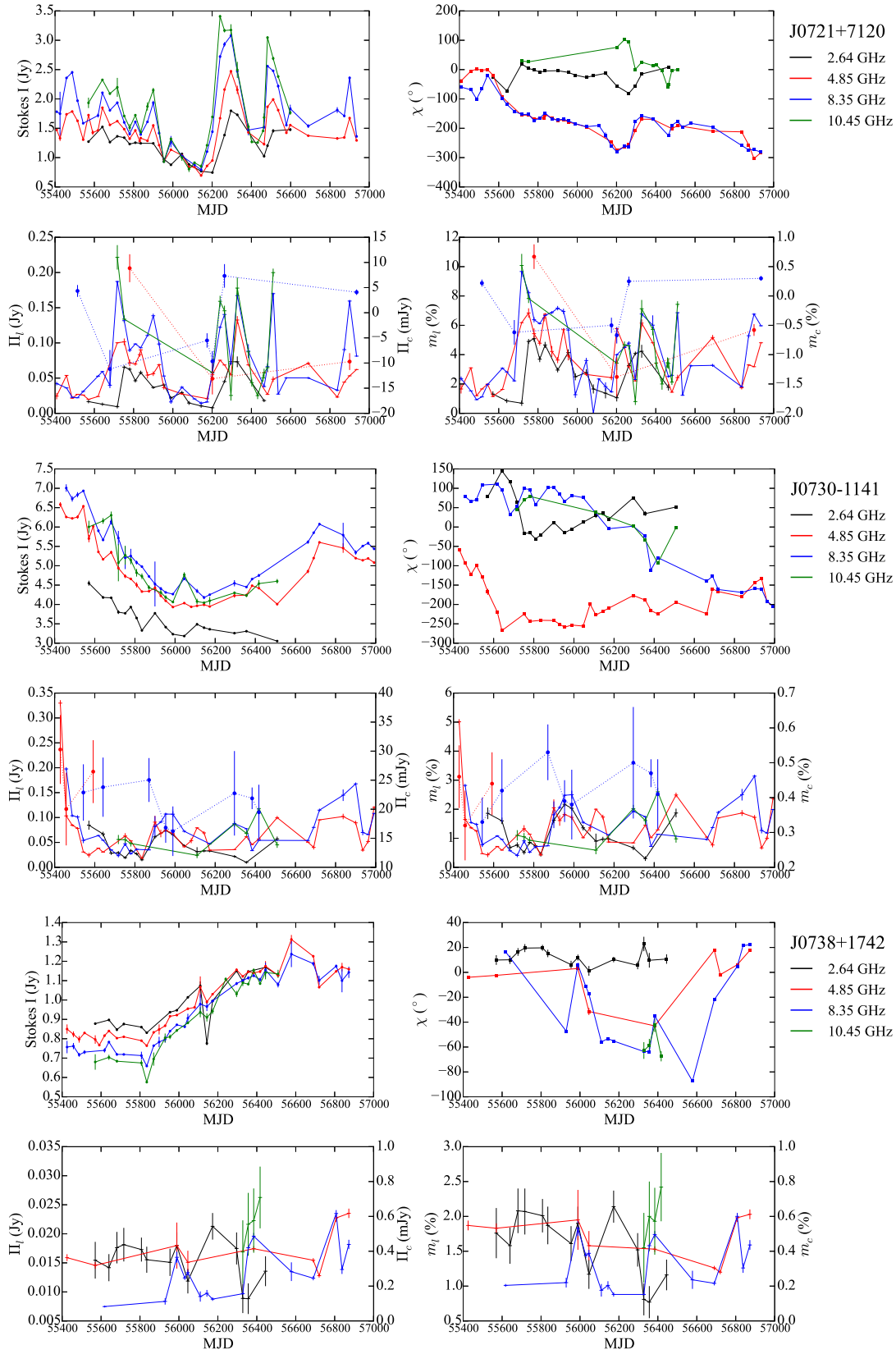


Figure B.9: continued

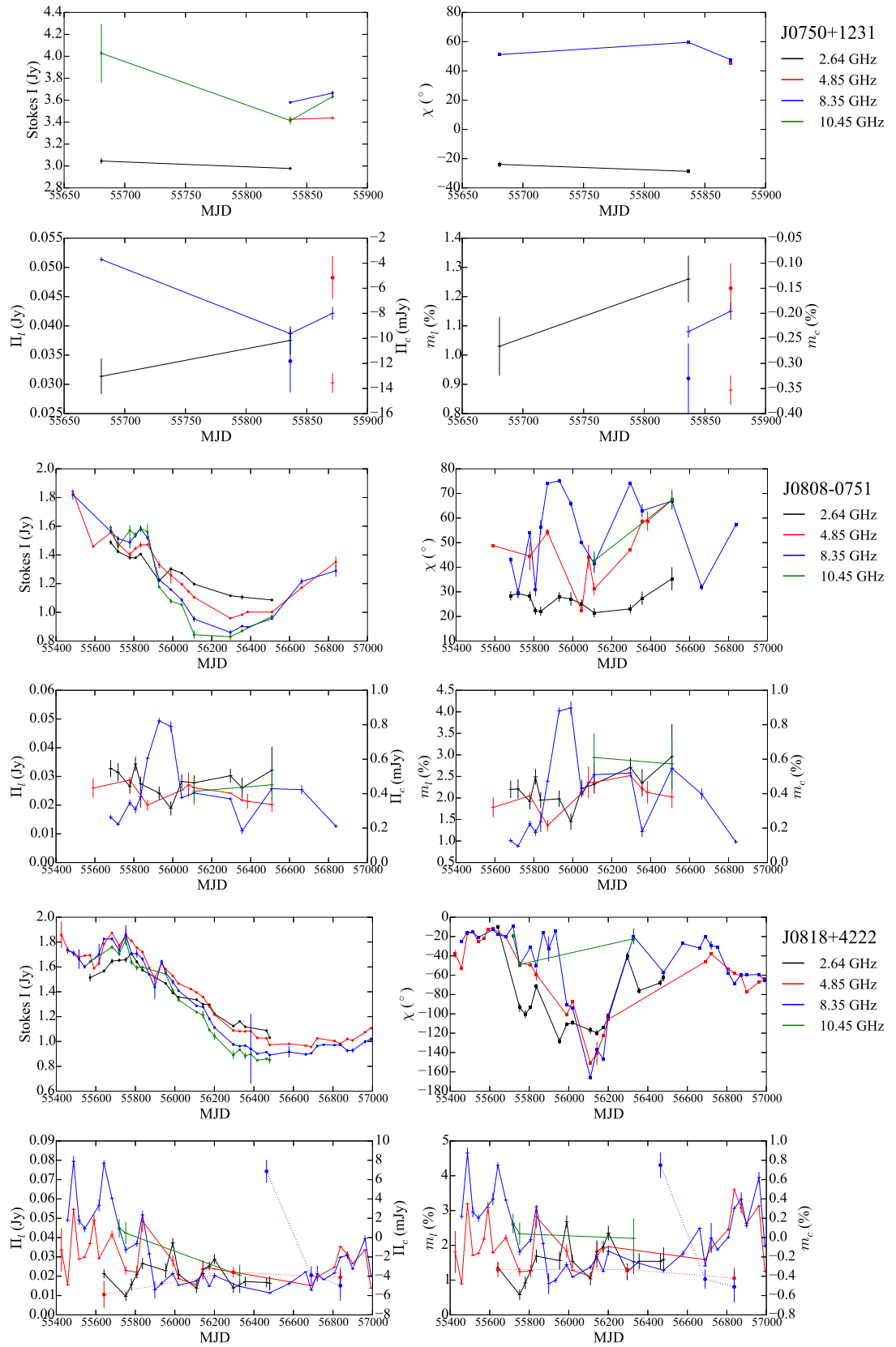


Figure B.10: continued

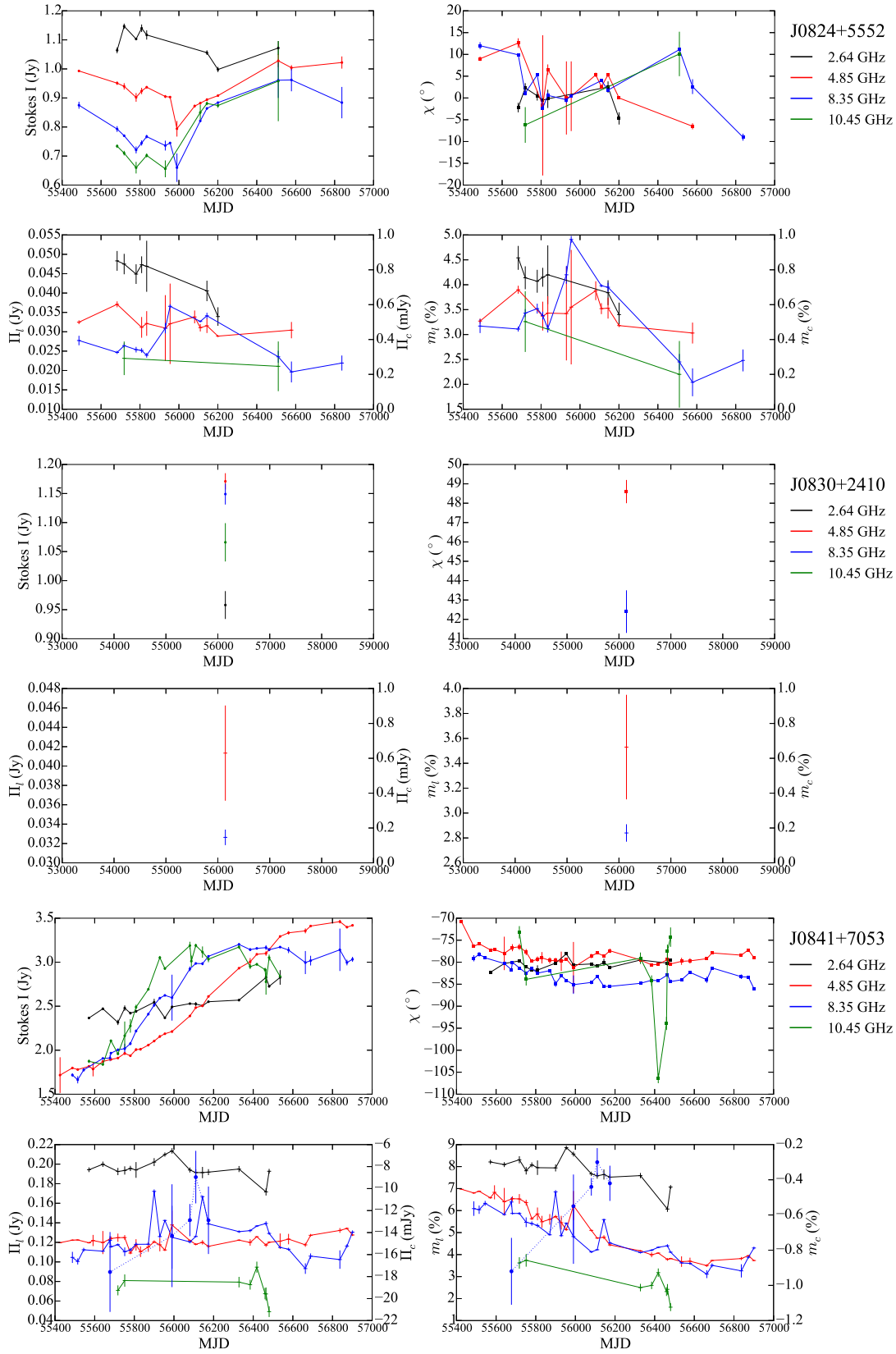


Figure B.11: continued

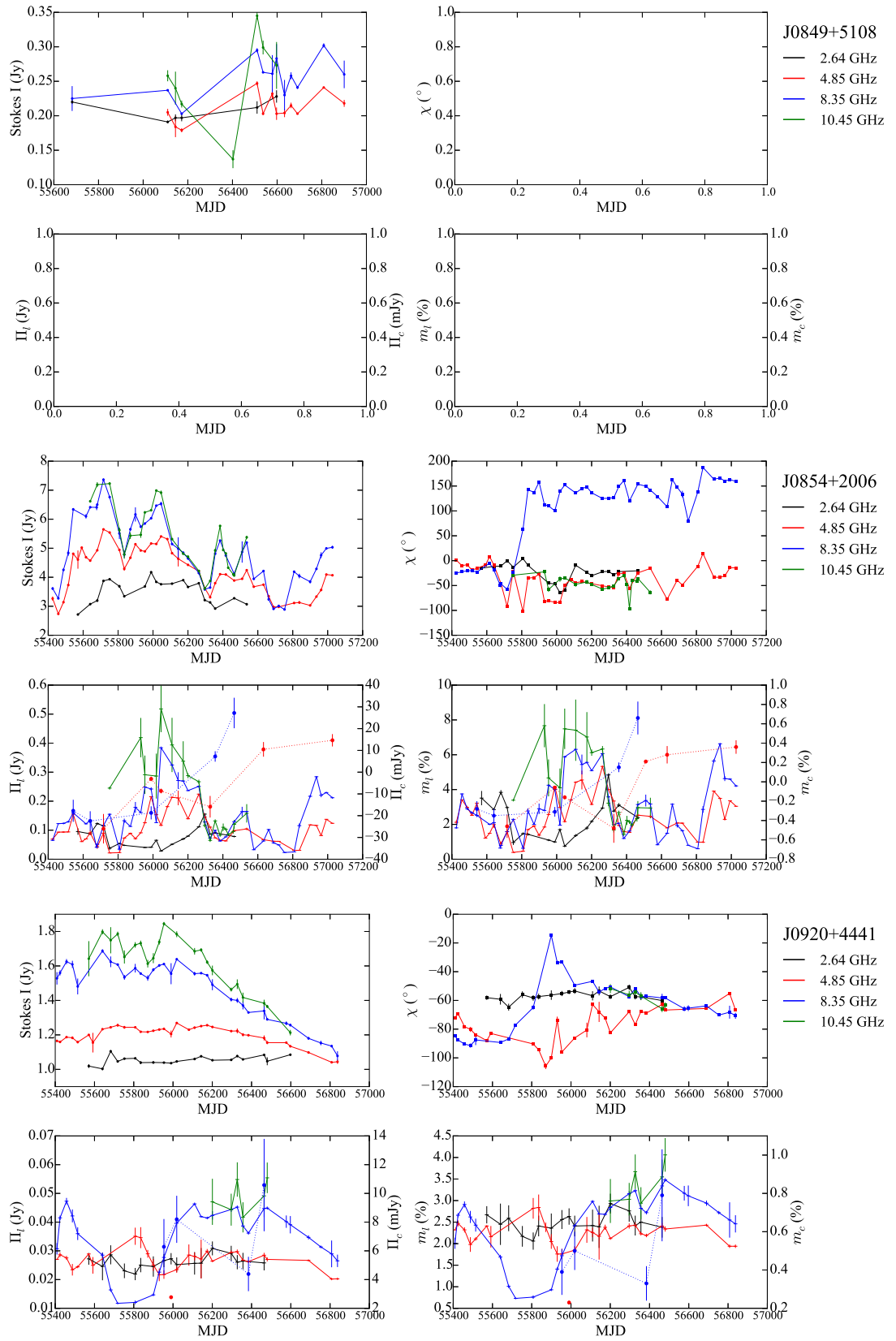


Figure B.12: continued

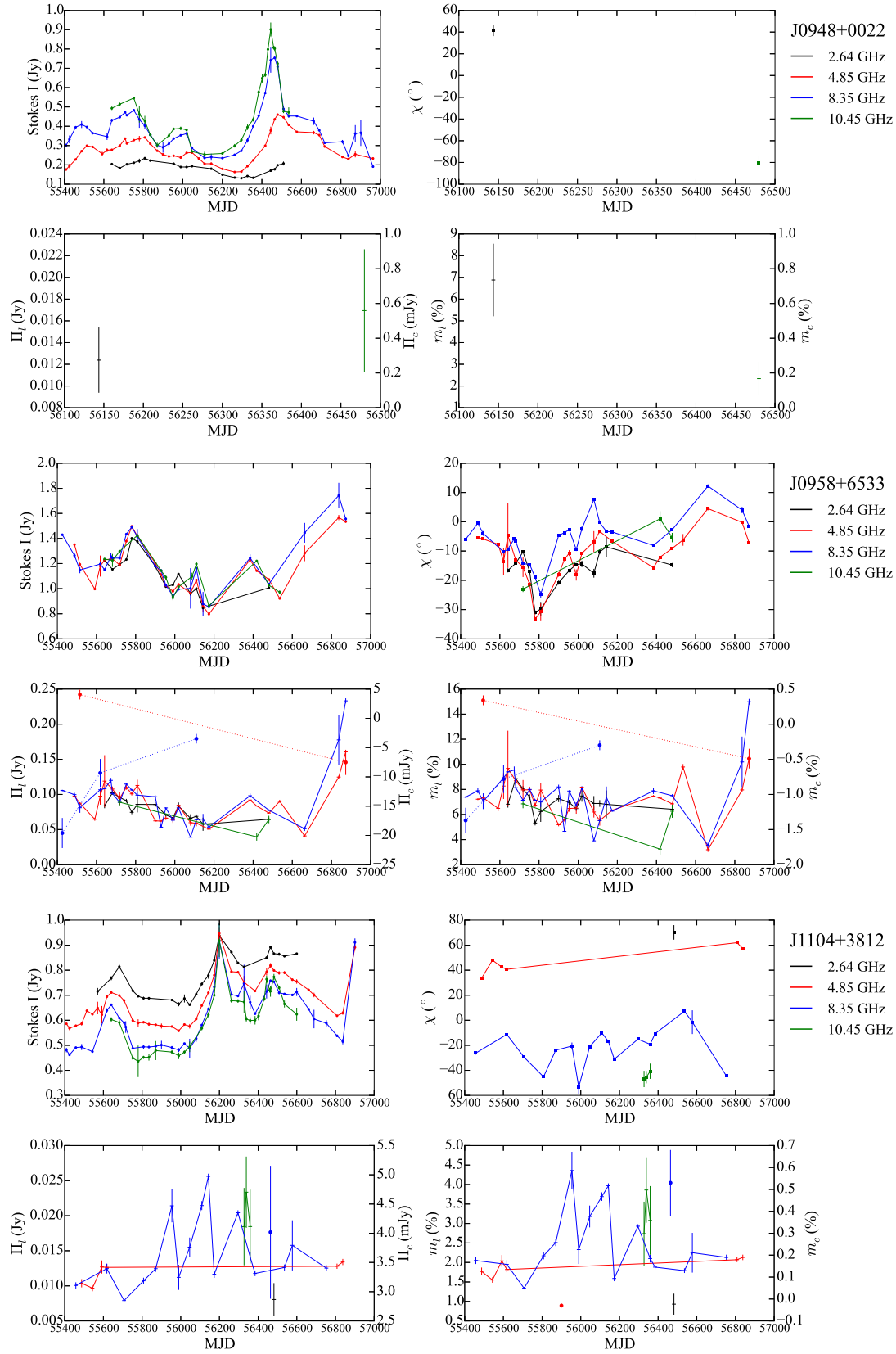


Figure B.13: continued

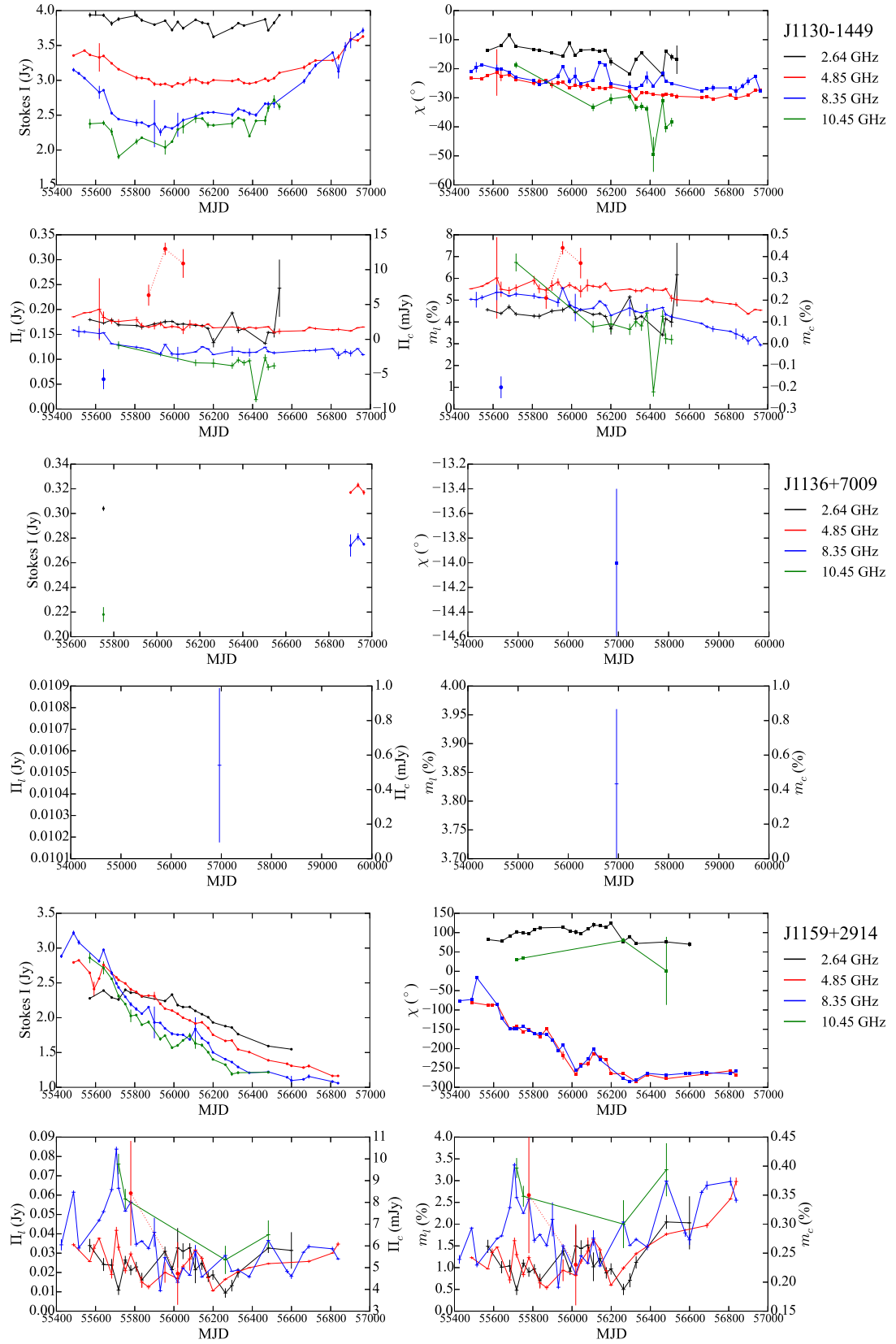


Figure B.14: continued

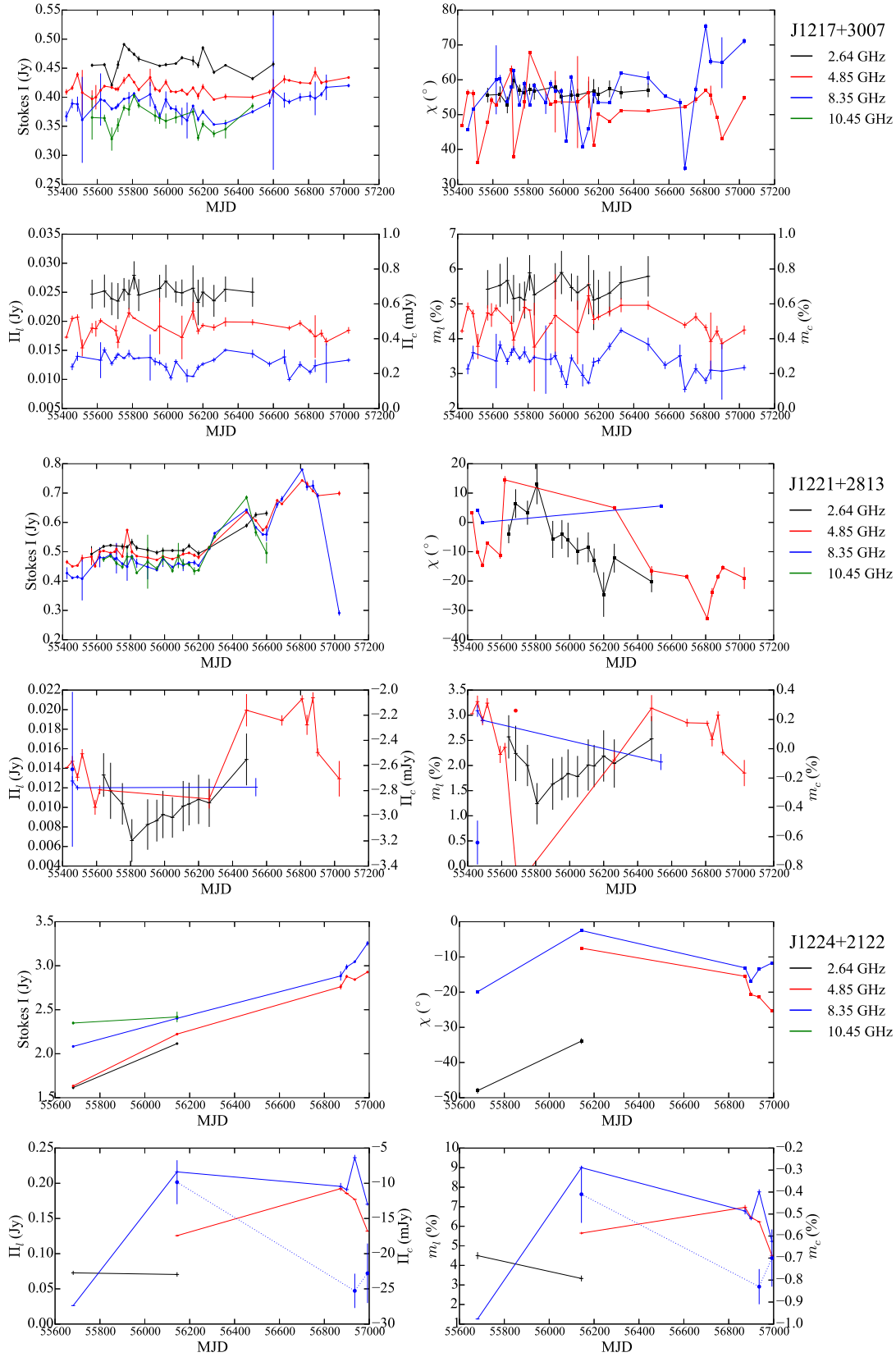


Figure B.15: continued

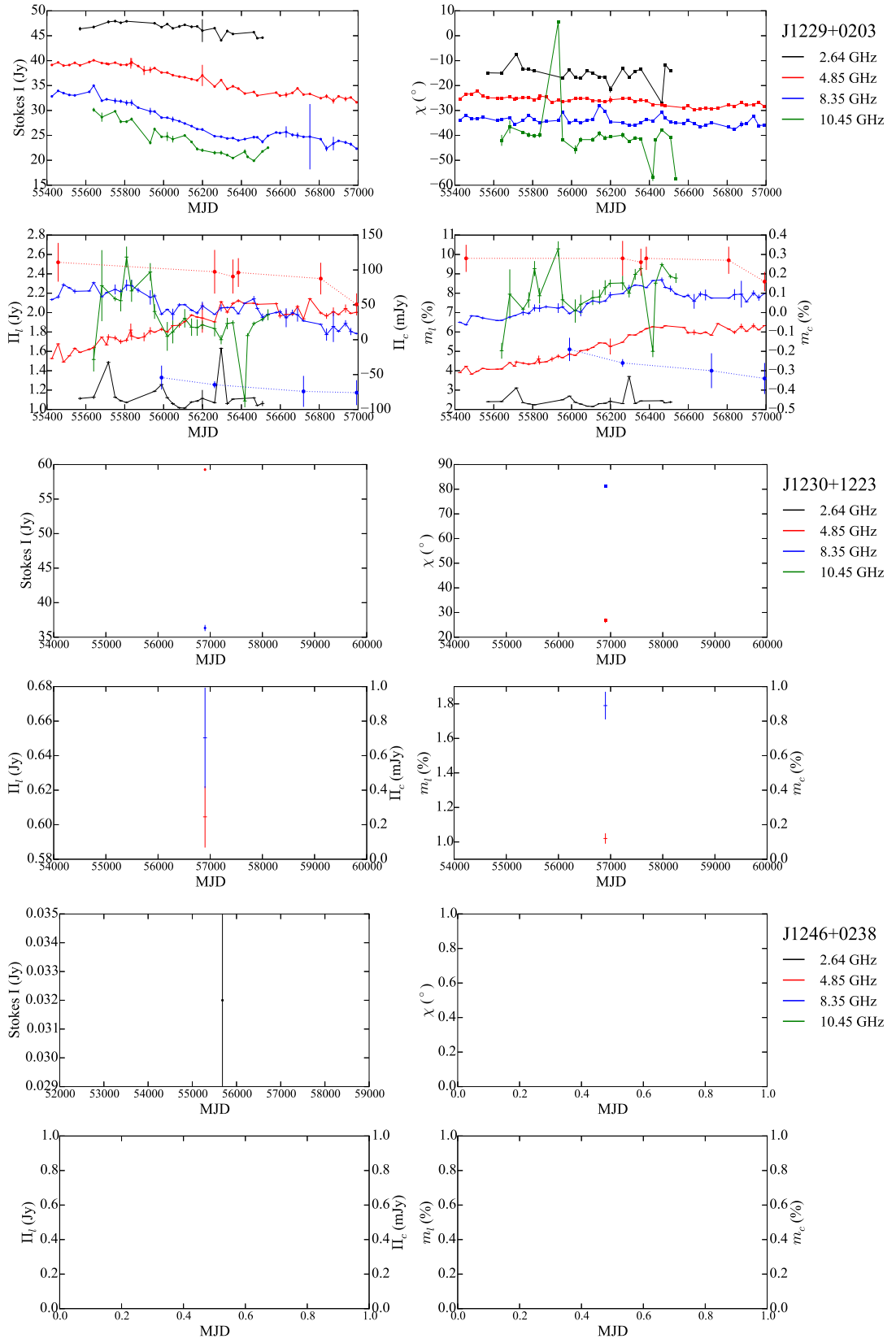


Figure B.16: continued

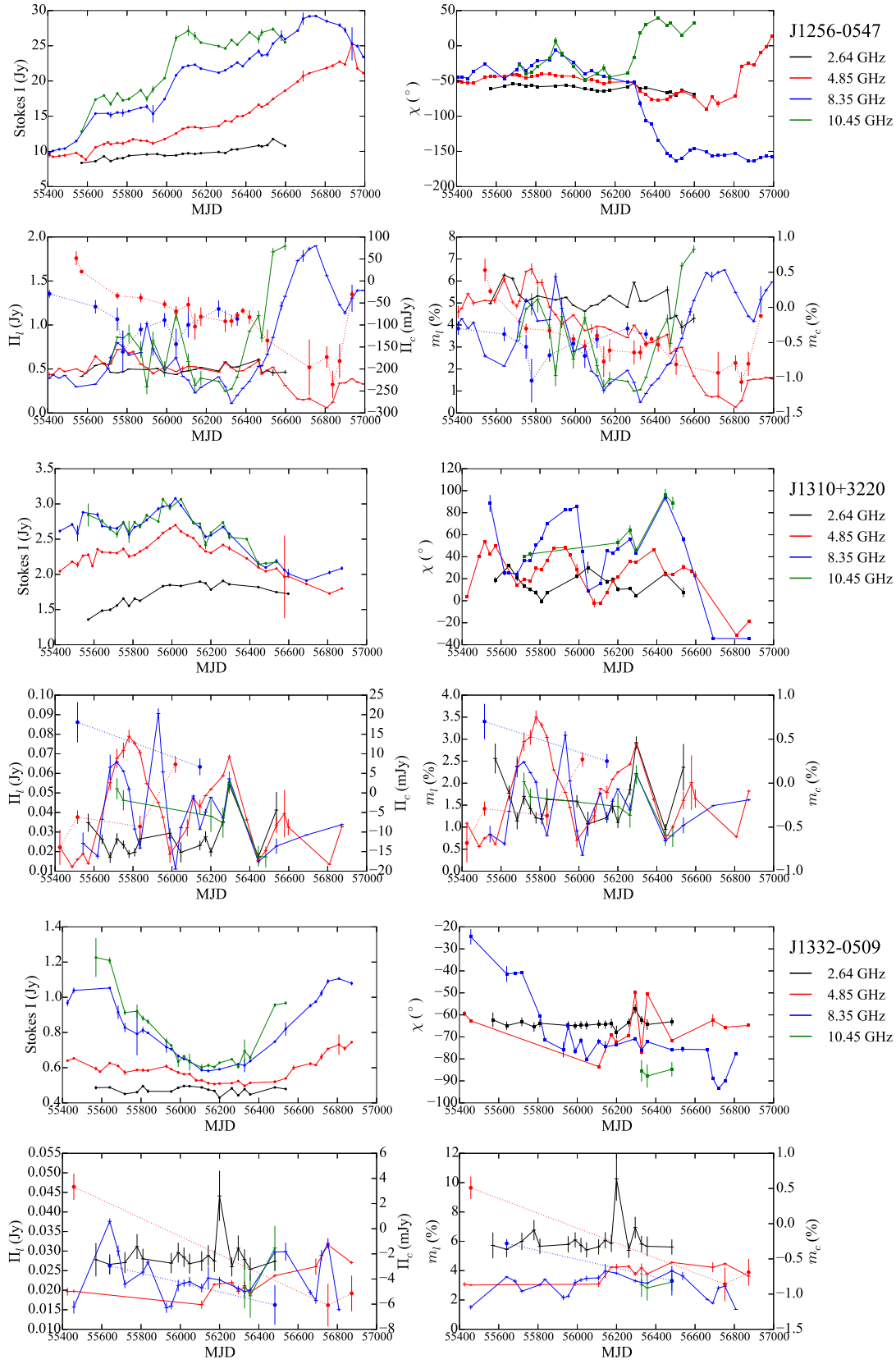


Figure B.17: continued

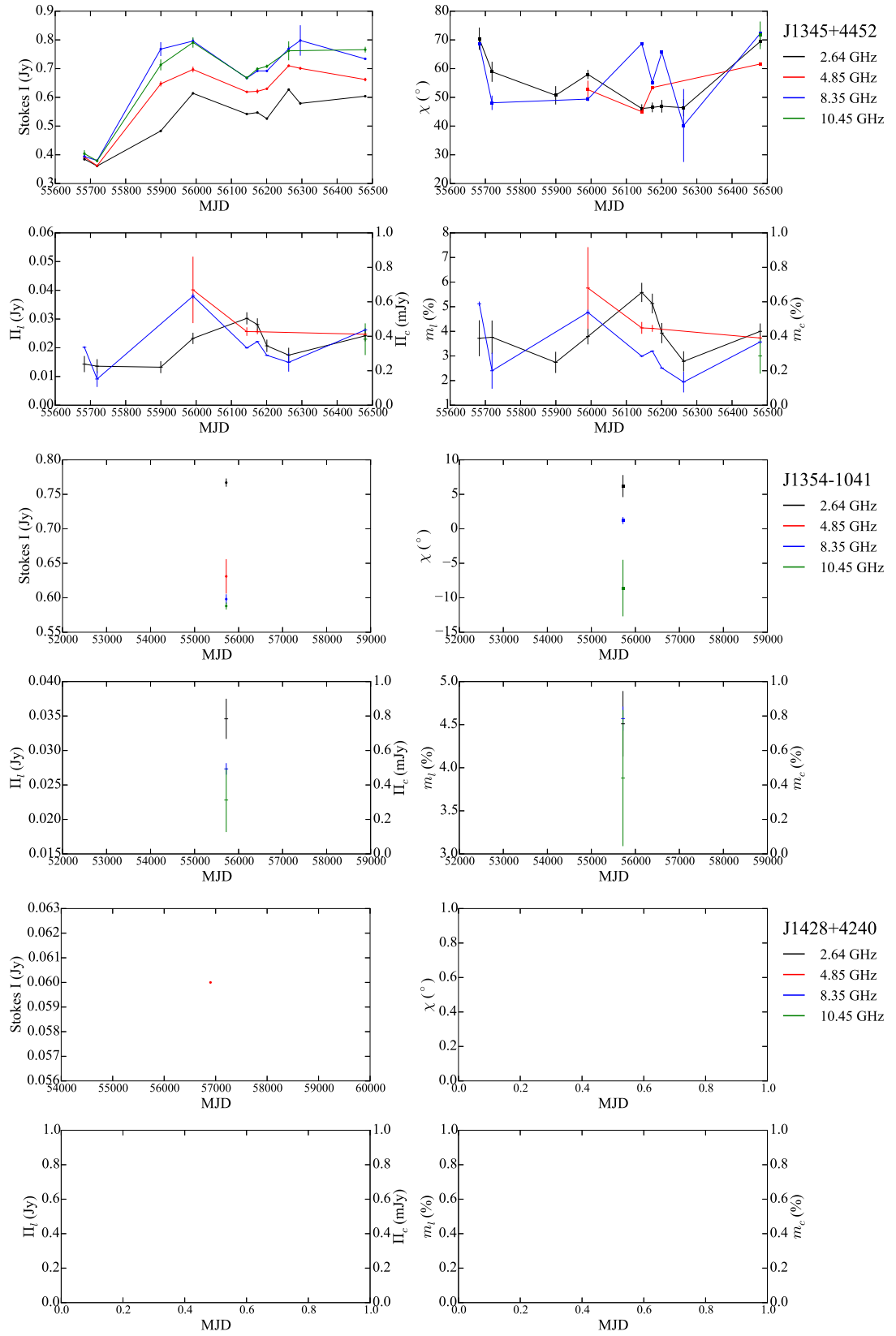


Figure B.18: continued

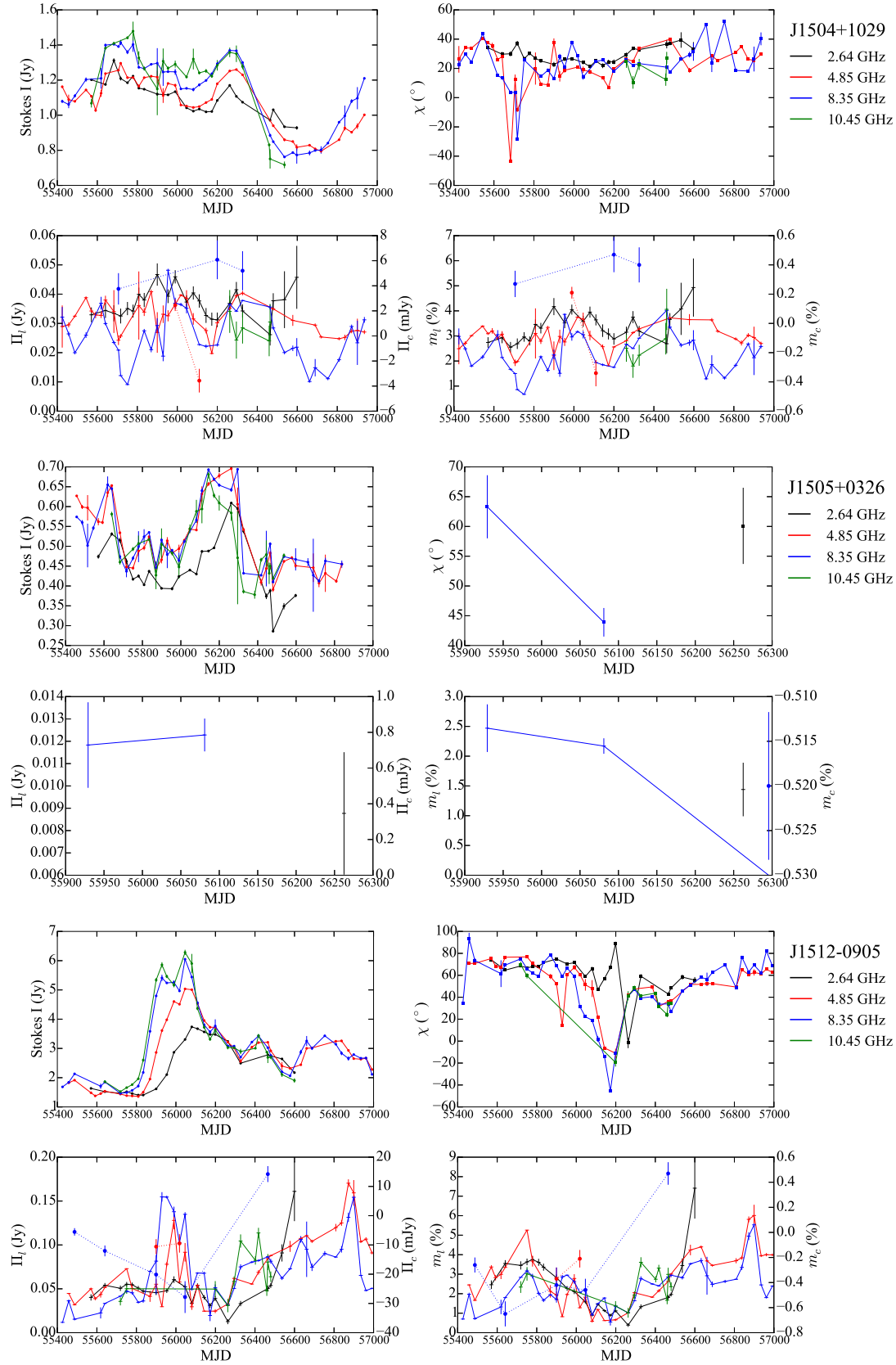


Figure B.19: continued

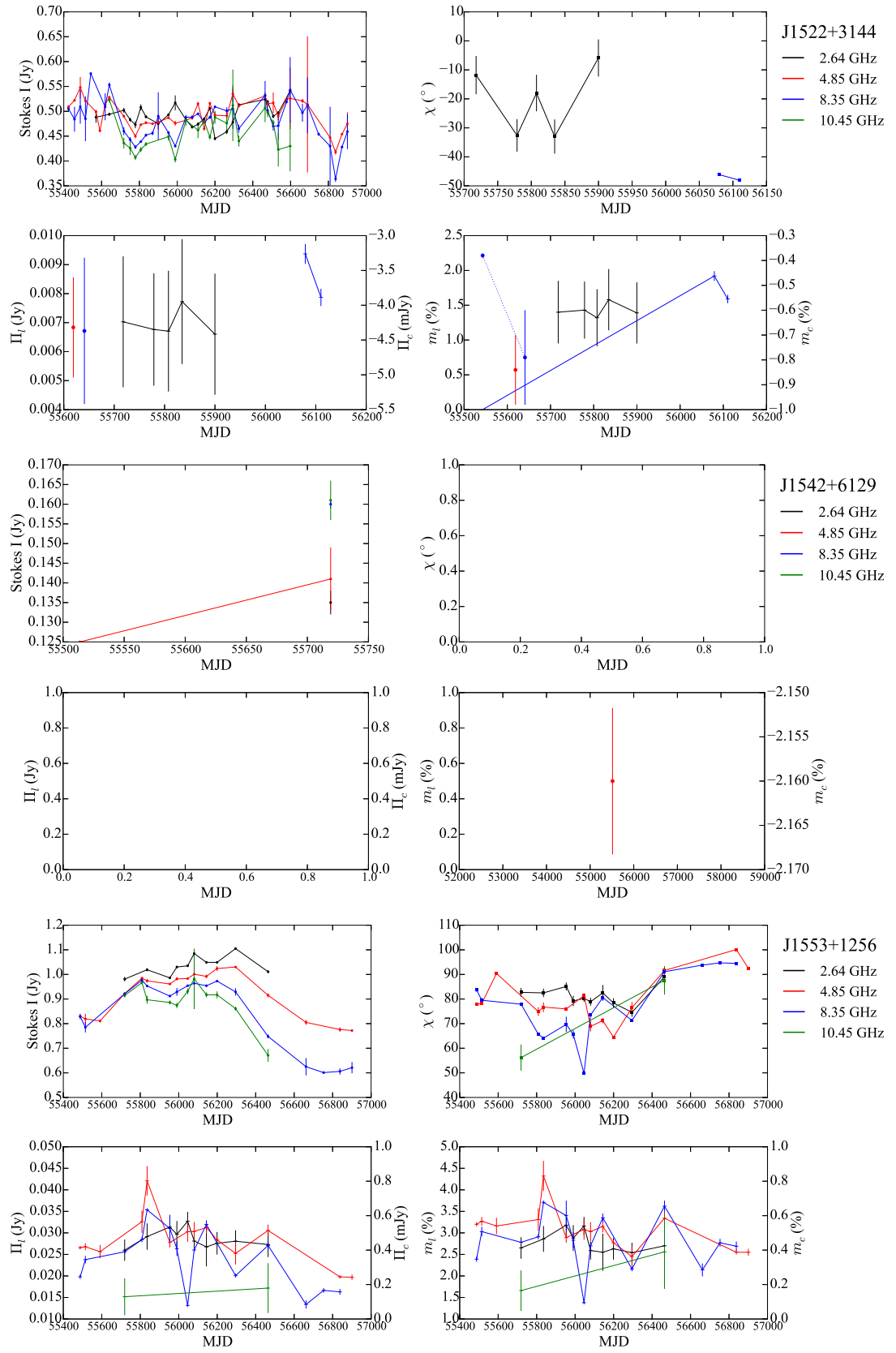


Figure B.20: continued

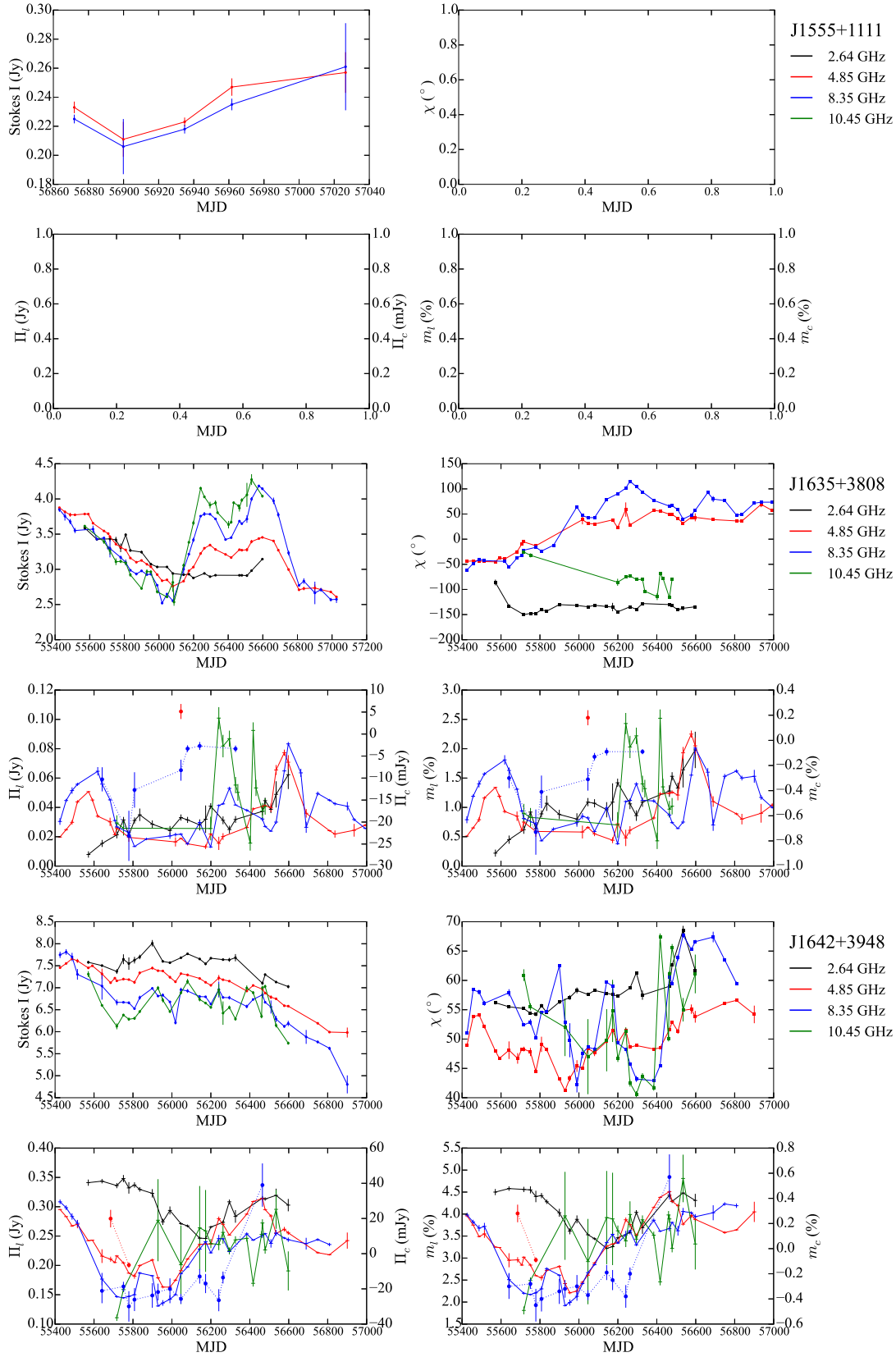


Figure B.21: continued

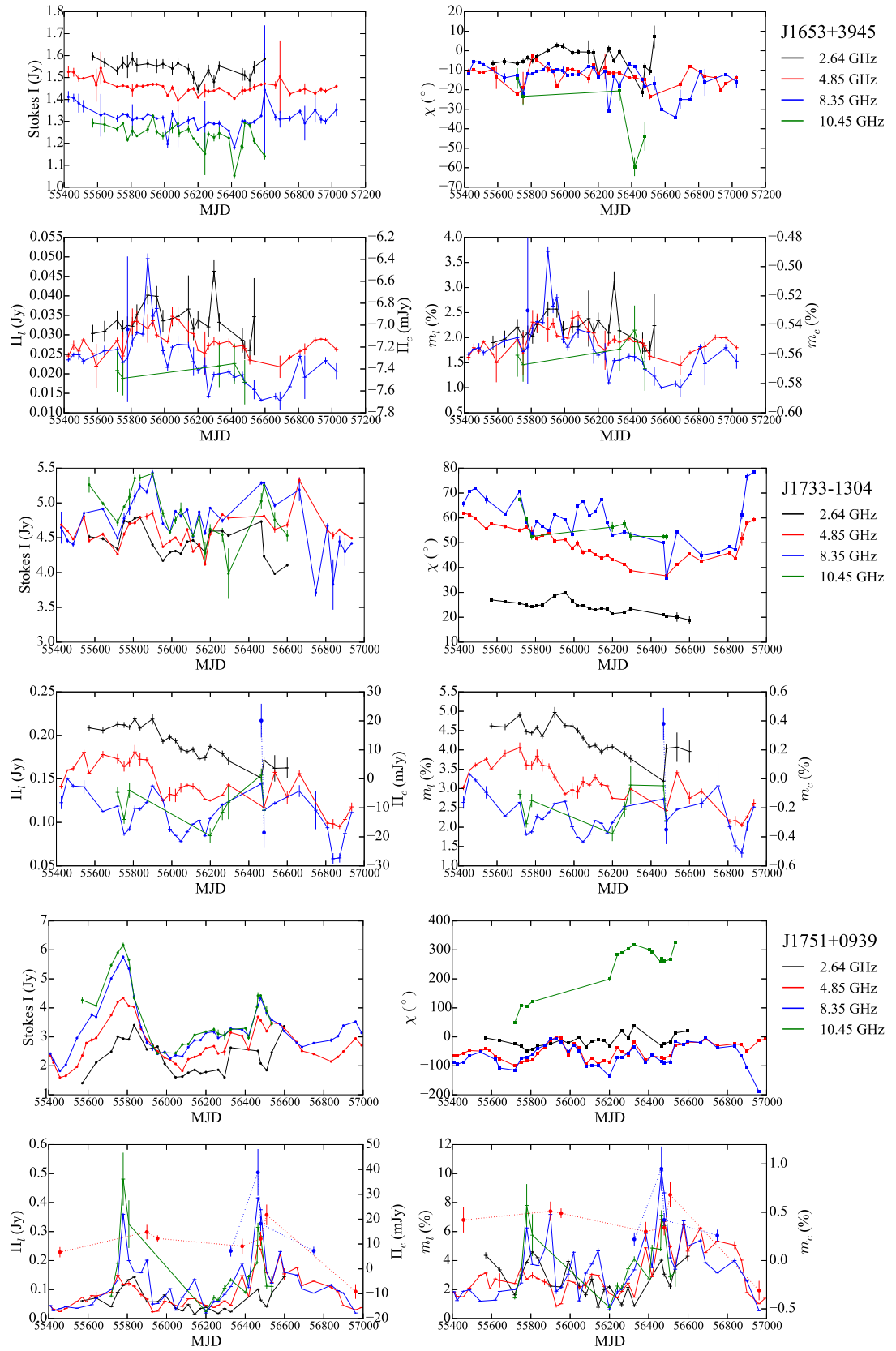


Figure B.22: continued

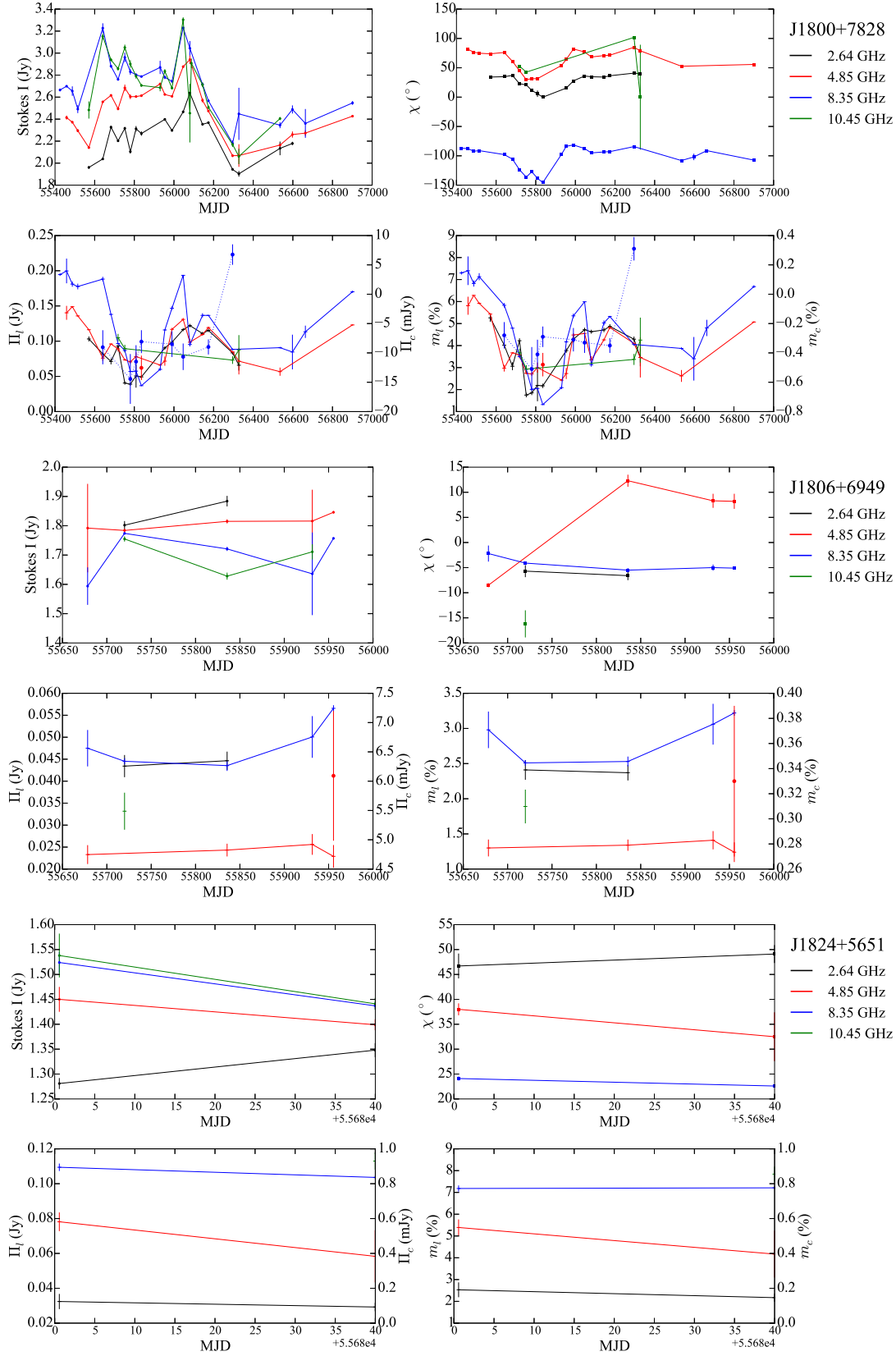


Figure B.23: continued

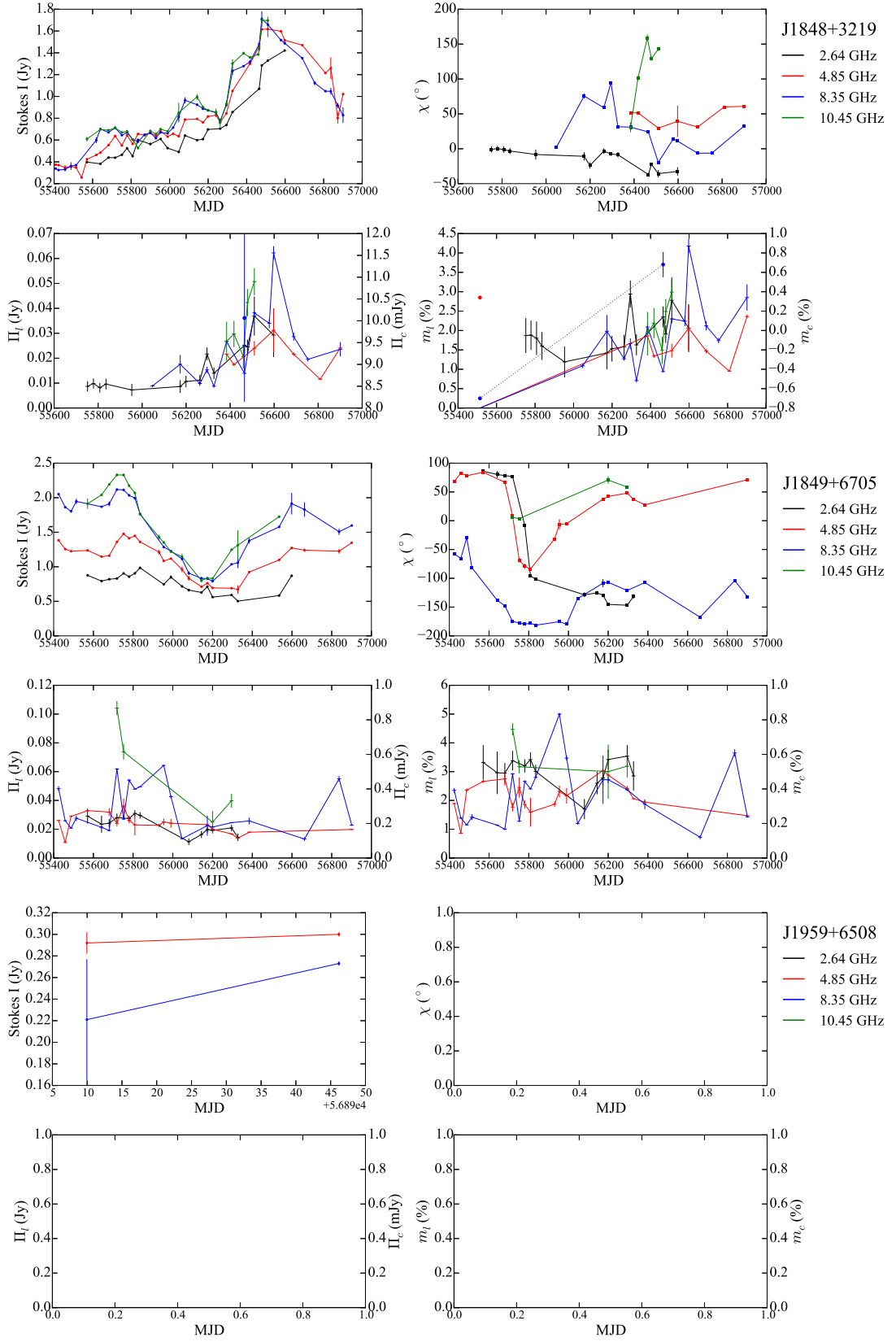


Figure B.24: continued

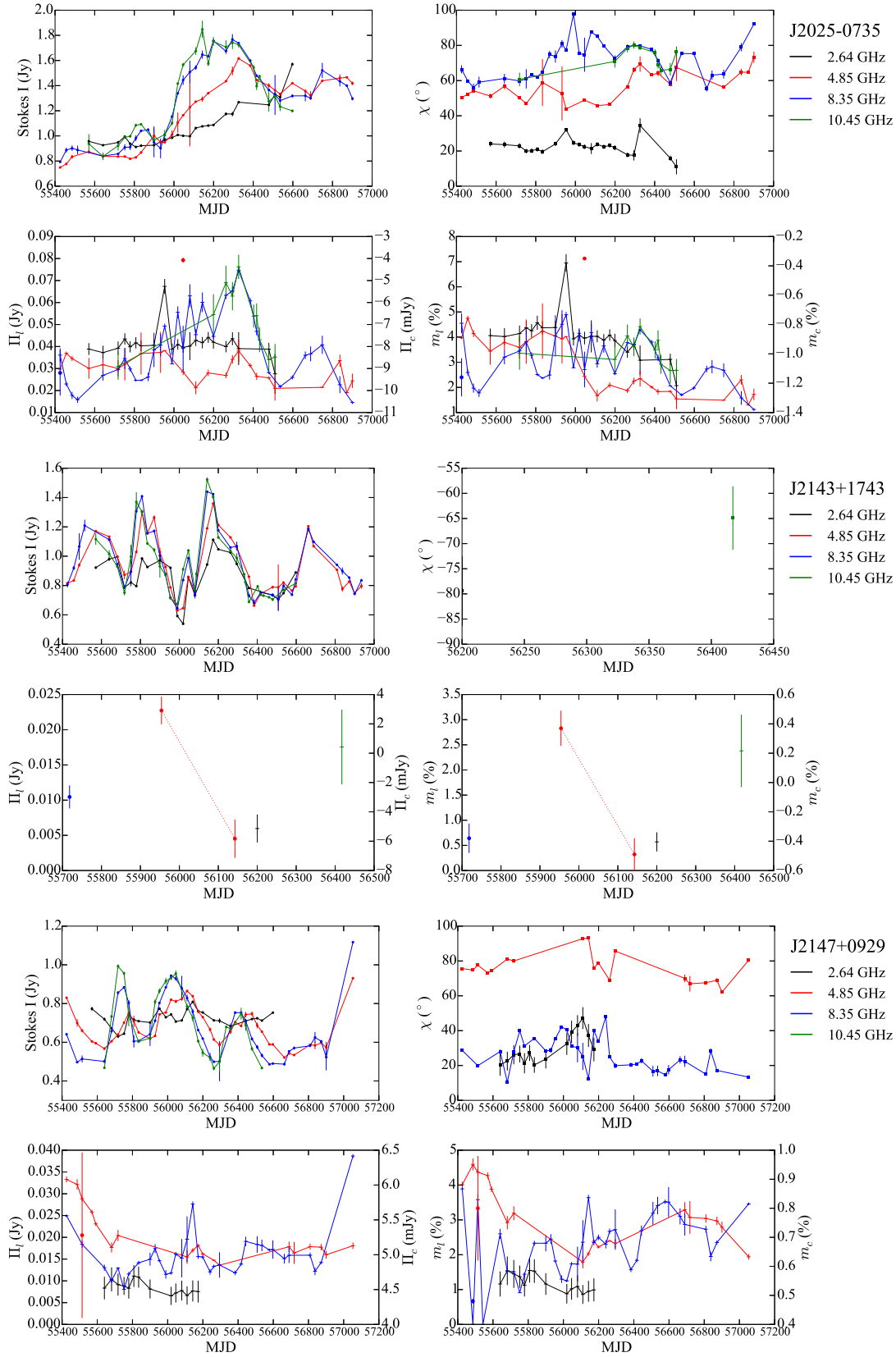


Figure B.25: continued

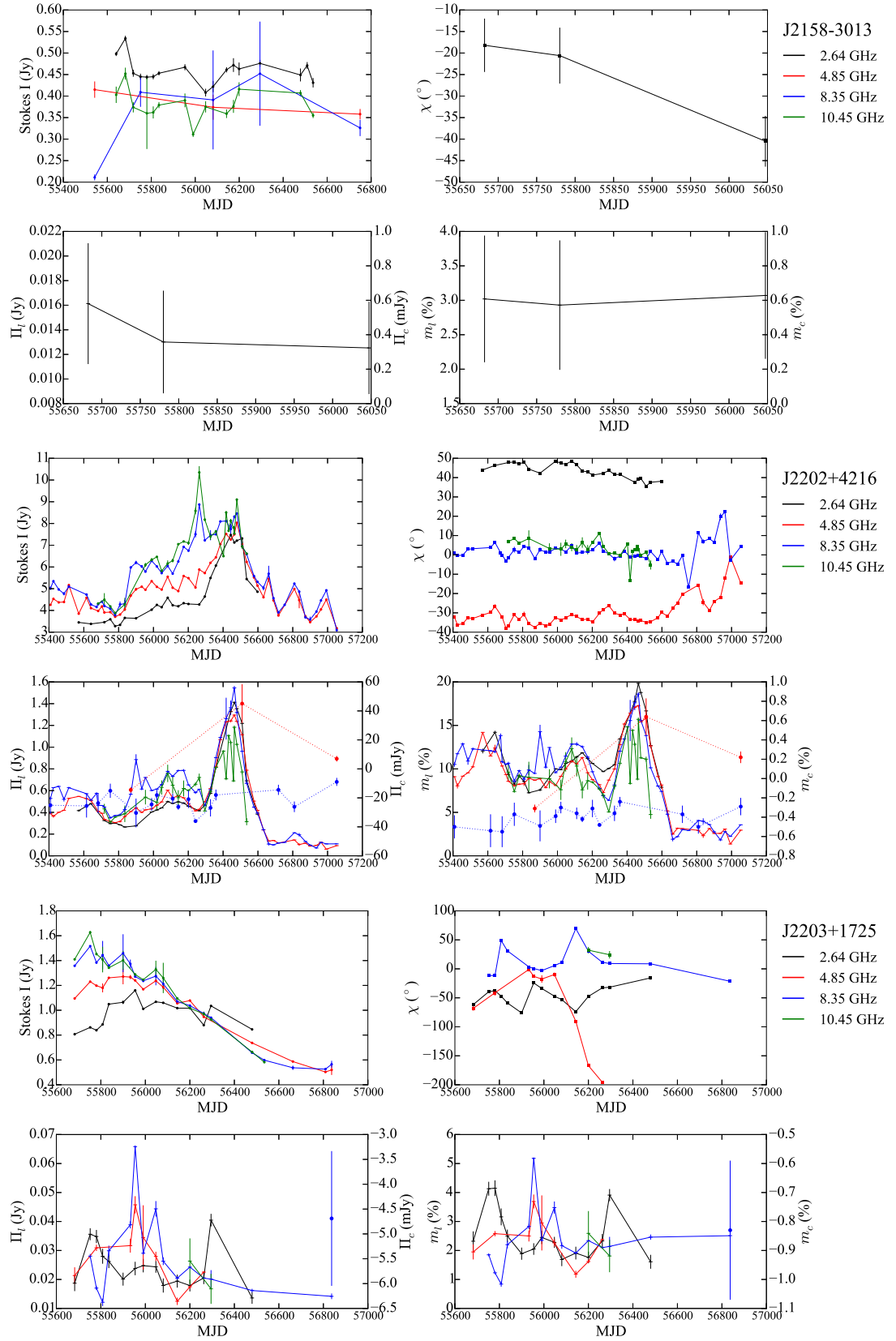


Figure B.26: continued

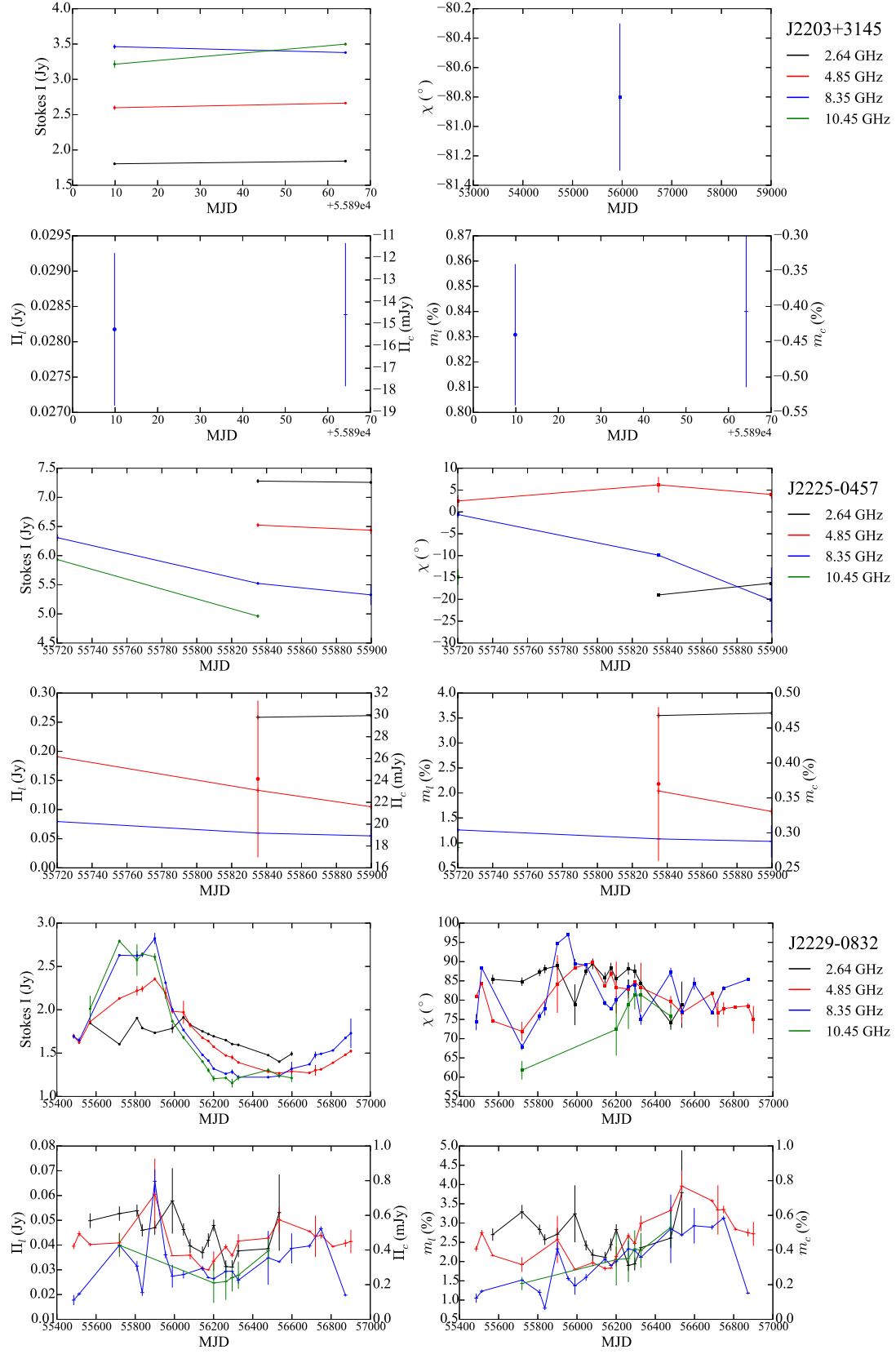


Figure B.27: continued

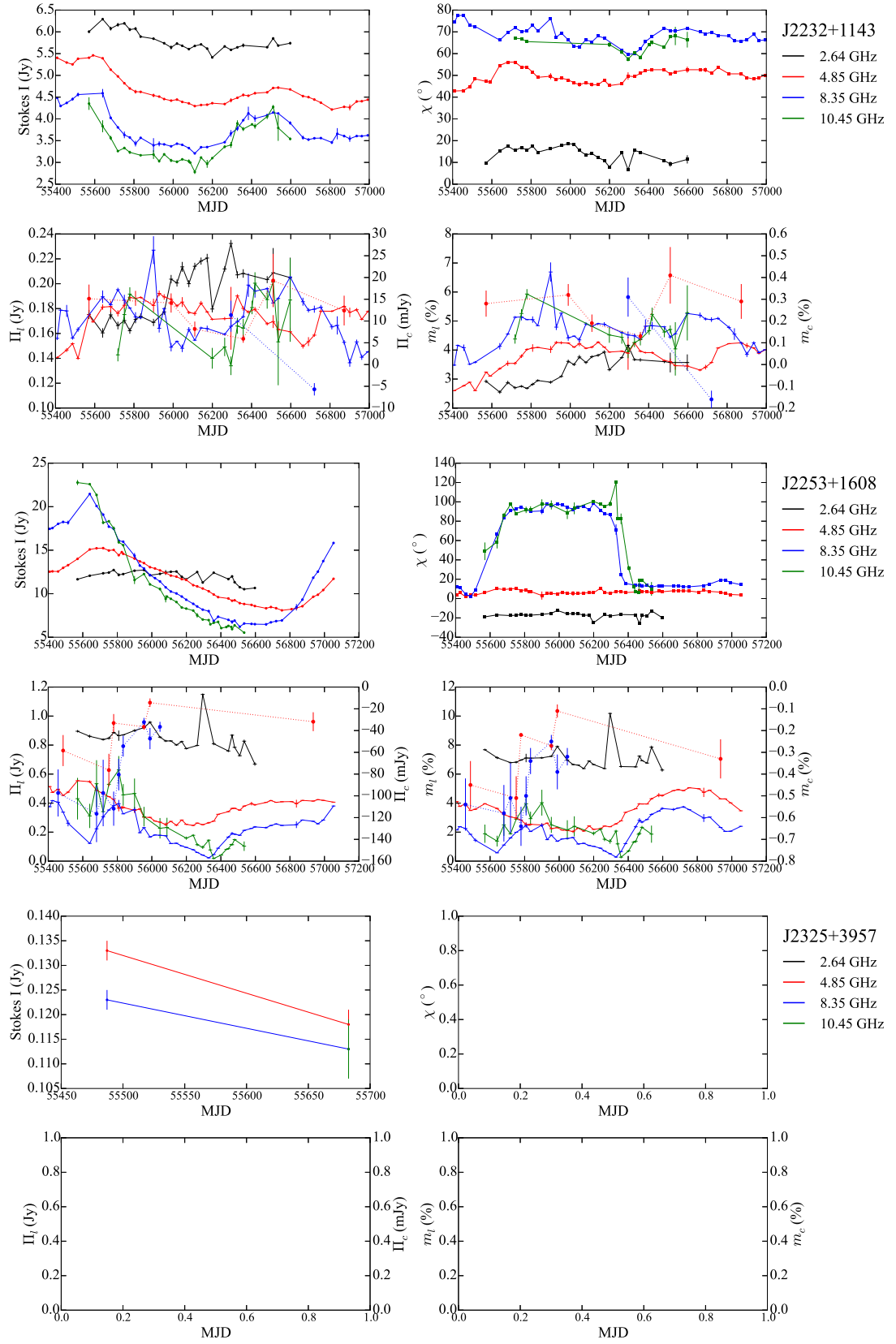


Figure B.28: continued

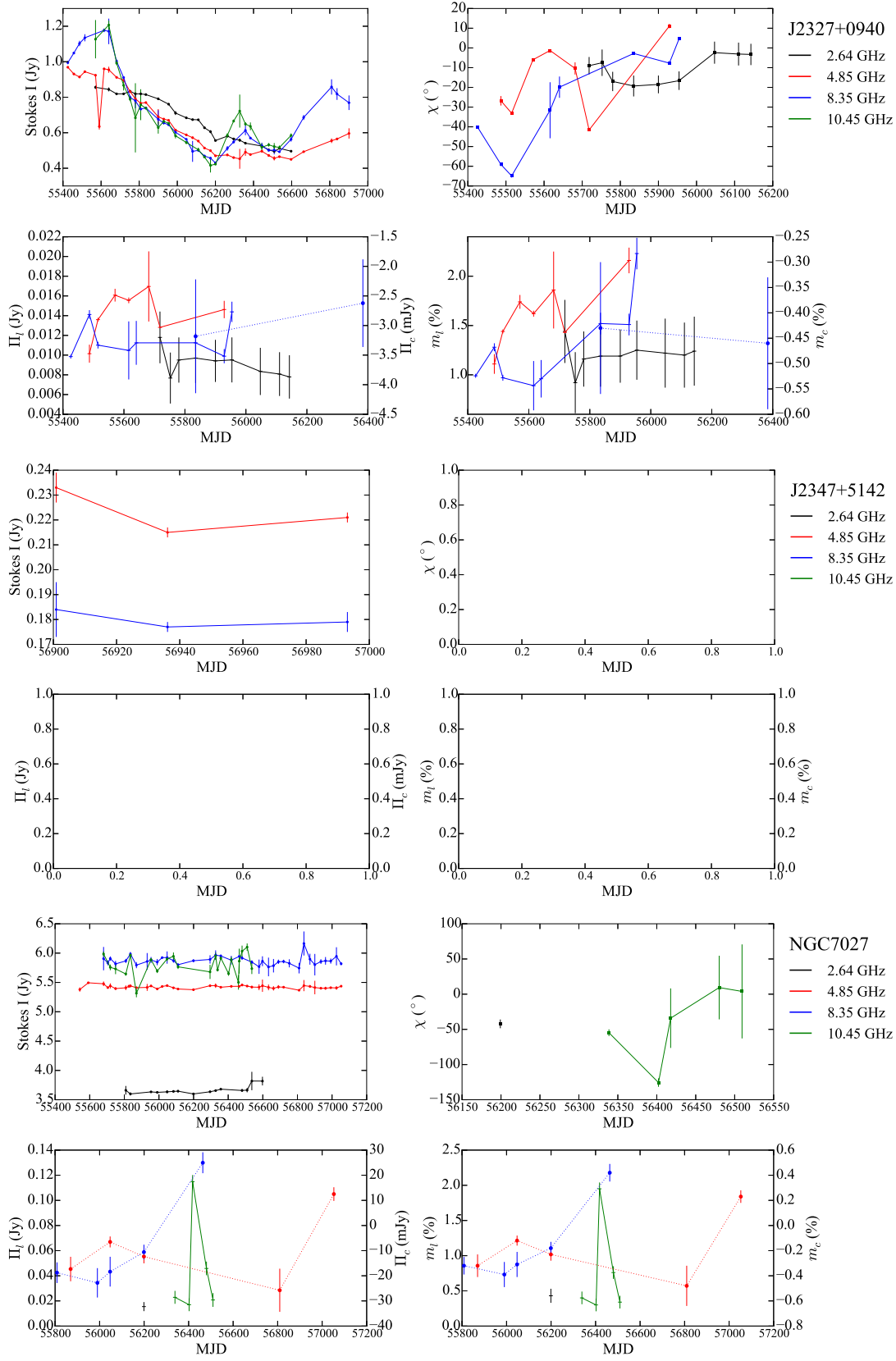


Figure B.29: continued

Appendix C

Spectra

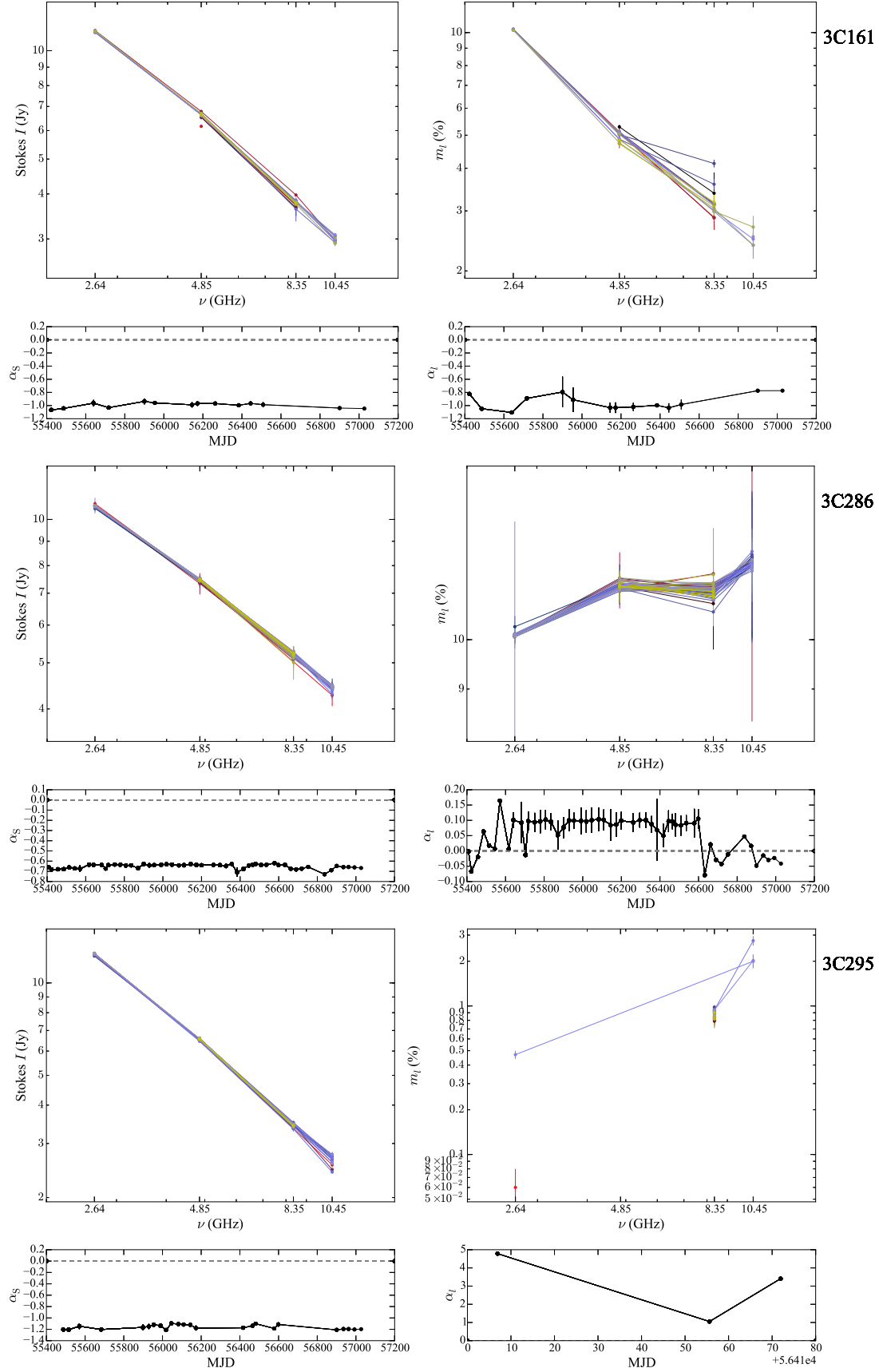


Figure C.1: Radio total flux density (left column) and linear polarization (right column) spectra extracted for all the observing sessions. In the bottom row, we plot the corresponding light curves of the spectral indices acquired by fitting a single power law through each spectrum.

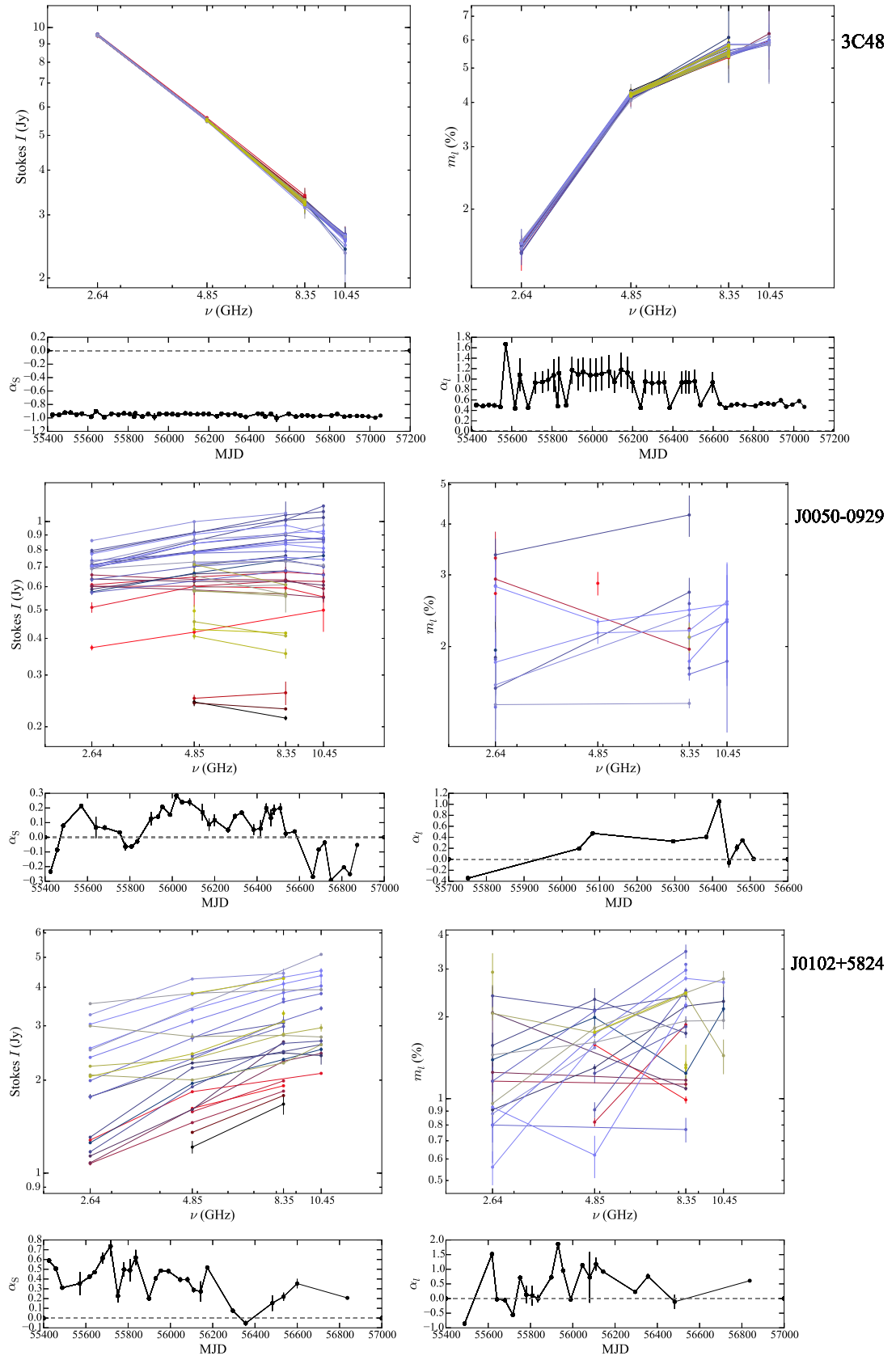


Figure C.2: continued

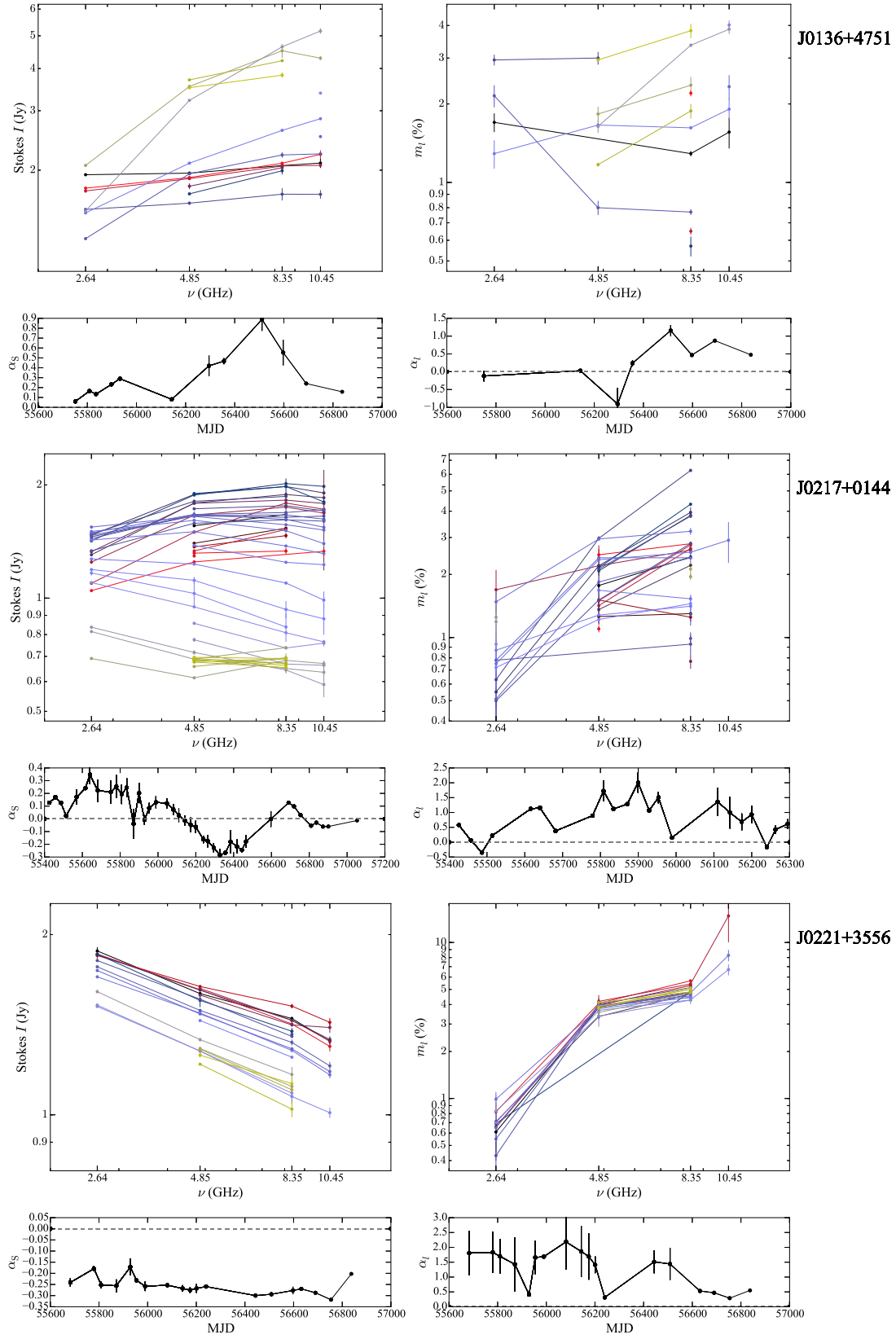


Figure C.3: continued

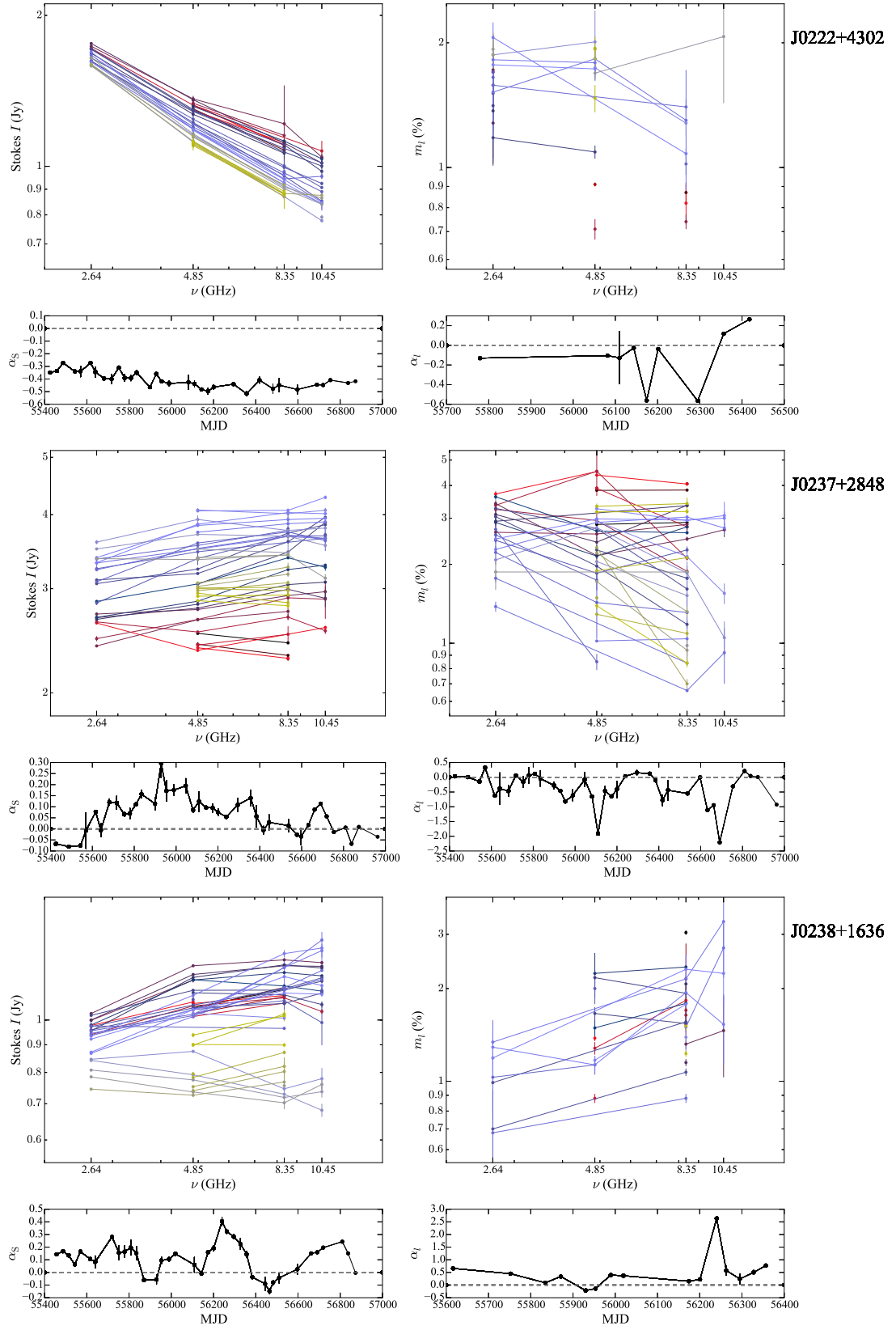


Figure C.4: continued

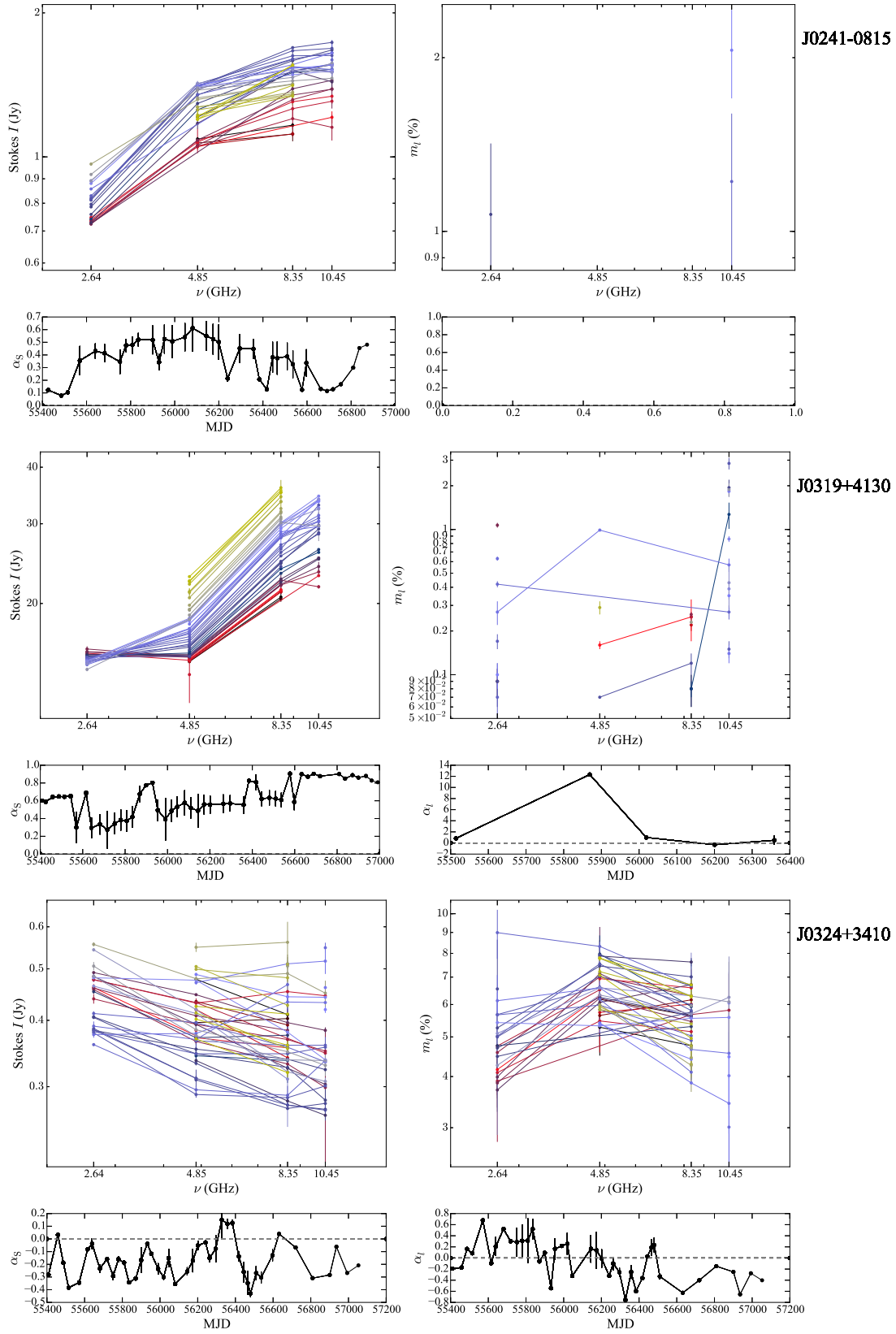


Figure C.5: continued

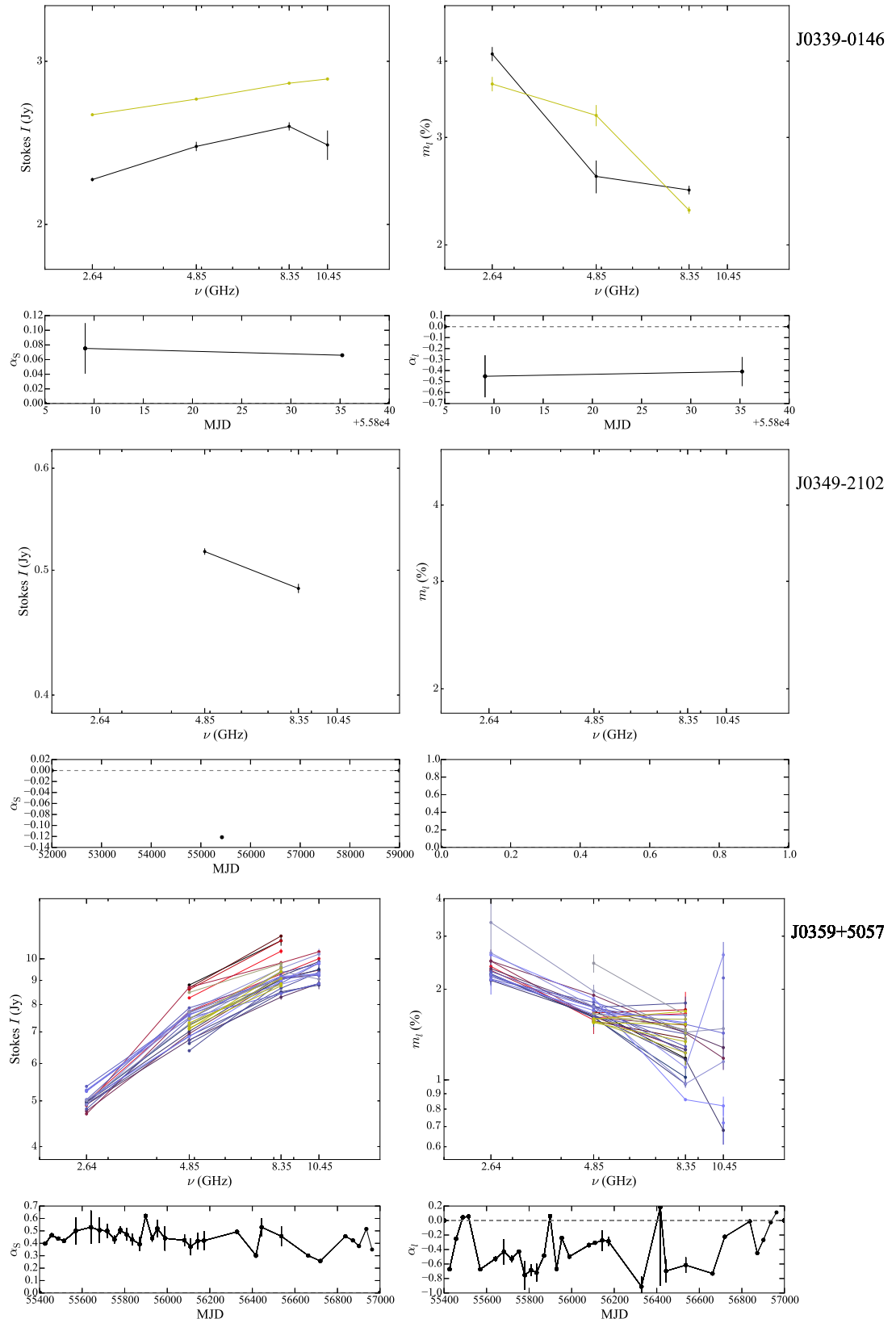


Figure C.6: continued

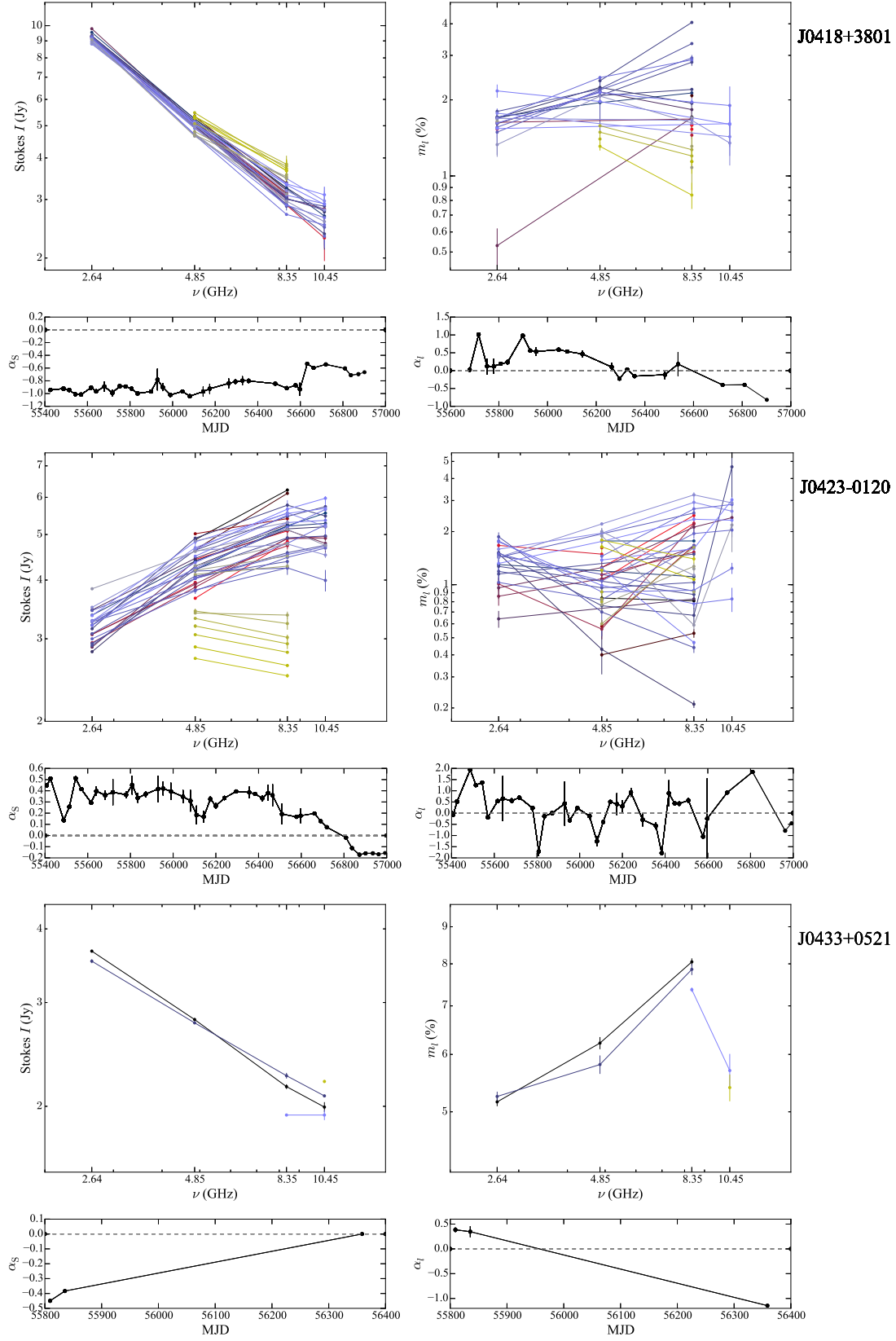


Figure C.7: continued

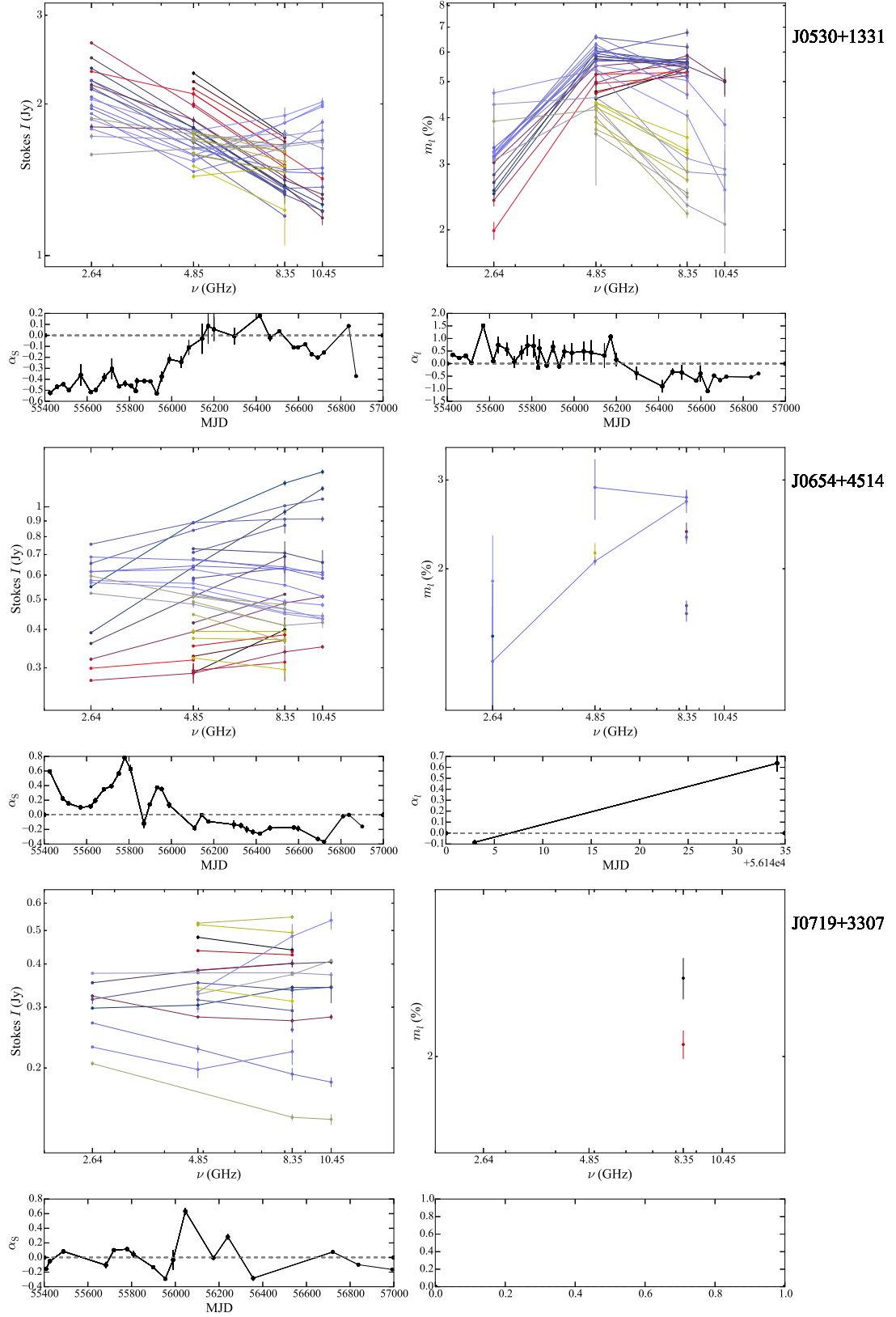


Figure C.8: continued

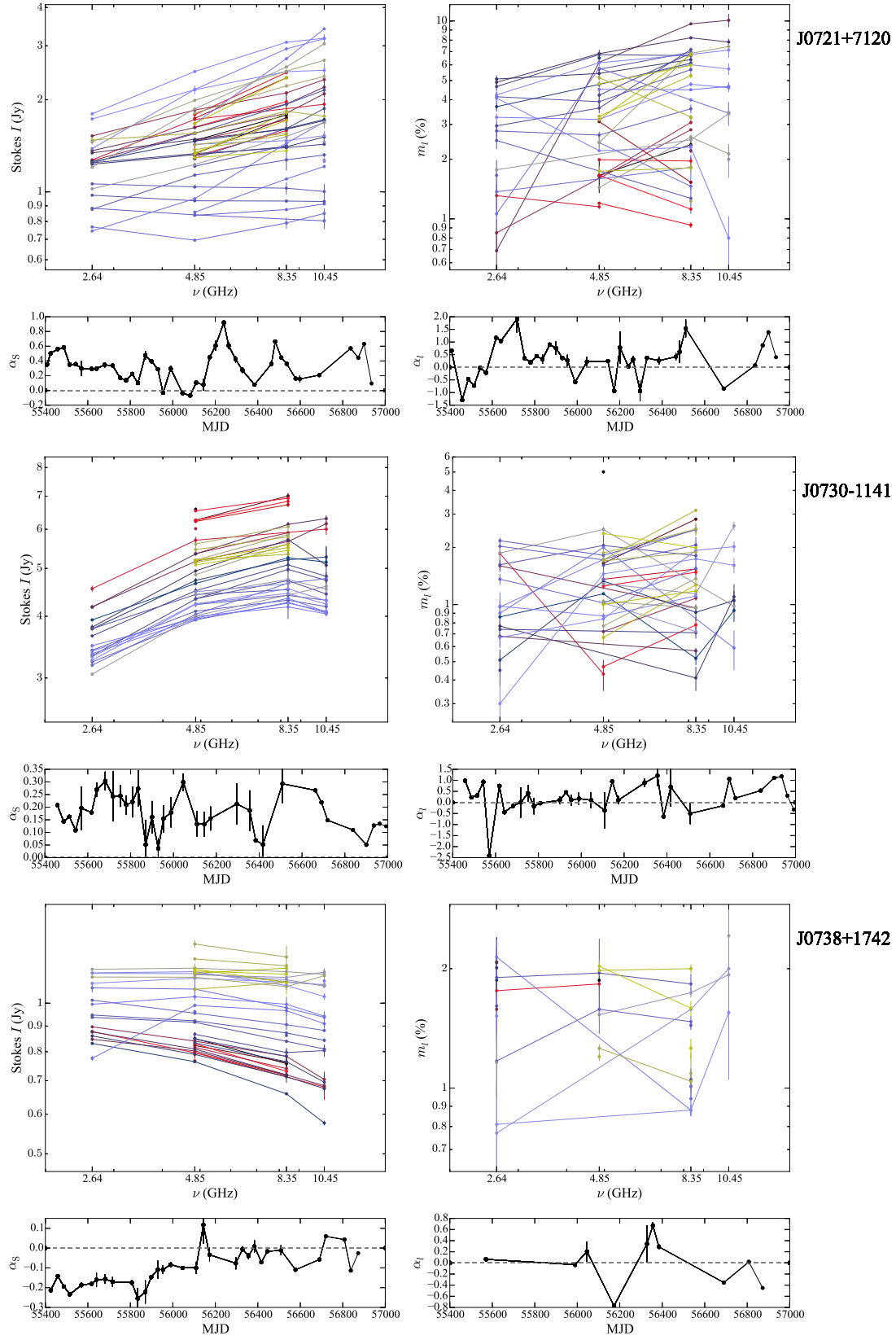


Figure C.9: continued

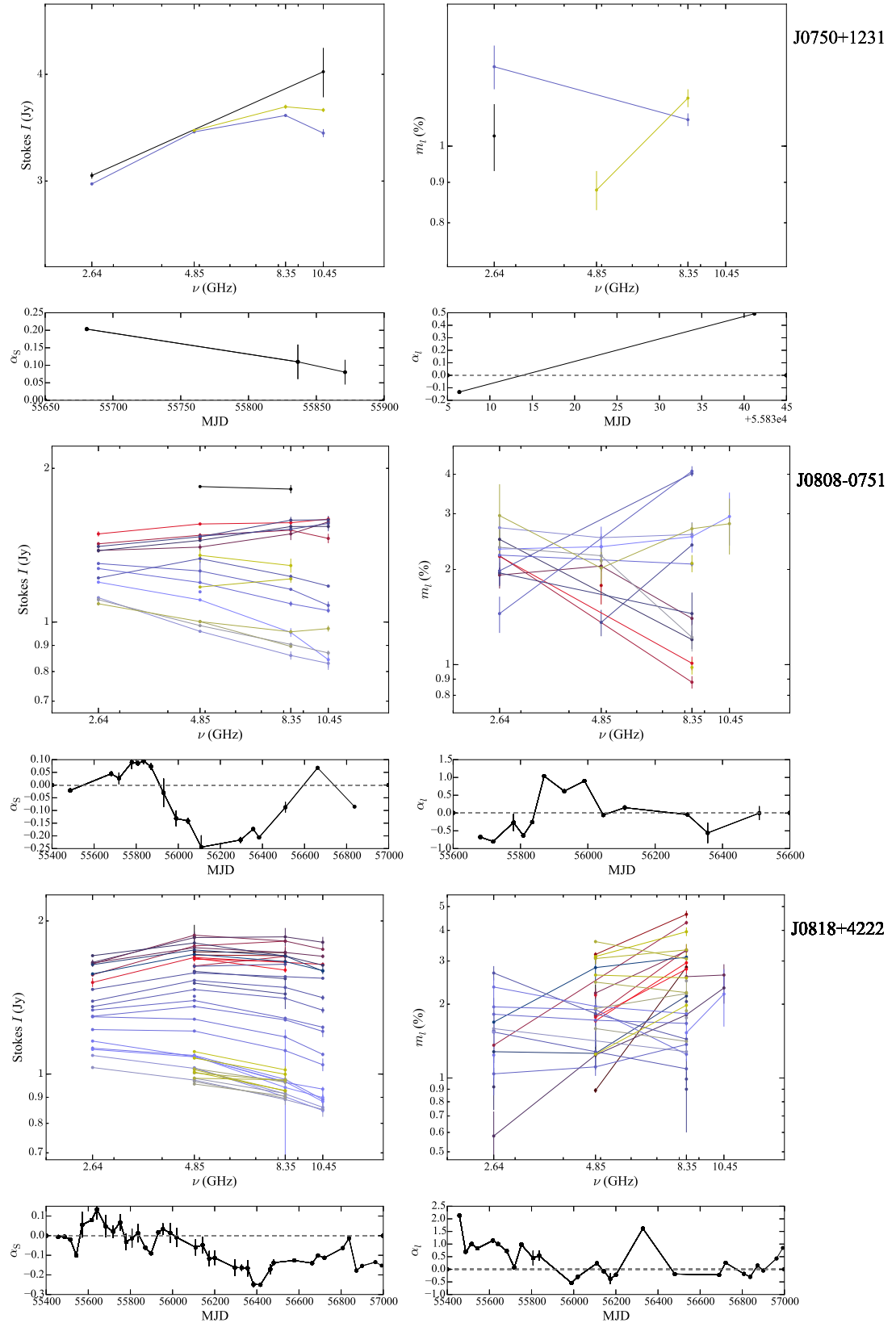


Figure C.10: continued

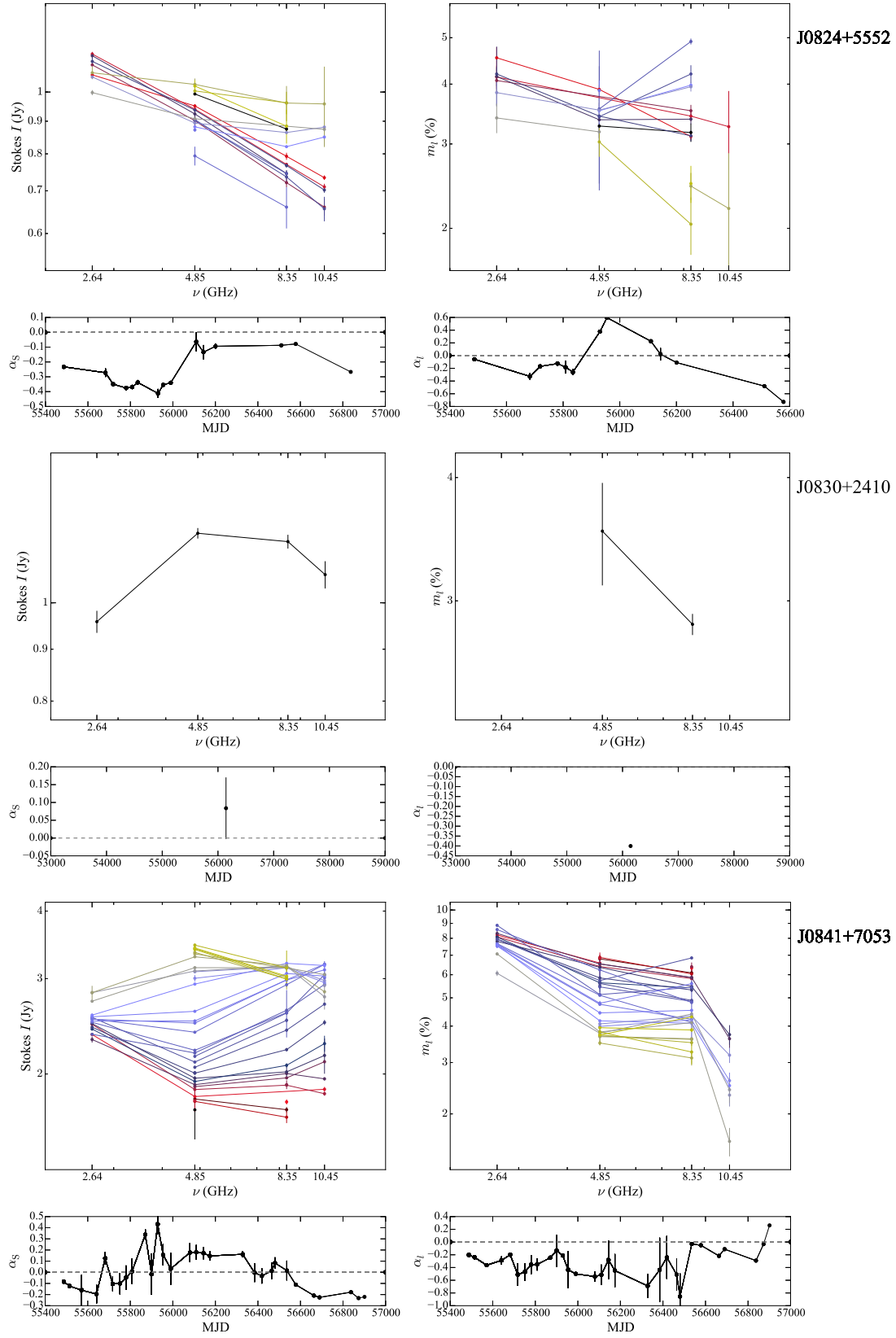


Figure C.11: continued

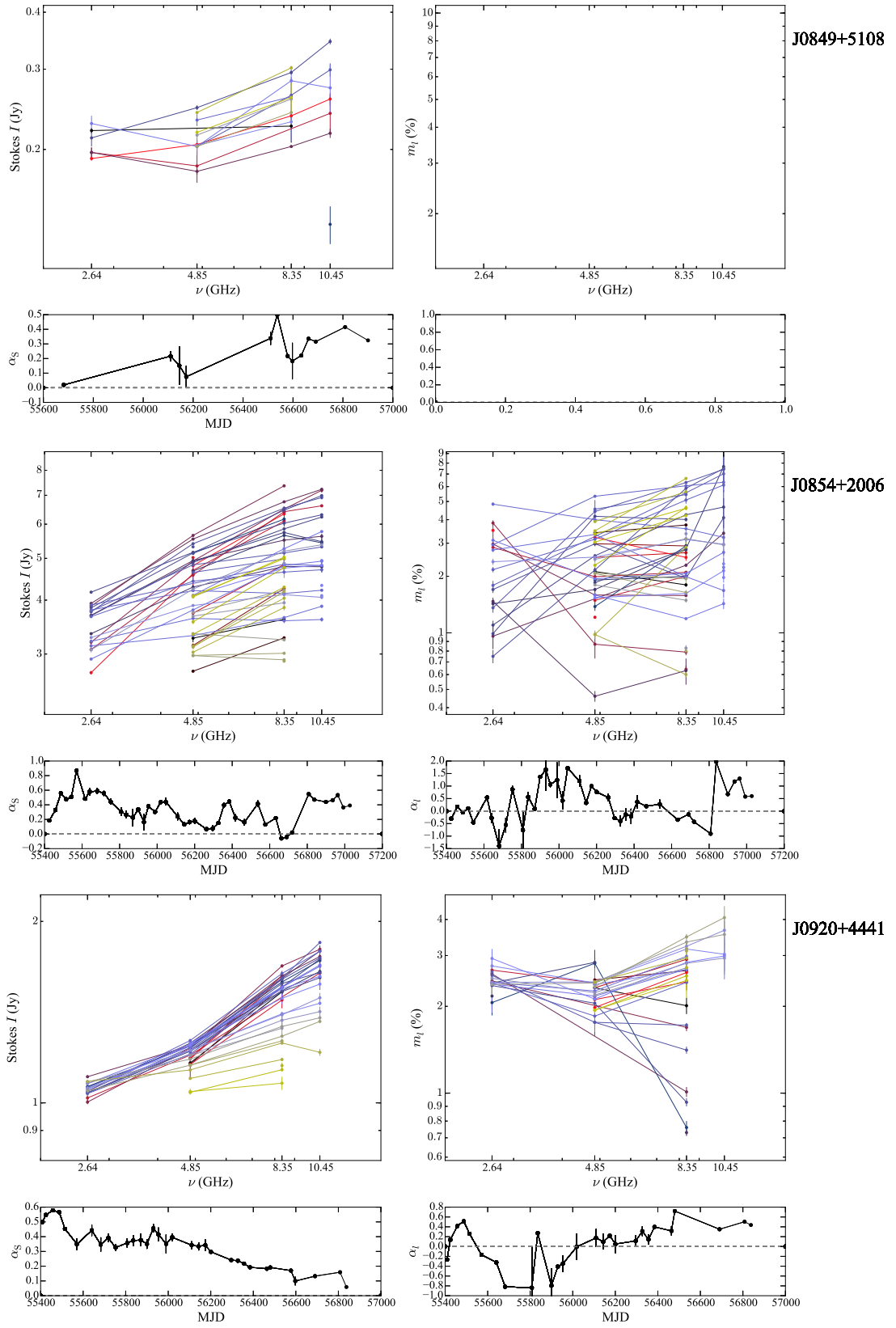


Figure C.12: continued

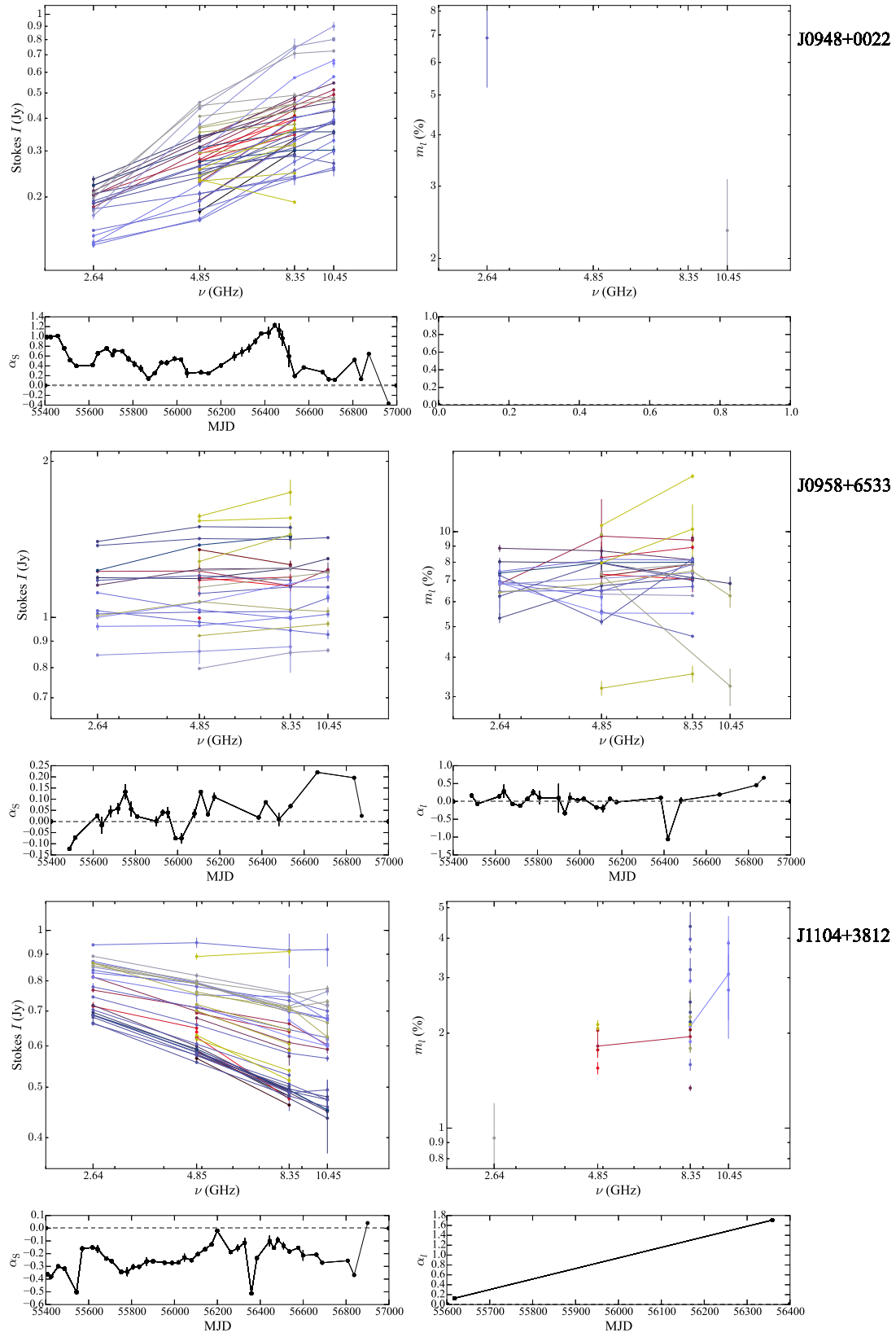


Figure C.13: continued

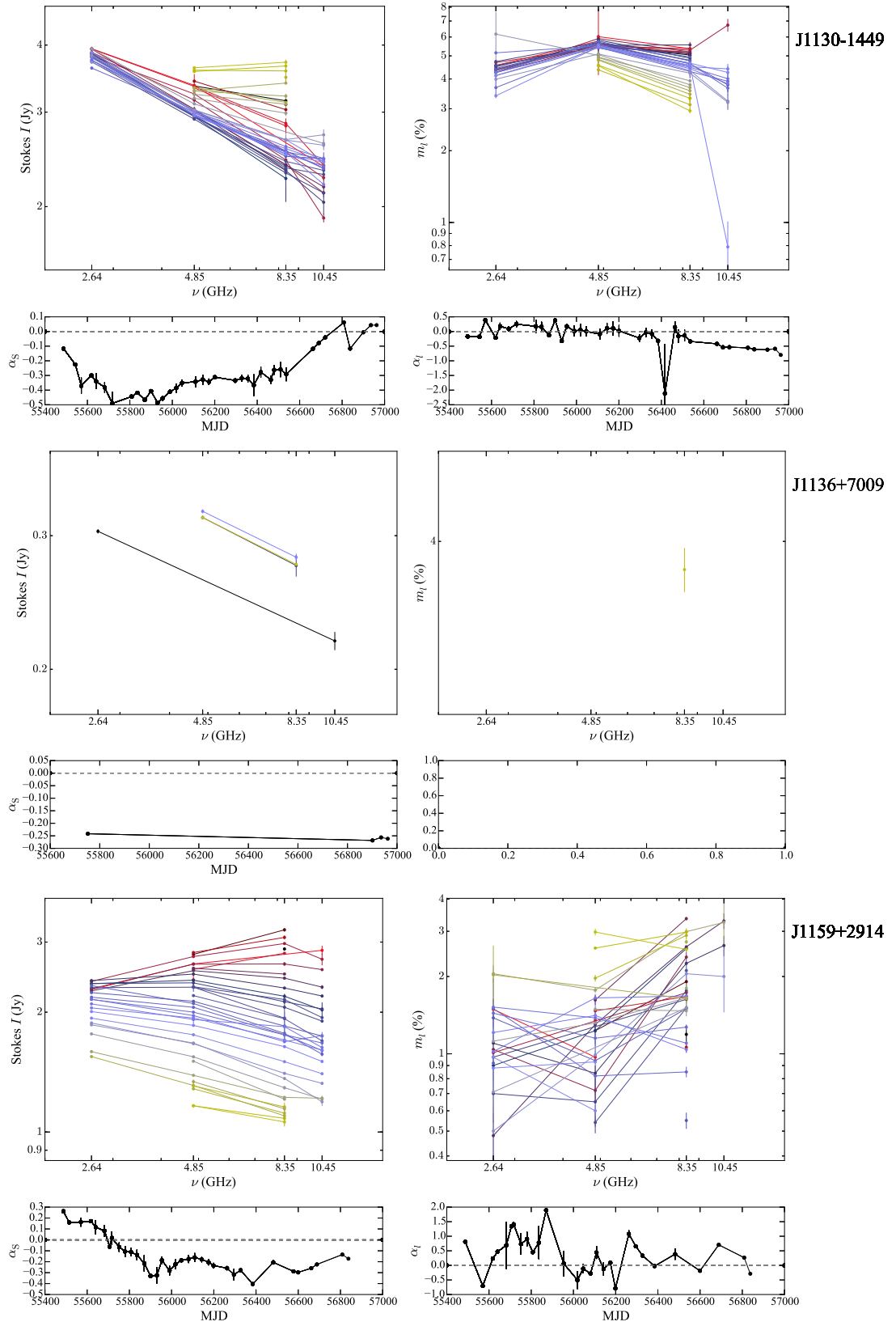


Figure C.14: continued

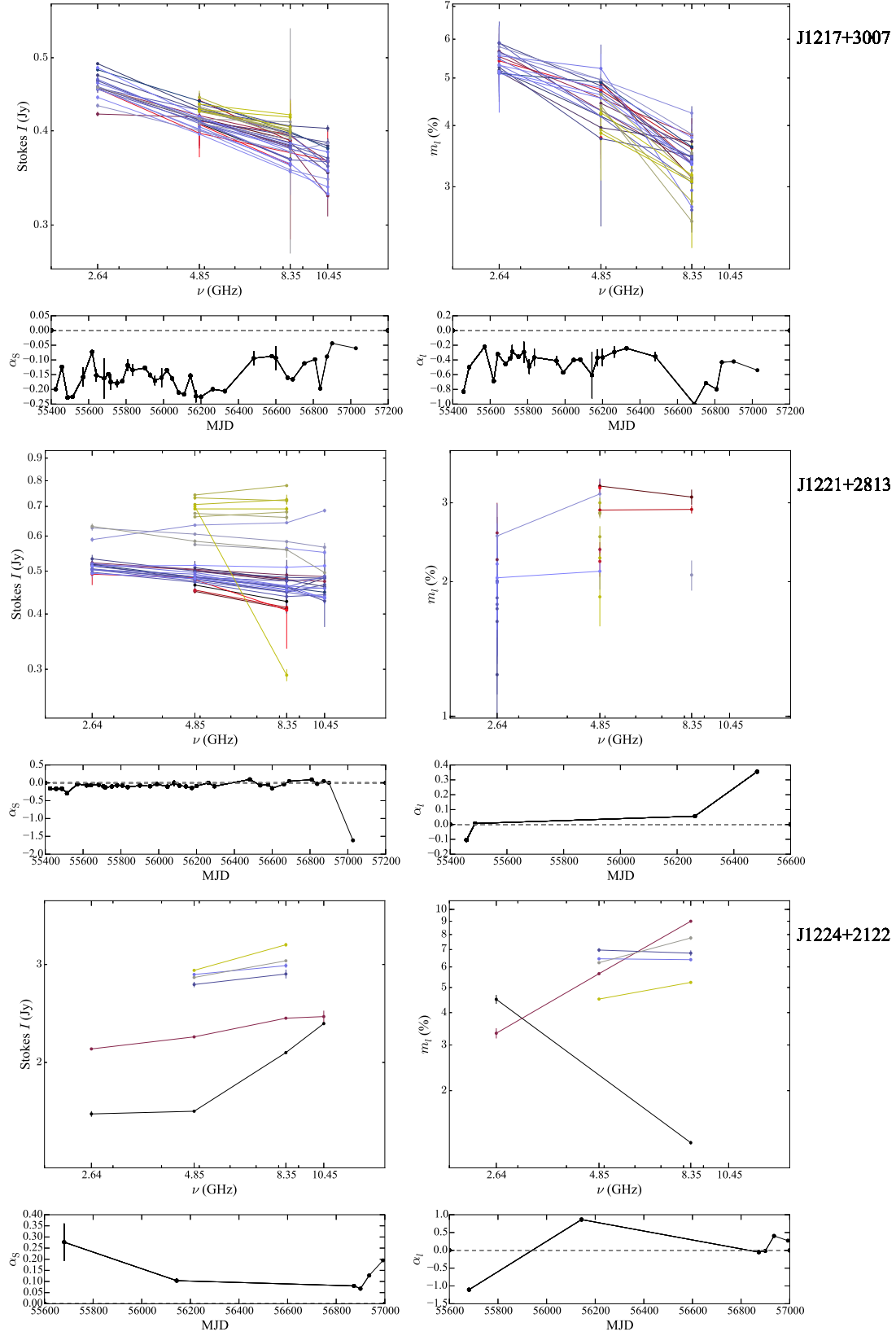


Figure C.15: continued

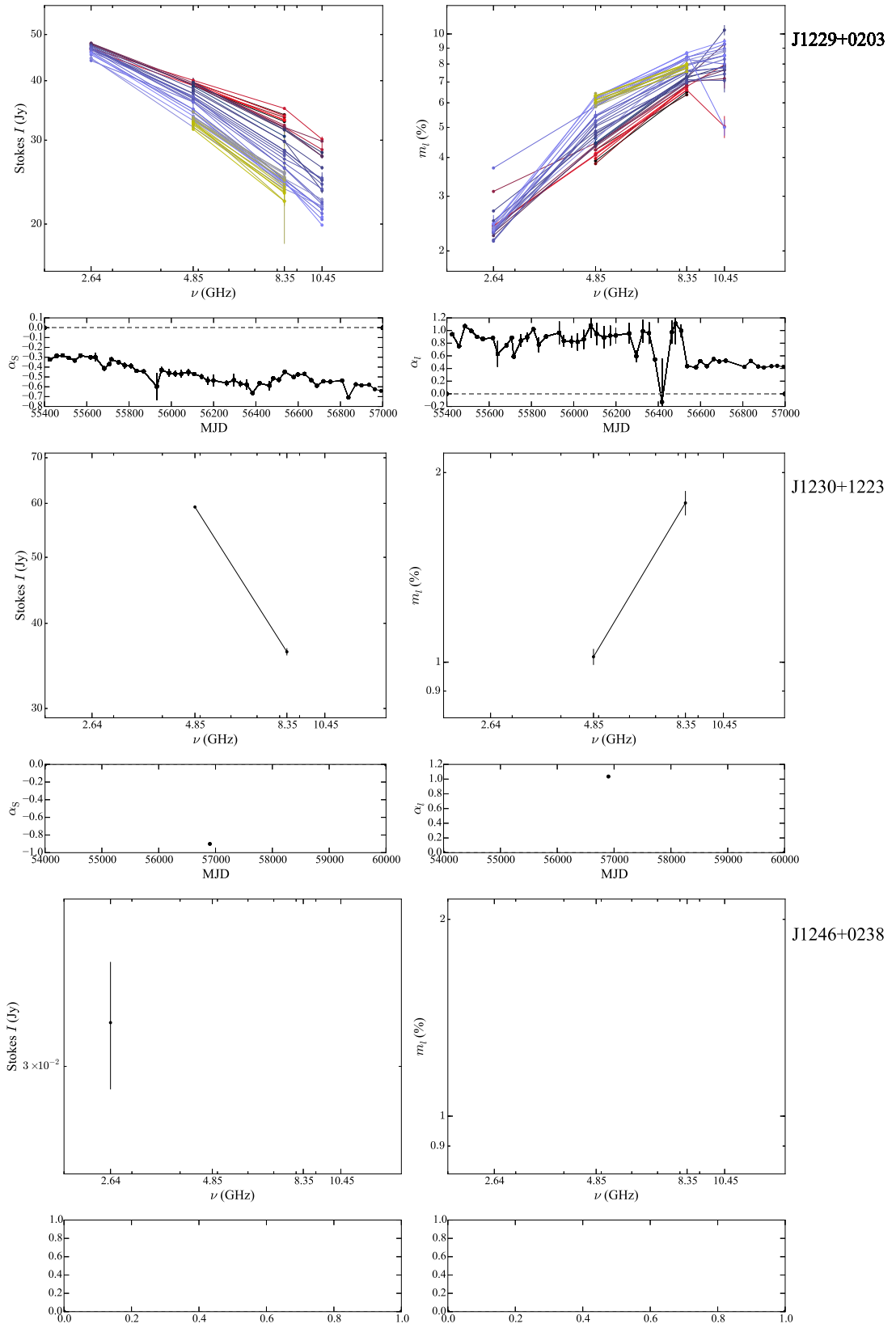


Figure C.16: continued

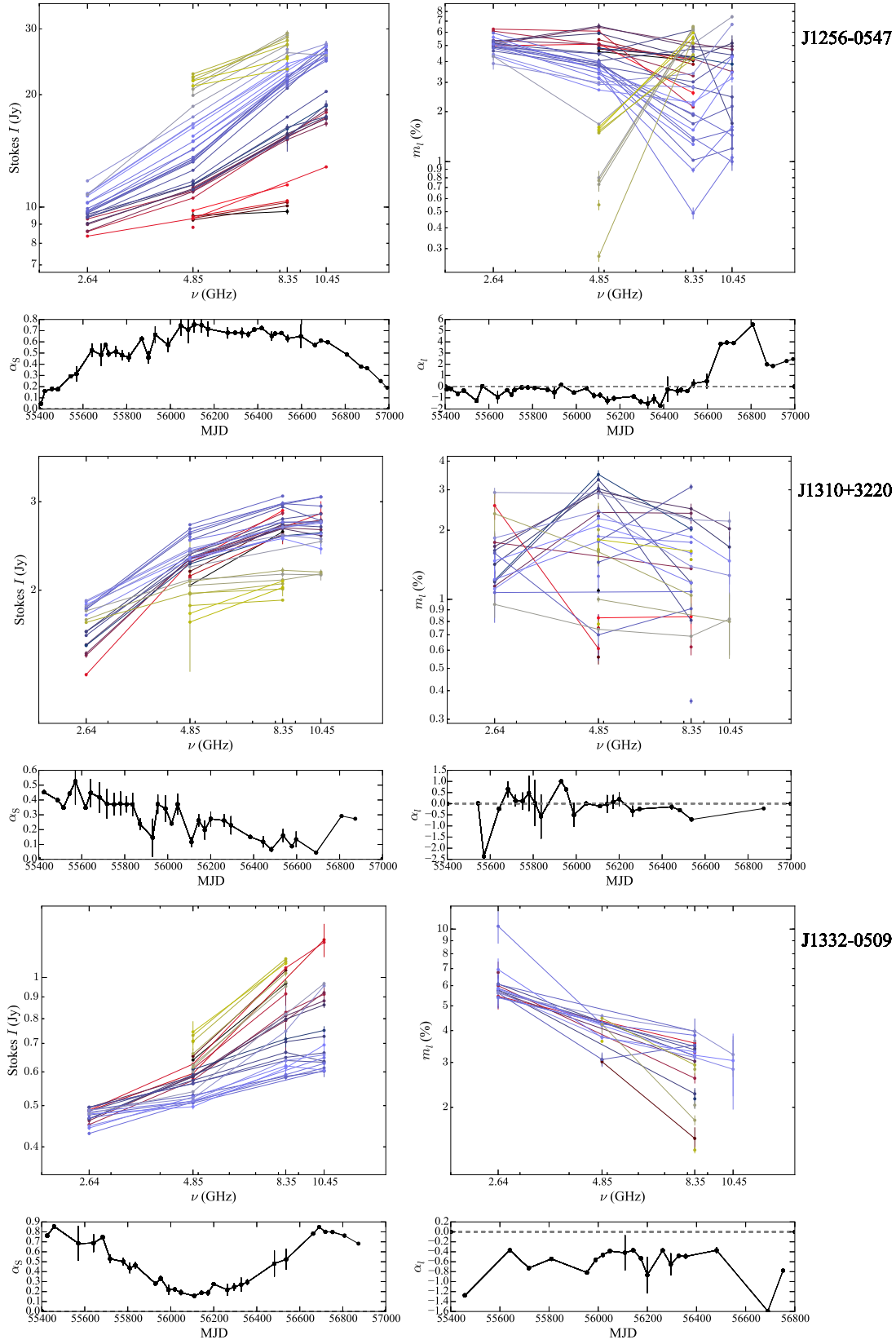


Figure C.17: continued

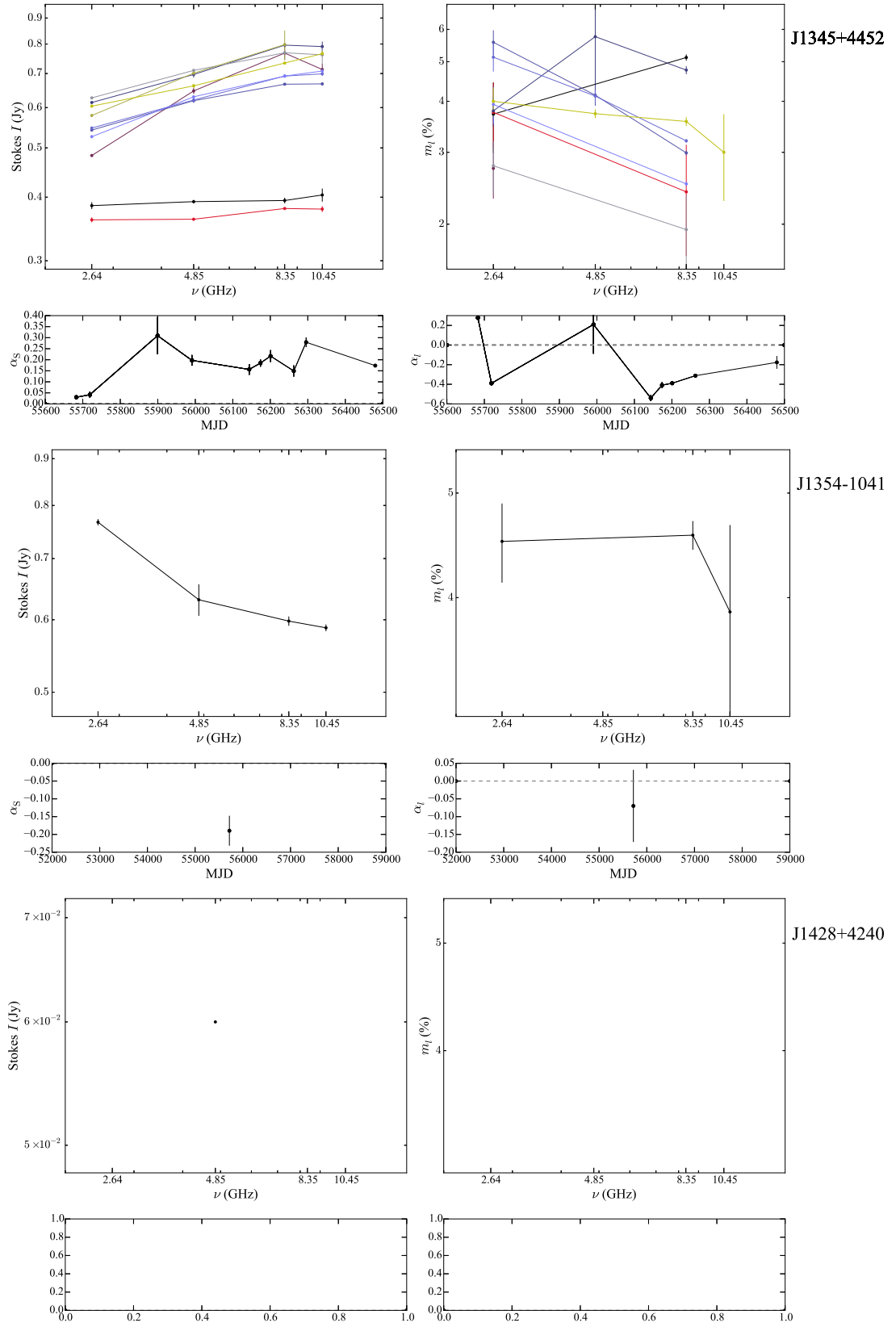


Figure C.18: continued

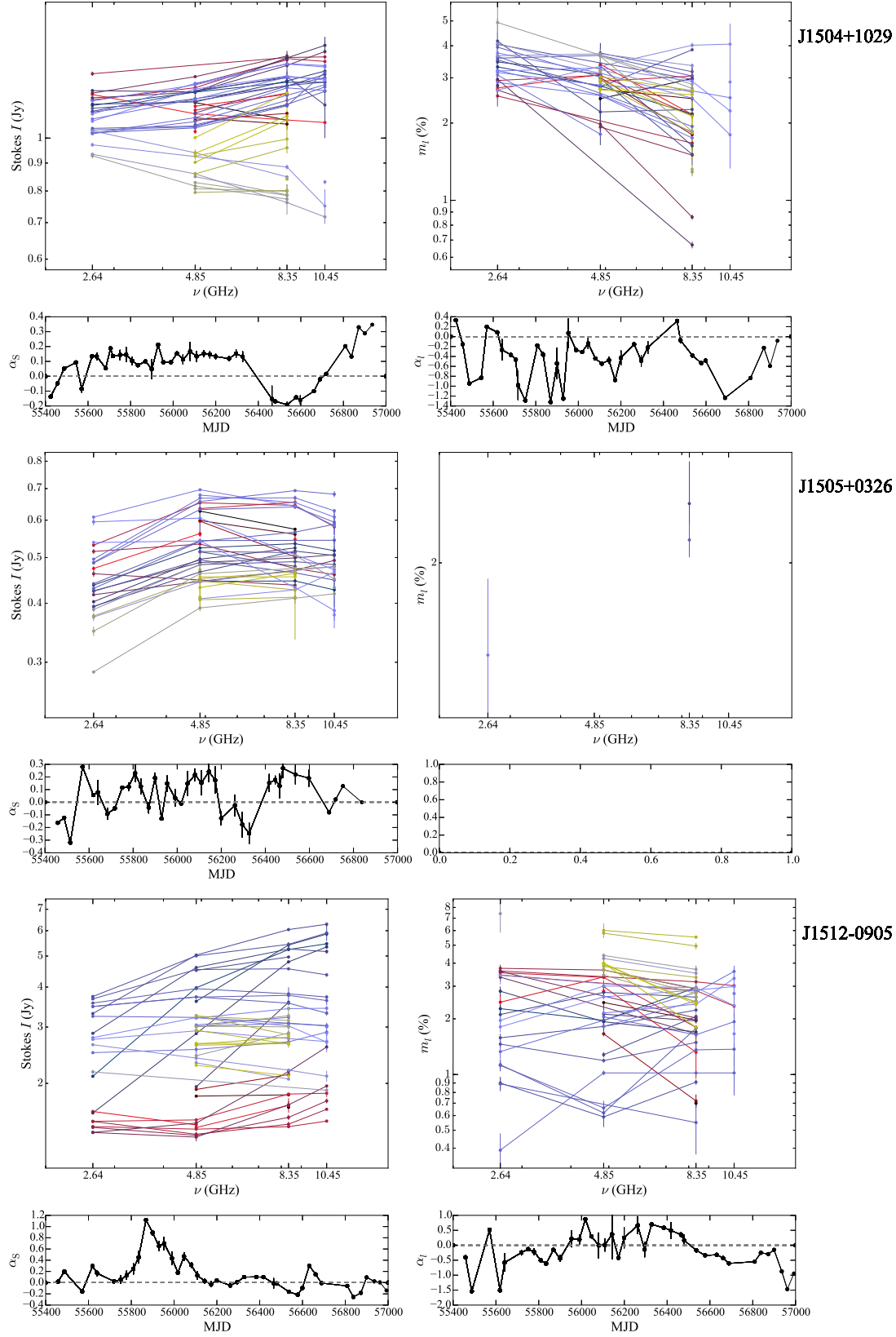


Figure C.19: continued

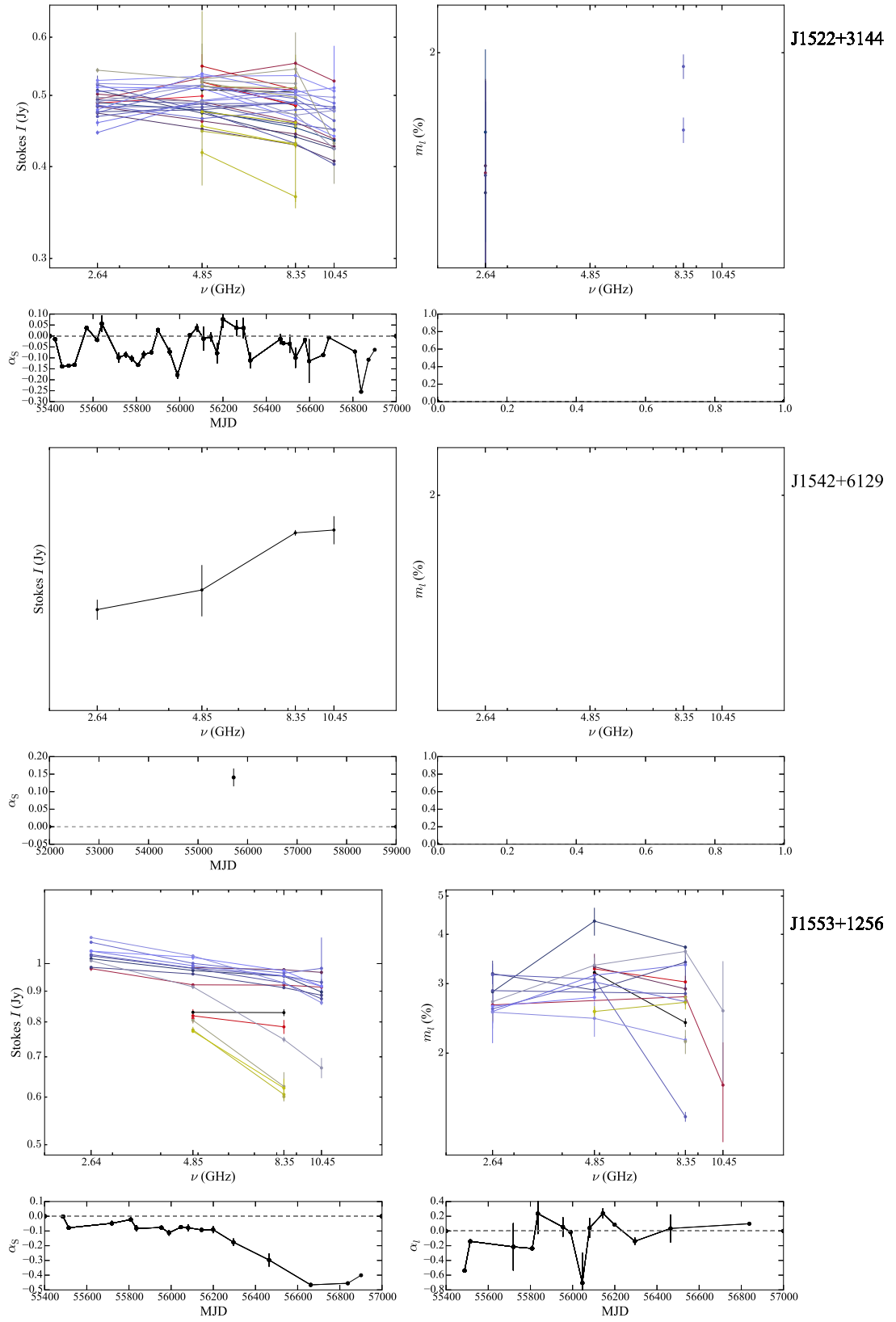


Figure C.20: continued

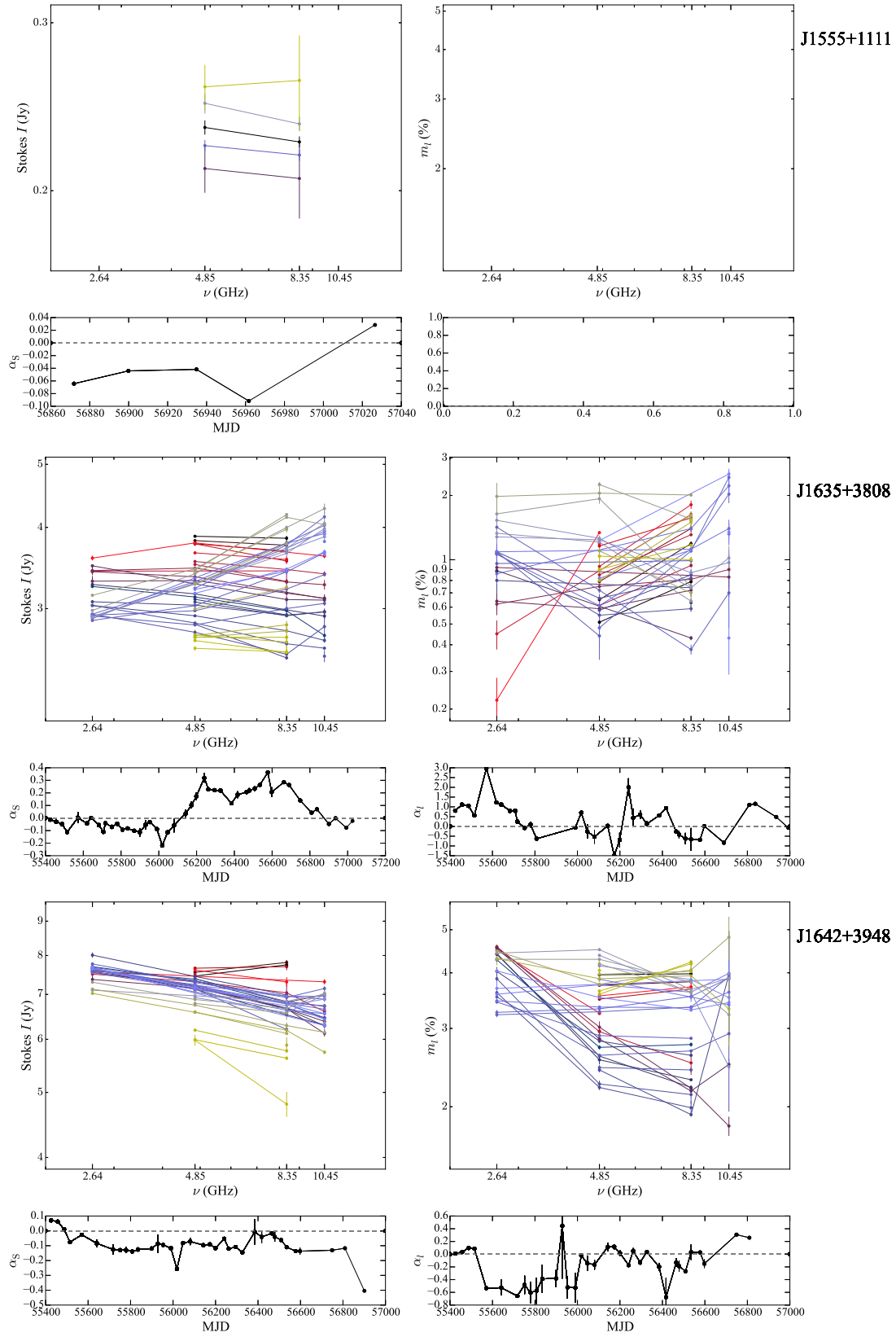


Figure C.21: continued

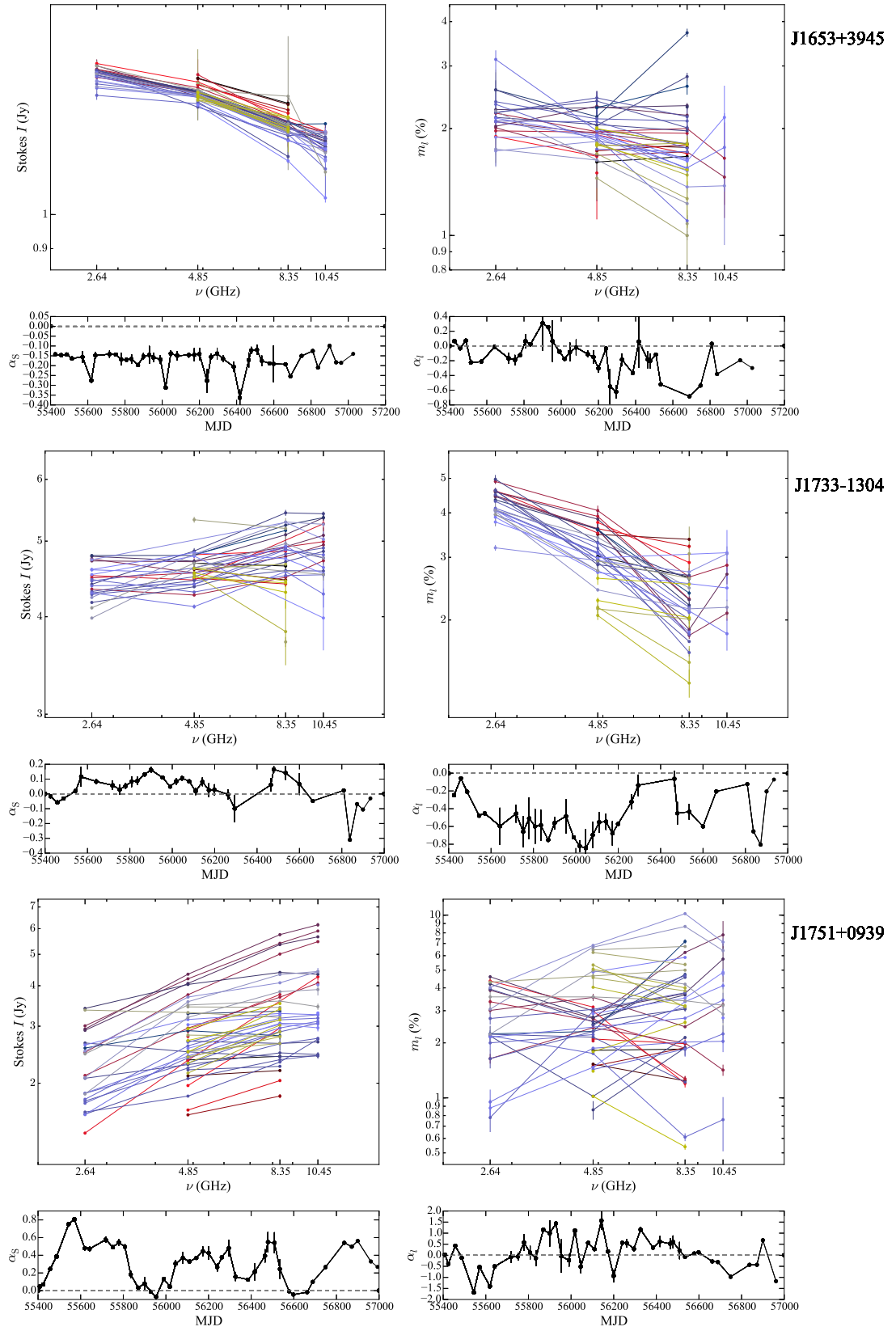


Figure C.22: continued

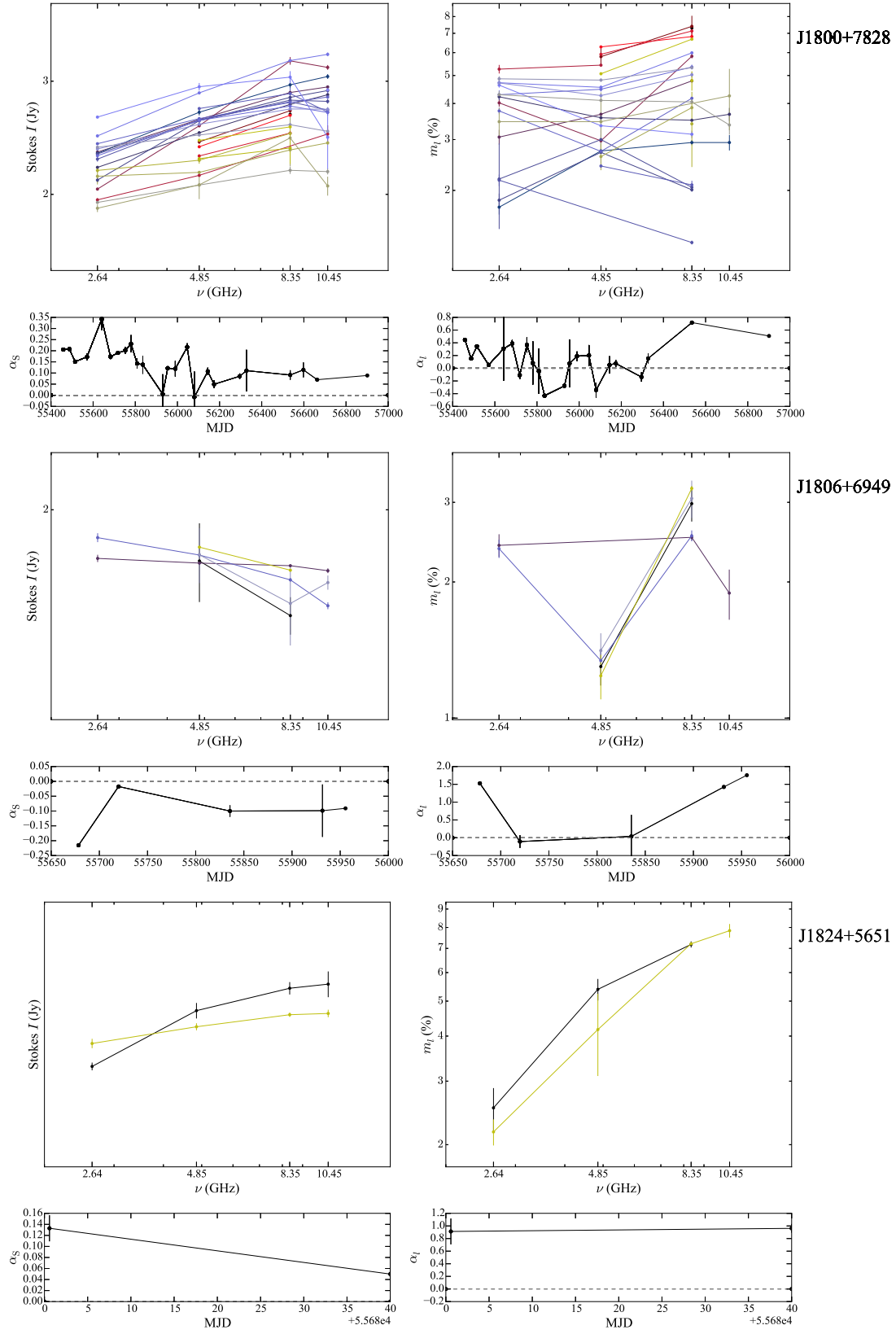


Figure C.23: continued

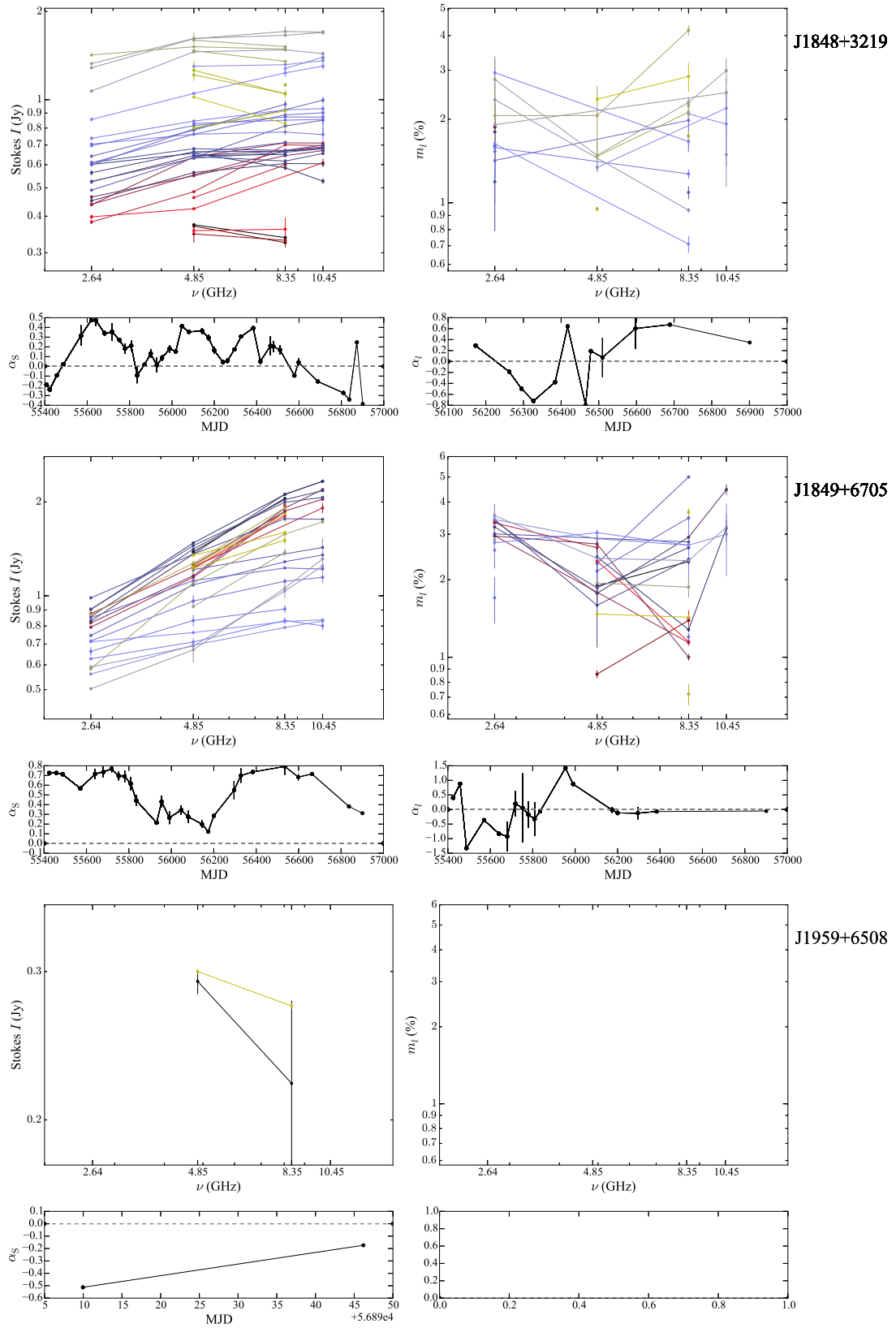


Figure C.24: continued

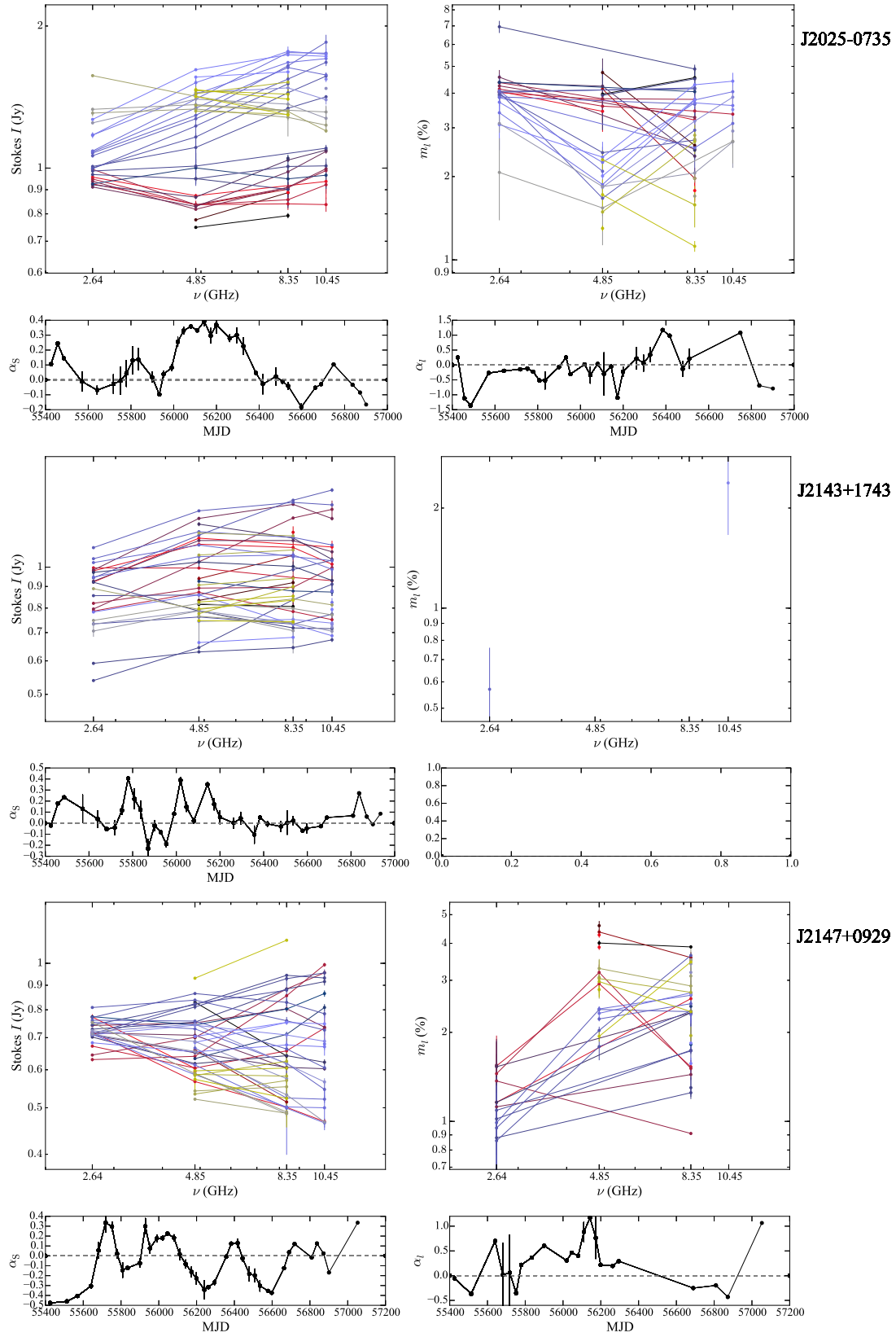


Figure C.25: continued

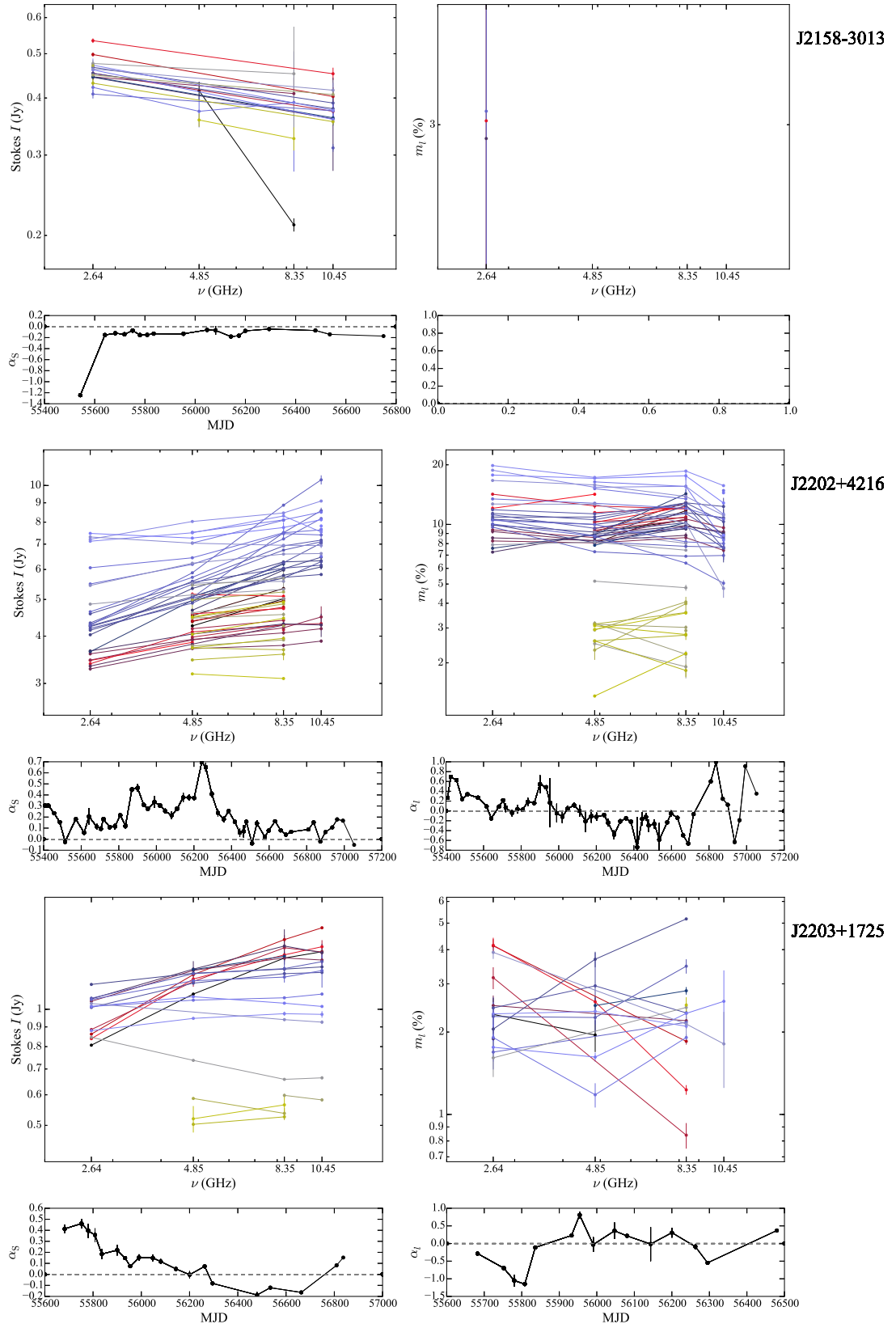


Figure C.26: continued

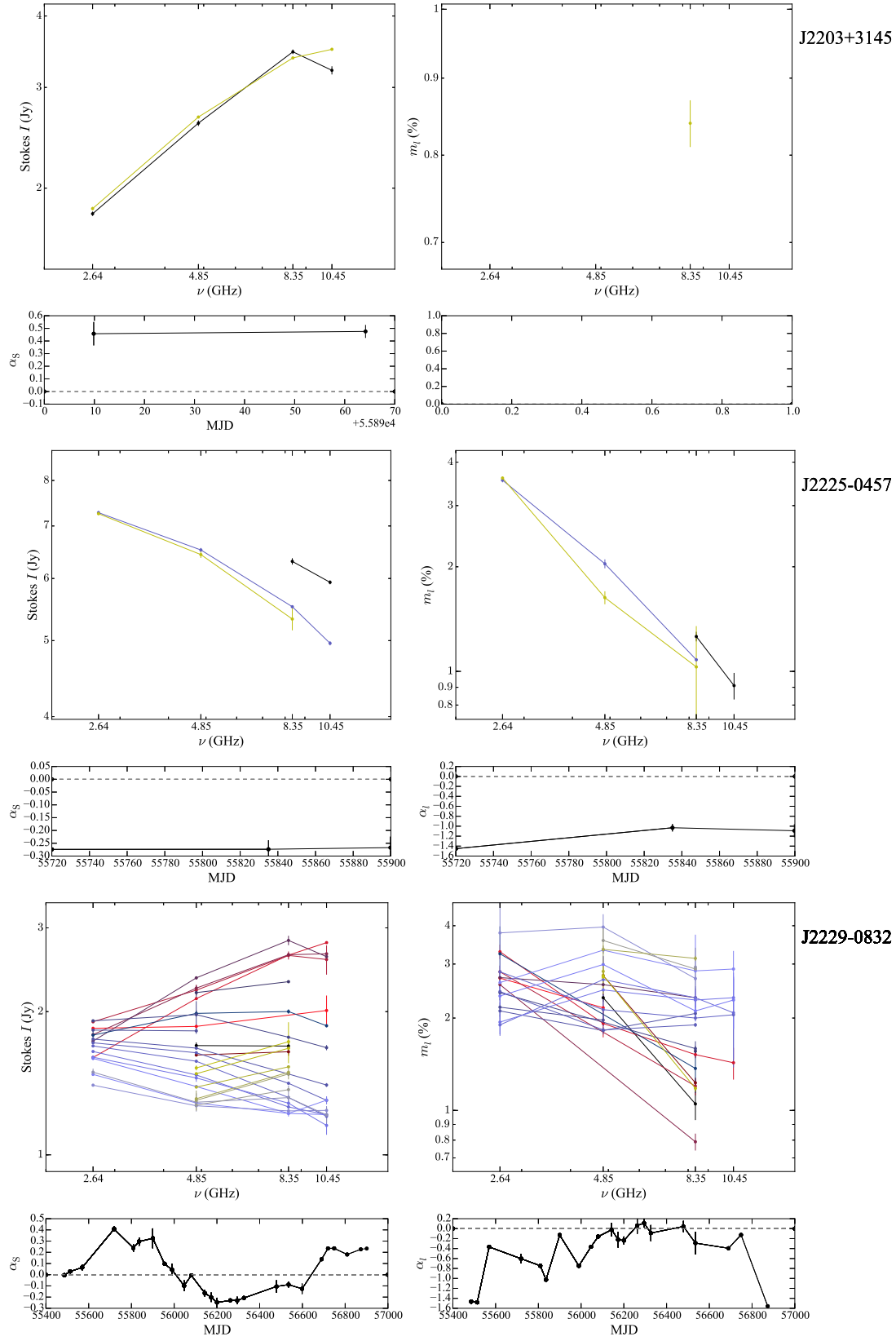


Figure C.27: continued

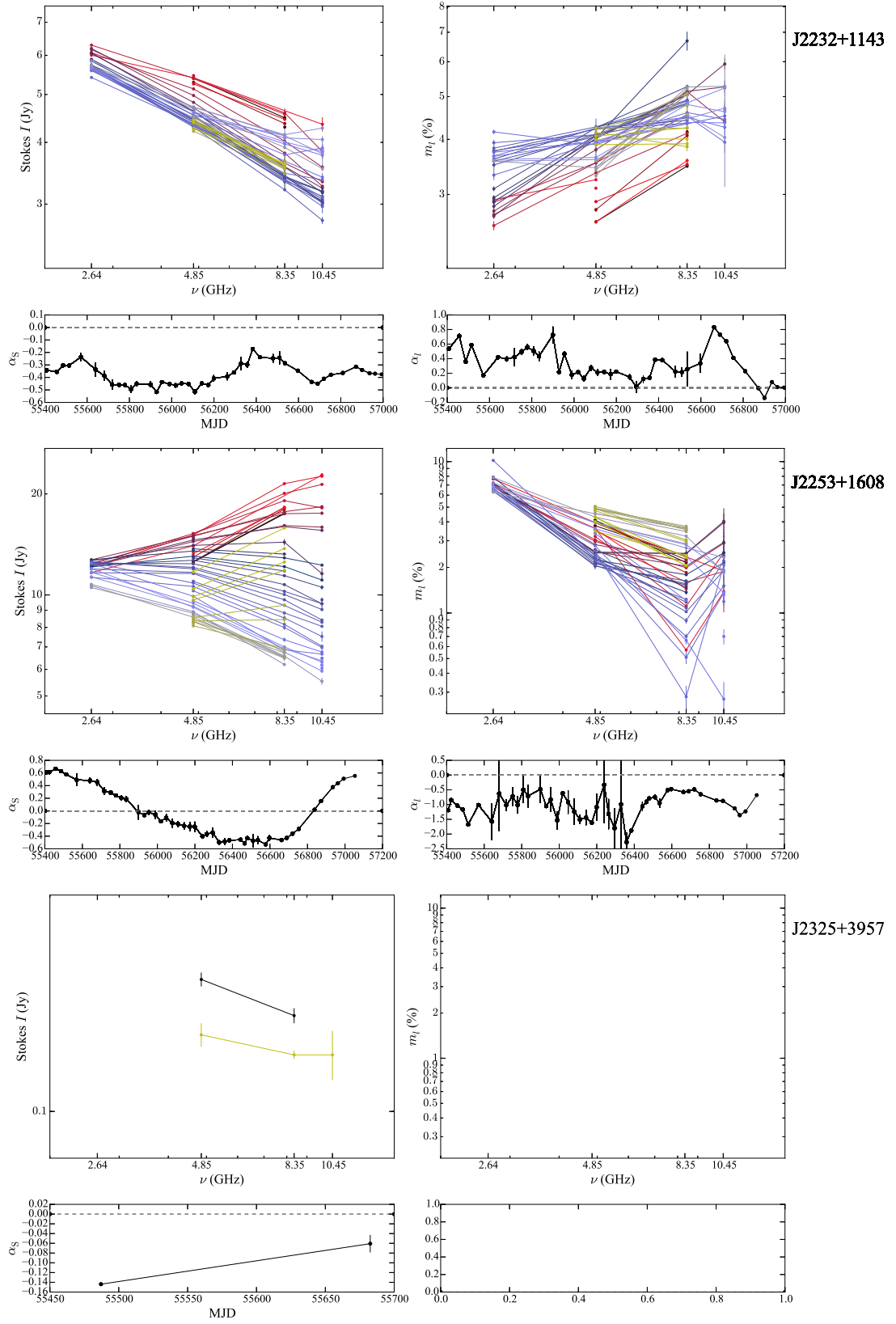


Figure C.28: continued

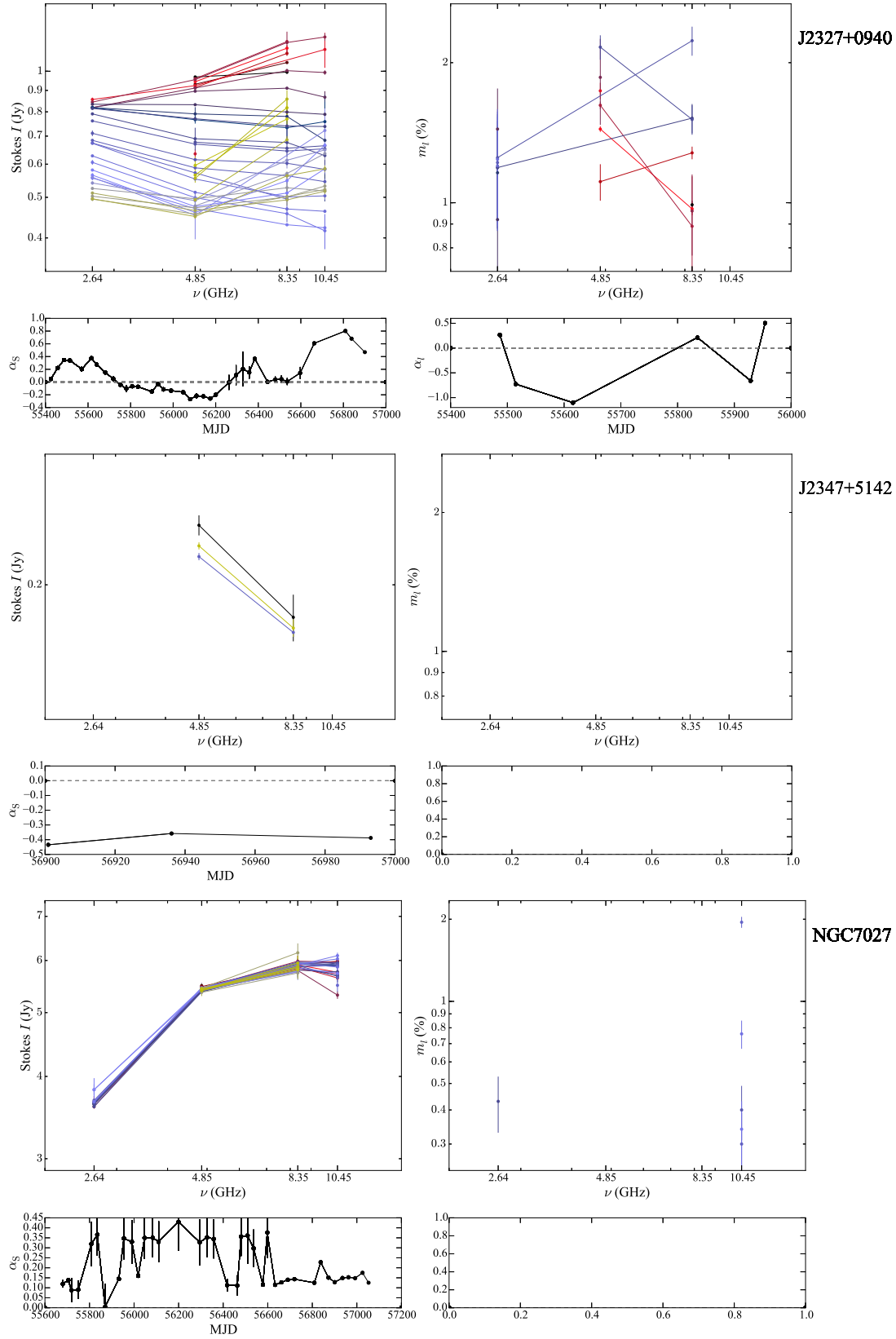


Figure C.29: continued

Appendix D

Rotation measure plots

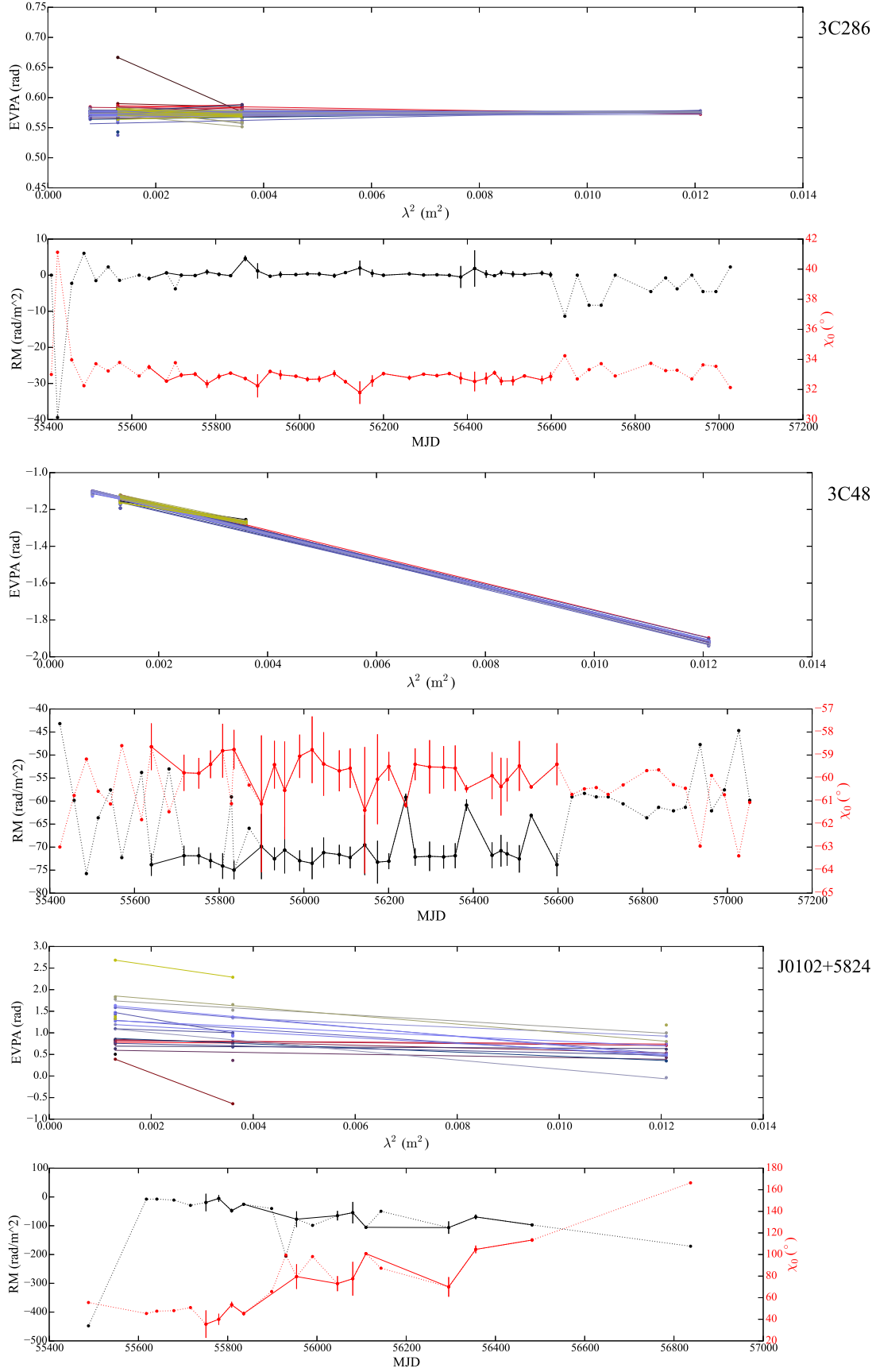


Figure D.1: In the top panel, we show the EVPA versus λ^2 plots constructed for each observing session. The plotted lines are the fits used to estimate the rotation measure (RM) and zero-wavelength EVPA (χ_0) for each session. The RM and χ_0 lightcurves are shown in the bottom panel with black and red color respectively. Notice that the χ_0 units are shown in the right axis.

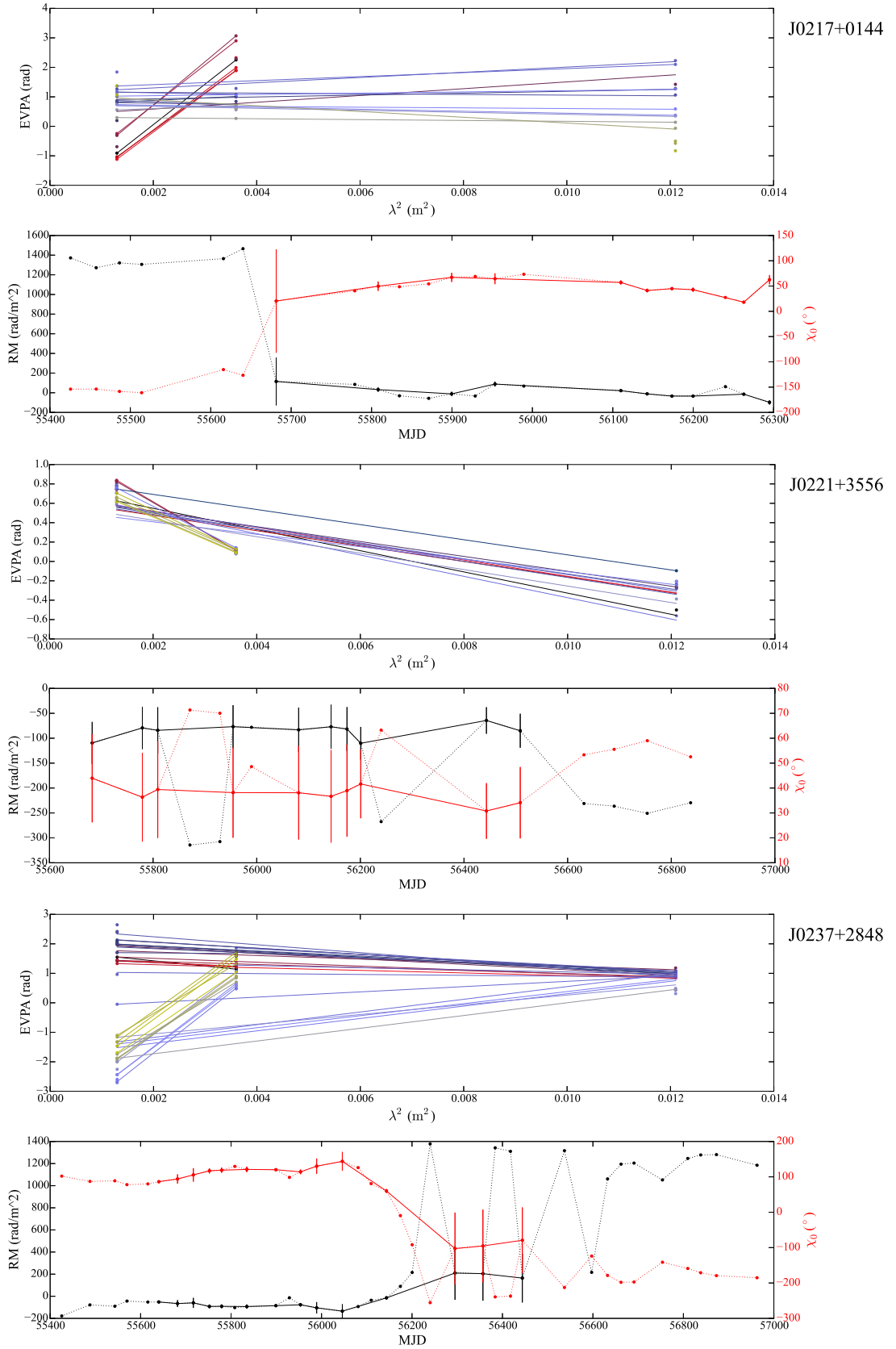


Figure D.2: continued

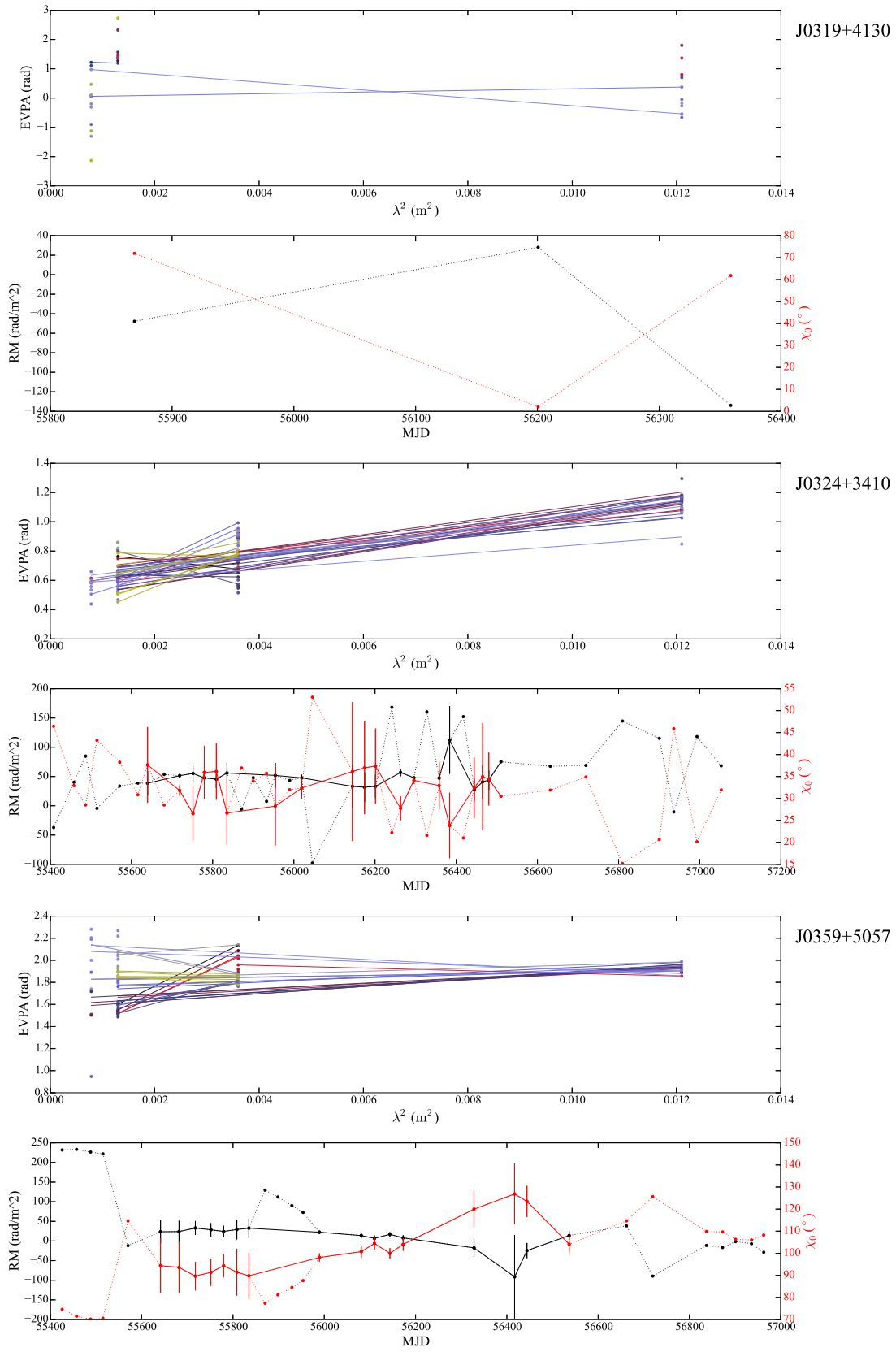


Figure D.3: continued

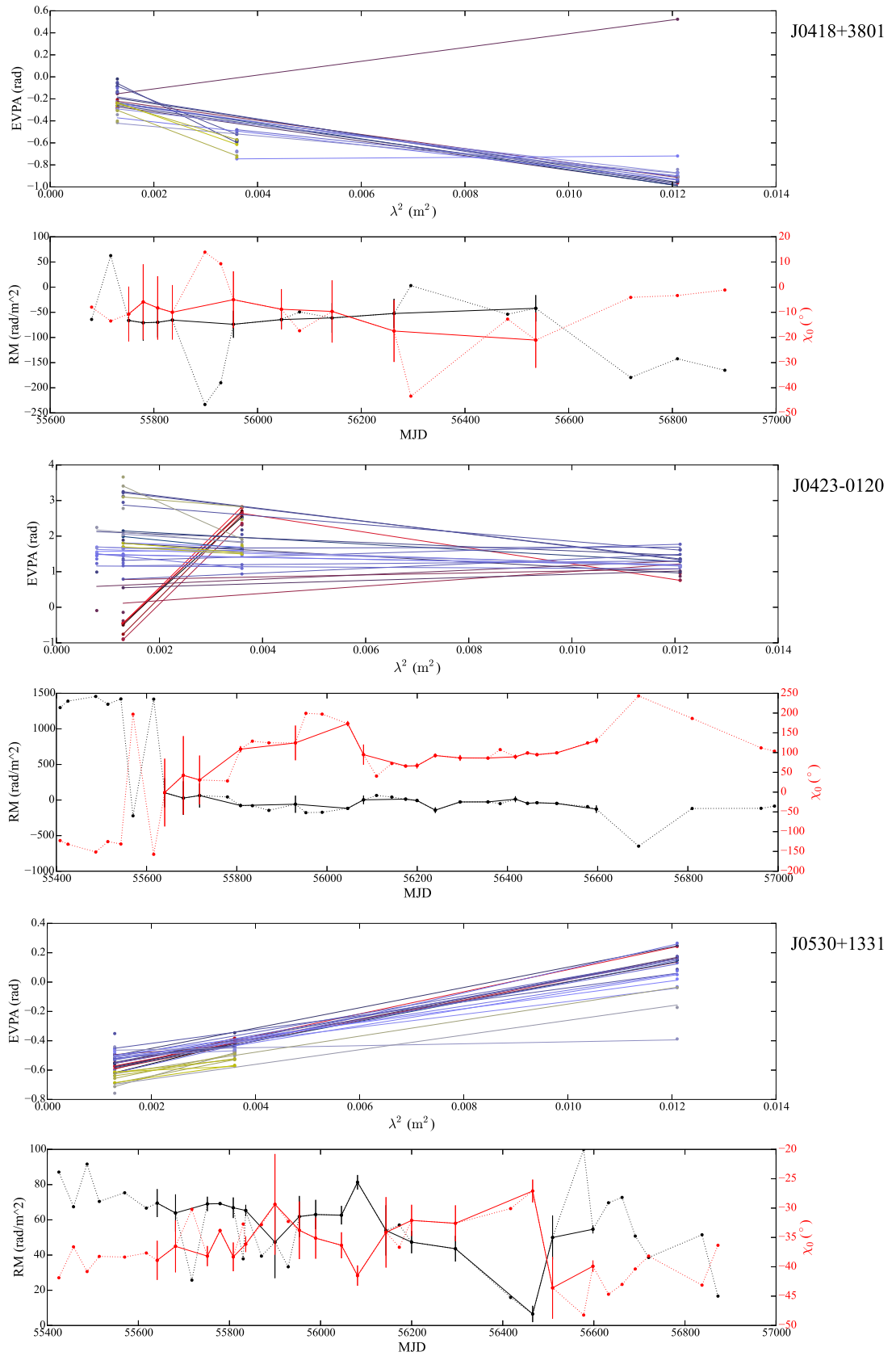


Figure D.4: continued

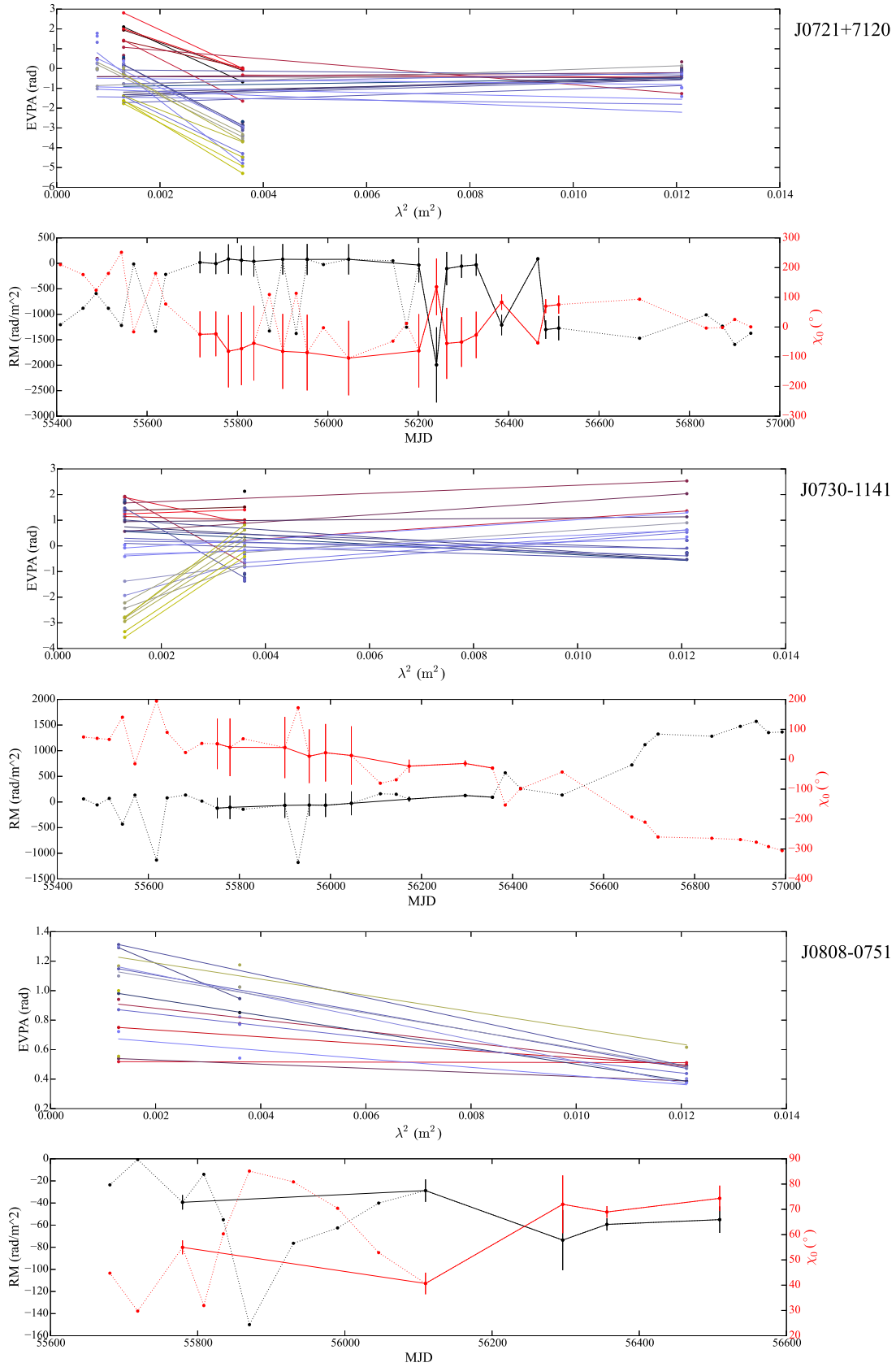


Figure D.5: continued

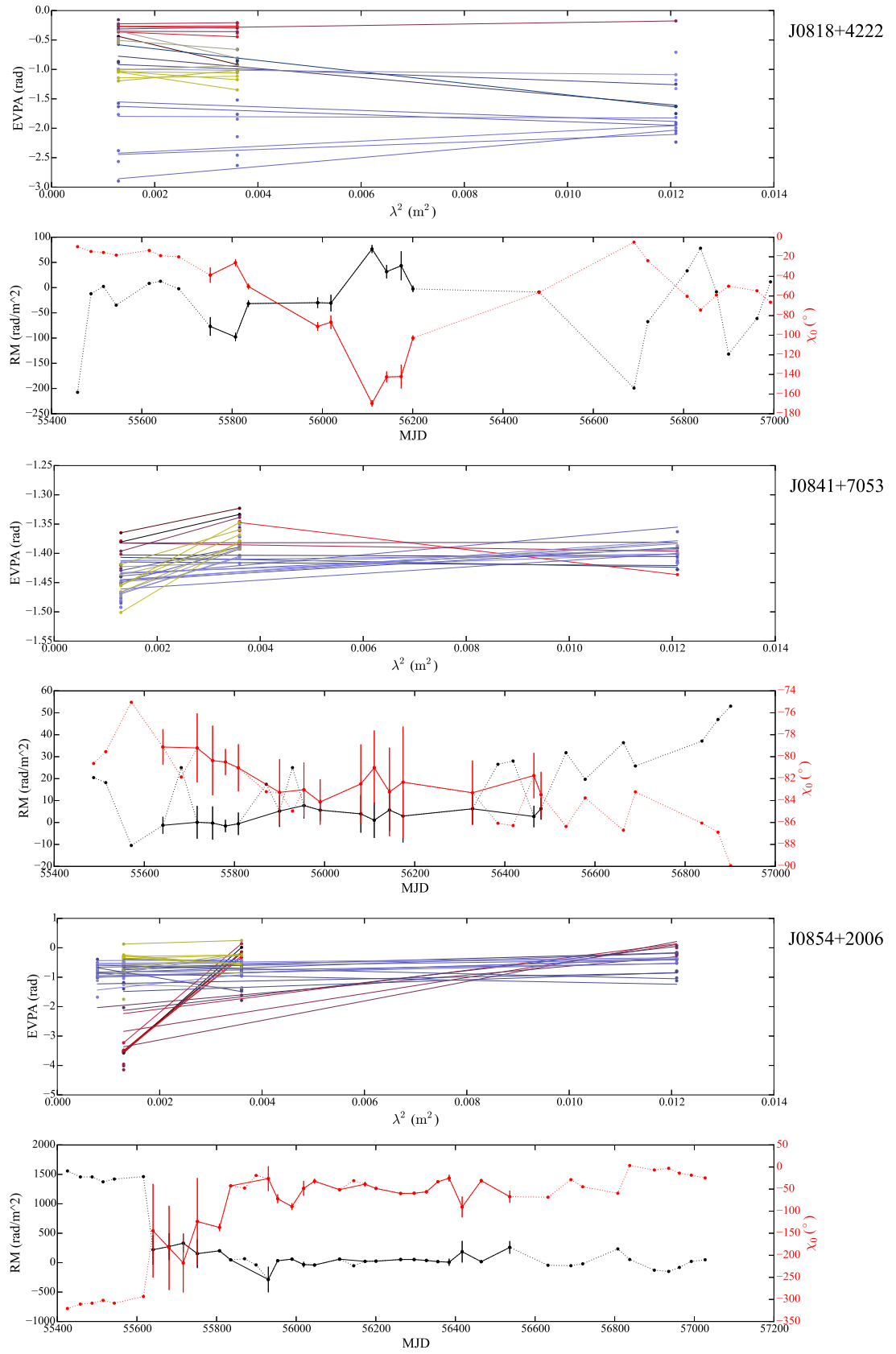


Figure D.6: continued

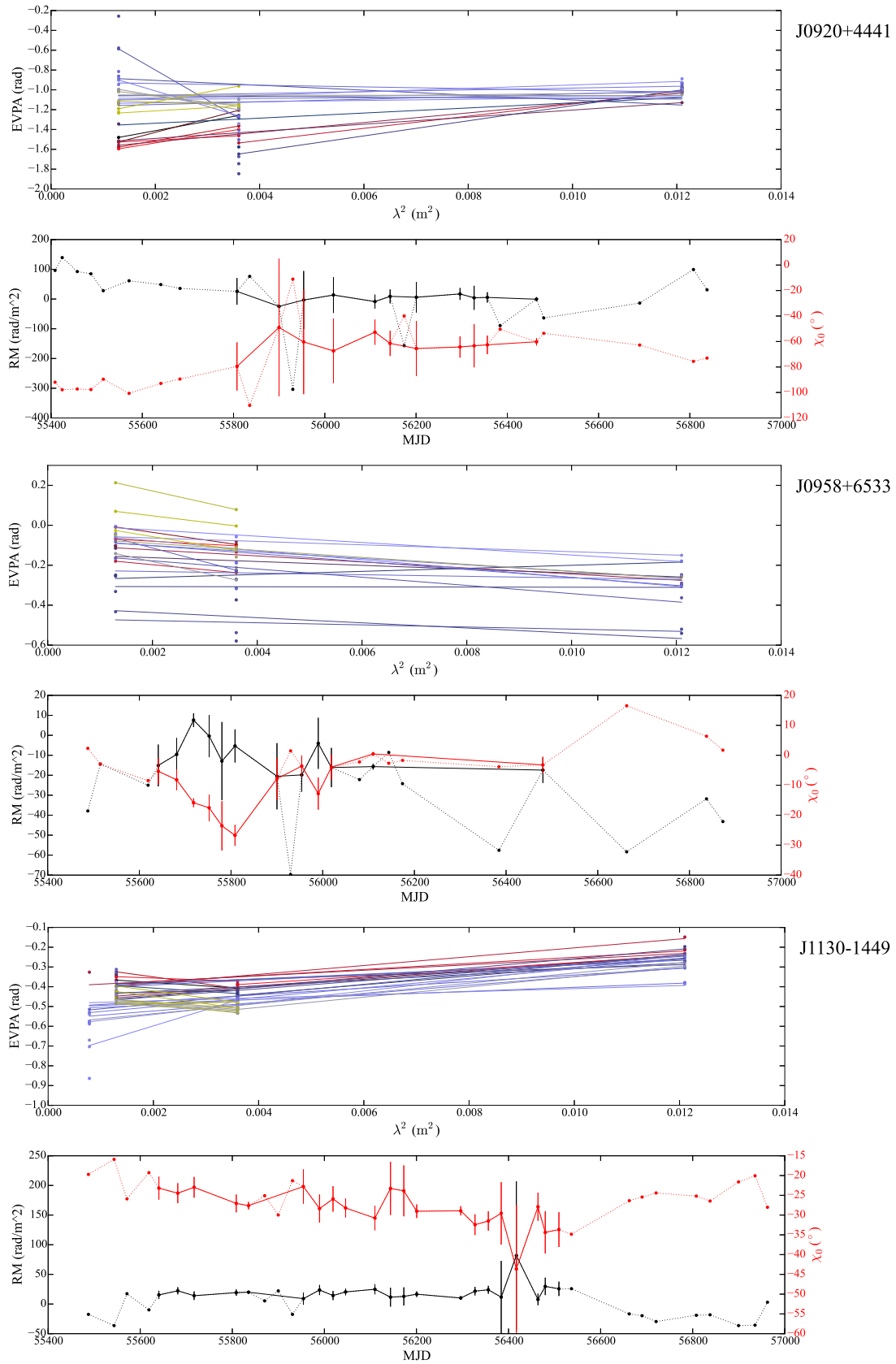


Figure D.7: continued

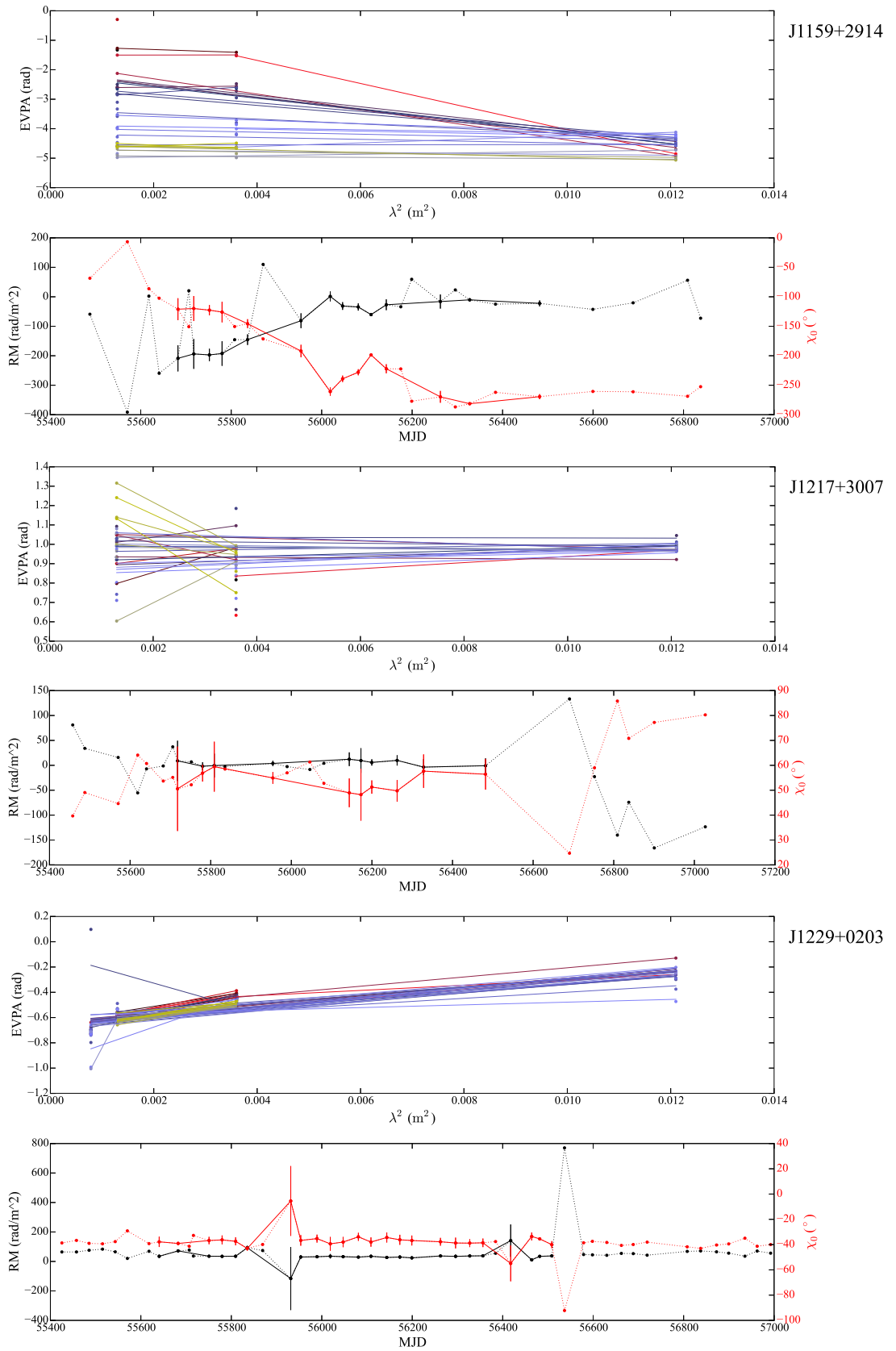


Figure D.8: continued

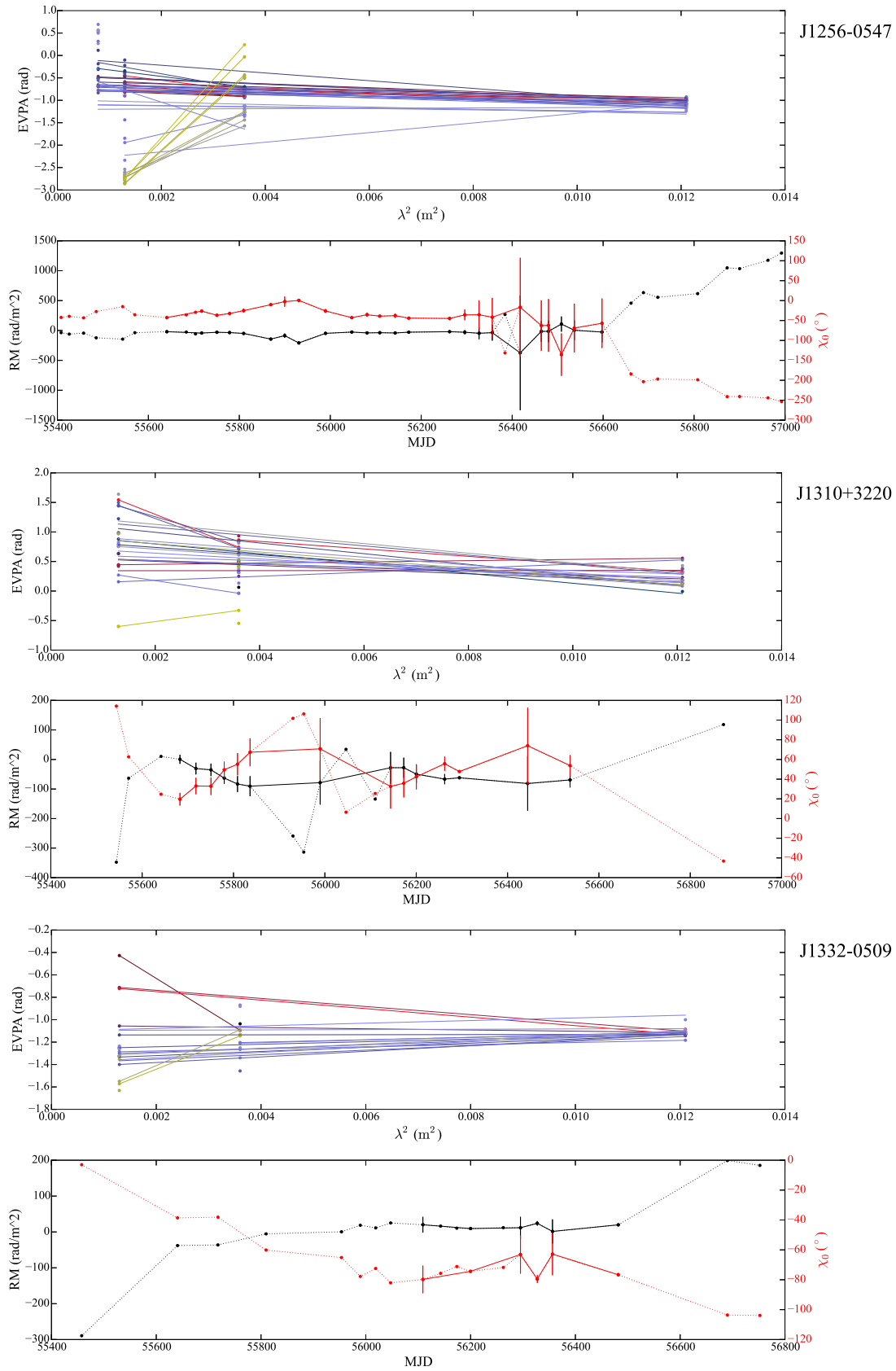


Figure D.9: continued

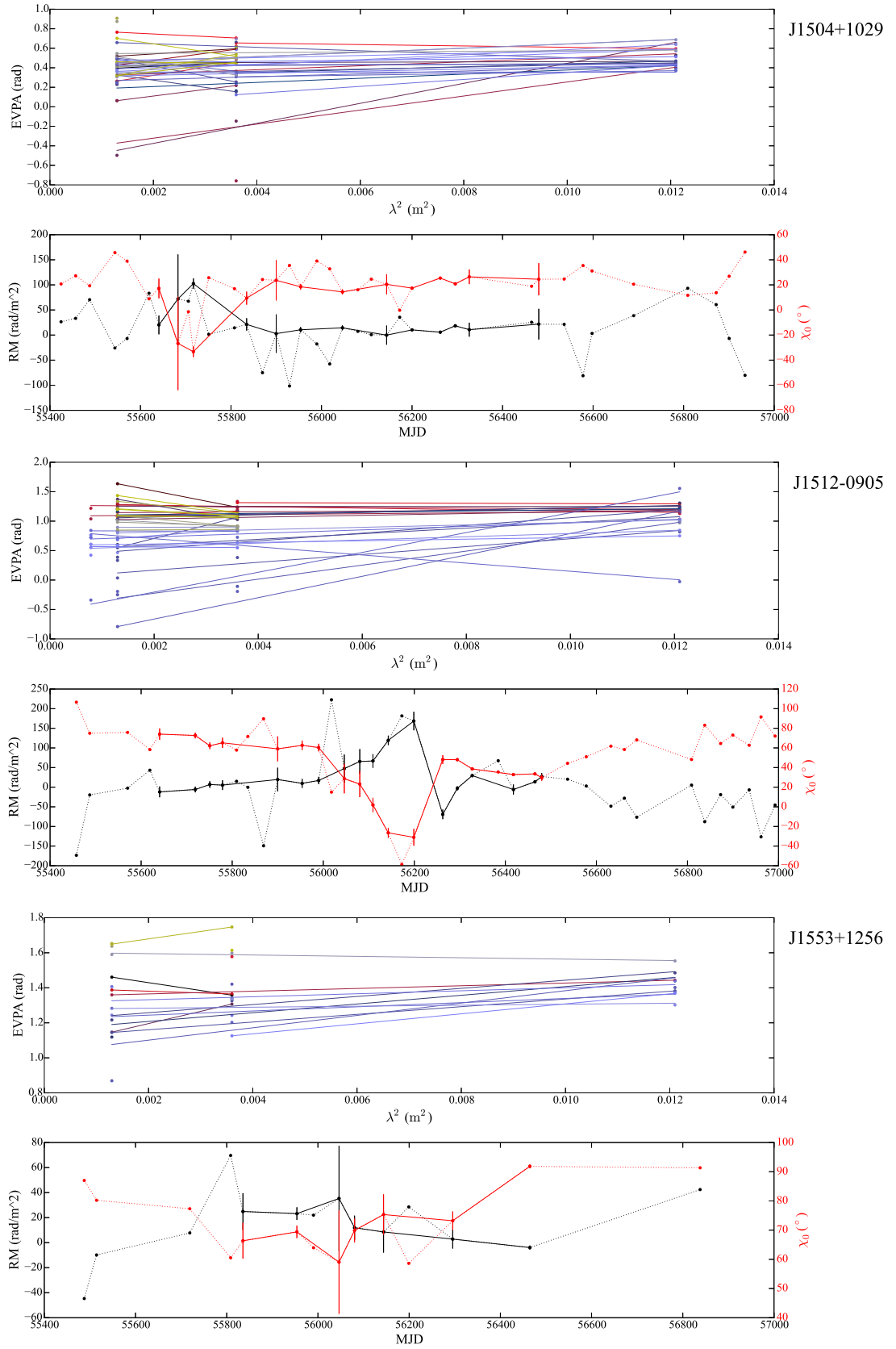


Figure D.10: continued

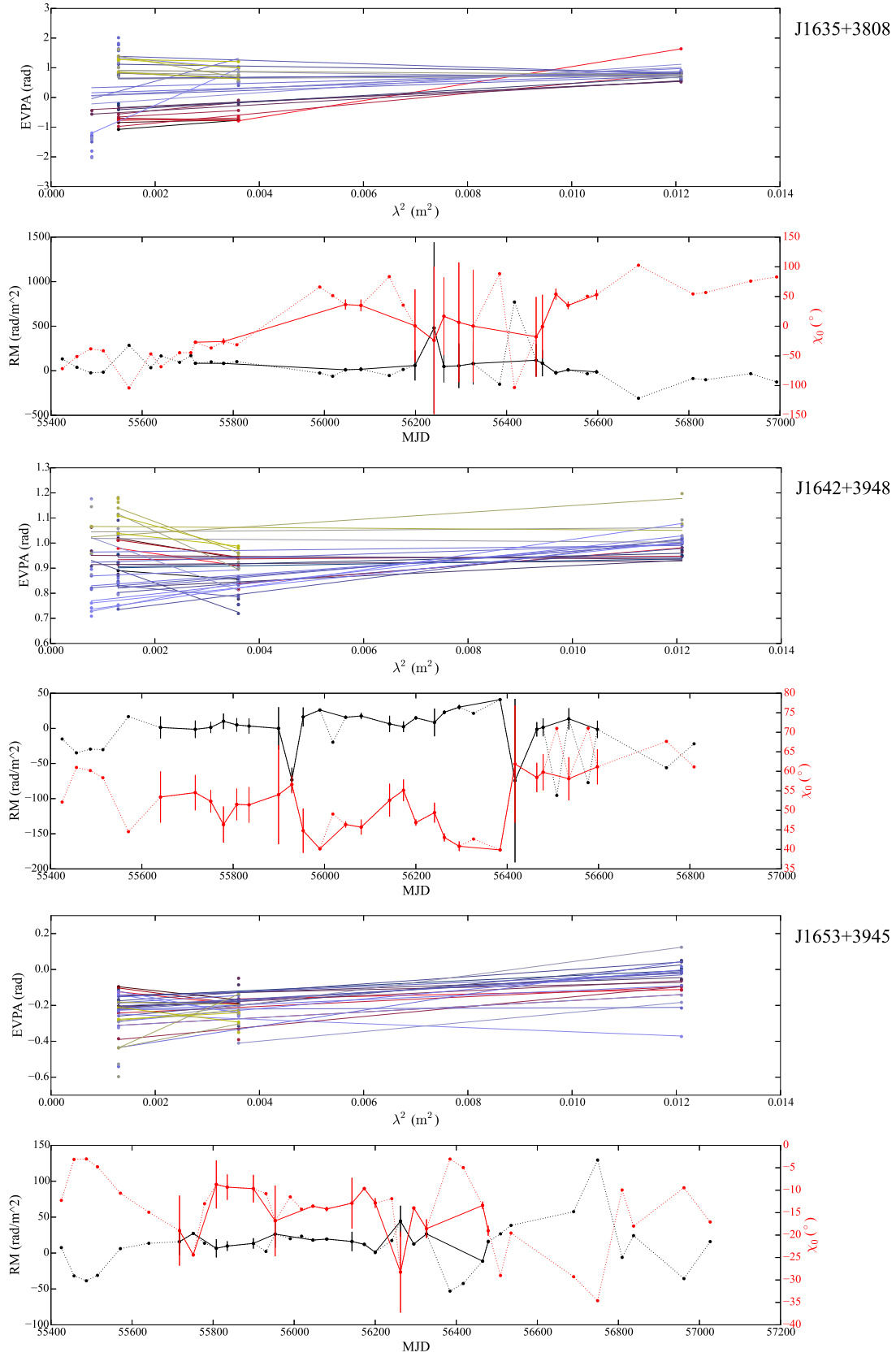


Figure D.11: continued

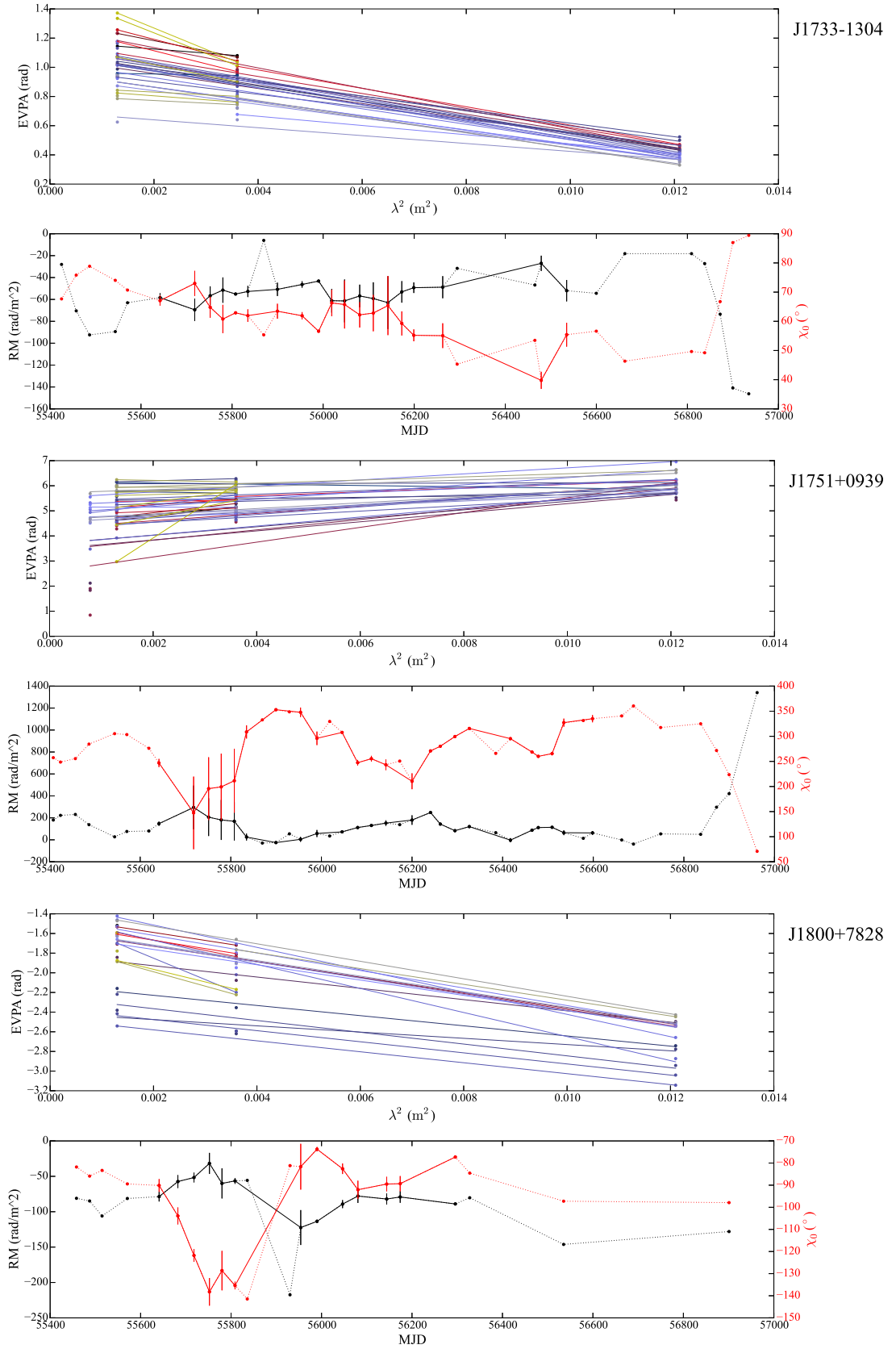


Figure D.12: continued

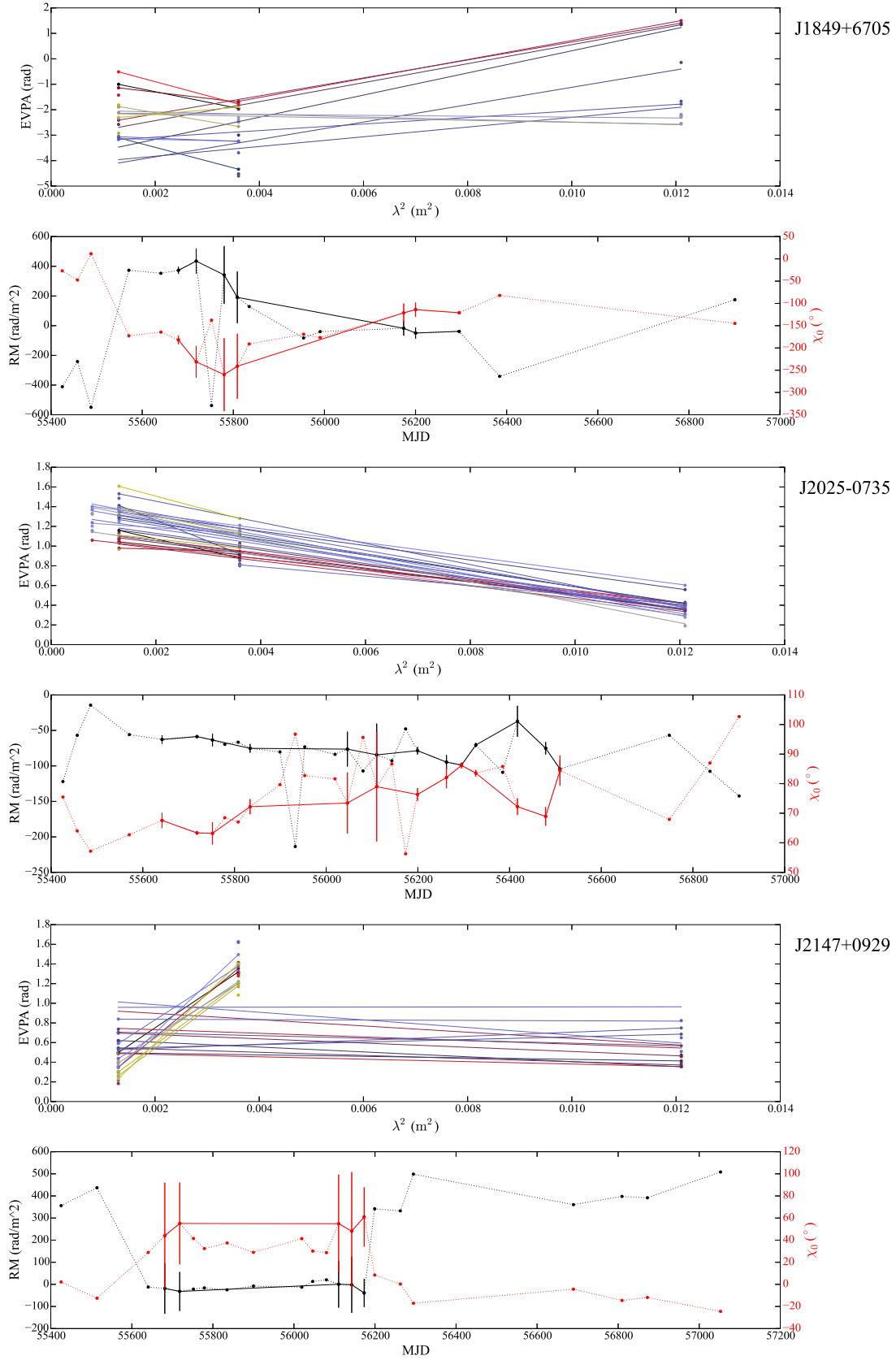


Figure D.13: continued

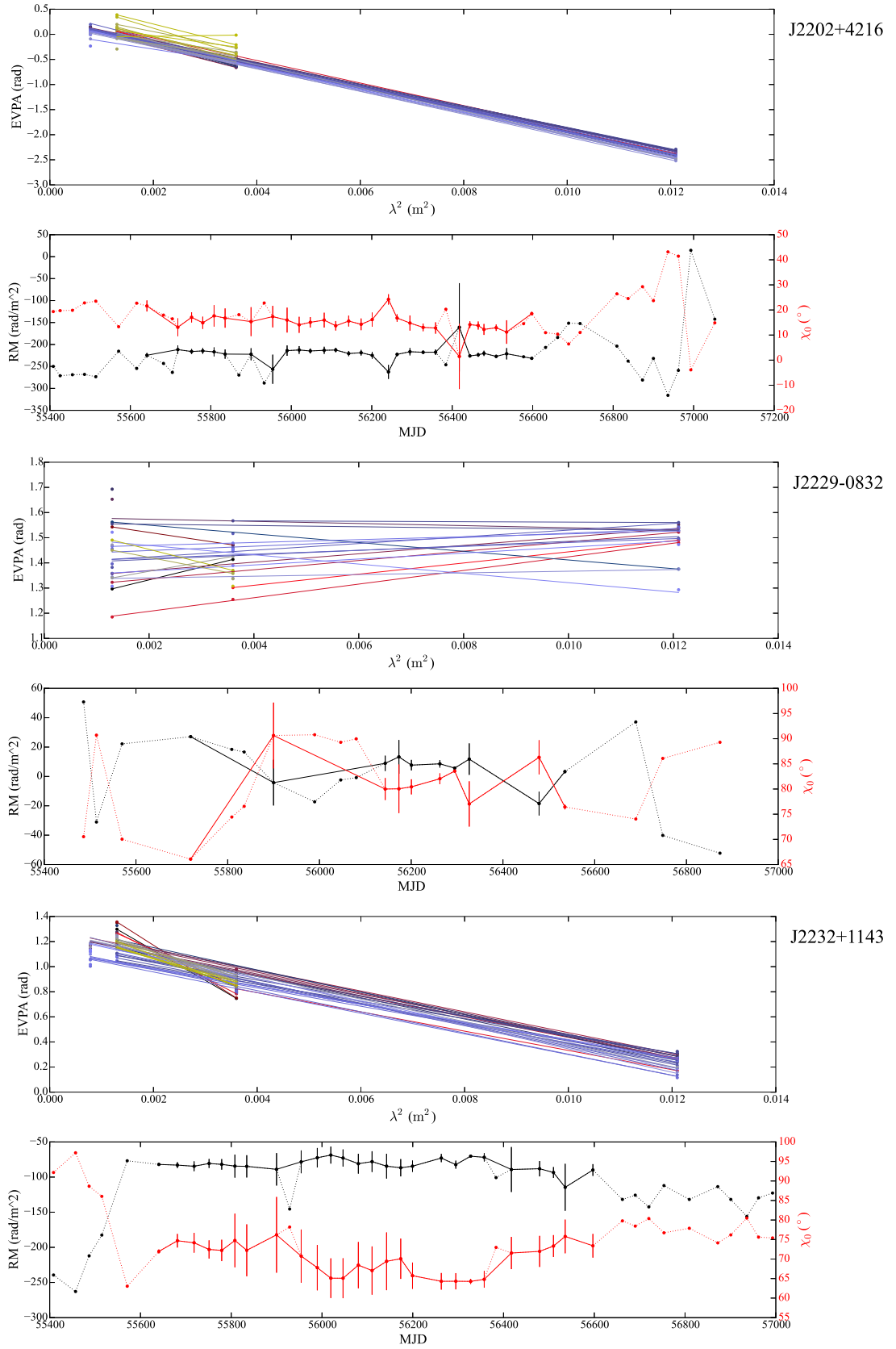


Figure D.14: continued

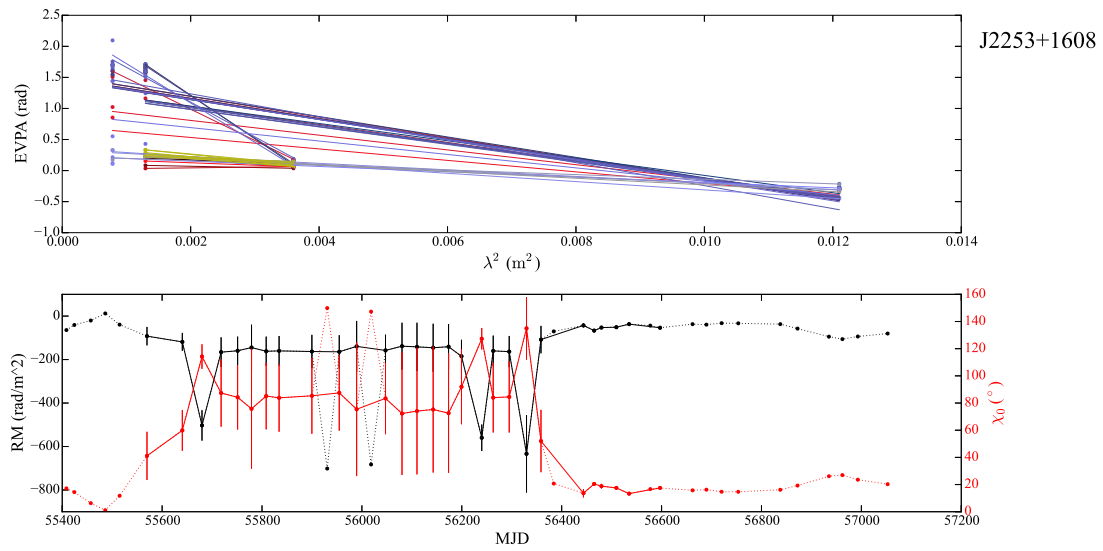


Figure D.15: continued

Appendix E

Optical polarization data

Table E.1: Representative statistical moments for the intensity and linear polarization characteristics of the observed sources in the R band. The corresponding quantities are given in the third column (x) and they are: the R-band magnitude, R, the linear polarization degree, m_l and the electric vector position angle (EVPA), χ . N_{sign} is the number of data points which passed a number of quality criteria over the total number of data points. For each quantity we provide the weighted average, $\langle x \rangle$, and standard deviation, σ_x , over the time that the quantity has been observed. The modulation index, $\frac{\sigma_x}{\langle x \rangle}$, as a measure of the variability amplitude of the source in that quantity as well as the median, minimum and maximum values are reported.

Source	x	N_{sign}	$\langle x \rangle$	σ_x	mi (%)	median	min	max
J0102+5824	R (mag)	14/15	17.57	0.46	0.03	17.80	18.93	17.00
	m_l (%)	13/15	14.8	0.3	0.0	14.4	5.8	22.4
	χ (°)	13/15	-78.6	22.3	...	-78.0	-110.5	-36.0
J0136+4751	R (mag)	23/23	17.17	0.40	0.02	17.06	17.72	16.08
	m_l (%)	19/23	14.2	0.2	0.0	11.7	5.0	22.9
	χ (°)	19/23	-32.4	92.9	...	-72.9	-135.0	140.8
J0221+3556	R (mag)	1/1	18.69	0.45	0.02	18.69	18.69	18.69
	m_l (%)	0/1	nan	nan	nan	nan	nan	nan
J0222+4302	R (mag)	21/21	14.44	0.17	0.01	14.43	14.69	14.15
	m_l (%)	21/21	8.1	0.1	0.0	8.4	3.0	11.8
	χ (°)	21/21	9.7	22.6	...	20.8	-38.6	36.4
J0324+3410	R (mag)	19/19	15.34	0.11	0.01	15.38	15.51	15.04
	m_l (%)	11/19	3.4	0.1	0.0	2.0	1.5	39.6
	χ (°)	11/19	-19.1	9.5	...	-19.5	-33.0	-0.0
J0339-0146	R (mag)	4/4	16.94	0.28	0.02	17.07	17.20	16.57
	m_l (%)	2/4	14.2	1.2	0.1	13.2	8.5	18.0
	χ (°)	2/4	37.3	4.9	...	37.3	32.4	42.2
J0423-0120	R (mag)	6/6	17.77	0.43	0.02	17.92	18.78	17.61
	m_l (%)	3/6	15.5	0.8	0.1	13.5	10.5	17.5
	χ (°)	3/6	-62.1	12.0	...	-53.9	-79.1	-53.4
J0721+7120	R (mag)	47/47	14.03	0.58	0.04	14.22	15.61	13.20
	m_l (%)	46/47	10.9	0.1	0.0	11.1	1.6	23.2

Table E.1: continued.

Source	x	N_{sign}	$\langle x \rangle$	σ_x	mi (%)	median	min	max
J0738+1742	χ (°)	46/47	-93.7	26.7	...	-93.4	-150.9	-43.2
	R (mag)	10/10	15.35	0.26	0.02	15.21	15.89	14.95
	m_l (%)	10/10	9.2	0.2	0.0	9.5	5.7	11.9
J0750+1231	χ (°)	10/10	25.1	26.0	...	24.3	-18.1	91.3
	R (mag)	10/10	17.48	0.62	0.04	17.66	17.85	15.96
	m_l (%)	2/10	5.9	0.7	0.1	8.7	5.4	12.0
J0818+4222	χ (°)	2/10	-29.6	1.2	...	-29.6	-30.9	-28.4
	R (mag)	9/9	17.90	0.72	0.04	17.97	18.86	16.35
	m_l (%)	3/9	16.7	1.1	0.1	17.2	15.2	17.7
J0830+2410	χ (°)	3/9	-19.8	1.8	...	-18.9	-22.3	-18.2
	R (mag)	6/6	16.49	0.46	0.03	17.32	17.44	16.45
	m_l (%)	1/6	3.8	0.8	0.2	3.8	3.8	3.8
J0841+7053	χ (°)	1/6	8.8	0.0	...	8.8	8.8	8.8
	R (mag)	15/15	16.79	0.92	0.05	17.36	18.13	14.42
	m_l (%)	5/15	3.2	0.3	0.1	3.1	1.7	146.9
J0849+5108	χ (°)	5/15	6.2	13.2	...	5.9	-14.5	24.0
	R (mag)	6/6	17.63	0.34	0.02	17.66	18.04	17.13
	m_l (%)	4/6	20.5	0.8	0.0	20.5	16.4	28.1
J0854+2006	χ (°)	4/6	14.6	23.0	...	12.3	-15.4	49.2
	R (mag)	32/32	14.92	0.44	0.03	14.89	16.59	14.53
	m_l (%)	31/32	11.3	0.1	0.0	11.8	1.0	24.4
J0948+0022	χ (°)	31/32	-27.2	29.5	...	-15.8	-87.3	12.9
	R (mag)	5/5	17.79	0.37	0.02	17.58	17.84	17.02
	m_l (%)	1/5	7.4	1.1	0.1	7.4	7.4	7.4
J0958+6533	χ (°)	1/5	132.2	0.0	...	132.2	132.2	132.2
	R (mag)	13/13	16.35	0.31	0.02	16.55	16.70	15.73
	m_l (%)	13/13	15.2	0.2	0.0	15.8	6.8	23.8
J1104+3812	χ (°)	13/13	4.5	13.7	...	4.1	-22.3	25.9
	R (mag)	1/1	12.21	0.05	0.00	12.21	12.21	12.21
	m_l (%)	1/1	7.5	0.2	0.0	7.5	7.5	7.5
J1136+7009	χ (°)	1/1	7.4	0.0	...	7.4	7.4	7.4
	R (mag)	14/14	14.93	0.11	0.01	14.94	15.08	14.71
	m_l (%)	6/14	3.1	0.2	0.1	3.0	2.1	4.3
J1159+2914	χ (°)	6/14	-28.9	28.2	...	-28.6	-69.7	6.1
	R (mag)	1/1	14.75	0.04	0.00	14.75	14.75	14.75
	m_l (%)	1/1	6.0	0.5	0.1	6.0	6.0	6.0
J1217+3007	χ (°)	1/1	-59.0	0.0	...	-59.0	-59.0	-59.0
	R (mag)	16/16	14.11	0.21	0.01	14.19	14.69	13.97
	m_l (%)	16/16	10.0	0.1	0.0	10.1	6.5	12.6
J1221+2813	χ (°)	16/16	-19.1	5.3	...	-20.2	-27.2	-4.5
	R (mag)	6/6	15.59	0.20	0.01	15.76	15.95	15.38
	m_l (%)	6/6	12.8	0.3	0.0	14.8	8.4	18.9
J1224+2122	χ (°)	6/6	75.2	14.3	...	69.1	63.8	104.8
	R (mag)	6/6	14.75	0.12	0.01	14.73	14.90	14.54

Table E.1: continued.

Source	x	N_{sign}	$\langle x \rangle$	σ_x	mi (%)	median	min	max
J1229+0203	m_l (%)	6/6	9.0	0.3	0.0	10.4	5.6	13.5
	χ (°)	6/6	-1.6	3.7	...	-1.1	-7.8	3.8
	R (mag)	1/1	12.35	0.07	0.01	12.35	12.35	12.35
J1256-0547	m_l (%)	1/1	1.4	0.1	0.0	1.4	1.4	1.4
	χ (°)	1/1	-9.3	0.0	...	-9.3	-9.3	-9.3
	R (mag)	13/13	15.12	0.24	0.02	15.03	15.41	14.68
J1354-1041	m_l (%)	13/13	19.6	0.2	0.0	18.6	10.7	28.1
	χ (°)	13/13	50.3	4.2	...	50.8	41.9	58.8
	R (mag)	1/1	16.65	0.42	0.03	16.65	16.65	16.65
J1428+4240	m_l (%)	0/1	nan	nan	nan	nan	nan	nan
	R (mag)	5/5	16.33	0.28	0.02	16.17	16.79	16.13
	m_l (%)	1/5	4.3	0.8	0.2	4.3	4.3	4.3
J1505+0326	χ (°)	1/5	-95.7	0.0	...	-95.7	-95.7	-95.7
	R (mag)	20/20	17.09	0.55	0.03	17.76	18.31	16.77
	m_l (%)	2/20	5.8	0.8	0.1	7.0	4.8	9.3
J1512-0905	χ (°)	2/20	-24.8	59.6	...	-24.8	-84.4	34.7
	R (mag)	41/42	15.19	1.50	0.10	15.49	20.50	12.82
	m_l (%)	30/42	7.5	0.1	0.0	5.9	2.5	21.2
J1542+6129	χ (°)	30/42	-11.6	61.5	...	-15.9	-108.8	105.6
	R (mag)	33/34	15.47	0.22	0.01	15.47	15.76	14.82
	m_l (%)	32/34	7.8	0.1	0.0	7.6	2.4	19.4
J1553+1256	χ (°)	32/34	-43.6	33.4	...	-43.6	-122.3	14.0
	R (mag)	25/25	17.14	0.12	0.01	17.17	17.33	16.94
	m_l (%)	2/25	5.4	0.9	0.2	6.5	3.9	9.1
J1555+1111	χ (°)	2/25	-33.4	16.8	...	-33.4	-50.2	-16.6
	R (mag)	3/4	14.10	0.29	0.02	14.03	14.27	13.70
	m_l (%)	3/4	12.6	0.3	0.0	5.9	3.1	20.8
J1635+3808	χ (°)	3/4	-25.4	19.1	...	-33.1	-44.0	0.9
	R (mag)	58/58	17.17	0.80	0.05	16.86	18.95	15.62
	m_l (%)	43/58	9.6	0.1	0.0	9.6	2.1	21.4
J1642+3948	χ (°)	43/58	-58.1	54.9	...	-68.9	-123.6	57.2
	R (mag)	29/29	17.46	0.40	0.02	17.32	18.12	16.45
	m_l (%)	17/29	5.7	0.3	0.1	5.1	3.4	15.4
J1653+3945	χ (°)	17/29	55.1	17.0	...	57.5	9.1	79.5
	R (mag)	59/59	13.70	0.06	0.00	13.65	13.86	13.52
	m_l (%)	59/59	2.9	0.1	0.0	2.7	1.1	7.1
J1751+0939	χ (°)	59/59	-45.4	10.7	...	-46.0	-67.1	-20.1
	R (mag)	51/51	14.35	1.04	0.07	16.34	17.85	9.67
	m_l (%)	47/51	9.2	0.1	0.0	9.2	1.5	24.0
J1800+7828	χ (°)	47/51	29.8	137.3	...	58.0	-199.2	238.2
	R (mag)	37/37	15.26	0.82	0.05	15.68	16.98	14.03
	m_l (%)	36/37	9.0	0.1	0.0	8.7	3.5	19.7
J1806+6949	χ (°)	36/37	-59.3	54.5	...	-62.2	-137.3	66.0
	R (mag)	44/44	14.57	0.15	0.01	14.56	14.93	14.24

Table E.1: continued.

Source	x	N_{sign}	$\langle x \rangle$	σ_x	mi (%)	median	min	max
J1824+5651	m_l (%)	40/44	6.5	0.1	0.0	5.3	1.7	55.6
	χ (°)	40/44	37.8	75.1	...	63.6	-129.9	186.2
	R (mag)	1/2	15.84	0.18	0.01	15.84	15.84	15.84
	m_l (%)	1/2	4.0	0.4	0.1	4.0	4.0	4.0
J1849+6705	χ (°)	1/2	-45.5	0.0	...	-45.5	-45.5	-45.5
	R (mag)	1/1	18.71	0.18	0.01	18.71	18.71	18.71
	m_l (%)	0/1	nan	nan	nan	nan	nan	nan
J1959+6508	R (mag)	30/30	14.58	0.30	0.02	14.47	15.07	14.06
	m_l (%)	29/30	4.0	0.1	0.0	4.3	2.0	7.2
	χ (°)	29/30	-23.4	6.7	...	-22.2	-39.9	-12.4
J2143+1743	R (mag)	33/33	15.91	0.04	0.00	15.89	15.98	15.81
	m_l (%)	16/33	1.8	0.1	0.1	1.8	1.3	2.3
	χ (°)	16/33	0.3	22.5	...	-5.9	-22.2	67.0
J2147+0929	R (mag)	1/1	18.59	0.01	0.00	18.59	18.59	18.59
	m_l (%)	0/1	nan	nan	nan	nan	nan	nan
J2202+4216	R (mag)	75/75	14.16	0.39	0.03	13.80	14.61	12.96
	m_l (%)	75/75	9.1	0.0	0.0	8.1	1.4	24.6
	χ (°)	75/75	-10.9	55.2	...	0.4	-189.9	73.0
J2225-0457	R (mag)	24/24	18.32	0.15	0.01	18.31	18.65	18.11
	m_l (%)	7/24	15.4	0.8	0.1	14.6	8.7	21.0
	χ (°)	7/24	-9.4	40.7	...	-27.3	-30.7	90.0
J2232+1143	R (mag)	54/54	16.66	0.18	0.01	16.65	16.94	16.16
	m_l (%)	39/54	5.2	0.1	0.0	4.7	1.6	16.4
	χ (°)	39/54	-118.1	111.0	...	-135.2	-357.6	59.9
J2253+1608	R (mag)	94/94	14.70	0.57	0.04	15.04	15.80	13.12
	m_l (%)	93/94	6.5	0.1	0.0	5.7	1.9	17.8
	χ (°)	93/94	-163.2	77.0	...	-194.1	-252.0	180.8
J2325+3957	R (mag)	1/1	18.04	0.64	0.04	18.04	18.04	18.04
	m_l (%)	0/1	nan	nan	nan	nan	nan	nan
J2347+5142	R (mag)	8/8	15.36	0.21	0.01	15.44	15.70	15.15
	m_l (%)	7/8	3.9	0.3	0.1	3.2	2.5	10.6
	χ (°)	7/8	-48.8	19.7	...	-49.3	-88.0	-25.5

Bibliography

- A. A. Abdo, M. Ackermann, M. Ajello, M. Axelsson, L. Baldini, J. Ballet, G. Barbiellini, D. Bastieri, B. M. Baughman, K. Bechtol, R. Bellazzini, B. Berenji, R. D. Blandford, E. D. Bloom, D. C.-J. Bock, J. R. Bogart, E. Bonamente, A. W. Borgland, A. Bouvier, J. Bregeon, A. Brez, M. Brigida, P. Bruel, T. H. Burnett, S. Buson, G. A. Caliandro, R. A. Cameron, P. A. Caraveo, J. M. Casandjian, E. Cavazzuti, C. Cecchi, Ö. Çelik, A. Chekhtman, C. C. Cheung, J. Chiang, S. Ciprini, R. Claus, J. Cohen-Tanugi, W. Collmar, L. R. Cominsky, J. Conrad, S. Corbel, R. Corbet, L. Costamante, S. Cutini, C. D. Dermer, A. de Angelis, F. de Palma, S. W. Digel, E. Do Couto E Silva, P. S. Drell, R. Dubois, D. Dumora, C. Farnier, C. Favuzzi, S. J. Fegan, E. C. Ferrara, W. B. Focke, P. Fortin, M. Frailis, L. Fuhrmann, Y. Fukazawa, S. Funk, P. Fusco, F. Gargano, D. Gasparrini, N. Gehrels, S. Germani, B. Giebels, N. Giglietto, P. Giommi, F. Giordano, M. Giroletti, T. Glanzman, G. Godfrey, I. A. Grenier, J. E. Grove, L. Guillemot, S. Guiriec, Y. Hanabata, A. K. Harding, M. Hayashida, E. Hays, D. Horan, R. E. Hughes, G. Iafrate, R. Itoh, M. S. Jackson, G. Jóhannesson, A. S. Johnson, W. N. Johnson, M. Kadler, T. Kamae, H. Katagiri, J. Kataoka, N. Kawai, M. Kerr, J. Knödlseider, M. L. Kocian, M. Kuss, J. Lande, S. Larsson, L. Latronico, M. Lemoine-Goumard, F. Longo, F. Loparco, B. Lott, M. N. Lovellette, P. Lubrano, J. Macquart, G. M. Madejski, A. Makeev, W. Max-Moerbeck, M. N. Mazziotta, W. McConville, J. E. McEnery, S. McGlynn, C. Meurer, P. F. Michelson, W. Mitthumsiri, T. Mizuno, A. A. Moiseev, C. Monte, M. E. Monzani, A. Morselli, I. V. Moskalenko, S. Murgia, I. Nestoras, P. L. Nolan, J. P. Norris, E. Nuss, T. Ohsugi, A. Okumura, N. Omodei, E. Orlando, J. F. Ormes, D. Paneque, J. H. Panetta, D. Parent, V. Pavlidou, T. J. Pearson, V. Pelassa, M. Pepe, M. Pesce-Rollins, F. Piron, T. A. Porter, S. Rainò, R. Rando, M. Razzano, A. Readhead, A. Reimer, O. Reimer, T. Reposeur, L. C. Reyes, J. L. Richards, L. S. Rochester, A. Y. Rodriguez, M. Roth, F. Ryde, H. F.-W. Sadrozinski, D. Sanchez, A. Sander, P. M. Saz Parkinson, J. D. Scargle, C. Sgrò, M. S. Shaw, C. Shrader, E. J. Siskind, D. A. Smith, P. D. Smith, G. Spandre, P. Spinelli, L. Stawarz, M. Stevenson, M. S. Strickman, D. J. Suson, H. Tajima, H. Takahashi, T. Takahashi, T. Tanaka, G. B. Taylor, J. B. Thayer, J. G. Thayer, D. J. Thompson, L. Tibaldo, D. F. Torres, G. Tosti, A. Tramacere, Y. Uchiyama, T. L. Usher, V. Vasileiou, N. Vilchez, V. Vitale, A. P. Waite, P. Wang, A. E. Wehrle, B. L. Winer, K. S. Wood, T. Ylinen, J. A. Zensus, M. Uemura, Y. Ikejiri, K. S. Kawabata, M. Kino, K. Sakimoto, M. Sasada, S. Sato, M. Yamanaka, M. Villata, C. M. Raiteri, I. Agudo, H. D. Aller, M. F. Aller, E. Angelakis, A. A. Arkharov, U. Bach, E. Benítez, A. Berdyugin, D. A. Blinov, M. Boettcher, C. S. Buemi, W. P. Chen, M. Dolci, D. Dultzin, N. V. Efimova, M. A. Gurwell, C. Gusbar, J. L. Gómez, J. Heidt, D. Hiriart, T. Hovatta, S. G. Jorstad, T. S. Konstantinova, E. N. Kopatskaya, E. Koptelova, O. M. Kurtanidze, A. Lahteenmaki, V. M. Larionov, E. G. Larionova, P. Leto, H. C. Lin, E. Lindfors, A. P. Marscher, I. M. McHardy, D. A. Melnichuk, M. Mommert, K. Nilsson, A. di Paola, R. Reinthal, G. M. Richter, M. Roca-Sogorb, P. Roustazadeh, L. A. Sigua, L. O. Takalo, M. Tornikoski, C. Trigilio, I. S. Troitsky, G. Umana, C. Villforth, K. Grainge, R. Moderski, K. Nalewajko, M. Sikora, Fermi LAT Collaboration, and Members of the 3C Multi-Band Campaign. A change in the optical polarization associated with a gamma-ray

- flare in the blazar 3C 279. *Nature*, 463(7283):919–23, February 2010. ISSN 1476-4687. doi: 10.1038/nature08841. URL <http://adsabs.harvard.edu/abs/2010Natur.463..919A>.
- M. Ackermann, M. Ajello, W. Atwood, L. Baldini, J. Ballet, G. Barbiellini, D. Bastieri, J. Gonzalez, R. Bellazzini, E. Bissaldi, R. Blandford, E. Bloom, R. Bonino, E. Bottacini, T. Brandt, J. Bregeon, R. Britto, P. Bruel, R. Buehler, S. Buson, G. Caliendo, R. Cameron, M. Caragiulo, P. Caraveo, J. Casandjian, E. Cavazzuti, C. Cecchi, E. Charles, A. Chekhtman, C. Cheung, J. Chiang, G. Chiaro, S. Ciprini, R. Claus, J. Cohen-Tanugi, L. Cominsky, J. Conrad, S. Cutini, R. D’Abrusco, F. D’Ammando, A. Angelis, R. Desiante, S. Digel, L. Venere, P. Drell, C. Favuzzi, S. Fegan, E. Ferrara, J. Finke, W. Focke, A. Franckowiak, L. Fuhrmann, A. Furniss, P. Fusco, F. Gargano, D. Gasparrini, N. Giglietto, P. Giommi, F. Giordano, M. Giroletti, T. Glanzman, G. Godfrey, I. Grenier, J. Grove, S. Guiriec, J. W. Hewitt, A. Hill, D. Horan, G. J’ohannesson, A. Johnson, W. Johnson, J. Kataoka, M. Kuss, G. Mura, S. Larsson, L. Latronico, C. Leto, J. Li, L. Li, F. Longo, F. Loparco, B. Lott, M. Lovellette, P. Lubrano, G. Madejski, M. Mayer, M. Mazziotta, J. McEnery, P. Michelson, T. Mizuno, A. Moiseev, M. Monzani, A. Morselli, I. Moskalenko, S. Murgia, E. Nuss, M. Ohno, T. Ohsugi, R. Ojha, N. Omodei, M. Orienti, E. Orlando, A. Paggi, D. Paneque, J. Perkins, M. Pesce-Rollins, F. Piron, G. Pivato, T. Porter, S. Rain’o, R. Rando, M. Razzano, S. Razzaque, A. Reimer, O. Reimer, R. Romani, D. Salvetti, M. Schaal, F. Schinzel, A. Schulz, C. Sgr’o, E. Siskind, K. Sokolovsky, F. Spada, G. Spandre, P. Spinelli, L. Stawarz, D. Suson, H. Takahashi, T. Takahashi, Y. Tanaka, J. Thayer, L. Tibaldo, D. Torres, E. Torresi, G. Tosti, E. Troja, Y. Uchiyama, G. Vianello, B. Winer, K. Wood, and S. Zimmer. The Third Catalog of Active Galactic Nuclei Detected by the Fermi Large Area Telescope. *Prepr. arXiv1501.06054*, page 76, January 2015. URL <http://arxiv.org/abs/1501.06054>.
- J. A. Acosta-Pulido, I. Agudo, R. Barrena, C. Ramos Almeida, A. Manchado, and P. Rodríguez-Gil. The redshift and broad-band spectral energy distribution of NRAO 150. *Astron. Astrophys.*, 519:A5, September 2010. ISSN 0004-6361. doi: 10.1051/0004-6361/200913953. URL <http://ads.nao.ac.jp/abs/2010A%26A...519A...5A>.
- I. Agudo, C. Thum, J. L. Gómez, and H. Wiesenmeyer. A simultaneous 3.5 and 1.3 mm polarimetric survey of active galactic nuclei in the northern sky. *Astron. Astrophys.*, 566:A59, June 2014. ISSN 0004-6361. doi: 10.1051/0004-6361/201423366. URL <http://ads.nao.ac.jp/abs/2014A%26A...566A...59A>.
- M. G. Akritas and M. A. Bershad. Linear Regression for Astronomical Data with Measurement Errors and Intrinsic Scatter. *Astrophys. J.*, 470:706, October 1996. ISSN 0004-637X. doi: 10.1086/177901. URL <http://adsabs.harvard.edu/abs/1996ApJ...470..706A>.
- M. F. Aller, H. D. Aller, P. A. Hughes, and G. E. Latimer. Centimeter-Wavelength Total Flux and Linear Polarization Properties of Radio-loud BL Lacertae Objects. *Astrophys. J.*, 512(2):601–622, February 1999. ISSN 0004-637X. doi: 10.1086/306799. URL <http://adsabs.harvard.edu/abs/1999ApJ...512..601A>.
- M. F. Aller, P. A. Hughes, H. D. Aller, G. E. Latimer, and T. Hovatta. Constraining the physical conditions in the jets of γ -ray flaring blazars using centimeter-band polarimetry and radiative transfer simulations. I. Data and models for 0420-014, OJ 287, and 1156+295. *Astrophys. J.*, 791(1):53, July 2014. ISSN 0004-637X. doi: 10.1088/0004-637X/791/1/53. URL <http://ads.nao.ac.jp/abs/2014ApJ...791...53A>.

- E. Angelakis. *Multi-Frequency Study of the NVSS Foreground Sources in the Cosmic Background Imager Fields*. PhD thesis, Max-Planck-Institut für Radioastronomie, eangelaki@mpifr-bonn.mpg.de, January 2007.
- E. Angelakis, A. Kraus, A. C. S. Readhead, J. A. Zensus, R. Bustos, T. P. Krichbaum, A. Witzel, and T. J. Pearson. Multi-frequency measurements of the NVSS foreground sources in the cosmic background imager fields. I. Data release. *A&A*, 501:801–812, July 2009. doi: 10.1051/0004-6361/200811267.
- E. Angelakis, L. Fuhrmann, I. Nestoras, J. A. Zensus, N. Marchili, V. Pavlidou, and T. P. Krichbaum. The F-GAMMA program: multi-wavelength AGN studies in the Fermi-GST era. *eprint arXiv:1006.5610*, 2010. URL <http://adsabs.harvard.edu/abs/2010arXiv1006.5610A>.
- E. Angelakis, L. Fuhrmann, I. Nestoras, C. M. Fromm, M. Perucho-Pla, R. Schmidt, J. A. Zensus, N. Marchili, T. P. Krichbaum, H. Ungerechts, A. Sievers, D. Riquelme, and V. Pavlidou. F-GAMMA: On the phenomenological classification of continuum radio spectra variability patterns of Fermi blazars. *J. Phys. Conf. Ser.*, 372(1):012007, July 2012. ISSN 1742-6596. doi: 10.1088/1742-6596/372/1/012007. URL <http://ads.nao.ac.jp/abs/2012JPhCS.372a2007A>.
- E. Angelakis, L. Fuhrmann, N. Marchili, L. Foschini, I. Myserlis, V. Karamanavis, S. Komossa, D. Blinov, T. P. Krichbaum, A. Sievers, H. Ungerechts, and J. A. Zensus. Radio jet emission from GeV-emitting narrow-line Seyfert 1 galaxies. *Astron. Astrophys.*, 575:A55, February 2015. ISSN 0004-6361. doi: 10.1051/0004-6361/201425081. URL <http://ads.nao.ac.jp/abs/2015A%26A...575A...55A>.
- R. R. J. Antonucci and J. S. Miller. Spectropolarimetry and the nature of NGC 1068. *Astrophys. J.*, 297:621, October 1985. ISSN 0004-637X. doi: 10.1086/163559. URL <http://adsabs.harvard.edu/abs/1985ApJ...297..621A>.
- V. Beckmann and C. R. Shrader. Active Galactic Nuclei. *Act. Galact. Nuclei, ISBN-13 978-3527410781. 350 pages. Wiley-VCH Verlag GmbH, 2012, -1*, August 2012. URL <http://ads.nao.ac.jp/abs/2012agn...book....B>.
- W. Bednarek, J. G. Kirk, and A. Mastichiadis. Production of gamma-rays by inverse Compton scattering in jets. *A&AS*, 120:571–574, December 1996.
- M. C. Begelman. Accretion disks in active galactic nuclei. *Astrophys. Act. galaxies quasi-stellar objects. Mill Val.*, pages 411–452, 1985. URL <http://adsabs.harvard.edu/abs/1985aagq.conf...411B>.
- Mitchell C. Begelman, Roger D. Blandford, and Martin J. Rees. Theory of extragalactic radio sources. *Rev. Mod. Phys.*, 56(2):255–351, April 1984. ISSN 0034-6861. doi: 10.1103/RevModPhys.56.255. URL <http://ads.nao.ac.jp/abs/1984RvMP...56..255B>.
- R. D. Blandford and A. Königl. Relativistic jets as compact radio sources. *Astrophys. J.*, 232:34, August 1979. ISSN 0004-637X. doi: 10.1086/157262. URL <http://adsabs.harvard.edu/abs/1979ApJ...232...34B>.
- A. Blandford, R. D.; Königl. Relativistic jets as compact radio sources. *Astrophys. J.*, 232: 34–48, 1979.

- D. Blinov, V. Pavlidou, I. Papadakis, S. Kiehlmann, G. Panopoulou, I. Liodakis, O. G. King, E. Angelakis, M. Baloković, H. Das, R. Feiler, L. Fuhrmann, T. Hovatta, P. Khodade, A. Kus, N. Kylafis, I. Myserlis, D. Modi, B. Pazderska, E. Pazderski, I. Papamastorakis, T. J. Pearson, C. Rajarshi, A. Ramaprakash, P. Reig, A. C. S. Readhead, K. Tassis, and J. A. Zensus. RoboPol: First season rotations of optical polarization plane in blazars. *eprint arXiv:1505.07467*, 2015. URL <http://adsabs.harvard.edu/abs/2015arXiv150507467B>.
- M. Boettcher, D. E. Harris, and H. Krawczynski. *Relativistic Jets from Active Galactic Nuclei*. Wiley, January 2012.
- T. V. Cawthorne and W. K. Cobb. Linear polarization of radiation from oblique and conical shocks. *Astrophys. J.*, 350:536, February 1990. ISSN 0004-637X. doi: 10.1086/168409. URL <http://adsabs.harvard.edu/abs/1990ApJ...350..536C>.
- L. Fuhrmann, J. A. Zensus, T. P. Krichbaum, E. Angelakis, and A. C. S. Readhead. Simultaneous Radio to (Sub-) mm-Monitoring of Variability and Spectral Shape Evolution of potential GLAST Blazars. In *AIP Conference Proceedings*, volume 921, pages 249–251. AIP, 2007. doi: 10.1063/1.2757314. URL <http://adsabs.harvard.edu/abs/2007AIPC...921..249F>.
- D. C. Gabuzda, E. A. Rastorgueva, P. S. Smith, and S. P. O’Sullivan. Evidence for cospatial optical and radio polarized emission in active galactic nuclei. *Mon. Not. R. Astron. Soc.*, 369(4):1596–1602, June 2006. ISSN 00358711. doi: 10.1111/j.1365-2966.2006.10433.x. URL <http://adsabs.harvard.edu/abs/2006MNRAS.369.1596G>.
- V. L. Ginzburg. Theoretical physics and astrophysics. *Int. Ser. Nat. Philos.*, 1979. URL <http://adsabs.harvard.edu/abs/1979tpa...book....G>.
- A. Hewitt and G. Burbidge. A revised optical catalog of quasi-stellar objects. *Astrophys. J. Suppl. Ser.*, 43:57, May 1980. ISSN 0067-0049. doi: 10.1086/190667. URL <http://cdsads.u-strasbg.fr/abs/1980ApJS...43...57H>.
- D. C. Homan, M. L. Lister, H. D. Aller, M. F. Aller, and J. F. C. Wardle. Full Polarization Spectra of 3C 279. *Astrophys. J.*, 696(1):21, May 2009. ISSN 0004-637X. doi: 10.1088/0004-637X/696/1/328. URL <http://arxiv.org/abs/0902.0810>.
- T. Hovatta, E. Valtaoja, M. Tornikoski, and A. Lähteenmäki. Doppler factors, Lorentz factors and viewing angles for quasars, BL Lacertae objects and radio galaxies. *Astron. Astrophys.*, 494(2):527–537, February 2009. ISSN 0004-6361. doi: 10.1051/0004-6361:200811150. URL <http://ads.nao.ac.jp/abs/2009A%26A...494..527H>.
- P. A. Hughes, H. D. Aller, and M. F. Aller. Polarized Radio Outbursts in BL-Lacertae - Part Two - the Flux and Polarization of a Piston-Driven Shock. *Astrophys. J.*, 298:301, November 1985. ISSN 0004-637X. doi: 10.1086/163611. URL <http://adsabs.harvard.edu/abs/1985ApJ...298..301H>.
- P. A. Hughes, H. D. Aller, and M. F. Aller. Synchrotron emission from shocked relativistic jets. I - The theory of radio-wavelength variability and its relation to superluminal motion. *Astrophys. J.*, 341:54, June 1989a. ISSN 0004-637X. doi: 10.1086/167471. URL <http://adsabs.harvard.edu/abs/1989ApJ...341...54H>.

- P. A. Hughes, H. D. Aller, and M. F. Aller. Synchrotron Emission from Shocked Relativistic Jets. II. A Model for the Centimeter Wave Band Quiescent and Burst Emission from BL Lacertae. *Astrophys. J.*, 341:68, June 1989b. ISSN 0004-637X. doi: 10.1086/167472. URL <http://adsabs.harvard.edu/abs/1989ApJ...341...68H>.
- P. A. Hughes, M. F. Aller, and H. D. Aller. Constraining the physical conditions in the jets of γ -ray flaring blazars using centimeter-band polarimetry and radiative transfer simulations. II. Exploring parameter space and implications. *Astrophys. J.*, 799(2):207, January 2015. ISSN 1538-4357. doi: 10.1088/0004-637X/799/2/207. URL <http://ads.nao.ac.jp/abs/2015ApJ...799..207H>.
- T. W. Jones and S. L. Odell. Transfer of Polarized Radiation in self-absorbed synchrotron sources. I. results for a homogeneous source. *Astrophys. J.*, 214:522–539, June 1977. ISSN 0004-637X. doi: 10.1086/155278. URL <http://adsabs.harvard.edu/full/1977ApJ...214..522J>.
- T. W. Jones, L. Rudnick, R. L. Fiedler, H. D. Aller, M. F. Aller, and P. E. Hodge. Magnetic field structures in active compact radio sources. *Astrophys. J.*, 290:627, March 1985. ISSN 0004-637X. doi: 10.1086/163020. URL <http://adsabs.harvard.edu/abs/1985ApJ...290..627J>.
- D. Kazanas and A. Mastichiadis. Relativistic Electrons in Blazars: A Hadronic Origin? *ApJ*, 518:L17–L20, June 1999. doi: 10.1086/312056.
- S. Kiehlmann, T. Savolainen, S. G. Jorstad, K. V. Sokolovsky, F. K. Schinzel, I. Agudo, A. A. Arkharov, E. Benítez, A. Berdyugin, D. A. Blinov, N. G. Bochkarev, G. A. Borman, A. N. Burenkov, C. Casadio, V. T. Doroshenko, N. V. Efimova, Y. Fukazawa, J. L. Gómez, V. A. Hagen-Thorn, J. Heidt, D. Hiriart, R. Itoh, M. Joshi, G. N. Kimeridze, T. S. Konstantinova, E. N. Kopatskaya, I. V. Korobtsev, Y. Y. Kovalev, T. Krajci, O. Kurtanidze, S. O. Kurtanidze, V. M. Larionov, E. G. Larionova, L. V. Larionova, E. Lindfors, E. López, A. P. Marscher, I. M. McHardy, S. N. Molina, D. A. Morozova, S. V. Nazarov, M. G. Nikolashvili, K. Nilsson, N. G. Pulatova, R. Reinthal, A. Sadun, S. G. Sergeev, L. A. Sigua, M. Sorcia, O. I. Spiridonova, L. O. Takalo, B. Taylor, I. S. Troitsky, L. S. Ugolkova, J. A. Zensus, and V. E. Zhdanova. Analyzing polarization swings in 3C 279. *EPJ Web Conf.*, 61:06003, December 2013. ISSN 2100-014X. doi: 10.1051/epjconf/20136106003. URL <http://ads.nao.ac.jp/abs/2013EPJWC...6106003K>.
- O. G. King, D. Blinov, A. N. Ramaprakash, I. Myserlis, E. Angelakis, M. Balokovi, R. Feiler, L. Fuhrmann, T. Hovatta, P. Khodade, A. Kougentakakis, N. Kylafis, A. Kus, D. Modi, E. Paleologou, G. Panopoulou, I. Papadakis, I. Papamastorakis, G. Paterakis, V. Pavlidou, B. Pazderska, E. Pazderski, T. J. Pearson, C. Rajarshi, A. C. S. Readhead, P. Reig, A. Steiakaki, K. Tassis, and J. A. Zensus. The RoboPol pipeline and control system. *Mon. Not. R. Astron. Soc.*, 442(2):1706–1717, June 2014. ISSN 0035-8711. doi: 10.1093/mnras/stu176. URL <http://adsabs.harvard.edu/abs/2014MNRAS.442.1706K>.
- J. P. Leahy and A. G. Williams. The bridges of classical double radio sources. *Mon. Not. R. Astron. Soc.*, 210:929–951, October 1984. ISSN 0035-8711. URL <http://ads.nao.ac.jp/abs/1984MNRAS.210..929L>.
- M. P. C. Legg and K. C. Westfold. Elliptic Polarization of Synchrotron Radiation. *Astrophys. J.*, 154:499, November 1968. ISSN 0004-637X. doi: 10.1086/149777. URL <http://adsabs.harvard.edu/abs/1968ApJ...154..499L>.

- K. R. Lind and R. D. Blandford. Semidynamical models of radio jets - Relativistic beaming and source counts. *Astrophys. J.*, 295:358, August 1985. ISSN 0004-637X. doi: 10.1086/163380. URL <http://adsabs.harvard.edu/abs/1985ApJ...295..358L>.
- M. L. Lister, M. H. Cohen, D. C. Homan, M. Kadler, K. I. Kellermann, Y. Y. Kovalev, E. Ros, T. Savolainen, and J. A. Zensus. MOJAVE: Monitoring of Jets in Active Galactic Nuclei with VLBA Experiments. VI. Kinematics Analysis of a Complete Sample of Blazar Jets. *AJ*, 138:1874-1892, December 2009. doi: 10.1088/0004-6256/138/6/1874.
- M. L. Lister, M. F. Aller, H. D. Aller, D. C. Homan, K. I. Kellermann, Y. Y. Kovalev, A. B. Pushkarev, J. L. Richards, E. Ros, and T. Savolainen. MOJAVE. X. Parsec-scale jet orientation variations and superluminal motion in active galactic nuclei. *Astron. J.*, 146(5):120, November 2013. ISSN 0004-6256. doi: 10.1088/0004-6256/146/5/120. URL <http://adsabs.harvard.edu/abs/2013AJ....146..120L>.
- M. S. Longair. High Energy Astrophysics. *High Energy Astrophys. by Malcolm S. Longair, Cambridge, UK Cambridge Univ. Press. 2011, -1*, February 2011. URL <http://ads.nao.ac.jp/abs/2011hea..book.....L>.
- M. Lyutikov, V. I. Pariev, and R. D. Blandford. Polarization of Prompt Gamma-Ray Burst Emission: Evidence for Electromagnetically Dominated Outflow. *Astrophys. J.*, 597(2):998-1009, November 2003. ISSN 0004-637X. doi: 10.1086/378497. URL <http://adsabs.harvard.edu/abs/2003ApJ...597..998L>.
- M. Lyutikov, V. I. Pariev, and D. C. Gabuzda. Polarization and structure of relativistic parsec-scale AGN jets. *Mon. Not. R. Astron. Soc.*, 360(3):869-891, July 2005. ISSN 00358711. doi: 10.1111/j.1365-2966.2005.08954.x. URL <http://adsabs.harvard.edu/abs/2005MNRAS.360..869L>.
- M. A. G. Maia, R. S. Machado, and C. N. A. Willmer. The Seyfert Population in the Local Universe. *Astron. J.*, 126(4):1750-1762, October 2003. ISSN 0004-6256. doi: 10.1086/378360. URL <http://adsabs.harvard.edu/abs/2003AJ....126.1750M>.
- A. P. Marscher and W. K. Gear. Models for high-frequency radio outbursts in extragalactic sources, with application to the early 1983 millimeter-to-infrared flare of 3C 273. *Astrophys. J.*, 298:114, November 1985. ISSN 0004-637X. doi: 10.1086/163592. URL <http://orca.cf.ac.uk/36464/>.
- A. P. Marscher, S. G. Jorstad, F. D. D’Arcangelo, P. S. Smith, G. G. Williams, V. M. Larionov, H. Oh, A. R. Olmstead, M. F. Aller, H. D. Aller, I. M. McHardy, A. Lähteenmäki, M. Tornikoski, E. Valtaoja, V. A. Hagen-Thorn, E. N. Kopatskaya, W. K. Gear, G. Tosti, O. Kurtanidze, M. Nikolashvili, L. Sigua, H. R. Miller, and W. T. Ryle. The inner jet of an active galactic nucleus as revealed by a radio-to-gamma-ray outburst. *Nature*, 452(7190):966-9, April 2008. ISSN 1476-4687. doi: 10.1038/nature06895. URL <http://adsabs.harvard.edu/abs/2008Natur.452..966M>.
- A. P. Marscher, S. G. Jorstad, V. M. Larionov, M. F. Aller, H. D. Aller, A. Lähteenmäki, I. Agudo, P. S. Smith, M. Gurwell, V. A. Hagen-Thorn, T. S. Konstantinova, E. G. Larionova, L. V. Larionova, D. A. Melnichuk, D. A. Blinov, E. N. Kopatskaya, I. S. Troitsky, M. Tornikoski, T. Hovatta, G. D. Schmidt, F. D. D’Arcangelo, D. Bhattarai, B. Taylor, A. R. Olmstead, E. Manne-Nicholas, M. Roca-Sogorb, J. L. Gómez, I. M. McHardy, O. Kurtanidze, M. G. Nikolashvili, G. N. Kimeridze, and L. A. Sigua. Probing the inner jet of the quasar PKS 1510-089 with multi-waveband monitoring during

- strong gamma-ray activity. *Astrophys. J.*, 710(2):L126–L131, February 2010. ISSN 2041-8205. doi: 10.1088/2041-8205/710/2/L126. URL <http://adsabs.harvard.edu/abs/2010ApJ...710L.126M>.
- E. Massaro, P. Giommi, C. Leto, P. Marchegiani, A. Maselli, M. Perri, S. Piranomonte, and S. Scavi. Roma-BZCAT: a multifrequency catalogue of blazars. *Astron. Astrophys.*, 495(2):691–696, February 2009. ISSN 0004-6361. doi: 10.1051/0004-6361/200810161. URL <http://ads.nao.ac.jp/abs/2009A%26A...495...691M>.
- A. Mücke, R.J. Protheroe, R. Engel, J.P. Rachen, and T. Stanev. BL Lac objects in the synchrotron proton blazar model. *Astropart. Phys.*, 18(6):593–613, March 2003. ISSN 09276505. doi: 10.1016/S0927-6505(02)00185-8. URL <http://adsabs.harvard.edu/abs/2003APh....18...593M>.
- I. Myserlis, E. Angelakis, L. Fuhrmann, V. Pavlidou, I. Nestoras, V. Karamanavis, A. Kraus, and J. A. Zensus. Multi-frequency linear and circular radio polarization monitoring of jet emission elements in *Fermi* blazars. *eprint arXiv:1401.2072*, 2014. URL <http://adsabs.harvard.edu/abs/2014arXiv1401.2072M>.
- K. Nalewajko. Polarization swings from curved trajectories of emitting regions. *Int. J. Mod. Phys. D*, 19(06):701–706, June 2010. ISSN 0218-2718. doi: 10.1142/S0218271810016853. URL <http://adsabs.harvard.edu/abs/2010IJMPD...19...701N>.
- P. L. Nolan, A. A. Abdo, M. Ackermann, M. Ajello, A. Allafort, E. Antolini, W. B. Atwood, M. Axelsson, L. Baldini, J. Ballet, G. Barbiellini, D. Bastieri, K. Bechtol, A. Belfiore, R. Bellazzini, B. Berenji, G. F. Bignami, R. D. Blandford, E. D. Bloom, E. Bonamente, J. Bonnell, A. W. Borgland, E. Bottacini, A. Bouvier, T. J. Brandt, J. Bregeon, M. Brigida, P. Bruel, R. Buehler, T. H. Burnett, S. Buson, G. A. Caliandro, R. A. Cameron, R. Campana, B. Cañadas, A. Cannon, P. A. Caraveo, J. M. Casandjian, E. Cavazzuti, M. Ceccanti, C. Cecchi, Ö. Çelik, E. Charles, A. Chekhtman, C. C. Cheung, J. Chiang, R. Chipaux, S. Ciprini, R. Claus, J. Cohen-Tanugi, L. R. Cominsky, J. Conrad, R. Corbet, S. Cutini, F. D’Ammando, D. S. Davis, A. de Angelis, M. E. DeCesar, M. DeKlotz, A. De Luca, P. R. den Hartog, F. de Palma, C. D. Dermer, S. W. Digel, E. do Couto e Silva, P. S. Drell, A. Drlica-Wagner, R. Dubois, D. Dumora, T. Enoto, L. Escande, D. Fabiani, L. Falletti, C. Favuzzi, S. J. Fegan, E. C. Ferrara, W. B. Focke, P. Fortin, M. Frailis, Y. Fukazawa, S. Funk, P. Fusco, F. Gargano, D. Gasparri, N. Gehrels, S. Germani, B. Giebels, N. Giglietto, P. Giommi, F. Giordano, M. Giroletti, T. Glanzman, G. Godfrey, I. A. Grenier, M.-H. Grondin, J. E. Grove, L. Guillemot, S. Guiriec, M. Gustafsson, D. Hadasch, Y. Hanabata, A. K. Harding, M. Hayashida, E. Hays, A. B. Hill, D. Horan, X. Hou, R. E. Hughes, G. Iafate, R. Itoh, G. Jóhannesson, R. P. Johnson, T. E. Johnson, A. S. Johnson, T. J. Johnson, T. Kamae, H. Katagiri, J. Kataoka, J. Katsuta, N. Kawai, M. Kerr, J. Knödseder, D. Kocevski, M. Kuss, J. Lande, D. Landriu, L. Latronico, M. Lemoine-Goumard, A. M. Lionetto, M. Llena Garde, F. Longo, F. Loparco, B. Lott, M. N. Lovellette, P. Lubrano, G. M. Madejski, M. Marelli, E. Massaro, M. N. Mazziotta, W. McConville, J. E. McEnery, J. Mehault, P. F. Michelson, M. Minuti, W. Mitthumsiri, T. Mizuno, A. A. Moiseev, M. Mongelli, C. Monte, M. E. Monzani, A. Morselli, I. V. Moskalenko, S. Murgia, T. Nakamori, M. Naumann-Godo, J. P. Norris, E. Nuss, T. Nymark, M. Ohno, T. Ohsugi, A. Okumura, N. Omodei, E. Orlando, J. F. Ormes, M. Ozaki, D. Paneque, J. H. Panetta, D. Parent, J. S. Perkins, M. Pesce-Rollins, M. Pierbattista, M. Pinchera, F. Piron, G. Pivato, T. A. Porter, J. L. Racusin, S. Rainò, R. Rando, M. Razzano, S. Razzaque, A. Reimer, O. Reimer, T. Reposeur, S. Ritz, L. S. Rochester, R. W. Romani, M. Roth, R. Rousseau, F. Ryde, H. F.-W. Sadrozinski, D. Salvetti,

- D. A. Sanchez, P. M. Saz Parkinson, C. Sbarra, J. D. Scargle, T. L. Schalk, C. Sgrò, M. S. Shaw, C. Shrader, E. J. Siskind, D. A. Smith, G. Spandre, P. Spinelli, T. E. Stephens, M. S. Strickman, D. J. Suson, H. Tajima, H. Takahashi, T. Takahashi, T. Tanaka, J. G. Thayer, J. B. Thayer, D. J. Thompson, L. Tibaldo, O. Tibolla, F. Tinebra, M. Tinivella, D. F. Torres, G. Tosti, E. Troja, Y. Uchiyama, J. Vandenbroucke, A. Van Etten, B. Van Klaveren, V. Vasileiou, G. Vianello, V. Vitale, A. P. Waite, E. Wallace, P. Wang, M. Werner, B. L. Winer, D. L. Wood, K. S. Wood, M. Wood, Z. Yang, and S. Zimmer. Fermi Large Area Telescope second source catalog. *Astrophys. J. Suppl. Ser.*, 199(2):31, April 2012. ISSN 0067-0049. doi: 10.1088/0067-0049/199/2/31. URL <http://ads.nao.ac.jp/abs/2012ApJS...199...31N>.
- S. P. O'Sullivan and D. C. Gabuzda. Magnetic field strength and spectral distribution of six parsec-scale active galactic nuclei jets. *Mon. Not. R. Astron. Soc.*, 400(1):26–42, November 2009a. ISSN 00358711. doi: 10.1111/j.1365-2966.2009.15428.x. URL <http://ads.nao.ac.jp/abs/2009MNRAS.400...26O>.
- S. P. O'Sullivan and D. C. Gabuzda. Three-dimensional magnetic field structure of six parsec-scale active galactic nuclei jets. *Mon. Not. R. Astron. Soc.*, 393(2):429–456, February 2009b. ISSN 00358711. doi: 10.1111/j.1365-2966.2008.14213.x. URL <http://ads.nao.ac.jp/abs/2009MNRAS.393...429O>.
- A. G. Pacholczyk. Radio astrophysics; nonthermal processes in galactic and extragalactic sources. *Ser. books Astron. Astrophys.*, -1:xxi, 269, 1970. URL <http://ads.nao.ac.jp/abs/1970ranp.book.....P>.
- A. G. Pacholczyk. Radio galaxies: Radiation transfer, dynamics, stability and evolution of a synchrotron plasmon. *Oxford*, 89, 1977. URL <http://adsabs.harvard.edu/abs/1977OISNP...89.....P>.
- I. I. K. Pauliny-Toth and K. I. Kellermann. Variations in the Radio-Frequency Spectra of 3c 84, 3c 273, 3c 279, and Other Radio Sources. *Astrophys. J.*, 146:634, December 1966. ISSN 0004-637X. doi: 10.1086/148941. URL <http://ads.nao.ac.jp/abs/1966ApJ...146...634P>.
- V. Pavlidou, E. Angelakis, I. Myserlis, D. Blinov, O. G. King, I. Papadakis, K. Tassis, T. Hovatta, B. Pazderska, E. Paleologou, M. Balokovi, R. Feiler, L. Fuhrmann, P. Khodade, A. Kus, N. Kylafis, D. Modi, G. Panopoulou, I. Papamastorakis, E. Pazderski, T. J. Pearson, C. Rajarshi, A. Ramaprakash, A. C. S. Readhead, P. Reig, and J. A. Zensus. The RoboPol optical polarization survey of gamma-ray-loud blazars. *Mon. Not. R. Astron. Soc.*, 442(2):1693–1705, June 2014. ISSN 0035-8711. doi: 10.1093/mnras/stu904. URL <http://adsabs.harvard.edu/abs/2014MNRAS.442.1693P>.
- R. A. Perley and B. J. Butler. An accurate flux density scale from 1 to 50 GHz. *Astrophys. J. Suppl. Ser.*, 204(2):19, February 2013a. ISSN 0067-0049. doi: 10.1088/0067-0049/204/2/19. URL <http://adsabs.harvard.edu/abs/2013ApJS...204...19P>.
- R. A. Perley and B. J. Butler. Integrated polarization properties of 3C48, 3C138, 3C147, and 3C286. *Astrophys. J. Suppl. Ser.*, 206(2):16, June 2013b. ISSN 0067-0049. doi: 10.1088/0067-0049/206/2/16. URL <http://ads.nao.ac.jp/abs/2013ApJS...206...16P>.
- B. M. Peterson. An Introduction to Active Galactic Nuclei. *An Introd. to Act. Galact. nuclei, Publ. Cambridge, New York Cambridge Univ. Press. 1997 Phys. Descr. xvi, 238 p. ISBN 0521473489*, -1, February 1997. URL <http://ads.nao.ac.jp/abs/1997iagn.book.....P>.

- A. Quirrenbach, A. Witzel, T. P. Kirchbaum, C. A. Hummel, R. Wegner, C. J. Schalinski, M. Ott, A. Alberdi, and M. Rioja. Statistics of intraday variability in extragalactic radio sources. *Astron. Astrophys. (ISSN 0004-6361)*, 258:279–284, 1992. URL <http://adsabs.harvard.edu/abs/1992A%26A...258..279Q>.
- G. B. Rybicki and A. P. Lightman. Radiative processes in astrophysics. *New York*, 1979. URL <http://adsabs.harvard.edu/abs/1979rpa...book....R>.
- D. J. Saikia and C. J. Salter. Polarization Properties of Extragalactic Radio Sources. *Annu. Rev. Astron. Astrophys.*, 26(1):93–144, September 1988. ISSN 0066-4146. doi: 10.1146/annurev.aa.26.090188.000521. URL <http://adsabs.harvard.edu/abs/1988ARA%26A...26...93S>.
- M. Sasada, M. Uemura, Y. Fukazawa, H. Yasuda, R. Itoh, K. Sakimoto, Y. Ikejiri, M. Yoshida, K. S. Kawabata, H. Akitaya, T. Ohsugi, M. Yamanaka, T. Komatsu, H. Miyamoto, O. Nagae, H. Nakaya, H. Tanaka, S. Sato, and M. Kino. Extremely high polarization in the 2010 outburst of blazar 3C 454.3. *Astrophys. J.*, 784(2):141, April 2014. ISSN 0004-637X. doi: 10.1088/0004-637X/784/2/141. URL <http://adsabs.harvard.edu/abs/2014ApJ...784..141S>.
- P. S. Smith, E. Montiel, S. Rightley, J. Turner, G. D. Schmidt, and B. T. Jannuzi. Coordinated Fermi/Optical Monitoring of Blazars and the Great 2009 September Gamma-ray Flare of 3C 454.3. *eprint arXiv:0912.3621*, 2009. URL <http://adsabs.harvard.edu/abs/2009arXiv0912.3621S>.
- J. Souchay, A. H. Andrei, C. Barache, S. Bouquillon, D. Suchet, F. Taris, and R. Peralta. The second release of the Large Quasar Astrometric Catalog (LQAC-2). *Astron. Astrophys.*, 537: A99, January 2012. ISSN 0004-6361. doi: 10.1051/0004-6361/201117954. URL <http://cdsads.u-strasbg.fr/abs/2012A%26A...537A..99S>.
- A. R. Taylor, J. M. Stil, and C. Sunstrum. A rotation measure image of the sky. *Astrophys. J.*, 702(2):1230–1236, September 2009. ISSN 0004-637X. doi: 10.1088/0004-637X/702/2/1230. URL <http://cdsads.u-strasbg.fr/abs/2009ApJ...702.1230T>.
- M. Turler. Shock-in-jet model for quasars and microquasars. *Mem. della Soc. Astron. Ital.*, page 8, 2010. URL <http://arxiv.org/abs/1010.0907>.
- Z. Turlo, T. Forkert, W. Sieber, and W. Wilson. Calibration of the instrumental polarization of radio telescopes. *Astron. Astrophys. (ISSN 0004-6361)*, 142:181–188, 1985. URL <http://adsabs.harvard.edu/abs/1985A%26A...142..181T>.
- C. M. Urry and P. Padovani. Unified Schemes for Radio-Loud Active Galactic Nuclei. *PASP*, 107:803, September 1995. doi: 10.1086/133630.
- H. Van der Laan. A Model for Variable Extragalactic Radio Sources. *Nature*, 211(5054): 1131–1133, September 1966. ISSN 0028-0836. doi: 10.1038/2111131a0. URL <http://adsabs.harvard.edu/abs/1966Natur.211.1131V>.
- M.-P. Véron-Cetty and P. Véron. A catalogue of quasars and active nuclei: 12th edition. *Astron. Astrophys.*, 455(2):773–777, August 2006. ISSN 0004-6361. doi: 10.1051/0004-6361:20065177. URL <http://ads.nao.ac.jp/abs/2006A%26A...455..773V>.
- S. von Hoerner. Design of large steerable antennas. *AJ*, 72:35, February 1967. doi: 10.1086/110198.

- W. Yuan, H. Y. Zhou, S. Komossa, X. B. Dong, T. G. Wang, H. L. Lu, and J. M. Bai. A Population of Radio-Loud Narrow-Line Seyfert 1 Galaxies with Blazar-Like Properties? *Astrophys. J.*, 685(2):801–827, October 2008. ISSN 0004-637X. doi: 10.1086/591046. URL <http://ads.nao.ac.jp/abs/2008ApJ...685..801Y>.
- H.-Y. Zhou, T.-G. Wang, X.-B. Dong, C. Li, and X.-G. Zhang. The Hybrid Nature of 0846+51W1: a BL Lac Object with a Narrow Line Seyfert 1 Nucleus. *Chinese J. Astron. Astrophys.*, 5(1):41–48, February 2005. ISSN 1009-9271. doi: 10.1088/1009-9271/5/1/005. URL <http://ads.nao.ac.jp/abs/2005ChJAA...5...41Z>.
- Y. Zhou, D.-H. Yan, and B.-Z. Dai. The optical variability properties of flat spectrum radio quasar 3C 454.3. *New Astron.*, 36:19–25, April 2015. ISSN 13841076. doi: 10.1016/j.newast.2014.09.010. URL <http://adsabs.harvard.edu/abs/2015NewA...36...19Z>.
- A. A. Zijlstra, P. A. M. van Hoof, and R. A. Perley. The Evolution of NGC 7027 at Radio Frequencies: A New Determination of the Distance and Core Mass. *Astrophys. J.*, 681(2): 1296–1309, July 2008. ISSN 0004-637X. doi: 10.1086/588778. URL <http://adsabs.harvard.edu/abs/2008ApJ...681.1296Z>.

Erklärung

Ich versichere, dass ich die von mir vorgelegte Dissertation selbständig angefertigt, die benutzten Quellen und Hilfsmittel vollständig angegeben und die Stellen der Arbeit, einschließlich Tabellen, Karten und Abbildungen, die anderen Werken im Wortlaut oder dem Sinn nach entnommen sind, in jedem Einzelfall als Entlehnung kenntlich gemacht habe; dass diese Dissertation noch keiner anderen Fakultät oder Universität zur Prüfung vorgelegen hat; dass sie, abgesehen von unten angegebenen Teilpublikationen – noch nicht veröffentlicht worden ist sowie, dass ich eine solche Veröffentlichung vor Abschluss des Promotionsverfahrens nicht vornehmen werde.

Die Bestimmungen dieser Promotionsordnung sind mir bekannt. Die von mir vorgelegte Dissertation ist von Prof. Dr. Andreas Eckart und Prof. Dr. J. Anton Zensus betreut worden.

Köln, den 17.08.2015

Publications / Teilpublikationen

- E. Angelakis, L. Fuhrmann, **I. Myserlis**, I. Nestoras, V. Karamanavis, T. P. Krichbaum, A. J. Zensus, N. Marchili, L. Foschini, H. Ungerechts, and A. Sievers. Properties of the radio jet emission of gamma-ray Narrow Line Seyfert 1s. In *Proceedings of Nuclei of Seyfert galaxies and QSOs - Central engine & conditions of star formation (Seyfert 2012)*. 6-8 November, 2012. Max-Planck-Institut für Radioastronomie (MPIfR), Bonn, Germany. Online at <http://pos.sissa.it/cgi-bin/reader/conf.cgi?confid=169>, id.58, page 58, 2012.
- E. Angelakis, L. Fuhrmann, and **I. Myserlis**. Properties of the radio jet emission of four gamma-ray Narrow Line Seyfert 1 galaxies. In *11th Hellenic Astronomical Conference*, pages 34–34, September 2013.
- E. Angelakis, L. Fuhrmann, N. Marchili, L. Foschini, **I. Myserlis**, V. Karamanavis, S. Kormoss, D. Blinov, T. P. Krichbaum, A. Sievers, H. Ungerechts, and J. A. Zensus. Radio jet emission from GeV-emitting narrow-line Seyfert 1 galaxies. *A&A*, 575:A55, March 2015. doi: 10.1051/0004-6361/201425081.
- M. Balokovic, T. Hovatta, O. King, T. Pearson, A. Readhead, D. Blinov, N. Kylafis, G. Panopoulou, I. Papadakis, I. Papamastorakis, V. Pavlidou, P. Reig, K. Tassis, P. Khodade, C. Rajarshi, A. Ramaprakash, R. Rouneq, E. Angelakis, **I. Myserlis**, L. Fuhrmann, J. A. Zensus, R. Feiler, A. Kus, B. Pazderska, and E. Pazderski. GRB 131030A - RoboPol optical afterglow polarimetry. *GRB Coordinates Network*, 15430:1, 2013.
- T. Beuchert, M. Kadler, J. Wilms, E. Angelakis, L. Fuhrmann, **I. Myserlis**, I. Nestoras, A. Kraus, U. Bach, E. Ros, C. Grossberger, and R. Schulz. Single-Dish Radio Polarimetry in the F-GAMMA Program with the Effelsberg 100-m Radio Telescope. In *European Physical Journal Web of Conferences*, volume 61 of *European Physical Journal Web of Conferences*, page 6006, December 2013. doi: 10.1051/epjconf/20136106006.
- D. Blinov, **I. Myserlis**, E. Angelakis, O. King, and V. Pavlidou. Optical and gamma-ray brightening of blazar OC 457. *The Astronomer's Telegram*, 4779:1, February 2013.
- D. Blinov, E. Angelakis, M. Balokovic, L. Fuhrmann, T. Hovatta, K. Katarzyski, P. Khodade, O. King, A. Kus, N. Kylafis, **I. Myserlis**, G. Panopoulou, I. Papadakis, I. Papamastorakis, V. Pavlidou, B. Pazderska, E. Pazderski, T. Pearson, C. Rajarshi, A. Ramaprakash, A. Readhead, P. Reig, R. Rouneq, K. Tassis, and A. Zensus. Optical polarization of gamma-ray bright blazars. In A. M. Mickaelian and D. B. Sanders, editors, *IAU Symposium*, volume 304 of *IAU Symposium*, pages 227–227, July 2014. doi: 10.1017/S1743921314003846.
- D. Blinov, V. Pavlidou, I. Papadakis, S. Kiehlmann, G. Panopoulou, I. Liodakis, O. G. King, E. Angelakis, M. Baloković, H. Das, R. Feiler, L. Fuhrmann, T. Hovatta, P. Khodade, A. Kus, N. Kylafis, **I. Myserlis**, D. Modi, B. Pazderska, E. Pazderski, I. Papamastorakis, T. J. Pearson, C. Rajarshi, A. Ramaprakash, P. Reig, A. C. S. Readhead, K. Tassis, and J. A. Zensus.

- RoboPol: First season rotations of optical polarization plane in blazars. *ArXiv e-prints*, May 2015.
- F. D’Ammando, M. Orienti, J. Finke, C. M. Raiteri, E. Angelakis, L. Fuhrmann, M. Giroletti, T. Hovatta, V. Karamanavis, W. Max-Moerbeck, **I. Myserlis**, A. C. S. Readhead, and J. L. Richards. Multifrequency studies of the narrow-line Seyfert 1 galaxy SBS 0846+513. *MNRAS*, 436:191–201, November 2013. doi: 10.1093/mnras/stt1560.
- L. Fuhrmann, J. L. Richards, U. Bach, T. Hovatta, M. Bremer, I. Nestoras, V. Karamanavis, K. Mooley, **I. Myserlis**, A. C. S. Readhead, C. C. Cheung, T. Pearson, and E. Angelakis. Follow-up radio observations of Nova Mon 2012 at 10 - 142 GHz. *The Astronomer’s Telegram*, 4376:1, September 2012.
- S. Jorstad, A. Marscher, V. Larionov, J. L. Gómez, I. Agudo, E. Angelakis, C. Casadio, M. Gurwell, T. Hovatta, M. Joshi, L. Fuhrmann, V. Karamanavis, A. Lähteenmäki, S. Molina, D. Morozova, **I. Myserlis**, I. Troitsky, H. Ungerechts, and J. A. Zensus. The Gamma-ray Activity of the high- z Quasar 0836+71. In *European Physical Journal Web of Conferences*, volume 61 of *European Physical Journal Web of Conferences*, page 4003, December 2013. doi: 10.1051/epjconf/20136104003.
- V. Karamanavis, **I. Myserlis**, L. Fuhrmann, E. Angelakis, I. Nestoras, T. P. Krichbaum, J. A. Zensus, H. Ungerechts, A. Sievers, and D. Riquelme. Gamma-ray blazar BL Lacertae: the highest recorded cm/mm radio flux over the past 30 years. *The Astronomer’s Telegram*, 4349:1, August 2012.
- V. Karamanavis, L. Fuhrmann, T. P. Krichbaum, E. Angelakis, J. Hodgson, **I. Myserlis**, I. Nestoras, A. J. Zensus, H. Ungerechts, and A. Sievers. Localizing the gamma rays from blazar PKS 1502+106. In *Proceedings of the 12th European VLBI Network Symposium and Users Meeting (EVN 2014). 7-10 October 2014. Cagliari, Italy. Online at <http://pos.sissa.it/cgi-bin/reader/conf.cgi?confid=230>, id.87*, page 87, 2014.
- V. Karamanavis, L. Fuhrmann, T. P. Krichbaum, E. Angelakis, J. Hodgson, **I. Myserlis**, I. Nestoras, J. A. Zensus, H. Ungerechts, and A. Sievers. Localizing the γ rays from blazar PKS 1502+106. *ArXiv e-prints*, April 2015.
- O. G. King, D. Blinov, D. Giannios, I. Papadakis, E. Angelakis, M. Baloković, L. Fuhrmann, T. Hovatta, P. Khodade, S. Kiehlmann, N. Kylafis, A. Kus, **I. Myserlis**, D. Modi, G. Panopoulou, I. Papamastorakis, V. Pavlidou, B. Pazderska, E. Pazderski, T. J. Pearson, C. Rajarshi, A. N. Ramaprakash, A. C. S. Readhead, P. Reig, K. Tassis, and J. A. Zensus. Early-time polarized optical light curve of GRB 131030A. *MNRAS*, 445:L114–L118, November 2014a. doi: 10.1093/mnras/slu149.
- O. G. King, D. Blinov, A. N. Ramaprakash, **I. Myserlis**, E. Angelakis, M. Baloković, R. Feiler, L. Fuhrmann, T. Hovatta, P. Khodade, A. Kougentakakis, N. Kylafis, A. Kus, D. Modi, E. Paleologou, G. Panopoulou, I. Papadakis, I. Papamastorakis, G. Paterakis, V. Pavlidou, B. Pazderska, E. Pazderski, T. J. Pearson, C. Rajarshi, A. C. S. Readhead, P. Reig, A. Steiakaki, K. Tassis, and J. A. Zensus. The RoboPol pipeline and control system. *MNRAS*, 442:1706–1717, August 2014b. doi: 10.1093/mnras/stu176.
- S. Komossa, D. Xu, L. Fuhrmann, D. Grupe, S. Yao, Z. Fan, **I. Myserlis**, E. Angelakis, V. Karamanavis, W. Yuan, and J. A. Zensus. What powers the radio-loud narrow-line Seyfert 1 galaxy RX J2314.9+2243?. A view onto its central engine from radio to X-rays. *A&A*, 574:A121, February 2015. doi: 10.1051/0004-6361/201424814.

- I. Myserlis.** Blazar physics through multi-band linear and circular polarization monitoring. In *11th Hellenic Astronomical Conference*, pages 35–36, September 2013.
- I. Myserlis, E. Angelakis, L. Fuhrmann, V. Karamanavis, I. Nestoras, T. P. Krichbaum, J. A. Zensus, H. Ungerechts, and A. Sievers.** Recent radio activity of the Fermi blazar S5 0716+714. *The Astronomer's Telegram*, 4447:1, October 2012a.
- I. Myserlis, E. Angelakis, L. Fuhrmann, V. Karamanavis, I. Nestoras, T. P. Krichbaum, J. A. Zensus, H. Ungerechts, and A. Sievers.** Recent radio activity of the Fermi blazar 4C +38.41. *The Astronomer's Telegram*, 4448:1, October 2012b.
- I. Myserlis, E. Angelakis, L. Fuhrmann, V. Karamanavis, I. Nestoras, T. P. Krichbaum, J. A. Zensus, H. Ungerechts, and A. Sievers.** Recent radio activity of the Fermi blazar CTA 102. *The Astronomer's Telegram*, 4449:1, October 2012c.
- I. Myserlis, J. Seiradakis, and M. Dogramatzidis.** Solar observations with a low frequency radio telescope. In I. Papadakis and A. Anastasiadis, editors, *10th Hellenic Astronomical Conference*, pages 5–5, January 2012d.
- I. Myserlis, E. Angelakis, L. Fuhrmann, V. Pavlidou, I. Nestoras, V. Karamanavis, A. Kraus, and J. A. Zensus.** Multi-frequency linear and circular radio polarization monitoring of jet emission elements in *Fermi* blazars. *ArXiv e-prints*, January 2014a.
- I. Myserlis, I. Liodakis, and G. Panopoulou.** Ongoing rotation of the optical polarization angle for the blazar GB6J1037+5711. *The Astronomer's Telegram*, 6261:1, June 2014b.
- G. Panopoulou, K. Tassis, D. Blinov, V. Pavlidou, O. G. King, E. Paleologou, A. Ramaprakash, E. Angelakis, M. Baloković, H. K. Das, R. Feiler, T. Hovatta, P. Khodade, S. Kiehlmann, A. Kus, N. Kylafis, I. Liodakis, A. Mahabal, D. Modi, **I. Myserlis**, I. Papadakis, I. Papamastorakis, B. Pazderska, E. Pazderski, T. J. Pearson, C. Rajarshi, A. C. S. Readhead, P. Reig, and J. A. Zensus. Optical polarization map of the Polaris Flare with RoboPol. *MNRAS*, 452: 715–726, September 2015. doi: 10.1093/mnras/stv1301.
- V. Pavlidou, E. Angelakis, **I. Myserlis**, D. Blinov, O. G. King, I. Papadakis, K. Tassis, T. Hovatta, B. Pazderska, E. Paleologou, M. Baloković, R. Feiler, L. Fuhrmann, P. Khodade, A. Kus, N. Kylafis, D. Modi, G. Panopoulou, I. Papamastorakis, E. Pazderski, T. J. Pearson, C. Rajarshi, A. Ramaprakash, A. C. S. Readhead, P. Reig, and J. A. Zensus. The RoboPol optical polarization survey of gamma-ray-loud blazars. *MNRAS*, 442:1693–1705, August 2014. doi: 10.1093/mnras/stu904.
- J. L. Richards, T. Hovatta, M. L. Lister, A. C. S. Readhead, W. Max-Moerbeck, T. Savolainen, E. Angelakis, L. Fuhrmann, M. F. Aller, H. D. Aller, **I. Myserlis**, and V. Karamanavis. An Exceptional Radio Flare in Markarian 421. In *European Physical Journal Web of Conferences*, volume 61 of *European Physical Journal Web of Conferences*, page 4010, December 2013. doi: 10.1051/epjconf/20136104010.
- D. Xu, S. Komossa, L. Fuhrmann, D. Grupe, E. Angelakis, **I. Myserlis**, V. Karamanavis, and A. Zensus. A multi-wavelength study of the radio-loud Narrow-line Seyfert 1 galaxy RXJ23149+2. In *The X-ray Universe 2014*, page 336, July 2014.

Lebenslauf

PERSÖNLICHE DATEN

Ioannis Myserlis

Geburtsdatum: 13. März 1988
Geburtsort: Thessaloniki, Griechenland
Staatsangehörigkeit: Griechisch

ANSCHRIFT

Max-Planck-Institut für Radioastronomie
Auf dem Hügel 69
53121 Bonn
Deutschland
email: imyserlis@mpifr-bonn.mpg.de

AUSBILDUNG

- 2012–2015 Doktorand an der Universität zu Köln und dem
Max-Planck-Institut für Radioastronomie in Bonn
Stipendium der International Max Planck Research School for
Astronomy and Astrophysics
wiss. Betreuer Prof. Dr. Andreas Eckart
Prof. Dr. J. Anton Zensus und
Dr. Emmanouil Angelakis
Titel: “A framework for the study of physical conditions in astrophysical plas-
mas through radio and optical polarization: Application to extragalactic jets”
- 2005–2011 Diplomstudent an der Aristotle University of Thessaloniki,
Diplom Physik
wiss. Betreuer Prof. Dr. John H. Seiradakis
Titel: “A low frequency radio telescope: First results of solar observations”
- 2002–2005 Allgemeine Hochschulreife am 2. Experimentelle Lyceum von Thessaloniki,
Thessaloniki